PHILIPS TECHNICAL REVIEW

VOLUME 37
1977

Philips Technical Review is published by the Research Laboratories of N.V. Philips' Gloeilampenfabrieken, Eindhoven, The Netherlands, and is devoted to the investigations, processes and products of the laboratories and plants which form part of or cooperate with enterprises of the Philips group of companies. In the articles the associated technical problems are treated along with their physical or chemical background. The Review covers a wide range of subjects, each article being intended not only for the specialist in the subject but also for the non-specialist reader with a general technical or scientific training.

The Review appears in three editions: English, Dutch and German, all identical in contents. There are twelve numbers per volume, each of about 32 pages. A yearly index is given for each volume and an index covering ten volumes appears every five years (the latest one was included in Volume 35, 1975).

Editors:	Drs J. W. Miltenburg, Editor-in-chief
	Dr J. W. Broer
	Ir D. van Dalen
	Dr E. Fischmann
	Drs K. J. Groenewolt
	Ir J. A. Klaassen
	Dr J. Ubbink
English edition:	D. A. E. Roberts, B.Sc., M. Inst. P., A.I.L. (Redhill, Surrey)
German edition:	Dipl.-Phys. R. Dockhorn (Hamburg)

© N.V. Philips' Gloeilampenfabrieken, Eindhoven, The Netherlands, 1978.

Articles may be reproduced in whole or in part provided that the source 'Philips Technical Review' is mentioned in full; photographs and drawings for this purpose are available on request. The editors would appreciate a complimentary copy.

Subject index, Volume 37, 1977

Page

Aluminate phosphors, behaviour of 221
Amplitude and phase contrast, simultaneous, in STEM 1
ASKA, application for TV picture tubes . . . 56
Bioceramic of sintered hydroxylapatite 234
Bismuth-silicon-oxide crystals, pulling large . . 250
Bubbles, microwave generation of 38
Camera for image processing, double-focus, edge-enhancing 180
Computer, speaker recognition by 207
Computer-aided design of LSI circuits 278
Cryogenics: a critical review 91
DAMA, 'Drop-out Annoyance Measuring Apparatus' 36
Data links, fast automatic equalizer for 10
Data transmission, modulation stage for . . . 291
Delta-modulation to PCM converter 313
Drop-outs in magnetic sound recording 29
Electron-beam pattern generator 334
Electron-image projector 347
Electron lithography 334
Electron microscope, scanning, detection method for producing phase and amplitude images simultaneously in 1
Equalizer for data links, fast automatic 10
Ferroelectric memory 51
Ferroxdure 157
Finite-element method and ASKA program, applied in stress calculations for TV picture tubes 56
Gallium-nitride LEDs 237
Gallium phosphide and gallium arsenophosphide, determination of zinc-diffusion profiles in . . 121
Glass fibres, optical, very smooth fracture faces for 89
Graphite, pyrolytic, products of 189
Holographic memory, $LiNbO_3$ for 109
Hydroxylapatite, sintered, as a bioceramic . . 234
Image intensifier, channel-plate, for hard X-rays 124
Image processing, edge-enhancing double-focus camera for 180
Image projector, electron- 347
Image sensor with resistive electrodes 303

Integrated circuits:

- automatic optical inspection of connecting-lead patterns for 77
- LSI (introduction to special issue) 265
- LSI — a revolution in electronics 267
- computer-aided design of LSI circuits 278
- I^2L digital modulation stage for data transmission 291
- image sensor with resistive electrodes 303
- delta-modulation to PCM converter 313
- Silicon Repeater 330
- electron-beam pattern generator 334
- electron-image projector 347

Page

Large-scale integration, see **Integrated circuits**
LEDs based on GaN 237
Liquid crystals for numerical displays 131
Lithium niobate as a material for holographic information storage 109
LSI, see **Integrated circuits**
Luminescence of aluminates 221
Macro- and microthermography, real-time . . . 241
Magnetic domains, microwave generation and manipulation of 38
Magnetic sound recording, annoyance due to modulation noise and drop-outs in 29
Magnetic tape, read-out by magnetoresistance effect 42
Magneto-optic storage wafer MOPS 197
Magnetoresistance effect, read-out of magnetic tape by 42

Memory:

- small analog, based on ferroelectric hysteresis 51
- holographic, with $LiNbO_3$ 109
- magneto-optic storage wafer MOPS 197

Mesogenic compounds 131
Micro- and macrothermography, real-time . . . 241
Modulation noise in magnetic sound recording 29
Modulation stage for data transmission, digital, I^2L 291
Modulation transfer with STEM 1
MOPS, a magneto-optic storage wafer of the discrete-bit type 197
Numerical display by means of liquid crystals . 131
OCR camera, edge-enhancing 180
Optical glass fibres, very smooth fracture faces for 89
Optical inspection of ICs 77
Pattern generator, electron-beam 334
Phase and amplitude contrast, simultaneous, in STEM 1
Phosphors with aluminate host lattices, behaviour of 221
Pyrolytic graphite, products of 189
Reverberation chamber, non-rectangular 176
Silicon Repeater 330
Speaker recognition by computer 207
STEM, simultaneous phase and amplitude contrast in 1
Storage, see **Memory**
Television picture tubes, stress calculations . . 56
Thermography, real-time macro- and micro- . . 241
Transmitting valves, grids for, of pyrolytic graphite 194
'VLP' player, ultra-compact optical scanner for 90
X-rays, image intensifier for hard 124
Zinc-diffusion profiles in GaP and $GaAs_xP_{1-x}$, determination of, with radioactive isotopes . . 121

Author index, Volume 37, 1977

Page

Admiraal, D. J. H., B. L. Cardozo, G. Domburg and J. J. M. Neelen
Annoyance due to modulation noise and drop-outs in magnetic sound recording 29
Baig, W. G.
An edge-enhancing double-focus camera for image processing 180
Beasley, J. P. and D. G. Squire
Electron-beam pattern generator 334
Bosma, H. and W. G. Gelling
LSI — a revolution in electronics 267
Boulou, M., M. Furtado and G. Jacob
Light-emitting diodes based on GaN 237
Bouwer, A. G., G. Bouwhuis, H. F. van Heek and S. Wittekoek
The Silicon Repeater 330
Bouwhuis, G., see Bouwer, A. G.
Brice, J. C., M. J. Hight, O. F. Hill and P. A. C. Whiffin
Pulling large bismuth-silicon-oxide crystals 250
Broek, C. A. M. van den and A. L. Stuijts
Ferroxdure 157
Bunge, E.
Speaker recognition by computer 207
Cardozo, B. L., see Admiraal, D. J. H.
Chalmeton, V.
A channel-plate image intensifier for hard X-rays . . . 124
Christiaens, M., see Jager, F. de
Dekkers, N. H. and H. de Lang
A detection method for producing phase and amplitude images simultaneously in a scanning transmission electron microscope 1
Domburg, G., see Admiraal, D. J. H.
Doorn, R. A. van and N. A. M. Verhoeckx
An I^{2}L digital modulation stage for data transmission 291
Dötsch, H.
The microwave generation and manipulation of magnetic domains 38
Eggermont, L. D. J., M. H. H. Höfelt and R. H. W. Salters
A delta-modulation to PCM converter 313
Elst, J. H. R. M. and D. K. Wielenga
The finite-element method and the ASKA program, applied in stress calculations for television picture tubes 56
Furtado, M., see Boulou, M.
Gelling, W. G., see Bosma, H.
Gestel, W. J. van, F. W. Gorter and K. E. Kuijk
Read-out of a magnetic tape by the magnetoresistance effect 42
Gorter, F. W., see Gestel, W. J. van
Heek, H. F. van, see Bouwer, A. G.
Heitmann, H., B. Hill, J.-P. Krumme and K. Witter
MOPS, a magneto-optic storage wafer of the discrete-bit type 197
Heyns, H., H. L. Peek and J. G. van Santen
Image sensor with resistive electrodes 303
Hight, M. J., see Brice, J. C.
Hill, B., see Heitmann, H.
Hill, O. F., see Brice, J. C.
Hily, C., J. J. Hunzinger, M. Jatteau and J. Ott
Real-time macro- and microthermography 241
Höfelt, M. H. H., see Eggermont, L. D. J.
Hoppe, W. J. J. van, G. D. Khoe, G. Kuyt and H. F. G. Smulders
Very smooth fracture faces for optical glass fibres . . . 89

Page

Hunzinger, J. J., see Hily, C.
Jacob, G., see Boulou, M.
Jager, F. de and M. Christiaens
A fast automatic equalizer for data links 10
Jatteau, M., see Hily, C.
Jeu, W. H. de and J. van der Veen
Liquid crystals for numerical displays 131
Khoe, G. D., see Hoppe, W. J. J. van
Knippenberg, W. F., B. Lersmacher and H. Lydtin
Products of pyrolytic graphite 189
Krumme, J.-P., see Heitmann, H.
Kuijk, K. E., see Gestel, W. J. van
Kurz, H.
Lithium niobate as a material for holographic information storage 109
Kuyt, G., see Hoppe, W. J. J. van
Lang, H. de, see Dekkers, N. H.
Lersmacher, B., see Knippenberg, W. F.
Lydtin, H., see Knippenberg, W. F.
Neelen, J. J. M., see Admiraal, D. J. H.
Niessen, C.
Computer-aided design of LSI circuits 278
Nieuwland, J. M. van, A. Petterson and C. Weber
The design and construction of a non-rectangular reverberation chamber 176
Ott, J., see Hily, C.
Peek, H. L., see Heyns, H.
Peelen, J. G. J., B. V. Rejda and J. P. W. Vermeiden
Sintered hydroxylapatite as a bioceramic 234
Petersen, A., P. Schnabel, H. Schweppe and R. Wernicke
A small analog memory based on ferroelectric hysteresis 51
Petterson, A., see Nieuwland, J. M. van
Rejda, B. V., see Peelen, J. G. J.
Salters, R. H. W., see Eggermont, L. D. J.
Santen, J. G. van, see Heyns, H.
Schnabel, P., see Petersen, A.
Schweppe, H., see Petersen, A.
Scott, J. P.
Electron-image projector 347
Smulders, H. F. G., see Hoppe, W. J. J. van
Sommerdijk, J. L. and A. L. N. Stevels
The behaviour of phosphors with aluminate host lattices 221
Squire, D. G., see Beasley, J. P.
Stevels, A. L. N., see Sommerdijk, J. L.
Stuijts, A. L., see Broek, C. A. M. van den
Thissen, F. L. A. M.
An equipment for automatic optical inspection of connecting-lead patterns for integrated circuits 77
Tijburg, R. P., see Verplanke, J. C.
Veen, J. van der, see Jeu, W. H. de
Verhoeckx, N. A. M., see Doorn, R. A. van
Vermeiden, J. P. W., see Peelen, J. G. J.
Verplanke, J. C. and R. P. Tijburg
Determination of zinc-diffusion profiles in gallium phosphide and gallium arsenophosphide with the aid of radioactive isotopes 121
Volger, J.
Cryogenics: a critical review 91
Weber, C., see Nieuwland, J. M. van
Wernicke, R., see Petersen, A.
Whiffin, P. A. C., see Brice, J. C.
Wielenga, D. K., see Elst, J. H. R. M.
Wittekoek, S., see Bouwer, A. G.
Witter, K., see Heitmann, H.

PHILIPS TECHNICAL REVIEW

VOLUME 37, 1977, No. 1

A detection method for producing phase and amplitude images simultaneously in a scanning transmission electron microscope

N. H. Dekkers and H. de Lang

Even in fields that appear to have been quite exhausted, discoveries are sometimes made that are so simple and fundamental in nature that they are totally unexpected. The article below presents a very simple method in which a pure phase image can be obtained with a scanning transmission electron microscope without recourse to defocusing and spherical aberration. At the same time an equally pure amplitude image is obtained separately. This again is an improvement since the structure of the film carrying the specimen is practically invisible in the image.

Introduction

In addition to the well known conventional electron microscope — the transmission electron microscope (TEM) — which has now been in use for thirty years and more, and the scanning electron microscope (SEM) of somewhat more recent date, a third microscope combining features of both (STEM) has come into use in the last few years. In this type of electron microscope the specimen is scanned in a raster pattern by a focused beam of electrons — in this the STEM is similar to the SEM — but the image is obtained by detection of the electrons which have passed through the specimen [1]. An STEM is not generally built as a separate instrument but is obtained from a TEM by the addition of certain accessories.

The STEM has various advantages over the conventional instrument. The electron-optics configuration can be simpler and the image is available in the form of a video signal. It has also been found that when dark-field illumination is employed, more efficient use can be made of the electrons: more of the scattered electrons are detected. This means that the specimen can be scanned with a less powerful electron beam and therefore sustains less radiation damage. At the same time it is relatively easy to analyse the inelastically scattered electrons in terms of energy, while because there is no further imaging after their passage through the specimen, the inelastically scattered electrons do not introduce chromatic blur into the image. A practical disadvantage of the STEM method is the need to use a very bright electron source, at least if it is desired to work with the highest resolution attainable.

Although it may not be obvious at first sight, it is equally possible to make phase specimens visible with an STEM as it is with a TEM or a phase-contrast (optical) microscope. In this article we shall describe a new detection method that makes it possible to obtain amplitude and phase images simultaneously [2]. As will be explained below, a detector consisting of two semicircular parts is used in the new method. With this method a phase image can be obtained without the need for defocusing or spherical aberration, as required in the TEM with coherent illumination. Before we examine the method in detail, we should like to compare imaging in the TEM with that in the STEM. It has been found possible to derive STEM imaging from TEM imaging by applying the principle of reciprocity, which reveals that phase contrast can in fact be obtained with the STEM.

Dr Ir N. H. Dekkers and Dr H. de Lang are with Philips Research Laboratories, Eindhoven.

[1] A. V. Crewe and J. Wall, Optik 30, 461, 1970.
[2] N. H. Dekkers and H. de Lang, Optik 41, 452, 1974.

Image formation in the TEM and STEM; amplitude and phase objects

The imaging in a conventional electron microscope has much in common with imaging in the optical microscope. In the same way that specimens in optical microscopy affect both the amplitude and the phase of the incident beam — but only the phase in the case of non-absorbent specimens — so also do specimens in the electron microscope. The phase change is determined by the optical path, i.e. the product of the geometrical path and the refractive index.

The refractive index for electron waves is found from the relation [3]:

$$n = 1 - \frac{eV}{E} \cdot \frac{E_0 + E}{2E_0 + E}, \qquad (1)$$

where e is the electronic charge and V the internal potential of the material; E is the electron energy eV_a, where V_a is the accelerating voltage; E_0 is the rest energy m_0c^2, where m_0 is the rest mass of the electron and c represents the velocity of light. The simpler expression

$$n = 1 - eV/2E = 1 - V/2V_a \qquad (2)$$

applies for the non-relativistic case. The phase change due to a layer of matter is given by

$$\int (n - 1)k \, dz, \qquad (3)$$

where k is the wave number:

$$k = \frac{2\pi}{\lambda} = \frac{mv}{\hbar} = \frac{\sqrt{2meV_a}}{\hbar}.$$

The *phase* is only affected if the electrons are only subjected to elastic collisions on the atomic scale, i.e. if they are affected by the field of the atomic nucleus and the electron cloud, but without actually exciting the electron cloud. In the case of excitation the electron undergoes an irreversible loss of energy (inelastic scattering). The elastically scattered and the non-scattered electrons together form the image, a point which will be discussed below.

The *amplitude* is affected if electrons are prevented from participating in the image-forming process described above. This is the case when elastically scattered electrons are not collected in the lens aperture and also when electrons are inelastically scattered; such electrons are now unable to interfere with the non-scattered electrons. Measurement of the energy lost by the inelastically scattered electrons can provide information about the substances present in the specimen. Inelastically scattered electrons can in fact produce an image, though it will not be very sharp for a number of reasons (delocalization [4], chromatic aberration), but the subject will not be discussed further here.

The imaging of phase structures in a conventional electron microscope

Let us consider a conventional electron microscope with coherent illumination. We shall take a weak, thin phase structure as our specimen. Let the amplitude of the incident wave be a. The wave transmitted by the object (coordinates x,y) is spatially phase-modulated and has an amplitude $a \exp i\phi(x,y)$, where the phase excursion ϕ is much less than 1. This wave, the object wave, can be thought of as consisting of the original unperturbed wave a and a (much weaker) scattered wave, caused by the structure, which is expressed by:

$$a_{\mathrm{Sp}} = a \exp i\phi(x,y) = a + ia\phi(x,y). \qquad (4)$$

From this we see that at the location of the specimen the scattered wave has a 90° phase difference from the unperturbed wave. An ideal optical system reproduces the object wave in the image plane (coordinates X,Y), where the amplitude A_{Im} can be written as:

$$A_{\mathrm{Im}} = A + iA\phi(X,Y). \qquad (5)$$

The intensity in the image is given by:

$$I_{\mathrm{Im}} = A_{\mathrm{Im}}A_{\mathrm{Im}}^* = A^2\{1 + \phi^2(X,Y)\}. \qquad (6)$$

Since $\phi \ll 1$, the term $\phi^2(X,Y)$ may be neglected and the result is a uniform intensity distribution; no structure is therefore perceptible in the image. To obtain a perceptible image structure we therefore have to abandon ideal imaging.

In F. Zernike's familiar phase-contrast technique — to return to optical microscopy for a moment — this is achieved by rotating the phase of the unperturbed wave through 90° (and possibly also attenuating it) in relation to the scattered wave; the image amplitude and intensity then become:

$$A_{\mathrm{Im}} = i\{\pm A + A\phi(X,Y)\}, \qquad (7)$$

$$I_{\mathrm{Im}} = A^2\{1 \pm 2\phi(X,Y)\}. \qquad (8)$$

There is now a perceptible image structure which, depending on the direction of the phase shift, is called a positive or a negative phase-contrast image.

---

[3] L. Reimer and H. Gilde, in: P. W. Hawkes (ed.), Image processing and computer-aided design in electron optics, Academic Press, London 1973, p. 138.
[4] H. Rose, Optik 45, 139 and 187, 1976.
[5] P. N. T. Unwin, Proc. Roy. Soc. London A 329, 327, 1972.
[6] See for example C. J. Rakels, J. C. Tiemeijer and K. W. Witteveen, Philips tech. Rev. 29, 370, 1968.
[7] See the article by Reimer and Gilde, note [3].
[8] J. M. Cowley, Appl. Phys. Lett. 15, 58, 1969.
[9] H. von Helmholtz, Crelle's J. 57, 1, 1859.
H. von Helmholtz, Wiss. Abhandl. Leipzig 1, 309, 1882.
[10] H. A. Lorentz, Versl. gew. Verg. Wis- en Natuurk. Afd. Kon. Akad. Wet. Amsterdam 14, 345, 1905, or Proc. Kon. Akad. Wet. Amsterdam 8, 401, 1905.
[11] M. von Laue, Ann. Physik (5) 23, 705, 1935.

It is in fact possible to process the unperturbed wave in this way in electron microscopy, but the operation is a difficult one [5]. The expedient generally adopted is to generate the phase-contrast effect by combining the spherical aberration of the objective lens with an appropriate amount of defocusing. The phase relation between the perturbed and the unperturbed wave can be adjusted in this way, as in Zernike's method. However, this method does not allow a 90° phase shift to be obtained over the entire spatial-frequency spectrum, and the phase-contrast effect remains imperfect. [6]

Another method of making phase structures perceptible in an electron microscope is based on the fact that the aperture angle of the objective has to be made small (of the order of 0.01 radian) to keep the effect of the unavoidable spherical aberration within reasonable bounds. The specimen invariably includes structures whose spatial frequency is so high that the scattered wave is not incident in the lens aperture, which means that imaging of these structures is not affected by interference of the scattered wave with the unperturbed wave: the structures are not 'resolved'. The scattering does however have another effect. Since the electrons scattered outside the lens aperture are lost for imaging purposes, this scattering can be regarded as 'virtual' absorption, so that the areas of the specimen where this scattering is more pronounced have a smaller amplitude in the image and therefore appear darker. We therefore have a situation in which a purely phase effect (we consider only elastic collisions) causes the specimen to become visible as an absorptive structure whose image shows all the properties of that of a genuine — i.e. absorptive — amplitude object.

The structure that produces this contrast is mainly the atomic structure of matter. A distinction can be made here between heavy and light elements. If we consider the properties of elastic scattering as a function of the atomic number [7], we find that the shape assumed by the angular distribution of the scattering hardly depends at all on the atomic number Z; the effective cross-section area, however, is approximately proportional to $Z^{3/2}$. Scattering is consequently much more pronounced for materials containing heavy atoms than for those containing light atoms, which explains why heavy elements are frequently used as (scattering) contrast media in electron microscopy. The contribution to the phase contrast made by a fragment of material depends very little on Z since the internal potential of all materials is of approximately the same order (several volts).

Image formation in an STEM; Helmholtz's reciprocity principle

We shall now discuss how image formation occurs in a scanning transmission electron microscope. It was originally thought that it must differ essentially from image formation in the conventional microscope because a scanning microscope would be free from the imaging peculiarities resulting from the use of coherent illumination. It soon became clear that this was not really true: the two imaging processes are completely analogous [8].

The similarity can be demonstrated by the reciprocity principle, which was first formulated for acoustic waves by H. von Helmholtz [9] and later for electromagnetic waves by H. A. Lorentz [10]. This theorem states that the transmission of radiation is, for very general conditions, invariant when the roles of source and detector are interchanged. It is widely applied in radiocommunication, in a version appropriate to transmitting and receiving antennas. As might be expected, the theorem also applies to electron waves [11]. For electron microscopy we formulate the theorem as follows: if a point source at P produces an intensity I at point Q, the same source located at Q will also produce an intensity I at point P.

In *fig. 1* we see next to one another a conventional transmission microscope (TEM) and a scanning transmission microscope (STEM). In the TEM the radiation from a surface element $d\sigma$, with position r, of the source, situated around point P, is incident on the specimen. In the image plane we choose a point Q conjugate to object point V with position ϱ on the specimen. The

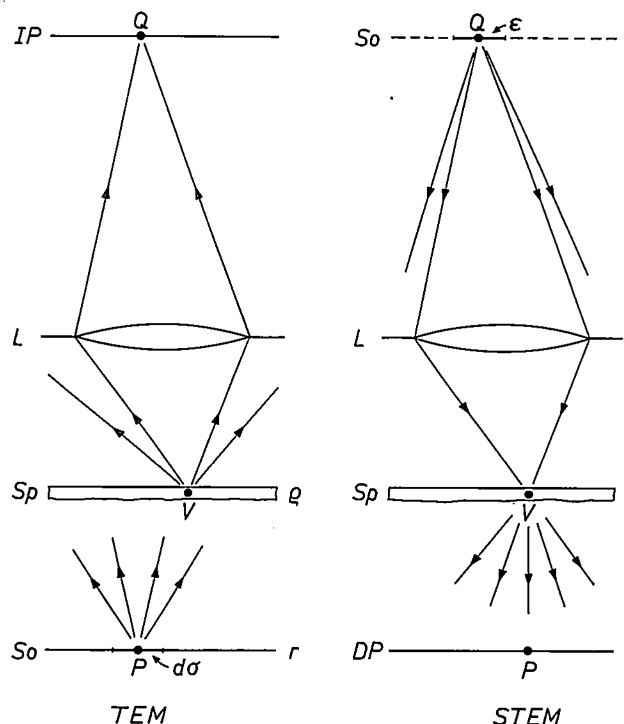

Fig. 1. The imaging principle in a conventional transmission electron microscope (TEM) and a scanning transmission microscope (STEM). One can be thought of as being derived from the other by interchanging the source and the detector (the reciprocity principle of Helmholtz). *So* electron source; r coordinate in the emitting plane. *Sp* specimen: ϱ coordinate in the object plane. *L* lens. *IP* image plane in TEM. *DP* detector plane in STEM. $d\sigma$ surface element around point P in the source plane of the TEM. ε (infinitesimal) surface area of the source in the STEM. Points V and Q are imaged in each other by the lens.

source element delivers an intensity contribution dI at Q, which depends on ϱ and can be written as:

$$dI(\varrho) = RT(\varrho)d\sigma. \quad (9)$$

R in this expression is the radiance of the source, i.e. the radiant flux per unit of surface area per unit of solid angle, and $T(\varrho)$ the transmission coefficient of the complete system, including the specimen.

In the STEM the source at Q has an infinitesimal area ε and a radiance R'. In the plane in which the source is located in the TEM there is now a detector. The intensity I' at point P of the detector plane is therefore

$$I'(\varrho) = R'T'(\varrho)\varepsilon, \quad (10)$$

where $T'(\varrho)$ again represents the transmission coefficient of the complete system, including the specimen. The reciprocity theorem now implies that the transmission coefficients are the same for both cases:

$$T(\varrho) \approx T'(\varrho). \quad (11)$$

From this it follows in particular that the intensity contribution dI' in the image plane of the TEM depends on ϱ in the same way as the intensity at point P of the detector plane. The equivalence of the two instruments for radiation travelling from P to Q in the TEM and from Q to P in the STEM is thus demonstrated.

Strictly speaking, this would only apply to electron microscopes with electrostatic lenses. Reciprocity does not apply for magnetic lenses because the movement of an electron along a path in a magnetic field is not reversible; it will be readily appreciated, however, that the analogy can be restored by reversing the magnetic field. Additionally, the inelastically scattered electrons will have to be ignored, i.e. they must be considered not to be detected.

In practice the source in the TEM will of course have finite dimensions. This means that we have to integrate over the source in (9), obtaining the following expression for the intensity:

$$I(\varrho) = T(\varrho)\int_{So} R d\sigma. \quad (12)$$

The detector in the STEM will also have finite dimensions. If the function G represents the sensitivity distribution of the detector in the STEM, the total detector signal becomes:

$$S(\varrho) = R'\varepsilon T'(\varrho)\int_{Det} G d\sigma. \quad (13)$$

Comparison of (12) and (13) shows that to maintain the equivalence of the TEM and the STEM the sensitivity distribution G over the detector must have the same shape as the radiance distribution R over the source in the TEM.

Principle of detection with a divided detector; simultaneous phase and amplitude contrast

As we have seen, phase contrast can be produced in the TEM by combining an appropriate amount of defocusing [6] with coherent illumination. This means that the source in fig. 1 as seen from the specimen must have a small angular diameter. The corresponding condition for the STEM is that the defocusing should be the same and that the detector should have the same (relative) position and size as the source in the TEM. It is at once obvious that such an STEM configuration is unpractical, for while it is difficult enough to obtain sufficient detected electrons in a reasonable time, only a very small proportion of the beam transmitted through the specimen is used in this case. A long exposure time would be necessary for a reasonable signal-to-noise ratio, with the added disadvantage that the probability of damage to the specimen would be increased by the large radiation dose.

However, it is possible to obtain phase contrast in the STEM by using a *detector of large area.* The use of a large detector has the added advantage that the resolution is increased. The reason for this is that when a detector does not completely fill the aperture of a beam that is not affected by a specimen, the resolution is the same as for a TEM with incoherent illumination, i.e. twice as high as with axial coherent illumination, which has long been known in optical microscopy.

We shall now explain our method with reference to *fig. 2*, which represents an STEM with a weak sinusoidal phase object. The complex amplitude of the scanning spot in the object plane will be called $a(x,y)$. The sinusoidal phase object whose spatial-frequency vector Ω is in the x-direction multiplies this amplitude by the object transmission T_ϕ:

$$T_\phi = \exp[i\phi_0 \cos\{\Omega(x-\xi)\}], \quad (14)$$

where ξ is the translation of the object in the x-direction and ϕ_0 the phase deviation. Since the object is weak:

$$\phi_0 \ll 1, \quad (15)$$

so that we can write for the transmission:

$$T_\phi = 1 + i\phi_0 \cos\{\Omega(x-\xi)\} = \\ = 1 + \tfrac{1}{2}i\phi_0[\exp\{i\Omega(x-\xi)\} + \exp\{-i\Omega(x-\xi)\}]. \quad (16)$$

On leaving the object the wave therefore consists of three components:
the undeflected wave a,
the wave deflected to the left $\frac{1}{2}ia\phi_0 \exp\{i\Omega(x-\xi)\}$,
the wave deflected to the right $\frac{1}{2}ia\phi_0 \exp\{-i\Omega(x-\xi)\}$.
The original beam is thus now accompanied by two deflected beams that can be thought of as having been derived from the original wave by rotation about the

axial point of the object through an angle Ω/k and an extra phase $\frac{1}{2}\pi \pm \Omega\xi$. In the detector plane, situated a (considerable) distance l away, the amplitude $A_\phi(X,Y)$ can be written as:

$$A_\phi(X,Y) = A(X,Y) + \tfrac{1}{2}\mathrm{i}\phi_0 A(X+\Omega l/k, Y)\exp(-\mathrm{i}\Omega\xi) + \\ + \tfrac{1}{2}\mathrm{i}\phi_0 A(X-\Omega l/k, Y)\exp(+\mathrm{i}\Omega\xi). \qquad (17)$$

The form of function A depends on the lens aberrations (e.g. spherical aberration) and the defocusing of the object. In practice $|A(X,Y)|$ will be constant inside and zero outside a circle of radius $\alpha_0 l$. If we assume for the time being that there are no aberrations and that the specimen is in focus, the phase of $A(X,Y)$ can also be regarded as constant. Hence $A(X,Y) = A_0$.

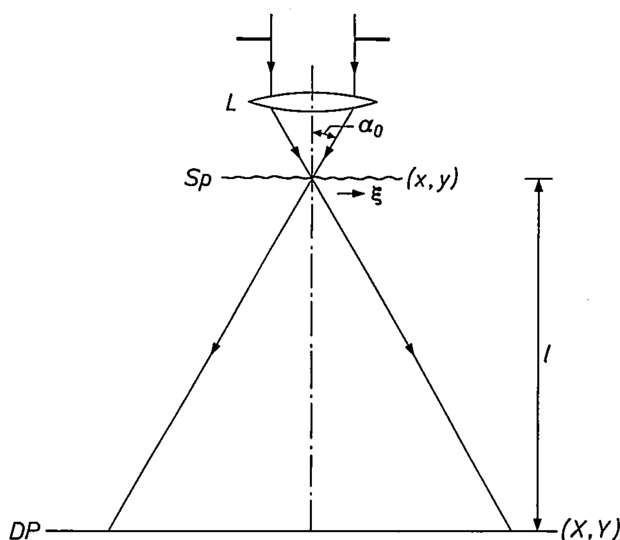

Fig. 2. Schematic presentation of imaging in the STEM, for calculating the behaviour of phase and amplitude objects. L lens that focuses the scanning beam, with angle of aperture α_0. *Sp* specimen plane; x and y coordinates of points on the specimen. ξ displacement of the specimen in the x-direction. *DP* detector plane; X,Y coordinates in *DP*.

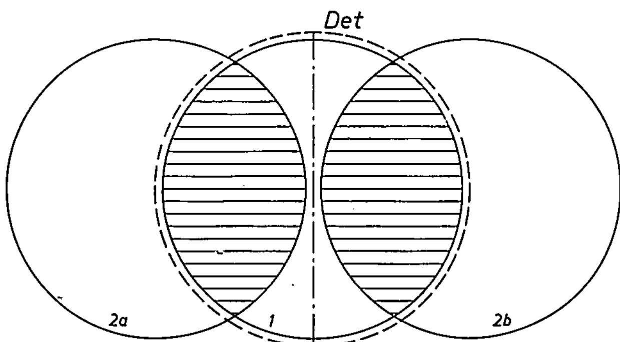

Fig. 3. At the output side of the specimen in the STEM we find not only the original beam *1*, shown here in section in the detector plane, but also two deflected beams *2*. The deflected beams have a rotation and a phase difference in relation to *1*, which depend on ξ (fig. 2). Interference occurs in the hatched areas and gives amplitude modulation when ξ is varied. The modulations of the two regions are in phase with each other in amplitude objects and in phase opposition in phase objects. A pure amplitude image or a pure phase image can therefore be obtained by dividing the detector (*Det*) into two parts along the vertical diameter and adding the signals from the two parts or subtracting them from each other.

Suppose now that the object is scanned by varying the position ξ of the object. The intensity in the detector plane will then be modulated in the hatched areas of *fig. 3* because interference between the undeflected beam and the beam deflected to the left will take place in the left-hand area, while interference between the undeflected beam and the beam deflected to the right will take place in the right-hand area. The phase of the undeflected beam is constant while the phases of the deflected beams decrease or increase with ξ as indicated by equation (17).

The intensity $I_{\phi,1}$ in the area on the left is given by:

$$I_{\phi,1} = A_0^2\{1 + \tfrac{1}{2}\mathrm{i}\phi_0 \exp(-\mathrm{i}\Omega\xi)\}\{1 - \tfrac{1}{2}\mathrm{i}\phi_0 \exp \mathrm{i}\Omega\xi\} = \\ = A_0^2(1 + \phi_0 \sin \Omega\xi), \qquad (18)$$

with the term in ϕ_0^2 neglected, of course.

Similarly for the area on the right:

$$I_{\phi,\mathrm{r}} = A_0^2(1 - \phi_0 \sin \Omega\xi). \qquad (19)$$

We therefore see that the modulations in the two areas of interference are opposite in phase, as should after all be expected since a phase object does not alter the total amount of power transmitted. Equations (18) and (19) also show that the intensity modulations differ by 90° in phase from the position of the object structure in relation to the scanning spot.

We next consider an amplitude object whose transmission T_a can be described by:

$$T_\mathrm{a} = 1 + p_0 \cos\{\Omega(x-\xi)\} = \\ = 1 + \tfrac{1}{2}p_0[\exp\{\mathrm{i}\Omega(x-\xi)\} + \exp\{-\mathrm{i}\Omega(x-\xi)\}]. \qquad (20)$$

Here again the wave leaving the specimen has three components:
the unperturbed wave a,
the wave deflected to the left $\frac{1}{2}ap_0 \exp\{\mathrm{i}\Omega(x-\xi)\}$, and
the wave deflected to the right $\frac{1}{2}ap_0 \exp\{-\mathrm{i}\Omega(x-\xi)\}$.

The amplitude at the detector plane is now

$$A_\mathrm{p}(X,Y) = A(X,Y) + \tfrac{1}{2}p_0 A(X+\Omega l/k, Y)\exp(-\mathrm{i}\Omega\xi) + \\ + \tfrac{1}{2}p_0 A(X-\Omega l/k, Y)\exp(+\mathrm{i}\Omega\xi), \qquad (21)$$

and the intensities in the areas of interference are:

$$I_{\mathrm{p},1} = A_0^2(1 + p_0 \cos \Omega\xi), \\ I_{\mathrm{p},\mathrm{r}} = A_0^2(1 + p_0 \cos \Omega\xi). \qquad (22)$$

We therefore see that with an amplitude object the intensity modulations in the two areas are in phase with each other and also with the position of the object in relation to the scanning spot.

Phase objects and amplitude objects therefore show up in different ways in the detector plane. We took advantage of this to divide the detector into two semicircular areas, as shown in fig. 3. If the signals from the two halves of the detector are added, the resulting

signal only contains amplitude information. If, however, one set of signals is subtracted from the other, then there is only phase information. The sum signal and the difference signal are obviously simultaneously available during the scanning process.

The phase structure appears differentiated in the image (see (18) and (19)) and is thus represented as a model in relief illuminated from the side.

The amplitude structure appears in the ordinary way, i.e. undifferentiated.

With this method of detection the contrast — and hence also the phase contrast — is obtained without any need for the defocusing or spherical aberration required in the TEM. Furthermore, as already noted, the resolution is just as high as in a TEM with incoherent illumination and therefore twice as high as in a TEM with coherent illumination in the radial direction.

An STEM detection method has also been published [12] in which the detector is divided into separate areas, as in our method, but these take the form of two or more annular zones. It will be clear from the explanation just given of the skew-symmetrical properties of modulation by phase structures that a configuration of this kind cannot give phase contrast without spherical aberration and defocusing, which means that a suitable combination of these aberrations has to be devised for this method, which we shall not discuss further here.

The analogy between the TEM and STEM illustrated in fig. 1 seems to indicate that it should be possible to obtain a pure phase image and a pure amplitude image with a TEM without having to use spherical aberration. This would necessitate two exposures with coherent illumination, the first with one half and the second with the other half of the illumination aperture covered. Summation of the exposures would yield the amplitude image and subtraction the phase image. This method is almost unusable in practice because perfect registration of the two exposures is difficult and also because they cannot be made simultaneously; images change shape in the interval between exposures. Another disadvantage is that the contrasts are poor.

Characteristics; experiments

Modulation transfer

We shall now look more closely at the characteristics of the method that has just been introduced.

First we shall discuss the modulation transfer ('contrast transfer') in the case of a focused system free from aberration. Image formation for weak structures can be completely characterized by the modulation transfer for phase and amplitude, since the imaging of such structures is a linear process: the intensity modulation in the image of two superimposed structures is the sum of the individual intensity modulations.

Here we define the modulation transfer for amplitude structures (with the sum signal of the two detectors) as the depth of modulation of the detected signal divided by the modulation depth of the absolute value of the amplitude transmission of a sinusoidal object structure.

For phase objects, which are detected by means of the difference signal from the two halves of the detector, the background signal is zero and the signal is a pure alternating-current signal. In defining modulation transfer, however, it is useful to attribute to the detector signal a background equal to the mean signal current for the total detector surface. This facilitates the treatment of signal-to-noise problems, since the electron

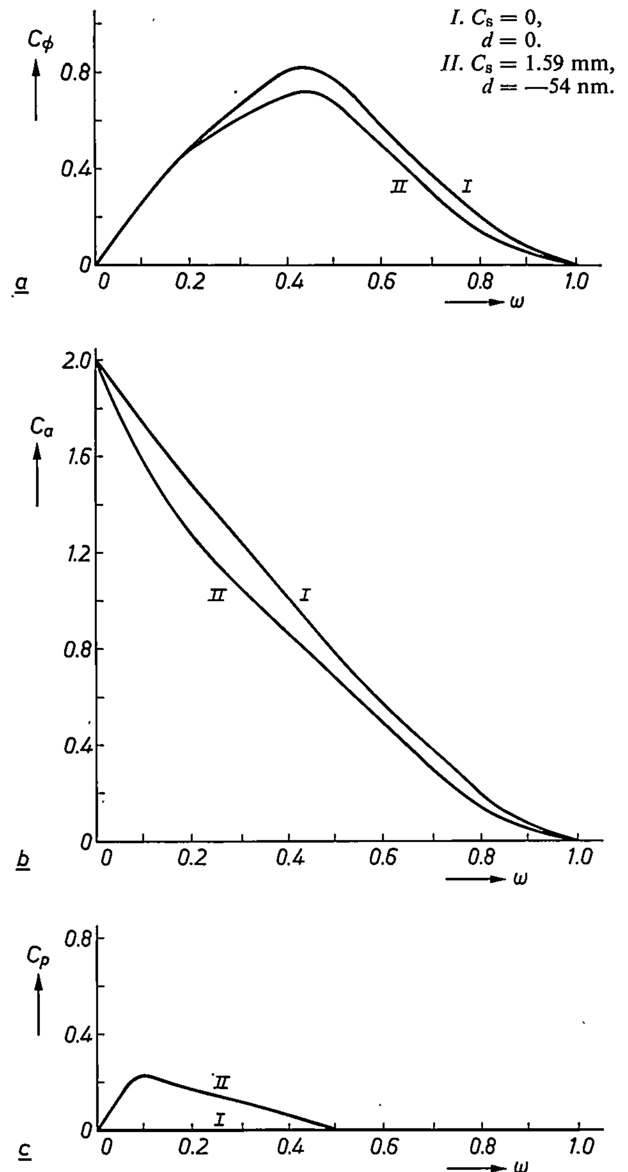

Fig. 4. *a*) Modulation transfer of phase structure (differentiated image) for (curve *I*) a specimen that is exactly in focus and imaged by an ideal lens and (curve *II*) one imaged by a lens with a spherical aberration C_s of 1.59 nm and with the optimum defocusing for that aberration ($d = -54$ mm). The ratio C_ϕ of the difference signal from the detector and the average signal are plotted against the phase deviation ω of the object transmission (assumed sinusoidal). *b*) As before, but for an amplitude structure (undifferentiated image). The modulation transfer C_a is defined here as the depth of modulation of the detected signal divided by that of the absolute value of the transmission of a specimen with a sinusoidal amplitude structure. *c*) In the presence of spherical aberration and defocusing the phase image (difference signal) contains unwanted information in the form of a weak, differentiated amplitude image (curve *II*). In an ideal system the contribution from this source is zero (curve *I*).

noise is proportional to the square root of the total area of the detector. For phase objects, therefore, the contrast transfer is defined as the ratio of the difference signal divided by the mean summation signal to the phase deviation of the sinusoidal object transmission. To calculate the modulation transfer we obviously have to know the ratio of the sum of the interference areas to the total area. For spatial frequencies that are so low that the interference regions overlap, the area of overlap does not count for the imaging of phase structures. This restriction does not apply to the imaging of amplitude structures.

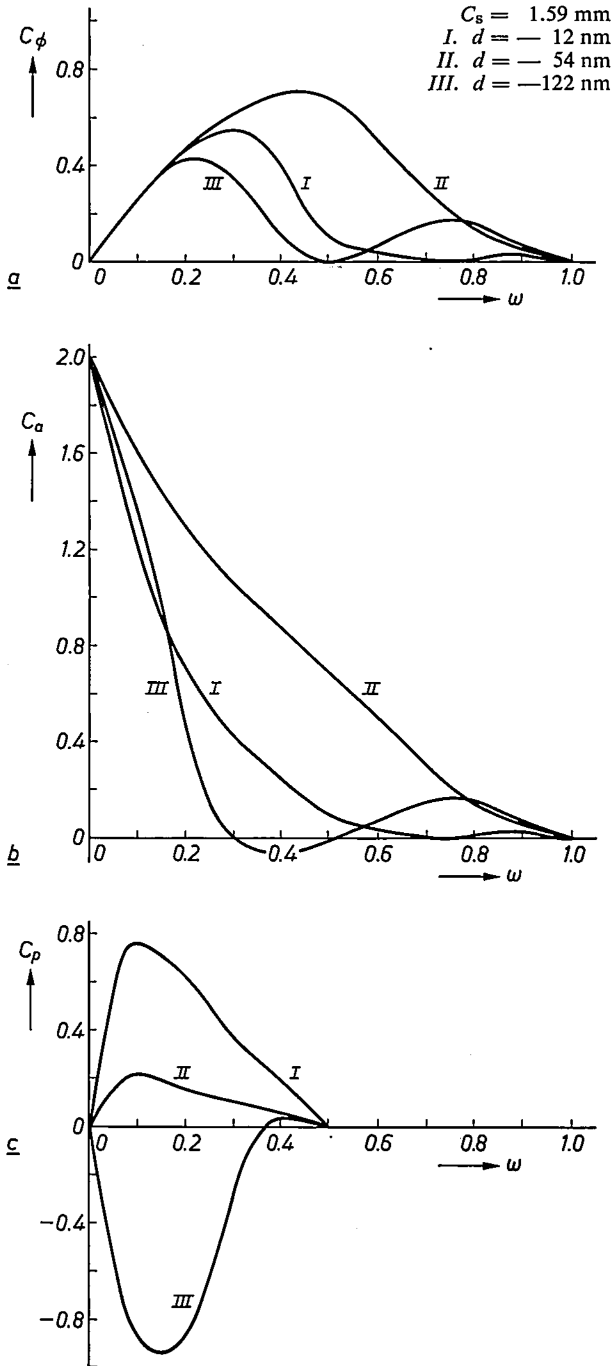

Fig. 5. Modulation transfer, with the same lens used as in fig. 4 (C_s = 1.59 mm), of phase structure (*a*), amplitude structures (*b*) and 'differentiated amplitude structures' (*c*), for three values of the defocusing *d*. *C* has the same sign over a large range of *d* values, which is by no means the case for the formation of phase contrast with a TEM using coherent illumination. The best situation is found for $d = -54$ nm (curves *II*).

The modulation transfer can be calculated in elementary terms and is shown in *fig. 4a* (curve *I*) for phase structures. The spatial-frequency vector is assumed perpendicular to the line separating the detector halves. The modulation transfer for amplitude structures is shown in fig. 4*b* (curve *I*).

If the spatial-frequency vector is rotated from the x-direction to the y-direction, the modulation transfer for phase structures decreases to zero, an effect that also occurs with lateral illumination of a relief. For a complete analogy the transfer would have to be proportional to the cosine of the angle between the spatial-frequency vector and the x-axis. Although this is not quite true in fact, the deviations are not significant.

For amplitude structures the modulation transfer is of course independent of the orientation of the object.

Spherical aberration and defocusing

It was assumed above that the lens was perfect and the object was in focus. In practice, however, both spherical aberration and defocusing are encountered, the first because some spherical aberration has to be admitted to obtain the maximum resolution, and the second because actual specimens are not always thin. We shall now consider the consequences of this for modulation transfer.

Let us call the coefficient of the third-order spherical aberration C_s and the defocusing d — the object lies a distance d inside the lens focus ('under-focusing'). The effect of C_s and d can be expressed by adding a phase factor to $A(X,Y)$, as follows:

$$A(X,Y) = A_0 \exp \mathrm{i}W(X,Y) = = A_0 \exp\left[\mathrm{i}k\left\{\frac{C_s}{4}\left(\frac{R}{l}\right)^4 + \frac{d}{2}\left(\frac{R}{l}\right)^2\right\}\right], \quad (23)$$

where $R^2 = X^2 + Y^2$. The effect of this phase factor is that the phase difference between the undeflected beam and the deflected beams is no longer constant in the interference areas. For the left-hand area the phase difference is

$$\Delta_l W(X,Y) = W(X + \Omega l/k, Y) - W(X,Y), \quad (24)$$

and for the right-hand area it is

$$\Delta_r W(X,Y) = \Delta_l W(-X,Y). \quad (25)$$

Introduction of this phase difference has the result that in expressions (18), (19) and (22), the modulation terms

[12] H. Rose, Optik 39, 416, 1974.
H. Rose, Optik 42, 217, 1975, particularly pp. 239 and 240.

acquire an extra phase $-\Delta_l W(X,Y)$ for the left-hand area and $+\Delta_r W(X,Y)$ for the right-hand area. Since this extra phase varies with position in the detector plane, the intensity modulation integrated over the interference area will be located closer to zero than in the case of aberration-free focusing, so that the modulation-transfer values will also be nearer zero. The calculation has to be performed numerically. We shall merely mention a few results here.

As a representative example let us consider a lens for which $C_s = 1.59$ mm. The best transfer is obtained for both phase and amplitude objects if the aperture angle α_0 is 9.0×10^{-3} rad and the defocusing d is -54 nm. The modulation-transfer functions for this case are shown in figs. 4*a* and *b* (curves *II*).

In addition to reducing the modulation transfer, spherical aberration and defocusing have another effect, for differentiated amplitude information is also found to occur in the difference signal. Fig. 4*c* shows the transfer function for this unwanted contrast for the same values of C_s, α_0 and d.

In all previous calculations it has been tacitly assumed that the sensitivity of the detector is constant over its entire surface area. If this is not the case, the modulation-transfer functions are affected in a manner that cannot be controlled. Some correction, but usually not enough, can be obtained by selecting an appropriate ratio for the two detector signals. Fortunately, semiconductor detectors with a sensitivity constant to a few per cent are now available.

Another important factor in connection with depth discrimination is the way in which the contrast formation depends on the defocusing. *Fig. 5* shows for the same values of C_s and α_0 the transfer of the three types of contrast for three values of defocusing, the optimum value and values on either side. It can be seen that the entire transfer function has the same sign over a wide range of defocusing. This is quite different from the behaviour of the transfer function in a TEM with coherent illumination, where the transfer function oscillates [6]. Closer examination also reveals that the depth discrimination is better because the transfer function decreases to zero with increased defocusing, although it oscillates in the process.

Some experiments

Experimental research into the new method of observation outlined in this article was conducted initially with a Philips EM 301 electron microscope and later with a Philips EM 400 electron microscope with an STEM unit. The thermal electron source of the microscope was replaced by a field-emission source [13], and the detection system described above, comprising two silicon detectors, was incorporated. These detectors were inserted in the input circuit of low-noise preamplifiers with a gain-bandwidth product of 18 GHz and capable of operating in the normal TV-frequency band [14]. The signals could be subtracted or added as desired, and the monitor image photographed. To avoid mains interference the line frequency was synchronized with the mains frequency. The monitor picture (1000 lines), which was obtained in 20 seconds, was photographed with a Polaroid camera. (The images derived from the sum or difference signals could of course also be obtained simultaneously.)

Fig. 6. Photographs of gold islands on a collodion film. The lower photograph was taken with the sum signal and the upper one with the difference signal, which means that they show an amplitude image and a differentiated phase image respectively. The direction of differentiation is from left to right. Since the collodion film behaves as a weak phase object, it remains practically invisible in the amplitude image, thus greatly enhancing the observability of the islands.

[13] These modifications were made at the Philips Scientific and Industrial Equipment (S & I) Division by Dr Ir K. D. van der Mast and others, who also helped to make the photographs shown (figs. 6 and 7).

[14] These amplifiers were developed at Philips Research Laboratories by Ir H. W. G. Haenen as preamplifiers in television cameras using 'Plumbicon' tubes.

[15] F. Nagata, T. Matsuda and T. Komoda, Jap. J. appl. Phys. **14**, 1815, 1975.

[16] See for example M. Françon, Optica Acta **1**, 50, 1954.

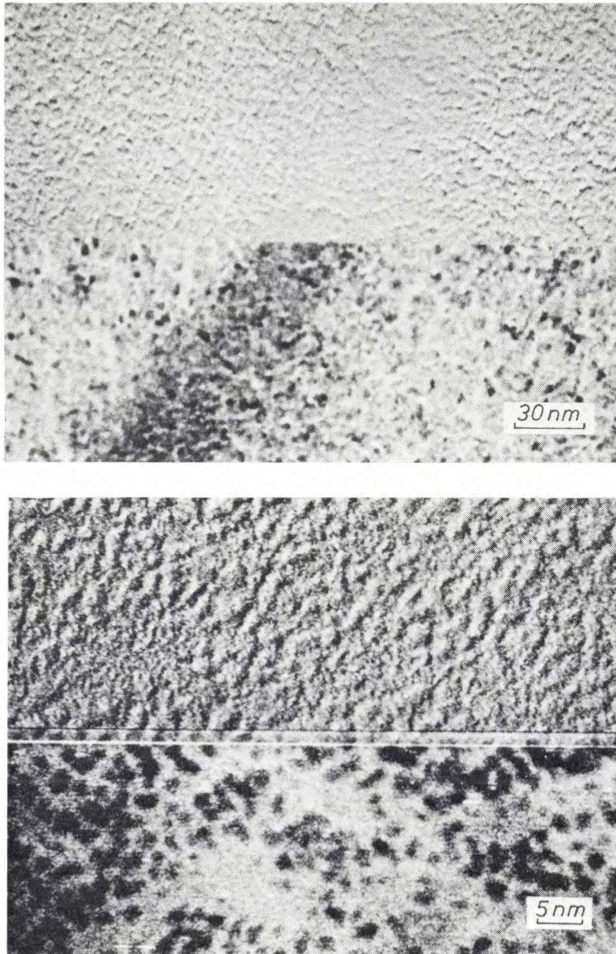

Fig. 7. As fig. 6, but now with tiny platinum spheres on a collodion film. The spheres are difficult to distinguish in the phase image (the two top illustrations) but clearly distinguishable in the amplitude image.

Fig. 6 shows photographs obtained by the above method of a specimen consisting of tiny islands of gold on a collodion film. The lower photograph was taken with the sum signal and shows the amplitude structure; the upper one was made with the difference signal and therefore represents the phase structure in differentiated form: the direction of differentiation is from left to right. In the lower photograph the islands are clearly visible as dark patches because the heavy gold atoms with their pronounced scattering result in amplitude contrast. The collodion film, on the other hand, consists chiefly of light atoms and therefore causes much less scattering and behaves like a weak phase object. As explained above in connection with sum detection, this type of structure is not imaged; this can also be seen from the photograph. In the upper photograph the amplitude contrast has been suppressed and the phase structure of the carrier and that of the gold are visible simultaneously.

Fig. 7 consists of similar photographs of small platinum spheres on a collodion film. These spheres form a weaker phase object than the islands in fig. 6 and are consequently almost imperceptible in the phase image. In the amplitude image the carrier is again almost imperceptible, enhancing the perceptibility of the specimen.

These results show that sum detection has to be used if heavy metals are used as stains. It is also important here for the structure of the carrier film and the unstained parts of the specimen not to be visible. (A similar situation arises in the TEM with incoherent illumination [15].)

If, however, it is desired to study unstained specimens only containing light elements, such as biological tissue, it is better to use the difference signal. The differentiation of the contrast image is in no way a disadvantage. Similar imaging methods are very widely used in optical microscopy [16].

The photographs in figs. 6 and 7 also show that instabilities in the emission of the electrons are not revealed in the difference images. The horizontal line in the amplitude pictures shows that such instabilities were present.

Imaging of individual atoms

It is interesting to consider whether individual atoms can be perceived with the method described. The imaging of heavy atoms ($Z \approx 80$) should indeed be readily possible in amplitude contrast. Calculation shows that heavy atoms behave like 'strong' phase-contrast objects so that to a large extent they have the character of amplitude objects [3] and can give a contrast of about 5%. Since a carrier consisting of light atoms (a phase object) is not visible with our method of perception, this should permit the observation of heavy atoms.

With difference detection the phase contrast of such atoms is reasonably high, but it disappears in the image of the noise structure of the carrier film. This method of detection is therefore unsuitable.

For the imaging of smaller atoms ($Z \approx 40$) sum detection is again inadequate because the amplitude contrast with these atoms is very small ($\propto Z^{3/2}$). In such cases dark-field methods have to be used.

Summary. Although it was not formerly thought possible, it has been found that an image of a phase object can be obtained with a scanning transmission (electron) microscope (STEM). A method has been devised in which either a phase image or an amplitude image — or, if desired, both simultaneously — can be obtained at will. The method employs a large circular solid-state detector divided into two halves. When the signals from both halves are added an infinitely thin object yields an amplitude image, while subtraction produces a differentiated phase image. Since a collodion film behaves like a weak phase object, it is practically invisible, which greatly enhances the visibility of amplitude objects situated on it. Instabilities in the emissions from the electron source are practically imperceptible in the phase image. The introductory section shows by reference to the reciprocity principle that the STEM can be regarded as a reciprocal transmission microscope (TEM), from which it follows that phase contrast is possible.

Philips tech. Rev. 37, 10-24, 1977, No. 1

A fast automatic equalizer for data links

F. de Jager and M. Christiaens

The increasing use of computers has led to a rapidly growing need for links for data transmission. This is particularly necessary when the facilities of a centrally located computer are required at several different locations. The obvious communication link here is the existing telephone system. However, this is not directly suitable for the transmission of data signals, especially at high bit rates. One of the measures then necessary is equalization, in which the circuits in use should adapt themselves, preferably automatically, to the characteristics of the transmission path. In this article the authors describe the principles of a circuit that offers significant advantages over the ones conventionally applied.

Introduction

When telephone circuits are used for the transmission of data signals, the difficulty arises that they do not completely meet the necessary requirements for a data-transmission system. Telephone circuits are designed for the transmission of speech, and the bandwidth of a telephone channel is therefore limited to the range of frequencies that will give adequate intelligibility: 300 to 3400 Hz. The spectrum of a data signal, however, usually contains a d.c. component, and a.c. components below 300 Hz and above 3400 Hz. The d.c. and low-frequency components are particularly important and must not be suppressed.

The transmission characteristics required for data transmission are also different from those required for telephony. The *amplitude characteristic* of a telephone circuit should ideally be flat, but appreciable deviation is permissible. The *group-delay characteristic* is subject to hardly any limitations at all; because filters are used this is always strongly curved, particularly at the edges of the transmitted band; see *fig. 1*. In speech transmission this is unimportant, since the ear reacts mainly to the *spectral distribution* of the acoustic energy. In data transmission, however, the *shape* of the received signals is of primary importance, and since sloping or curved amplitude and group-delay characteristics change the shape of a signal, it is important that these two characteristics should be as flat as possible for a data link.

Ir F. de Jager is with Philips Research Laboratories, Eindhoven; Ir M. Christiaens is with MBLE, Brussels.

As well as the non-ideal shape of the characteristics, there is another factor that increases the distortion of the signals. This is the use of *carrier systems* on trunk telephone circuits. In these systems there is usually a small frequency difference between the carrier signal modulated at the transmitting end and the carrier signal used for demodulation at the receiving end. This results in a small frequency shift (0-10 Hz) for all components in the spectrum of the signal. Again, this does not degrade speech quality. Data signals, however, undergo unacceptable distortion because this shift upsets the harmonic relation between the components.

Transmission of the data signals is possible if a d.c. component and the required a.c. components are allowed to modulate a special carrier at the transmitter.

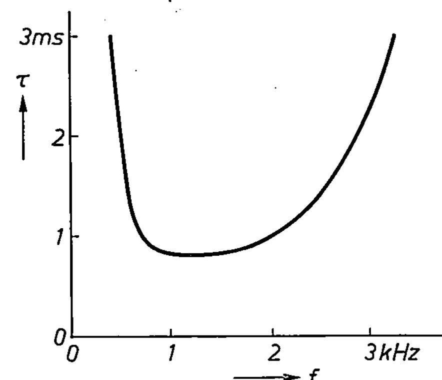

Fig. 1. Typical group-delay characteristic for a telephone channel. τ group delay, f frequency.

The frequency of this carrier is chosen in such a way that the components of the data signal fall in the frequency band available for telephony. The original signal is recovered at the receiver by demodulation. A piece of data-transmission equipment for the transmission and reception of signals is called a 'modem', because it contains both a *mo*dulator and a *dem*odulator.

The 'data carrier', together with the signal, must be sent from the transmitter to the receiver, or must be recovered from the signal at the receiver. Now if a frequency shift of the spectrum arises in the transmission path, this same shift also applies for the data carrier. After demodulation with this carrier the components of the signal reappear at the correct frequencies.

However, the undesired effects of sloping or curved amplitude and group-delay characteristics still remain. The correction of the distortion thus introduced is known as 'equalization'. Before looking at this in more detail we shall give a general picture of the requirements that a transmission circuit of limited bandwidth must meet for data transmission.

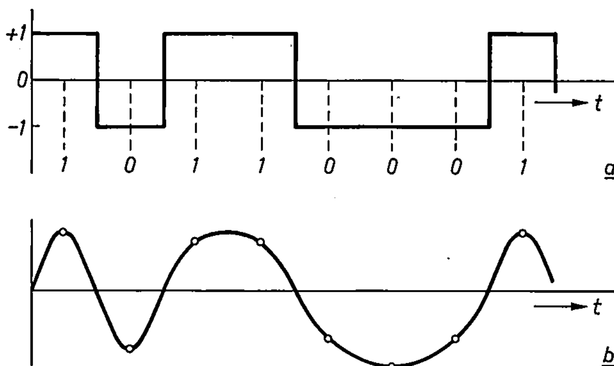

Fig. 2. *a*) Rectangular waveform used in the transmission of data signals. At certain times established by a clock signal the bit value ('1' or '0') is determined by the polarity. *b*) Waveform that can be obtained after passing the signal through a lowpass filter. The small circles indicate the sampling times.

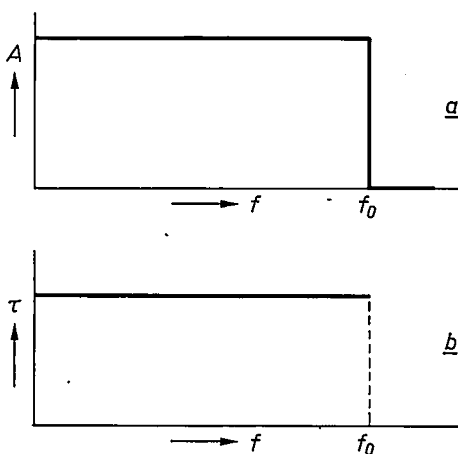

Fig. 3. Amplitude characteristic (*a*) and group-delay characteristic (*b*) that are both flat up to a cut-off frequency f_0.

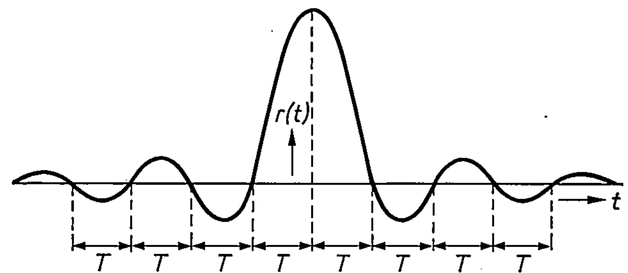

Fig. 4. Response $r(t)$ for a short pulse received via a transmission path with characteristics like those of fig. 3. Oscillatory 'tails' are produced, with zeros at times occurring at integer multiples of T before and after the maximum; $T = 1/(2f_0)$.

Transmission of binary signals in a limited bandwidth

The bits that form the information to be transmitted are usually indicated as 1 and 0. They are transmitted by means of pulses, which can be used in various ways to indicate the bit values [1]. Pulses of opposite polarities are mostly used, e.g. with a positive pulse for the bit value 1 and a negative pulse for the bit value 0. If the duration of each pulse is equal to the bit period, then the signal has a rectangular waveform (*fig. 2a*). Since the transmission path has a limited bandwidth, a lowpass filter is generally included at the transmitter, so that the transmitted waveform becomes rather like that of fig. 2*b* [2]. This signal is sampled at the receiver at fixed times established by a clock signal, so that the polarity, and hence the bit value, is determined. It must therefore be possible to recover the polarity of the received signal reliably at the sampling times. This condition can be satisfied, even with limited bandwidth, provided the characteristics meet certain requirements, which we shall now examine more closely.

We consider first the simple case in which a very short pulse is transmitted. The spectrum of such a pulse occupies a wide band of frequencies and in transmission over a circuit of limited bandwidth the signal is distorted, even if the amplitude and group-delay characteristics are flat in the transmitted part of the band. If the characteristics are flat up to the cut-off frequency f_0 (*fig. 3*), the original short pulse is received as a signal which is given as a function of time by [3]

$$r(t) = \sin(2\pi f_0 t)/(2\pi f_0 t). \qquad (1)$$

This response is shown in *fig. 4*. It can be seen that there are 'tails' before and after the pulse. The zeros of

[1] See for example W. R. Bennett and J. R. Davey, Data transmission, McGraw-Hill, New York 1965.

[2] The transmission path is taken to include not only the cables and any microwave links between transmitter and receiver, but also all the other circuits that the signal passes through in transmitter and receiver, such as filters, modulators and demodulators, and hence the lowpass filter in the transmitter referred to in fig. 2*b*.

[3] See R. W. Lucky, J. Salz and E. J. Weldon Jr, Principles of data communication, McGraw-Hill, New York 1968.

the signal occur at times that fall an integer multiple of T before and after the maximum, where $T = 1/(2f_0)$.

If a *train* of short pulses is transmitted, then there is overlapping of the received signals, so that the height of the maximum of the response can be affected by the previous and succeeding pulses. The sampling of this signal can give rise to incorrect bits. If, however, the pulse rate is $2f_0$, and the pulse period therefore T, then the maximum of each pulse response coincides with the zeros of the other pulse responses at the receiver. The maxima of the received pulses do not then affect one another and on sampling at the correct times the bits have the correct value.

If the characteristics are not flat, the response differs from the shape shown in fig. 4. It could perhaps have the shape shown in *fig. 5*. The zeros do not appear at equal intervals, and it is therefore not possible to choose the frequency of a series of transmitted pulses in such a way that the maxima are not affected [4]. The probability of receiving incorrect bits is of course further increased by interfering signals, such as noise. Imperfections in the characteristics of a transmission path therefore increase the sensitivity to interference.

A flat group-delay characteristic can be produced in practice, but a flat amplitude characteristic that stops at a particular frequency cannot. H. Nyquist [5] showed however that satisfactory performance can be obtained with an amplitude characteristic that has skew symmetry about the half-value points at the boundary of the passband at the nominal cut-off frequency f_0 (see *fig. 6*). While this 'Nyquist' shape does not give a short-pulse response corresponding to the relation (1), the zeros do appear at equal time intervals of $1/(2f_0)$. A flat group-delay characteristic is again necessary in this case.

In the above discussion it has been assumed that the transmitted signal consisted of short pulses. The spectrum of such a pulse is flat, and this is one of the reasons why the zero crossings in the response of each pulse appear at equal intervals in time. Frequently, however, pulses are used whose duration is not small compared with the pulse-repetition period. The signal spectrum is then not flat and if a transmission path with a characteristic like that of fig. 6 is used, the desired regular spacing of the zero crossings is not achieved. Zero crossings at equal time intervals can however be produced if the signal is passed through a filter that compensates the deviation between the actual and the desired spectrum.

The spectrum of a rectangular pulse of duration T_0 is given by the shape of the function

$$\sin(\pi f T_0)/(\pi f T_0).$$

If the pulse duration is equal to the pulse period

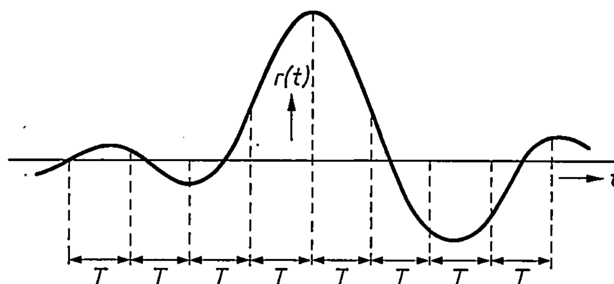

Fig. 5. Example of the response $r(t)$ of a short pulse received via a transmission path whose amplitude and group-delay characteristics are not flat. The zeros are not now equally spaced in time.

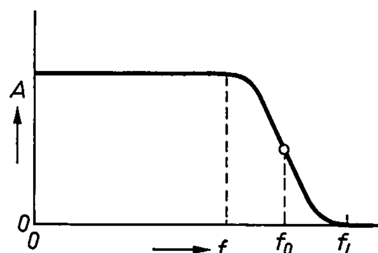

Fig. 6. Amplitude characteristic that is skew symmetrical about the nominal cut-off frequency ('Nyquist cut-off'). A amplitude, f frequency, f_0 nominal cut-off frequency, f_l limiting frequency.

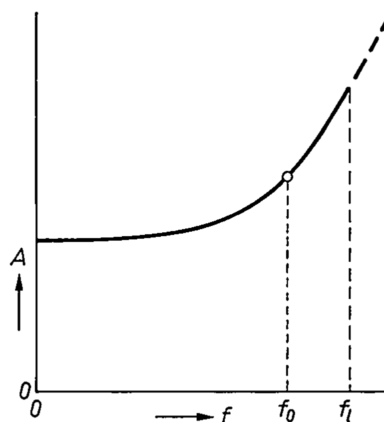

Fig. 7. Amplitude characteristic of a filter that will give a flat spectrum from a rectangular pulse of length T (fig. 4).

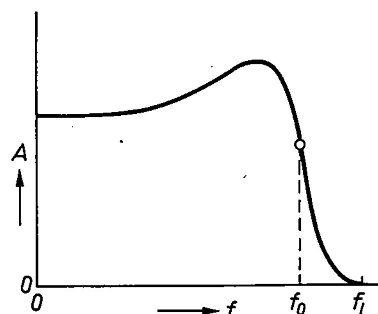

Fig. 8. Amplitude characteristic of a transmission path on which a rectangular voltage waveform can be transmitted without the received pulses affecting one another at the sampling times. The sampling rate must be equal to twice the nominal cut-off frequency f_0.

(fig. 2*a*), then $T_0 = T = 1/(2f_0)$. The spectrum is therefore given by the function

$$\sin(\pi f/2f_0)/(\pi f/2f_0).$$

To produce a flat spectrum the signal must pass through a filter whose amplitude characteristic is the reciprocal of this function; see *fig. 7*. Only the part of this characteristic below the limiting frequency f_g is of importance, of course.

If a signal like that of fig. 2*a* is used with the filter characteristic of fig. 7 and a transmission path with the characteristic of fig. 6, then even though the response of each pulse has tails the received pulses do not affect one another at the sampling times. It is however necessary for the bit frequency to be correctly matched to the bandwidth; our starting point in the foregoing was that the nominal bandwidth f_0 was equal to half the bit rate. The specified bandwidth of a telephone channel thus sets a limit to the bit rate.

A filter with the characteristic of fig. 7 does not have to be added to the transmission path as a separate element. The filter can also be considered as a part of this path, for which the total transmission characteristic must then have the form given by multiplying the ordinates of fig. 6 and fig. 7. A transmission characteristic of the form thus obtained is shown in *fig. 8*.

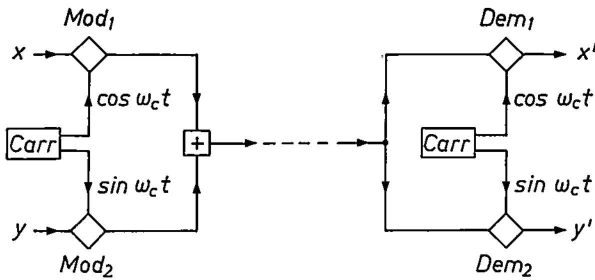

Fig. 9. Circuit for a transmission system with orthogonal modulation. Mod_1 and Mod_2 modulators in which the input signals x and y modulate two carriers at the same frequency but differing in phase by 90°. *Carr* carrier-signal generators. Dem_1 and Dem_2 demodulators.

Modulation methods

In many data-transmission systems a bit rate of 2400 bits/s is used. This requires a nominal bandwidth of 1200 Hz. Such a signal could be put on to a telephone channel by amplitude modulation of a carrier at say 1800 Hz. Since there would then be two sidebands, a frequency band from 600 to 3000 Hz would be necessary. Because of the curvature of the amplitude and group-delay characteristics, however, the signals would then be distorted to such an extent that in many cases reliable data transmission could not be guaranteed.

A better utilization of the available frequency band can be obtained with a modulation method in which two independent streams of information are carried on a single transmission channel. The principle used, known as 'orthogonal modulation', is shown in *fig. 9*. It offers the possibility of transmitting more than one bit per sampling, so that the sampling rate, and hence the bandwidth, can be reduced. Two balanced modulators are used, supplied by carriers at the same frequency, but 90° out of phase. These carriers are modulated independently by two signals, denoted by x and y. If now the demodulation at the receiver makes use of two carrier signals, each in phase with one of the transmitter carriers, then the demodulators yield the transmitted signals x' and y' independently of each other. If for example two bits are to be transmitted per sampling, the signal to be transmitted is applied to a coding circuit (*fig. 10*), which sets the values of x and y to +1 or —1 for each two bits. Since four combinations are possible the four bit combinations 0-0, 0-1, 1-0 and 1-1 can be coded in this way. At each change of sign for x or y a phase change is produced in the balanced modulator for the corresponding carrier sig-

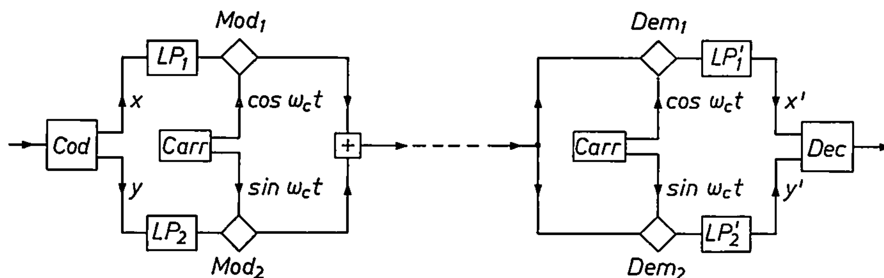

Fig. 10. Circuit for transmission of data signals in a system for orthogonal modulation. *Cod* coder that gives particular values of the signals x and y for 2, 3 or 4 bits. *LP* lowpass filters. *Dec* decoder for recovering the bits from the magnitude of x' and y'.

[4] See H. C. van den Elzen, On the theory and the calculation of worst-case eye openings in data-transmission systems, Philips Res. Repts. **30**, 385-435, 1975.

[5] H. Nyquist, Certain topics in telegraph transmission theory, A.I.E.E. Trans. **47**, 617-644, 1928. The frequency $f_0 = 1/(2T)$ is called the Nyquist rate or the Nyquist frequency.

nals. Since the signals x and y are passed through lowpass filters, these phase changes take place gradually; but at the sampling times they amount in effect to a change in polarity. The total transmitted signal now has a constant amplitude at the sampling times and can appear in four different phases differing by 90° (*fig. 11*). This modulation method is consequently also known as four-phase shift keying, or 4 PSK.

If the phase angles in the received signal are to be detected with certainty, the received components x' and y' should have the values +1 or —1 as accurately as possible at the sampling times. This means that the channels $x - x'$ and $y - y'$ should both satisfy the Nyquist criterion, which can be achieved with an appropriate choice for the transmission characteristics of the lowpass filters in transmitter and receiver. At a bit rate of 2400 bits/s a sampling rate of 1200 Hz is necessary. The nominal bandwidth of the filters is thus 600 Hz. Since two sidebands are produced again in the modulation, a bandwidth of 1200 Hz is necessary for the transmission path. A data signal such as this can be sent over a standard telephone channel without the curvature in the characteristics giving rise to error bits on reception.

Nowadays, however, there is an increasing demand for transmission channels for higher bit rates, since with the aid of a multiplier system it is then possible for the same link circuit to serve a number of users. A higher bit rate may also be necessary when the data received from a data link is to be presented on a visual display. Various systems therefore operate at a bit rate of 4800 bits/s. Orthogonal modulation is again used here, but now with three bits transmitted at each sampling. The coding circuit is then arranged so that the signal is transmitted with a constant amplitude but in eight different phases, differing by 45°. A picture of the end-points of the appropriate vectors, known as the 'signal constellation', is shown in *fig. 12*. Each of these points corresponds to one of the eight possible combinations of three bits.

The need for an even higher bit rate has led to the development of systems for a rate of 9600 bits/s. In this case a combination of phase and amplitude modulation is used. Both output terminals of the coding circuit now deliver a quaternary signal, i.e. one that can have four values. In this case the values are +3, +1, —1 and —3 (*fig. 13*). The signal constellation for the transmitted signal is shown in *fig. 14*. The 16 different combinations of four bits can be coded in this way.

The signal constellation represented in fig. 14 illustrates only one of the many possible ways of coding the bits. With a circuit like that of fig. 10 it is also possible to modulate the two carriers in such a way that a different arrangement of these points is obtained. An

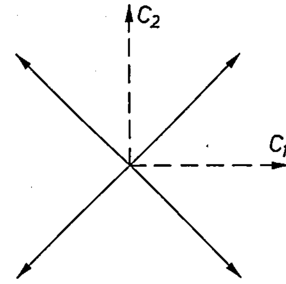

Fig. 11. Vector diagram of a signal with orthogonal modulation, obtained with a circuit like that of fig. 10. C_1 and C_2 are the two carriers. With this system two bits can be transmitted at each sampling.

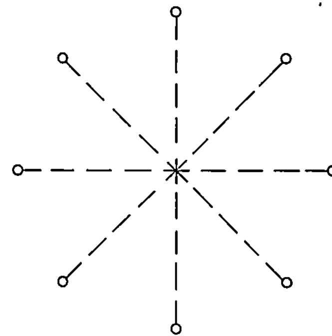

Fig. 12. Signal constellation that can transmit three bits per sampling. The signal can occur in eight different phase states at the sampling times.

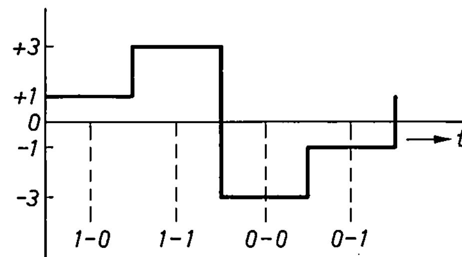

Fig. 13. Quaternary signal with the four discrete values +3, +1, —1 and —3.

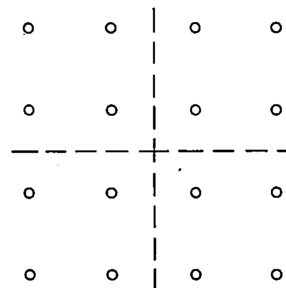

Fig. 14. Signal constellation that can transmit four bits per sampling. This signal is produced by quaternary amplitude modulation of the two carriers in the circuit of fig. 10.

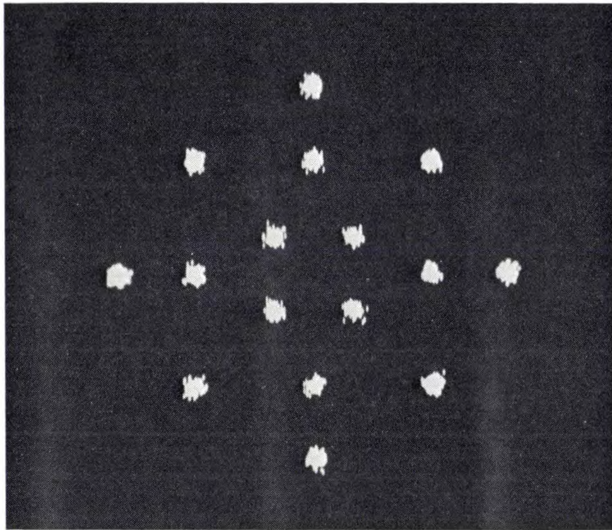

Fig. 15. Signal constellation recommended by CCITT (V 29) for transmission at 9600 bits/s. With this arrangement of the points the signals are less affected by phase fluctuations than in the arrangement of fig. 14.

example, which is laid down in an international recommendation [6], is given in *fig. 15*. This picture was obtained by making the signals x' and y' visible as analog signals on an oscilloscope at the sampling times. It has been found that a transmission system with such an arrangement of these points is less susceptible to phase fluctuations that appear as small angular displacements of the diagram of fig. 15 and are due to noise in the oscillators of (mainly older) carrier systems.

In the transmission system just discussed the sampling rate is 2400 Hz, so that a nominal bandwidth of 1200 Hz is necessary. The carrier frequency used in this system is 1700 Hz, which means that the nominal frequency band of the transmission circuit must extend from 500 to 2900 Hz. As stated earlier, data signals of such a bandwidth cannot be reliably transmitted over an ordinary unmodified telephone channel. Circuits are required that will compensate for the departure of the amplitude and group-delay characteristics from the ideal flat curve. We shall now discuss the principles and design of several such circuits.

Circuits for equalization

A circuit that will provide equalization (an equalizer) corrects the amplitude and group-delay characteristics in such a way that they meet a particular criterion. For data transmission over a channel of narrow bandwidth a correction is required such that the complete circuit satisfies the condition derived by Nyquist for the prevention of interaction between the received pulses at the sampling times (the Nyquist criterion).

If a transmission path is used whose characteristics are fixed, an equalizer can be built up from a number of fixed circuit elements. In many cases, however, the characteristics of the transmission path are not known before a connection is made. This is the case when the existing telephone system is used. The connection between two subscribers can then be made along various paths, and a different equalizer setting is generally required for each path. Since manual adjustment is difficult and time-consuming, equalizers have been developed that adjust themselves automatically after a connection has been made. As a rule a test signal is transmitted before the actual information signal; the equalizer then adjusts itself automatically and the setting remains unchanged during the transmission of the information. In this case we have a *preset equalizer*.

For such an equalizer to be of use in practice, the characteristics of the transmission path should not of course change during the transmission of the information. Often, however, there are changes. In a carrier system, for example, phase changes in the carrier signal may occur that change the transmission characteristics to an impermissible degree. In these cases there is a need for an automatic equalizer whose setting is continually adjusted during the transmission of the information. Such a device is called an *adaptive equalizer*.

Equalizers operating in the time domain

In most of the automatic equalizer circuits that have so far been used the test signal consists of a series of positive and negative pulses of equal amplitude. If the transmission path was ideal, the sampled values in the response would all be of equal amplitude and could only differ in sign. If the characteristics deviate from the correct form the maximum of each pulse can be affected by tails from the preceding and the following pulses. This can cause variations between the sampled values. The basic principle used in many equalizer circuits is that the received series of test pulses is compared with a series of pulses originating in the receiver and corresponding to the transmitted pulses [7]. A difference signal is produced from the received and the comparison pulses, and this signal, the 'error signal', is applied to a control circuit. This circuit determines for every received pulse the extent to which the preceding and following pulses contribute to the deviation from the correct height. For such an operation to be possible a number of pulses must always be simultaneously available. This is arranged by applying the incoming signal to a delay line after sampling; see *fig. 16*. The

[6] CCITT recommendation No. V29.

[7] See for example R. W. Lucky, Automatic equalization for digital communication, Bell Syst. tech. J. **44**, 547-588, 1965, and A. Gersho, Adaptive equalization of highly dispersive channels for data transmission, Bell Syst. tech. J. **48**, 55-70, 1969.

delay line consists of a number of sections, each with a delay time equal to the sampling period T. The signals at the beginning and at the end of the line, and also those between the sections, are multiplied by coefficients $c_1 \ldots c_N$ and applied to an adder *Ad*. The output signal z from this circuit is the equalized signal.

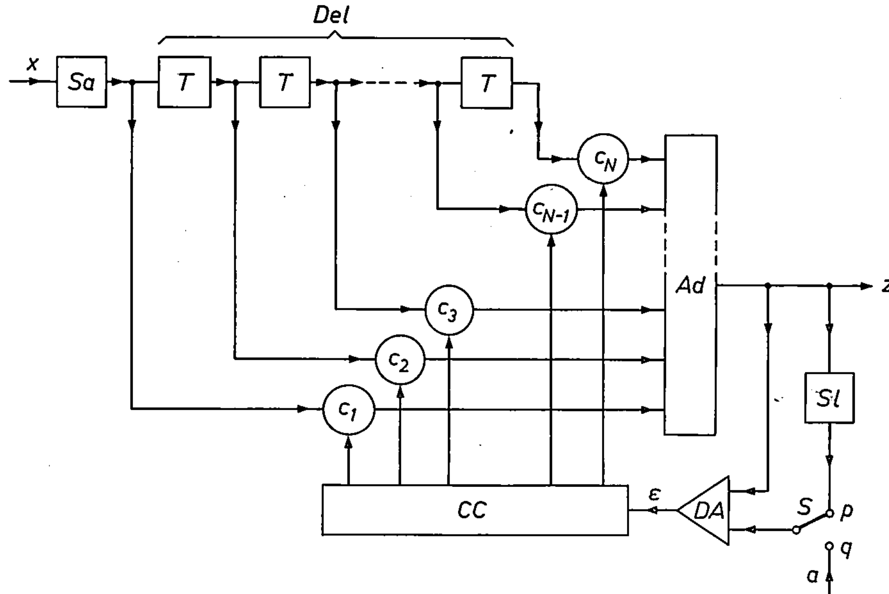

Fig. 16. Schematic circuit of an automatic equalizer that operates in the time domain. When the switch S is in position q the circuit operates as a preset equalizer. When switch S is in position p the circuit becomes an adaptive equalizer. *Del* delay line, consisting of a number of sections of delay time T equal to the sampling period. *Sa* sampling circuit. *Ad* adder. $c_1 \ldots c_N$ transmission coefficients. *DA* differential amplifier. *CC* control circuit. x input signal. z output signal. a comparison signal. ε error signal.

The signal z and the comparison signal a are applied to the inputs of the differential amplifier *DA*, which provides the error signal ε. (The switch S is in the position q.) This error signal is applied to the control circuit *CC*, which changes the coefficients $c_1 \ldots c_N$ in accordance with one of several specially developed algorithms. Since the output signal is affected by the signals at all the taps, a direct determination of the desired magnitude for each of the coefficients is not possible. The procedure is therefore carried out with a series of test pulses, and the correct setting is obtained by an iterative method. The coefficients finally receive the values for which the error signal ε has the minimum value. The equalizer is then set so that the combined characteristics of transmission path and equalizer satisfy the Nyquist criterion. The values of the coefficients $c_1 \ldots c_N$ thus obtained are now fixed and the information can be transmitted.

After the equalizer has been set up the circuit forms a 'transversal' filter [8]. Filters of this type can often be used to meet specifications that are almost or completely impossible to satisfy with conventional filters. In the case in question both the amplitude and the group-delay characteristics must be matched to various transmission paths for the signals. This would not be possible with filters consisting of inductors, capacitors and resistors.

In the application of the principle we have described a series of pulses must be available that is exactly like the series of test pulses originating from the transmitter. These comparison pulses can be generated separately in the receiver, but it is also possible to derive the comparison signal from the output signal of the equalizer. A circuit of this type is formed when the switch S in fig. 16 is set to position p. The signal then passes through a 'slicer' *Sl*, which limits both positive and negative pulses. If the equalizer is not yet set up correctly, the pulses that form the signal z have different heights. The pulses in the output signal of the slicer, however, do all have the same height. This signal is therefore approximately equal to the desired signal and can be used as a comparison signal. This circuit operates not only while the test pulses are being received, but also while the information is being transmitted. The unit therefore forms an adaptive equalizer.

A feature of the equalizers that we have looked at so far is that the criterion for the control of the circuit is derived from the *time* function of the signal. These equalizers are therefore said to work in the *time domain*. Since the output signal from the equalizer is the controlling time function, these circuits in fact make use of a form of feedback. Because of the ever-present danger

of instability in feedback circuits it is only possible to use small steps in the iterative procedure for establishing the coefficients $c_1 \dots c_N$. This means that a long series of test pulses (perhaps 1000) may be necessary to reach the stable final state.

It can happen that a transmission path is so poor that the non-equalized signal has the wrong polarity at some of the sampling times. This can appreciably lengthen the setting-up time, particularly in the case of an adaptive equalizer, and depending on the algorithm for the control circuit, it may happen that the stable

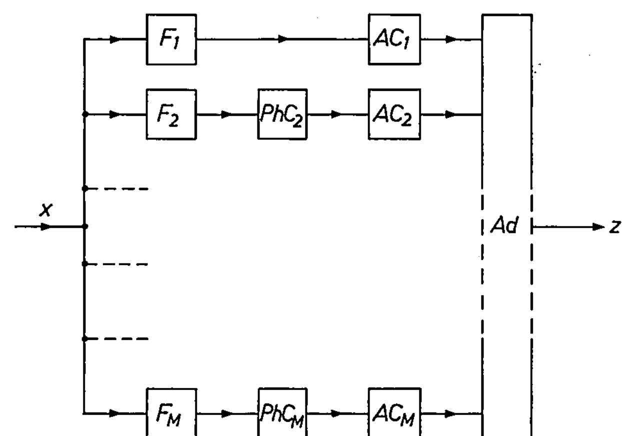

Fig. 17. Schematic circuit of an equalizer operating in the frequency domain. $F_1 \dots F_M$ filters. $PhC_2 \dots PhC_M$ phase-correcting circuits. $AC_1 \dots AC_M$ amplitude-correcting circuits. Ad adder. x input signal. z output signal.

setting is not reached at all. For this reason circuits are used that initially operate with locally generated comparison pulses; once the setting-up procedure has gone far enough for the error signal ε to be sufficiently small, the system is switched to the adaptive mode of operation.

An equalizer operating in the frequency domain

We shall now describe an equalizer developed at our laboratories that does not have the disadvantage just mentioned. The criterion for setting up is not derived from the time function here, but from the spectrum of the test signal; operation is in the *frequency domain.* The principle used depends on the fact that a periodic signal has a line spectrum with a finite number of components in a limited bandwidth. If the change in amplitude and phase arising in the transmission path is determined for each of these components, then these changes can be compensated and the transmitted signal can be recreated from the sum of the corrected components. By applying this process to a test signal consisting of a series of periodically repeated pulses, the data link is equalized for this test signal. In this case, provided a particular condition is satisfied, equalization has then also been established for the data signals to be transmitted.

This principle could be put into practice with a circuit corresponding to the block diagram of *fig. 17.* The received test signal is applied to a number of filters $F_1 \dots F_M$, which each pass one of the components of the spectrum. A phase-correcting network PhC and an amplitude-correcting network AC are provided for each component [9]. The way in which these circuits are set up automatically will be described later. After passing through the networks PhC and AC the components are recombined in the adder Ad.

Since there is no feedback in the application of this principle, there is no danger of instability and no need for an iterative procedure in setting up. This means that setting up is much faster than for equalizers operating in the time domain.

The test signal

As will be shown later, the setting up can be performed with a single test pulse. However, to explain the operation we shall at first take the signal to consist of a series of short pulses with a pulse period NT, where T is again the sampling time and N an integer. The spectrum of the signal contains a d.c. component and a number of harmonic components at regular frequency intervals of f_1, where

$$f_1 = 1/(NT).$$

If we assume that the transmission path limits the bandwidth to the 'Nyquist rate' $f_0 = 1/(2T)$, the highest frequency in the spectrum is q/NT, with $q = (N - 1)/2$. (We confine ourselves here to the simple case in which N is odd.) The relation for the transmitted test signal is then:

$$f(t) = E\{\tfrac{1}{2} + \sum_{k=1}^{q} \cos(2\pi k f_1 t)\}. \qquad (2)$$

If we make use of the following relations (which can be derived from the summation of a geometric series):

$$\sum_{k=-q}^{q} e^{jk\alpha} = \frac{\sin \alpha(q + \frac{1}{2})}{\sin(\alpha/2)}, \qquad (3)$$

and we substitute

$$\alpha = 2\pi f_1 t = 2\pi t/NT,$$

[8] See for example H. E. Kallmann, Transversal filters, Proc. I.R.E. 28, 302-310, 1940. An explanation of the operation of such filters has also been given by P. J. van Gerwen in the article 'The use of digital circuits in data transmission', Philips tech. Rev. 30, 71-81, 1969.

[9] The d.c. component, which is passed by the filter F_1, is of course only corrected in magnitude.

then we can also write (2) in the form:

$$f(t) = \tfrac{1}{2}E \frac{\sin(\pi t/T)}{\sin(\pi t/NT)}. \qquad (4)$$

This function has zeros at integer multiples of T, except at multiples of the pulse period NT of the test pulses.

If as a result of the characteristics of the transmission path the spectrum components of the test signal undergo changes in phase and amplitude, then a signal is received of the form

$$x(t) = E\{\tfrac{1}{2}a_0 + \sum_{k=1}^{q} a_k \cos(2\pi k f_1 t + \phi_k)\}. \qquad (5)$$

The 'task' of the equalizer is now to bring the phase angles ϕ_k back to zero and to make the coefficients a_k equal to 1, so that the shape of $x(t)$ will correspond to that of $f(t)$.

The filters

The performance required of the filters F is very different from that usually required of filters for other applications. Generally a filter should pass all signals in a particular band of frequencies and suppress all signals outside that band as much as possible. In the case considered here, however, each filter must pass one of the components from the line spectrum of the test signal and suppress the other components. Since this line spectrum only has components at integer multiples of the repetition rate of the pulses, the filters must have transmission characteristics with zeros at regular intervals along the frequency axis.

Even though these filters operate at a fixed setting, unlike those in the equalizers discussed earlier, it is very difficult to realize them with classical filter circuits. A solution is again offered here by the transversal filters. The complete circuit can still remain comparatively simple, since a separate delay line is not necessary for every filter; it is sufficient to have a common delay line for all the filters. The number of taps is made equal to N, the ratio introduced earlier of the period of the test pulses to that of the data pulses. The number of sections is therefore $N-1$. The delay time per section is again equal to the sampling interval T. Since a sharp cut-off of a particular passband is not necessary, the value of N can remain relatively small (e.g. 15). However, the number of sections should be sufficiently large for the total delay time $(N-1)T$ for the signal to be at least equal to the duration of a received pulse with its tails (the pulse response).

We shall consider first the filter F_1 that gives the d.c. component of the test signal. This can be a transversal filter, with the voltages at the taps on the delay line added directly together. Since the transmittance function of each section is equal to $e^{-2\pi j f T}$, the transmittance function of the filter thus formed is

$$H_0'(f) = \sum_{k=0}^{N-1} e^{-2\pi j k f T} =$$

$$= e^{-2\pi j f q T}\{1 + 2\sum_{m=1}^{q} \cos 2\pi m f T\}. \qquad (6)$$

Making use of equation (3) again and substituting $\alpha = 2\pi f T = 2\pi f/Nf_1$, we then have:

$$H_0'(f) = e^{-2\pi j f q T} \frac{\sin(\pi f/f_1)}{\sin(\pi f/Nf_1)}. \qquad (7)$$

Since q is equal to $(N-1)/2$, the first factor of (7) corresponds to the transmission characteristic of the part of the delay line between the input and the centre. The delay time of this part of the filter is independent of the frequency, so that this term need be considered no further. The fraction appearing in (7)

$$H_0(f) = \frac{\sin(\pi f/f_1)}{\sin(\pi f/Nf_1)} \qquad (8)$$

is the transmission characteristic of the filter. This is shown in *fig. 18*. The curve has zeros at integer values of f/f_1, except at integer multiples of Nf/f_1. With the assumption that the nominal cut-off frequency of the transmission path is equal to the Nyquist rate $f_0 = 1/(2T)$, however, only the d.c. component is passed.

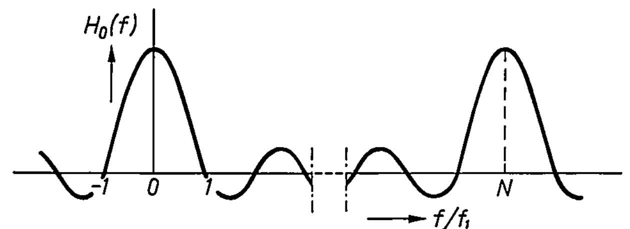

Fig. 18. Transmission characteristic of a transversal filter in which the delay line has N taps. The number of sections is therefore $N-1$. The coefficients $c_1 \ldots c_N$ (see fig. 16) are all equal. This characteristic is represented by eq. 8. In addition to the d.c. component this filter passes the harmonic component at the frequency Nf_1.

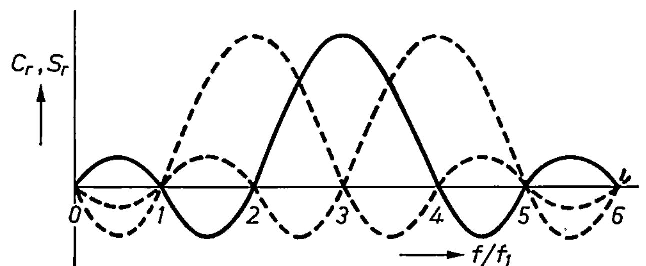

Fig. 19. Some examples of transmission characteristics of transversal filters that each pass one of the harmonic components of the test signal. The frequencies of the transmitted components are $2f_1$, $3f_1$ and $4f_1$.

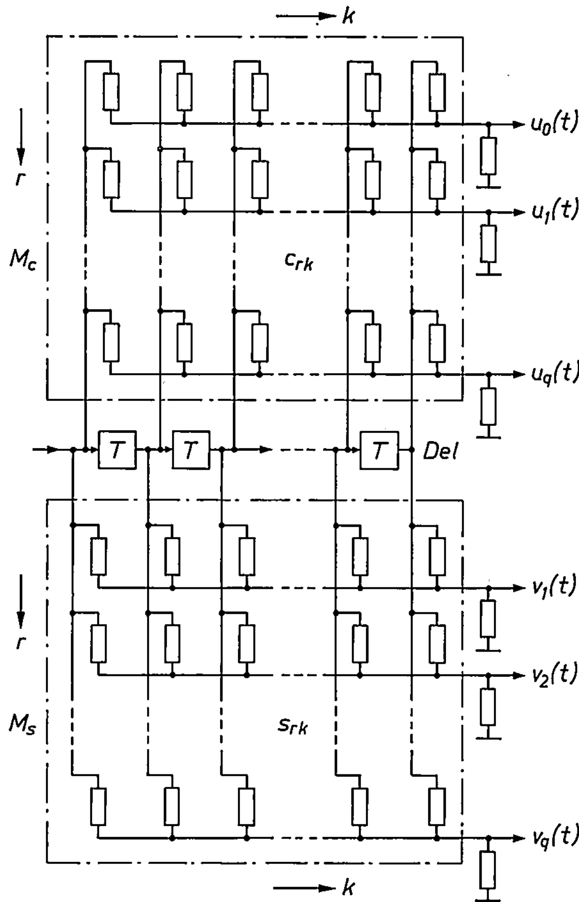

Fig. 20. Circuit of the transversal filters that split the test signal into harmonic components. *Del* delay line. M_c and M_s resistance networks for the cosine and sine filters. r is the number of the row and k that of the column of the resistances. c_{rk} and s_{rk} transmission coefficients of the signals from the taps of the delay line to the output terminals of the filters. $u_0(t)$ ... $u_q(t)$ and $v_1(t)$ ... $v_q(t)$ output signals from the filters.

Filters that pass one of the harmonic components and suppress the others (thus including the d.c. component) can be derived from the filter for the d.c. component by a simple transformation. This depends on the theorem [10] that the transmission characteristic $H_0(f)$ of a lowpass filter is shifted to a central frequency f_r if the pulse response appropriate to $H_0(f)$ is multiplied by $\cos 2\pi f_r t$ or $\sin 2\pi f_r t$. In the first case the transmission function

$$C_r(f) = \tfrac{1}{2}\{H_0(f+f_r) + H_0(f-f_r)\} \qquad (9)$$

is produced, while in the second case the corresponding function is:

$$S_r(f) = \tfrac{1}{2}\mathrm{j}\{H_0(f+f_r) - H_0(f-f_r)\}. \qquad (10)$$

From now on we shall call these filter types 'cosine filters' and 'sine filters'. Both filters have the same transmission characteristics; but at the frequency f_r the output voltages of the two types differ in phase by 90°. Since this phase difference is made use of for the phase correction in the equalizer, both a cosine filter and a sine filter are used for each value of f_r. *Fig. 19* shows three examples of these transformed transmission characteristics, for $f_r = 2f_1, f_r = 3f_1$ and $f_r = 4f_1$.

The various filters can be realized by connecting fixed resistances to the taps on the delay line. A configuration of this type is shown in *fig. 20*. The resistances belonging to the cosine filters and sine filters are shown on opposite sides of the delay line. Each row of resistances, together with the delay line, forms a transversal filter. The number of a row is indicated by r (going from 0 to q), and the number of a column, and hence that of a tap on the delay line, is indicated by k (going from 1 to N). The transmission coefficients from the taps to the output terminals of the cosine filters are indicated by c_{rk} and those to the output terminals of the sine filters by s_{rk}. The factors $\cos 2\pi f_r t$ and $\sin 2\pi f_r t$ mentioned above, by which the pulse response of the d.c. filter must be multiplied to obtain the filters that pass the harmonic components rf_1, are now obtained by substituting $f_r = r/NT$ and $t = (k-q-1)T$. The resistances must therefore be given values such that these transmission coefficients satisfy

$$\left.\begin{aligned} c_{rk} &= \cos 2\pi r(k-q-1)/N \\ \text{and} \qquad s_{rk} &= \sin 2\pi r(k-q-1)/N. \end{aligned}\right\} \qquad (11)$$

(Where negative values are necessary for these coefficients, the resistances concerned are connected to the delay line via inverters.) The total number of transversal filters in the arrangement of fig. 20 is then $2q + 1 = N$. This corresponds to the number of taps on the delay line.

The principle of the equalizer described here depends on the 'discrete Fourier transform' (DFT) [11] of the test signal. In the usual expansion of a periodic function of time as a Fourier series, this function corresponds at every instant to the sum of a series of components, a series that in general contains an infinite number of terms. In DFT this correspondence is only required at a finite number of instants. A finite number of terms in the series expansion is therefore sufficient. These terms are not found by integrating with respect to time, as in the usual Fourier expansion, but by summation of a number of discrete values. If it is desired to expand a function $x(t)$, periodic in t and of period 1, in a series that corresponds with the values x_k of $x(t)$ at the times $t = k/N$ (N is a positive integer), then we can write:

$$x_k = \frac{1}{N}\sum_{n=0}^{N-1} X_n \mathrm{e}^{2\pi \mathrm{j} nk/N}, \qquad (12)$$

where

$$X_n = \sum_{k=0}^{N-1} x_k \mathrm{e}^{-2\pi \mathrm{j} nk/N}. \qquad (13)$$

[10] A. Papoulis, The Fourier integral and its applications, McGraw-Hill, New York 1962.
[11] A. V. Oppenheim and R. W. Schafer, Digital signal processing, Prentice-Hall, Englewood Cliffs 1975.

The relation between the equations for x_k and X_n depends on the fact that the expression

$$\frac{1}{N}\sum_{n=0}^{N-1} e^{2\pi j n r/N}$$

is equal to 1 for $r = mN$ (m is an integer) and is equal to zero for all other integer values of r.

The analogy between the equations for the time function x_k and the spectrum X_n is expressed in the case we have considered by the correspondence between equations (4) and (8).

In the above discussion the starting point was the application of an analog signal of limited bandwidth to the input of the transversal filters. It was tacitly assumed that the sampling of the equalized signal took place at the output of the equalizer. It is however also possible to sample the signal before it is applied to the filters, even though the input signal to each transversal filter then has a wide spectrum and, because of the periodicity of the passband of such a filter, many of these components reach the output. This is because a transversal filter whose output signal is sampled at a particular instant has the property that the input signal can also be sampled with a period corresponding to the delay time per section. In the first case the analog voltages $f(t)$, $f(t-T)$, $f(t-2T)$, etc. at the taps are first combined to give the voltage

$$s_1(t) = c_1 f(t) + c_2 f(t-T) + \ldots c_N f\{t-(N-1)T\},$$

in which $t = t_1$ is substituted on sampling. In the second case the sampled voltages $f(t_2)$, $f(t_2+T)$, $f(t_2+2T)$, etc. are passed through the delay line, and

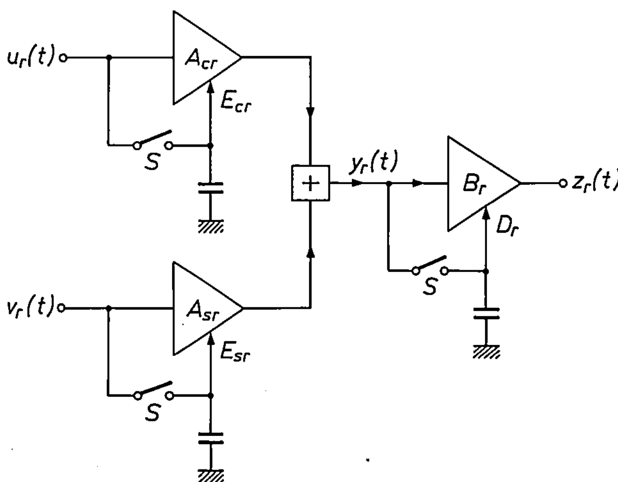

Fig. 21. Circuit for correcting phase and amplitude of the test signal. A_{cr} and A_{sr} control amplifiers whose gains are proportional to the control voltages E_{cr} and E_{sr}. B_r control amplifier with gain inversely proportional to the control voltage D_r. The input signals to the amplifiers are sampled at the time $t = 0$ with the switches S. $u_r(t)$ and $v_r(t)$ output signals from one of the cosine filters and the corresponding sine filter, respectively (see fig. 20). $y_r(t)$ and $z_r(t)$ input and output signals of the amplifier B_r.

then give rise to the discontinuous voltage

$$s_2(t_2) = c_1 f(t_2 + (N-1)T) + \\ + c_2 f(t_2 + (N-2)T) \ldots c_N f(t_2).$$

The voltages $s_1(t_1)$ and $s_2(t_2)$ will clearly be equal when the difference between the sampling times t_1 and t_2 is equal to the total delay time $(N-1)T$ of the delay line.

Sampling the signal at the input to the equalizer has the advantage that a much simpler design can be used for the delay line.

The phase and amplitude correction

The principle of the circuit used for correcting the phase and amplitude of each component of the spectrum of the test signal is shown in *fig. 21*. The cosine filter for the component under consideration, which has a transmission function $C_r(f)$ as given by (9), delivers the output signal

$$u_r(t) = \tfrac{1}{2}NEa_r \cos(2\pi r f_1 t + \phi_r), \qquad (14)$$

while the output signal from the sine filter with the transmission function $S_r(f)$ given by (10) is

$$v_r(t) = \tfrac{1}{2}NEa_r \sin(2\pi r f_1 t + \phi_r). \qquad (15)$$

The voltages are applied to the two amplifiers of gain A_{cr} and A_{sr}, proportional to the control voltages E_{cr} and E_{sr}, so that

$$A_{cr} = hE_{cr} \quad \text{and} \quad A_{sr} = hE_{sr},$$

where h is the constant of proportionality. The control voltages E_{cr} and E_{sr} are derived from the input signals by sampling them at a particular instant with the aid of the switches S. This instant can be chosen as the time $t = 0$ without loss of generality. The control voltages are then

$$E_{cr} = u_r(0) = \tfrac{1}{2}NEa_r \cos\phi_r$$

and

$$E_{sr} = v_r(0) = \tfrac{1}{2}NEa_r \sin\phi_r.$$

Since the amplifiers are then set up such that

$$A_{cr} = hu_r(0) \quad \text{and} \quad A_{sr} = hv_r(0), \qquad (16)$$

the output voltages are

$$y_{cr}(t) = Ka_r^2 \cos\phi_r \cos(2\pi r f_1 t + \phi_r)$$

and

$$y_{sr}(t) = Ka_r^2 \sin\phi_r \sin(2\pi r f_1 t + \phi_r).$$

The constant K here is equal to $hN^2E^2/4$. The two signals are added together, giving the sum signal

$$y_r(t) = A_{cr}u_r(t) + A_{sr}v_r(t) = Ka_r^2 \cos 2\pi r f_1 t. \qquad (17)$$

We see that this voltage is independent of the unknown phase angle ϕ_r.

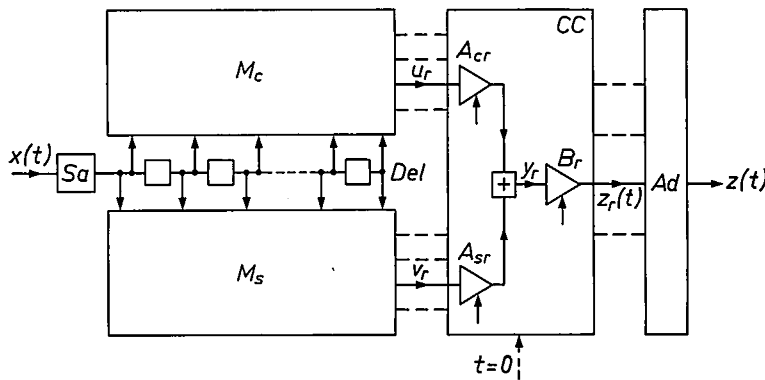

Fig. 22. Block diagram of the equalizer, operating in the frequency domain. The control circuit *CC*, which is set up at time $t = 0$, contains q circuits like those of fig. 21. The output signals $z_r(t)$ are added in the adder *Ad*. $z(t)$ is the equalized output signal.

For amplitude correction the signal $y_r(t)$ is applied to the amplifier of gain B_r. The gain of this amplifier can also be controlled, by the voltage D_r, but now in such a way that the gain is *inversely* proportional to D_r. We can therefore write:

$$B_r = h'/D_r. \qquad (18)$$

The control voltage D_r is again derived from the input signal by sampling this signal immediately after the time $t = 0$. The control voltage then obtained is

$$D_r = y_r(0) = h\{u_r^2(0) + v_r^2(0)\} = Ka_r^2, \qquad (19)$$

so that the output voltage of the amplifier becomes

$$z_r(t) = B_r y_r(t) = h' \cos 2\pi r f_1 t. \qquad (20)$$

This voltage is clearly independent of both the unknown phase angle ϕ_r and the unknown amplitude a_r of the appropriate component from the spectrum.

We make the constant h' the same for all the components, except the d.c. component, which is obtained from the cosine filter for which $r = 0$. In the latter case we make the corresponding quantity equal to $h'/2$. The sum of all the corrected components then becomes

$$z(t) = h'(\tfrac{1}{2} + \sum_{r=1}^{q} \cos 2\pi r f_1 t). \qquad (21)$$

This equation corresponds to (2) and therefore, in connection with (4), gives the pulse response of a network that satisfies the Nyquist condition, which is the intended result for the equalizer. The setting of the amplifiers is now fixed, which is represented in fig. 21 by capacitances. All subsequently transmitted data signals are therefore also equalized.

The complete circuit of an equalizer designed in accordance with the principles described is shown in *fig. 22*. The resistance networks M_c and M_s correspond with those of fig. 20. The control circuit *CC* contains a correction circuit like that of fig. 21 for each component of the test signal. In the circuit *Ad* the output signals from all the *B* amplifiers are added, giving rise to the equalized signal $z(t)$.

In the above description of the operation of the circuit it was assumed that the analog signal received via the transmission path was applied to the input of the delay line. In this case the signal $z(t)$ given by (21) is obtained at the output of the equalizer. Sampling this signal at the correct times gives the values of the bits. However, a significant advantage can be obtained by making use of the possibility of sampling the signal before the delay line, as mentioned earlier. If a circuit *Sa* is included that samples the signal periodically at the frequency $1/T$, as indicated in fig. 22, then the transversal filters give the corresponding discrete values of $u_r(t)$ and $v_r(t)$ at periodic times.

The use of a non-periodic test signal

In the above mathematical treatment it was assumed that the test signal consisted of a series of pulses with a repetition period of NT. If now the significant response time of each pulse is smaller than NT, then all the information necessary for setting the equalizer is present at an instant at which the response of the first pulse has been completely entered into the delay line. It therefore does not matter whether the test signal is a periodically recurring pulse or just a single pulse. The setting time can therefore in principle remain limited to the time necessary for the delay line to take in the response of a single pulse.

The effect of components above the Nyquist rate

Another initial assumption was that the received signal only contained components below the Nyquist rate f_0 (see fig. 3). Since a transmission path is used that has a Nyquist-type characteristic at the cut-off frequency (fig. 6), components above f_0 can however be transmitted. The fact that transversal filters have periodically repeated passbands (fig. 18) means that some of the filters pass components that are above f_0. For each of these filters the two transmitted components are located symmetrically about the Nyquist rate. It can be shown from relations that apply to the discrete Fourier transform that the appropriate correc-

tion is also achieved with the equalizers we have described when these two components are both passed by the same filter.

Digital version

An equalizer as in fig. 22 could be built up from standard elements. The delay line could be a 'bucket-brigade' line [12], or a charge-coupled device (CCD)[13], with which a signal can be shifted in steps. Other components of the circuit, a sampling circuit, inverters, control amplifiers and circuits for setting the voltages are well known from other branches of electronics.

It is however possible, and indeed a much more attractive idea, to construct the complete equalizer from digital circuits. The principle of such a design is shown in *fig. 23*. The receiver now consists of an analog-to-digital converter A/D operating at a sampling rate $2f_0$ and a digital processor Pr. The receiver is controlled by a clock circuit Cl that is synchronized with the data signals. The received signal $x(t)$ is coded in the analog-to-digital converter A/D in a binary code, typically of 8 bits, corresponding to $2^8 = 256$ levels. The signals $x_k(t)$ at the taps of the delay line (see fig. 20) can be expressed in terms of the input signal $x(t)$ by writing:

$$x_k(t) = x(t'),$$

where $t' = t - (k-1)T$. These signals can therefore also be obtained by sampling the input signal with a period T. The output signals from the filters now follow from the equations

$$\left.\begin{aligned} u_r(t) &= \sum_{k=1}^{N} c_{rk}x_k(t) \\ \text{and} \quad v_r(t) &= \sum_{k=1}^{N} s_{rk}x_k(t), \end{aligned}\right\} \quad (22)$$

with $r = 0 \ldots q$. In the digital design the values of $x_k(t)$ for $t = 0$ are stored in a register that forms part of the memory *Mem*. The constants c_{rk} and s_{rk} (see 11) are also stored here. The output signals $u_r(0)$ and $v_r(0)$ are then calculated in the arithmetic unit *Cal* from the above equations. From these quantities, which are also stored in the memory, the setting of the (now simulated) amplifiers A_{cr}, A_{sr} and B_r follows. The appropriate calculations are performed with the aid of the equations (16), (18) and (19).

On the subsequent reception of the data signals, the corrected value of the spectrum components is given, as can be seen from fig. 21, by the equation

$$z_r(t) = A_{cr}B_r u_r(t) + A_{sr}B_r v_r(t). \quad (23)$$

The sum of these components gives the output signal

$$z(t) = \sum_{r=0}^{q} z_r(t). \quad (24)$$

In calculating $u_r(t)$ and $v_r(t)$ from the equations given above N^2 products would have to be calculated for each sampling. This procedure can be considerably simplified, however. After substituting (22) and (23), the equation (24) takes the form

$$z(t) = \sum_{k=1}^{N} c_k x_k(t), \quad (25)$$

in which

$$c_k = \sum_{r=0}^{q} (A_{cr}c_{rk} + A_{sr}s_{rk})B_r. \quad (26)$$

The coefficients c_k, which are again stored in the memory, only have to be calculated once for the setting of the equalizer. When these quantities are used, then only N products have to be calculated at each sampling on reception of the data signals. The values of c_k calculated in the way described above and stored correspond completely with the coefficients $c_1 \ldots c_N$ that are used in an equalizer operating in the time domain as in fig. 16.

The digital version offers possibilities that cannot be obtained, or can only be obtained with difficulty, with analog circuits. For example, when standard elements are used it is necessary to limit the number of taps on the delay line, and hence the value of N. With the digital version, however, there is no objection to choosing higher values for N, say up to 32. In practice the pulse-response time can amount to 13 ms. It has been found that to achieve the desired accuracy the arithmetic unit requires about 10 ms to determine the coefficients c_k. A total time of only 23 ms is thus required for equalization of the data link.

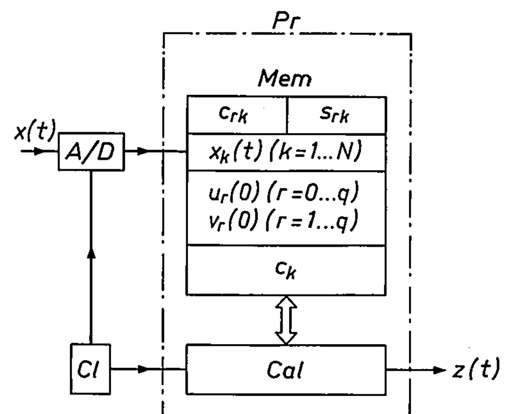

Fig. 23. Digital version of an equalizer operating on the principles illustrated in fig. 22. A/D analog-to-digital converter. Pr processor. *Mem* memory. *Cal* arithmetic unit. *Cl* clock-signal generator. $x(t)$ input signal. $z(t)$ output signal. The quantities stored in the memory are discussed in the text.

Once the coefficients c_k have been established, the computer has a surplus of arithmetic capacity. This can be used for applying corrections to the values of c_k during the transmission of the information. The principle of adaptive equalization in the time domain, as described earlier, is then applied (see fig. 16). This also allows corrections to be made for a not completely correct setting of the equalizer, which can occur when an interfering signal is received at the same time as the test pulse.

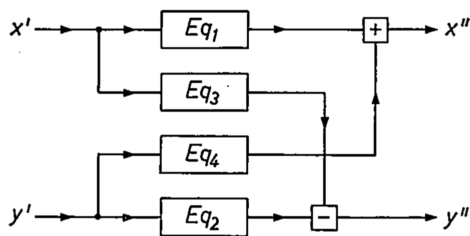

Fig. 24. Circuit with four equalizers, applied in the receiver section of a modem for 9600 bits per second. Eq_1 is the equalizer for the x channel, Eq_2 the equalizer for the y channel. Eq_3 and Eq_4 compensate interaction between the two channels.

should of course *both* satisfy the Nyquist condition. This can be achieved in part by the lowpass filters LP_1, LP_1' and LP_2, LP_2', which are included in the signal path in the transmitter and receiver. Even then the uncertainty in the characteristics of the transmission path makes it necessary to use equalization, which should be separate for each channel. This is still not sufficient, since errors can also arise when the shape of the characteristics of the transmission path is such that there is insufficient separation between the two channels, so that the signal y' is affected by the signal x at the sampling times, and vice versa [4]. This 'crosstalk' effect can be corrected by including two extra equalizers in the receiver. The corresponding circuit is shown in *fig. 24*. Eq_1 and Eq_2 are (identical) equalizers for the x channel and the y channel; Eq_3 and Eq_4 (also identical) compensate for the effects of interaction. All the equalizers are set up at the same time. The test pulse is transmitted on one of the channels, e.g. the x channel. Eq_1 is set up with the aid of this. This setting is taken over by Eq_2. Eq_3 follows a programme that makes y'' zero at all sampling times. Eq_4 takes over the resulting setting

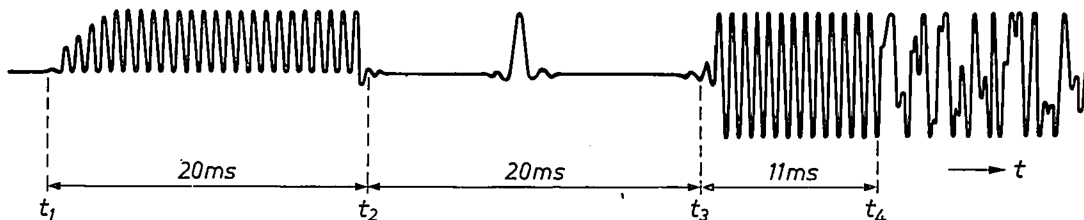

Fig. 25. The signal used in setting up the equalizers in the equipment described. From t_1 to t_2 a 1200-Hz signal is transmitted, together with a d.c. component. In the interval t_2 to t_3 the test pulse is transmitted. During the subsequent calculation time t_3 to t_4 a 1200-Hz signal is transmitted again. At t_4 the actual data transmission commences.

of Eq_3, but gives a compensation voltage of the opposite sign.

For the correct operation of a system with orthogonal modulation as described here, the frequency of the carrier signal used in demodulation at the receiving end must be exactly equal to the frequency of the carrier signal modulated at the transmitter. If there is a small difference between these frequencies there will be a phase error in the received signal, associated with a gradual

Application of digital equalization in a system for data transmission with 9600 bits per second

We stated at the beginning of this article that the need for higher bit rates has led to the development of systems in which more than one bit is transmitted per sampling. Here the use of digital circuits offers possibilities that are hardly practical with analog circuits. We should like to illustrate this by describing a transmission system for 9600 bits/s. A sampling rate of 2400 Hz is used in this system, so that each sampling contains information about 4 bits. The nominal bandwidth is therefore 1200 Hz. The transmission takes place by a combination of phase and amplitude modulation of the data carrier, a method that was discussed earlier with reference to fig. 10.

To give reliable transmission of a signal with a modulation system like that of fig. 10, the x and y channels

[12] F. L. J. Sangster, The 'bucket-brigade delay line', a shift register for analogue signals, Philips tech. Rev. 31, 97-110, 1970.
F. L. J. Sangster and K. Teer, Bucket-brigade electronics — new possibilities for delay, time-axis conversion, and scanning, IEEE J. SC-4, 131-136, 1969.

[13] L. J. M. Esser, Peristaltic charge-coupled devices: what is special about the peristaltic mechanism, in: P. G. Jespers, F. van de Wiele and M. H. White (ed.), Solid-state imaging, Noordhoff, Leiden 1976, pp. 343-425.

rotation of the diagram of fig. 15. By detecting this error the frequency of the demodulating carrier can be corrected. Variations in the clock frequency can be corrected in a similar way.

The signal pattern applied to one of the channels in the transmitter to set up the equalization system is shown in *fig. 25*. First of all a 1200-Hz signal is transmitted for 20 ms. This modulates a carrier at 1700 Hz to produce sidebands at the frequencies 500 and 2900 Hz, and since the signal also contains a d.c. term the carrier is also transmitted. These three signals are now used for setting the carrier-signal and clock-signal generators in the receiver to the correct phases.

The test pulse is next transmitted during an 'interval', which also lasts for 20 ms. During the calculation time of 11 ms, which now follows, a 1200-Hz signal is again transmitted to ensure that the phase of the clock signal is correct. The transmission of the data signals then starts, in which the decoded values of x' and y' of the signal constellation from fig. 15 appear at the output in groups of four bits. As we said earlier, the correct phase of the data carrier and of the clock signal can now be derived from the data signals, and the processor algorithm is switched over to the slower adaptive correction to the principle of fig. 16.

Summary. A transmission path for data signals should have characteristics very different from those for telephony. Nevertheless, the rapidly increasing need for data links has made it necessary to make extensive use of existing telephone circuits for data transmission. Since the characteristics of the telephone circuits can differ very considerably from one another, reliable transmission of data signals at high bit rates is only possible if a circuit is used that makes the characteristics of the complete transmission path conform to the Nyquist criterion for data transmission, preferably automatically. Many of these equalizers take the information for setting up from the time function of a transmitted test signal; they operate in the time domain. Disadvantages associated with these equalizers are that the setting-up time is long and that there is a danger of instability in the circuit. The article describes an equalizer that operates in the frequency domain and does not have these disadvantages. Special features of this type of equalizer are that preset transversal filters are used and that only a single test pulse is required for the setting up. The algorithm used is based on the discrete Fourier transform of the response of this test pulse. An equalizer of this type has been made with digital circuits. Four of the equalizers have been combined in a modem for transmitting data signals at a rate of 9600 bits per second.

Recent scientific publications

These publications are contributed by staff of laboratories and plants which form part of or cooperate with enterprises of the Philips group of companies, particularly by staff of the following research laboratories:

Philips Research Laboratories, Eindhoven, The Netherlands	*E*
Philips Research Laboratories, Redhill, Surrey, England	*M*
Laboratoires d'Electronique et de Physique Appliquée, 3 avenue Descartes, 94450 Limeil-Brévannes, France	*L*
Philips GmbH Forschungslaboratorium Aachen, Weißhausstraße, 51 Aachen, Germany	*A*
Philips GmbH Forschungslaboratorium Hamburg, Vogt-Kölln-Straße 30, 2000 Hamburg 54, Germany	*H*
MBLE Laboratoire de Recherches, 2 avenue Van Becelaere, 1170 Brussels (Boitsfort), Belgium	*B*
Philips Laboratories, 345 Scarborough Road, Briarcliff Manor, N.Y. 10510, U.S.A. (by contract with the North American Philips Corp.)	*N*

Reprints of most of these publications will be available in the near future. Requests for reprints should be addressed to the respective laboratories (see the code letter) or to Philips Research Laboratories, Eindhoven, The Netherlands.

M. Adriaansz & L. Vriens: Laser Raman scattering from metal-halide arcs.
Philips Res. Repts. **31**, 193-198, 1976 (No. 3). *E*

J. P. André, J. Hallais & C. Schiller: Heteroepitaxial growth of GaP on silicon.
J. Crystal Growth **31**, 147-157, 1975. *L*

J. P. Beasley & D. G. Squire: Electromask generator. *(Abstract.)*
J. Vac. Sci. Technol. **12**, 1251, 1975 (No. 6). *M*

V. Belevitch: Simultaneous canonic synthesis of two dual impedances.
Int. J. Circuit Theory & Appl. **3**, 311-317, 1975 (No. 3). *B*

V. Belevitch: The lateral magnetic skin-effect in thin plates.
Philips Res. Repts. **31**, 199-215, 1976 (No. 3). *B*

M. Binet: Fast and nondestructive method of $C(V)$ profiling of thin semiconductor layers on an insulating substrate.
Electronics Letters **11**, 580-581, 1975 (No. 24). *L*

G. M. Blom, J. J. Daniele, T. Kyros & A. F. Witt (M.I.T., Cambridge, Mass.): Interface demarcation during LPE growth of GaAs.
J. Electrochem. Soc. **122**, 1541-1544, 1975 (No. 11). *N*

P. F. Bongers: Magnetic properties and chemical bonding.
Crystal structure and chemical bonding in inorganic chemistry, editors C. J. M. Rooymans & A. Rabenau, publ. North-Holland, Amsterdam 1975, pp. 27-45. *E*

A. H. Boonstra & C. A. H. A. Mutsaers: Relation between the photoadsorption of oxygen and the number of hydroxyl groups on a titanium dioxide surface.
J. phys. Chem. **79**, 1694-1698, 1975 (No. 16). *E*

A. H. Boonstra & C. A. H. A. Mutsaers: Adsorption of hydrogen peroxide on the surface of titanium dioxide.
J. phys. Chem. **79**, 1940-1943, 1975 (No. 18). *E*

P. W. J. M. Boumans & F. J. de Boer: An assessment of the inductively coupled high-frequency plasma for simultaneous multi-element analysis.
Proc. Anal. Div. Chem. Soc. **12**, 140-152, 1975 (No. 5). *E*

J. C. Brice, J. M. Robertson, W. T. Stacy & J. C. Verplanke: Strain induced effects in the LPE growth of garnets.
J. Crystal Growth **30**, 66-76, 1975 (No. 1). *E*

T. W. Bril: Raman spectroscopy of crystalline and vitreous borates.
Thesis, Eindhoven 1976. (Philips Res. Repts. Suppl. 1976, No. 2.) *E*

T. M. Bruton, O. F. Hill, P. A. C. Whiffin & J. C. Brice: The growth of some gamma bismuth oxide crystals.
J. Crystal Growth **32**, 27-28, 1976 (No. 1). *M*

K. H. J. Buschow: Magnetic properties of $MgCo_2$, $MgNi_2$ and Mg_2Ni.
Solid State Comm. **17**, 891-893, 1975 (No. 7). *E*

K. H. J. Buschow, H. H. van Mal & A. R. Miedema: Hydrogen absorption in intermetallic compounds of thorium.
J. less-common Met. **42**, 163-178, 1975 (No. 2). *E*

T. A. C. M. Claasen & M. J. C. van Gemert: Approximate solutions in multiple reflection time domain spectroscopy.
J. chem. Phys. **63**, 68-73, 1975 (No. 1). *E*

T. A. C. M. Claasen, W. F. G. Mecklenbräuker & J. B. H. Peek: On the stability of the forced response of digital filters with overflow nonlinearities.
IEEE Trans. **CAS-22**, 692-696, 1975 (No. 8). *E*

J. Cornet: Les applications optiques des verres semi-conducteurs.
Rev. Phys. appl. **10**, 409-416, 1975 (No. 6). *L*

H. Damsma & E. E. Havinga: Pressure dependence of superconductive transition temperatures in alloyed compounds $LaTl_{3-x}Pb_x$.
Solid State Comm. **17**, 409-411, 1975 (No. 4). *E*

P. Delsarte: On subfield subcodes of modified Reed-Solomon codes.
IEEE Trans. **IT-21**, 575-576, 1975 (No. 5). *B*

J. P. Deschamps: Binary simple decompositions of discrete functions.
Digital Processes **1**, 123-140, 1975 (No. 2). *B*

J. G. Dil: Brillouin scattering from metals.
Thesis, Rochester, N.Y., U.S.A., 1975. *E*

C. Z. van Doorn: Dynamic behavior of twisted nematic liquid-crystal layers in switched fields.
J. appl. Phys. **46**, 3738-3745, 1975 (No. 9). *E*

L. D. J. Eggermont: Measured signal/quantising-distortion ratio of high-information delta modulation.
Electronics Letters **11**, 242-244, 1975 (No. 11). *E*

J. Georges: Design aspects of a language for interactive computing.
Interactive systems, Proc. Conf. London 1975, pp. 19-30. *B*

M. Gleria & R. Memming: Photoelectrochemical studies of tris[2,2′-bipyridyl]ruthenium(II) at semiconductor electrodes.
Z. phys. Chemie neue Folge **98**, 303-316, 1975 (No. 1-6). *H*

M. Goscianski, L. Léger & A. Mircea-Roussel: Field induced transitions in smectic A phases.
J. Physique Lettres **36**, L 313-316, 1975 (No. 12). *L*

J. J. de Groot & J. A. J. M. van Vliet (Philips Lighting Division, Eindhoven): The measurement and calculation of the temperature distribution and the spectrum of high-pressure sodium arcs.
J. Physics D **8**, 651-662, 1975 (No. 6).

J. A. G. Hale & P. Saraga: Control of a PCB drilling machine by visual feedback.
Adv. Papers 4th Int. Joint Conf. on Artificial intelligence, Tbilisi 1975, pp. 775-781. *M*

W. K. Hofker (Philips Research Labs., Amsterdam Division): Determination of moments of experimental range distributions of boron implanted in silicon.
Radiation Effects **25**, 205-206, 1975 (No. 3).

W. K. Hofker*, H. W. Werner, D. P. Oosthoek* & N. J. Koeman* (* Philips Research Labs., Amsterdam Division): Redistribution of background impurities in silicon induced by ion implantation and annealing.
Ion implantation in semiconductors, editor S. Namba, publ. Plenum Press, New York 1975, pp. 201-209. *E*

A. Humbert: Study of the growth of epitaxial layers and its application to (Ga,In)As composites.
Philips Res. Repts. **31**, 216-243, 1976 (No. 3). *L*

L. Jacomme: Modal dispersion in multimode graded-index fibers.
Appl. Optics **14**, 2578-2584, 1975 (No. 11). *L*

B. A. Joyce & C. T. Foxon: Kinetic studies of the growth of III-V compounds using modulated molecular beam techniques.
J. Crystal Growth **31**, 122-129, 1975. *M*

J. J. Kelly & C. H. de Minjer: An electrochemical study of undercutting during etching of duplex metal films.
J. Electrochem. Soc. **122**, 931-936, 1975 (No. 7). *E*

J. J. Kelly & J. K. Vondeling: The nucleation reaction on photosensitive TiO_2 films.
J. Electrochem. Soc. **122**, 1103-1107, 1975 (No. 8). *E*

J. T. C. van Kemenade & R. K. Eijnthoven: Sintern von ZnO für spannungsabhängige Widerstände.
Ber. Dtsch. Keram. Ges. **52**, 243, 1975 (No. 7). *E*

Th. J. van Kessel: Welke nieuwe mogelijkheden geeft de IC-technologie aan de analoge elektronica?
T. Ned. Elektronica- en Radiogen. **40**, 83-90, 1975 (No. 4). *E*

G. D. Khoe: Power coupling from junction lasers into single mode optical fibres.
First Eur. Conf. on Optical fibre communication, London 1975 (IEE Conf. Publn No. 132), pp. 114-116. *E*

U. Killat: Revised dynamical theory of thermoplastic deformation.
J. appl. Phys. **46**, 5169-5172, 1975 (No. 12). *H*

J. E. Knowles: On the origin of the 'second level of drive' effect in quartz oscillators.
Proc. 29th Ann. Frequency Control Symp., Fort Monmouth (N.J.) 1975, pp. 230-236. *M*

J. Koenings, D. Küppers, H. Lydtin & H. Wilson: Deposition of SiO_2 with low impurity content by oxidation of $SiCl_4$ in a nonisothermal plasma.
Chemical vapor deposition, 5th Int. Conf., publ. Electrochem. Soc., pp. 270-280, 1975. *A*

W. L. Konijnendijk: Structural differences between borosilicate and aluminosilicate glasses studied by Raman scattering.
Glastechn. Ber. **48**, 216-218, 1975 (No. 10). *E*

F. Kools: Herstellung und Kennzeichnung von Hexaferrit-Pulvern und -Suspensionen.
Ber. Dtsch. Keram. Ges. **52**, 213-215, 1975 (No. 7). *E*

G. Kowalski: Suppression of scattered radiation in radiography and improvement of resolution by spatially modulated intensity.
Appl. Optics **15**, 648-655, 1976 (No. 3). *H*

K. E. Kuijk: Het ontwerpen van analoge IC's met behulp van basisschakelingen.
T. Ned. Elektronica- en Radiogen. **40**, 91-97, 1975 (No. 4). *E*

D. Küppers & H. Lydtin: Decomposition of methane on a hot carbon surface after multiple collisions.
J. Crystal Growth **31**, 98-100, 1975. *A*

J. Ladell, A. Zagofsky & S. Pearlman: Cu Kα_2 elimination algorithm.
J. appl. Cryst. **8**, 499-506, 1975 (No. 5). *N*

J. G. M. de Lau, P. F. G. Bongaerts, J. L. H. M. Wijgergangs & A. L. Stuijts: Untersuchung chemischer Inhomogenitäten in Ferrit-Pulvern unter Verwendung des Heißpressens.
Ber. Dtsch. Keram. Ges. **52**, 207-210, 1975 (No. 7). *E*

F. H. de Leeuw & J. M. Robertson: Bubble velocities in $(YLa)_3(FeGa)_5O_{12}$ films.
AIP Conf. Proc. **24**, 601-602, 1975. *E*

F. K. Lotgering: Photomagnetic effects and disaccommodation in Co-doped YIG.
J. Phys. Chem. Solids **36**, 1183-1191, 1975 (No. 11). *E*

C. Loty: A real time oscilloscope and photodetector device with picosecond resolution.
Proc. 2nd ISPRA Nuclear Electronics Symp., Stresa 1975, pp. 439-440. *L*

M. H. van Maaren & W. van Haeringen: Anomalous influence of Ce-impurities on the superconducting transition temperatures in $LaIn_{3-x}Sn_x$.
Proc. 14th Int. Conf. on Low temperature physics, Otaniemi 1975, Vol. 2, pp. 533-536. *E*

R. Madar, G. Jacob, J. Hallais & R. Fruchart: High pressure solution growth of GaN.
J. Crystal Growth **31**, 197-203, 1975. *L*

J. Magarshack, P. Harrop & A. Rabier: Investigation of transferred-electron amplifier diodes with a doping notch.
Philips Res. Repts. **31**, 257-277, 1976 (No. 3). *L*

H. H. van Mal: Stability of ternary hydrides and some applications.
Thesis, Delft 1976. (Philips Res. Repts. Suppl. 1976, No. 1.) *E*

R. Metselaar, M. A. H. Huyberts & H. Logmans: Light-induced changes in permeability of *n*- and *p*-type YIG films.
J. appl. Phys. **46**, 3171-3174, 1975 (No. 7). *E*

K. H. Meyer: Über den Einfluß von Oberwellen auf das Verhalten des Hysteresemotors.
Thesis, Eindhoven 1976. (Philips Res. Repts. Suppl. 1976, No. 3.) *A*

J. Michel, A. Mircea & E. Fabre: Computer analysis of back-surface field silicon solar cells.
J. appl. Phys. **46**, 5043-5045, 1975 (No. 11). *L*

A. R. Miedema, R. Boom* & F. R. de Boer* (* Universiteit van Amsterdam): Simple rules for alloying.
Crystal structure and chemical bonding in inorganic chemistry, editors C. J. M. Rooymans & A. Rabenau, publ. North-Holland, Amsterdam 1975, pp. 163-196. *E*

R. F. Mitchell & R. Stevens: Diffraction effects in small-aperture acoustic surface wave filters.
Wave Electronics **1**, 201-218, 1975 (No. 3). *M*

A. Mitonneau: Investigation of deep traps in GaAs by a capacitive method.
Philips Res. Repts. **31**, 244-256, 1976 (No. 3). *L*

J. F. Olijhoek & H. C. A. Nauts: Anomalies in the low temperature specific heat of $Gd_xEr_{1-x}Rh$ compounds.
Proc. 14th Int. Conf. on Low temperature physics, Otaniemi 1975, Vol. 3, pp. 196-199. *E*

J. W. Orton, A. H. M. Kipperman* & J. A. Beun* (* Eindhoven University of Technology): An experimental study of the electrical properties of the contact between two similar semiconductor crystals.
J. Physics D **9**, 69-82, 1976 (No. 1). *M*

J. A. Pals & L. H. J. Graat: *I-V* characteristics of a superconductive film with a locally applied magnetic field.
Proc. 14th Int. Conf. on Low temperature physics, Otaniemi 1975, Vol. 2, pp. 251-254. *E*

K. Pasedach: Über die Auflösung eines Systems von Integralgleichungen.
Z. angew. Math. Mech. **56**, T 262-263, 1976 (No. 3). *H*

J. Périlhou & J. Kamkar (Hôpital Esquirol, Saint-Maurice): De la réfraction des rayons ultrasonores dans les tissus, de l'influence sur les images et des conséquences pour l'appareillage.
Journée d'étude d'échotomographie en obstétrique et gynécologie, Saint-Maurice 1975, pp. 35-40. *L*

G. Piétri: Towards picosecond resolution. Contribution of microchannel electron multipliers to vacuum tube design.
Proc. 2nd ISPRA Nuclear Electronics Symp., Stresa 1975, pp. 397-405. (*Also in* IEEE Trans. **NS-22**, 2084-2092, 1975 (No. 5).) *L*

J. A. de Poorter & A. Bril: Absolute x-ray efficiencies of some phosphors.
J. Electrochem. Soc. **122**, 1086-1088, 1975 (No. 8). *E*

Th. J. A. Popma & A. M. van Diepen: Non-crystalline $Y_3Fe_5O_{12}$ studied by Mössbauer effect and magnetization.
AIP Conf. Proc. **24**, 123-124, 1975. *E*

W. Puschert: Optisches Heterodyn-Verfahren zur Messung von Betrag und Phase mechanischer Schwingungsamplituden im Angströmbereich.
Feinwerktechnik & Messtechnik **83**, 316-317, 1975 (No. 7). *A*

P. J. Rijnierse, H. Logmans, R. Metselaar & W. T. Stacy: Optical measurement of magnetic anisotropy in thin garnet films.
Appl. Phys. **8**, 143-150, 1975 (No. 2). *E*

A. P. Severijns: Compact design for dilution refrigerators.
Proc. 14th Int. Conf. on Low temperature physics, Otaniemi 1975, Vol. 4, pp. 25-28. *E*

P. J. Severin & F. C. Eversteyn: On the correction to be applied to the thickness of an epitaxial layer measured with infrared multiple interference.
J. Electrochem. Soc. **122**, 962-964, 1975 (No. 7). *E*

J. M. Shannon, K. Board, S. D. Brotherton & A. Gill: Charge coupled F.E.T. devices (C.C.F.E.T.).
IEEE 1975 Int. Electron Devices Meeting, Washington, pp. 320-323. *M*

F. A. Staas & H. C. M. van der Waerden: A dilution refrigerator with circulation of both ^{3}He and ^{4}He.
Proc. 14th Int. Conf. on Low temperature physics, Otaniemi 1975, Vol. 4, pp. 17-20. *E*

H. E. M. Stassen (Philips Elcoma Division, Eindhoven), **J. G. M. de Lau & D. Veeneman:** Herstellung dichter Mn-Zn-Ferrite für Magnetköpfe.
Ber. Dtsch. Keram. Ges. **52**, 204-207, 1975 (No. 7). *E*

M. D. Sturge, E. Cohen, L. G. Van Uitert (all with Bell Laboratories, Murray Hill, N.J.) **& R. P. van Stapele:** Microscopic order parameters in $PrAlO_3$.
Phys. Rev. B **11**, 4768-4779, 1975 (No. 12). *E*

A. Thayse: La détection des aléas dans les circuits logiques au moyen du calcul différentiel booléen.
Digital Processes **1**, 141-169, 1975 (No. 2). *B*

C. van Trigt & N. Blom: Solution of a multi-level model of an optically thick sodium plasma.
J. quant. Spectrosc. rad. Transfer **15**, 905-917, 1975 (No. 10). *E*

T. S. te Velde: The production of the cadmium sulphide - copper sulphide solar cell by means of a solid-state reaction.
Energy Conversion **14**, 111-115, 1975 (No. 3/4). *E*

J. D. B. Veldkamp & M. I. L. Uijterschout (Technische Hogeschool Twente): The variation of Young's moduli with temperature of α SiC.
Proc. Brit. Ceramic Soc. **25**, 211-216, 1975. *E*

K. Weiss: Transport und mechanisches Gleichgewicht in einem elastischen Kristall.
Z. phys. Chemie neue Folge **96**, 215-228, 1975 (No. 4-6). *E*

G. F. Weston: Plasma panel displays.
J. Physics E **8**, 981-991, 1975 (No. 12). *M*

G. F. Weston: Gas discharge data displays.
Progress in electro-optics, editor E. Camatini, publ. Plenum Press, New York 1975, pp. 127-160. *M*

M. C. H. M. Wouters, H. M. Eijkman & L. J. van Ruyven (all with Philips Semiconductor Development Laboratory, Nijmegen): The electrical conductivity of silicon between 500 °C and 1200 °C.
Philips Res. Repts. **31**, 278-283, 1976 (No. 3).

Contents of Philips Telecommunication Review **34**, No. 2, 1976:

H. Bouwman, H. J. de Jong & J. Lindelöw: Philips teleprinters PACT 200 and 500 (pp. 45-54).
G. Baltzer: RUT 200/500 teleprinter for military applications (pp. 55-63).
N. H. Hamers & W. Hermes: 1400 km TV transmission on coaxial cable (pp. 64-71).
J. B. Buchner: Ternary line codes (pp. 72-86).

Contents of Electronic Applications Bulletin **33**, No. 4, 1976:

Components for industrial microwave power generators (pp. 151-156).
Audio power amplifiers with Darlington output transistors (pp. 157-169).
A. J. M. Coolen: The effect of temperature on u.h.f. circulator input v.s.w.r. (pp. 173-185).
J. A. den Ouden: Single chip, integrated digital voltmeter (pp. 187-198).
H. F. Tack: Microwave measurements on components fitted with SMA connectors (pp. 199-203).
Nomogram: the inductance of multi-layer, air-cored coils (pp. 204-205).

Contents of Mullard Technical Communications **13**, No. 130, 1976:

M. H. Dryden: Design for reliability (pp. 395-432).

Contents of Mullard Technical Communications **14**, No. 131, 1976:

A. J. Terry: Switched-mode field deflection for 20AX television using TDA2600 (pp. 2-18).
P. J. Hart: Transmitter design with v.h.f. broadband amplifier modules (pp. 19-43).
J. E. Saw: Microwave doppler intruder alarms (pp. 44-52).

Volume 37, 1977, No. 1 pages 1-28 Published 30th June 1977

PHILIPS TECHNICAL REVIEW

VOLUME 37, 1977, No. 2/3

Annoyance due to modulation noise and drop-outs in magnetic sound recording

D. J. H. Admiraal, B. L. Cardozo, G. Domburg and J. J. M. Neelen

It is possible to carry out many kinds of physical measurement with great accuracy on a product intended for human use and still not obtain a conclusive answer to the question of the product's usability. This is because human perception also enters into the picture. If the investigation is extended to include a representative number of human subjects it will be discovered, however, that human perception obeys certain laws. These can often be quantified, as has been done for example in the theory of the chromaticity diagram and in the international definitions of loudness. More particularly in the context of noise abatement, a further step has been taken and efforts have been made to express the concept of annoyance in numerical terms, leading to reproducible results. Something of the same sort is attempted in the article below, which deals with the annoyance caused to the listener by two imperfections of magnetic sound recording that are hard to avoid: modulation noise and the spontaneous occurrence of short interruptions or 'drop-outs'. The subject belongs naturally to the range of studies performed by the Institute for Perception Research (IPO), where the authors carried out the work.

Noise and 'drop-outs' in magnetic sound recording

The recording of sound on magnetic tape has reached a high degree of perfection. An inherent imperfection of the process, however, is the noise added to the original audio signal. When the conditions are good the noise may be barely perceptible, but under less favourable conditions it is distinctly audible and can sometimes be annoying. In this article we shall be concerned with the audibility of one particular type of noise and with the annoyance it causes.

There are in fact two kinds of noise. In the first place there is the background noise, which is always present during playback and is particularly obtrusive in the absence of a signal or when the signal is weak. Efforts are made to reduce this noise by improving the quality of the tapes and also by magnetizing the tape as fully as possible. One method includes a process of signal compression and expansion (the Dolby system). Another approach is to attenuate the highest frequencies during the reproduction of weak signals, since these are the components of the noise that are most disturbing to the listener ('Dynamic Noise Limiter').

Drs B. L. Cardozo is with the Institute for Perception Research, Eindhoven; Ing. D. J. H. Admiraal, Ing. G. Domburg and Ir J. J. M. Neelen were formerly with the Institute. Ing. G. Domburg is now with the Philips Medical Systems Division, Eindhoven, and Ir J. J. M. Neelen is with Hollandse Signaalapparaten B.V., Hengelo.

Apart from this noise, which is an independent addition to the signal and may therefore be called additive noise, there is also what is termed multiplicative noise. This only occurs when a signal is recorded on the tape (i.e. during the 'modulation' of the tape); its strength is proportional to that of the signal. It takes the form of amplitude modulation of the signal. It is this kind of noise, called 'modulation noise', that will be dealt with here. Under certain conditions modulation noise can be annoying, as appears from listening tests that we have carried out and which will be described below. Its reduction deserves just as much attention as that of additive noise.

Another annoying effect that has been the subject of considerable attention is the effect known as 'drop-out', i.e. short interruptions (really attenuations) of the signal that occur during the playback of magnetic tapes. They may be caused by inhomogeneities in the magnetic layer, or they may be due to dirt, fingerprints, creases in the tape, etc. This effect is most troublesome with cassette tapes. For a fraction of a second the signal almost or completely vanishes. The effect might be regarded as a very low-frequency component of modulation noise, but in an oscillogram of the playback signal (*fig. 1*) it can be clearly distinguished from the

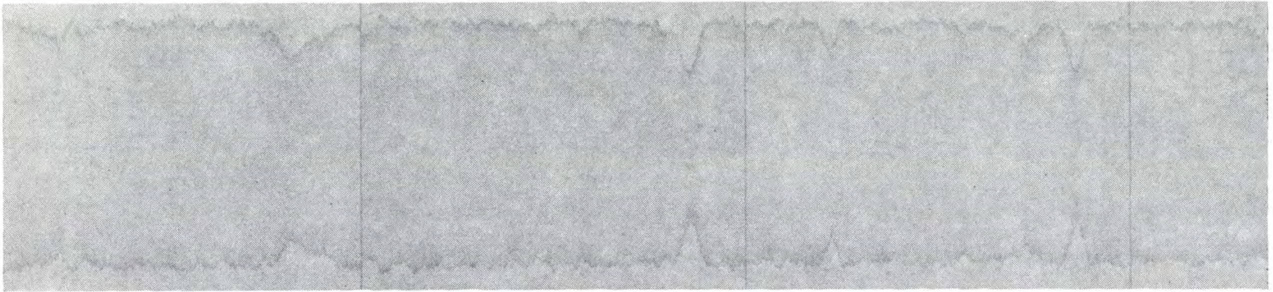

Fig. 1. Oscillogram of a sinusoidal tone at 5000 Hz, obtained from a magnetic tape. It shows, in addition to the low-frequency amplitude modulation in which the modulation noise appears, a number of short attenuations in the signal amplitude ('drop-outs'). The distance between two vertical lines corresponds to 0.1 second.

other amplitude variations, and it makes a quite different impression on the listener.

Our listening tests have shown that the annoyance caused by drop-outs depends on their duration, the degree of signal attenuation and their distribution in time. A measuring instrument has been developed in which these aspects are evaluated in the same way as they were in the listening tests; the instrument gives a reading of the results in terms of a numerical 'annoyance rating'. Some forty of these instruments are now being used in the laboratories of magnetic-tape manufacturers and users all over the world [1].

Causes of modulation noise

Although in this article we are only concerned with the perception and subjective evaluation of the interfering effects mentioned above, it will nevertheless be useful to touch briefly on the causes of modulation noise.

An important cause is the inhomogeneous distribution of the magnetic particles in the tape. The particles each form a single magnetic domain and are thus fully magnetized; consequently they tend to form clusters during the manufacture of the tape [2]. In magnetizing the tape the maximum magnetization will consequently vary from place to place. Another contributory factor is that the thickness of the magnetic layer is not completely uniform.

Yet another important cause of modulation noise is the variation in the gap between tape and magnetic head. This may be due to surface roughness of the tape, but also to soiling of the head or of the tape. As a result there are fluctuations in the field that records the signal on the tape. The resulting modulation noise (called 'asperity noise' [3]) is often the most serious in practice.

In this last form of modulation noise the lowest frequencies are strongest. The spectral power density (noise power per Hz bandwidth) can be approximately represented by a curve that is flat below 35 Hz and decreases by 6 dB per octave above it; see *fig. 2.*

Hearing threshold and masking

The characteristics of the ear obviously play an important part in the perception of modulation noise. In the first place its perception depends on whether or not the modulation noise exceeds the threshold of audibility. The lower curve in *fig. 3* gives the threshold for single (sinusoidal) tones; a logarithmic plot is given of the intensity required for a tone of a particular frequency to be just perceptible to the average ear. The sensitivity of the human ear is highly frequency-dependent and is greatest between 3000 Hz and 4000 Hz.

Whether or not a sound is heard depends not only on its intensity but also on whether or not other sounds are present. A stronger sound may mask a weaker one, i.e. make it inaudible. In this way the modulation noise is often masked by the sound signal itself. The masking is also frequency-dependent, and is particularly pronounced at closely adjacent frequencies. This can be seen from the other curves in fig. 3, which relate to the masking of single tones by noise in a narrow frequency band around 1000 Hz; the nearer the tone is to 1000 Hz, the stronger it must be to be heard. As can be seen, the masking effect of the noise band extends much farther towards the higher frequencies than towards the lower frequencies.

Audibility and annoyance

A sound, or more generally an acoustic effect, can be made so weak that it becomes inaudible to the human ear. When the sound is then made stronger again, the threshold of audibility will eventually be exceeded. In this process it is essential that the listener should know the sound and thus be able to recognize it. Only then does a threshold value have any significance. In our experiments we always ensured that the subjects taking part were thoroughly familiar with and capable of recognizing the modulation-noise effect and the drop-outs. This is vital to the manner in which the degree of annoyance is determined. Our initial assumption is that the annoyance increases monotonically with the mod-

ulation depth, or, in the case of the drop-outs, with the modulation depth and also with the duration of the interruption.

To indicate the annoyance due to unwanted sound in terms of a number on a scale, we can take the threshold of audibility as the zero of the scale. We also found that after some practice the subjects could in fact give quantitative estimates of annoyance that increased monotonically with the intensity of the unwanted sound. We therefore asked the subjects to give their judgement of the annoyance h due to the modulation noise in certain passages of music, on the following scale:

$h = 0$ no modulation noise audible,
1 modulation noise audible but not annoying,
2 modulation noise annoying,
3 modulation noise very annoying.

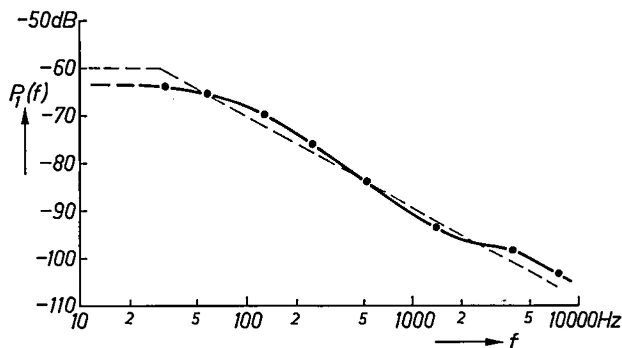

Fig. 2. Frequency spectrum of modulation noise measured on a tape containing a recording of a sinusoidal tone at 1000 Hz (*solid curve*), and curve approximating to it (*dashed*). $P_1(f)$ is the power density of the noise, i.e. the power in a frequency band 1 Hz wide, given in dB relative to the power of the sinusoidal tone. f frequency.

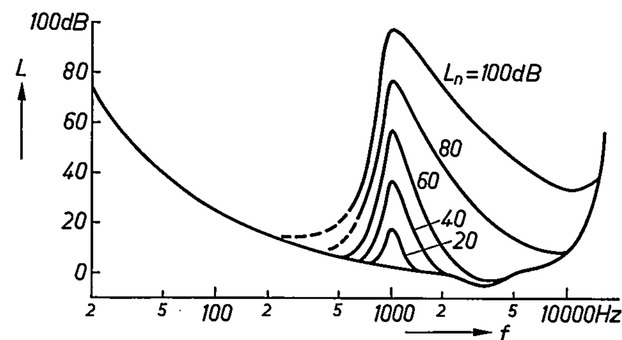

Fig. 3. Threshold curves for the human ear. The lower curve gives the hearing threshold for sinusoidal tones, and is a plot of the level L which a sinusoidal tone of frequency f must have to be only just audible to the average human ear (0 dB corresponds to a sound-pressure amplitude of 2×10^{-5} N/m²). The other curves show how this threshold curve changes when noise at a level L_n is present in a narrow band around 1000 Hz. The narrow noise band has a masking effect here, which is particularly marked at the higher frequencies. (From E. Zwicker and R. Feldtkeller, Das Ohr als Nachrichtenempfänger, 2nd edition, S. Hirzel Verlag, Stuttgart 1967.)

The subjects were allowed not only to interpolate on this scale but also to extrapolate. Extrapolation is important since the annoyance scale does not have any natural upper limit as it has a natural lower limit. Fixing an upper limit would face the subject with a problem: he would be inclined to evaluate the most annoying stimulus at the highest scale value permitted. Since he does not know beforehand whether there is an even more annoying stimulus to come, he will tend to avoid the upper limit.

Modulation noise

A problem in listening tests with modulation noise is that it is difficult to present the subjects with music without modulation noise for comparison. This would require music that had not in any way been recorded.

Logically, we should therefore have had the same music played live during the listening tests. But this seemed too drastic a solution in the circumstances. In any case, we found that it was not absolutely necessary, since tape recordings of high quality are available (the 'master tapes' used in making records) on which the modulation noise is negligible; indeed, artificial modulation noise has to be added for the audibility determination.

In determining the audibility of modulation noise we also used sinusoidal signals generated directly by electrical methods. In addition, tape recordings of these signals were made with very low modulation noise, and these recordings again confirmed that, provided sufficient precautions are taken in these experiments, there is no need to avoid the use of recorded music.

Audibility

In the design of listening tests in which the subjects are asked to assess the annoyance they experience from modulation noise, it is important to know where the limits of audibility lie. We therefore carried out preliminary audibility tests, first using well defined signals of simple form, including a single sinusoidal tone modulated by white noise, i.e. noise with a uniform spectral power density P_1. This noise was limited in frequency by a lowpass filter with a variable cut-off frequency f_n. The modulated signal then consists of a carrier at the frequency f_c of the sinusoidal tone with two sidebands extending to $f_c - f_n$ on one side and to $f_c + f_n$ on the other.

The amplitude of these sidebands depends on the modulation depth. This indicates the ratio of the mod-

[1] The inclusion of a measurement of this type in an international standard on which to judge the quality of audio tapes is currently being studied in the IEC (International Electrotechnical Commission).

[2] G. Frens, H. F. Huisman, J. K. Vondeling and K. M. van der Waarde, Suspension technology, Philips tech. Rev. **36**, 264-270, 1976 (No. 9).

[3] E. G. Trendell, The measurement and subjective assessment of modulation noise in magnetic recording, J. Audio Engng. Soc. 17, 644-653, 1969.

ulating-signal amplitude to the amplitude of the carrier. In the case of our noise band, however, we cannot simply speak of an amplitude. We therefore put the modulation depth at $m = 1$ when, as in the modulation by a sinusoidal tone, the total mean power P_n of the sidebands is half that of the carrier P_c; as an equation:

$$m = \sqrt{2P_n/P_c}. \qquad (1)$$

In practice we prefer to use the signal-to-noise ratio S/N, i.e. the difference in dB between the level of the wanted signal and that of the modulation noise:

$$S/N = -10 \log_{10}(P_n/P_c)\,\text{dB} = -20 \log_{10} m + 3\,\text{dB}. \quad (2)$$

The larger the value of S/N, the less is the likelihood that the noise will be audible.

We are interested in the signal-to-noise ratio $(S/N)'$ at which the modulation noise is only just audible. This depends on the frequency and amplitude of the sinusoidal tone and on the highest frequency f_n of the noise. We can determine this audibility limit experimentally with the arrangement shown by the block diagram in *fig. 4*, where a subject hears the signal through the headphones and can adjust the level of the noise to his audibility threshold. The mean result obtained in this experiment by a number of subjects with a sinusoidal signal at 1000 Hz is indicated by the measured points in *fig. 5*. We see that as the bandwidth of the noise increases, the noise level has to decrease very rapidly if the modulation noise is to remain inaudible.

An explanation for this, and for the clearly defined plateau at 1000 Hz, can be found from the threshold curves in fig. 3. We consider the threshold curve for a signal level of 80 dB and show it in *fig. 6* on a linear frequency scale, since this simplifies the representation of the sinusoidal tone with the two sidebands of equal width.

Depending on the bandwidth f_n of the modulating noise, there are four different cases.

A. The noise sidebands remain within the 'critical bandwidth' B_c. The human ear can integrate the incident acoustic energy within such a critical frequency band into a single total impression. In our case the noise will not then be distinguishable from the sinusoidal tone, but will be heard, if the noise level is high enough, as a distinct fluctuation in the amplitude of the sinusoidal tone. The critical band for our experimental tone of frequency $f_c = 1000$ Hz is about $\frac{1}{6} f_c$ wide; the noise bandwidth in this case is thus given by $f_n < \frac{1}{12} f_c \approx 80$ Hz. It appears from the measurements (fig. 5) that the audibility threshold here lies at a signal-to-noise ratio $(S/N)' \approx 20$ dB. It follows from equation (2) that this corresponds to a modulation index of $m = 0.14$. The definition we have taken for the modulation index for noise signals implies that at $m = 1$ the standard deviation σ of the noise is equal to $1/\sqrt{2}$ times the amplitude a of the carrier. If $m = 0.14$, then $\sigma = 0.14a/\sqrt{2} = 0.1a$. This means that the amplitude fluctuates between $0.9a$ and $1.1a$ for 68% of the time, a variation of $\pm$ 0.8 dB. It is known that these are in fact fluctuations in level that are only just audible.

B. The noise exceeds the critical bandwidth, but has not yet reached the frequency f_1, where there is a minimum in the masked hearing threshold. We see in fig. 6 that the 'left shoulder' of the noise spectrum, i.e. the frequencies around $f_c - f_n$, will now be audible first. Because of the steep left-hand side of the masking curve, the audibility threshold falls rapidly with rising f_n (the steeply falling part of the curve in fig. 5).

C. The noise extends beyond f_1. The modulation noise is audible at f_1, irrespective of where the lower limit of the noise lies between 0 Hz and f_1 Hz. This explains the plateau in fig. 5.

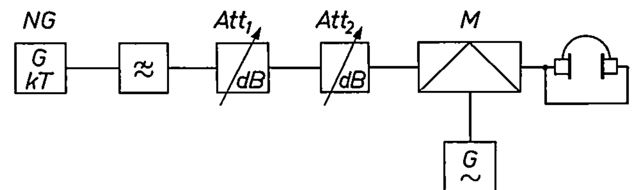

Fig. 4. Experimental arrangement for determining the audibility threshold of modulation noise, when the signal consists of a single sinusoidal tone. The noise, from a noise generator *NG*, is limited in bandwidth by a lowpass filter to a frequency f_n before being passed through two variable attenuators Att_1 and Att_2. In the modulator *M* a sinusoidal tone from a sine-wave generator is modulated by this noise; the subject hears the output signal through headphones. The subject adjusts the attenuator Att_2 to a level at which he can only just hear the modulation noise. There is a risk that in doing so he will be unconsciously influenced by the setting for a previous experiment; the experimenter therefore always sets the attenuator Att_1 to a different position between the individual experiments.

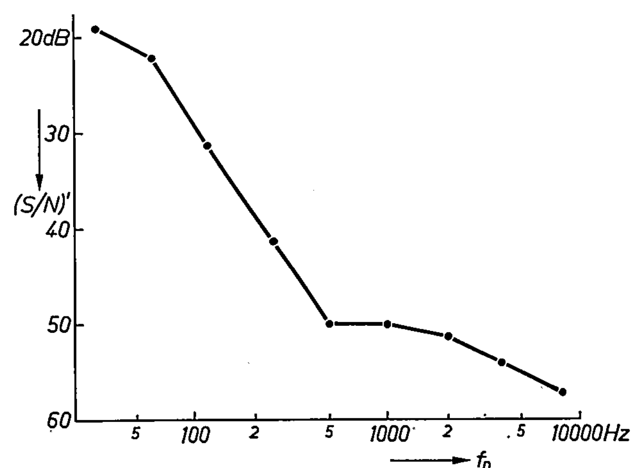

Fig. 5. Audibility threshold of modulation noise for a sinusoidal tone at 1000 Hz. The signal-to-noise ratio $(S/N)'$ at which the noise is only just audible is plotted as a function of the bandwidth f_n of the noise modulating the sinusoidal tone. The tone has a sound-pressure level of 80 dB.

D. If the bandwidth of the noise is greater than 1000 Hz, then 'the lower sideband is reflected against 0 Hz'. This implies that the energy content of the lower part (up to f_n — 1000 Hz) is doubled, so that the level rises by 3 dB. In fig. 6 this is shown for $f_n = 1500$ Hz, and the doubled sideband thus extends beyond f_1. Because of this the threshold has still fallen by 3 dB; the modulation noise is audible at f_1 as it was before.

On the right-hand side of the masking curve the hearing threshold has a second minimum, whose frequency we call f_2. For the masking curve relating to a signal level of 80 dB, both minima are at about the same level (fig. 3). For the 60-dB curve, however, the second minimum is about 10 dB lower. If the noise band at a signal level of 60 dB is made so wide that the upper sideband reaches this minimum, then modulation noise at a level about 10 dB lower becomes audible, and we would then have to distinguish a fifth and subsequent cases.

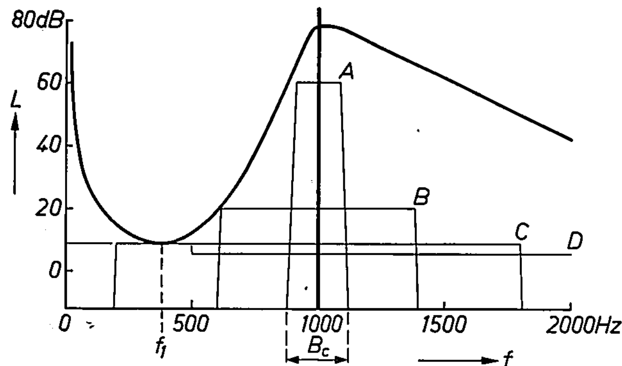

Fig. 6. The threshold curve for $L_n = 80$ dB from fig. 3, displayed on a linear frequency scale. The figure includes the frequency spectrum of a sinusoidal tone at 1000 Hz modulated in amplitude by noise in the band 0 to f_n Hz, for different values of f_n (cases *A*, *B*, *C*, *D*). In each case the level is shown at which the modulation noise is only just audible. B_c critical bandwidth at 1000 Hz. f_1 frequency of the left-hand minimum of the threshold curve.

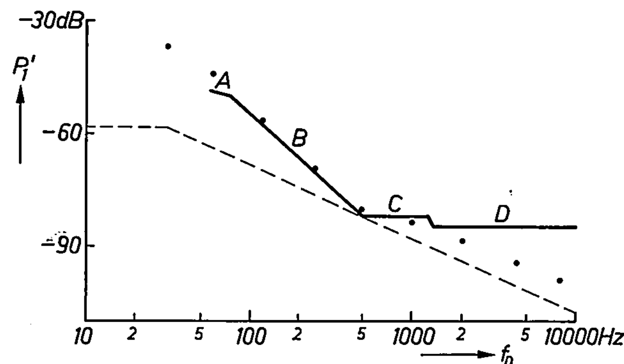

Fig. 7. Power density $P_1'(f)$ at which the noise sidebands of a sinusoidal tone at 1000 Hz are only just audible; the sinusoidal tone is amplitude-modulated by white noise in a frequency band $0 - f_n$. The curve was derived from the masked hearing threshold for a sinusoidal tone at a level of 80 dB (fig. 3). The measurement points are from fig. 5. The dashed curve gives the frequency spectrum of modulation noise of a level that can only just be heard.

We shall confine ourselves here, however, to the one case of a sinusoidal tone of 80 dB. From the foregoing we can deduce the power density P_1' (the power per Hz of bandwidth) that the noise sidebands should have as a function of the cut-off frequency f_n for the noise to be raised to the audibility threshold. This is shown in *fig. 7*. In this figure we have repeated the measurement points from fig. 5, but now the power density of the noise is plotted instead of the signal-to-noise ratio. In both cases the power of the 1000-Hz sinusoidal tone is the reference (0 dB), but since the power in 1 Hz of the noise band is very small, the ratios to this reference, and hence the difference in decibels, are much greater. It can be seen that the calculated threshold levels are in reasonable agreement with the measurements.

From fig. 7 we can also read off the maximum permissible level of the modulation noise occurring in practice around a sinusoidal tone of 1000 Hz if the noise is to remain inaudible. For this purpose we can draw in fig. 7 the approximating spectrum from fig. 2. As soon as the modulation-noise spectrum goes above the dashed curve, the modulation noise becomes audible, first of all at frequencies around f_1.

Annoyance

Annoyance may be said to be experienced when the modulation noise occurs with a signal having a meaningful content, and that is usually not a sinusoidal tone but music. Here, however, the *audibility* of the noise is different from that in the experiments described above; the noise is now less easily perceived. This is because its occurrence is unpredictable, owing to the continual changes of volume and frequency in music. What is more, music never consists of a single sinusoidal tone but always contains more than one frequency and often very many frequencies, so that the noise may be masked over a large part of the hearing spectrum.

It follows from this that recordings of a solo instrument will be more vulnerable than those of an orchestra. Looking for the most vulnerable situation in which to carry out the annoyance determinations, we compared twelve solo instruments with each other: violin, cello and double-bass; piccolo, flute, oboe, clarinet and bassoon; trumpet, horn, trombone and tuba. A passage played by each instrument, lasting 25 seconds, was recorded a number of times, modulated by noise at different levels. The subjects were asked to make an assessment in terms of the *h*-scale described above. The most vulnerable instrument proved to be the flute, followed by the piccolo, oboe and horn. The double-bass, cello, tuba and bassoon were relatively unaffected. This confirms that modulation noise is heard most easily in music with a single (high) fundamental tone and with a small number of higher harmonics.

The somewhat breathy character of the flute did not apparently lessen the audibility of the modulation noise, particularly in its third octave.

We also tried to find the most sensitive listening conditions. These were to listen through headphones to a stereophonic signal. The annoyance determinations were carried out under these conditions, incoherent noise being presented in the left-hand and right-hand channels as it would be in actual listening to stereophonic recordings.

After these preparations we were ready to begin with the annoyance determination proper. This was done in a listening experiment on a somewhat larger scale. Eighteen subjects took part, including eight audio technicians who were professionally responsible for the quality control of sound recordings.

These subjects were presented with 12 identical fragments of music each lasting 20 seconds and recorded in random order with six different signal-to-noise ratios; each signal-to-noise ratio was thus presented twice. The modulation noise approximated the actual frequency spectrum, as described earlier (fig. 2): flat up to 35 Hz, and decreasing by 6 dB per octave above this frequency. The subjects assigned an h-value to each fragment.

The series of 12 fragments belonged to different categories: orchestral (Handel, *Water Music*), piano (Schumann, First Sonata) and a passage from a flute solo (Debussy, *Le Syrinx*). In addition to these fragments the subjects were also occasionally presented with a sinusoidal tone of 1000 Hz (also lasting 20 seconds), again recorded on magnetic tape. This was done to enable us to deduce the influence of the use of magnetic recordings from a comparison with the experiments using a directly generated sinusoidal tone. All the fragments were presented at a volume such that the loudest passages were 70 dB above the threshold of audibility.

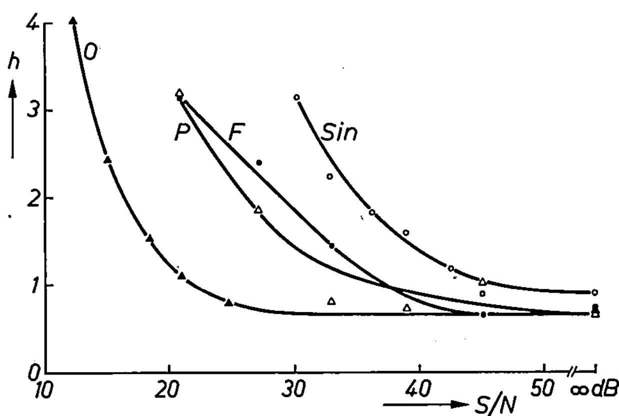

Fig. 8. The annoyance value h of modulation noise at different signal-to-noise ratios S/N for different categories of music and for a sinusoidal tone at 1000 Hz. O orchestra. P piano. F flute. *Sin* sinusoidal tone. The results are mean values for eighteen subjects. The fact that the mean values are not at $h = 0$ (modulation noise inaudible) even in the absence of deliberately applied modulation noise, must be attributable to the tendency of subjects to avoid extreme values of the h-scale.

The means of the assessments made by the eighteen subjects are presented in *fig. 8*. The results confirm that flute music is the most sensitive of all to modulation noise. For flute music the modulation noise is perceptible as soon as the signal-to-noise ratio goes below about 40 dB. We know (see fig. 6) that the modulation noise then becomes audible in a frequency band near 500 Hz, and is thus clearly distinguishable from the music.

With orchestral music, on the other hand, the modulation noise does not become audible until the signal-to-noise ratio is less than about 20 dB. Here only the very low-frequency components of the noise are not masked by the signal and these are heard as an audible amplitude modulation of the music. With increasing modulation depth this is soon experienced as very annoying: curve O in fig. 8 rises steeply.

With the sinusoidal tone the modulation noise becomes audible when the signal-to-modulation-noise ratio is less than about 45 dB. The experiments described above can be compared with experiments using a 1000-Hz sinusoidal tone that had not been recorded on tape by referring to the dashed curve in fig. 7; this gives the spectral power density of modulation noise with the spectrum used here, which is only just audible with a 1000-Hz sinusoidal tone at 80 dB. In this case, a recalculation gives a signal-to-noise ratio of 42.5 dB. The figure of about 45 dB found with a sinusoidal tone on tape agrees sufficiently well with this to make it reasonable to assume that the modulation noise inherent in this tape recording did not play any significant role.

Drop-outs

As we saw earlier, the short interruptions (drop-outs) that may occur during the playback of a magnetic tape can be attributed not only to inhomogeneities in the tape but also to dirt, creases in the tape, etc. Nevertheless, there are considerable differences on this point between various types of tape, and a low number of drop-outs is regarded as an indication of tape quality [4].

The drop-outs vary in duration from a few milliseconds to more than 100 milliseconds; the short drop-outs, however, are much more numerous than the long ones. The attenuation D is generally lower in the short drop-outs, since the level seldom changes at a rate faster than 1 dB/ms.

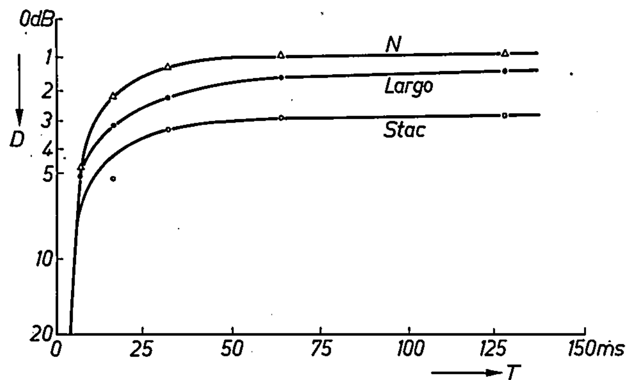

Fig. 9. The depth D which drop-outs of duration T must have to be only just audible. Curve N relates to 'white' noise, curve *Largo* to slow, sustained music and curve *Stac* to staccato music. Mean values for two subjects for regular repetition of the effect at a frequency of 2 Hz.

Drop-outs of this kind are difficult to avoid entirely. In sound recording it is sufficient if they cause no significant perceptual disturbance. It is therefore important to examine the conditions under which they are audible — depending also on the programme on the tape — and, going a step further, to consider how much annoyance they cause when they are audible. This annoyance can then be a measure of the quality of the tape in this respect. The answer to these questions can again only be obtained from listening experiments in which the questions are put to the subjects.

To determine audibility and annoyance, it is desirable to have drop-outs whose parameters can be varied. A special instrument was therefore built for the listening experiments; this instrument permits attenuations of variable duration and depth to be inserted in a signal. The fall and rise times of the signal can also be varied.

Audibility

The effect we are considering may be regarded as amplitude modulation of short duration. This means that sidebands will appear for a short time in the frequency spectrum. These sidebands are most likely to be heard when the acoustic signal itself is a narrow-band signal. When a sinusoidal tone drops out and recovers sufficiently quickly clicks can in fact be heard which are louder the steeper the transition.

In reality we rarely encounter pure sinusoidal tones, so that clicks are not heard. For an initial exploratory audibility experiment we therefore chose a signal consisting of 'white' noise; even when the transitions are steep, no clicks are heard.

This initial experiment was carried out with two subjects, who heard the noise signal through headphones. At a rate of twice per second the signals were then interrupted for periods of 4, 8, 16, 32 and 64 milliseconds; the subjects were asked to adjust the depth of the attenuations to a level at which they were only just audible. The settings chosen by the two subjects showed good agreement; the mean results are given as curve N in *fig. 9*. Attenuations lasting 4 ms are found to be inaudible in white noise, however deep; longer attenuations, on the other hand are found to be audible when their depth is only 1 dB.

To make the experiments more realistic, we repeated them using music. Since the nature of the music was likely to have some influence, two contrasting pieces were chosen: one was a slow and solemn piece (Handel's '*Largo*' arranged for string orchestra) and the other was a dynamic and staccato piece (Schubert's *Marche Militaire* No. 1 played by a symphony orchestra). The results are also given in fig. 9. As might be expected, the interruptions in staccato music are not so readily audible as in sustained music.

It may in any case be concluded from these audibility experiments that interruptions shorter than 10 ms are in practice inaudible. When interpreting the results it should also be borne in mind that the perceptibility of the drop-outs is virtually at a maximum, because of the periodic repetition used and because the subject can adjust the threshold himself. In practice the drop-outs occur at unpredictable moments and the attenuations must therefore be deeper for them to be audible. We shall return to this point presently. The limits of audibility thus found provide indications as to how long and how deep the drop-outs have to be in listening experiments designed to determine their annoyance value.

Annoyance

The subject's assessment of the annoyance caused by drop-outs will naturally depend to a great extent on how interested he is, on the nature of the music and on the listening conditions. We have already mentioned that the effect is more annoying in slow and sustained music than in fast, staccato music; the interruptions are also more noticeable in recordings with a great deal of reverberation than in those with little reverberation, and more noticeable with solo instruments than in orchestral playing. More annoyance is experienced with single-track recordings than with stereophonic two-track recordings, where the two tracks are not usually affected simultaneously. The drop-outs are more clearly perceptible when listening through headphones than when listening to loudspeakers; sound

[4] W. van Keuren, An examination of drop-outs occurring in the magnetic recording and reproduction process, J. Audio Engng. Soc. 18, 2-19, 1970.

reflections in the room then appear to have some smoothing effect.

To avoid having to differentiate the results to allow for all these conditions, we concentrated the experiments on the worst case: sustained music with much reverberation, heard through headphones. Very suitable pieces were an organ solo (M. E. Bossi, *Thème et variations*, Op. 115) and a violin solo (J. S. Bach, Sonata No. 1 in G, BWV 1001).

To allow more weight to be attached to the annoyance evaluations a larger number of subjects was selected: fourteen, including six audio technicians. In assessing a number of fragments of music they were asked to express their opinion in a numerical value on the h-scale referred to above.

The annoyance of the short drop-outs depends partly on whether they occur in isolation or in groups. In the listening experiments the two cases were kept distinct. First of all, fragments of music 20 seconds long were played in which one drop-out occurred with a length of 10, 30, 128 or 474 ms and a depth of 4, 8 or 16 dB (the combination of 10 ms and 4 dB was omitted). The annoyance values were averaged over all the subjects and over all the pieces of music and the result is shown in *fig. 10*. The scatter in the values that were averaged was such that 95% fell within a region of 0.2 to 0.5 units. In this figure, curves for $h = 0, 1, 2, 3$ have been interpolated between the measured values.

The h-scale is seen to have been fully used by the subjects, and there was even some extrapolation beyond $h = 3$. The annoyance experienced from a drop-out longer than 100 ms is apparently not very dependent on the duration, and this dependence is greatest when the attenuation is very high.

Fig. 10 also shows the audibility threshold for slow and sustained music, as represented by the *Largo* curve in fig. 9. As can be seen, this does not coincide with the curve $h = 0$ but lies about 1.5 dB above it. The difference can be explained from the fact that the signal did not drop out at fixed times during the annoyance experiments, but unexpectedly, and furthermore the subjects could not adjust the magnitude of the attenuation to the audibility threshold. The curve $h = 0$ is therefore more realistic than the *Largo* curve.

The effect of repetition on the annoyance experienced was investigated by introducing the drop-outs in the same piece of music not once but twice, four times or eight times; in this case the drop-out duration was always 31 ms and the attenuation 8 dB. The annoyance then appears to increase almost linearly with the number of drop-outs per fragment (*fig. 11*), at least as long as the drop-outs do not follow one another too rapidly. If the interval between them becomes less than 1 s, this causes additional annoyance (*fig. 12*).

The DAMA annoyance meter

For comparing different tape samples the manufacturer cannot of course keep on recruiting subjects to take part in listening experiments. The DAMA annoyance meter was therefore designed ('Drop-out Annoyance Measuring Apparatus'). A photograph is shown in *fig. 13*. This instrument detects short interruptions during the playback of the tape, and on the basis of

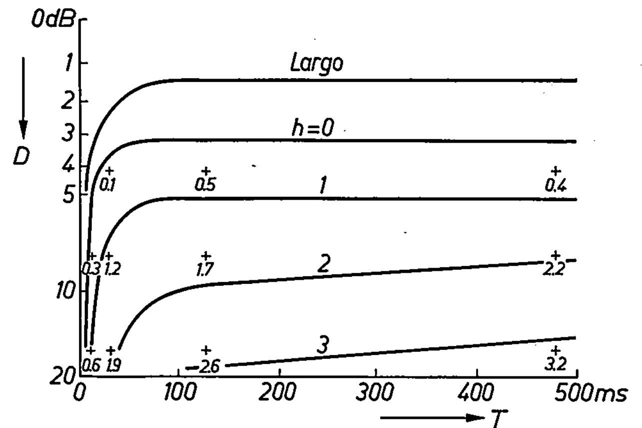

Fig. 10. Lines of equal annoyance rating h, drawn in a field of annoyance evaluations of drop-outs of duration T and depth D. The experiments were made with fragments of music lasting 20 s, each containing one drop-out. The h-values at the measured points are the mean assessments for 14 subjects. The *Largo* curve from fig. 9 is repeated here.

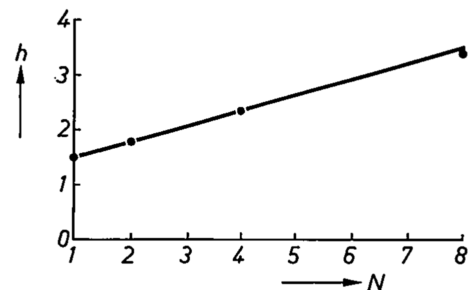

Fig. 11. The annoyance rating h (mean for 14 subjects) plotted against the number of drop-outs N contained in one fragment of music lasting 20 s. Each additional drop-out increases the annoyance rating h by about $\frac{1}{4}$.

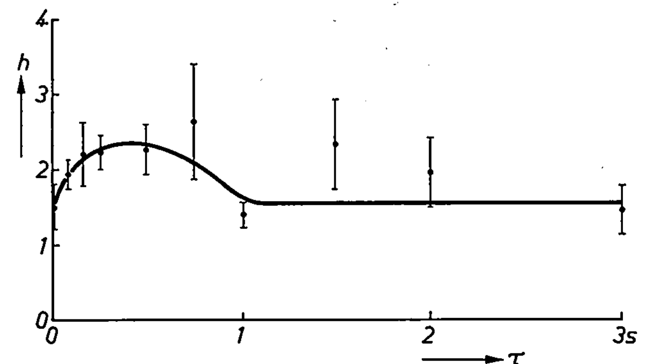

Fig. 12. When the time τ between two drop-outs is shorter than about one second, the annoyance caused is greater than that corresponding to the curve in fig. 11. If the h-values there are reduced to $N = 1$, i.e. if they are reduced by $\frac{1}{4}(N - 1)$, the result is $h \approx 1\frac{1}{2}$. If the interval τ is taken into consideration, however, this h-value only applies when $\tau > 1$ second.

Fig. 13. The DAMA annoyance meter ('Drop-out Annoyance Measuring Apparatus'), which automatically determines the annoyance ratings of drop-outs in the signal on an audio tape.

their duration, depth and frequency it calculates an annoyance value that links up as closely as possible with the findings of the listening experiments described [5]. The instrument gives a digital reading of the annoyance value, which can also be recorded on paper. The measurements are carried out on tapes on which a continuous sinusoidal tone, typically at 3000 Hz, is recorded.

The instantaneous value of the signal, measured by a peak detector, is compared in the annoyance meter with various thresholds, which are in a fixed ratio to the signal amplitude averaged over a long period. Differential amplifiers detect which thresholds are exceeded and thus determine the magnitude of the attenuation. In another part of the instrument, which contains delay lines for 10 ms, 20 ms and 50 ms, the duration is divided into different categories. A switching matrix then delivers an annoyance value, depending on the depth and duration of the drop-out, which corresponds to the h-numbers in fig. 10. The annoyance value is stored in a register.

The annoyance meter divides the signal into periods of 20 seconds. If the signal drops out repeatedly in one period, h-points are added as 'penalty points'. If the repetitions occur within one second, the annoyance values are further increased. The annoyance meter sums the annoyance values over 20 seconds. A typical recording is shown in *fig. 14.*

[5] D. J. H. Admiraal, A drop-out annoyance measuring apparatus 'DAMA' to check magnetic tapes, to be published shortly.

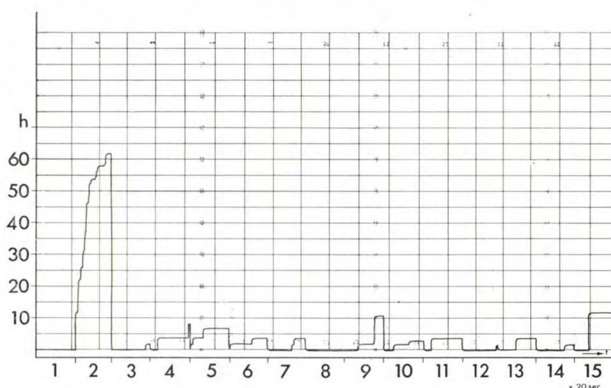

Fig. 14. Example of an automatic recording of the annoyance rating h during 15 successive periods of 20 s, i.e. during a time of five minutes. During each period the h-values are accumulated; at the end of each period the h-counter is reset to zero. In period *2* the annoyance value is by far the greatest. In period *3* some annoyance is registered only towards the end (up to $h = 2$), in period *8* no annoyance is registered at all. To avoid fractions, the figures on the h-scale here are four times greater than in the listening tests.

Summary. In addition to a constant background noise, sound recordings on magnetic tape may also suffer from modulation noise and 'drop-outs'. The level of the modulation noise is proportional to that of the signal. Modulation noise is more readily audible in recordings of solo instruments than in orchestral music; listening tests have shown that for the flute the audibility threshold lies at a signal-to-noise ratio as high as 40 dB. The frequency with which drop-outs occur is a matter of tape quality. Listening tests have been carried out to determine the annoyance caused by drop-outs as a function of their duration, the degree of attenuation and the frequency of occurrence. The results of these experiments have been applied in the DAMA annoyance meter, which can measure these quantities for an audio tape and assign a quality rating to it.

Philips tech. Rev. 37, 38-41, 1977, No. 2/3

The microwave generation and manipulation of magnetic domains

Cylindrical magnetic domains ('bubbles') can be generated in a thin magnetic film of substituted yttrium iron garnet, epitaxially grown on a non-magnetic substrate [1]. These domains are stable between certain values of an external magnetic field, and considerable interest has been shown in them because of possible applications in information storage. Since their volume is very small — only a few microns in height and diameter — they can give a high information density.

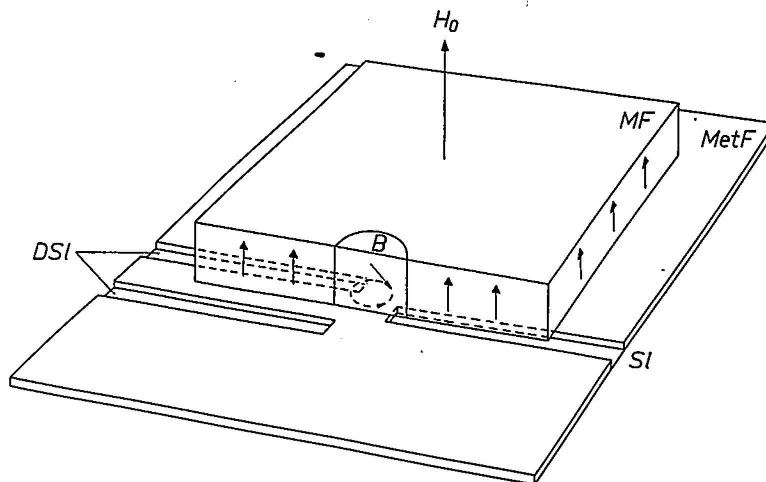

Fig. 1. Precession of the spins in a bubble domain B, at the maximum of the r.f. magnetic field from slotline waveguides, located underneath the magnetic film MF (schematic). The waveguides include an input slotline Sl and a double slotline DSl (coplanar waveguide) in a thin metallic layer $MetF$; H_0 static magnetic field.

If an r.f. magnetic field is applied in the plane of the magnetic film, to which the bias field is perpendicular, the electron spins in the film start to precess. The amplitude of the precession reaches a maximum when the frequency of the r.f. field coincides with the precession frequency, which is usually the case at lower microwave frequencies. This ferrimagnetic resonance is used nowadays for measuring material parameters, such as anisotropy constants and saturation magnetization. In these tests a uniform spin precession is set up in the film.

More complicated effects are observed if spin precession is generated locally in regions of the size of a bubble domain. In our experiments we have used special waveguide configurations for this [2] [3]. We have found that the strong spin precession that can be generated in this way can be used to create domains; it can also be made visible. The forces exerted on the domains by the spin precession also result in special movements or ordering of the domains; we should like to point out the possible uses of this property in bubble technology or in optics.

The experimental arrangement; bubble generation

To illustrate the arrangement a magnetic film containing a bubble domain is represented schematically in *fig. 1*. The bias field is indicated by $\boldsymbol{H}_0$. The spin precession inside the bubble is excited by the field from the waveguides underneath the magnetic film. These consist of a double slotline (coplanar waveguide) and an input slotline with a width of 3 μm, which are etched in a thin layer of metal; where the two meet they are short-circuited. Between the short-circuits in these transmission lines the high-frequency currents are

[1] See W. F. Druyvesteyn, F. A. Kuijpers, A. G. H. Verhulst and C. H. M. Witmer, Single-mask bubble memory with rotating-field control, Philips tech. Rev. 36, 149-159, 1976 (No. 6).
[2] H. Dötsch and H. J. Schmitt, Interaction of microwaves with ring domains in magnetic garnet films, Appl. Phys. Letters 24, 442-444, 1974.
[3] H. Dötsch, Stability and dynamics of microwave generated ring domains, AIP Conf. Proc. 29, 78-83, 1976.

'pinched' into a small area, which gives very high amplitudes of precession locally.

The areas of high spin precession can be made visible by making use of the Faraday effect: the plane of polarization of linearly polarized light that passes through the magnetized film at right angles rotates through an angle proportional to the magnetization. This magnetization is reduced by the spin precession. The areas of precession can be identified as dark patches in *fig. 2*, while the waveguides are visible as straight lines. In this experiment the magnetic film was saturated by a strong bias field. The variation of the Faraday rotation with position can be measured; it is closely related to the r.f. magnetic field of the slotline. An arrangement of this kind can be used to obtain information about the distribution of the r.f. field in planar waveguides.

The area between the short-circuits in the slotlines is about 10 μm in diameter, and in saturated material we can observe precession angles here of more than 90°. However, if the bias field is reduced to a level at which bubble domains can exist, such large precession angles can no longer be obtained. The spins then reverse as soon as the precession angle reaches a critical value, and a bubble domain is formed. On the other hand, the strong spin precession in the region in which the bubbles are excited produces a decreased local static magnetic field, with an approximately radial gradient. The bubble domains are subjected to forces directed along this gradient.

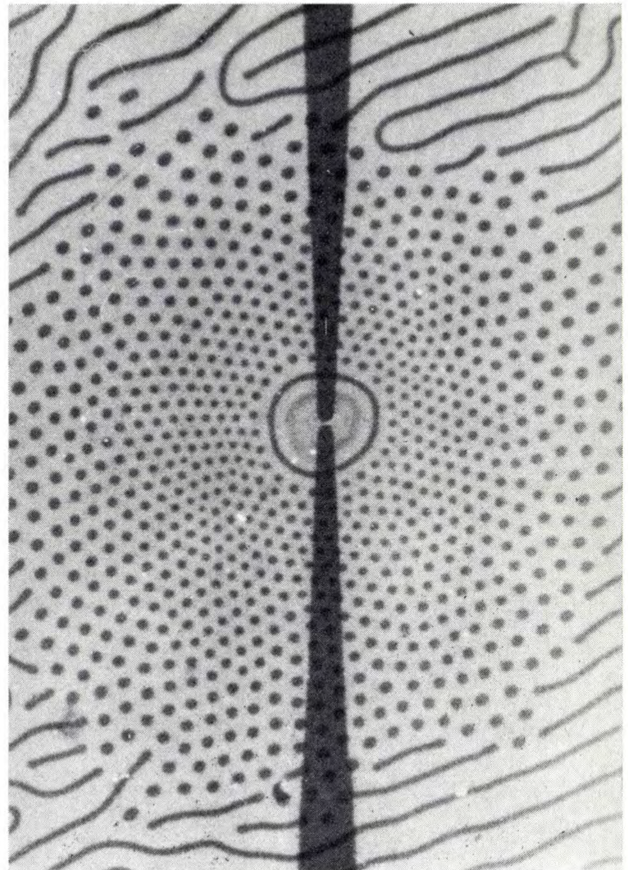

Fig. 3. Bubbles describing a circular path around the area in which they were excited (*blurred circle*). The force acting radially outwards on the bubbles is compensated by the bubble lattice and a ring domain (*dark circle*). In this experiment a second single slotline was used to 'pinch' the r.f. current of the input slotline and hence help to generate the bubbles.

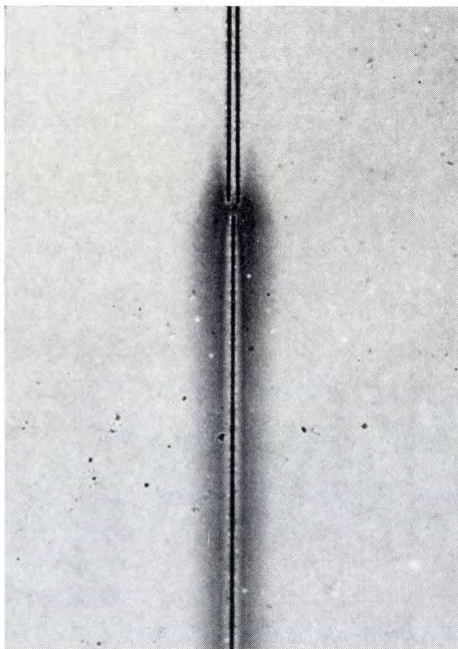

Fig. 2. The darker areas are areas with strong spin precession in a magnetically saturated film close to a slotline waveguide; they have been made visible by means of the Faraday effect. The dark straight lines are the input slotline and the double slotline.

Circulating bubbles

At relatively high values of the bias field the bubbles are small in comparison with the area in which they are excited and they are pushed away from this area. This movement also sets up a deflecting force that is perpendicular to the velocity of the bubble at any given moment, while the magnitude of this force depends on the state of the bubble wall. Bubbles whose walls are not in the same state receive different angles of deflection and can be separated with the aid of this effect.

Since our waveguides are a continuous source of bubbles, a lattice of bubbles is produced. The magnetostatic repulsion force from these bubbles opposes the radial component of the force that pushes the bubbles outwards, so that the bubbles eventually describe a circular path around the area in which they were excited. This behaviour can be seen in *fig. 3*, where a ring domain (see below) is used in addition to the bubble lattice to compensate the radial component of the force. The dark circle in the photograph is the ring domain, while the blurred circle inside it is due to the circulating bubbles. This effect can be used to produce

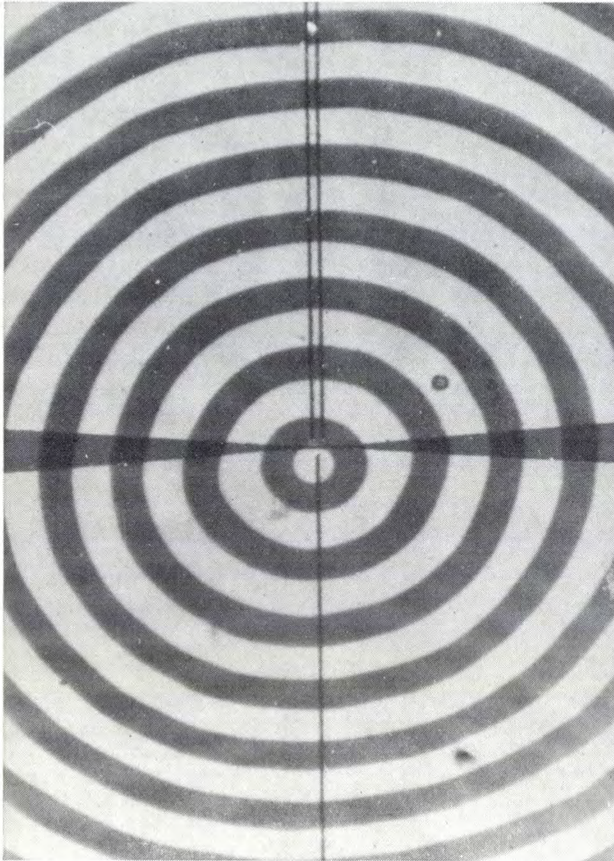

Fig. 4. A system of concentric ring domains formed by generating a new bubble inside the last bubble to be generated; the system is statically stable. The wedge-shaped slots separate the input slotline from the double slotline and have no special significance in the experiment.

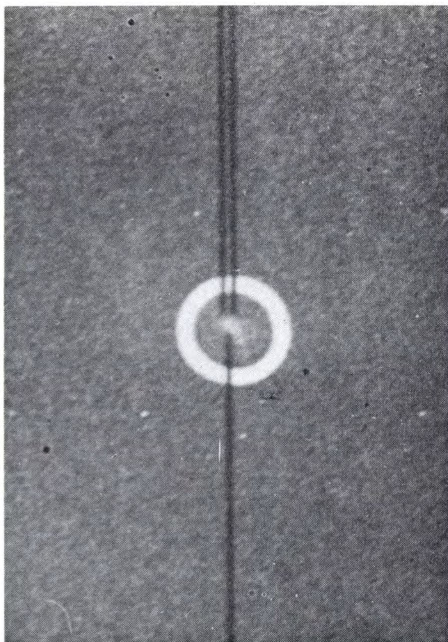

Fig. 5. A single ring domain stabilized by the spin precession maintained by microwave energy in the inside.

a rotation of a complete bubble lattice containing information.

The forces acting on the bubbles because of the interaction of the spin precession can also be used to capture bubbles at locations where the precession angle is at a minimum. A suitable configuration for this purpose is a slotline that is locally widened and forms a circle of slightly greater diameter than a bubble; the bubble in such a circle is caught in a potential well where the precession angle is at a minimum and the forces on the bubble are radially inwards.

Ring and strip domains

At weaker bias fields the bubble diameter is larger. If a bubble is large with respect to the area in which it was produced, it will remain at that location, while the spins continue to precess inside the bubble. The bubble is then in a state of unstable equilibrium, however, since it is situated at a maximum of the spin precession where the forces on the domain are radially outwards; its diameter is then greater than that of an ordinary bubble with no spin precession.

If the precession angle inside the bubble is increased, then a critical value is again reached, just as in the original excitation of the bubble; the spins reverse again and create a bubble within a bubble, so that a ring domain is formed. If this process is continued, a complete system of many concentric rings can be produced. A system of this kind is shown in *fig. 4*; it will even retain static stability as the microwave power decreases to zero.

Unlike these static ring systems, a single ring domain in a low-coercivity film has to be stabilized by using microwave energy. A single ring domain is shown in *fig. 5*; the light patch in the centre clearly indicates strong spin precession. The diameter of the ring increases as the microwave power increases or the bias field decreases; the stability range of the ring domain extends far beyond the field-strength at which static domains collapse. If the microwave energy stabilizing such a ring is modulated in amplitude, the ring reacts with a radial oscillation. This oscillation is usually heavily damped, so that its amplitude decreases as the modulation frequency increases; the frequency at which the amplitude has decreased to half the initial value is generally between 100 and 200 kHz. By making use of this dynamic behaviour of the ring domains it is possible to determine the eigenfrequency of a ring for a particular value of the bias field. The mean rate at which a ring collapses can be derived from measurements of the 'critical switch-off time' for the microwave energy, i.e. the duration of the interruption during which the ring shrinks to its limiting radius but only just fails to

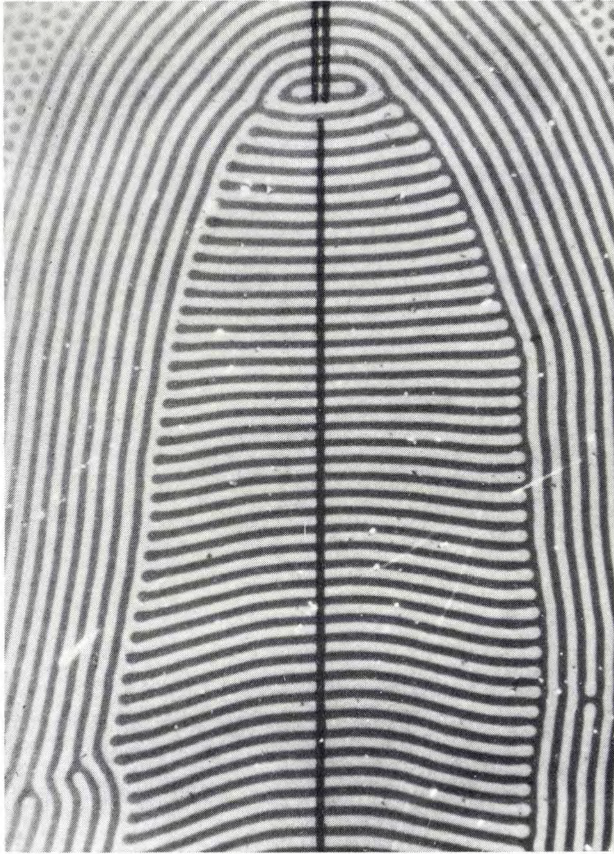

Fig. 6. Strip domains. In the centre these are parallel to the gradient of the static magnetization; at the edges they are at right angles to it. The gradient is related to the spin precession in the vicinity of the slotline.

collapse. These two quantities can be used to characterize the magnetic material. This domain-oscillation technique can also be used to check the quality of magnetic films, since the oscillating domains become fixed in position ('pinned') by point imperfections.

When the bias fields are very weak, strip domains are produced in the film. The forces on these domains produce an ordering like that shown in *fig. 6*, a photograph of a crystal in which the spin precession spreads relatively far from the slotline: close to the slotline the domains are parallel to the gradient of the static magnetization but further away they are perpendicular to it. The regular domain patterns shown in fig. 6 and in fig. 4 can be used for the diffraction of light; the width of the domains can be varied by means of the bias field.

H. Dötsch

Dr H. Dötsch is with Philips GmbH Forschungslaboratorium Hamburg, Hamburg, West Germany.

Philips tech. Rev. 37, 42-50, 1977, No. 2/3

Read-out of a magnetic tape by the magnetoresistance effect

W. J. van Gestel, F. W. Gorter and K. E. Kuijk

The discovery of a new physical effect or a new property of a material is often completely unrelated to its technical exploitation. A clear example of this is the magnetoresistance effect, which can occur in alloys that are ferromagnetic. In this effect the magnitude of the electrical resistivity depends on the angle between the direction of the current and the ferromagnetic magnetization. It was discovered in both nickel and iron in 1857, but it is only in the last few years that there has been any recognition of its significance in magnetic recording.

Introduction

Although it has already been known for more than 100 years [1], there has been an increasing interest in the technical exploitation of the magnetoresistance effect. Thin-film technology has advanced so far that it is now worthwhile to investigate whether the effect could be used for measuring magnetic fields, in particular for information read-out [2]. Here we should not only think of information recorded on magnetic tape — although this is the principal subject of this article — but also information stored in a magnetic-bubble memory.

The basic concept can be more clearly explained with the aid of *fig. 1*. Information is stored on a magnetic tape in the form of a magnetization that varies both in direction and in magnitude as a function of position on the tape. This produces an external magnetic field, whose strength varies with position. If the tape now moves in relation to the reading head, which is a strip of a ferromagnetic alloy mounted vertically, the variation of the magnetic-field component H_y (perpendicular to the plane of the tape) causes the direction of the magnetization in the reading head to vary. The moving tape therefore produces indirectly a variation in the electrical resistivity, which can be readily observed.

It will also be clear that the magnetoresistance effect can also be used for the measurement of constant magnetic fields.

Since it has to be extremely thin, the strip is mounted on a substrate — we shall return to this point later. Because a high resistance to wear is required, both sides of the device are coated with a layer of wear-resistant material; see *fig. 2*.

Instead of a vertically mounted strip it would also be possible to use a strip mounted parallel to the tape, but although this is an interesting arrangement the problem of wear is almost insurmountable. It cannot be solved by allowing the tape to run along the substrate because the distance between the tape and the strip then becomes too great.

The most important advantage of reading out magnetic information by means of variations in magneto-

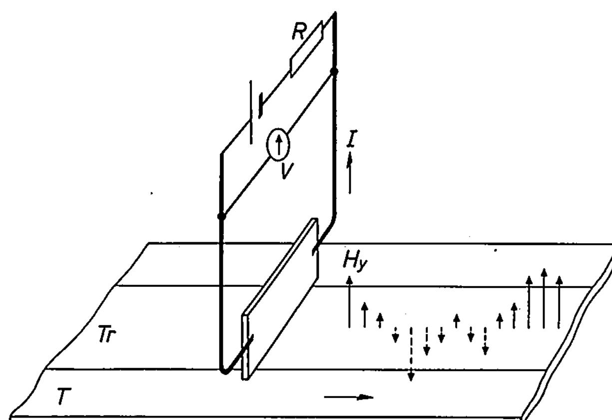

Fig. 1. Principle of operation of a reading head based on the magnetoresistance effect. Above the tape T, with track Tr, there is a strip of a ferromagnetic alloy, whose resistance is continuously measured with the aid of a measuring current I. Variations in the component H_y of the magnetic field from the travelling tape change the direction of the magnetization of the strip, and this produces a change in its resistance. A magnetoresistive head therefore records H_y as a function of time, whereas a conventional reading head records the time derivitive of H.

Ir W. J. van Gestel and Dr F. W. Gorter are with Philips Research Laboratories, Eindhoven; Ir K. E. Kuijk, formerly with Philips Research Laboratories, is now teaching at the Hogere Technische School, Eindhoven.

resistance lies in the possibility of making the reading head very small without reducing the sensitivity to an unacceptably low value. This is of interest if a magnetic tape with more than one track has to be read out, or if the presence of magnetic bubbles at a particular location in magnetic-bubble material has to be determined by means of a reading head.

The performance of a magnetoresistive head (MRH) optimized for the particular application can certainly compete, in terms of sensitivity, noise, crosstalk, and whether it can be included in a tape recorder, with the conventional reading head, which is based on the observation of the change of the magnetic flux in a high-permeability ferromagnetic yoke. With the conventional inductive method the reading and writing functions can often be combined in one head, which is of course an advantage. On the other hand it is not so easy to miniaturize the inductive reading head as it is a strip like the one in fig. 2, and this must be taken into account when a multiple head has to be designed. For example, a decrease in the number of turns that measure the variation of the flux density in the yoke causes a proportional reduction in sensitivity. This demonstrates an important difference between the two methods of read-out. In fig. 1 the y-component of the field of the magnetic tape is measured directly; however, with an inductive head, it is not the field (or the associated flux density) that is measured, but the rate at which the field varies. It is self-evident that at low frequencies (low tape speeds) the inductive method only produces a weak signal.

In the following section we first analyse the response of a magnetoresistive head to a variation in H_y. Then we consider the problem of the linearization of the response function, with emphasis on a method that has been discovered and investigated at our laboratories [3]. In the remaining sections of the article we look at the frequency characteristic, the noise behaviour and the technology of our experimental MRHs, and also the possibility of using the head for certain special applications.

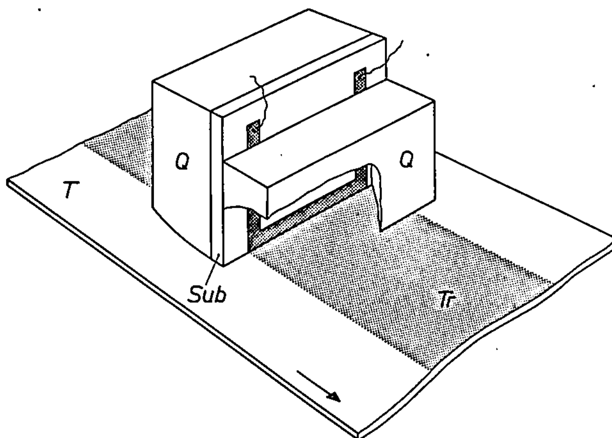

Fig. 2. In a reading head based on the magnetoresistance effect the ferromagnetic strip and its supply leads are mounted on a substrate *Sub*. In practice the thickness of the strip is 0.02 to 0.3 μm, its width is of the order of 10 μm and its length is equal to the width of the track (between 20 μm and a few mm). The substrate and strip are placed between two plates of wear-resistant material *Q*. The surface of the head next to the tape is made slightly rounded.

The electrical resistance of an MRH in a homogeneous magnetic field

The electrical resistivity in an ordinary metal can also be a function of the angle between the direction of the current and that of the magnetization. The special feature of ferromagnetic metals is that the effect can be relatively large at room temperatures and also occurs in polycrystalline material. The angular dependence can be represented by

$$\varrho = \varrho_0(1 + \beta \cos^2 \theta), \tag{1}$$

where ϱ is the resistivity, θ the angle between current I and magnetization M and ϱ_0 and β are constants of the material. The extreme values for the resistivity are found for $\theta = 0°$ and $\theta = 90°$; the resistivity is lowest at $\theta = 90°$. Obviously, the alloy chosen for the ferromagnetic strip should have the highest possible value for β. In addition, it should be easy to rotate the magnetization in a magnetic field of the order of 8000 A/m (about 100 Oe) as produced by the magnetic tape. Alloys with a high permeability, a small coercive force and a relatively large β that are suitable for this application include $Ni_{89}Fe_{11}$ or $Ni_{70}Co_{30}$ [4]. At low temperatures β can lie between 0.1 and 0.2; at room temperature β is much smaller. For most of the strips we have used this effect amounts to only a few per cent.

We shall now analyse the relationship between the resistivity and H_y, the field to be measured. It will be apparent that the dimensions of the MRH, i.e. the length l, thickness t and width w, play an important role in this relationship; see *fig. 3*. Starting with a strip mounted vertically we assume that the strip is in a homogeneous magnetic field. (In practice H_y decreases with distance from the tape.)

If H_y is equal to zero, the magnetization will lie preferentially in the longitudinal direction, that is to

[1] W. Thomson, Phil. Mag. (4) **15**, 469, 1858.
[2] A comprehensive analysis of the possibilities has been given by R. P. Hunt, IEEE Trans. **MAG-7**, 150, 1971. An initial report of the work carried out at our Laboratories will be found in F. W. Gorter, J. A. L. Potgiesser and D. L. A. Tjaden, IEEE Trans. **MAG-10**, 899, 1974.
[3] K. E. Kuijk, W. J. van Gestel and F. W. Gorter, IEEE Trans. **MAG-11**, 1215, 1975.
[4] A. R. Miedema and J. W. F. Dorleijn, Philips tech. Rev. **35**, 29, 1975.

say along the z-axis. This is related to the demagnetization energy $\frac{1}{2}\mu_0 N M_S^2$ (N is the demagnetization factor, $\mu_0 M_S$ the saturation magnetization), which is a measure of the energy of the magnetic field produced externally by a magnetized body. The larger the cross-section of the body in the direction of magnetization, the smaller the energy. When the direction of magnetization is rotated from z to y, the demagnetization energy changes in accordance with the relation

$$E = \tfrac{1}{2}(N_y - N_z)\mu_0 M_S^2 \sin^2\theta. \quad (2a)$$

In the case $t \ll w \ll l$, N_z can be neglected and N_y approaches t/w. Also, in the presence of H_y the energy contains a term

$$E_H = -\mu_0 H_y M_S \sin\theta. \quad (2b)$$

The resultant θ can be found by minimizing the sum of (2a) and (2b), and differentiating with respect to θ we find:

$$\mu_0 M_S \cos\theta \,\{H_y - (t/w)M_S \sin\theta\} = 0. \quad (3)$$

If we now set $(t/w)M_S \equiv H_0$ (an r.m.s. field), then we see that as long as $H_y \leqslant H_0$ the solution is given by $\sin\theta = H_y/H_0$, while for larger values of H_y we have $\cos\theta = 0$ and hence $\theta = 90°$. Using the result from relation (1) that there is a quadratic relationship between the change in resistivity and $\sin\theta$, we find:

$$\left.\begin{aligned} &\Delta R/(\Delta R)_{max} = 1 - (H_y/H_0)^2 \quad \text{for} \quad H_y < H_0 \\ &\text{and} \\ &\Delta R/(\Delta R)_{max} = 0 \qquad\qquad\quad \text{for} \quad H_y > H_0. \end{aligned}\right\} \quad (4)$$

This response function is shown in *fig. 4* (curve *1*). A reading head with a response function such as curve *1* of fig. 4 could not of course be used in practice as a linear transducer; for low fields ($H_y \ll H_0$) the change in resistivity is almost zero and for high fields the response is independent of H_y. In practice the response function is somewhat flatter. This is related to the assumption, in the above derivation of the direction of orientation of M, that M has the same direction over the complete strip; this is not the case. In fact, it is only possible to speak of a demagnetization factor N and a corresponding demagnetization field for magnetized bodies in the form of an ellipsoid of revolution. In practice, if the shape deviates from an ellipsoid then N has a kind of mean value, but the demagnetization field will no longer have the same direction and magnitude everywhere. Moreover, local inhomogeneities and anisotropic fields can be introduced during the fabrication of the strip. The results of numerical calculations for the case of an inhomogeneous demagnetization field [5] have been shown as curve *2* in fig. 4. Even though the situation is thus better than curve *1* would suggest, a good practical reading head can only be obtained when special precautions are taken. These will be discussed in the following section.

Dimensions of the strip

A direct conclusion about the preferred dimensions of the strip can be drawn from the above calculations. The reading head is sensitive to field-strengths approximately equal to H_0 and hence to $(t/w)M_S$. Since $\mu_0 M_S$ has a magnitude of about 1 W/m² and w cannot be chosen greater than about 10 µm — otherwise the field from the tape would not extend beyond the strip — t follows directly from H_0. For a field H_0 of 10^4 A/m we obtain $t = 0.1$ µm.

Limits can also be defined for the thickness of the strip. The thickness should not be made less than about

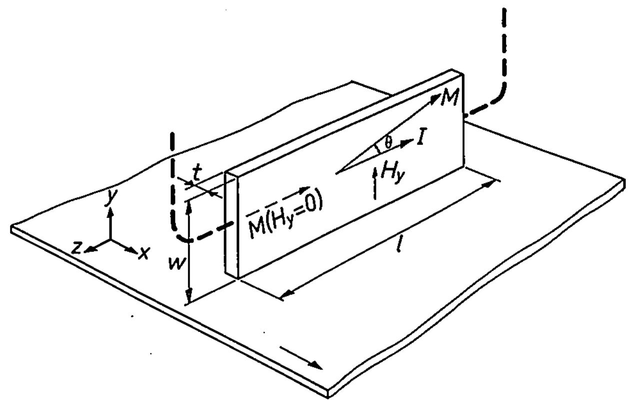

Fig. 3. The definition of the coordinate system x,y,z and the length l, width w and thickness t, as used in the description of the magnetoresistance effect. H_y is the field to be measured. M is the magnetization of the strip, I the measuring current; θ is the angle between these two vectors.

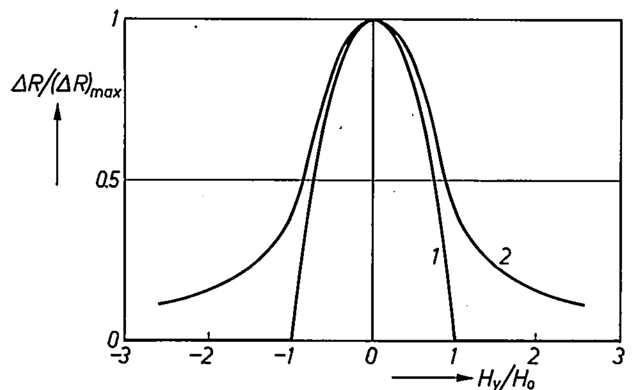

Fig. 4. Calculated response curves for a magnetoresistive head; the relative change in resistance $\Delta R/\Delta R_{max}$ is plotted against H_y, normalized to the demagnetization field H_0 (see eq. 4). Curve *1* refers to the case of an ellipsoidal reading head, in which the demagnetizing field is homogeneous. Curve *2* is based on assumptions that correspond more closely with reality. The relationship between the variables is approximately linear in the region around the point of inflexion in the curve; at the associated field-strength ($H_y/H_0 \approx 0.9$), θ is about 45°.

20 nm, since it is difficult to deposit films that are both homogeneous and mechanically reliable at thicknesses less than this value; in the second place there is an increase in the resistivity of metals when the thickness is less than the mean free path for electron scattering. This extra resistance will not be anisotropic, so that the maximum effect will diminish. In nickel this free pathlength is about 30 nm at room temperature. On the other hand, the strip must not be made so thick that its resistance is no longer large with respect to the contact resistance; this occurs when $t > 1$ μm.

The linearization of the response function

In a reading head it is important that the output signal, and hence the change in electrical resistance, are proportional to the input signal, i.e. the variation in H_y. The response function obtained when the unperturbed magnetization is oriented along the z-axis is an even function of the field H_y, and consequently for small values of H_y the sensitivity is small and the distortion is large.

This can be improved by making use of the fact that the response curve has a point of inflexion and is approximately linear in a small region around this point. Closer study has shown that for the associated value of H_y the magnetization M is inclined at an angle of about 45° to the direction of the current (the z-axis). We can therefore obtain a linear response for small variations in H_y if we ensure that the current and magnetization are inclined at an angle of about 45°. There are two methods of achieving this result.

In the first method use is made of an auxiliary field H_b in the y-direction, whose magnitude is made comparable with the anisotropic demagnetization field H_0; the field from the tape can now be considered as a relatively small variation h_y. If H_y in equation (4) is replaced by $H_b + h_y$, then provided $\theta < 90°$ we obtain:

$$\Delta R/(\Delta R)_{\max} = 1 - \frac{H_b^2}{H_0^2} - \frac{2H_b h_y}{H_0^2} - \frac{h_y^2}{H_0^2}. \quad (5)$$

When the last term is small ($h_y \ll H_0$), this relation is almost linear, with a slope of $2H_b/H_0^2$. The condition $H_0 \gg h_y$ determines the demagnetization field (and hence the thickness) and H_b/H_0 determines the sensitivity. Linearization of the response by using an auxiliary field — either external or in the form of an anisotropic field — is certainly possible in practice, but it does present some problems. There is also the danger that such a field could affect the information written on the tape.

[5] R. L. Anderson, C. H. Bajorek and D. A. Thompson, AIP Conf. Proc. 10, 1445, 1973.

The 'barber pole'

The difficulties associated with the use of an auxiliary field are avoided in the solution that has been found at our laboratories [3]. As explained above, it is desirable to start from the situation in which the current and the preferred direction of magnetization are at an angle of 45° to each other. An alternative method of obtaining this angle of 45°, instead of using an auxiliary field, is to make the current in a ferromagnetic material flow obliquely in the way illustrated in *fig. 5*. If the magnetic strip is partially covered by oblique stripes of a material of a much higher electrical conductivity, then the equipotential planes will also lie obliquely and the current through the intervening areas of NiFe will be at an angle of about 45° to the (unchanged) easy direction of the magnetization. The design shown in fig. 5 is called a 'barber pole' because of its resemblance to the red and white striped pole still sometimes seen outside barber's shops.

The response function of the barber pole can be calculated from equation (4):

$$\Delta R/(\Delta R)_{\max} = 1 - \sin^2(\theta + \theta_B),$$

with (6)

$$\sin\theta = H_y/H_0.$$

Here θ_B is the angle imposed by the construction between the current and the direction of the magnetization in the unperturbed state. On rearranging and substituting $\theta_B = 45°$ we obtain:

$$\Delta R/(\Delta R)_{\max} = \tfrac{1}{2} - \frac{H_y}{H_0}\left\{1 - \left(\frac{H_y}{H_0}\right)^2\right\}^{\frac{1}{2}}. \quad (7)$$

When $\theta_B = 0$ the response function is of course that of an 'ordinary' MRH, as already shown in fig. 4, curve *1*.

We have now obtained a linear response function for small values of H_y ($H_y \ll H_0$), with the gradient — i.e. the sensitivity of the head — determined by H_0. The complete response function for an ellipsoid, also for large H_y, is compared with that of an ordinary MRH in *fig. 6*. It can be seen that a linear relation between H_y and $\Delta R/\Delta R_{\max}$ exists over a large range of fields ($-0.7 < H_y/H_0 < +0.7$); this range is greater than in

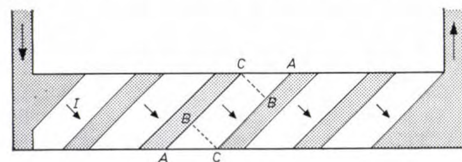

Fig. 5. The 'barber pole'. The current I in the ferromagnetic strip flows at an angle of 45° to the longitudinal direction, and hence to the preferred direction of magnetization, because stripes of a relatively good electrical conductor (shaded grey) are applied to the surface of the strip. In this way a linear response can be obtained without the use of an auxiliary field. At the edges of the strip — in a region roughly corresponding to the triangles ABC, the direction of the current does of course differ somewhat from the ideal.

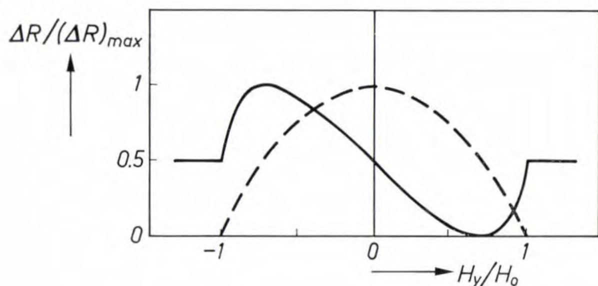

Fig. 6. The response curve for a 'barber pole', calculated for homogeneous magnetization. The curve has an approximately linear section around $H_y = 0$. Curve *1* from fig. 4 is also shown for comparison; this curve is an even function of H_y, whereas the curve for the barber pole is not.

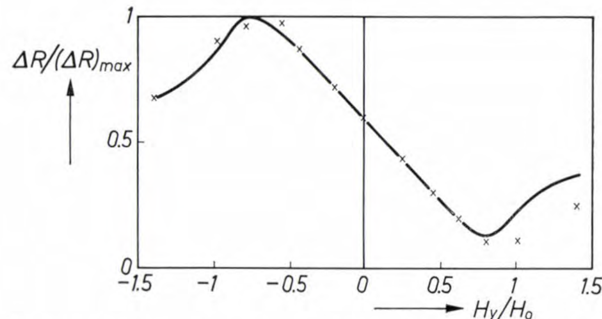

Fig. 8. Calculated response curve for the barber pole when the effect of the edge of the strip on the current distribution (see fig. 7) is taken into consideration. The crosses are measured values.

the case of an auxiliary field H_b. Both for large values of H_y and for $H_y = 0$, the magnetization is at an angle of 45° to the current and the value of the resistance is given by $R_0(1 + \frac{1}{2}\beta)$.

The calculated curve in fig. 6 again refers to the ideal case. As before, it is assumed that M is uniform, but in addition it is assumed that the current has the same direction everywhere. This is not true along the edges of the strip, of course, and the effect of the different current distribution in the triangles ABC in fig. 5 must really be studied in detail. An example of the calculated position of the equipotential planes at the edge of the strip is given in *fig. 7*. It is also possible to calculate the response function for this complicated case. The results are compared with the experimental values in *fig. 8*. The agreement is good. An important difference from the ideal curve given in fig. 6 is the asymmetry between positive and negative values of H_y.

A minor complication is caused by the fact that although the magnetization M aligns itself preferentially along the z-axis it does not differentiate between the positive or negative z-direction. In an ordinary MRH this gives no cause for concern ($\theta = 45°$ and $\theta = 135°$ give the same value of resistance), but in the barber pole this difference is certainly of importance; see *fig. 9*. This duality can be avoided by using a weak longitudinal auxiliary field, sufficiently strong to overcome the coercivity.

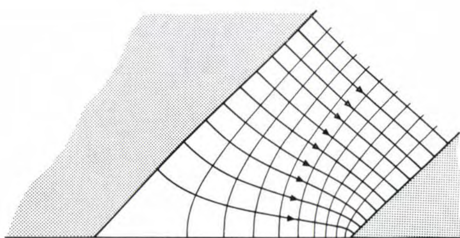

Fig. 7. The effect of the edges of the strip on the current distribution in the barber pole (see fig. 5). The thin lines represent the equipotential surfaces.

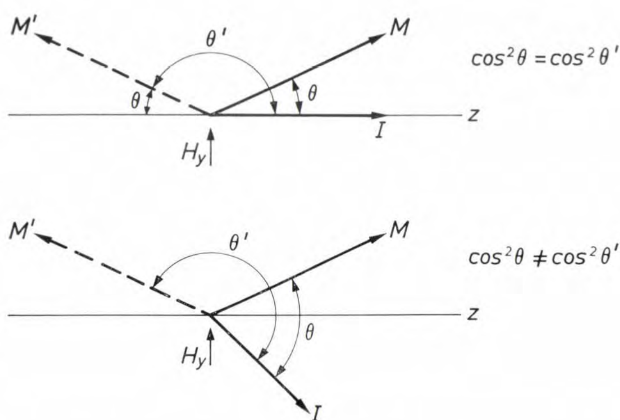

Fig. 9. In a conventional MRH it makes no difference if the magnetization M at $H_y = 0$ aligns itself in the positive or the negative z-direction; in both cases a particular value of H_y gives the same value of $\cos^2\theta$ and hence the same change in resistance (see eq. 1). In the barber pole, however, where the direction of the current is *not* along the z-axis, it does make a difference.

Characteristics of an MRH

Sensitivity

From what has been said above it is easy to deduce the type of output signal to be expected from a reading head — with or without a barber pole. It can be assumed that this will differ depending on the application. The extent of the linearity region will always have to be matched to the maximum field-strength, which leads to different values of H_0. For γ-Fe_2O_3 tapes, for which the maximum undistorted field emergent from the tape has a field-strength of about 12×10^3 A/m (150 Oe), the value of H_0 should not be made less than about 24×10^3 A/m (300 Oe). A value of $w = 10$ μm then gives a thickness t of 0.3 μm, the maximum permissible value. If the track width is now assumed to be fixed, say at 100 μm, then the total resistance of the strip is known (10 Ω) and the total change in resistance that can be obtained in the linear region is about 0.1 Ω.

For tapes containing CrO_2 and metal powder the field emergent from the tape should be taken to be rather stronger. In situations where the head is not in contact with the tape, the field should be taken as weaker.

By making H_0 very small, a very large sensitivity can be obtained and very weak fields (such as the Earth's magnetic field) can be measured provided that they are not superimposed on another stronger field. At very small values of H_0 the anisotropy field H_K of the strip is not negligible (it is about 10^2 A/m) and the sensitivity is no longer proportional to H_0^2 (eq. 4).

Finally, there is the measuring current to be considered. This is limited by warming-up effects and possibly by diffusion due to electromigration (atoms being 'pulled along' by the current-carrying electrons). With a strip of dimensions 0.3×10 μm, a current of up to about 100 mA is possible in practice (current density 3×10^{10} A/m^2; in strips that have been protected against corrosion a value of about 10^{11} A/m^2 can be obtained [6]). The maximum output voltage is then about 3 mV, which is much more than can be obtained from a conventional inductive head at this track width and at low tape speeds (0.03 mV).

Frequency characteristic

The dynamic behaviour is no less important than the static behaviour that we have been discussing so far. By dynamic behaviour we mean the way in which the response function depends on the frequency of the signals from the tape.

The rate at which the magnetization in the strip (and hence its resistance) can follow changes in H_y is very great and has very little effect on the frequency characteristic; this is determined by spatial factors. It is therefore better in the first instance to look at the *wavelength* characteristic.

For sinusoidally magnetized tapes, there is an exponential decrease in H_y in the y-direction, which depends on λ. Sine-wave signals recorded on the tape at equal amplitudes but different frequencies give spatial distributions of H_y that differ not only in the x-direction but also in the y-direction. This can be expressed by the equation

$$H_y(x,y) = \hat{H}_{sur}\, e^{-2\pi y/\lambda} \sin(2\pi x/\lambda), \tag{8}$$

where $\hat{H}_{sur}$ is the amplitude of the field at the surface of the tape ($y = 0$). If we assume that the change in resistance is proportional to the mean value $\overline{H}_y$ of the external field over the strip, we can derive the wavelength characteristic as follows:

$$\overline{H}_y = \frac{1}{w} \int_a^{a+w} \hat{H}_{sur}\, e^{-2\pi y/\lambda}\, dy =$$

$$= \hat{H}_{sur} \frac{1 - e^{-2\pi w/\lambda}}{2\pi w/\lambda}\, e^{-2\pi a/\lambda}. \tag{9}$$

Here a is the distance from the lower side of the strip to the tape. The exponential decrease in H_y with y imposes a clear upper limit to the value of a.

Theoretical wavelength characteristics for strips with different values of width w are shown in *fig. 10*. It can be seen that the wavelength at which the curve begins to fall depends on w. This follows obviously from equation (9), since the mean field-strength over the strip increases as w becomes smaller.

Measured characteristics are shown in *fig. 11*. In principle, the decrease in sensitivity as a function of decreasing wavelength might be expected to be a disadvantage in read-out with an inductive head. In

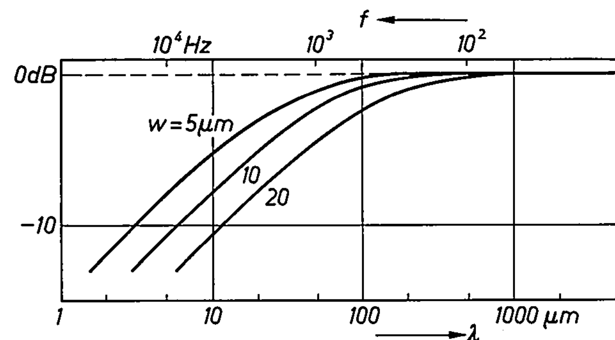

Fig. 10. The calculated wavelength characteristic (log-log scale) for conventional magnetoresistive heads (fig. 1) for different widths w. It has been assumed that the amplitude of the field-strength at the surface of the tape is always the same. The sensitivities at the long wavelengths have been adjusted to be equal. The corresponding frequencies are plotted along the upper scale for a tape speed of 4.75 cm/s. The frequency at which the curve begins to fall off increases as w becomes smaller. The dashed line indicates the characteristic for an ideal inductive reading head.

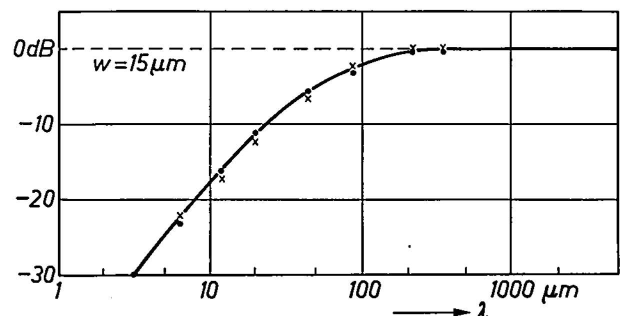

Fig. 11. The measured characteristic for a conventional MRH (•) and a barber pole of the same width (×) compared with that of an inductive reading head with a gap of 0.7 μm (the curve). The sensitivities have been equalized at the longer wavelengths. (In practice, the sensitivity at a tape speed of 4.75 cm/s of an MRH with an auxiliary field is about 30 dB higher and that of a barber pole is about 27 dB higher.)

[6] R. I. Potter, IEEE Trans. **MAG-10**, 502, 1974.

practice, however, the sensitivity of an MRH is so much larger, even at measuring currents much less than 100 mA, that the effect is not all that important in comparison. Moreover, the characteristic of an MRH of the type shown in fig. 1 has no zero points like those that occur with an inductive head.

Noise

When a magnetic tape is read in a reading head there are four different sources of noise: the amplifier, the head itself, the tape and the mechanical contact between the head and the tape. In designing a reading head every attempt is made to make the noise contributions from the amplifier, head and the tape-head contact so small that the total noise is determined principally by the tape. The MRH can almost always meet these requirements because of its superior sensitivity. This is not the case with the inductive head, however, if it is used with a low-noise tape, a very narrow track, a low tape speed or if the head has a small number of turns. In addition it should be borne in mind that some contributions to the noise (such as the amplifier noise) are constant, whereas others depend on factors such as the gain or the measuring current, so that they cannot be compared directly.

The amplifier noise is not very important — good modern amplifiers have an equivalent noise resistance of less than 100 ohms. This contribution is much less important for an MRH than for an inductive head, because the output signal of the MRH is much larger.

The tape noise is a consequence of the fact that the tape is not a continuous magnetic medium, but consists of a 'suspension' of magnetic particles in a polymeric carrier. The tape noise should therefore be considered as a given quantity, in the same way as the signal to be read.

The head noise is mainly resistance noise arising from the ohmic resistance of the MRH. Barkhausen noise is also present sometimes, especially when the strip contains more than one magnetic domain; this form of noise can easily be avoided by using a longitudinal auxiliary field of several hundred A/m. In the barber-pole head this field is already present for other reasons.

It might be thought that an MRH with a higher resistance would produce more head noise. This is indeed true in an absolute sense, but not relatively. Resistance noise is proportional to the square root of the resistance. The measured signal, however, is derived from the relative change in the resistance, and is therefore proportional to R, so that the signal-to-noise ratio increases as R increases.

An important additional contribution is the 'temperature noise' [7]. The resistance of the MRH does not only change because of the effect of a magnetic field, it also changes because of variations in temperature. These variations can be relatively large: 0.25% per °C. Because of irregularities in the surface roughness of the tape there are variations in the heat generated at the contact surface between the MRH and the moving tape, and there are also variations in the dissipation of the heat produced by the measuring current in the MRH. These effects can lead to temperature variations that affect the resistance significantly. It is therefore necessary to ensure that there is good heat dissipation. We use a wafer of silicon as the substrate. This material gives a good compromise between the different requirements demanded of the substrate: it is wear-resistant, a good conductor of heat, non-magnetic and a poor conductor of electricity. Temperature noise mainly contains components at low frequencies.

Finally, we should say something about the measuring current. Since the amplifier noise and the resistance noise are independent of the measuring current and since the shot noise is negligible, it seems desirable to make the measuring current as high as possible. However, this increases the temperature difference between the head and its surroundings, and hence the temperature noise. An MRH is so sensitive, however, that even with relatively insensitive heads ($t \approx 0.3$ µm) and a track width of 200 µm, it is possible to use a measuring current of much less than 100 mA without the other noise contributions exceeding the tape noise. The noise performance of an MRH is better than that of an inductive reading head, particularly at narrow track widths and at low tape speeds.

Technology; special designs

The manufacture of a magnetoresistive head places no very high demands on technology. For thin NiFe films we use compositions such as $Ni_{89}Fe_{11}$ and for films thicker than 0.1 µm we use $Ni_{80}Fe_{20}$ because of its low magnetostriction. The alloy is applied to the substrate by evaporation, with the use of a thin film of Ti as an adhesion layer, or by sputtering, when an adhesion layer is unnecessary. During the subsequent treatment the temperature should remain below about 400 °C, principally because the magnetoresistance effect would otherwise become weaker (β becomes smaller). The barber-pole design has in fact few complications. The oblique stripes are obtained by sputtering a 'sandwich' of molybdenum (adhesive layer, 0.1 µm), gold (conductor, 1 µm) and a second adhesion layer, typically of molybdenum. The exact shape can be obtained by the use of well known photoresist-and-etching methods. In the light of present-day semiconductor technology, no great difficulties are encoun-

tered in mounting the contact leads or in applying a coating of silica to prevent corrosion.

Reading heads for special applications can also be made by the same process. A good example is the 'track-sensing' head, which can be used to find out whether the position of a track is asymmetrical with respect to the MRH. The two halves of the barber pole are connected together in opposing sense, and no signal will be produced if the track is symmetrical. Another example is the interference-suppressor head, which consists of two detectors connected in opposition and mounted close together. The field from the tape affects only one of the two detectors, so that normally only one signal is obtained, but interfering magnetic signals from the surroundings will produce signals that will very nearly cancel. A three-track head in which this principle is applied is shown in *fig. 12.*

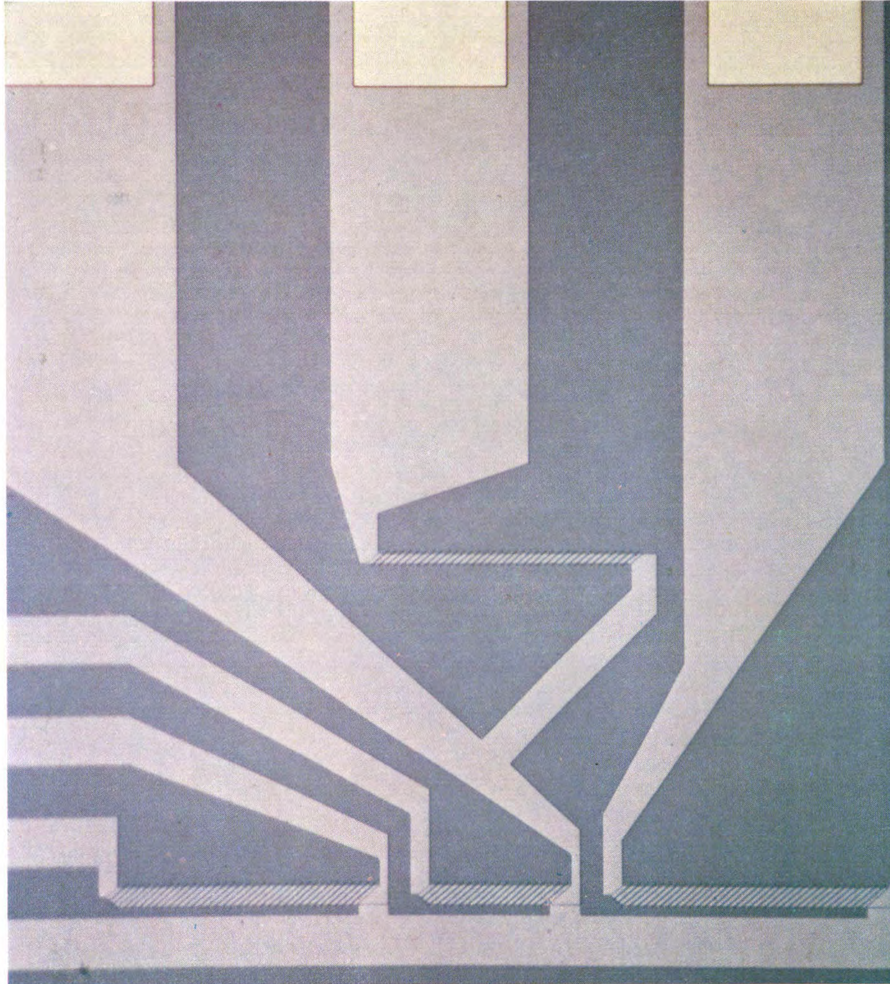

Fig. 12. Ferromagnetic strips and connecting leads forming part of a three-track MRH with barber poles mounted on a substrate. The light-coloured stripes are the conductors. When plates of wear-resistant material have been applied to both sides, the lower part of the unit is ground away. The resistance of the horizontal conductor is continuously measured during the grinding to give an indication of the rate of progress. A fourth strip located rather higher up does not respond to the field from the tape but compensates for the interference signals detected by the central reading strip.

Finally, we ought to mention that it is possible to make reading heads that are sensitive at very short wavelengths, without this causing saturation at the longer wavelengths. This is done by placing a plate of soft magnetic material such as Permalloy on either side of the strip and a short distance away from it [8]. The plates shield the strip from contributions from parts of the tape that are further away, and they also conduct the magnetic flux; see *fig. 13a.* These heads are of course developed for weak fields.

[7] See the article by Gorter, Potgiesser and Tjaden in note [2].
[8] C. H. Bajorek and A. F. Mayadas, AIP Conf. Proc. **10**, 212, 1973.

When an MRH is used it is possible to work with narrow tracks (high track density), and with an MRH of the type just described it appears that information recorded at a density of over 1.5×10^7 bits/cm^2 can be read [6]. An MRH strip can readily be combined with an inductive writing head of the thin-film type [9]. In such a writing head the tape runs along two soft magnetic plates, which function as shields for the MRH strip (fig. 13*b*).

To summarize and conclude, we believe we have made it clear that the use of the magnetoresistance effect in a ferromagnetic metal as a method of measuring magnetic fields with a high spatial resolution could become extremely important for applications related to magnetic recording. In this article we have only described read-out from magnetic tape, and we have compared the MRH with a conventional alternative, the inductive head. If we consider read-out from magnetic-bubble memories, however, the only acceptable possibility at the moment is read-out by means of the magnetoresistive anisotropy.

[9] J. C. van Lier, G. J. Koel, W. J. van Gestel, L. Postma, J. T. Gerkema, F. W. Gorter and W. F. Druyvesteyn, IEEE Trans. **MAG-12**, 716, 1976.

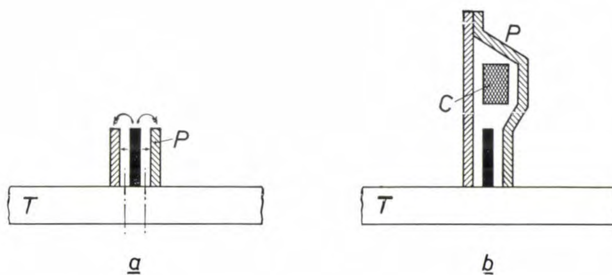

Fig. 13. *a*) An MRH that is sensitive to very short wavelengths yet does not saturate at the longer wavelengths can be made by shielding the strip (black) with a plate *P* of soft magnetic material. The sections of the tape beyond the chain-dotted lines do not contribute to the flux in the strip. *b*) If a coil *C* is included in a similar configuration then a combination of an MRH of the type shown in (*a*) and a thin-film type of inductive head is obtained.

Summary. The magnetoresistance effect in a narrow strip of a suitably chosen NiFe alloy has much to offer for the detection of magnetic fields, and hence for reading out from magnetic tape or from a bubble memory. An approximately linear response can be obtained if the angle between the magnetization of the strip in the absence of a magnetic field and the direction of the measuring current is about 45°. Since the direction of the easy axis of magnetization is longitudinal and therefore coincides with the direction of the current, this is not possible without special precautions. In the solution described here, the 'barber pole', the strip is covered by oblique (45°) stripes of a relatively good conductor, and the current crosses 'at right angles' between the stripes. Except at very short wavelengths the MRH is much more sensitive than an inductive reading head, so that the amplifier noise plays a less important role. An MRH can be made very small and the principle allows special versions to be made for special applications, such as track-sensing heads and interference-suppressor heads. The technology is analogous to that required for thin-film circuits, but the temperature must remain below 400 °C.

A small analog memory based on ferroelectric hysteresis

A. Petersen, P. Schnabel, H. Schweppe and R. Wernicke

Efforts have long been made to find means of utilizing the polarization of ferroelectric materials for information storage in memories, in a method analogous to the use of the magnetization of ferromagnetic materials. The ferroelectrics previously available, however, had such high coercive field-strengths that it was not possible to make memory cells with acceptably low write voltages. Recent developments have provided ferroelectric ceramics that have much lower coercive field-strengths, so that write voltages compatible with transistor circuits are now feasible. With an appropriate composition, these materials can be given a square hysteresis loop, enabling them to be used for the storage of both digital and analog data. The memory can be designed to receive the required write voltages from an integrated circuit.

Introduction

It may be useful to provide modern electronic equipment with a small memory device for storing control data and similar information. For such purposes the memory should be 'non-volatile', i.e. the information must remain stored without any external input of energy. Memories of this type can be used to store data for selecting radio or television channels, data for the adjustment of brightness, contrast and colour saturation in television receivers, set-point data in control units, and frequently used telephone numbers. If the data is in analog form, an analog memory can be a great advantage in many cases, since it dispenses with the need for an analog-to-digital converter. The stored data must be readily erasable and the read-out must be non-destructive.

There are various devices that would meet the above requirements. Motor-driven potentiometers could be used, or non-volatile semiconductor circuits. Also well suited for memories of this type, however, are devices that employ hysteresis effects with stable remanent states. The magnetization of ferromagnetic materials has long been used for this purpose, but nowadays it is also possible to use the polarization of modern ferroelectric ceramics. This may in fact be preferable for some applications, since all that is required to produce the polarization is an electric field between a pair of electrodes on the material. There is not the power dissipation always associated with the magnetization of ferromagnetics.

Provided the hysteresis loop of the material is reasonably rectangular, the remanent polarization after removal of the polarizing field will be almost identical with the polarization in the presence of the field (*fig. 1*). The remanent polarization increases with increasing polarizing field-strength; any polarization between maximum positive and maximum negative can be obtained by tracing out appropriate sub-loops of the hysteresis curve. These properties make the material ideally suited for the storage of analog information.

Non-destructive read-out of the information is achieved by utilizing the piezoelectric effect that is always present in polarized ferroelectrics. Mechanical vibrations of a polarized ferroelectric generate an alternating electric field between the electrodes attached

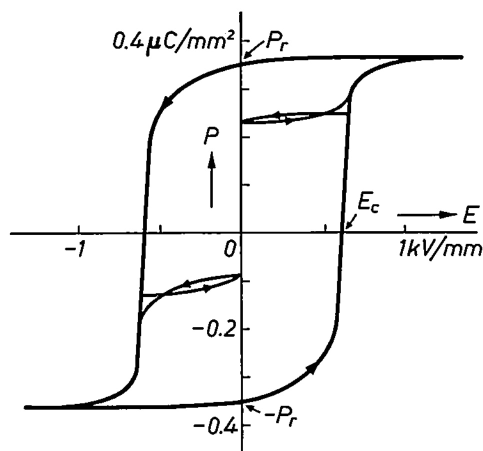

Fig. 1. Polarization P as a function of field-strength E, the hysteresis loop, for a lanthanum-doped mixed crystal of $PbTiO_3$ and $PbZrO_3$. The chemical composition of the material and the parameters of the sintering process are selected to give a reasonably square loop and a low coercive field-strength E_c. Two sub-loops are drawn to show how all remanent polarization values between $+P_r$ and $-P_r$ can be obtained.

Dipl.-Phys. A. Petersen is with Valvo, Hamburg; Dr P. Schnabel, Dipl.-Phys. H. Schweppe and Dr R. Wernicke are with Philips GmbH Forschungslaboratorium Aachen, Aachen, West Germany.

to the material. The amplitude of the alternating voltage is proportional to the polarization of the material between the electrodes. Conversely, an alternating voltage between two electrodes on a polarized ferroelectric body can make the body vibrate mechanically.

In the following sections we shall look at the construction of ferroelectric analog memories and give some details of the applications mentioned at the beginning of the article.

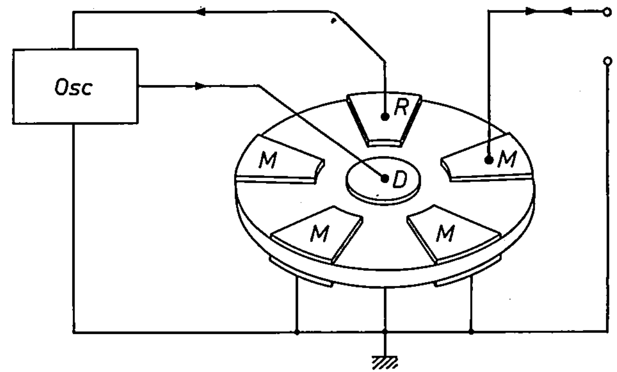

Fig. 2. A ferroelectric memory device. A ferroelectric ceramic disc is provided with an identical electrode pattern on both faces. The central electrode pair D excites a radial vibration piezoelectrically; the material between the electrodes D is permanently polarized. The pair R is used for generating a feedback signal that drives the disc at its resonant frequency; here again the material between the electrodes must be permanently polarized. The electrode pairs M around the circumference form the memory cells.

Construction of a ferroelectric analog memory

Ceramic materials based on mixed crystals of lead zirconate and lead titanate with a perovskite structure are very suitable for the fabrication of a ferroelectric memory. They exhibit pronounced ferroelectric behaviour, they can be made inexpensively by conventional sintering techniques, and they can easily be cut, lapped and metallized. By adjusting the chemical composition of the material and the conditions for the sintering process, the ferroelectric properties can be varied over a wide range [1]. The Philips laboratories in Aachen have developed varieties of this material that have a low coercive field-strength and the required rectangular hysteresis loop (fig. 1). The low coercive field-strength enables the memory devices made with this material to be driven with relatively low voltages.

We have made a memory device that consists of a thin ferroelectric disc with identical electrode patterns on both faces (*fig. 2*). The patterns are in the form of a central pair of electrodes and a number of electrode pairs arranged around the circumference.

The outer electrode pairs constitute the individual memory cells. As described above, information is written in by applying a voltage between a pair of electrodes. It is also possible, however, to apply a low direct current to the electrodes through a high resistance, in other words to apply a polarizing charge. In this way an accurately defined polarization can be achieved, even in materials for which the hysteresis loop has vertical or almost vertical sides.

The central electrode pair excites the disc piezoelectrically in a radial mechanical vibration; the material between these electrodes is given the maximum polarization. The disc is included in a feedback loop of the driving oscillator. The feedback signal is provided by one of the outer electrode pairs, again with maximum polarization of the ferroelectric between the electrodes. The circuit used (*fig. 3*) drives the disc at its resonant frequency and ensures that the amplitude of the mechanical vibration remains constant even if there are temperature variations or changes in polarization between the drive electrodes. For simplicity the ground electrodes can often be combined.

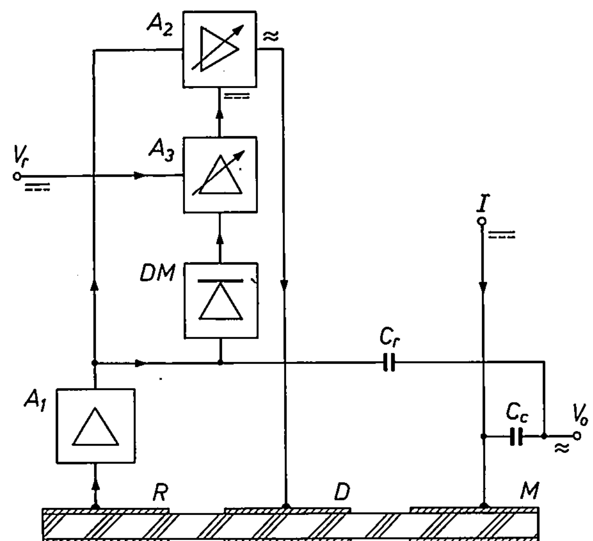

Fig. 3. Circuit for the piezoelectric excitation of a memory disc and for writing in and reading out information. The drive electrode D, the reference electrode R and the amplifiers A_1 and A_2 form a feedback system that oscillates at the mechanical resonant frequency of the disc (200 kHz for a disc of diameter 12 mm and thickness 0.3 mm). The discriminator DM and the d.c. amplifier A_3 control the vibration amplitude, using the voltage V_r as reference. The write-in signal I gives a polarization proportional to this signal under the electrode M. The vibration of the disc generates an alternating voltage of amplitude proportional to this polarization, and hence to I. This alternating voltage contributes to the output voltage V_o through the capacitor C_c. The voltage generated at the reference electrode also contributes to the output voltage through capacitor C_r, so that the negative half of the hysteresis loop can also be used.

The alternating voltage that appears across the storage electrodes during mechanical vibration of the disc corresponds in amplitude to the magnitude of the local polarization in the ferroelectric, but gives no indication of the sign of the polarization. However, when the feedback signal for the drive is used as a phase reference and compared with the storage signal, as also

indicated in fig. 3, a uniquely defined signal can be extracted from the memory for any polarization between $+P_r$ and $-P_r$. This technique doubles the storage capacity. A memory disc of this type is shown in *fig. 4*.

Reduction of the write voltage

If a ferroelectric memory is to be used in combination with transistors and integrated circuits, the voltage for the polarization should be no more than 30 to 50 V. Since the coercive field-strength in the most favourable case is 600 V/mm (fig. 1), the thickness of the material between the storage electrodes must be no more than about 50 μm. For reasons of mechanical strength, however, the memory disc should not be thinner than 0.2 mm; this means that the polarizing voltage would have to be 120 V, which is much too high.

The first experimental design we produced in an attempt to solve this problem is illustrated in *fig. 5*. A photo-etching technique was used to reduce the thickness of the storage-electrode regions to about 50 μm. This hardly affects the mechanical strength of the disc and the resonant frequency while the voltage required is brought down to 30-50 V. The relation between the d.c. polarizing voltage V_p and the amplitude of the alternating read-out voltage V_a with this design is shown in *fig. 6*.

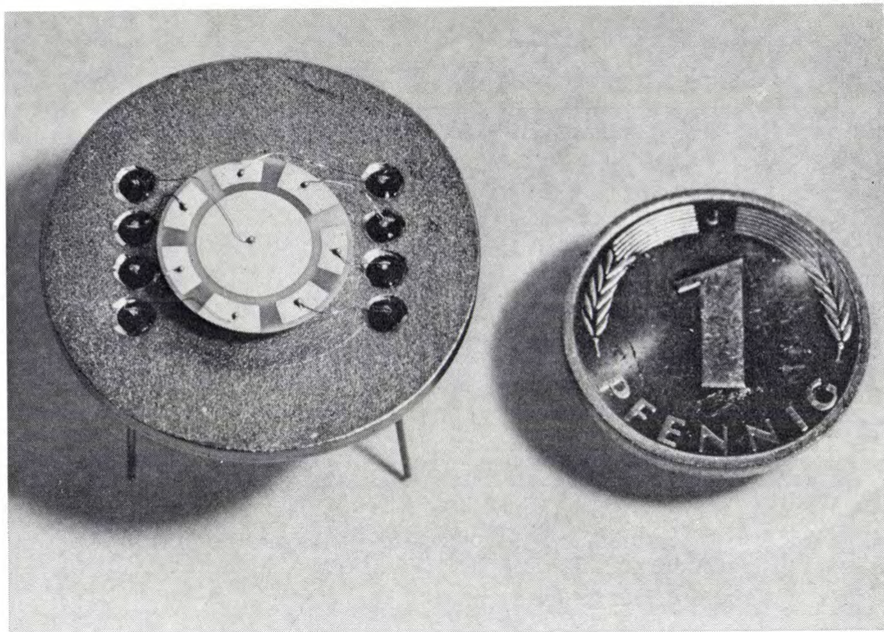

Fig. 4. A ferroelectric memory disc. The centre of the disc is attached to a piece of elastic material. The disc is mounted inside the encapsulation of a power transistor to protect it from undesirable ambient effects. To simplify the design some of the ground electrodes are combined.

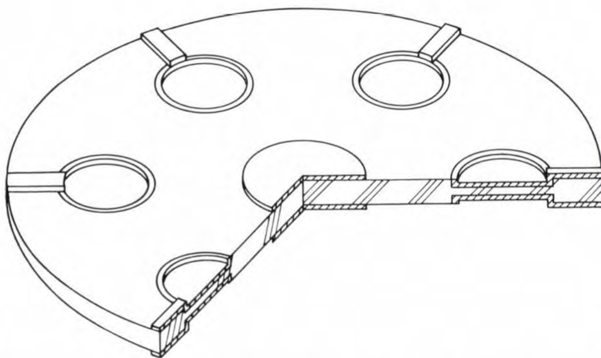

Fig. 5. To reduce the write voltage the ferroelectric ceramic can be etched away under the memory electrodes to a thickness of 50 μm. A voltage of 30-50 V is then sufficient for complete polarization. The mechanical stability and resonant frequency of the entire disc are largely determined by the thickness of the unetched material (0.3 mm).

In another arrangement designed to reduce the write voltage we used two closely spaced parallel electrodes on one face of the disc. When a voltage is applied between the electrodes, the polarization of the ferroelectric is then mainly parallel to the surface (*fig. 7a*). As in the previous case, radial mechanical vibration of the disc generates an alternating voltage proportional to the local polarization. The write voltage is now determined by the spacing of the electrodes, which can easily be made 20 μm or less with modern techniques. The design based on this principle is illustrated in fig. 7*b*. The memory electrodes and the reference electrode are placed around the circumference of the disc.

[1] K. Carl and K. H. Härdtl, Ber. Dtsch. Keram. Ges. **47**, 687, 1970.

The common annular counter-electrode is earthed to avoid a capacitive coupling between the memory electrodes and the central drive electrode. The circuits used with this arrangement are similar to those described earlier. With an electrode spacing of 20 μm, write voltages as low as 20-30 V have been achieved. A further reduction in the gap width, and hence in the write voltage, would not present much difficulty. Apart from the low write voltage, this arrangement has the additional advantage that each memory cell requires a much smaller ceramic volume, so that more information can be stored in the same disc.

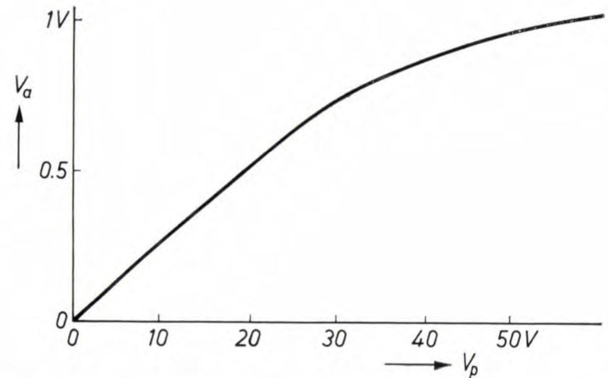

Fig. 6. The amplitude V_a of the alternating read-out voltage as a function of the write voltage V_p for a ferroelectric memory as in fig. 5.

Applications

Remote control of a television set

A television set can be made much more convenient to use if remote control of the brightness, contrast and colour saturation settings is provided. This is usually done with an ultrasonic signal and some kind of memory device to store the selected settings. The main requirements to be met by such a memory are exactly those a ferroelectric memory can meet: non-volatility and non-destructive read-out.

Fig. 8 shows the principle of the circuit that we have designed for this application. The memory cells on the piezoelectrically driven ceramic disc deliver an alternating signal voltage that is taken to the output through a coupling capacitor C_c; this voltage is then converted into a control signal. The connection to the feedback electrode through C_r allows the full storage capacity of the memory to be used. Each cell can be connected by the remote controller to a selected positive or negative voltage, depending on whether it is desired to increase or decrease the control signal, and hence the polarization. A fairly high resistance in the connection to the voltage generator determines the rate at which the setting is changed. The button for increasing or decreasing one of the settings is kept depressed until the desired change takes place; the magnitude of the control signal at the moment the button is released is stored in the memory. The circuit for this 'armchair control' is given in more detail in *fig. 9*.

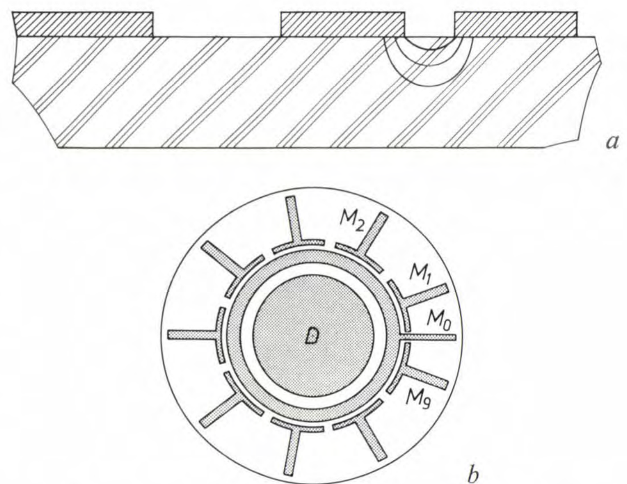

Fig. 7. Electric-field distribution (*a*) and a possible electrode configuration (*b*) for a ferroelectric memory disc with memory electrodes on one face of the disc. $M_1 \ldots M_9$ are the memory electrodes; the common counter-electrode M_0 forms an effective electrostatic screen between the memory electrodes and the drive electrodes *D*. The polarization of the ferroelectric, which contains the information, is mainly parallel to the surface, but for read-out the same radial extensional vibration can be used as in the case of an axial polarization.

Storage of set-point data for process controllers

In process control a non-volatile memory can be used for retaining set-point data during power failures for one reason or another. The data can be set by hand or obtained from measurements of particular parameters. They can be stored as either digital or analog signals. Precautions are necessary to prevent interfering signals due to power-failure transients being stored instead of the desired signals. Here again a ferroelectric memory

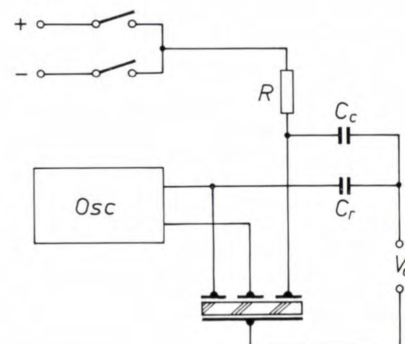

Fig. 8. Basic diagram of the circuit used for data storage in the remote control of a television set. When the remote control is used one of these memory electrodes is connected to a positive or negative voltage via a high resistance *R*. This causes a slow change in the polarization of the memory cell and of the output signal V_o, which controls one of the settings of the television set. Once the desired result has been reached, the remote-control button is released and the data for the settings remains stored in the memory.

can be used instead of a number of motor-driven potentiometers.

Another application in process control is the storage of the maximum or minimum value of a signal in a particular time interval.

so as to store a total of say ten digits, which will be sufficient for local and trunk calls and for most international calls. The writing and reading speeds must of course be matched to the requirements of the local telephone exchange.

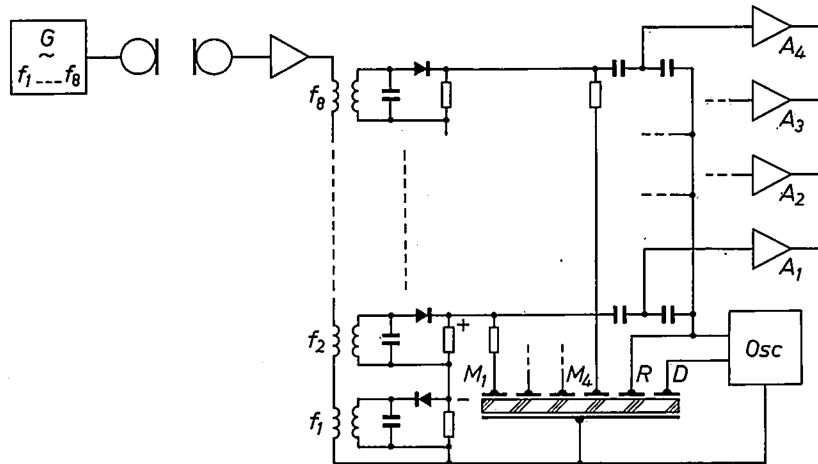

Fig. 9. Block diagram of the remote control of four different settings of a television set. When one of eight buttons is depressed, the ultrasonic oscillator G generates one of the eight frequencies $f_1 \ldots f_8$. This signal is transferred through a loudspeaker and a microphone to the television set, where it is amplified. The output signal of the amplifier is selected by frequency with the aid of the eight tuned LC circuits $f_1 \ldots f_8$. Because of the diodes connected in series with the load resistors of these circuits, a signal of frequency f_1 produces a negative polarization under the memory electrode M_1, while a signal of frequency f_2 produces a positive polarization. The oscillator *Osc* delivers the drive signal for the memory disc; the amplifiers $A_1 \ldots A_4$ pass the setting signals to the appropriate circuits in the television set.

Storage of telephone numbers

A telephone can be made much easier to use if frequently called numbers can be stored in a memory device and retrieved by simply pressing a button. A ferroelectric memory can also be used for this automatic facility. Each digit of a telephone number then has to be stored as an analog signal with ten possible levels. This can be done by arranging a memory disc

Summary. The development of suitable ferroelectric materials now allows ferroelectric hysteresis to be used for information storage as well as the long-established methods based on ferromagnetic hysteresis. The $PbTiO_3$-$PbZrO_3$ mixed crystals we have used have a relatively low coercive field-strength, so that it is possible to design memory devices that can be polarized with voltages as low as about 30 V. The ease with which the degree of polarization can be controlled makes ferroelectric memories suitable for the storage of analog information. Non-destructive read-out of the information is obtained by utilizing the piezoelectric properties of polarized ferroelectrics. The article concludes with a description of some applications of ferroelectric analog memories.

Philips tech. Rev. 37, 56-71, 1977, No. 2/3

The finite-element method and the ASKA program, applied in stress calculations for television picture tubes

J. H. R. M. Elst and D. K. Wielenga

The mechanical behaviour of very complicated structures such as aircraft, ships or pressure vessels is almost impossible to calculate by the classical methods of analysis. A numerical approximation method was developed in the fifties for the solution of such problems. This was the finite-element method, in which the calculations are applied to a model of the structure. These calculations can give a sufficiently accurate approximation to the behaviour of the actual structure without taking up too much computer time. Philips have purchased computer software based on this method — the ASKA system — from its designers, the Institut für Statik und Dynamik der Luft- und Raumfahrtkonstruktionen, Stuttgart. Several modifications have been introduced into the system at Philips, making it more suitable for calculating the stresses in the glass envelopes for television picture tubes at an early stage in the design.

Introduction

In 1941 A. Hrennikoff put forward a method for calculating the mechanical behaviour of an elastic body by substituting for it an equivalent framework, in which he assigned elastic properties to the cells of the framework in such a way that the behaviour of the framework would be expected to resemble that of the continuous body [1]. A theoretical basis for this method was first established in the middle fifties in publications in Europe and America [2]. This was the origin of the 'matrix method for structural analysis', which rapidly came into more general use.

Before this method was available, the only methods for calculating the elastic behaviour of mechanical structures were analytical methods in which a solution is sought through a description of the mechanical behaviour in terms of differential equations, possibly with the aid of finite-difference methods or by numerical integration. In practice these methods could only be applied to structures of relatively simple geometry and with fairly straightforward boundary conditions.

In the matrix method, which is essentially an approximation method, the starting point is an idealized representation of the structure, built up from discrete elements with simplified elastic properties. Since these elements have finite dimensions (and are not infinitesimally small like those used in deriving the equations of equilibrium for the continuum), the method is usually called the Finite-Element Method, abbreviated to FEM. In applying this method so much computation is necessary that a high-speed computer with a large memory is necessary for the calculations to be completed within a reasonable time. Wider application of the method has therefore only become a practical possibility after the introduction of the third-generation computers.

The matrix method was initially mainly used for stress calculations in aircraft design, and later in such calculations for ships, pressure vessels, building construction, etc. Later again the method was taken up for applications outside mechanical engineering: heat-conduction problems, fluid flow, the calculation of electrical and magnetic potential distributions, etc.[3]. There has also been an increasing interest in recent years in the fundamental mathematical basis of the method [4].

An example of a structure whose increasing complexity has made it even less amenable to the classical analytical methods is the glass envelope for a television picture tube. The main feature of interest here is the mechanical stress produced when the envelope is evacuated; it is highly desirable to establish at the design stage whether the envelope will be strong enough. In the earlier tubes the geometry was sufficiently simple

Ir J. H. R. M. Elst is with the Philips Electronic Components and Materials Division, Eindhoven; D. K. Wielenga is with the Philips Mechanical Engineering Works, Eindhoven; both were formerly with Philips Research Laboratories, Eindhoven.

(the first tubes had rotational symmetry) for analytical methods to give a reasonable accuracy. But as the geometry increased in complexity more and more simplifications had to be introduced into the calculations, giving results that were less and less satisfactory. The mechanical strength of the tubes then had to be checked by means of strain-gauge measurements on a prototype of the envelope (*fig. 1*). Since a prototype had to be made for every design, this was a very time-consuming and expensive procedure. The finite-element method now enables the stresses to be calculated to the desired accuracy in the actual design stage.

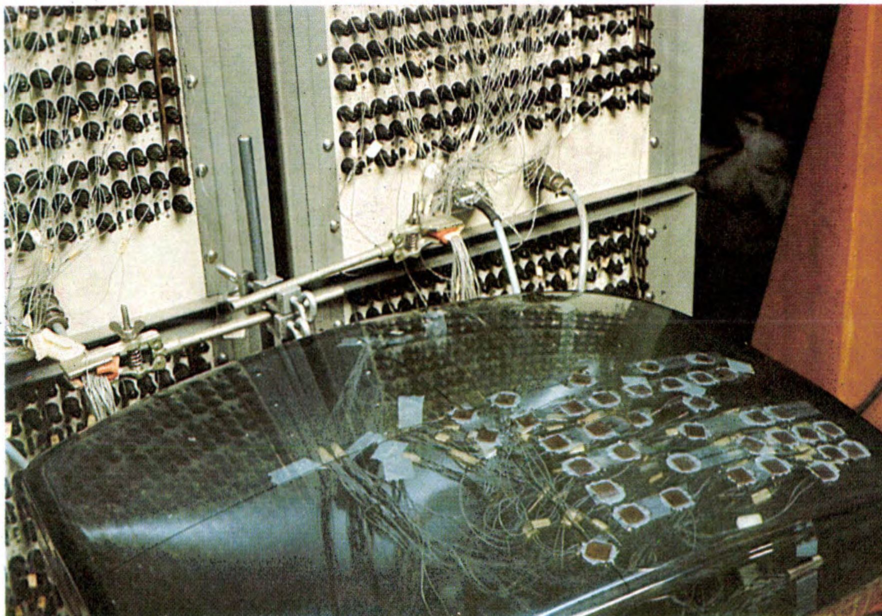

Fig. 1. Strain-gauge measurement of the deformation of the envelope for a television picture tube. The gauges are attached to the inside of the envelope before the two components of the tube — the screen and the cone — are bonded together. After the tube has been evacuated the strain gauges are automatically scanned by the equipment visible in the background, and the measured strain values are recorded on punched tape.

To gain some experience with the method some simple programs for solving two-dimensional problems were developed at Philips Research Laboratories. This work showed however that developing our own programs for stress calculations in picture tubes would have taken many man-years, and it was therefore decided to purchase software that had already been developed elsewhere. After a few experimental calculations we purchased the ASKA system in 1970.

The ASKA software system

The ASKA system consists of a set of programs for solving mechanical stress and vibration problems by the finite-element method; it was designed by the Institut für Statik und Dynamik der Luft- und Raumfahrtkonstruktionen (ISD) at the University of Stuttgart. The name ASKA is an acronym for Automatic System for Kinematic Analysis. The system was chosen because it was eminently suitable for calculating three-dimensional stress patterns (like those in the television picture tube). At the time of our purchase ISD had already put 120 man-years into its development.

The system now consists of four parts:

ASKA I for linear static analysis,
ASKA II for linear dynamic analysis,
ASKA III-1 for elasto-plastic and creep analyses and
ASKA III-2 for buckling analysis.

In this article we shall confine ourselves to the ASKA I program used for the calculation of the picture-tube envelope. This part has been furthest developed and has already been taken up by a number of users at Philips. The other parts are still subject to various restrictions,

[1] A. Hrennikoff, Solution of problems of elasticity by the framework method, J. appl. Mech. **8**, A 169-175, 1941.
[2] J. H. Argyris and S. Kelsey, Energy theorems and structural analysis, Butterworth, London 1960 (appeared earlier as a series of articles in Aircraft Engng. **26** and **27**, 1954/55).
M. J. Turner, R. W. Clough, H. C. Martin and L. J. Topp, Stiffness and deflection analysis of complex structures, J. aeronaut. Sci. **23**, 805-823 & 854, 1956.
[3] O. C. Zienkiewicz, The finite element method in engineering science, McGraw-Hill, London 1971.
[4] J. R. Whiteman (ed.), The mathematics of finite elements and applications, Academic Press, London 1973.

both in technical possibilities and in practical applications.

The ASKA programs are mostly written in FORTRAN, to give the greatest independence from the type of computer (at Philips the IBM 370/168 computer is used for ASKA at present). In the design of ASKA every attempt was made to make it both a useful tool for the practical design of structures, and also a system that can serve as the starting point for further research. To facilitate practical design work an input/output system has been provided that is matched as far as possible to the convenience of the user, who must of course possess an adequate knowledge of the finite-element method. The programs that perform the actual calculations do not concern the user at all, since they are activated automatically. To make ASKA suitable for research as well, it is largely built up from modules, which makes it easy to include alterations and additions. Even so, the use and further development of a computer system such as ASKA requires considerable skill and experience; cooperation with software specialists is essential.

The facility for including modifications in ASKA has been used to adapt the ASKA I program to the specific requirements of the picture-tube problem. The program is used at Philips for a large number of other problems besides the calculation of these picture tubes. These include the calculation of the deformations and stresses in a hydraulic motor, in a centrifuge, in the base-plate of an automatic coffee-maker, in the cooler housing of a hot-gas engine, and in a helical-groove bearing. ASKA is also increasingly used in the calculation of the dynamic behaviour of structures. The suitability of ASKA as a research tool can be seen from the application for calculating the resonant frequencies of a reverberation chamber and for calculating the flow of a highly viscous fluid along an open cavity, since these problems do not resemble those that ASKA was designed to solve.

In this article we shall start by giving a description of the finite-element method and deriving the equations used. Next we shall look at the ASKA I program and modifications to it. Finally we shall describe the application of the system to the calculation of the mechanical behaviour of the envelopes of television picture tubes.

Calculations for an elastic body

Let us consider a linear-elastic body of volume V with a surface S of which a part S_P is subjected to a known load. It is required to find the deformations and stresses that are produced in the body by the load (it is assumed that the deformations remain small).

Three sets of differential equations apply for such a problem: the equations that express the relation between the strains ε_{ij} and the displacements u_i, the equilibrium equations, given in terms of the stresses σ_{ij}, and Hooke's law, which gives the relation between the stresses and the strains. From these equations it is possible to derive a set of three partial differential equations expressed in terms of the displacements u_i and their derivatives, which can be used to describe any linear elastic problem (see the Appendix). By using variational methods it can be shown that solving these equations to obtain the displacements is mathematically equivalent to finding a displacement field $u_i(x,y,z)$ that satisfies the boundary conditions and for which a certain 'functional' (a quantity whose value is defined by the function u_i and its derivatives) is at a minimum. For the body described above this functional is:

$$\Phi = \int_V \tfrac{1}{2} E_{ijkl}\, \varepsilon_{ij}\, \varepsilon_{kl}\, \mathrm{d}V - \int_{S_P} p_i u_i\, \mathrm{d}S. \qquad (1)$$

Here E_{ijkl} is the tensor from Hooke's law, which contains the elastic constants of the material; p_i represents the components of the load on the surface S_P. The indices i, j, k and l take the values 1, 2 and 3, which indicate the coordinates x, y and z. The summation convention also applies here: a summation must be made over indices that occur twice in a term. The functional Φ has the dimensions of energy; the method described is known in elasticity theory as 'the principle of minimum potential energy'.

The principle of minimum potential energy forms the basis of the finite-element method in the form known as the displacement method. In this method approximations are introduced for the distribution of the displacements. It is also possible to derive variational methods that lend themselves to the introduction of approximations for the distribution of the stresses (force method) or of displacements and stresses (mixed methods). In this article only the displacement method will be described.

The finite-element method

In solving an elasticity problem by the finite-element method the body is considered to be built up from a number of small regions of relatively simple geometry, the *elements* (e.g. bars, triangles, tetrahedra). A number of points in these elements are chosen as *nodes*; these usually lie on the boundaries of the elements, particularly at the corners. This *network* of nodes forms the idealized model of the body, and the calculations are made on the model. For each element *interpolation functions* are chosen which express uniquely the displacements in the elements in terms of the displacements of the nodes. The displacement field is then calculated for which the functional Φ from equation (1)

has a minimum value. This displacement field, characterized by the displacement of the nodes, is an approximate solution to the problem.

Since the matrix notation is the most suitable for describing the finite-element method, particularly for computer processing, we shall rewrite equation (1) in matrix notation:

$$\Phi = \int_V \tfrac{1}{2}\boldsymbol{\varepsilon}^{\mathrm{T}}\boldsymbol{E}\boldsymbol{\varepsilon}\,\mathrm{d}V - \int_{S_{\mathrm{P}}} \boldsymbol{u}^{\mathrm{T}}\boldsymbol{p}\,\mathrm{d}S. \qquad (2)$$

Here $\boldsymbol{E}$ is the elasticity matrix, formed from the elements of the elasticity tensor E_{ijkl}; $\boldsymbol{\varepsilon}$ is a column matrix with the strains as the elements (column matrices are written as a row of elements between curly brackets):

$$\boldsymbol{\varepsilon} = \{\varepsilon_{xx}\,\varepsilon_{yy}\,\varepsilon_{zz}\,\varepsilon_{xy}\,\varepsilon_{yz}\,\varepsilon_{zx}\}$$

and $\boldsymbol{\varepsilon}^{\mathrm{T}}$ is its transpose, the row matrix

$$\boldsymbol{\varepsilon}^{\mathrm{T}} = [\varepsilon_{xx}\,\varepsilon_{yy}\,\varepsilon_{zz}\,\varepsilon_{xy}\,\varepsilon_{yz}\,\varepsilon_{zx}].$$

In addition $\boldsymbol{u}^{\mathrm{T}}$ is the row matrix $[u_x u_y u_z]$ and $\boldsymbol{p}$ is the column matrix $\{p_x p_y p_z\}$.

The functional Φ is obtained for a body divided into N elements by summing the contributions from the separate elements:

$$\Phi = \sum_{n=1}^{N} \Phi_n = \sum_{n=1}^{N} \left[\int_{V_n} \tfrac{1}{2}\boldsymbol{\varepsilon}_n^{\mathrm{T}} \boldsymbol{E}_n \boldsymbol{\varepsilon}_n\,\mathrm{d}V_n - \int_{S_{\mathrm{P}n}} \boldsymbol{u}_n^{\mathrm{T}} \boldsymbol{p}_n\,\mathrm{d}S_n \right]. \qquad (3)$$

This summation is only permissible if the boundaries of the elements themselves make no contribution to Φ. This will certainly not be the case if it is arranged that the strains at the boundaries are finite. Consequently the interpolation functions must be such that there are no discontinuities in the displacements at the boundaries of the elements: the continuity of the structure may not be broken.

For the displacement field of element n we can write:

$$\boldsymbol{u}_n = \boldsymbol{F}_n \boldsymbol{d}_n, \qquad (4)$$

where $\boldsymbol{d}_n$ is the column matrix of the nodal displacements and $\boldsymbol{F}_n$ contains the interpolation functions.

We can illustrate the subdivision into elements and the selection of the interpolation functions by the simple case of a thin plate loaded in its own plane. The problem can be considered as two-dimensional ('plane stress'). We can divide the plate into triangular elements; for each element (see *fig. 2a* and *b*):

$$\boldsymbol{u} = \{u_x(x,y)\; u_y(x,y)\}, \text{ and}$$
$$\boldsymbol{d} = \{u_{x1}\, u_{y1}\, u_{x2}\, u_{y2}\, u_{x3}\, u_{y3}\}.$$

For simplicity the subscript n is omitted here. The displacements in this element can clearly be interpolated linearly. This can be expressed in matrix notation by:

$$\begin{bmatrix} u_x \\ u_y \end{bmatrix} = \begin{bmatrix} F_1 & 0 & F_2 & 0 & F_3 & 0 \\ 0 & F_1 & 0 & F_2 & 0 & F_3 \end{bmatrix} \cdot \begin{bmatrix} u_{x1} \\ u_{y1} \\ u_{x2} \\ u_{y2} \\ u_{x3} \\ u_{y3} \end{bmatrix},$$

where F_1, F_2 and F_3 are linear functions of x and y:

$$F_i(x,y) = a_i x + b_i y + c_i.$$

By including the conditions $F_1(x_1,y_1) = 1$ and $F_1(x_2,y_2) = F_1(x_3,y_3) = 0$ the coefficients a_1, b_1 and c_1 can be expressed in terms of the coordinates of the nodes. The coefficients of the functions F_2 and F_3 can be determined in an analogous way.

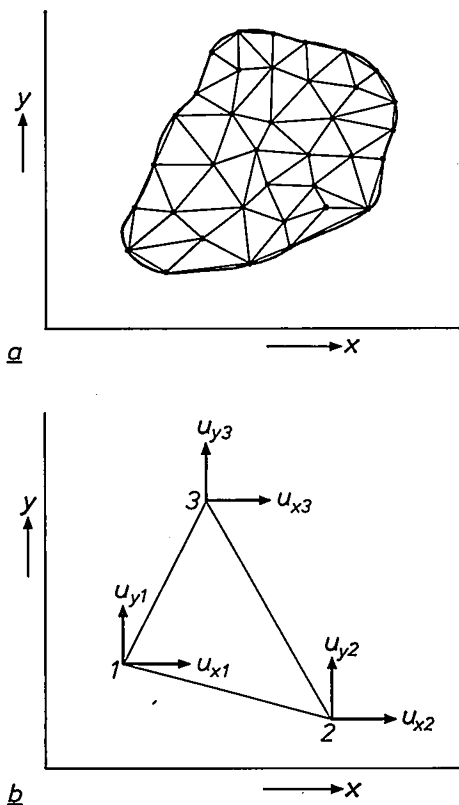

Fig. 2. *a*) Division of a thin flat plate into triangular elements. The three corners of each triangle are taken as 'nodes'. This means that the displacements of the other points of each element are expressed in terms of the displacements u_{xi} and u_{yi} of these points by using interpolation functions. (*b*) Linear interpolation functions are chosen for these triangular elements.

After selecting the interpolation functions $\boldsymbol{F}_n$ the strain can be calculated from

$$\boldsymbol{\varepsilon}_n = \boldsymbol{B}_n \boldsymbol{d}_n, \qquad (5)$$

where the matrix $\boldsymbol{B}_n$ is obtained from equation (4) by differentiation. This gives the functional Φ for element n:

$$\Phi_n = \int_{V_n} \tfrac{1}{2}\boldsymbol{d}_n^{\mathrm{T}}\boldsymbol{B}_n^{\mathrm{T}}\boldsymbol{E}_n\boldsymbol{B}_n\boldsymbol{d}_n\,\mathrm{d}V_n - \int_{S_{\mathrm{P}n}} \boldsymbol{d}_n^{\mathrm{T}}\boldsymbol{F}_n^{\mathrm{T}}\boldsymbol{p}_n\,\mathrm{d}S_n =$$
$$= \tfrac{1}{2}\boldsymbol{d}_n^{\mathrm{T}}\boldsymbol{k}_n\boldsymbol{d}_n - \boldsymbol{d}_n^{\mathrm{T}}\boldsymbol{q}_n, \qquad (6)$$

where

$$\boldsymbol{k}_n = \int_{V_n} \boldsymbol{B}_n^{\mathrm{T}}\boldsymbol{E}_n\boldsymbol{B}_n\,\mathrm{d}V_n \quad \text{and} \quad \boldsymbol{q}_n = \int_{S_{\mathrm{P}n}} \boldsymbol{F}_n^{\mathrm{T}}\boldsymbol{p}_n\,\mathrm{d}S_n;$$

$\boldsymbol{k}_n$ is the stiffness matrix of the element and $\boldsymbol{q}_n$ contains

the forces at the nodes equivalent to the external load p_n exerted on the element. For the complete body therefore

$$\Phi = \sum_{n=1}^{N} \Phi_n = \sum_{n=1}^{N} (\tfrac{1}{2}d_n^{\mathrm{T}}k_n d_n - d_n^{\mathrm{T}}q_n). \qquad (7)$$

The nodal displacements of the complete network are then combined in a single column matrix r; numbers are assigned to the nodes of the body for this operation. The relation between the nodal displacements d_n arranged element by element and the global nodal displacements r is stated by the *connection matrix* A:

$$\{d_1 d_2 d_3 \ldots d_N\} = \{A_1 A_2 A_3 \ldots A_N\}r, \text{ or } d = Ar. \qquad (8)$$

This matrix also relates to the transformation of local coordinate systems associated with the elements to a general system that applies to the complete body. If these systems are the same A is a Boolean matrix (which only contains ones and zeros).

Substituting from (8), (7) becomes:

$$\Phi = \tfrac{1}{2}r^{\mathrm{T}}A^{\mathrm{T}}kAr - r^{\mathrm{T}}A^{\mathrm{T}}q, \qquad (9)$$

where $k = \lceil k_1 k_2 k_3 \ldots k_N \rfloor$ (these brackets indicate a diagonal matrix), and $q = \{q_1 q_2 q_3 \ldots q_N\}$. We now define

$$K = A^{\mathrm{T}}kA \quad \text{and} \quad f = A^{\mathrm{T}}q; \qquad (10)$$

K is the stiffness matrix of the body subdivided into elements and f contains the nodal-point forces equivalent to the external load p. Therefore

$$\Phi = \tfrac{1}{2}r^{\mathrm{T}}Kr - r^{\mathrm{T}}f. \qquad (11)$$

Since E is symmetrical, k and K are also symmetrical.

To determine the displacements and hence the values of r for which the functional Φ has a minimum value, we calculate the derivatives of Φ with respect to the various elements of r, and set them equal to zero. This gives the set of linear equations

$$Kr = f. \qquad (12)$$

The column matrix f contains all the forces that act upon the body, and hence the forces at the points where we wish to support the body. These forces are in equilibrium; their interdependence is expressed by the six equilibrium equations for the complete body. This dependence has the result that the matrix K is singular (i.e. it has no inverse), so that the set of equations (12) has an infinite number of solutions; a rigid-body motion is still possible.

To eliminate this interdependence, the values of a number of nodal displacements must be given in the statement of the problem; this number must be at least as many as are necessary to prevent rigid-body motion. All the displacements whose values have been given before-hand are called 'prescribed' displacements r_{P}; the associated unknown reaction forces are denoted by f_{P}. The remaining unknown nodal displacements, called 'local' displacements are denoted by r_{L}, the associated known forces by f_{L}. A corresponding arrangement of the matrix K now gives:

$$\begin{bmatrix} K_{\mathrm{LL}} & K_{\mathrm{LP}} \\ K_{\mathrm{PL}} & K_{\mathrm{PP}} \end{bmatrix} \begin{bmatrix} r_{\mathrm{L}} \\ r_{\mathrm{P}} \end{bmatrix} = \begin{bmatrix} f_{\mathrm{L}} \\ f_{\mathrm{P}} \end{bmatrix}. \qquad (13)$$

Multiplied out this gives:

$$K_{\mathrm{LL}}r_{\mathrm{L}} + K_{\mathrm{LP}}r_{\mathrm{P}} = f_{\mathrm{L}}, \quad \text{and} \qquad (14)$$

$$K_{\mathrm{PL}}r_{\mathrm{L}} + K_{\mathrm{PP}}r_{\mathrm{P}} = f_{\mathrm{P}}. \qquad (15)$$

From (14) it follows that

$$r_{\mathrm{L}} = K_{\mathrm{LL}}^{-1}(f_{\mathrm{L}} - K_{\mathrm{LP}}r_{\mathrm{P}}), \qquad (16)$$

and the reaction forces can be determined from this and (15).

After the calculation of the unknown displacements r_{L} the nodal displacements d for each element can be determined from the now completely known matrix r with the aid of equation (8). From these and equation (5) the distribution of the strain can then be found, and the distribution of the stress in the different elements can now be found with the aid of Hooke's law. The stresses and strains for each separate nodal point can now be calculated as the mean of the values that have been calculated in the elements that share the node. These values are not in general exactly equal; this is inherent in the nature of the displacement method.

From (12), with the aid of equations (10) and (8) it can be shown that

$$q_r = kd, \qquad (17)$$

where q_r represents the internal nodal forces for each element. These can be calculated if d is known. The resulting nodal forces $f_r = \{f_{\mathrm{L}} f_{\mathrm{P}}\}_r$ can then be calculated from eq. (10); $f_{\mathrm{L}r}$ must of course be equal to the originally introduced load f_{L}, while $f_{\mathrm{P}r}$ gives the reaction forces. In the ASKA system this method is used instead of equation (15) to calculate the reaction forces.

A numerical calculation on a computer, based on the finite-element method, thus consists in general of the seven following stages.

— Idealization of the structure. Formation of the connection matrix A.

— Calculation of the element stiffness matrices k_n and formation of the matrices K_{LL} and K_{LP}.

— Calculation of the equivalent nodal forces $f_{\mathrm{L}} - K_{\mathrm{LP}}r_{\mathrm{P}}$.

— Calculation of the displacements r_{L}.

— Calculation of the nodal displacements d_n, the stresses σ_n and the strains ε_n for each element.

— Calculation of the mean strains and stresses for each node.
— Calculation of the reaction forces f_P.

In practice the calculation of the various quantities does not follow these formulae exactly. For example, the matrix A, which contains very many zeros, is not formed as a complete matrix, and the stiffness matrix K is not determined from the formal matrix multiplication A^TKA. More efficient methods have been developed for these processes, but we shall not pursue the matter further here.

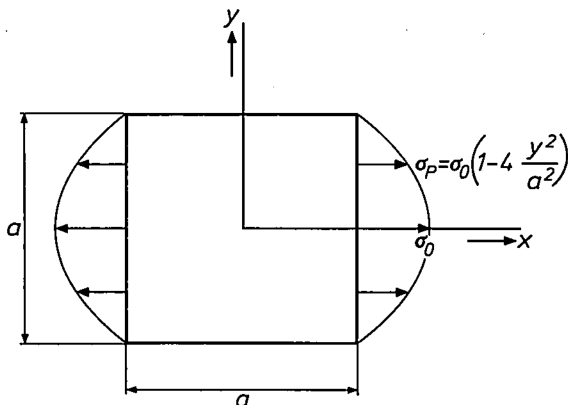

Fig. 3. Square plate loaded by a parabolically distributed tension on two opposite sides. The dimensions of the plate are $0.8\times0.8\times0.01$ m, the modulus of elasticity E is 2×10^{11} N/m^2 and Poisson's ratio ν is 0.3. The load σ_P is indicated as a line load (force per unit length) and is assumed to act over the complete thickness of the plate; $\sigma_0 = 16\times10^5$ N/m.

The ASKA I program

As we said in the introduction, the ASKA I program was specially developed for the solution of linear static problems by the finite-element method. The program can be applied for structures in which the displacements and the strains remain small at the loads imposed. The material must also have linear elastic behaviour; it may be anisotropic with the anisotropy defined in terms of local coordinate systems.

The program consists of a total of 250 000 instructions, distributed over about 2500 subroutines. The total storage required for the program is about 2.3 Mbytes (eight-bit bytes); by applying 'overlay' techniques the main-memory capacity necessary can be limited to about 310 kbytes. In overlay techniques only those parts of the program necessary for a particular phase of the calculation are present in the main memory during that phase. The rest of the program is stored in a disc memory. During an ASKA program there is therefore an intensive traffic of programs and numerical data between the disc and the main memory.

Procedure for solution

In applying ASKA I for the solution of a practical problem [5] there are a number of separate phases: the statement of the problem, the idealization of the structure, the preparation of the numerical data and the actual calculation. We shall now discuss this procedure; by way of illustration we shall indicate what happens in the solution of the simple problem of *fig. 3*. This refers to a thin square plate, loaded on two opposite sides by a parabolically distributed tension. It is required to find the displacements and stresses in the plate. Analytical solutions to this problem are known [6] [7], and we shall compare the ASKA results with these.

The statement of the problem

The problem must first of all be clearly described; this means that the *geometry, properties of the materials* and the *load* must be established. (Fig. 3 and its caption together form the statement of the problem of our example.) For a complicated structure it is sometimes necessary to simplify the structure a little, before dividing it up into elements, so as to arrive at a model that can be calculated by the finite-element method. The mechanical behaviour of this model must of course correspond sufficiently well with that of the actual structure.

The idealization of the structure

As we emphasized earlier, the subdivision of the structure into elements is the most important phase of the solution process. First the types of element are selected that might be expected to represent the behaviour of the structure as closely as possible. The size and location of the elements are then determined; the topology of the network is thus established.

To choose the degree of fineness of the network (mesh), it is necessary to have some knowledge of the behaviour of the structure under load; at places where large gradients in the stresses can be expected, the network should be made finer than elsewhere. A finer network does not just give a more accurate solution, however, it also requires more computer time and is therefore more expensive. In practice the idealization of a structure is always a compromise between the accuracy desired and the expense.

[5] See also: ASKA part I — Linear static analysis, user's reference manual, ISD report No. 73, Univ. Stuttgart 1971 (Revision C, 1975).
[6] S. Timoshenko and J. N. Goodier, Theory of elasticity, 2nd edn, McGraw-Hill, New York 1951.
[7] G. R. Cowper, G. M. Lindberg and M. D. Olson, A shallow shell finite element of triangular shape, Int. J. Solids & Struct. 6, 1133-1156, 1970.

In the ASKA I program element types are available for many categories of problems: for example for structures built up from bars and beams, continua subjected to planar stress or strain, axisymmetric continua, plates, thin- and thick-walled shells and three-dimensional continua. The element library of ASKA I now contains 48 elements, in various families, such as bar elements, two-dimensional elements, ring elements, plate elements, shell elements and three-dimensional elements. The location of the nodes is fixed for each element, and also the number of degrees of freedom and the form of the interpolation functions. These degrees of freedom can for example be displacements and their derivatives, and rotations. In the remainder of this article we shall only refer to displacements.

With a number of elements there is the possibility of applying them together with other elements in the same structure. The condition for this is that the variation of the displacement should be the same at the adjacent boundary surfaces of the elements. The user himself can also add new elements to the system.

In idealizing a structure it is not only necessary to set up the subdivision into elements, the *boundary conditions* have to be laid down as well. At a kinematic boundary condition the displacement at a node can be either prescribed or 'suppressed'. If it is suppressed the prescribed value is zero (e.g. at a support). As was explained on p. 60, at least as many displacements must be specified as are necessary to prevent rigid-body motion. A boundary condition can also be laid down by setting the displacements of various nodes equal to one another, without assigning a specific value. Finally, initial strains can be specified at nodes or for each element. Possible static boundary conditions are: external forces at nodes, distributed loading on the element surfaces and thermal loading specified by initial strains. The distributed loading can be line load (force per unit length), surface load (force per unit area) or volume load (force per unit volume). Both the prescribed displacements and the forces can be specified in local coordinate systems selected by the user. Various loading cases for a structure can be calculated in a single ASKA calculation.

It is appropriate to mention some of the important features of the idealization here.

— If there are symmetries in the structure and the loading it is sufficient to calculate only part of the structure.

— By assigning appropriate numbers to the nodes a band structure can be produced in the stiffness matrix; the elements not equal to zero are then located in a band on both sides of the diagonal. Since the width of this band strongly affects the computation time (a wide 'bandwidth' requires a great deal of computer time), it is important to keep this width as small as possible (see *fig. 4*).

— Programs can be developed that can generate the subdivision into elements for some structures completely automatically. These 'mesh-generator' programs start from the geometrical description of the structure and some basic information about the degree of fineness desired for the network. They give both the topological description of the network and the coor-

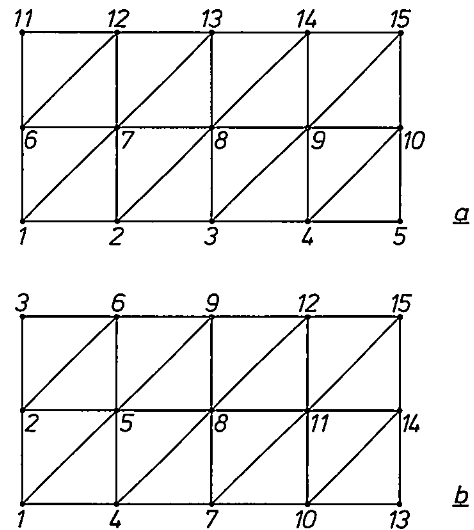

Fig. 4. Simple network of triangular elements with the nodes numbered. The numbering should be arranged to make the resultant bandwidth of the stiffness matrix of the structure as small as possible (the bandwidth of a matrix is the width of the region, on either side of the diagonal, where the elements are different from zero). This can be arranged by ensuring that the difference in node numbers is as small as possible for each element. For the sample given in this figure this means that the numbering should not run parallel to the long side (*a*) but parallel to the short side (*b*).

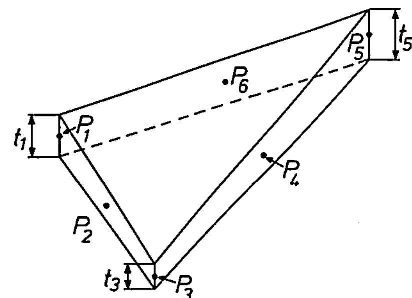

Fig. 5. The two-dimensional element code-named 'TRIM 6', used in the idealization of the structure of fig. 3. This element has six nodes (P_1 to P_6) with three degrees of freedom at each node. These are the displacements in the direction of the three coordinate axes. The element only possesses stiffness, however, for the displacements in its own plane. These displacements follow quadratic curves, i.e. the interpolation functions F are quadratic. t_1, t_2 and t_3 give the thicknesses at the three corners.

dinates of the nodes. The use of a mesh generator saves a considerable amount of time, because setting up such an idealization 'by hand' is usually the most time-consuming part of the procedure. At Philips we now have mesh generators for two-dimensional problems and for calculating picture-tube envelopes.
— There may be advantages in using substructures; this procedure will be discussed separately below.

The idealized structure (types of elements used, num-

The preparation of the numerical data

The numerical data necessary for the performance of a calculation is now collected. This includes:
— The nodal coordinates; if they are not generated by a mesh generator they will have to be measured off from drawings, or from the actual structure, usually a very time-consuming activity.
— The geometrical data for the elements (e.g. the thickness).

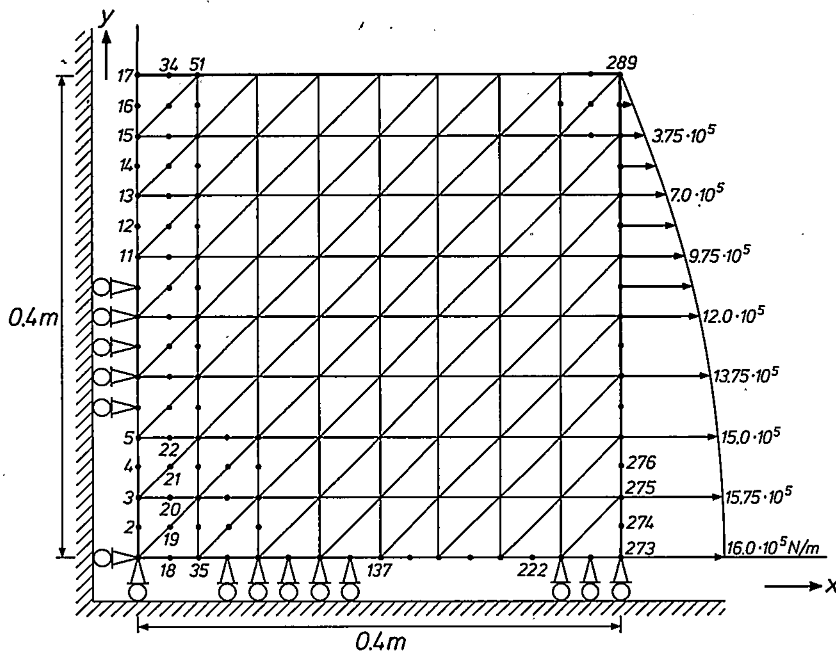

Fig. 6. Subdivision into elements for the calculation of the structure of fig. 3. Because of the symmetry in geometry and loading it is only necessary to consider a quarter of the structure. At all the nodes along the lines of symmetry the displacements perpendicular to these lines must be suppressed (drawn as roller supports for a number of nodes). For node *1* this means that it is fully supported. The value of the load at the nodes is given on the right. The smallest bandwidth for the stiffness matrix is obtained by numbering the nodes parallel to one of the axes.

bering of the nodes, suppressed and prescribed displacements) is defined in the 'topological description', which makes use of a specially designed programming language.

We shall now return to our example of fig. 3. Since the plate is in plane stress, a two-dimensional element should obviously be chosen; the most suitable one here is the element known as TRIM 6 (*fig. 5*). This element has zero stiffness for displacements perpendicular to the plane of the element. Because the structure is symmetrical in shape and in loading, only a quarter of the plate needs to be taken into consideration; we choose the element distribution of *fig. 6*.

— The elastic constants of the elements. In the isotropic case these are Young's modulus E and Poisson's ratio ν; in the anisotropic case the complete elasticity matrix must be given.
— The values of the load quantities (prescribed displacements, nodal forces, distributed loads, initial strains).
— Any local systems of axes in which the load is given or the anisotropic elasticity matrices are defined.

This data is input into the computer in blocks each containing a particular kind of data, e.g. the nodal coordinates. Each block is preceded by a code indicating the contents of the block.

The calculation

In the ASKA I program a calculation is divided into a number of logical stages, such as the data input, the calculation of the elemental stiffness matrices, the assembly of the stiffness matrix of the structure, etc. The program modules that perform these stages are called 'processors' in the ASKA system, and are activated by the user by calling subroutines in a FORTRAN program. This program, which directs the actual running of the program, is called ASKA Processor Control, or APC for short; it consists of a list of processors that have to be worked through in succession.

Fig. 7 shows a block diagram of a simple calculation with the ASKA program. Each block represents an ASKA processor; the function it performs or the quantity to be calculated is indicated inside the block, and the name of the processor is indicated in the upper right-hand corner of the block. The data that is processed by the processors is grouped in logical entities, called 'books'; these books are each given an alphanumeric name. The user can perform certain operations with these books by using this name as argument in a processor call. In this way the user can decide for example which books he would like to output as the result of the calculation, such as displacements, stresses or reaction forces.

The computer time required for a calculation with the ASKA I program varies from a few minutes to several hours, depending on the magnitude of the problem. For the more complicated problems it is desirable to run the calculation in several stages, rather than all at once; the 'books' with the intermediate results (e.g. the stiffness matrices) are then put on tape and read in again in the following stage or stages. Special input-output processors are available in ASKA for this.

During the complete calculation checks are carried out to see if errors have arisen. An extensive error-diagnosis system has been built into ASKA that can give some 600 different error messages. Sometimes these only contain comments that are of use to the user, while the calculation continues in the normal way; but if the error is serious the calculation is immediately stopped.

Substructures

The ASKA system also offers the possibility of splitting a structure into several parts and dividing each into elements separately. A partial network of this type is called a *substructure*; see *fig. 8*. The substructures are then interconnected by the nodes that lie on the boundaries, which means that the displacements at these nodes are made equal to one another for the various substructures. In this case we refer to *external* displacements. The nodes combining the substructures in this way together form the *main net*. The assembly of substructures to form a main net is essentially analogous to the combination of elements to form a network [8].

Fig. 7. Block diagram of a calculation of mechanical strength with the ASKA I program. Each block represents a processor, i.e. a program that performs a particular logical stage of the calculation. The code name for calling the processor in the control program APC (ASKA Processor Control) is indicated in each block. In this program the user must establish the procedure to be followed in the calculation and he determines which results must be calculated and output.

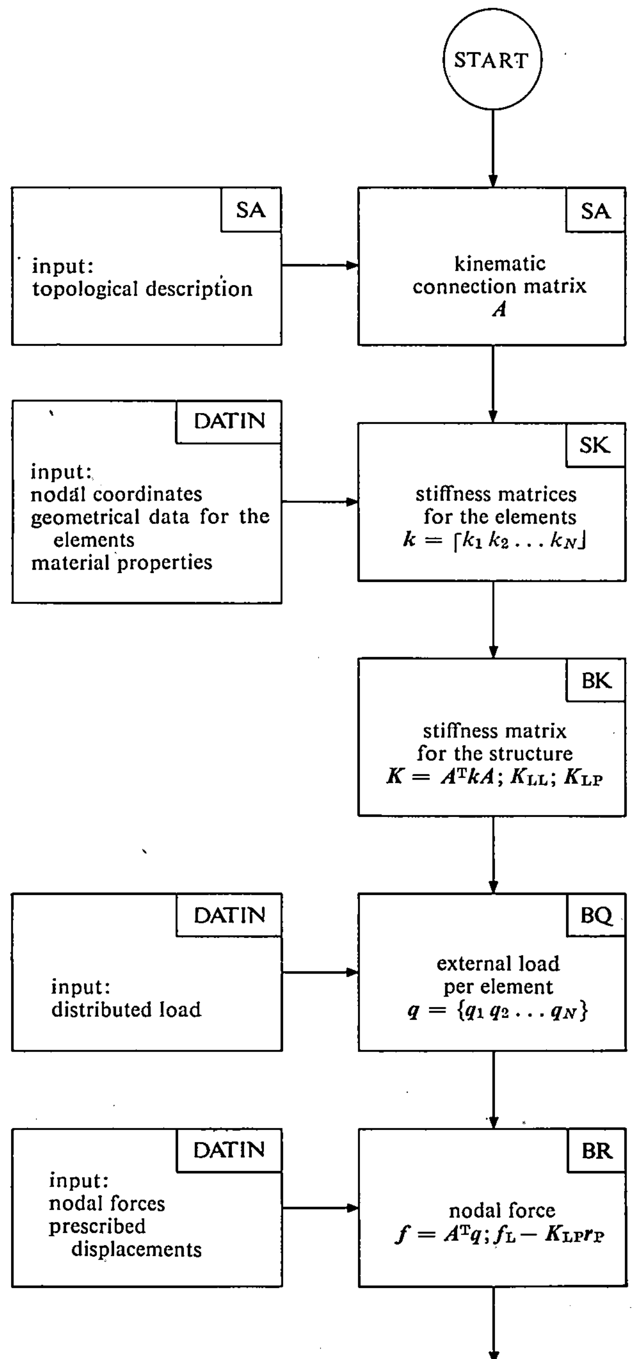

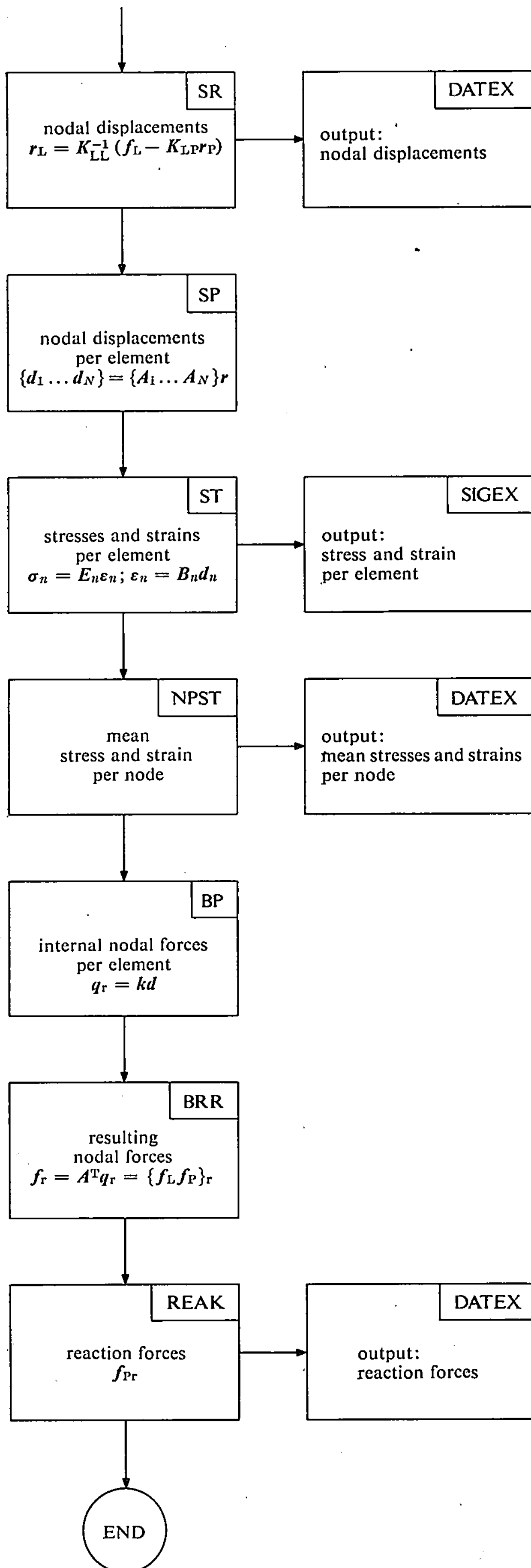

The application of substructuring can offer various advantages:
— It simplifies the idealization of the structure, since this can now be done separately for each substructure.
— It introduces the possibility of making standardized 'presolved' substructures for parts of structures that are used a number of times (in the same or in different structures). This can save a great deal of computer time.
— Alterations in the element distribution or in the actual structure itself can be made much more quickly and inexpensively, since they are now made for individual substructures where appropriate.
— Substructures permit hinges and sliding contacts to be included.
— Errors in the input data can be traced and corrected for the appropriate substructure.
— Selective data output can be made substructure by substructure.

The ASKA system can now also be used to divide a substructure even further into subsubstructures (recursive substructuring).

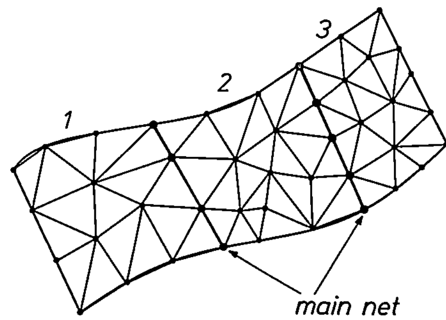

Fig. 8. Diagram of a structure divided into three substructures (*1*, *2* and *3*). The substructures are interconnected by the nodes at the boundaries, which together constitute the 'main net'.

Assessment of the results

A critical appraisal of the results of an ASKA calculation is desirable. There will always be some uncertainty about the accuracy of the results, because of the free choice in the degree of fineness of the network, particularly if it is not possible to make any predictions about the behaviour of the structure. Experience will bring confidence here; in some cases, however, the user will only be satisfied when he finds that a second calculation with a finer distribution gives results only marginally different. If results obtained from experiments or analytical calculations are also available, then comparison will obviously give a check on the calculation. When a certain type of structure has to be cal-

[8] J. S. Przemieniecki, Theory of matrix structural analysis, Mc-Graw-Hill, New York 1968.

culated repeatedly it is particularly useful to use an element distribution whose accuracy has been verified by such a comparison.

Table I shows by way of illustration some results from the calculation of our example. The displacements and the mean stresses are given at a number of nodes and these are compared with the results of an analytical calculation. It can be seen that a good agreement has been achieved with the selected idealization. The highest deviation is less than 2%.

Table I. Some results from the ASKA calculation of the example of fig. 3, compared with the results from an analytical calculation [9]. Values are quoted for a few displacements u_i (in m) and stresses σ_{ij} (in N/m²) at the nodes 1, 17, 273 and 289, of the idealized structure; see fig. 6.

	ASKA	Exact	Deviation %
u_{y17}	-0.8828×10^{-4}	-0.8852×10^{-4}	0.27
u_{x273}	2.9467×10^{-4}	2.9548×10^{-4}	0.27
u_{x289}	0.7363×10^{-4}	0.7439×10^{-4}	1.02
u_{y289}	0.1058×10^{-4}	0.1039×10^{-4}	1.83
σ_{xx1}	1.3742×10^{8}	1.3745×10^{8}	0.02
σ_{yy1}	-0.2289×10^{8}	-0.2255×10^{8}	1.51
σ_{xx17}	0.6552×10^{8}	0.6571×10^{8}	0.29
σ_{yy17}	0.0002×10^{8}	0	—
σ_{yy289}	0.0075×10^{8}	0	—

In a calculation of some magnitude the number of results is large and their interpretation is often difficult. To obtain a good interpretation the user will often find it necessary to apply further processing to the results. He could for example find it useful to apply transformations to coordinate systems of his own selection, or to display the results. It would then be necessary for him to write his own programs for such processing, because the facilities that ASKA has to offer here are very limited.

Some modifications

To adapt the ASKA system to specific needs such as those encountered in calculating television picture tubes, a number of additions and alterations to the program have been developed at Philips Research Laboratories.

The preparation of the data to be input for an ASKA calculation is a considerable task, which can only be automated in a few special cases. The chance that errors are made in this preparation is consequently so large that it is necessary to make an effective check on the correctness of this data before the expensive computation procedure is set under way. This is done in an 'ASKA prerun' (a procedure with a shortened APC); a special processor has been developed for this (VERIFY), which starts from the topological description and the numerical data to make a drawing of the structure that has been input. The user can then check from the drawing whether the topological description

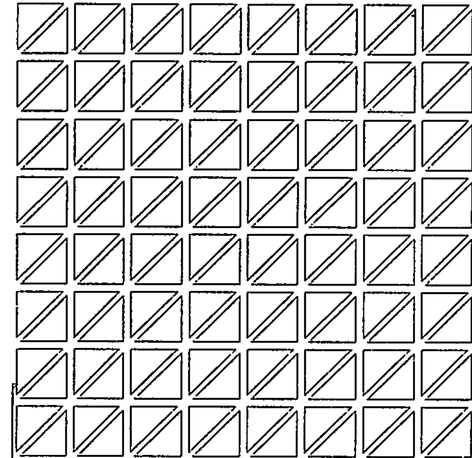

Fig. 9. Drawing of the network of fig. 6, made with the processor VERIFY to check the input data. All the elements are shown here, so that the user can check whether all the elements that should have been defined are in fact present in the topological description.

and the nodal coordinates are correct. *Fig. 9* shows such a plot of the input for the problem of fig. 3 as an example. The user can choose the viewing point for the structure in VERIFY, and also the scale of the drawing.

A simple extension to the VERIFY processor allows a drawing to be made of the deformed structure by superposing the calculated displacements at the coordinates of the nodes. A readily comprehensible presentation of the other results, the stresses and strains at the various nodes, is a rather intractable problem, particularly for three-dimensional structures. For two-dimensional structures a processor has been developed that draws lines of equal stress, and for picture tubes a processor has been produced that represents the calculated results (displacements, stresses, strains) along the line of interaction of an arbitrary plane with the inner or outer surface of the envelope.

The ASKA I program can be used to calculate structures with very large numbers of unknowns (10 000 or more). Equally large numbers of equations arise in the process, so that a great deal of computer time is required. A considerable reduction in this computer time can be obtained if the subroutines that perform the various matrix manipulations are rewritten in the symbolic language of the computer instead of in FORTRAN. These operations can then be performed twice as fast as in the original version.

Even when the calculation has been speeded up in this way the computation of a large structure requires several hours of computer time. Since the chance of a computer failure in such a length of time is by no means inconsiderable, it is important to be able to preserve the intermediate results of the calculation. Then if there is a machine failure it is not necessary to start the whole calculation all over again, but merely at the intermediate point. This is called a 'checkpoint/restart' facility. Such a facility has been simultaneously introduced at both Philips Research Laboratories and ISD, but in rather different ways; in calculating picture-tube envelopes a combination of the two methods is used. Although retrieving the intermediate results in such a situation is expensive in computer time and transport costs, this safety measure is a prudent one for the longer calculations.

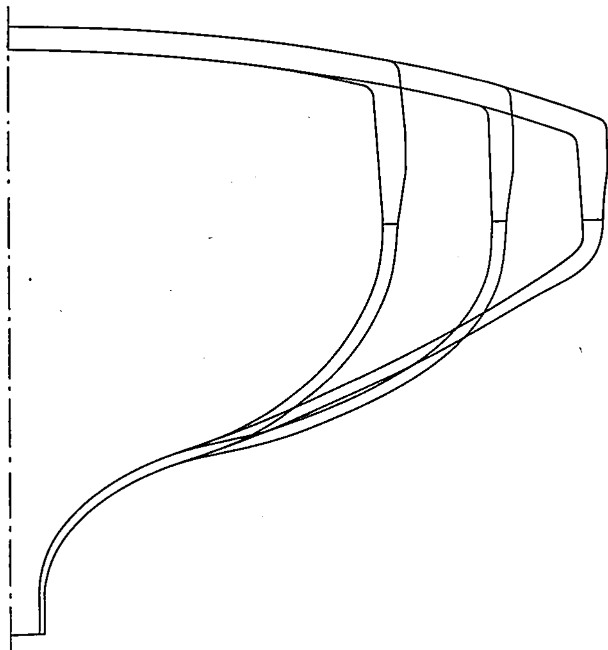

Fig. 10. The diagonal cross-section and the two symmetry cross-sections of the envelope of the 26-inch 110° colour-television picture tube. The envelope thickness is 12 mm at the centre of the screen.

A recent development permits the user to introduce linear dependences between degrees of freedom. This can be important for structures idealized with different kinds of elements, hinged structures or structures containing rigid subassemblies. The theoretical basis of this development was established at Delft University of Technology [10]; it has been included in the ASKA system at Philips, with about 80% of the program made up from existing ASKA modules.

Calculation of a picture-tube envelope

The calculation of the 26-inch 110° colour-television envelope will now be discussed as a representative example. Calculation of the mechanical behaviour of television envelopes has the advantage that it is then possible to determine at the design stage whether the envelope will bear the stresses due to the evacuation. The alternative of making strain-gauge measurements on a prototype is time-consuming and expensive. The calculations therefore reduce the design time and design costs for a new type of envelope. They also provide more information about permissible temperature variations and hence indicate the way to design an envelope with the optimum glass thickness for manufacture.

An incidental effect is the possibility of making calculations for the press tools as well.

The statement of the problem

The two symmetry cross-sections and the diagonal cross-section of the 26-inch 110° envelope are shown in *fig. 10*. The envelope consists of a glass screen and a glass cone; the two are bonded together by devitrifying enamel. The bond is not taken into account in the calculation.

We shall only consider the loading case in which the envelope is subjected to an external overpressure of 1 atm. Because of symmetry in load and geometry it is only necessary to calculate a quarter of the envelope.

The Young's modulus of the glass is taken as 0.67×10^{11} N/m^2 and Poisson's ratio as 0.27.

The idealization of the structure

Since the envelope is fairly thick, and since a three-dimensional stress pattern is to be expected in the transition from the front of the screen to the raised edge — a region where high strains will occur — a three-dimensional type of element was selected. Elements that appeared suitable were the TET-10, a tetrahedron with 10 nodes and a quadratic displacement field, or an element from the HEXE family — particularly the HEXEC-27 (see *fig. 11*). Although trial calculations showed that the HEXEC-27 required more computer time, and gave results that were only slightly more accurate than those from the TET-10, the element distribution with the HEXEC-27 was so much more convenient that this element was adopted.

The element distribution that was used for the calculation (see *fig. 12*) consists of a single layer of 304 elements; it was assumed that the variation in stress

[9] The exact values were taken from the article of note [7].

[10] H. A. C. M. Spaas, J. G. M. van de Reek and D. K. Wielenga, Linear constraints in the ASKA programming system, PROGEL report PRGL-SYST-R 75-2, Laboratorium voor Energievoorziening en Kernreactoren van de Technische Hogeschool, Delft.

over the thickness of the glass could be represented sufficiently accurately in this way. Substructuring was applied; the red lines in fig. 12 and the boundary between screen and cone divide the structure into six substructures. Since the feature of most interest is the stress variation at the transition between the front of the screen and the raised edge the network was made rather finer here, whereas a relatively coarse network was satisfactory for the cone. The narrow neck at the end of the cone was not included in the calculation. The tube was assumed to be sealed off there; the effect of this approximation will be local. The lowest point of the cone is supported in the z-direction (this is the direction of the axis of the tube). *Table II* gives the values of some of the characteristic quantities from the six substructures and the main net.

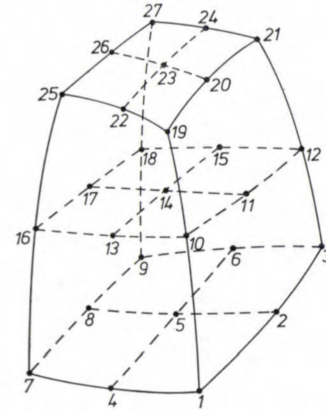

Fig. 11. The HEXEC-27 element, which is used in the idealization of the envelope of a picture tube. The element has 27 nodes; the sides are all parabolic. There are three degrees of freedom at each node: u_x, u_y and u_z; the displacement function is given by a polynomial of the fourth degree.

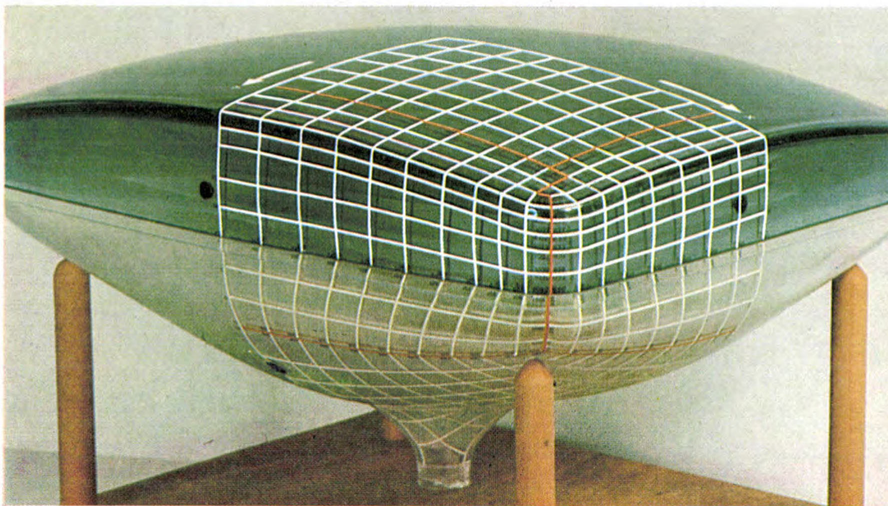

Fig. 12. Idealization for the calculation of the mechanical behaviour of a picture-tube envelope. Because of the symmetry in shape and loading it is only necessary to calculate a quarter of the envelope. This part is idealized by a single layer of elements of the type in fig. 11. It is divided into six substructures; the red lines and the boundary between screen and cone separate the substructures.

Table II. Characteristic quantities for the six substructures of the idealized envelope and for the main net connecting these substructures. The suppressed displacements (with prescribed value zero) are at the symmetry cross-sections and at the sealed-off neck of the envelope, the external displacements couple the substructures together and the local displacements are the remaining unknown displacements. The number given at the far right of the table for each substructure is a measure of the 'bandwidth' B of the stiffness matrix.

Substructure	No. of elements	No. of nodes	No. of displacements			$\frac{1}{2}(B+1)$
			local	external	suppressed	
1	48	663	1644	255	90	290
2	68	921	2229	489	45	319
3	54	741	1761	417	45	319
4	30	441	885	417	21	145
5	24	357	705	345	21	145
6	80	1071	2771	327	115	348
Total	304	—	9995	—	—	—
Main net	—	375	1107	—	—	—

The preparation of the numerical data

The coordinates of the corners of the elements were obtained by measuring the envelope in fig. 10 on a coordinate table (the intermediate points were determined by interpolation). This is only possible for the calculation of an existing tube, of course; if it is desired to calculate a tube at the design stage then the coordinates will have to be derived from an engineering drawing. If a mesh generator for this problem is available, this will give the nodal coordinates as well as the element distribution.

The nodal-point loads were calculated by special ASKA processors from the values of the external load, which were given for each element.

A check was of course also made in this case on the correctness of the input data: drawings of the element distribution were made with the processor 'VERIFY'. These plots for all six substructures have been combined in a single diagram in *fig. 13*.

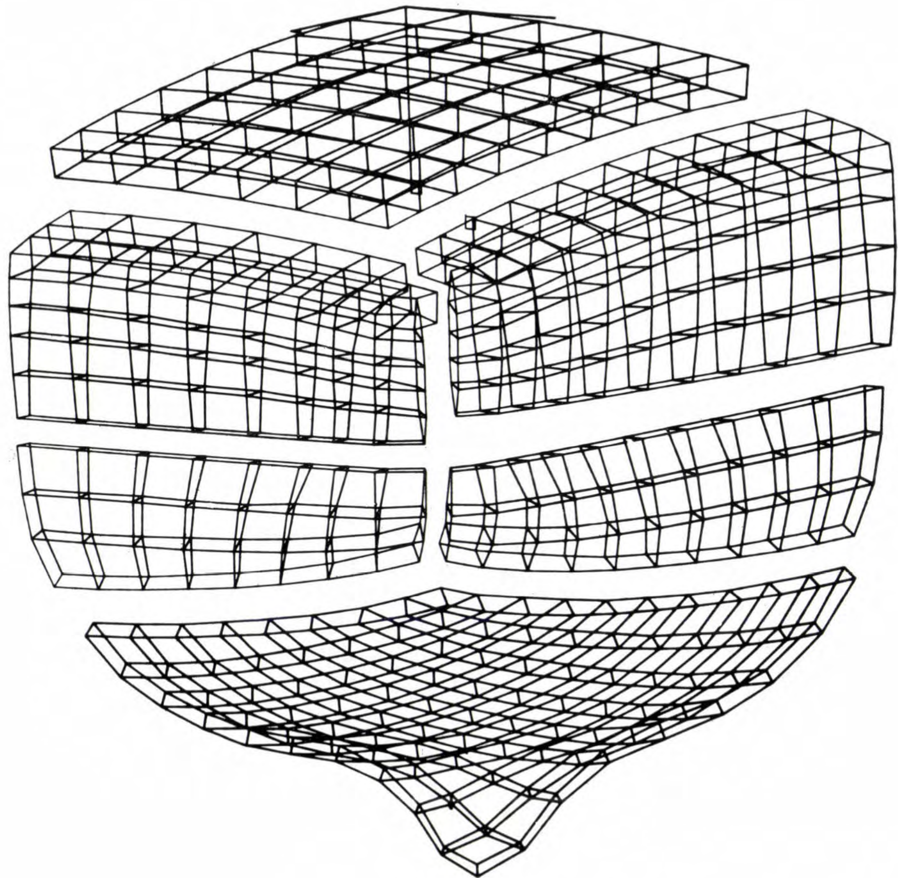

Fig. 13. Drawing of the network of fig. 12, made with the processor VERIFY. The drawing was produced by combining the plots of the six separate substructures with a small spacing between them.

Performance

The calculation of this structure with some 11 000 unknowns required about seven hours of computer time when it was first performed on the IBM 360/75 computer. The costs were correspondingly high. These costs have now been reduced by about a half by using the procedures for reducing the computer time and for minimizing the memory capacity required.

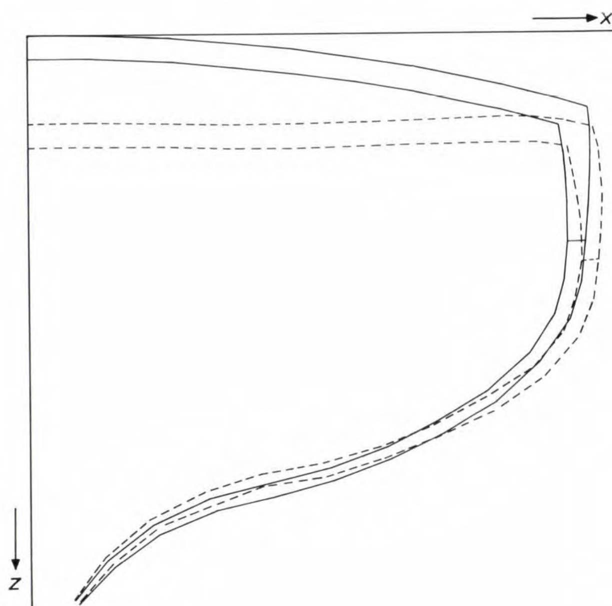

Fig. 14. Deformation of the largest symmetry cross-section of the envelope under the overpressure of 1 atm due to the evacuation. The scale on which the displacements are plotted is larger than the scale on which the geometry of the tube is shown; the largest deflection at the centre of the screen is about 0.2 mm.

Fig. 14 shows the calculated deformation of the largest symmetry cross-section of the envelope. From experience it has been found that in assessing the strength of a glass structure the most informative quantity is the strain produced, particularly its positive maximum. Glass is much less sensitive to pressure.

The calculated strains at the glass surface in the smallest symmetry cross-section of the envelope are shown in *figs. 15* and *16*; comparison of the measured and calculated values indicates good agreement. The greatest deviation is at the point R (the transition from the front of the screen to the raised edge) and at the end of the cone. We should remember here that in the idealization the rounded transition to the raised edge is replaced by a sharp edge, while the measurements at this location are also less accurate. The deviations at the end of the cone can be explained by the coarser element distribution for the cone and the 'sealed-off' idealization, which does not correspond with reality. Good agreement is obtained however in the practically important region on either side of the point R in figs. 15 and 16, where there is considerable bending. There are

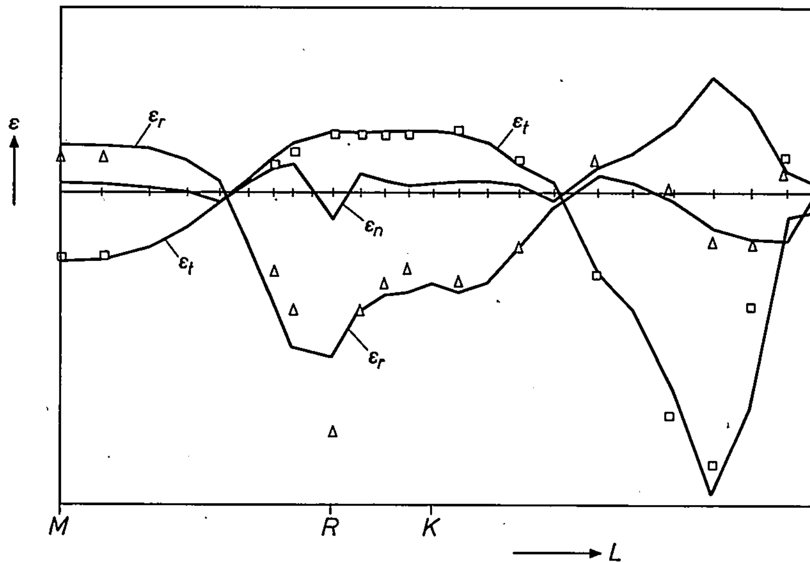

Fig. 15. The strain ε in the glass along the inside of the envelope at the smallest symmetry cross-section. The strain has been plotted against the position L on the developed line of intersection of this cross-section and the inside surface; the point M corresponds to the centre of the screen, the point R to the transition between the front of the screen and the raised edge and the point K to the transition between the screen and the cone. The solid lines connect the calculated values, transformed to local coordinate systems defined by the normal n to the glass surface and the tangents to the surface in the plane of the cross-section (radial r) and perpendicular to it (tangential t). Measured values are also given for ε_r (triangles) and ε_t (squares). The agreement between the measured and calculated values is very good.

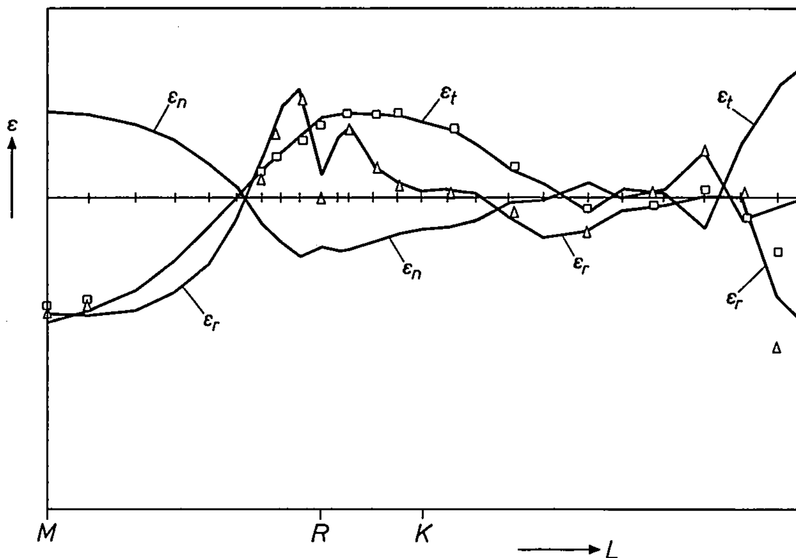

Fig. 16. As fig. 15, but now for the strains at the outer surface, plotted on the developed line of intersection between the smallest symmetry cross-section and the outer surface.

two positive peaks in ε_r here on the outside of the tube, which are approximated very closely in the calculation.

We can conclude that ASKA has been found to be an indispensable design tool in achieving the aims stated at the beginning of this section. The ASKA programs have greatly assisted in reducing the time and expense required in the design of a television picture tube.

Other systems

In addition to ASKA there are a large number of comparable systems available or accessible for use. Each of these systems has its strong and weak points; we shall mention here ICES-STRUDL, also available at Philips, and NASTRAN, SESAM, ASAS, BERSAFE and MARC [11]. The MARC system is very suitable for solving nonlinear problems, and will also shortly be available at Philips. All of these systems can be applied to large groups of very diverse problems. They all have one feature in common with ASKA: specialist knowledge and experience is necessary in use for advanced applications. Again, it will in practice often be necessary to adapt the system to the user's particular requirements, which means that close cooperation with software specialists is essential.

Finally, we should like to emphasise that the finite-element method is a numerical method of solution. This means that an understanding of the behaviour of a structure as a function of various parameters can only be obtained after repeated calculations, which may not be permissible in practice. Analytical methods, giving

[11] A survey of the various systems is given in: K. E. Buck, D. W. Scharpf, E. Stein and W. Wunderlich (ed.), Finite Elemente in der Statik, Ernst, Berlin 1973.
[12] See K. Washizu, Variational methods in elasticity and plasticity, Pergamon Press, Oxford 1968.

more closed solutions in which the effect of the parameters is immediately visible, are still preferable. Unfortunately, the kinds of problem that can be solved by such methods are becoming relatively fewer. The finite-element method, on the other hand, has considerably increased the range of kinds of problem that are amenable to calculation.

Appendix: The equations of the theory of linear elasticity

In the theory of linear elasticity the following relations (they are given here in tensor notation) are applicable.
here in tensor notation) are applicable.

The relation between the strains ε_{ij} and the displacements u_i is:

$$\varepsilon_{ij} = \tfrac{1}{2}(u_{i,j} + u_{j,i}), \tag{A1}$$

where the subscripts i and j take the successive values 1, 2 and 3, indicating the coordinates x, y and z, while a subscript following a comma indicates a differentiation with respect to the appropriate coordinate.

For $i = j = 1$ eq. (A1) gives:

$$\varepsilon_{xx} = \tfrac{1}{2}\left(\frac{\partial u_x}{\partial x} + \frac{\partial u_x}{\partial x} = \frac{\partial u_x}{\partial x},\right.$$

so that the strain in the x-direction is the derivative with respect to x of the displacement in the x-direction. If $i = 1, j = 2$, then we have:

$$\varepsilon_{xy} = \tfrac{1}{2}\left.\frac{\partial u_x}{\partial y} + \frac{\partial u_y}{\partial x}\right),$$

where $2\varepsilon_{xy}$ is the shear in the x,y-plane (the angular change of a right angle between the x- and the y-direction). The quantities ε_{yy}, ε_{zz}, ε_{yz} and ε_{zx} follow from (A1) in the same way.

The equilibrium equations for the stresses σ_{ij} are expressed as

$$\sigma_{ij,j} = 0. \tag{A2}$$

In addition to the convention for differentiation as mentioned above, the summation convention is also applied: if an index appears twice in a term then a summation must be made over this index. For $i = 1$ eq. (A2) then gives:

$$\frac{\partial \sigma_{xx}}{\partial x} + \frac{\partial \sigma_{xy}}{\partial y} + \frac{\partial \sigma_{xz}}{\partial z} = 0.$$

This equation can be derived from the equilibrium of the normal and shear forces acting on a volume element dxdydz in the x-direction. Corresponding equations for the y- and z-directions can be derived from (A2) for $i = 2$ and 3. From the equilibrium of moments it also follows that $\sigma_{ij} = \sigma_{ji}$.

Hooke's law, which gives the relation between the stresses σ_{ij} and the strains ε_{ij}, can be expressed as

$$\sigma_{ij} = E_{ijkl}\varepsilon_{kl}, \tag{A3}$$

where E_{ijkl} contains the elasticity constants of the material. For a three-dimensional isotropic body this gives six equations that can be expressed in matrix notation as:

$$\begin{bmatrix}\sigma_{xx}\\ \sigma_{yy}\\ \sigma_{zz}\\ \sigma_{xy}\\ \sigma_{yz}\\ \sigma_{zx}\end{bmatrix} = \frac{E}{(1+\nu)(1-2\nu)}\begin{bmatrix}1-\nu & \nu & \nu & 0 & 0 & 0\\ \nu & 1-\nu & \nu & 0 & 0 & 0\\ \nu & \nu & 1-\nu & 0 & 0 & 0\\ 0 & 0 & 0 & \frac{1-2\nu}{2} & 0 & 0\\ 0 & 0 & 0 & 0 & \frac{1-2\nu}{2} & 0\\ 0 & 0 & 0 & 0 & 0 & \frac{1-2\nu}{2}\end{bmatrix}\begin{bmatrix}\varepsilon_{xx}\\ \varepsilon_{yy}\\ \varepsilon_{zz}\\ 2\varepsilon_{xy}\\ 2\varepsilon_{yz}\\ 2\varepsilon_{zx}\end{bmatrix}$$

Here E is Young's modulus and ν is Poisson's ratio.

Substituting (A1) in (A3) gives

$$\sigma_{ij} = E_{ijkl}\cdot\tfrac{1}{2}(u_{k,l} + u_{l,k}),$$

so that (A2) becomes

$$E_{ijkl}\cdot\tfrac{1}{2}(u_{k,lj} + u_{l,kj}) = 0. \tag{A4}$$

This equation represents a set of three partial differential equations, for $i = 1$, 2 and 3. The terms are summed over the subscripts j, k and l; the terms $u_{k,lj}$ and $u_{l,kj}$ represent second derivatives.

These differential equations (A4) can be used to describe any problem in linear elasticity theory; in obtaining solutions it is of course always necessary to take into account the boundary conditions for the particular problem. If a numerical solution of the equations is desired, difference methods must be used; however, setting up the difference equations and finding their solution is so difficult for a three-dimensional body that there is a strong incentive to find other methods. One such possibility gives us the *variational calculus*; it can be shown from this that solving the elasticity equations is mathematically equivalent to finding a displacement field $u_i(x,y,z)$ that satisfies the kinematic boundary conditions and gives a minimum for a particular 'functional' (a quantity whose value is defined by the function u_i and its derivatives). For a body of volume V and with an area S_P of its surface subjected to a load p_i, this functional is

$$\Phi = \int_V \tfrac{1}{2}E_{ijkl}\,\varepsilon_{ij}\,\varepsilon_{kl}\,\mathrm{d}V - \int_{S_P} p_i\,u_i\,\mathrm{d}S. \tag{A5}$$

We shall give no proof of this here [12].

Summary. The finite-element method (FEM) is a numerical approximation method for carrying out stress calculations on structures that are too complicated for the classical analytical methods. The structure is divided into elements (e.g. bars, triangles, tetrahedra), and a number of points in these elements are selected as nodes. To calculate the stiffness of an individual element the displacements of the points of the element are expressed in terms of the displacements of the nodes with the aid of interpolation functions. The stiffness of the structure divided into elements is next calculated; the displacements of the nodes can then be determined as a function of the external load. From these it is possible to calculate the displacements, stresses and strains in each separate element, as well as the reaction forces at the places where the structure is supported.

In the article the theory of the finite-element method is derived from the general equations of elasticity theory; the ASKA computer system that Philips have purchased for carrying out calculations by this method is also described. The ASKA I program for linear elastic problems, which is applied here, consists of 250 000 instructions, distributed over 2500 subroutines; it occupies 2.3 Mbytes (eight-bit bytes) of memory capacity and requires a main memory of 310 kbytes. The element library contains 48 elements for various kinds of structures. A description is given of the solution procedure: the input of the topological and numerical data from the idealized structure, the application of substructures, the actual calculation and the assessment of the results. Some modifications have been introduced into the ASKA program, in particular for checking the input data, displaying the results and speeding up the calculation. The calculation of the envelope of the existing 26-inch 110° colour-television tube is given as an example. Because of symmetry in shape and loading only a quarter of this tube has to be calculated. This part is idealized by a single layer of elements of the type HEXEC-27, divided into six substructures. The results of the calculations, which took seven hours on the IBM 360/75, are in fairly good agreement with the results of strain-gauge measurements on the tube. Making these calculations while a new television tube is still in the design stage allows the design procedure to be speeded up considerably.

Recent scientific publications

These publications are contributed by staff of laboratories and plants which form part of or cooperate with enterprises of the Philips group of companies, particularly by staff of the following research laboratories:

Philips Research Laboratories, Eindhoven, The Netherlands	*E*
Philips Research Laboratories, Redhill, Surrey, England	*M*
Laboratoires d'Electronique et de Physique Appliquée, 3 avenue Descartes, 94450 Limeil-Brévannes, France	*L*
Philips GmbH Forschungslaboratorium Aachen, Weißhausstraße, 51 Aachen, Germany	*A*
Philips GmbH Forschungslaboratorium Hamburg, Vogt-Kölln-Straße 30, 2000 Hamburg 54, Germany	*H*
MBLE Laboratoire de Recherches, 2 avenue Van Becelaere, 1170 Brussels (Boitsfort), Belgium	*B*
Philips Laboratories, 345 Scarborough Road, Briarcliff Manor, N.Y. 10510, U.S.A. (by contract with the North American Philips Corp.)	*N*

Reprints of most of these publications will be available in the near future. Requests for reprints should be addressed to the respective laboratories (see the code letter) or to Philips Research Laboratories, Eindhoven, The Netherlands.

J. J. Andriessen & H. Bouma (Institute for Perception Research, Eindhoven): Eccentric vision: adverse interactions between line segments.
Vision Res. **16**, 71-78, 1976 (No. 1).

H. Bacchi & H. Tchen (CCETT, Rennes): Réalisation d'un transformateur d'images en temps réel.
Ann. Télécomm. **30**, 363-373, 1975 (No. 9/10). *L*

V. Belevitch: On the synthesis of passive reciprocal two-ports with prescribed $S_{12}(p)$.
Arch. Elektronik & Übertragungst. (AEÜ) **29**, 473-476, 1975 (No. 11). *B*

V. Belevitch: On frequency-power relations.
Int. J. Circuit Theory & Appl. **4**, 93-98, 1976 (No. 1). *B*

U. K. P. Biermann: The lithium/sulphurhexafluoride heat source in combination with a Stirling engine as an environmental independent underwater propulsion system.
Record 10th Intersociety Energy Conversion Engng. Conf. (IECEC), Newark 1975, pp. 1023-1030. *E*

L. Blok: Characterization of vapor grown (001) $GaAs_{1-x}P_x$ layers by selective photo-etching.
J. Crystal Growth **31**, 250-255, 1975. *E*

P. M. Boers, M. T. Vlaardingerbroek & M. Danielsen (Technical University of Denmark, Lyngby): Dynamic behaviour of semiconductor lasers.
Electronics Letters **11**, 206-208, 1975 (No. 10). *E*

H. M. van den Bogaert, D. J. Zwanenburg & Th. A. M. M. Maas: Structure analysis of the reaction products of 1′,3′,3′-trimethylspiro[2*H*-1-benzopyran-2,2′-indolines] with 1,1-bis[4-(dimethylamino)phenyl]ethylene and related compounds.
Recueil Trav. chim. Pays-Bas **94**, 218-220, 1975 (No. 9/10). *E*

H. van den Boom & R. E. Breemer: Simple setup for Raman difference spectroscopy.
Rev. sci. Instr. **46**, 1664-1666, 1975 (No. 12). *E*

A. H. Boonstra & C. A. H. A. Mutsaers: Photohydrogenation of ethyne and ethene on the surface of titanium dioxide.
J. phys. Chem. **79**, 2025-2027, 1975 (No. 19). *E*

P. W. J. M. Boumans & F. J. de Boer: Studies of an inductively-coupled high-frequency argon plasma for optical emission spectrometry, II. Compromise conditions for simultaneous multi-element analysis.
Spectrochim. Acta **30B**, 309-334, 1975 (No. 9). *E*

P. W. J. M. Boumans, F. J. de Boer, F. J. Dahmen*, H. Hoelzel* & A. Meier* (* E. Merck AG, Darmstadt): A comparative investigation of some analytical performance characteristics of an inductively-coupled radio frequency plasma and a capacitively-coupled microwave plasma for solution analysis by emission spectrometry.
Spectrochim. Acta **30B**, 449-469, 1975 (No. 10/11). *E*

P. Branquart, J.-P. Cardinael, J. Lewi, J.-P. Delescaille & M. Vanbegin: An optimized translation process and its application to ALGOL 68.
Lecture Notes in Computer Science **38**, 1976, IX + 334 pp. (Springer, Berlin). *B*

J. C. Brice, J. M. Robertson & H. van der Heide: A new method of stirring for LPE growth.
J. Crystal Growth **31**, 375-379, 1975. *M, E*

J.-J. Brissot & C. Belouet: Cellules solaires au silicium polycristallin.
Rev. int. Héliotechnique 2ème semestre 1975, 42-47. *L*

H. E. Brockman: Improved yields for MOST's using ion implantation.
J. appl. Phys. **47**, 1716-1718, 1976 (No. 4). *M*

F. J. A. den Broeder & H. Zijlstra: Relation between coercive force and microstructure of sintered $SmCo_5$ permanent magnets.
Proc. 3rd Eur. Conf. on Hard magnetic materials, Amsterdam 1974, pp. 118-129; 1975. *E*

C. A. M. van den Broek (Philips Ceramics Laboratory, Uden): Introduction of various grades of raw materials in ferrite magnet production.
Proc. 3rd Eur. Conf. on Hard magnetic materials, Amsterdam 1974, pp. 53-61; 1975.

A. Broese van Groenou: Grinding of ferrites, some mechanical and magnetic aspects.
IEEE Trans. **MAG-11**, 1446-1451, 1975 (No. 5). *E*

H. H. Brongersma & T. M. Buck: Selected topics in low-energy ion scattering: surface segregation in Cu/Ni alloys and ion neutralization.
Surface Sci. **53**, 649-658, 1975. *E*

S. D. Brotherton: Measurement of deep-level spatial distributions.
Solid-State Electronics **19**, 341-342, 1976 (No. 4). *M*

M. Brouha & K. H. J. Buschow: Thermomagnetic history effects in $LaCo_5$, $ThCo_5$ and related compounds.
IEEE Trans. **MAG-11**, 1358-1360, 1975 (No. 5). *E*

M. Brouha & K. H. J. Buschow: Magnetic properties of $LaCo_{5x}Cu_{5-5x}$.
Proc. 3rd Eur. Conf. on Hard magnetic materials, Amsterdam 1974, pp. 162-165; 1975. *E*

E. Bruninx & E. van Meyl: The analysis of surface waters for iron, zinc and lead by coprecipitation on iron hydroxide and x-ray fluorescence.
Anal. chim. Acta **80**, 85-95, 1975 (No. 1). *E*

K. H. J. Buschow: Magnetic interactions in intermetallic compounds.
J. less-common Met. **43**, 55-67, 1975 (No. 1/2). *E*

K. H. J. Buschow: Magnetic properties of rare earth — magnesium compounds (RMg_3).
J. less-common Met. **44**, 301-306, 1976. *E*

F. M. A. Carpay: Die Morphologie der in-situ-gewachsenen Verbundwerkstoffe.
Handbuch der Mikroskopie in der Technik VII, Umschau Verlag, Frankfurt a.M. 1975, pp. 355-368. *E*

T. A. C. M. Claasen, W. F. G. Mecklenbräuker & J. B. H. Peek: Quantization noise analysis for fixed-point digital filters using magnitude truncation for quantization.
IEEE Trans. **CAS-22**, 887-895, 1975 (No. 11). *E*

M. G. Collet: An experimental method to analyse trapping centres in silicon at very low concentrations.
Solid-State Electronics **18**, 1077-1083, 1975 (No. 12). *E*

C. D. Corbey, R. Davies & R. A. Gough (University of Bradford): Wide-band varactor-tuned coaxial oscillators.
IEEE Trans. **MTT-24**, 31-39, 1976 (No. 1). *M*

M. Delfino: Solution crystal growth of ionic salts by electrolytic solvent decomposition.
J. Crystal Growth **32**, 378-380, 1976 (No. 3). *N*

G. Diemer: Scientific films; a look from inside a research laboratory.
Registratie 7, No. 3, 11-16, 1975. *E*

A. M. van Diepen, K. H. J. Buschow & H. W. de Wijn (Rijksuniversiteit Utrecht): On the origin of the high uniaxial magnetocrystalline anisotropy in $SmCo_5$.
Proc. 3rd Eur. Conf. on Hard magnetic materials, Amsterdam 1974, pp. 45-48; 1975. *E*

J. W. F. Dorleijn & A. R. Miedema: On the sign of the anomalous Hall effect in ferromagnetic alloys.
Physics Letters **55A**, 118-120, 1975 (No. 2). *E*

H. Durand & G. J. Naaijer: Water pumps driven by photovoltaic solar energy conversion.
Rev. int. Héliotechnique 2ème semestre 1975, 35-41. *L*

W. F. K. van den Eijnde: Taak en organisatie van technische produktinformatie.
Polytechn. T. pt/aktueel 1975, No. 39, pp. 3, 4, 10 & 12. *E*

F. L. Engel (Institute for Perception Research, Eindhoven): Visual conspicuity as an external determinant of eye movements and selective attention.
Thesis, Eindhoven 1976. (Philips Res. Repts. Suppl. 1976, No. 6.)

H. A. van Essen: I^2L en zijn toepassing in een digitale datazender.
T. Ned. Elektronica- en Radiogen. **40**, 127-134, 1975 (No. 5). *E*

W. G. Essers, G. Jelmorini & G. W. Tichelaar: The plasma-MIG process.
Advanced welding technology, Proc. 2nd Int. Symp. Japan Welding Soc., Osaka 1975, pp. 157-162. *E*

M. J. C. van Gemert: Radiative decay in the afterglow of strongly depleted Na-Ne-Ar low-pressure discharges.
J. appl. Phys. **46**, 4899-4903, 1975 (No. 11). *E*

G. Gerlagh & P. Baeyens (Philips Philite and Metalware Manufacturing Division, Eindhoven): A new etchant for photochemical milling of aluminium.
Trans. Inst. Met. Finish. **53**, 133-137, 1975 (No. 3).

C. J. Gerritsma, J. J. M. J. de Klerk & P. van Zanten: Changes of twist in twisted nematic liquid-crystal layers by frequency switching of applied electric fields.
Solid State Comm. **17**, 1077-1080, 1975 (No. 9). *E*

J. A. Geurst, F. A. Staas & W. van Haeringen: On the minimum temperature attainable in dilution refrigerators.
Physics Letters **55A**, 251-254, 1975 (No. 4). *E*

U. Goebel, E. Dormann (both with Technische Hochschule Darmstadt) **& K. H. J. Buschow:** On the electronic structure of LaAg and LaZn.
J. Physics F **5**, 2198-2207, 1975 (No. 11). *E*

W. Goedbloed (Philips Elcoma Division, Eindhoven): Thin film M.I.C. activities in respect of reproducibility and reliability.
Internepcon/Europa '75, Int. Microelectronics Conf., Stuttgart 1975, session III, 13 pp.

A. H. Goemans & L. J. van Ruyven (Philips Semiconductor Development Laboratories, Nijmegen): Control of slip in horizontal silicon epitaxy with profiled susceptors.
J. Crystal Growth **31**, 308-311, 1975.

H. J. van Gorkom, M. P. J. Pulles (both with Huygens Laboratory, Leiden) **& J. S. C. Wessels**: Light-induced changes of absorbance and electron spin resonance in small photosystem II particles.
Biochim. biophys. Acta **408**, 331-339, 1975 (No. 3). *E*

L. Guidoux (Télécommunications Radioélectriques et Téléphoniques — TRT, Le Plessis-Robinson, France): Egalisation autoadaptive des lignes téléphoniques.
Thesis, Paris-Sud, Centre d'Orsay, 1974. (Philips Res. Repts. Suppl. 1976, No. 7.)

G. J. van Gurp (I, II) **& C. Langereis** (I): Cobalt silicide layers on Si: I. Structure and growth, II. Schottky barrier height and contact resistivity.
J. appl. Phys. **46**, 4301-4307, 4308-4311, 1975 (No. 10). *E*

J. Haisma, K. L. L. van Mierloo, W. F. Druyvesteyn & U. Enz: Static conversion of Bloch-line number and the self-collapse of hard bubbles.
Appl. Phys. Letters **27**, 459-462, 1975 (No. 8). *E*

H. W. Hanneman & M. J. J. Theunissen: Charge transfer devices and signal processing applications.
Journées d'Electronique 1975 on Advanced signal processing technology, Lausanne, pp. 101-130. *E*

J. 't Hart & R. Collier (Institute for Perception Research, Eindhoven): Integrating different levels of intonation analysis.
J. Phonetics **3**, 235-255, 1975.

N. Hazewindus: On non-constant orbit axial injection in a cyclotron.
Nucl. Instr. Meth. **128**, 169-171, 1975 (No. 1). *E*

N. Hazewindus (I, II), **A. Petterson** (II) **& B. J. Driessen** (II) (Philips Scientific and Industrial Equipment Division, Eindhoven): The axial injection system of the SIN Injector Cyclotron: I. Design considerations, II. Description and experiments.
Nucl. Instr. Meth. **129**, 325-329, 331-340, 1975 (No. 2). *E*

J. C. M. Henning & J. H. den Boef: Strain-modulated electron spin resonance of $MgO:Fe^{2+}$.
Phys. Stat. sol. (b) **72**, 369-373, 1975 (No. 1). *E*

W. J. van den Hoek & W. Klessens (Philips Lighting Division, Eindhoven): Carbon-fluorine transport reactions in carbon-filament incandescent lamps.
High Temp. Sci. **7**, 215-219, 1975 (No. 3).

W. J. van den Hoek & W. Klessens (Philips Lighting Division, Eindhoven): Carbon-hydrogen and carbon-chlorine transport reactions in carbon-filament incandescent lamps.
Carbon **13**, 429-432, 1975 (No. 5).

H. Hörster, R. Kersten & F. Mahdjuri: Sonnenkollektoren mit hohem Wirkungsgrad.
Klima+Kälte-Ing. **4**, 113-118, 1976 (No. 3). *A*

A. Huijser & J. van Laar: Work function variations of gallium arsenide cleaved single crystals.
Surface Sci. **52**, 202-210, 1975 (No. 1). *E*

A. Humbert, L. Hollan & D. Bois: Incorporation of deep centres in VPE GaAs.
Appl. Phys. **9**, 117-119, 1976 (No. 2). *L*

M. Jatteau & M. Tissot (SODERN, Limeil-Brévannes): Instruments de radiométrie infrarouge.
Mesures Régul. Autom. **40**, No. 12, 37-45, 1975. *L*

H. D. Jonker, A. E. Morgan & H. W. Werner: Secondary ion mass spectrometry of compositional changes in garnet films.
J. Crystal Growth **31**, 387-391, 1975. *E, H*

E. M. H. Kamerbeek: Comparison between permanent-magnet motors and other types of electric motor.
Proc. 3rd Eur. Conf. on Hard magnetic materials, Amsterdam 1974, pp. 214-224; 1975. *E*

A. Klopfer & W. Lems: Verbesserungsmöglichkeiten von Glühlampen.
Elektrotechn. Z. etz.b **28**, 86-87, 1976 (No. 4). *A*

A. J. R. de Kock, P. J. Roksnoer & P. G. T. Boonen: The introduction of dislocations during the growth of floating-zone silicon crystals as a result of point defect condensation.
J. Crystal Growth **30**, 279-294, 1975 (No. 3). *E*

W. L. Konijnendijk & J. M. Stevels: The structure of borate glasses studied by Raman scattering.
J. non-cryst. Solids **18**, 307-331, 1975 (No. 3). *E*

F. Kools: Some aspects of Sr-hexaferrite powders and suspensions.
Proc. 3rd Eur. Conf. on Hard magnetic materials, Amsterdam 1974, pp. 98-101; 1975. *E*

B. Kramer & C. Balzano: Observation of a peak in the negative-resistance/r.f.-voltage curve for high-low GaAs IMPATT diodes.
Electronics Letters **11**, 509-511, 1975 (No. 21). *L*

P. Kramer, C. H. F. Velzel, M. R. de Haan, K. Compaan (Philips Electro-Acoustics Division, Eindhoven), **J. J. M. Braat & K. A. Immink**: Het 'VLP' systeem: Het optische uitleessysteem; De signaalverwerking; Toepassingen van het 'VLP' medium; De detectie van positioneringsfouten; De servosystemen.
T. Ned. Elektronica- en Radiogen. **40**, 153-175, 1975 (No. 6). *E*

G. S. Krijtenburg (Philips Elcoma Division, Eindhoven) **& A. L. Stuijts**: The sintering behaviour of Sr-hexaferrites prepared from $SrCO_3$ containing some $SrSO_4$.
Proc. 3rd Eur. Conf. on Hard magnetic materials, Amsterdam 1974, pp. 83-86; 1975. *E*

J.-P. Krumme, G. Bartels, P. Hansen & J. M. Robertson: Control of the growth-induced magnetic anisotropy in ferrimagnetic garnet films grown by liquid-phase epitaxy.
Mat. Res. Bull. **11**, 337-346, 1976 (No. 3). *H, E*

K. E. Kuijk, W. J. van Gestel & F. W. Gorter: The Barber Pole, a linear magnetoresistive head.
IEEE Trans. **MAG-11**, 1215-1217, 1975 (No. 5). *E*

F. A. Kuijpers: Single-mask bubble memories: bit/chip organization with decoding.
IEEE Trans. **MAG-11**, 1136-1138, 1975 (No. 5). *E*

F. P. J. Kuijpers, L. Blok & A. T. Vink: Growth and characterization of GaP and $GaAs_{1-x}P_x$.
J. Crystal Growth **31**, 165-171, 1975. *E*

H. K. Kuiken: The cooling of a low-heat-resistance cylinder moving through a fluid.
Proc. Roy. Soc. London A **346**, 23-35, 1975 (No. 1644). *E*

S. K. Kurtz: Measurement of nonlinear optical susceptibilities.
Quantum electronics: a treatise, Vol. I. Nonlinear optics, Part A, publ. Academic Press, New York 1975, pp. 209-281. *N*

M. Laguës: Contribution à l'étude de la ségrégation de surface.
Thesis, Paris XI, Centre d'Orsay, 1975. (Philips Res. Repts. Suppl. 1976, No. 5.) *L*

J. G. M. de Lau: De invloed van chemische samenstelling en microstructuur op magnetische eigenschappen van nikkel-zink-cobalt-ferrieten.
Klei en Keramiek **25**, 185-192, 1975 (No. 10). *E*

W. A. Ledeboer & P. J. Schophuizen (Philips Elcoma Division, Eindhoven): Use of computer calculations for the design of low stray field loudspeaker systems.
Proc. 3rd Eur. Conf. on Hard magnetic materials, Amsterdam 1974, pp. 257-260; 1975.

F. K. Lotgering, A. M. van Diepen & J. F. Olijhoek: Mössbauer spectra of iron-chromium sulphospinels with varying metal ratio.
Solid State Comm. **17**, 1149-1153, 1975 (No. 9). *E*

D. Meyer-Ebrecht, K. Bethe, R. Hoefert & J. Lemmrich: Signale frequenzanalog dargestellt.
Elektronik (München) **25**, No. 6, 36-41, 1976. *H*

B. J. Mulder: Preparation of ultrathin, helium-tight, unbacked, unsealed metal windows for gas discharge lamps.
J. Physics E **8**, 1046-1048, 1975 (No. 12). *E*

K. H. Nicholas: A rapid method of predicting the sheet resistances of boron implanted layers.
Radiation Effects **28**, 177-181, 1976 (No. 3/4). *M*

T. J. A. Popma & M. G. J. Kamminga: The polar magneto-optic Kerr rotation of ferromagnetic perovskites (La, Bi, Sr)MnO_3.
Solid State Comm. **17**, 1073-1075, 1975 (No. 9). *E*

A. Rabier, J. Magarshack & P. Harrop: Influence of the structure of a cathode doping notch on the performance of TE diodes.
Proc. 1975 Cornell Electr. Engng. Conf., Ithaca, pp. 237-245. *L*

G. W. Rathenau: Change and permanence in magnets.
Proc. 3rd Eur. Conf. on Hard magnetic materials, Amsterdam 1974, pp. 7-16; 1975. *E*

H. Rau: Energetics of defect formation and interaction in pyrrhotite $Fe_{1-x}S$ and its homogeneity range.
J. Phys. Chem. Solids **37**, 425-429, 1976 (No. 4). *A*

R. Rautschke, G. Amelung, N. Nada (all with Martin-Luther-Universität, Halle/Saale), **P. W. J. M. Boumans & F. J. M. J. Maessen** (Universiteit Amsterdam): Beitrag zur Kinetik thermochemischer Reaktionen von Uranverbindungen in einer Graphitmatrix im Gleichstrombogen — Grundsätzliche Überlegungen über die Rolle thermochemischer Vorgänge als Partnereffekte in der spektrochemischen Analyse.
Spectrochim. Acta **30B**, 397-415, 1975 (No. 10/11). *E*

K. Rennicke & E. Polak (Philips Scientific and Industrial Equipment Division, Eindhoven): A computer controlled strategy for an open channel waste water system.
System simulation in water resources, editor G. C. Vansteenkiste, North-Holland Publ. Co., Amsterdam 1976, pp. 383-391. *H*

W. Rey: Commentaire à propos de 'Lissage de fractile par M. Cramer'.
Rev. fr. Autom. Inform. Rech. opérat. (R.A.I.R.O.) **9**, oct. 1975, 93-94 (No. V-3). *B*

W. Rey & L. J. Martin (Hôpital St. Pierre, Brussels): Estimation of hazard rate from samples.
40th Session Int. Stat. Inst., Warsaw 1975, pp. 686-688. *B*

J. M. Robertson & J. C. Brice: New flux systems for the LPE growth of thin garnet films.
J. Crystal Growth **31**, 371-374, 1975. *E, M*

J. M. Robertson, P. K. Larsen & P. F. Bongers: Epitaxially grown Bi-substituted iron garnet films for magneto-optic devices.
IEEE Trans. **MAG-11**, 1112-1114, 1975 (No. 5). *E*

T. E. Rozzi: A new approach to the network modelling of capacitive irises and steps in waveguide.
Int. J. Circuit Theory & Appl. **3**, 339-354, 1975 (No. 4). *E*

B. Schiek & J. Köhler: An improved microstrip-to-microslot transition.
IEEE Trans. **MTT-24**, 231-233, 1976 (No. 4). *H*

P. C. Scholten: Magnetic measurements on particles in suspension.
IEEE Trans. **MAG-11**, 1400-1402, 1975 (No. 5). *E*

G. B. Scott, D. E. Lacklison, J. L. Page & J. Hewett: Absorption spectra and magneto-optic figures of merit in the $Bi_xSm_{3-x}Fe_{5-y}Ga_yO_{12}$ system.
Appl. Phys. **9**, 71-77, 1976 (No. 1). *M*

J. M. Shannon: Recoil-implanted antimony-doped surface layers in silicon.
Applications of ion beams to materials 1975, Proc. Conf. Coventry (Inst. Phys. Conf. Ser. No. 28), pp. 37-43; 1976. *M*

A. Slob: Toekomstige ontwikkelingen in digitale schakelingen.
Polytechn. T. Elektr. **30**, 724-726, 1975 (No. 21). *E*

C. G. Sluijter: Scientific uses of television.
Science Film No. 9, 16-20, 1975. *(Also in French, pp. 11-15.)* *E*

W. L. N. van der Sluys: A lithium/sodium/sulphurhexafluoride heat source in combination with a Stirling engine as a propulsion system for small submersibles.
Record 10th Intersociety Energy Conversion Engng. Conf. (IECEC), Newark 1975, pp. 1031-1037. *E*

F. A. M. Snijders, N. A. M. Verhoeckx, H. A. van Essen & P. J. van Gerwen: Digital generation of linearly modulated data waveforms.
IEEE Trans. **COM-23**, 1259-1270, 1975 (No. 11). *E*

J. L. Sommerdijk, J. M. P. J. Verstegen (Philips Lighting Division, Eindhoven) **& A. Bril:** On the luminescence of $LiBaF_3:Eu^{2+}$.
J. Luminescence **10**, 411-413, 1975 (No. 6). *E*

W. T. Stacy & A. B. Voermans: Thermally activated stress relief in garnet layers grown by liquid phase epitaxy.
J. Crystal Growth **31**, 380-386, 1975. *E*

A. M. Stark: Fundamental one-dimensional analysis of transistors.
Thesis, Surrey 1975. (Philips Res. Repts. Suppl. 1976, No. 4.) *M*

S. Strijbos: Pressure filtration of permanent magnetic powders.
Proc. 3rd Eur. Conf. on Hard magnetic materials, Amsterdam 1974, pp. 102-105; 1975. *E*

K. Teer: Communication and telecommunication.
IEEE Trans. **COM-23**, 1040-1045, 1975 (No. 10). *E*

J. P. Thiran: On unit element structures for wave digital filters.
Proc. Conf. on Digital signal processing, Florence 1975, pp. 124-131. *B*

J. C. Tranchart & P. Bach: A gas bearing system for the growth of CdTe.
J. Crystal Growth **32**, 8-12, 1976 (No. 1). *L*

C. Wellekens: Simultaneous flat approximations of the ideal low-pass filter.
Proc. Conf. on Digital signal processing, Florence 1975, pp. 43-50. *B*

C. J. Werkhoven & R. C. Peters: On the kinetics of nitrogen incorporation in GaP LPE layers using NH_3 vapour doping.
J. Crystal Growth **31**, 210-214, 1975. *E*

P. A. C. Whiffin, T. M. Bruton & J. C. Brice: Simulated rotational instabilities in molten bismuth silicon oxide.
J. Crystal Growth **32**, 205-210, 1976 (No. 2). *M*

J. te Winkel: Past and present of the charge-control concept in the characterization of the bipolar transistor.
Adv. in Electronics & Electron Phys. **39**, 253-289, 1975. *E*

S. Wittekoek, T. J. A. Popma, J. M. Robertson & P. F. Bongers: Magneto-optic spectra and the dielectric tensor elements of bismuth-substituted iron garnets at photon energies between 2.2-5.2 eV.
Phys. Rev. B **12**, 2777-2788, 1975 (No. 7). *E*

J. M. Woodcock: Enhancement of the donor activity of implanted selenium in GaAs by gallium implantation.
Appl. Phys. Letters **28**, 226-227, 1976 (No. 4). *M*

H. E. J. Wulms: Integreerbare injectielogica (I^2L).
Polytechn. T. Elektr. **30**, 827-838, 1975 (No. 25). *E*

D. J. Zwanenburg & Th. A. M. M. Maas: The reactions between 1′,3′,3′-trimethylspiro[2*H*-1-benzopyran-2,2′-indolines] and 1,1-bis[4-(dimethylamino)phenyl]-ethylene; products and mechanism.
Recueil Trav. chim. Pays-Bas **94**, 215-218, 1975 (No. 9/10). *E*

M. de Zwart & Th. W. Lathouwers: Electric field-induced pitch contraction in the planar cholesteric texture of a liquid crystal with a large negative dielectric anisotropy.
Physics Letters **55A**, 41-42, 1975 (No. 1). *E*

Contents of Philips Telecommunication Review **34**, No. 3, 1976:

H. L. Bakker: A new 12/18 MHz coaxial transmission system for 3600 channels (pp. 89-101).
G. J. Kamerbeek, G. A. Klein & A. C. Steenhuisen: TCP 18 Central Control for PRX telephone switches (pp. 103-121).
L. H. Slotboom: DS 714/81, a new telegraph and data processor (pp. 122-135).
H.-J. Schmidt: A versatile equalizer theory (pp. 137-141).

Contents of Electronic Applications Bulletin **34**, No. 1, 1976:

Audio power amplifiers with Darlington output transistors, Part 2. Theory into practice (pp. 4-14).
L. E. Jansson: Power capacity of ferrite-cored transformers and chokes in switched-mode power supplies (pp. 20-47).

Volume 37, 1977, No. 2/3 pages 29-76 Published 20th September 1977

PHILIPS TECHNICAL REVIEW

VOLUME 37, 1977, No. 4

An equipment for automatic optical inspection of connecting-lead patterns for integrated circuits

F. L. A. M. Thissen

When every product from quantity production is separately examined by an inspector to see whether it meets the specifications, some 'bad' ones will almost inevitably slip through. It is therefore desirable to automate such 'visual inspection' as far as possible. This applies even more to the growing number of products that are virtually impossible to inspect visually in practice, for example because they are very small or the production runs are very large. Automated inspection is then an essential. We shall call this process 'automatic optical inspection', since the information travels by an optical path from the product to the inspection system. Work on this inspection system has been in progress at the Centre for Technology (CFT), where members of some of the Philips product divisions and the Research Laboratories cooperate on technology projects. An initial result of this work is a machine that makes an automatic optical inspection of the connecting-lead patterns on the flexible plastic 'tape' for mounting integrated circuits (called IC spiders). An important contribution to this project was made by G. P. J. Janssen of the Electrical Mechanization Department of the Video Division, which developed the electronic units for the system. A vital component of this system is the 'data formatter', which will also be used in other inspection systems. The mechanical units of the system were designed by the Mechanical Mechanization Department of the Video Division.

Introduction

The final inspection of many quantity-produced products is carried out by an inspector, who judges visually whether the product meets the specifications. For some products occasional sample checks will be sufficient; for others it may be necessary to subject every completed item to this visual inspection. A familiar example in the electronics industry of a product that has to be individually inspected is the printed-circuit board. Although it is no exception to have production runs of hundreds of thousands of such boards, every single one still has to be inspected visually. This means that many people are required to do this work, and since it is tedious and uninspiring it is inevitable that human errors will occur and that products with defects will be passed as satisfactory. Automation of this inspection is highly desirable, and it also seems perfectly feasible since the criteria are all clearly defined (the conducting tracks must all be present, there must be no short-circuits or near-short-circuits, etc.). As in visual inspection, the information from automated inspection will also pass along an optical path from the product to the inspection system. To indicate this we shall use the term 'automatic optical inspection'.

As a first move towards automatic optical inspection a machine has been developed for inspecting the 'pattern' of connecting leads on the flexible plastic 'tape' used for mounting integrated circuits [1]. These connecting leads are applied to a plastic tape by an electroplating process; see *fig. 1*. Each pattern of leads measures about 20×8.2 mm; the narrow tracks in the centre, on which the IC is mounted (the 'bonding zone'), are only 0.1 mm wide. The pattern has to

Ing. F. L. A. M. Thissen is with Philips Research Laboratories, Eindhoven.

[1] A. van der Drift, W. G. Gelling and A. Rademakers, Integrated circuits with leads on flexible tape, Philips tech. Rev. 34, 85-95, 1974.

meet very close tolerances. In the bonding zone only very slight dimensional deviations are permitted, because of the play encountered during the positioning of the IC on the pattern. The same requirements have to be met by the solder lands, i.e. the broad contacts at the end of the tracks with which the connecting leads are mounted on a board. The only requirements for the rest of the pattern are that there should be no restriction to the current flow and that there should be no short-circuits or leakage paths.

The situation for the inspection of the connecting leads differs from that for printed-circuit boards: the fabrication of the connecting leads is not yet combined with visual inspection; before the inspection system was put into use only a few pilot runs were made. where possible defects could cause trouble (for example the type number, which is also included in the pattern, is not inspected). Another advantage is that the various test specifications can easily be met in the various areas of the pattern.

The centre-line method is a 'global' method, that is to say one in which the whole pattern (or most of it) has to be accessible for inspection. This is no problem with connecting-lead patterns, but with large printed-circuit boards it can present difficulties. In addition to these and other global methods there are also methods for purely localized inspection, e.g. for determining local deviations in the regularity of the pattern, or for finding tracks that are too close together, etc.[2]. These other methods will not be considered here.

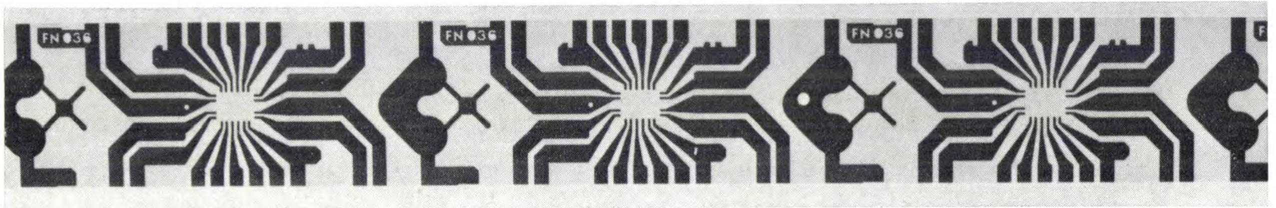

Fig. 1. Part of a tape with connecting-lead patterns for mounting integrated circuits. The copper tracks are applied by an electroplating process to a tape of transparent plastic with a width of 8.2 mm. An integrated circuit is soldered to the narrow tracks in the central region of each pattern; this is called the bonding zone; with the broad leads from the tracks the whole pattern, after having been cut from the tape, is mounted on a printed-circuit board. The system has found a fault in the centre pattern (a hole in a track bottom right). The pattern is then marked by punching a hole in the broad track on the right of it.

Owing to the small dimensions of the connecting-lead pattern, which makes it essential to use a microscope, and because of the diversity of the test specifications in the various zones, visual inspection of the millions of patterns produced in a year would be quite impossible. In other words there is no question of automating human labour, for without automatic inspection it just would not be possible to produce the required numbers of patterns. This trend will become increasingly apparent with other products in the future.

For the automatic optical inspection of connecting-lead patterns we use one of the methods developed for the inspection of printed-circuit boards, the *centre-line method*. This method consists in verifying the width of each conducting track and of each strip of insulation between two tracks. Each pattern to be inspected is compared with a model in which the centre-lines of these tracks and insulation strips have been established, as well as the minimum value for the width. A great advantage of the centre-line method compared with other methods, in which the whole pattern is scanned point by point, is that only the areas are inspected

A general picture of the system

The inspection system consists essentially of two television cameras that take pictures of the patterns, a transport system that moves the tape with the patterns past the cameras, and a minicomputer that compares the pictures from the cameras with the centre-line model stored in its memory (*fig. 2*). Each pattern is viewed in four parts: one camera takes three fields that together cover the whole pattern, and the other camera, with greater magnification, views a field that only includes the bonding zone (*fig. 3*). The tape is illuminated by transmitted light — the material is transparent — to obtain a good contrast between the tracks and the insulation (the plastic) between them.

At the same time as a picture is scanned by the camera the video information is digitized and stored in the computer memory. The picture consists of 400 lines. To obtain the same resolution horizontally and vertically, the lines are divided into 450 picture points in the digitizing process with the information 'black' or 'white', '1' or '0', corresponding to 'track' or 'no track'. For each field a total of 400×450 bits of infor-

mation are thus stored. Immediately after one of the fields of a pattern has been recorded in this way, its image information is compared with the centre-line model of this field, which is stored in the computer. Simultaneously the stepping motor is actuated to transport the next field in front of the camera, or a switch is made to the other camera (or both).

The installation, shown in fig. 2, operates semi-automatically or entirely automatically, as required. In semi-automatic operation the inspection process is interrupted as soon as the computer finds a fault and a teletypewriter types out coded data relating to the fault, including the dimensions. In addition the location of the fault is displayed on a television monitor, which always shows a picture of the field being inspected. The location of the fault is indicated on the display by a cross (*fig. 4*) or 'cursor'. The data will allow the user to decide whether or not he should reject the pattern, and he types in his decision. In entirely automatic operation the computer itself makes the decision from the reject criteria stored in its memory. When a pattern is rejected, a hole is punched into a particular place on the pattern (see fig. 1) and the inspection continues with the first field of the next pattern.

Before discussing the operation of the system in more detail, we shall first give a description of the centre-line method.

The centre-line method

In the centre-line method the model with which the inspected pattern is compared — four models for the connecting-lead patterns, one for each picture field — consists of the centre-line of all the tracks and insulation strips of the pattern; see fig. 3. Each of these centre-lines is assigned a test criterion that indicates the minimum required width of the track, and which also shows whether the centre-line belongs to a track or an insulation strip. When the width of a track in the pattern varies along a centre-line, different test criteria are given for the various parts of the centre-line.

The centre-lines can be established in a model in two ways. Lines that run horizontally or vertically or at an angle of 45° (by horizontal we mean here the longitudinal dimension of the pattern) are represented by the coordinates of the origin or starting point, the direction in which the line runs (designated by a figure between 1 and 8) and the length of the line (expressed in the number of image points). Lines at an arbitrary angle are indicated by the coordinates of the starting and end points. The required track widths are always indicated for a horizontal or vertical intersection with the track.

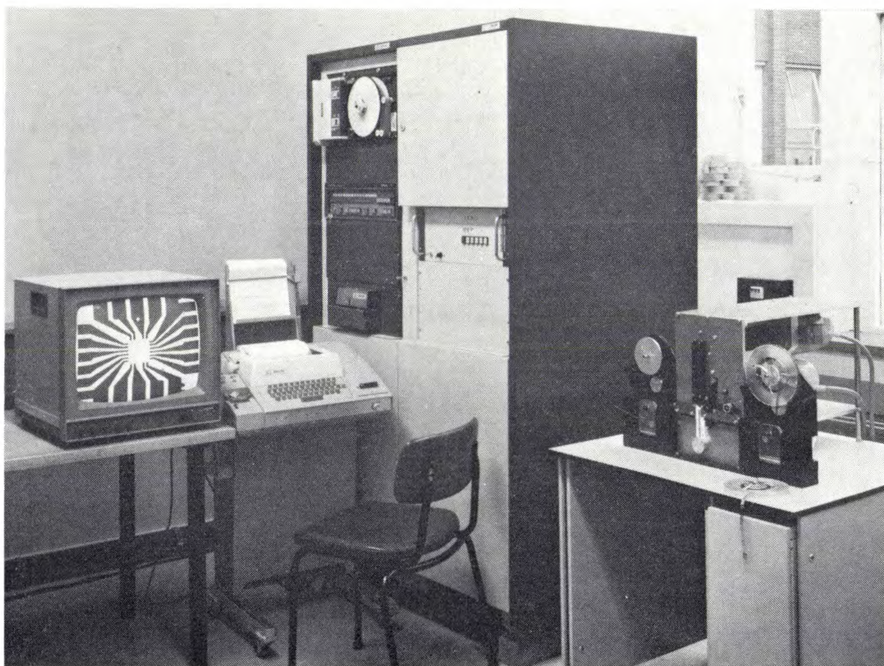

Fig. 2. System for the automatic inspection of connecting-lead patterns on tape. In the part on the right the plastic tape is transported past a light source so that the patterns can be viewed one at a time by two television cameras (for two different magnifications). One of the pictures taken is displayed on the monitor. The central unit is a Philips P 855 minicomputer, which compares the pictures with a model of the pattern stored in its memory.

[2] M. Ejiri, T. Uno, M. Mese and S. Ikeda, A process for detecting defects in complicated patterns, Computer Graphics and Image Processing 2, 326-339, 1973.

The centre-line models, four for each type of pattern to be inspected, are drawn up once, punched in a tape and stored in the computer memory. A special computer program has been developed for drawing up the model in a direct dialogue with the computer by means of an interactive display [3]. We shall not deal with this here.

The inspection of a track proceeds as follows. For each centre-line point a check is made to determine whether there are a sufficient number of 'track' points

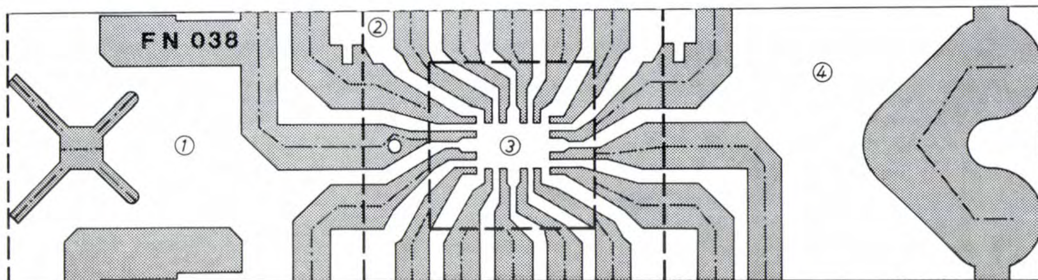

Fig. 3. Division of a pattern into four image fields. Fields *1*, *2* and *4* are recorded by the same camera and together cover the whole pattern; field *3*, recorded by a second camera with a greater magnification, covers only the bonding zone, which has to meet the tighter specifications for the accuracy. In fields *1*, *2* and *4* the centre-lines of the tracks in the centre-line model are indicated. The fields are recorded and inspected in the sequence *1*, *2*, *3*, *4*.

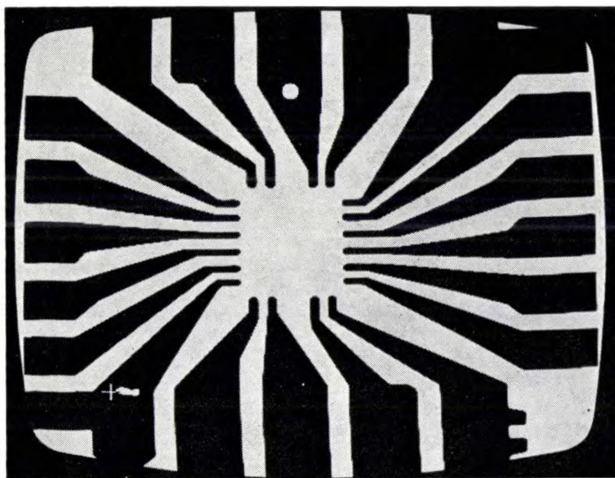

Fig. 4. Television-monitor display of field *2* of a pattern in which a fault has been found. This fault, a hole in a track, is marked by the computer with a cross (a 'cursor'). In semi-automatic operation of the system the user decides from the position of the error and its dimensional data, which are printed out by a teletypewriter, whether or not to reject the pattern. In automatic inspection this fault will certainly lead to rejection. The pattern with this fault is also shown in fig. 1.

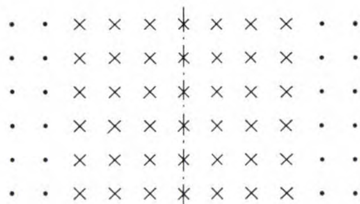

Fig. 5. Stored image of a vertical track with a width of seven points. The 'track' points are indicated by a cross, the insulation spacing by dots; the position of the centre-line from the model is indicated by a chain-dotted line. Since peripheral points may be missing as a result of quantization noise, a track width of only five points is required in the test criterion in this case. No fault is then found in the track in this example.

symmetrically arranged around each point in the stored video information. This check is made at a horizontal or vertical intersection with the track, depending on how the track width in the model is defined. It is of course necessary to know which points of the stored image correspond to the centre-line points of the model: image and centre-line model must be correctly positioned in relation to each other. We shall touch on this aspect later.

Let us now look at the actual situation for a track with a width of seven points (*fig. 5*). Owing to quantization noise during the recording and digitizing of the image, we cannot be certain whether the peripheral points of the track are present. When drawing up the centre-line model a width specification of five points is therefore laid down in the test criterion for this track. If we now examine the five points arranged symmetrically around the centre-line at the intersection, we may find any of the following situations.

1) The five points are all present.

2) All five points are there except for a peripheral point.

3) One or more points *in* the track are missing (and possibly a peripheral point as well).

In the first case the intersection is correct, as it is for all of the part of the track displayed. In the second case we find only four of the five points. This intersection would therefore really be faulty, but the fact that a *peripheral point* is missing indicates that the model may be positioned wrongly in relation to the picture, since it may happen that the centre-line does not coincide exactly with the centre of the track. This situation is shown in *fig. 6*. Here the first three intersections satisfy the criterion, but in the fourth a peripheral point is

missing. However, if the centre-line is moved one image point to the left, then this intersection also satisfies the criterion, without faults arising in the other intersections. The intersection is then passed as correct. In the actual inspection of connecting-lead patterns (where

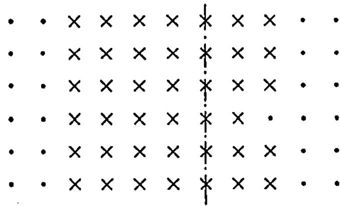

Fig. 6. Stored image of a vertical track in which a fault is found on inspection with a track width of five points. This fault, however, arises because the centre-line does not coincide with the centre of the track. Such positioning errors can be remedied by repeating the inspection of the intersection with a displaced centre-line when a peripheral point is found to be missing. When the centre-line in the example shown here is moved one point to the left the track satisfies the criterion.

the narrowest track always has a width of 10 to 15 points) the centre-line is moved through two points when peripheral points are missing.

In the third case, where one or more points are missing in an intersection, a fault has been discovered. Not all faults, of course, necessarily lead to the rejection of the pattern; for example a small hole in a wide track is indeed discovered as a fault, but it will have no practical consequences. To avoid an unnecessarily high reject percentage, therefore, the seriousness of a fault must first be judged before the decision 'pass' or 'reject' is taken.

Fault appraisal

When a fault is discovered, a subroutine that determines the dimensions of the fault is initiated. This is done by making a *fault projection*; see *fig. 7*. Starting with the first intersection in which the fault occurs, the intersections are scanned and a record is made in a projection buffer *PB* of the points that are missing. Part of the main memory is reserved for this buffer. In addition to the track points, some surrounding points are also examined in each intersection. This subroutine stops as soon as a completely correct intersection is found; the buffer then contains a projection of the fault.

The following data can be read from the projection. If the fault is an isolated one, e.g. a hole in a track as in fig. 7, the maximum width of the hole and also the widths of the two free conducting paths beside the hole can be determined from the projection. If the fault is a constriction, as in *fig. 8*, the remaining free conducting path can be determined from the projection. The length of the fault always appears from the number of successive intersections in which part of the fault is visible. The same procedure is of course used when the fault is an island of copper in an insulation strip or a protrusion from a track.

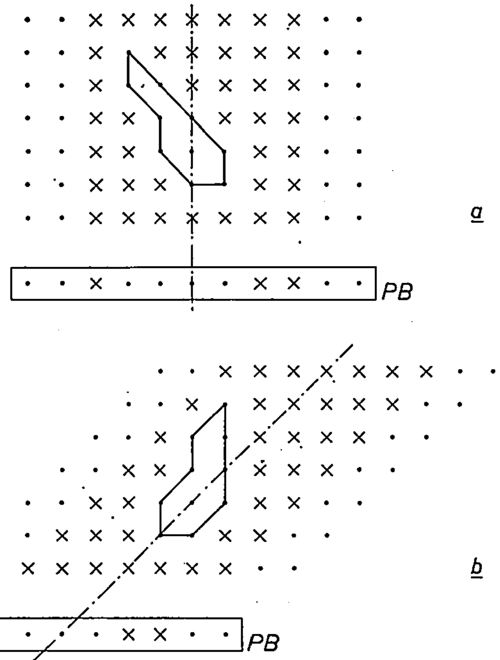

Fig. 7. Making a fault projection. When a fault is discovered in a track, the missing points are recorded in a projection buffer *PB* for all successive intersections in which the fault is visible. Two points on either side of the track are also examined. If the fault is a hole in a horizontal or vertical track, a projection of this hole is produced in *PB* on a perpendicular intersection of the track (*a*). From the contents of *PB* it is now possible to read the maximum widths of the free conducting parts next to the hole (here one and two points). If the track is not horizontal or vertical, but runs in an arbitrary direction, a similar result is achieved by giving the centre-line point for all intersections in the buffer the same position, in other words the fault is projected parallel to the centre-line on to a horizontal or vertical line (*b*).

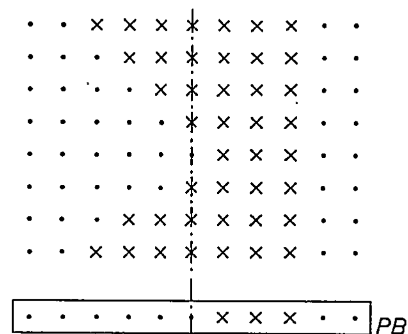

Fig. 8. Fault projection for a constriction in a track. From the contents of the projection buffer *PB* the remaining free path can now be read (here three points).

[3] A similar application of an interactive display is described in: P. Blume, Computer-aided design, Philips tech. Rev. 36, 162-175, 1976 (No. 6).

The necessity of a procedure including fault projection appears from the example in *fig. 9*. Here a thin scratch in a track has broken the electrical connection. Nevertheless there is only a small fault present at each intersection — in all cases no more than one point is missing — which in itself is not a reason for rejecting the pattern. It can only be seen from the projection that the connection is broken and that the pattern must therefore be rejected.

Whether a fault of certain dimensions should result in a reject depends to a great extent on its position in the connecting-lead pattern. Different rejection criteria apply to the bonding zone, the zone with the tracks and the zone with the solder lands. In the model each centre-line section in addition to the width criterion is given information indicating to which of these zones it belongs. From this information and the rejection criteria for the three zones, which are stored in the computer, a decision subroutine can determine whether or not the discovery of a fault must be followed by rejection.

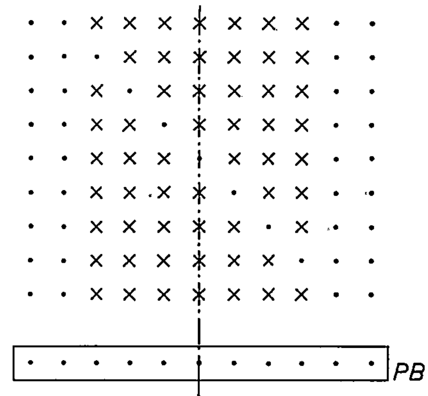

Fig. 9. Illustrating the necessity for a fault projection. For the fault shown here, which runs right across a track, only one missing point is found in each intersection; this alone would not result in a reject. The projection, however, shows that the connection is completely broken.

Technical design

The camera arrangement

The camera used for inspecting the connection patterns is an XG 7302 type, developed by the Philips Electro-acoustics Division for use in X-ray systems. The camera has very high stability for the horizontal and vertical deflection. The line generator has been modified to produce a rectangular picture instead of the original circular one. The 875 picture lines originally used (in two interlaced fields) have been increased to 876, and a field of 438 lines is scanned every 20 milliseconds without interlacing [4]. A number of these lines must be suppressed (for the field flyback, for example); about 400 lines remain in each field.

Inspection of the bonding zone of a pattern requires a resolution of 10 μm; the optical system of the camera that takes the picture of the bonding zone is therefore arranged in such a way that the distance between two picture points corresponds to 10 μm in the pattern. With a field of 400 lines with 450 picture points this means that the camera must cover an image field of 4×4.5 mm, large enough for the bonding zone (see fig. 3). For the rest of the pattern a resolution of 20 μm is adequate. The second camera is therefore set for an image field of 8×9 mm, so that the complete pattern can be recorded in three steps.

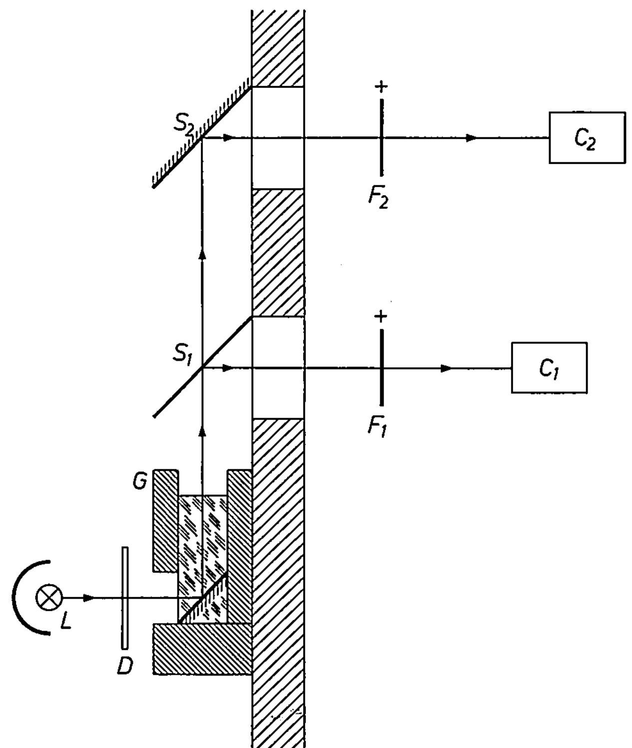

Fig. 10. Diagram of the optical part of the system. The tape runs through a guide G over a glass block through which it is illuminated by the light source L via a diffuser D (a ground-glass plate). The semi-transparent mirror S_1, the lens system F_1, the mirror S_2 and the system F_2 form the images in the two cameras C_1 and C_2. The lens systems and the object and image distances are chosen in such a way that C_1 operates with a resolution of 10 μm and C_2 with 20 μm.

The arrangement of the camera in relation to the tape is illustrated schematically in *fig. 10*. The tape runs through a guide groove G over a small glass block through which it is diffusely illuminated. By means of the semi-transparent mirror S_1, the mirror S_2 and the lens systems F_1 and F_2, images of the pattern are formed in cameras C_1 and C_2. With a suitable choice of lenses and of object and image distances, camera C_1 has a resolution of 10 μm and camera C_2 of 20 μm.

The tape is transported by means of a stepping motor that drives a spindle against which the tape is pressed by a rubber roller. In the detail photograph in *fig. 11* the roller can be seen to the right of the position where the tape is illuminated. The transport commands are given by the computer. The tape is wound on take-up and feed reels driven by servomotors. This ensures that the tape always hangs in a loop at both ends.

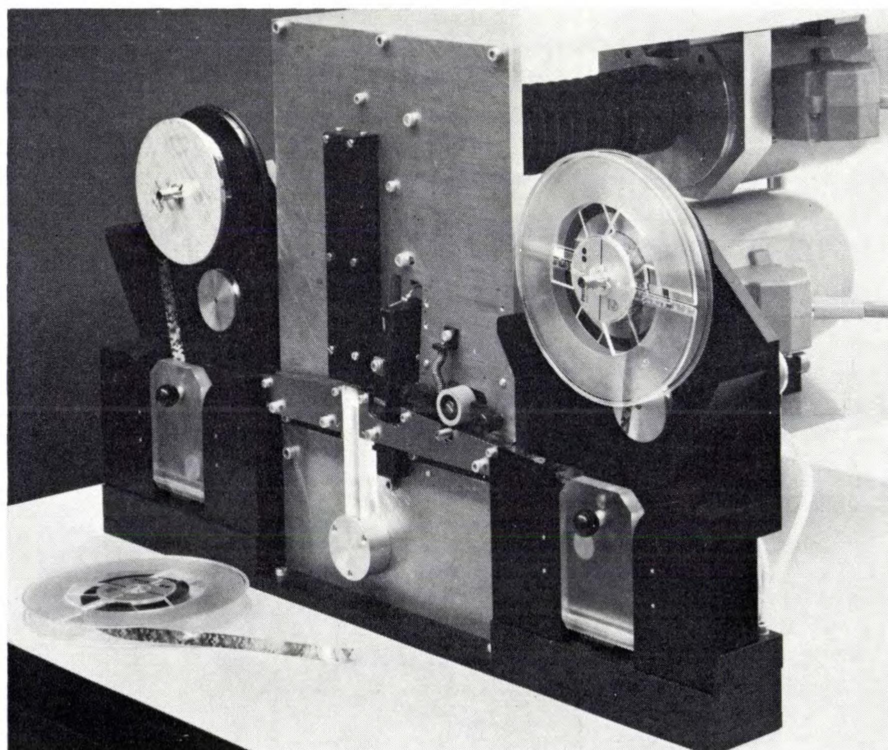

Fig. 11. Camera arrangement and tape-transport mechanism. The two cameras are situated behind the vertical front plate. The glass block through which the tape is diffusely illuminated can be seen at the centre of the plate; the black box above it contains the two mirrors that project the light on to the cameras (see fig. 10). The tape with the patterns is transported from the left-hand reel along the horizontal guide groove to the take-up reel on the right. The drive is supplied by a stepping motor that drives a spindle against which the tape is pressed by a rubber roller (right of centre on the front plate). Each reel is driven by a servomotor controlled in such a way that the tape hangs down in a loop loaded by a counterweight. In this way the tape is kept in equilibrium in the middle of the system by the weights on the left and right. Tape transport is therefore not affected by the feed and take-up of the tape, but is controlled solely by the stepping motor.

Interface with the computer

Fig. 12 shows a block diagram of the complete inspection system. The control circuits of the cameras C_1 and C_2 are contained in the control units CU_1 and CU_2; the synchronization pulses for the two cameras are supplied by a single generator *SG*. The video signals are fed to the multiplexer *M*, an electronic switching device that passes on one of the two signals to the level discriminator *Ds* when a command is given by the computer. The video signal is converted here into a binary signal with the discrete values 0 V or 5 V, representing 'no track' or 'track'. The video mixer *VM*, which also receives the synchronizing pulses from *SG*, makes the video signal visible on the television monitor *Mon*.

In the circuit following *Ds*, the 'data formatter' *Df*, the signal is digitized and then fed to the computer. The data formatter consists of two shift registers, each of which can contain the image information from one line. These registers are filled alternately; while the information from a line is being read into the input for one of the registers, the information is being read out of the other register by the computer. The shift frequency during the filling of the registers is such that the video signal presented to the inputs is divided into the required

[4] The modifications of the camera system were made by B. J. van Donselaar of these Laboratories.

450 discrete values per picture line during the input process. Inputting thus takes place synchronously with the scanning of the picture; the speed is determined by the camera system and is slightly more than 12×10^6 bits per second. The registers are read out discontinuously in groups of 16 bits (the word length of the computer) and at the higher speed of 19.2×10^6 bits per second, determined by the speed of the computer.

The computer is a Philips P 855 minicomputer, whose main memory has a storage capacity of 32×1024 words of 16 bits and a store cycle time of 0.8 μs. By means of a special input channel *DMA* (Direct Memory Access) the video information from the data formatter is transferred straight to the main memory. The information from one picture occupies about 12 000 words, which are stored at consecutive addresses. The programs and the model data are read in by a punched-tape reader *TR*; the main memory is large enough to contain this data in addition to the video information, so that the inspection system requires no backing storage, such as a magnetic-disc file. The modular input/output system *MIOS* of the computer controls the multiplexer *M*, the stepping motor *S* (via the servo-controller *SC*), the punch *P* used for marking the rejected patterns, and the cursor generator *CG*. The MIOS also includes an operating panel *OP* for starting and stopping the system, selecting automatic or semi-automatic inspection and switching the cursor on or off.

In the semi-automatic operation of the system the user communicates with the computer by means of the teletypewriter. This can also supply statistical data about the faults discovered. Such data may reveal certain manufacturing errors that would otherwise be difficult to trace, such as a slight undulation in the series of patterns on the tape caused when the tape is cut from the wide plastic strip on which the patterns are made. The system also contains the tape reader *TR* and a tape punch *TP* for entering the model data when making the centre-line model. In the arrangement shown in fig. 2 the left-hand part of the cabinet contains the computer; the other circuits are contained in the right-hand part on which the operating panel is located.

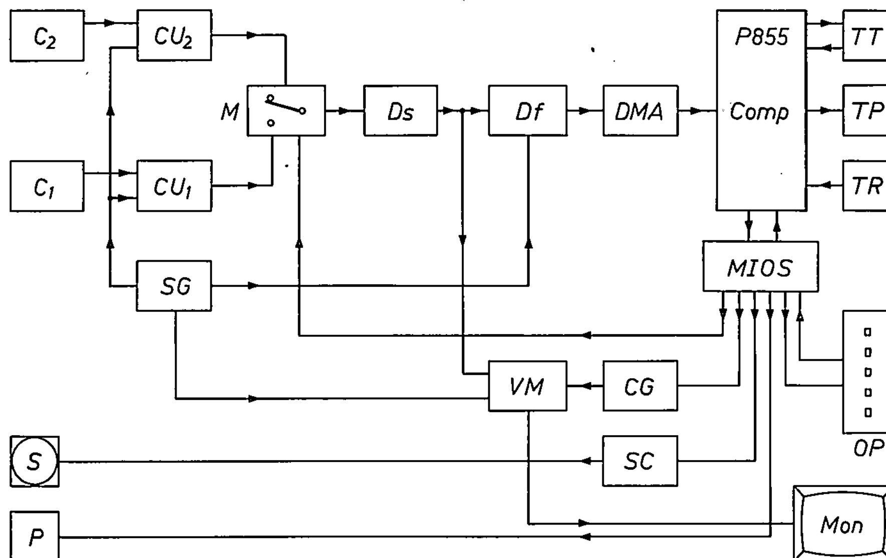

Fig. 12. Block diagram of the inspection system. C_1 and C_2 cameras with control units CU_1 and CU_2 and sync generator *SG*. *M* multiplexer. *Ds* level discriminator. *VM* video mixer. *Mon* television monitor. *Df* data formatter. *DMA* input system (Direct Memory Access). *MIOS* modular input and output system. *CG* cursor generator. *S* stepping motor with servo controller *SC*. *P* punch mechanism. *TT* teletypewriter. *TP* tape punch. *TR* punched-tape reader. *OP* operating panel.

The inspection cycle

We shall now deal with some aspects of the system in more detail. The inspection cycle for the four fields of a pattern is shown in *fig. 13*. The smallest unit along the time axis of this diagram is the field-scan period of the cameras (20 ms). The upper line (*In*) indicates when an image is read into the computer. By using the data formatter the image can be read in while the camera is taking the picture, so that this input takes no longer than one field-scan period. The following line (*Tr*) indicates when the stepping motor is actuated. The line marked *Insp* shows the periods in which the four image fields are inspected by the computer, and the fourth

and fifth lines indicate which camera is switched on.

The inspection of a field begins as soon as the video information it contains has been read in; at the same time the tape transport can start to bring the next field in front of the cameras. Inspection and transport will thus coincide to some extent. If the inspection of a field takes longer than the transport to the next one, the new field is read in as soon as the inspection is completed (see transition *C*, after the inspection of field *3* and the transport of field *3* to field *4*). If on the other hand the inspection takes less time than the transport, the input is started by a signal that indicates that the stepping motor is ready (transitions *A* and *D*). This takes a little longer. During the inspection of field *2* there is no transport, since field *3* is the bonding zone and is recorded with the tape in the same position as for field *2*, but with the other camera. After the input of field *2* a switch is therefore made to camera *1*; field *3* is input when the inspection of field *2* is complete (transition *B*).

It follows from the timing diagram that the duration of a cycle is mainly determined by the speed of the computer: inspection of the more complicated fields *2* and *3* requires about half the entire inspection time. During the inspection of fields *1* and *4* the tape transport is the longer process; in principle some improvement could be achieved here with a faster stepping motor. The system can inspect a tape with its patterns at a speed of about one pattern per second.

Positioning

During the inspection the pattern must occupy the same position in the image field as the centre-line model: the centre-lines in pattern and model must coincide. As we saw when discussing the centre-line model, a slight deviation in the relative positioning can be remedied by moving the centre-lines through a distance of one or two image points during the inspection, but a deviation of three or more points makes the inspection impossible.

Because there are no mechanical references such as guide perforations in the tape, the patterns cannot be placed in the same position under the cameras for inspection; transport by the stepping motor cannot guarantee exact positioning of the patterns. It was therefore decided to use a method in which the pattern itself serves as a reference. After the picture has been taken the positioning of the pattern in the image field is measured; if this differs from the positioning of the model, the model is then moved until it takes up the same position as the pattern [5]. In practice this is done by correcting all centre-line coordinates by the measured difference before the inspection begins.

The position of the pattern is determined by means of two measuring windows, one for a horizontal track edge and the other for a vertical one. When the model

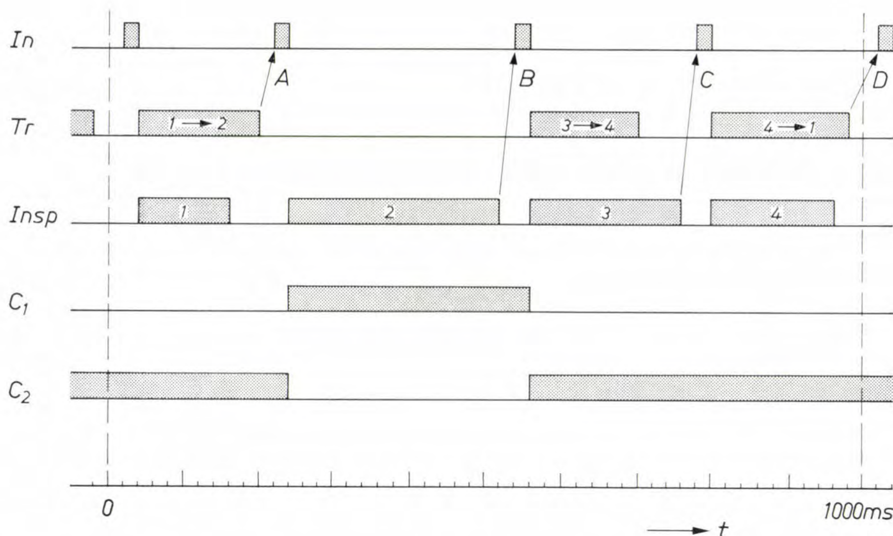

Fig. 13. Timing diagram of the inspection cycle for a pattern. The periods for image input *In*, tape transport *Tr*, inspection of the four fields *Insp*, operation of camera C_1 and of camera C_2 are indicated from top to bottom. The field-scan period of the camera is plotted along the time axis as the smallest unit. In the case shown, the complete cycle takes one second; the cycle time depends to some extent on the complexity of the pattern.

[5] The principle of this positioning method was proposed by T. Ing. F. A. C. Brouckaert of these Laboratories.

is being made these windows are located in such a way that the edge of the track falls at the centre of each window; see *fig. 14*. The coordinates x_m and y_m of these track edges in the model are called the nominal model positions. The coordinates of the track edges inside the windows are also determined in the image of the pattern after it has been transferred to the memory for storage. Let these values be x_{obj} and y_{obj}, then image and model can be brought into position by reducing all coordinates of the centre-lines by $x_m - x_{obj}$ and $y_m - y_{obj}$.

The measuring windows must on the one hand be large enough to ensure that the track edge always falls inside the window after the transport of each field, but on the other hand not so large that another edge could be visible in it. The size L_x of the x-window must therefore be adapted to the accuracy of the tape transport by the stepping motor (the x-direction is the direction in which the tape travels). The tape is transported in steps with a magnitude of five measuring points. If the value $x_m - x_{obj}$ after transport is greater than five points, a correction step follows, so that the positioning measurement is also used for adjusting the stepping motor. The size of the y-window is dictated by the nonlinearity of the tape travel in the guide and by the accuracy of the positioning of the patterns on the tape. In practice the system uses two windows each of 16 × 16 measuring points.

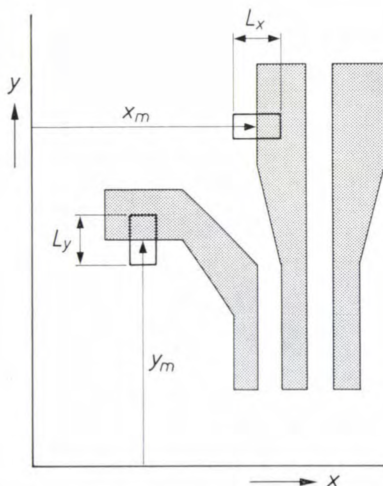

Fig. 14. Measuring windows for determining the position of the pattern. The location of the windows is such that when the model is being made a vertical track edge appears in the centre of one window and a horizontal track edge in the centre of the other. The values x_m and y_m then establish the position of the model. When a picture of a pattern has been taken and stored in the memory, the position of the track edges in this picture is determined in these same windows; the difference between these measured values and the values of x_m and y_m then indicates how far the model must be displaced to cause the centre-lines of the model to coincide with the inspected pattern. The dimensions L_x and L_y of the windows are such that after the tape transport the edges to be measured fall inside the windows. The x-direction is the longitudinal direction of the tape.

The computer program

Fig. 15 shows a diagram of the part of the computer program that carries out the actual inspection of the image field. It begins with the input of the model data for the first centre-line: the coordinates of the starting point, the direction and the length of the centre-line, and the test criterion (*1*). It is then known whether the centre-line belongs to a track or to an insulation strip; in the first case the 'ones' are inspected and in the other the 'zeros'. The next question in the program after (*1*), whether all the centre-lines have been inspected, is answered in this stage by 'no'. After the input of the data the starting point of the centre-line is corrected from the result of the position measurement, so that the centre-lines in the image and the model coincide (*2*). The program then selects the appropriate inspection subroutine; depending on the direction of the centre-line, horizontal or vertical intersections are made and inspected (*3*). These subroutines are virtually identical; the scheme here shows only the inspection of vertical intersections in full.

The inspection subroutine starts with the intersection through the first centre-line point (*4*). If this intersection satisfies the test criterion (*5*), the subroutine investigates whether there is another centre-line point to follow (*6*), moves to this point (*7*) and again makes an intersection. In this way all the points of the centre-line are dealt with in sequence. The cycle (*4*, *5*, *6*, *7*) is thus very frequently repeated, and it was therefore desirable to make the cycle as fast as possible. This was achieved by having as much data available as possible about the track and the centre-line in the inspection subroutine and in a number of fast-access registers. If no faults are found in the track, the data for the next centre-line is read in (*1*) and the procedure starts again from the beginning. Once all the centre-lines have been inspected in this way (*8*), another part of the program takes over to see that the information of a new image field is read in.

If it is found during the inspection of an intersection that the test criterion is not satisfied, the inspection cycle is abandoned and a projection is made of the intersection that contains the fault (*9*). The program then remains in the projection cycle (*9*, *10*, *11*, *12*), in which the intersection is made at each successive centre-line point, inspected and projected until either the centre-line has been worked through or an intersection with no fault is found. (In this subroutine the intersection is made and inspected at the same time as the projection.) The next step is to determine from the fault projection the dimensions of the fault (*13*); the program then decides from the rejection criteria whether or not to reject the pattern (*14*). If a fault does not lead to rejection, the program returns to the inspection cycle,

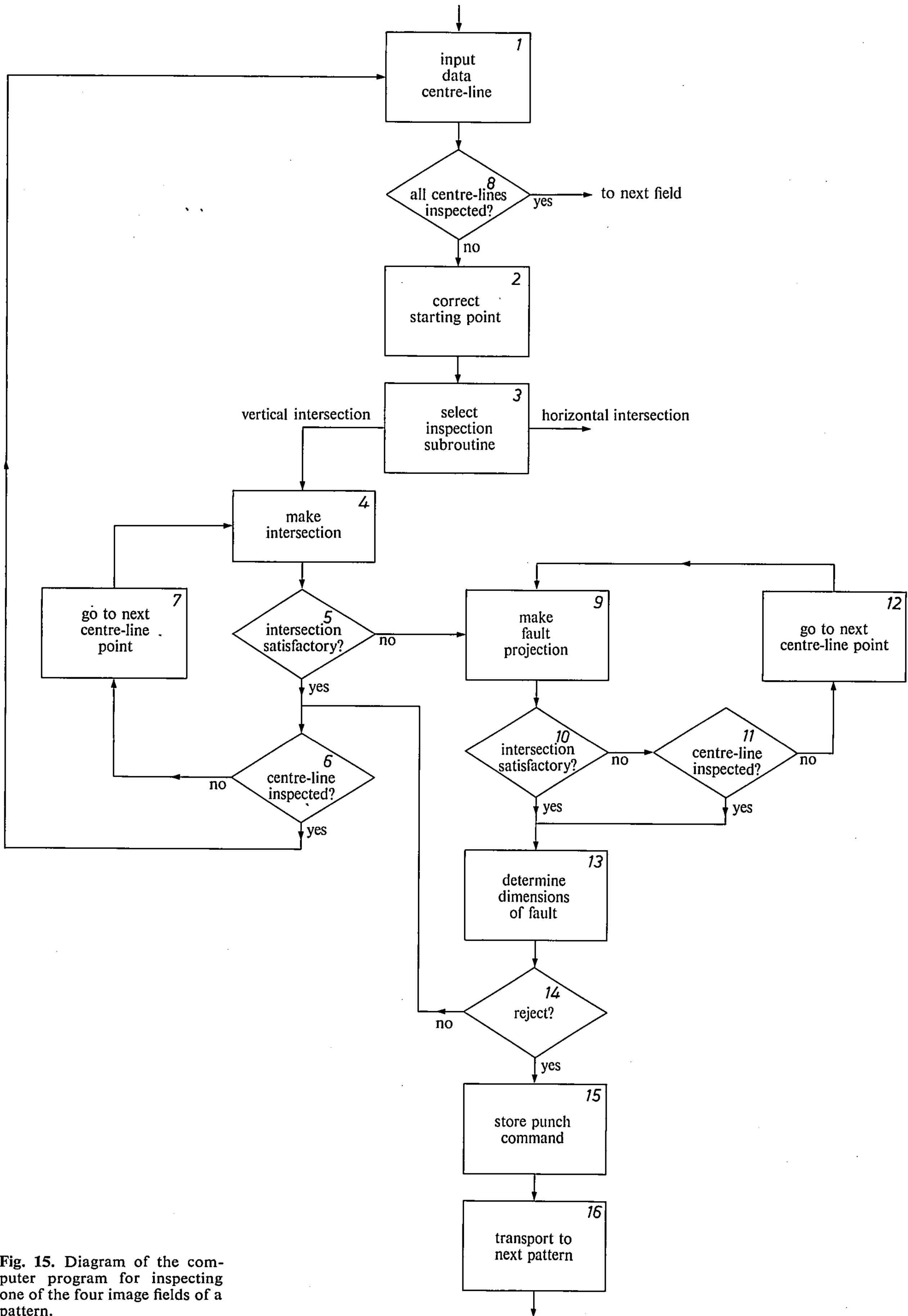

Fig. 15. Diagram of the computer program for inspecting one of the four image fields of a pattern.

which then works through the rest of the centre-line. If the pattern is rejected, an instruction is stored in the memory (*15*) to the effect that a hole must be punched in the pattern when it arrives under the punch (this is located above the transport guide near the position where the picture was taken). Inspection of the field is then promptly discontinued and the tape is transported to the first field of the next pattern in front of the cameras (*16*): any subsequent fields of the rejected pattern are then omitted.

Results

The inspection system was recently put into use in the Philips Video Division. During the period in which the system was tested in the laboratory about a million connecting-lead patterns were inspected. During this trial period the system was steadily improved by comparing, in sample checks, the results of automatic inspection with those of semi-automatic inspection (where the operator decides on rejects), and then by appropriately adapting the rejection criteria. A stage was in fact reached where the sample check showed that the system made fewer errors in automatic operation than in semi-automatic operation. Of course, we cannot conclude from this that the system will be better than a human inspector in all circumstances. For the inspection of large series of patterns, however, the system certainly has the advantage that it is able to decide upon approval or rejection from quantitative measurements and exactly defined criteria, whereas human inspectors make their decisions from rather general impressions, which may also vary considerably as a consequence of fatigue and changes in personnel. The system is also faster and the results are fully reproducible.

When all these factors are taken into account, we are led to the conclusion that the system comes up to expectations. The millions of patterns made in a year can be inspected entirely automatically and at high speed, which would not be possible with conventional visual inspection.

Summary. The connecting-lead patterns on plastic tape used for mounting integrated circuits must all be inspected for faults after production. An inspection system is described in which the patterns are viewed in succession by a television camera, and the video information is then compared with a model in a minicomputer. The model consists of the centre-lines of the tracks and of the insulation strips between the tracks, and for each centre-line there is a test criterion that specifies the required widths of the tracks and insulation strips. A computer program carries out the inspection by checking all the centre-lines, making intersections through the track or the strip at each centre-line point, and verifying whether the test criteria are completely satisfied. If a fault is found, its dimensions are determined and rejection criteria are used to decide whether the pattern should be passed or rejected. The system, which has recently been introduced in production, is capable of inspecting a tape with its patterns entirely automatically at a speed of one pattern per second. A hole is punched in the rejected patterns.

Very smooth fracture faces for optical glass fibres

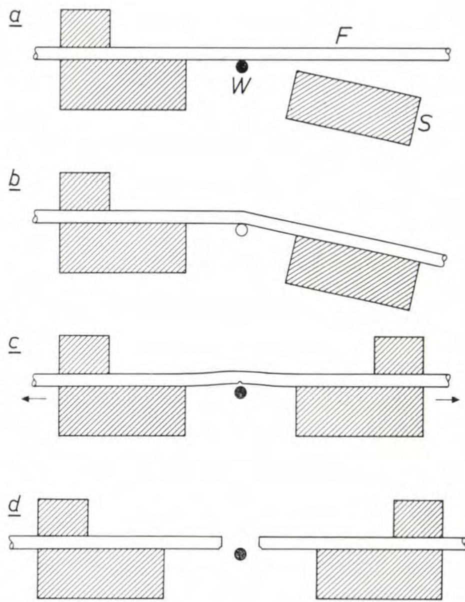

1

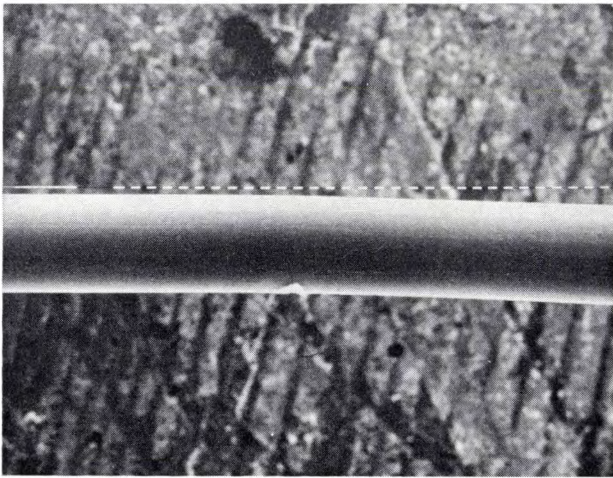

2

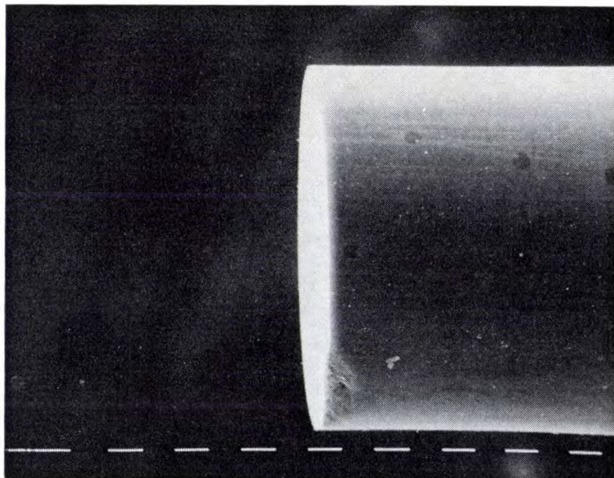

3

Optical glass fibres used for transmission must have end faces that are very smooth and reasonably perpendicular to the longitudinal axis to minimize optical losses.

In the existing method for breaking off glass fibres, a notch is made with a diamond on the outside of a glass fibre held in tension around the outside of a cylinder. The ends of the fibre are then pulled, causing the fibre to snap at the notch, where the tensile stress is greatest. This kind of method has the disadvantages that glass particles may be left behind on the end faces and that very sharp cutting tools have to be used with great accuracy.

In the new method that we have developed a wire filament is used to make a 'notch' and at the same time to determine the place where the tensile stress is at a maximum. The successive stages of the method are illustrated diagrammatically in *fig. 1*. The glass fibre *F* is clamped at one end and placed across the filament *W* (fig. 1*a*). When the filament is heated (fig. 1*b*) the fibre bends and the free end comes to rest on a support *S*. The fibre is then returned to its original position, clamped and subjected to a tensile force (fig. 1*c*). Because of the bend in the glass fibre the tensile stress is at a maximum at the notch, as desired. The fibre will therefore fracture across the axis (fig. 1*d*), leaving two perfectly smooth fracture faces.

The SEM photomicrograph in *fig. 2* shows a glass fibre (diameter 113 μm) after it has been heated locally by a filament with a diameter of 80 μm. *Fig. 3* shows the fracture face of a glass fibre. (The imprint of the filament can still be seen at the bottom.)

We have now made a hundred fibre end faces in this way, all of mirror quality, with the aid of a small easily operated machine. The filament, which replaces the much more expensive diamond, remains completely intact.

W. J. J. van Hoppe
G. D. Khoe
G. Kuyt
H. F. G. Smulders

W. J. J. van Hoppe, Ir G. D. Khoe, Ing. G. Kuyt and H. F. G. Smulders are with Philips Research Laboratories, Eindhoven.

Philips tech. Rev. 37, 90, 1977, No. 4

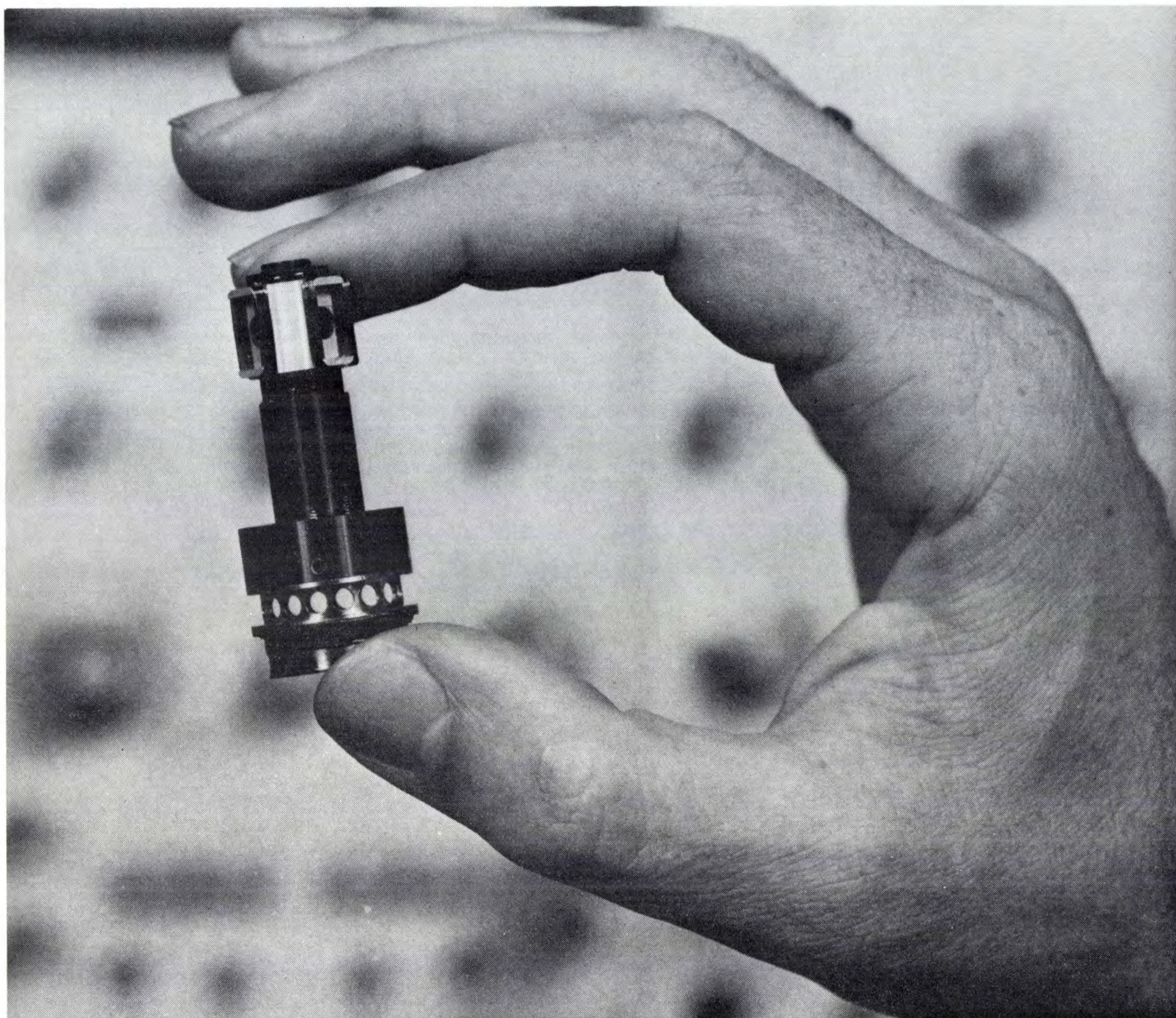

Ultra-compact optical scanner for 'VLP' player

Studies have been made at Philips Research Laboratories in Eindhoven to see how the scanning optics of a 'VLP' player can be simplified and made smaller by the use of a miniature semiconductor laser.

The result of these studies is shown in the photograph. The device that can be seen here contains an experimental AlGaAs laser, made at these laboratories, which functions as both light source and detector, as well as the associated optics. It is 4 cm long, the diameter is 1 cm and it weighs only 16 grams. Because the functions are combined the number of components can be kept to a minimum. Since the new scanner is so small and light the track and the surface of the disc do not have to be followed with a pivoting mirror [1]. The scanner is moved as a whole in the radial, tangential and vertical directions by means of three actuators. It has been found that this scanner (numerical aperture 0.6) gives just as good a picture quality from the disc as the existing one.

Further studies are continuing on the reliability and life of the semiconductor scanner. There is very indication that a considerable simplification in the 'VLP' player will be obtained in the future.

[1] P. J. M. Janssen and P. E. Day, Philips tech. Rev. 33, 190, 1973.

Cryogenics: a critical review

J. Volger

The article below is a slightly modified version of a recent article by Prof. Volger in Interdisciplinary Science Reviews (ISR), and is published here by kind permission of ISR's Editor-in-chief. Although no references were given in the original version, we have included a few references to other articles in Philips Technical Review for the benefit of those who may wish to study some aspects of the subject in more detail.

Man must have been able to distinguish hot and cold through direct sensation of the skin, long before he had a precise concept of what temperature really is. Through an early technology of fire, the burning of wood and later of coal, high temperatures became familiar to our ancestors. The development of our civilization depended on this. The physics and technology of temperatures below ambient appeared only recently and the penetration of cryotechnology — the technology of low temperatures — into our modern world is still modest. It is, however, undoubtedly a growth area, the more so since cooling equipment of all kinds, down to the very lowest temperatures, is now becoming steadily cheaper and more reliable. Household refrigerators are used worldwide and in some industrialized countries they may consume some 10-15% of domestic electric power.

In order to obtain high temperatures exothermal chemical or nuclear reactions are used and the heat so produced is led by conduction or radiation to the desired place. The whole biosphere of our planet profits from the thermal radiation of the Sun.

Low temperatures may be obtained when heat can be lost to low-temperature heat sinks, such as the cold universe. Radiation measurements of the dark parts of the universe have shown it to be extremely cold indeed, a few degrees absolute. The existence of our atmosphere does not permit us to profit from the low temperatures of space on a large scale when really low temperatures are wanted. Spaceships are of course an exception. Also, very little may be expected of the use of endothermal chemical reactions. The classical cooling method of mixing ice and salt lowers the temperature by some 20 °C only.

So we are left with the conclusion that substantial cooling requires tricks of a more sophisticated kind. Before going on to a discussion of these and other items that make the world of low temperatures so exciting, we shall first look at the basic concept of temperature, including some simple statistical mechanics.

Prof. Dr J. Volger is a Deputy Director of Philips Research Laboratories, Eindhoven.

The thermodynamical definition of temperature

We think of a body as a system of atoms exhibiting a scheme of energy levels, determined by quantum mechanics. When the body is heated, higher energy levels are excited. Obviously, the distribution of a given amount of energy U over all these atomic levels may be achieved in many ways, each having a certain probability P. Usually internal energy transitions will rapidly bring about the most probable distribution, i.e. the maximum value of P for given U, and then we speak of thermal equilibrium. From P a quantity S, the entropy, can be derived: $S = k \ln P$. The factor k (Boltzmann's constant) is independent of the nature of the system.

If two systems A and B are brought in thermal contact, energy can be exchanged and the combination reaches a new equilibrium, i.e. equal and uniform temperatures in A and B. Thermal equilibrium means that the distribution of the total energy U over the now combined collection of energy levels has reached the maximum probability. The law of combination of probabilities is to form a product, $P_{AB} = P_A \times P_B$. So, upon an infinitesimally small energy transfer $dU_A = -dU_B$ between A and B we then require

$$\frac{\partial P_{AB}}{\partial U_A} = 0,$$

so that

$$\frac{\partial}{\partial U_A} \ln P_A = \frac{\partial}{\partial U_B} \ln P_B, \quad \text{or} \quad \frac{\partial S_A}{\partial U_A} = \frac{\partial S_B}{\partial U_B}.$$

This means equalized temperatures indeed when — as is the case in thermodynamics — the basic definition of

temperature (i.e. absolute temperature) is $T = \partial U/\partial S$, a definition that appears to coincide, fortunately, with the absolute temperature as measured in an ideal or perfect gas thermometer. $S = 0$ means that P is minimal, equal to 1 in fact, and this will be the case if the whole system of atoms has arrived in what quantum-mechanically is called a non-degenerate ground state. We call this situation perfect order, the absolute zero point of temperature.

The equilibrium distribution of energy at the various levels of a system is thus governed or indicated by the temperature. By way of illustration we calculate T in a model system: a set of N very simple atoms, each with a ground state at, say, zero energy and one excited state with energy ε only. The total energy $U = n\varepsilon$ is given. We seek P, the number of ways in which the n excitations can be accommodated in the level scheme. From the theory of combinations we arrive at

$$P = \frac{N!}{n!(N-n)!},$$

and to a good approximation it follows that

$$\frac{S}{k} = \ln P = N \ln N - n \ln n - (N-n) \ln (N-n),$$

and so

$$T = \frac{\partial U}{\partial S} = \frac{\partial U/\partial n}{\partial S/\partial n} = \frac{\varepsilon}{k \ln \{(N-n)/n\}}.$$

This expression may also be read in reverse order: it then gives us the ratio between the occupation numbers of the two levels in our model system as a function of temperature:

$$\frac{n}{N-n} = \exp(-\varepsilon/kT).$$

This is the familiar Boltzmann equation. It also holds for a many-level scheme.

Fig. 1 shows the relation between U, S and T in this simple model system. The lower part of the curve is typical for the normal thermal excitation of any system. Of course, the higher the scheme of atomic-energy levels, the further extends the simultaneous increase of U and S when raising the temperature. For $0 < T < \infty$ in our two-level scheme $0 < n < \frac{1}{2}N$. A negative temperature means an artificial non-equilibrium situation, so that the occupation number of the upper level has been made larger than the one of the ground level, e.g. by a vigorous excitation 'pump' as used in a maser.

The transition probabilities between the relevant levels play a role here. Sometimes atoms tend to stay in excited states, which are then called metastable with respect to those lower levels to which they do not decay. Usually it is possible to distinguish between subsystems that exhibit their own internal equilibrium, i.e. temperature. One should keep in mind that nature provides energy-level schemes extending over millions of electron volts, if the nuclear levels are included. (The atomic energy of the chemical bond has a magnitude of only a few eV.) Owing to its boisterous history the part of the universe in which we live has enormous quantities of nuclear matter in an excited state: so, if conditions permit, this is unstable with respect to nuclear fission or fusion. Also, enormous quantities of biological matter in our biosphere are in an excited state, chemically metastable with respect to oxidation. This does not mean, of course, that we should consider our daily world as having a negative temperature.

Fig. 1 also shows that the internal energy U of a system is determined by both T and ε, the latter parameter, moreover, being susceptible to an external influence, such as a magnetic field. If only heat is supplied the increase of U is obtained by proceeding along one specific curve, such as depicted for a fixed value of ε. Also, U may be changed by affecting ε, but the number n of excitations in the model system remains constant in such a process, and likewise the entropy.

Principles of cooling

In general, for any object for which a temperature can be defined U can be plotted as a monotonic function of S. External parameters X, such as pressure or magnetic field, mark out a set of $U(S)$ curves. Each has a positive second derivative, which means that decreasing U by extracting heat (X constant) leads to a fall in

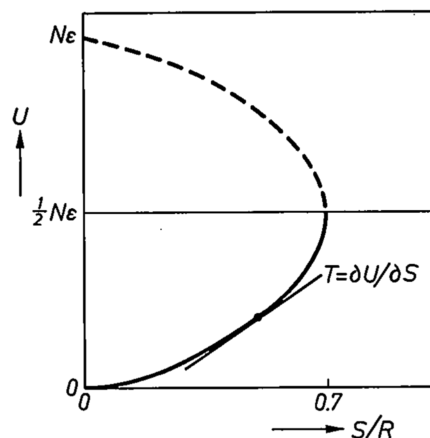

Fig. 1. The relation between the total energy U and the entropy S in a model substance, consisting of N atoms which have only two energy levels. The temperature at a particular part of the curve is equal to the slope of the tangent: $T = \partial U/\partial S$. The quantity R is the constant from the well known law $PV = RT$.

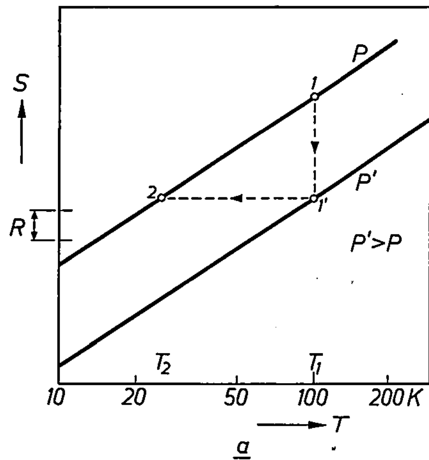

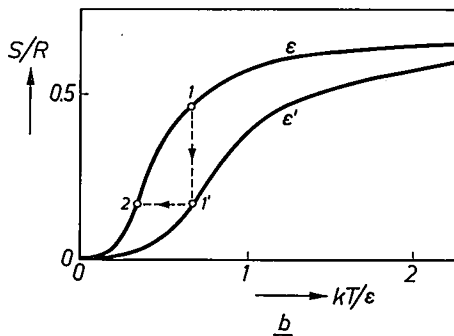

Fig. 2. *a*) The entropy S of a monatomic ideal gas, plotted as a function of T for two values of the pressure P. Cold can be produced by compressing the gas isothermally ($1 \rightarrow 1'$) and then allowing it to expand isentropically (i.e. thermally insulated ($1' \rightarrow 2$)). In the stage ($1' \rightarrow 2$) the temperature falls from T_1 to T_2. From thermodynamics it follows that in this idealized case we have for one mole of gas:

$$S = R \ln (T^{5/2}/P) + \text{const.}$$

The process $1 \rightarrow 1' \rightarrow 2$ therefore leads to a decrease in temperature that satisfies

$$T_2/T_1 = (P/P')^{2/5}.$$

In the process work is performed by the expanding gas, and an amount of heat

$$Q = RT_2 \ln (P'/P) \qquad (1)$$

is extracted from it. In the graph $P' = 12P$. The temperature is plotted on a logarithmic scale, the entropy linearly (the quantity R is indicated as a measure). *b*) The entropy of a system of two-level atoms (see fig. 1), as a function of temperature. It is assumed that in a magnetic field H the energy distance ε of the two levels is proportional to H (Zeeman splitting). From statistical mechanics it can be shown that in this case

$$S = R \ln \{1 + \exp(-\varepsilon/kT)\} \times \varepsilon/kT \times \frac{\exp(-\varepsilon/kT)}{1 + \exp(-\varepsilon/kT)}.$$

The entropy is therefore a function of kT/ε only. The process $1 \rightarrow 1' \rightarrow 2$ (adiabatic demagnetization) leads to a decrease in temperature as

$$T_2/T_1 = \varepsilon/\varepsilon' = H/H'. \qquad (2)$$

The distribution of the atoms over the two kinds of level remains the same during the adiabatic demagnetization. In the graph ε' has been made equal to 2ε. The temperature is plotted in units of ε/k (k is equal to R divided by the number of molecules per mole).

temperature. If we cannot lower the temperature by direct heat transfer to a colder body — which may be cumbersome below ambient temperature — we may try to squeeze entropy out of the system by varying isothermally a suitable parameter. Thereafter its original value is restored under thermal isolation, or 'adiabatically', which means that entropy is conserved. This principle is illustrated in *fig. 2a* and fig. 2*b* and we put up these two cases because they are the basis of two important cooling methods, using expansion refrigerators and adiabatic demagnetization respectively.

The physical basis of these two methods is explained in the caption of fig. 2. From equations (1) and (2) as given there it would seem as if arbitrary low temperatures were obtainable by just decreasing P or H to extremely low values. The actual situation, however, is different since in any real physical system the particles always interact, causing deviations from the ideal conditions: a real gas at low temperatures condenses into a fluid or solid, and magnetic particles feel each other's magnetic moment to the effect that a minimum level splitting ε_0, however small, exists.

Here the third law of thermodynamics is relevant, stating that any real system at the limit of zero temperature must have zero entropy. It is easily verified that in our model system of magnetic atoms on which fig. 2*b* is based a basic splitting of energy levels ε_0 does indeed cause the entropy to be zero at $T = 0$. This third law sets a limit for the attainment of low temperatures. In equation (2), for example, the smallest value of the numerator is ε_0. The general conclusion is that for the production of ultra-low temperatures nearly ideal systems must be used such as helium atoms, which of all atoms have the least interaction, and zero nuclear spin. Very sophisticated cooling methods have been developed along these lines.

The gas-cycle refrigerating machines, all akin to the one discussed (fig. 2*a*) and perfected with the help of heat exchangers and regenerators, provide effective cooling, permitting liquefaction of all gases, down to the most difficult, helium, with a boiling point of 4.2 K. A well known cryogenerator is the Stirling-Philips

[1] J. W. L. Köhler and C. O. Jonkers, Fundamentals of the gas refrigerating machine, Philips tech. Rev. **16**, 69-78, 1954/55.
J. W. L. Köhler and C. O. Jonkers, Construction of a gas refrigerating machine, Philips tech. Rev. **16**, 105-115, 1954/55.
G. Prast, A gas refrigerating machine for temperatures down to 20 K and lower, Philips tech. Rev. **26**, 1-11, 1965.
A. A. Dros, An industrial gas refrigerating machine with hydraulic piston drive, Philips tech. Rev. **26**, 297-308, 1965.
G. J. Haarhuis, The Philips helium liquefier, Philips tech. Rev. **29**, 197-204, 1968.
A. Daniels and F. K. du Pré, Miniature refrigerators for electronic devices, Philips tech. Rev. **32**, 49-56, 1971.

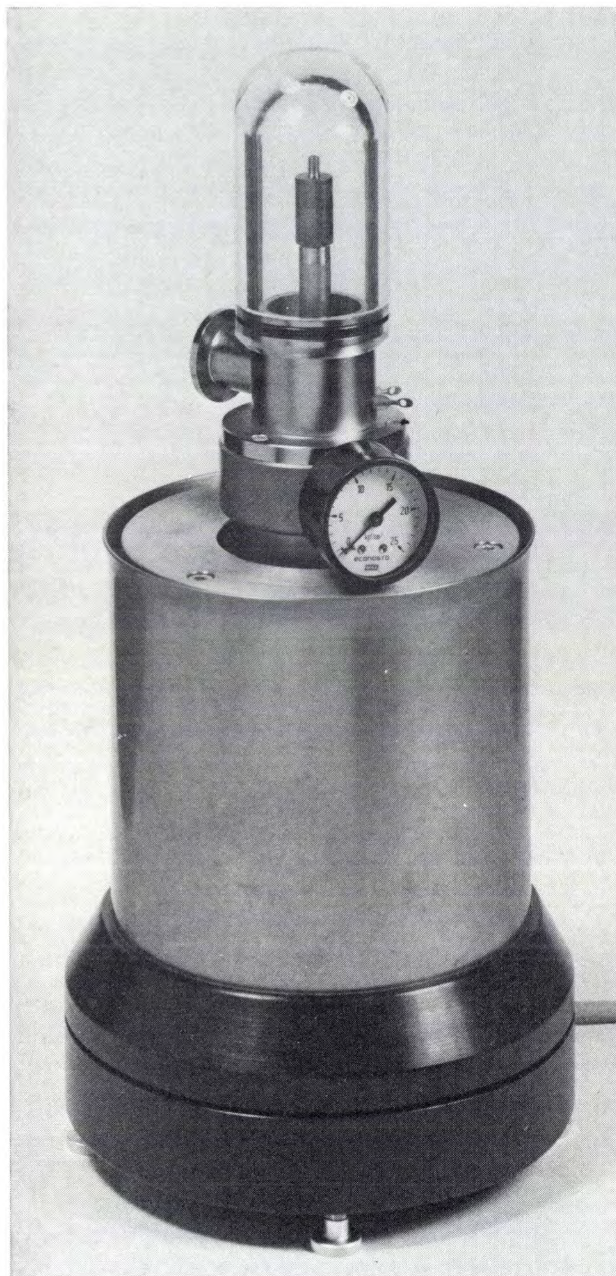

Fig. 3. The Philips MC 80 Stirling refrigerator. This small machine is driven by an electromechanical vibrator like that of a loudspeaker. It produces 0.5 W of cold at 80 K.

refrigerator [1], which is shown in *fig. 3*. Below 1 K other cooling methods take over, for instance the adiabatic-demagnetization method (*fig. 4*), with which a temperature of about 1 mK can be obtained.

The cyclic operation discussed above must here be contrasted with another group of methods with rather different features. These methods have in common that a steady flow of particles (atoms, molecules, electrons) is forced through a border zone, the particles being in different thermodynamical conditions before and after passing this zone; this also means different levels of energy transport per particle. Consequently, upon passing the contact area the particles either deliver or take up energy (depending on the direction of flow) and this makes itself felt as a thermal effect.

In *fig. 5* some principles are illustrated. A classical cooling method is by evaporation (fig. 5*a*) of a liquid: molecules migrate through the surface from the liquid to the vapour, where they are practically free, in so doing they have to take up energy which is extracted from the liquid. By letting helium boil at reduced pressure a temperature slightly below 1 K is obtainable, with ^{3}He even as low as 0.25 K.

A similar case is the Joule-Thomson effect (fig. 5*b*). A gas is expanded from high pressure to low pressure and at the nozzle a thermal effect occurs. When the flow is thermally isolated and the temperature is low enough a decrease of the temperature of the gas results. When the flow is to occur isothermally the cooling power must be consumed externally. Still another,

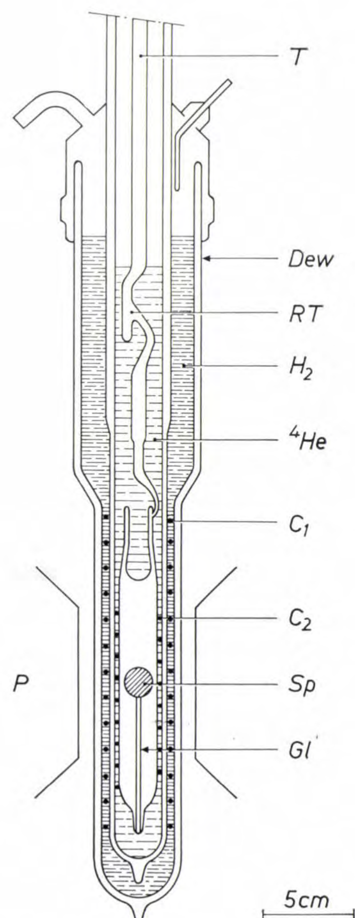

Fig. 4. Diagram of classical apparatus for cooling by adiabatic demagnetization. *Dew* dewar vessel. H_2 liquid hydrogen. ^4He liquid helium. *Sp* paramagnetic specimen. *Gl* glass support. $C_{1,2}$ coils for measurement purposes. The specimen can be magnetized by a magnet whose poles *P* are shown. Thermal contact is provided by a contact gas, which can be pumped away later through tube *T*. The radiation trap *RT* prevents external radiation from reaching the neighbourhood of the specimen.

essentially similar, case is the Peltier effect (fig. 5*c*). Here electrons are flowing from (for example) a *P*-type semiconductor to an *N*-type semiconductor and at the junction thermal energy is needed to promote these carriers from the lower transport levels (valency band) to the higher ones (conduction band). So thermal energy is taken up from the surroundings, which results in an overall cooling.

Cryotechnology

Cryotechnology as a professional and industrial discipline dates from the middle of the last century. The most important economic aspect of cryotechnology is the liquefaction of such gases as air, oxygen, nitrogen, argon, methane, and natural gas. Equally important is the separation of pure components from a mixture, e.g. oxygen from air. Various chemical and metallurgical technologies depend on the application of pure gases, as commercially supplied in the liquid phase. Oxygen, indispensable in steel production, has become a raw material of utmost importance. Helium — once an esoteric gas available only in minute quantities in two or three laboratories of the world — is now available in millions of cubic metres; it plays a key role in space technology. Many more examples can be given. Big companies supply very large quantities indeed of cryoliquids to steel foundries and other customers. The business turnover is many thousands of million dollars and the growth rate of the cryoindustry is approximately 10% per year. *Fig. 6* is a photograph of a large plant where helium is separated from natural gas.

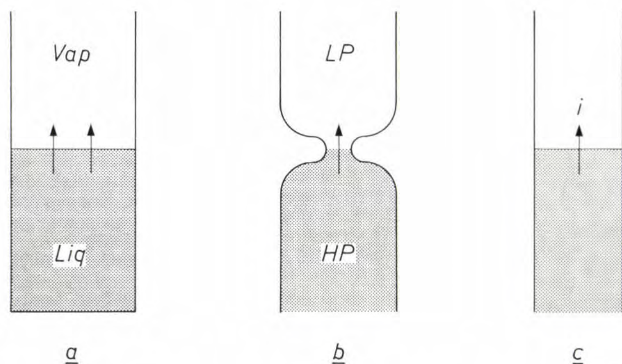

Fig. 5. The principle of three related cooling effects in which a steady flow of particles is forced through a border zone: evaporation by pumping away the vapour (*a*), the Joule-Thomson effect (*b*) and the Peltier effect (*c*). *Liq* liquid. *Vap* vapour. *HP* high pressure. *LP* low pressure. The temperature is assumed constant (the cooling power is externally consumed); under these circumstances the cooling power per unit of flow is equal to the difference in enthalpy below and above the interface. In the case of a gas or a liquid the enthalpy is essentially the heat taken up under constant pressure, i.e. including the amount of work necessary for the change in volume. In the case of Peltier cooling the corresponding enthalpy difference is called the Peltier coefficient Π, so that the heat Q produced at the Peltier junction by a current i is equal to Πi. In the best Peltier devices Π is about 200 mV.

The liquefaction of helium and its ready availability for laboratory experiments has opened vast new fields in pure and applied physics. During the last three decades, the introduction of liquefiers of the Kapitza-Collins type and the Stirling-Philips type have provided a safe, easy and local production of some 10 litres of liquid helium per hour, thus answering the demands of hundreds of laboratories in the world. This development is one of the highlights of contemporary scientific history.

All these installations for gas liquefaction, whatever their size, are based on gas-cycle refrigerating machines, including those in which the expansion engine is a turbine, or on the Joule-Thomson effect.

Domestic refrigerators, air conditioners and the like are big business, producing cooling and hence safe storage of fish, fruits and other consumables, aboard ship and ashore, in the air and on spacecraft. These facilities provide temperatures down to, say, −40 °C and rely on cooling by evaporation. The compressor type, used in countless domestic refrigerators, employs ammonia, or an organic fluid like CCl_2F_2. This chemical is evaporated, and the vapour compressed and recondensed in a condenser where the heat of condensation must be removed by some cooling mechanism. This liquid is fed back again to the evaporator. In the absorption type of refrigerator, the vapour from an evaporator, where cooling is produced, is absorbed in some solvent (for instance NH_3 in H_2O), thus providing the mass flow. Either continuously or intermittently, the gas is distilled from the solvent, recondensed and conducted back to the evaporator. Such refrigerators have reached a high degree of perfection, efficiency and reliability, their lifetime often being many decades.

In the fifties and early sixties determined efforts were made to develop Peltier cooling [2]. It was then thought that with existing basic knowledge of electrical conductivity, including the thermoelectric phenomena, only some further materials research was needed to begin a new era in refrigeration. This hope has not come true. Thermoelectric cooling did not establish itself in refrigeration, except for a few very specialized applications, because it proved commercially not competitive. A heavy d.c. current is needed, which requires expensive auxiliary apparatus. Certainly in household refrigerators, a Peltier cooler is more expensive than the cheap compressor type of cooling.

Reduced running costs could compensate if the coefficient of performance η, the ratio between cooling power and electrical input power, were suf-

[2] W. Lechner, Peltier cooling, Philips tech. Rev. 27, 113-130, 1966.

ficiently high. However, from very intensive materials research all over the world it has become apparent that this ratio has an unpromising upper limit. For all heat pumps η is at best the (inverse) Carnot efficiency, $T_{\mathrm{cold}}/(T_{\mathrm{hot}}-T_{\mathrm{cold}})$, as follows from the laws of thermodynamics. In actual practice, however, η is lowered considerably by dissipative processes, such as ohmic heat caused by resistance in the branches of the Peltier modules, and by thermal losses. The reduction factor appears to depend on the value of the Peltier coefficient Π (see fig. 5*c*), and indeed on the resistivities and thermal conductivities of the materials used.

The Peltier coefficient Π is immediately related to the energy difference of the levels at which the transport of charge carriers occurs in the two branches. The coefficient should not be chosen too large as high resistivity, predicted by the theory of conductivity, would follow. The optimum for Π is at a few hundred millivolts, produced by heavily doped semiconductors. These then should have as large a carrier mobility as can be found and at the same time a minimal thermal conductivity. After many years of research the best compromise was found in Bi_2Te_3/Bi_2Se_3 alloys. When these are used for Peltier cooling, a temperature drop of 50 °C is obtained, the cooling power there becoming negligible. An efficiency of some 50% is possible if the cooling power is consumed at 30 °C below ambient.

The millikelvin region has been an area of great progress in the last decades, of discovering and applying interesting new physical phenomena. As yet there are no industrial applications. But let us first look at some of the remarkable features of the physical world at very low temperatures.

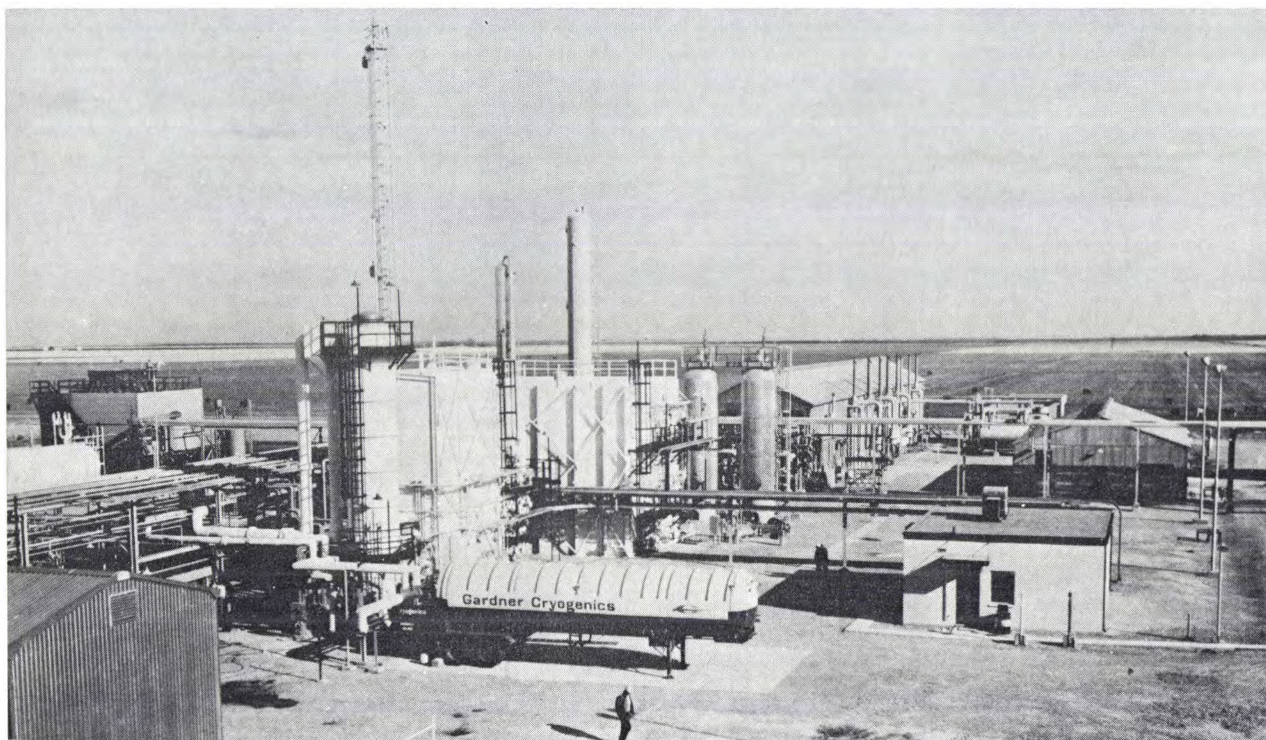

Fig. 6. A liquefaction plant where 650 litres of liquid helium per hour are separated from natural gas (Richfield, Kansas, U.S.A.).

Solid-state research at low temperatures

Low-temperature physics has now been a frontier science for a century [3]. Whenever new temperature regions have been opened up, interesting new properties or phenomena have been discovered. At present some 25% of the contents in the physical 'letters' journals deals with investigations at very low temperatures.

Liquid helium is essential in research laboratories when physicists require lengthy measurements at low temperature. At low temperature signals are often stronger, disturbing noise is weaker and, most important of all, energy quantization manifestly affects the properties of matter.

A striking example is the specific heat of solids, the ratio between heat taken up and increase of temperature, $c = \partial U/\partial T$. The specific heat vanishes when approaching the absolute zero of temperature because

in any real system there is always a finite energy difference between the lowest levels, whatever their particular features. In fact, our two-level model (see the first part of this article) is an example for the general phenomenon: suppose the number of excitations, n, that is the number of energy quanta taken up by the model system, is still very small as compared with N. The energy content is then to a good approximation

$$U = n\varepsilon = N\varepsilon \exp(-\varepsilon/kT),$$

and the specific heat

$$c = \frac{\partial U}{\partial T} = Nk(\varepsilon/kT)^2 \exp(-\varepsilon/kT).$$

Due to the exponential function, c vanishes rapidly near $T = 0$.

In a small temperature interval near $T = \varepsilon/k$ this specific-heat function shows a distinct peak. In many paramagnetic salts, whose magnetic ions have characteristic energy-level splitting schemes, such a behaviour has indeed been observed.

The most important way in which solids can accommodate additional energy is by more vigorous atomic or molecular excitation and vibrations. These thermal lattice vibrations reflect the dynamics of the atoms, as determined by their mass and by the specific forces keeping the lattice of the solid together. Whatever complications may thwart the accurate solution of these quantum-mechanical problems, the general features of lattice specific heat are always the same: near absolute zero the thermal energy is found to be proportional to T^4 and, consequently, the specific heat is proportional to T^3; the proportionality factor is a function of the mass and force constants of the constituent atoms. At $T = 0$ the total energy of a solid has not vanished; some potential energy and a residual value of the vibrational energy are still present. This is known as the zero-point energy. The entropy, however, should have vanished at $T = 0$; the residual motions of the particles and their positions should then have reached perfect order.

In the temperature dependence of their electrical resistivity, metals clearly reflect the scattering effect which the thermally activated lattice vibrations have on the electrons that carry the current. In the early days of low-temperature physics great interest was evinced as to what would happen to these conduction electrons near $T = 0$. We now know that a low residual resistivity is usually left, due to scattering of the electrons by lattice defects unless, of course, the metal has become superconducting (see below). Determining the finer details of conduction electrons, such as their concentration, their energy levels and their mobility, requires extensive low-temperature research, both for metals and semiconductors. True metals retain their huge concentration of conduction electrons even at the very lowest temperature, but semiconductors do not.

The conduction of heat in solids shows a somewhat different pattern, but basically similar concepts. The thermal conductivity of metals is strongly related to their electrical conductivity, as heat is mainly carried by free conduction electrons. However, only a small fraction of them, proportional to the absolute temperature, T, is fit to take up any extra kinetic energy. A remarkable exception occurs when the metal has become superconducting and the accompanying ordering of the conduction electrons excludes them from heat conduction altogether. Moreover, in all solids, including non-metals, heat can be propagated by wave-like lattice vibrations. These will undergo little perturbation in a fine, pure crystal at very low temperatures, this by itself enhancing thermal conductivity. However, if the vibrational thermal energy is extinguished, as it is near $T = 0$, no vehicles are left and so any solid will ultimately be a perfect thermal insulator at absolute zero.

Another field of solid-state research which has gained much from low temperatures is the study of magnetic materials. In magnetically ordered systems, like ferromagnets, the elementary magnetic moments of the electrons tend to take up parallel positions. Above a certain temperature, the Curie temperature, this order vanishes. At $T = 0$ the ordering is perfect. The interesting thing is to discover what happens just above the absolute zero, when a small fraction of the elementary magnets are already starting to withdraw from their ordered positions. More dilute magnetic systems are now also being investigated, with materials that have their Curie temperatures in the liquid-helium range, or, more spectacular still, in the millikelvin region or lower — with substances in which the tiny elementary magnets of some atomic *nuclei* take up parallel positions. Such research is not only important for pure science but equally valuable as background knowledge which provides the electronics industry with its best magnetic materials, be they for computer memories or tape recorders. The work on magnetic resonance [4] should also be mentioned (*fig. 7*). This dynamic phenomenon is usually best observed at low temperatures and its study has led to new materials for sophisticated microwave components and devices, such as radar and masers.

The use of low temperatures enhances research in many other and quite different domains, for instance luminescence, electrical breakdown or semiconduction.

[3] An introduction is given in J. Volger, Solid-state research at low temperatures, Philips tech. Rev. **22**, 190-195, 226-231 and 268-277, 1960/61.

[4] D. J. Kroon, Nuclear magnetic resonance, Philips tech. Rev. **21**, 286-299, 1959/60.

Yet all these success stories are surpassed by the impact of two typically low-temperature phenomena: superconductivity and superfluidity. At very low temperatures many physical properties can be studied 'under the magnifying glass', as it were. However, in the two phenomena just mentioned we have a unique feature of the physical world such as has not hitherto been observed under ordinary circumstances.

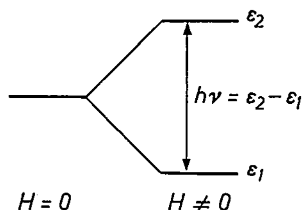

Fig. 7. The principle of magnetic resonance. Nuclear levels or atomic-energy levels split under the influence of a magnetic field (the Zeeman effect). Radiation for which the quantum energy $h\nu$ is equal to the distance $\varepsilon_2 - \varepsilon_1$ between two partial levels — there can also be many more — can be absorbed. This spectroscopy at radio frequencies gives important information about the nuclear magnetic moments and atomic magnetic moments in all kinds of substances, and in particular about the effects of neighbouring atoms. The method is of interest in solid-state physics, organic chemistry, biology, etc. At low temperatures the lines of the absorption spectra are usually sharp and strong.

Superconductivity and superfluidity

Upon cooling, a good many metals and alloys will eventually become superconducting, but ferromagnetic metals are among the exceptions. The superconducting condition is such that, from the thermodynamical point of view, the superconductor is to be considered as a different phase, compared to the metal in its normal state. The transition temperature at which superconductivity begins marks a phase transition — comparable with the transition of a liquid into a solid. Though superconductivity has been known since 1911 when H. Kamerlingh Onnes and G. Holst discovered the phenomenon while working with mercury, a true understanding of it, including the interpretation of such a basic datum as transition temperature, did not come until the late fifties, primarily due to the work of the Nobel prize winners J. Bardeen, L. N. Cooper and J. R. Schrieffer. It seems appropriate to give here a brief account of some characteristics of this wonderful phenomenon and its analogue, superfluidity. Their applications and interdisciplinary aspects will be dealt with in the subsequent sections [5].

Superconductivity in essence means zero electrical resistance. One of the striking consequences is the possibility of maintaining an eternally persistent ring current, once it has been established. A superconductor is also a perfect diamagnet: up to a characteristic field-strength it excludes a magnetic field by spontaneous, persistent currents at its surface, thus compensating for the outer field, with the effect that internally, whatever its previous history, it is absolutely field-free. Both features are a consequence of the strong organization of the conduction electrons. The basic concept is that the superconducting state is a quantum state on a macroscopic scale: one single wave function, a concept already familiar in nuclear, atomic and molecular problems, is considered suitable to describe the mean behaviour of all electrons and the physical properties of the entire superconducting body. This ordering process results essentially from a pairing of electrons, an attractive binding through interaction with the lattice. These pairs, consisting of two electrons with virtually equal and opposite velocity, are looked upon as a species of pseudo-particles. Governed by their macroscopic wave function the conduction electrons, particularly the centres of gravity of the pairs, behave in perfect unison; the common velocity, which is only small, determines the current, if any. Strangely enough, the electrons themselves are scattered fiercely by the impurities that are always present in a metal, but the pairing overrules these disturbing effects: the pairs, even in ever-changing combinations of partners, may be considered as the stable surviving entities, carrying the frictionless current in perfect match.

Yet the scattering process has an observable effect. When the mean free path of the individual electrons is very small, as is the case with alloys, the stiffness of the macroscopic wave function is also somewhat limited. This gives rise to a subclass of superconductors called superconductors of the second kind. Superconductors of the first kind resist a magnetic field by generation of surface currents, up to a characteristic field-strength H_c, typically of the order of magnitude of 100 kA/m, followed by a complete breakdown into the 'normal' condition. However, a superconductor of the second kind will resist the field completely only up to a much lower field-strength H_{c1}, after which the superconducting body starts admitting magnetic flux in the form of millions of 'flux tubes'. These are tiny vortex-like structures, typically 100 μm in diameter, each containing the same quantized amount of flux, 2×10^{-15} Wb. This flux is generated by a certain density of the persistent ring current circulating around its thread-like non-superconducting core.

The occurrence of flux quantization is one of the most striking aspects of the macroscopic wave function mentioned. In between the flux tubes the sample remains superconducting, until at last at a relatively high magnetic field H_{c2}, in exceptional cases even above 10 MA/m, the body is crammed full of flux tubes and normal conductivity is restored. The picture has now become somewhat more complex and in *fig. 8* the essentials are illustrated. When the average magnetic

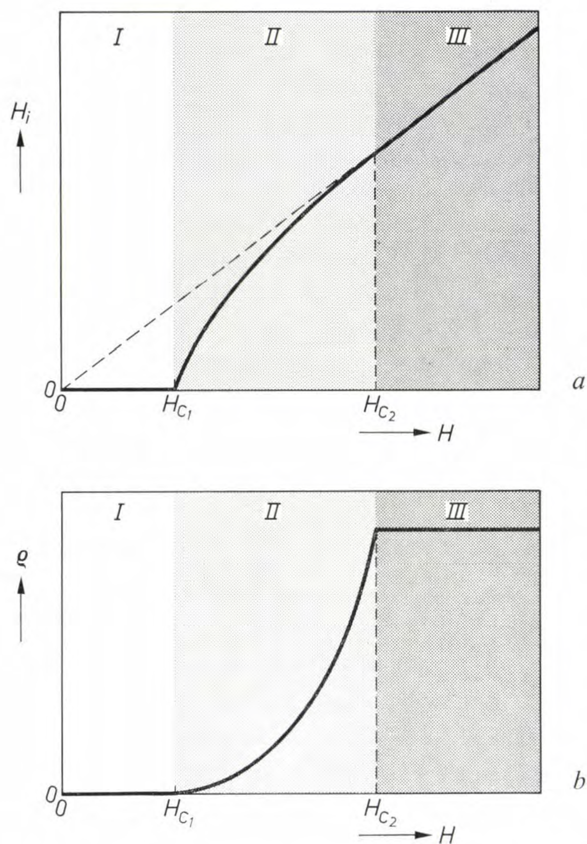

Fig. 8. Schematic representation of the magnetic and electrical properties of a superconductor of the second kind in an outer magnetic field.
a) The internal field H_i, plotted against H. In zone *I* ($H < H_{c1}$) there is no difference from a superconductor of the first kind: the field cannot penetrate the conductor, which behaves as a perfect diamagnet. In zone *II* ($H_{c1} < H < H_{c2}$) flux tubes can penetrate the conductor (the 'mixed' state). In the range $H > H_{c2}$ the superconductivity has completely disappeared.
b) The resistivity ϱ as a function of H. In zone *II* the resistivity is in general not zero, but is however zero at sites where the flux tubes are firmly pinned, e.g. at dislocations. In a superconductor of the first kind the interval H_{c1}–H_{c2} has disappeared; if the outer field increases, the superconductor suddenly changes from a perfect diamagnet into a normal metal. The resistivity of a superconductor of the second kind will remain zero up to H_{c2} if enough pinning sites for flux tubes are available in the material. Such materials are popularly referred to as 'hard superconductors'.

Table I. The transition temperatures T_c of a number of superconductors of the first and second kinds and the field-strength (H_c or H_{c2}) at which they change over to normal conduction. The H-values have been extrapolated to $T = 0$.

First kind	T_c (K)	H_c (A/m)
Aluminium	1.18	9×10^3
Indium	3.40	22×10^3
Lead	7.23	65×10^3
Second kind	**T_c (K)**	**H_{c2} (A/m)**
$Nb_{0.75}Ti_{0.25}$ (alloy)	10.0	7×10^6
$Nb_{0.75}Zr_{0.25}$ (alloy)	10.8	7×10^6
Nb_3Sn (compound)	18.3	22×10^6
V_3Ga (compound)	14.4	18×10^6

behaviour is considered, the superconductor of the second kind in the interval H_{c1}-H_{c2}, the 'mixed state', is not a perfect diamagnet. Moreover, a current through the sample exerts a force upon the flux tubes — not different from the interaction between a current and a magnet in every electric motor. If the flux tubes are not pinned they will move perpendicular to the current and it is found that this brings about a measurable potential difference in the conductor. This is, of course, nothing other than the occurrence of a resistance in the mixed state, its specific value being determined by the fraction of the sample's volume that is taken up by the non-superconducting vortex cores.

From a practical point of view those superconductors of the second kind are most interesting which have substantial irregularities in the build-up of their crystal, e.g. fluctuations in the composition of alloys, fine precipitates, or stress fields of lattice defects. Such irregularities may act as pinning points for the flux lines, immobilizing them even if heavy currents pass through the specimen. This ensures that the conductor remains really non-resistive, even in very high magnetic fields. The application of superconductors in heavy-current systems for power transmission is therefore now a largely solved technological problem.

Two other matters from the rapidly growing body of knowledge of the superconducting state should be mentioned; these relate to the transition temperature and the Josephson effect.

The transition temperatures of thousands of alloys and intermetallic compounds have now been determined to see if they fit the theory of Bardeen, Cooper and Schrieffer and if there is any hope for a really high-temperature superconductor. The results of all this work are partly disappointing. With their basic equation Bardeen *et al.* predict that T_c is dependent on the dominating lattice frequency, the electron density and a parameter characterizing the pair-forming interaction between lattice and electrons. Generally speaking this has been verified, but many physicists feel that a genuine, precise prediction of T_c is not yet possible, as quantitative knowledge of the details of interaction is missing. In the meantime it has become clear that superconductors with T_c above 20 K are extremely rare and that a T_c of, say, 30 K is unlikely ever to be found. *Table I* shows data relating to a number of superconductors of the first and second kinds. *Fig. 9* shows the historical record, the trend being an increase of 0.25 K per year so far.

The Josephson effect occurs in a weak link between two superconductors, the most striking example per-

[5] A more detailed treatment of superconductivity and the theory of Bardeen *et al.* is given in J. Volger, Superconductivity, Philips tech. Rev. **29**, 1-16, 1968.

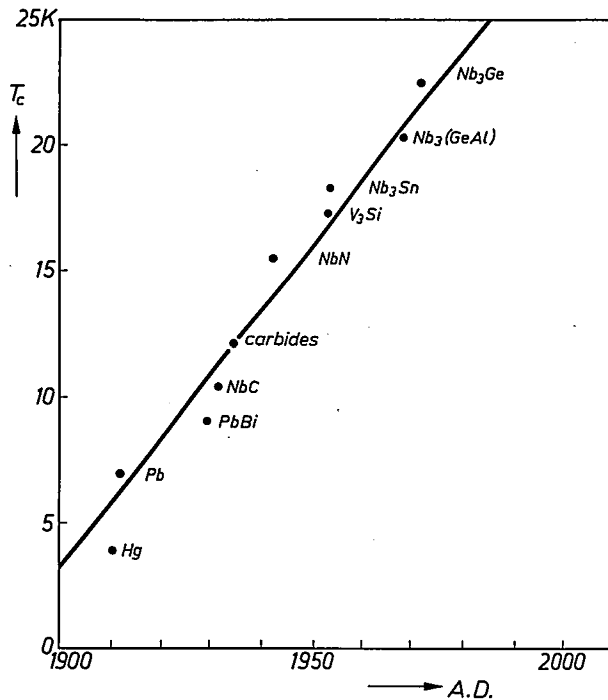

Fig. 9. The historical development of the highest known transition temperature T_c of superconductors.

haps being two superconductors in contact with each other through a thin layer of isolating material such as Al_2O_3, obtained by oxidation of aluminium. The typical property of superconductors is the long-range phase coherence of their wave function and, as wave functions are known to extend even through such isolating thin barriers, the two superconducting bodies can remain phase-locked. This means, as B.D. Josephson predicted in 1962, that a supercurrent may flow through the barrier and, indeed, zero resistance has been experimentally verified. In retrospect it can be concluded that experimental evidence for this effect existed for many years without ever being properly recognized.

The maximum supercurrent through the Josephson contact is determined by the overlap of the partial wave functions. When this maximum value is exceeded the junction becomes resistant. It is not necessary to dwell upon the many interesting features of Josephson junctions, including their a.c. behaviour and their response in magnetic fields. However, one very sensitive measuring device should be mentioned: this is known as SQUID (an acronym for Superconducting Quantum Interference Device), and consists of a closed superconducting circuit into which a Josephson junction has been inserted. As long as the loop, including the junction, is superconducting, the basic laws of electromagnetism require that it should contain a fixed number of flux quanta. When placed in an outer magnetic field, a loop current must and will be generated to preserve the flux. Since this current may bring the junction into the resistive state the SQUID is able to detect magnetic field variations, and that to a fabulous degree of sensitivity, better than 10^{-8} A/m. This may prove most useful, for instance in magnetocardiography (see below).

When *liquid helium*, the normal isotope ^{4}He, is below 2.18 K it assumes an ordered state (He II), comparable in many respects to the superconducting state of metals. The helium atoms are then partially condensed into a superfluid phase in which the liquid shows no viscosity, at least not at low velocities. Here, too, the physical situation is characterized by one macroscopic wave function, or order parameter, which is phase-coherent over the whole volume of the liquid. This stiffness leads to the hydrodynamical property that vortices and vortex rings, once generated, may persist for ever and that their circulation is quantized.

The physics of superfluidity is as intriguing as the physics of superconductivity. At finite temperature, but below 2.18 K, a fraction of the molecules do not participate in the ordering, so that the entropy differs from zero. Now, one curious aspect is that when the liquid is passed through a tube filled with very fine porous material, such a porous plug being called a 'superleak', virtually only the ordered part of the liquid flows through. Ideally, the superleak produces helium with zero entropy, i.e. essentially at zero temperature, but in actual practice some disturbing imperfection or dissipative process always occurs.

Cryogenic engineering

Liquefaction, handling, storage and use of oxygen, argon, methane and helium have, as we saw earlier, developed into large-scale industrial activities. A very spectacular application is in space technology. The large rockets that put a spacecraft into orbit contain thousand-ton quantities of liquid hydrogen as fuel and liquid oxygen as oxidizer; big quantities of helium are needed as pressurizing gas.

In interdisciplinary terms, perhaps the most interesting scope of large-scale cryogenic engineering is the application in electrical power equipment, in which superconducting wires can be used: cables, transformers and rotating machines [6]. The expectations of this revolutionary kind of engineering have been great indeed, yet in reality there is no breakthrough and it is worthwhile discussing the underlying factors.

The superconductors of the second kind mentioned above may yet become the ultimate fulfilment of Kamerlingh Onnes's anticipation that they could become vital to electrical engineering. This anticipation was frustrated in his time; it was soon discovered that for inconsiderable values of the current, and of the

outer magnetic field too, the superconducting state in metals like tin or lead is destroyed. This is typical of superconductors of the first kind, which happened to be the ones then investigated (see Table I). It is a historical accident that systematic investigations of alloys have come much later: superconductivity of the second kind was not properly identified before the fifties.

Hard, type II, superconductors are now available with current-carrying capacities, indicating the limit of resistanceless conduction, of the order of magnitude of 3×10^5 A/cm^2 for d.c., and very high upper critical fields, at least 10 MA/m. We have already discussed the need for flux pinning in the material and this can, in fact, be done. However, as is typical for any type-II superconductor, flux lines must have penetrated the wire to some extent at least when the field-strength is between H_{c1} and H_{c2}.

We are, in fact, facing a contradiction here: when the magnetic field is increasing, an occasional jerky motion of flux-line packages is unavoidable. This redistribution of magnetic flux in the metal gives rise to induction, i.e. dissipation of energy and rise of temperature, which may locally drive the material into its normal state. If no countermeasures are taken, flux jumps may occur in adjacent regions, due to magnetic and thermal coupling, and soon the whole wire will be normal, though the true limiting value of current or field has not yet been reached. This quenching phenomenon would of course have disastrous consequences.

Fortunately, stabilization of superconducting wires can be achieved, bringing the practical limit of overloading close to the true limit, as determined by the flux-pinning properties of the material. The methods adopted to stabilize superconductors are the reduction of the wire diameter and the embedding of the wire in high-purity copper. Reduction of the wire diameter causes the energy released during a flux jump to be too small to restore normality to the metal. By cladding the superconducting wire with a layer of copper, one provides for an electrical and thermal bypass, so that the full current can at least be taken temporarily if the quenching effect threatens to set in. Multifilament Nb_3Sn cable is now commercially available, and often contains more than a thousand very fine (e.g. diameter of 60 μm) filaments, as the cross-section in *fig. 10* shows. It is very attractive, extra stability and quench protection being offered by copper or other low-resistivity metal fillers between the filaments.

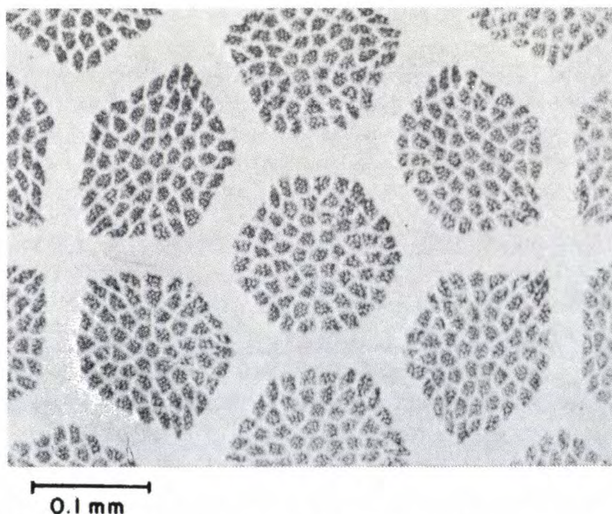

Fig. 10. A cross-section of an Nb_3Sn superconductor wire, with $61 \times 61 \times 19$ filaments (each of less than 2.5 μm diameter). (From H. Kuckuck, E. Springer and G. Ziegler, Cryogenics **16**, 350, 1976.)

With the advent of well stabilized, hard superconducting wires electrical engineering may eventually take an entirely new course. For instance, take the construction of superconducting a.c. generators. Five-megawatt prototypes have been built and tested, demonstrating their technical feasibility as high-power electric generators in aircraft and even as utility turbine generators. The electromagnet of the rotor is made of a superconducting wire carrying a current density two orders of magnitude greater than the conventional conductors, and with a magnetic field two or three times that of conventional rotors. Such generators will weigh less than a third of what a generator of like power and conventional design would weigh.

Moreover, the construction of homopolar generators and a.c. generators with superconducting stators has been tried. However, the reductions in size and, when the equipment is fairly large, its cost reduction, are not enough to bring about a breakthrough. The complex cryogenic requirements, liquefier and thermal insulation, especially of the helium-cooled rotor, remain a very weak point in the eyes of electrical engineers, who rightly demand maximum system reliability. Today the refrigeration circuits are still too delicate and vulnerable for the heavy requirements of a power system for, say, a town, a ship or a hospital. The same holds true for superconducting transformers and power cables.

Very interesting design specifications for power-transmission cables have been made, based on successful experiments with short test lines. These include sophisticated electrical insulation up to 400 kV, terminals, joints and other equipment. Although non-dissipative power transmission may become highly desirable or even necessary in heavily powered areas such as London or New York, at present the state of the art is by no means advanced enough to make the

[6] An application in magnet coils for laboratory use has been described in A. L. Luiten, Superconducting magnets, Philips tech. Rev. **29**, 309-322, 1968, and **30**, 147, 1969.

introduction of superconducting cables, during the next ten or twenty years, say, probable. The same applies to cryocables of non-superconducting metals, like aluminium, used at temperatures of, say, 20 K so that their resistance is dramatically reduced by a factor of a hundred or so.

As has occurred so often in the history of industrial technology, large-scale application of a revolutionary development can be furthered by a convincing demonstration of a successful vehicle. It has been, and still is, the hope of many workers in this field that the use of superconducting coils in magnetic levitation for high-speed rail transport may prove to be the breakthrough vehicle. The idea appears sound enough. In the densely populated areas of the world, millions of people every day demand fast public transport over ever-increasing distances, now up to hundreds of kilometres. Air traffic does not yet appear to be the best solution to this demand.

It is difficult to exceed the 200 km/h limit of rail cars with normal rolling wheels because of problems in stability. However, at 400 or 500 km/h, the best solution may be magnetic levitation, with vehicles floating on a bed of repellant magnetic forces. This would mean an entirely new railway technology. At low velocity the train could run on normal wheels, at higher velocity strong magnets in the vehicles would induce magnetic reaction fields in special, strongly conductive plates on the track, so that both lift and guidance would be obtained. Propulsion too would be by magnetic force and here the linear induction motor may find one of its best applications.

The greatest problem in the development of a levitation train is the construction of sufficiently powerful magnets. This type of transport is considered seriously particularly in Japan but also to some extent in Europe. In test facilities of intermediate size the feasibility of superconducting magnet coils has already been demonstrated, the advantages being more magnetic energy for smaller size and weight, without energy loss. However, the tremendous task remains of developing a reliable cryogenic system capable of operating on board a train. Also, the electrodynamic parts of the development programmes have still to be completed, needing large-scale effort for the careful analysis of drag forces, geometric tolerances and elastic deformation, tests of measuring, control and steering equipment, the study of starting and landing problems and so forth. At present it is by no means clear what specifications will finally emerge for a safe 500 km/h levitation train. Some policy makers have already decided that a big expenditure for such a train would not be appropriate at present. After all, it is by no means yet clear whether the pressing human communications problem will ultimately be solved by fast human transport or by electronic data transmission.

Large-scale cryogenic engineering is used for the gigantic magnetic coils of the elementary-particle accelerators like those in the CERN unit in Geneva, Switzerland, shown under construction in *fig. 11*, and in the Fermi Laboratory, Batavia, Ill., U.S.A. Particles coming from these accelerators collide, giving rise to a variety of events and these can be made visible in a hydrogen bubble chamber. The particles taking part in an event leave tracks in the liquid hydrogen at 20 K in the form of tiny vapour bubbles which can be photographed. The bubble chamber may consist of a vessel 4 m in diameter containing liquid hydrogen, and with large windows in the thermally insulating walls. Around the chamber a huge superconducting magnet coil produces a magnetic field of, say, 3 Wb/m^2 in that large volume of liquid hydrogen, so as to deflect the particle tracks, an essential tool in the analysis and identification of the events.

In electronics, it was once believed that mass production of the essential logic and memory elements for the very large computers could best be done with the aid of superconductivity. These elements, cryotrons, were considered for miniaturization and large-scale production with the help of cheap planar techniques. Today, this approach is not considered to have much chance of success, though the packing density, extreme speed and negligible heat dissipation of recently conceived elements, based upon the Josephson effect, are very impressive indeed.

Cryobiology

Life itself cannot bear cold. Below −5 °C all elementary processes usually come to a standstill. Tissue may become irreparably damaged at still lower temperatures and the lethal effects of ice crystals in tissues are especially to be feared. For certain micro-organisms it was an important discovery that after immersion in glycerol they could be subjected to slow, reversible cooling and thawing. This led to the widespread low-temperature banking of living cells, especially spermatozoa and red blood cells. These may survive the state of anabiosis. However, there is as yet no hope for those who want to preserve themselves or others in a state of suspended animation by deep freezing. Cooling to low temperatures takes too long for larger bodies; before a temperature low enough to arrest decay and vital processes can be reached, blood circulation will have stopped, followed a few minutes later by irreversible damage to the human brain.

Cryobiology includes investigations of living organisms under the influence of intense cold, such as

work on food preservation, botanical studies, the banking of skin and organs for transplantation, and the question of what really sets the hazard limit of exposure to extreme cold, in particular when the exposure is under controlled conditions.

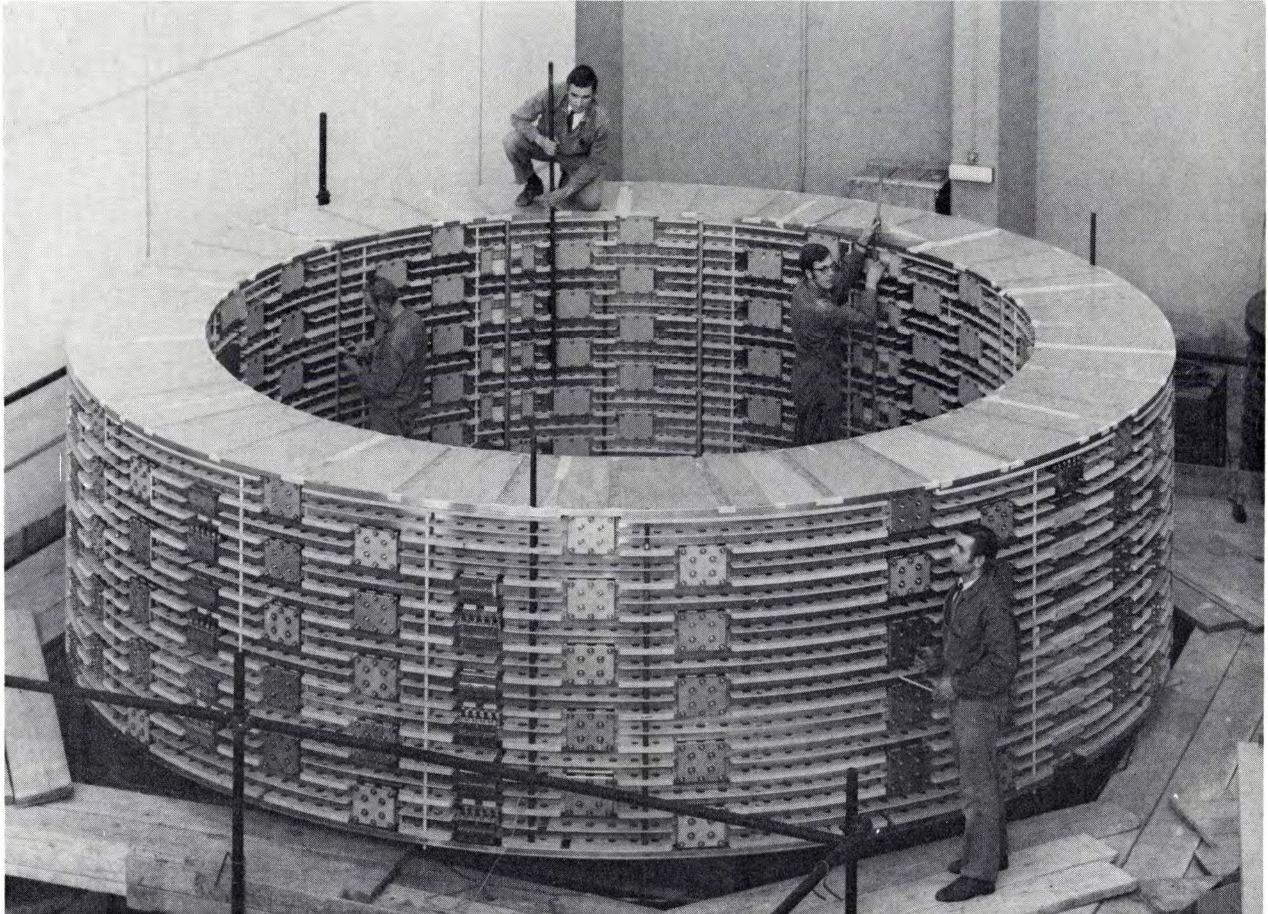

Fig. 11. The construction of a superconducting magnet (inner diameter 430 cm), to be used with the hydrogen bubble chamber at CERN, Geneva. This magnet will produce a field of 3.5 Wb/m^2 (35 000 gauss).

As a practical application, artificial insemination (AI) must be mentioned first. It may be considered one of the most important methods for the development and improvement of livestock, including the prevention of diseases: it therefore has high priority in agricultural development programmes. By adopting systematic breeding programmes many characteristics, such as the quality of beef or milk, can be improved. It is now easy to have a wide variety of selected bovine semen available in AI centres even after the death of the donors. A large stock of semen is collected and frozen, and thus enables the centre to meet the requirements of many breeders throughout the year. The semen can be diluted with a mixture of chemicals including glycerol. It is spread out over small sample holders, slowly frozen and preferably stored at liquid-nitrogen temperature (—196 °C), ensuring a virtually infinite storage life. *Fig. 12* shows liquid-nitrogen production and storage equipment [7] made by Philips, together with some of the containers needed in an AI centre. A typical centre will store the semen of ten bulls, processed in such a way that 100 000 cows can be inseminated twice a year with it. Fertilized egg cells, of mice for example, have also been stored at — 196 °C.

Gradually, many other tissue banks are coming into existence, for bone marrow, blood platelets, and certain tissue-culture cells. Automatically controlled apparatus for slow cooling to liquid-nitrogen temperatures are now being developed. Some tissues, such as skin and cornea, can be successfully stored but for whole organs, a task more urgent every day, much still needs to be done, and effective preservation methods are still problematic.

[7] The principle of operation of this equipment has been described in J. van der Ster and J. W. L. Köhler, A small air fractionating column used with a gas refrigerating machine for producing liquid nitrogen, Philips tech. Rev. 20, 177-187, 1958/59.

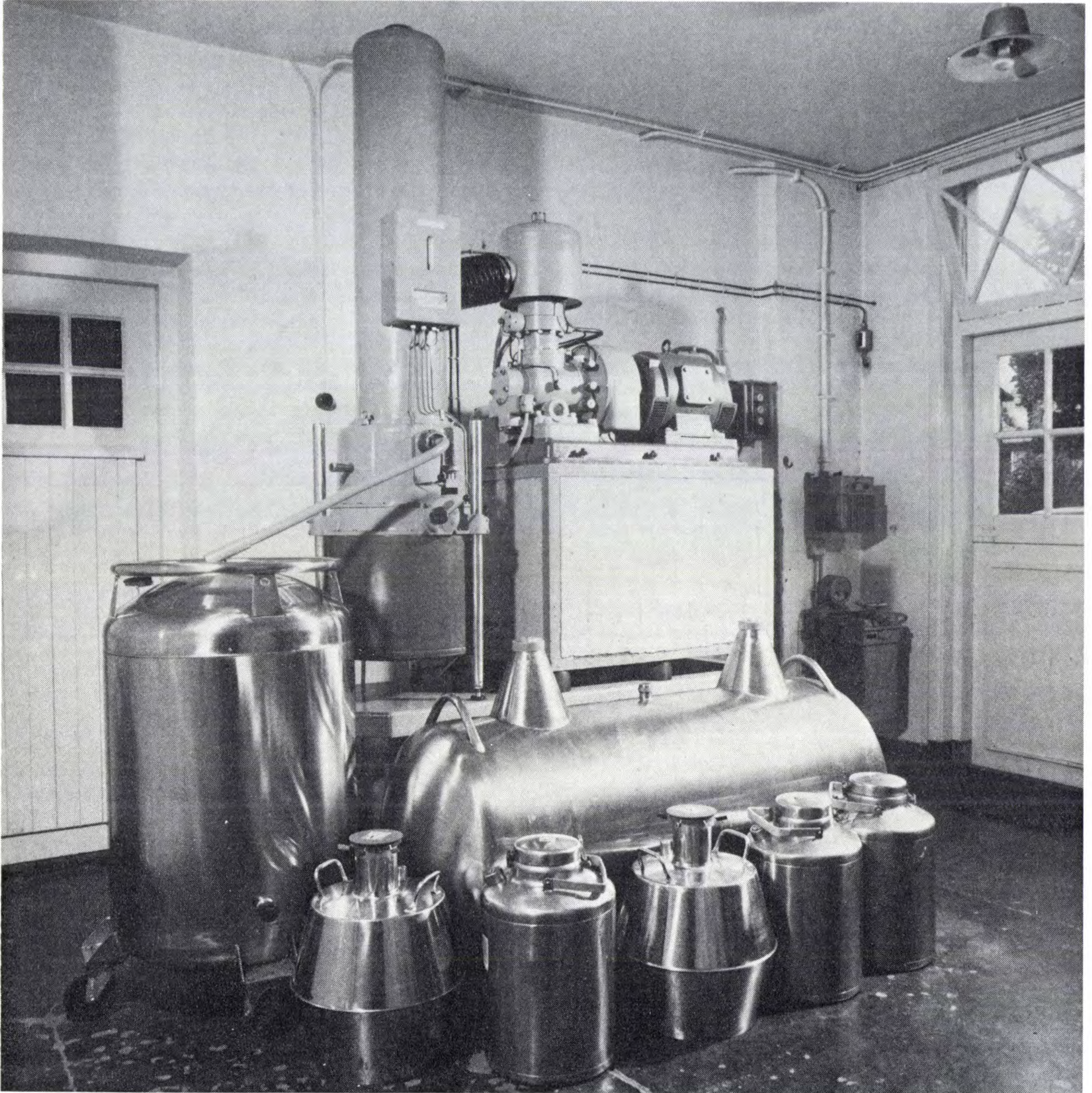

Fig. 12. Equipment for the production and storage of liquid nitrogen. The Philips PLN 106 liquid-nitrogen unit can be seen in the background; it consists of the PW 7160 refrigerating machine (right) and the PW 7170 air fractionating column (left). In the foreground are two large containers for liquid nitrogen alongside containers for the storage of bovine semen.

Cryophysics may obtain entry into medicine in yet another interesting way. Superconducting magnet coils may be the only solution where very strong fields are needed, for instance when magnet-tipped catheters have to be guided to places not otherwise accessible. Nuclear-magnetic-resonance measurements on an entire patient may become a matter of routine, if identification of malignant tissue by nuclear-magnetic-resonance mapping methods does, as expected, develop into a powerful diagnostic tool. Magnetic fields extending over a sufficient distance and having sufficient intensity and homogeneity could only be produced by using superconducting magnets.

Cardiography has recently been enriched by a magnetometric method. In addition to the electrocardiogram (ECG) one can now measure the magnetocardiogram (MCG); this reflects the fluctuating magnetic field — at a level of 10^{-10} Wb/m^2 — produced by the electrical (ion) current in the beating heart muscle. Such measurements require an extremely sensitive method, made possible by using a superconducting pick-up coil with a Josephson junction, SQUID, as indicated above.

Magnetocardiograms can be taken in a non-invasive way and by probing around the torso at least as much information can be obtained as from ECGs. The introduction of this new clinical diagnostic technique, however advantageous it is, could be retarded by sound medical conservatism and by the complexity and cost of the cryogenic facilities; the helium liquefier and its accessories would take some $ 50 000 of the clinic's yearly budget.

Finally, cryogenic surgery; cold can be used as a surgical tool, for instance for the inhibition and destruction of malignant cells. In cryosurgery a cannula of small dimensions is currently being used, with thermally insulated walls except for the very tip, in which liquid nitrogen circulates. The probe produces lesions according to its shape and size and the method is believed to be a very safe approach to the removal of certain diseased tissues. In practice, cryosurgery has been applied to skin neoplasms, and controlled destruction of prostatic obstruction has also been achieved. In neurological surgery an important application is the accurate placement of lesions in the basal ganglia of the brain as a treatment of Parkinson's disease and similar disorders of movement.

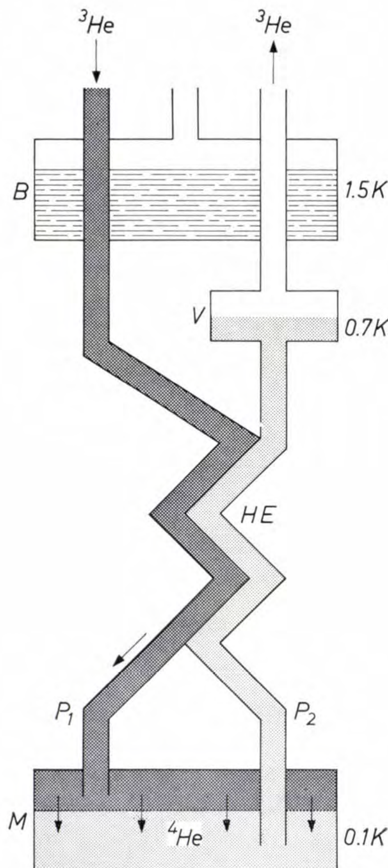

Fig. 13. Basic diagram of a dilution refrigerator. The cooling takes place in the mixing chamber M, where two phases are present: concentrated ^{3}He (dark shading) and superfluid ^{4}He that contains only a small percentage of ^{3}He (light shading). There is a continuous flow of ^{3}He across the interface from the concentrated to the dilute phase. This mixing process closely resembles evaporation, and takes up heat in a similar way. The ^{3}He passes through the pipe P_2 and enters the vaporization chamber (or still) V, from which it is pumped away; the vapour consists almost entirely of ^{3}He, owing to the great difference in the vapour pressures of ^{3}He and ^{4}He. The ^{3}He is compressed again, condensed and returned to M via the pipe P_1. B ^{4}He bath. HE heat exchanger.

Towards the absolute zero

The millikelvin temperature range had already been entered during the thirties, by cleverly designed adiabatic-demagnetization experiments with paramagnetic salts. This technique is still in use, but the more spectacular results are now in the microkelvin temperature range; for this the paramagnetic properties of the nuclear system in a solid are used instead of those of an ordinary paramagnetic salt in which the magnetic properties stem from the electronic shells of the constituent atoms.

What is really fascinating, however, and an absolute winner in terms of cooling capacity in the millikelvin range, is the ^{3}He-^{4}He dilution refrigerator; much work has been done on it over the last decade. A short discussion of its principle is in keeping with this review.

In the dilution refrigerator use is made of a remarkable property of liquid mixtures of ^{3}He and ^{4}He. At sufficiently low temperature, below about 0.5 K, the mixture spontaneously separates into two phases, both liquid, the one being rich in ^{4}He and superfluid, the other being very rich in ^{3}He, not superfluid and floating on top of the first one. As ^{3}He atoms from the almost pure ^{3}He phase evaporate into the diluted phase they must pick up energy, so that cooling is produced. The dissolved ^{3}He atoms are scarcely hindered in the superfluid ^{4}He phase and can be considered as forming a gas in it. We have here, in fact, another example of the second category of cooling phenomena discussed earlier.

The principle of the dilution refrigerator is outlined in *fig. 13*. The device works so well because it is indeed possible to remove ^{3}He selectively from the diluted phase and to recirculate it towards the concentrated phase so that ^{3}He atoms will continuously pass the phase boundary. As is to be expected this cooling device also needs the proper use of heat exchangers for efficient operation. This is by no means easy because, as we have seen, the thermal conductivity of the materials from which a heat exchanger may be made, copper for instance, vanishes at very low temperature. Moreover, the heat transfer from the helium liquid to the copper surface becomes extremely difficult at this point; this is due to the almost total reflection of the wave-like

vibrational modes carrying the heat bouncing against the metal surface.

Recently, ingenious improvements for the classical dilution refrigerator have been published. A flow pattern of both liquids is added with respect to each other, so that practically an ideal heat exchange results from direct contact between the two phases [8]. It should be noted that the order of magnitude of the cooling power of such devices, in the millikelvin range, is still well below 1 mW. However, thermal insulation techniques are almost perfect and the specific heat of physical objects to be investigated at those low temperatures is also usually small. The obvious advantage of the dilution refrigerator is its continuous operation, never achieved in adiabatic demagnetization. The latter is essentially a one-stroke method.

A short final remark about another spectacular discovery along the never-ending road to the absolute zero. Many have speculated whether pure ^{3}He, cooled to sufficiently low temperature, would also become superfluid. For some years now the answer has been known: at a few millikelvins, roughly a factor of 1000 lower than ^{4}He, ^{3}He becomes superfluid. The reason for the differences in the properties of both isotopes is, of course, that their nuclei are different. The ^{3}He atom has a magnetic nucleus and in terms of statistical behaviour it is akin to the electron. Consequently, the superfluidity of ^{3}He resembles the superconductivity phenomenon, the ^{3}He atoms forming pairs just as the electrons do in a superconductor. Research on ^{3}He is presently considered to be one of the main interests of cryophysics.

Outlook

In this review many aspects of cryogenics have not been mentioned, for instance, the sophisticated thermal insulation, indispensable in all cryogenic engineering, or cryopumping. This is the condensation of gases to liquids or solids with very low vapour pressures when in contact with a very cold surface. It is probably the fastest, cleanest and most effective way of obtaining an ultra-high vacuum. If and when the large-scale use of hydrogen as an energy carrier becomes an important contribution to the solution of the world's energy problems, cryogenic engineering will then be one of the most essential technologies.

It has been my aim to illustrate the beauty of a frontier science, which has found interesting applications to boot. In this respect low-temperature physics does not differ from many other branches of physics which are also developing at high speed, surprising us again by the discovery of entirely new phenomena or by the formulation of new basic concepts, helpful in an understanding of nature. As was pointed out, low-temperature physics has been and will remain one of the pillars of the science of condensed matter, some of its concepts having very wide application indeed. Take superfluidity for instance: this phenomenon is known so well now that it has been quite natural for astronomers to include superfluidity in their picture of neutron stars! Some scientists believe that certain aspects of the theory of superfluidity may be found to be of crucial importance for the full understanding of life.

What else has nature in store for us as we manage to produce ever-lower temperatures? We do not know. It might be that in the microkelvin range the solid system of nuclear magnetic moments with their feeble interaction could disclose intriguing structures. Or that the very low-frequency thermal excitation of complicated crystals turns out to be interesting in that temperature range. For the time being many properties of both helium isotopes remain puzzling.

The future may bring many practical surprises, particularly in the use of superconductivity; unfortunately the prospects for essentially higher transition temperatures remain dim. The wide field of cryogenic engineering, developing in interdisciplinary coherence with low-temperature physics, will certainly remain the interesting growth field it has been during the past century.

[8] F. A. Staas, Continuous cooling in the millikelvin range, Philips tech. Rev. 36, 104-114, 1976; this article also gives further references to the technical literature.

Summary. Some of the highlights and disappointments in low-temperature physics and technology are presented in this article. The emphasis is on concepts and trends rather than on a rigorous and complete treatment. Cooling methods and the properties of matter at low temperatures are discussed, both from a purely scientific and an applied point of view, with some emphasis on superconductivity.

Recent scientific publications

These publications are contributed by staff of laboratories and plants which form part of or cooperate with enterprises of the Philips group of companies, particularly by staff of the following research laboratories:

Philips Research Laboratories, Eindhoven, The Netherlands	*E*
Philips Research Laboratories, Redhill, Surrey, England	*M*
Laboratoires d'Electronique et de Physique Appliquée, 3 avenue Descartes, 94450 Limeil-Brévannes, France	*L*
Philips GmbH Forschungslaboratorium Aachen, Weißhausstraße, 51 Aachen, Germany	*A*
Philips GmbH Forschungslaboratorium Hamburg, Vogt-Kölln-Straße 30, 2000 Hamburg 54, Germany	*H*
MBLE Laboratoire de Recherches, 2 avenue Van Becelaere, 1170 Brussels (Boitsfort), Belgium	*B*
Philips Laboratories, 345 Scarborough Road, Briarcliff Manor, N.Y. 10510, U.S.A. (by contract with the North American Philips Corp.)	*N*

Reprints of most of these publications will be available in the near future. Requests for reprints should be addressed to the respective laboratories (see the code letter) or to Philips Research Laboratories, Eindhoven, The Netherlands.

H. Bacchi: Considérations sur le choix des transformations orthogonales et sur leurs perspectives.
Acta Electronica **19**, 299-332, 1976 (No. 4). *L*

G. Bioul & J. J. Quisquater: Application of shortest-path problems to design automation of circuit layouts.
Philips Res. Repts. **31**, 423-465, 1976 (No. 5). *B*

O. Boser: Hydrogen sorption in $LaNi_5$.
J. less-common Met. **46**, 91-99, 1976 (No. 1). *N*

M. R. Boudry, J. A. Morice & E. J. Millett: Real-time multi-access computing system for laboratory instrumentation.
Biomed. Computer Technol. **1**, 48-52, 1976 (No. 1). *M*

R. Brehm & M. Helmig: Messung hoher Geschwindigkeiten in einem Glas-Drosselejektor.
Raumfahrtforschung **19**, 314-317, 1975 (No. 6). *E*

F. M. A. Carpay, G. Y. Chin*, S. Mahajan* & J. J. Rubin* (* Bell Laboratories, Murray Hill, N.J.): Constrained deformation of molybdenum single crystals.
Acta metall. **23**, 1473-1478, 1975 (No. 12). *E*

T. A. C. M. Claasen & L. O. G. Kristiansson (Royal Institute of Technology, Stockholm): Necessary and sufficient conditions for the absence of overflow phenomena in a second-order recursive digital filter.
IEEE Trans. **ASSP-23**, 509-515, 1975 (No. 6). *E*

J. Daniels (I, II, V), **K. H. Härdtl** (I), **D. Hennings** (III) **& R Wernicke** (IV, V): Defect chemistry and electrical conductivity of doped barium titanate ceramics: Part I. Electrical conductivity at high temperatures of donor-doped barium titanate ceramics, Part II. Defect equilibria in acceptor-doped barium titanate, Part III. Thermogravimetric investigations, Part IV. The kinetics of equilibrium restoration in barium titanate ceramics, Part V. New aspects of an improved PTC model.
Philips Res. Repts. **31**, 487-559, 1976 (No. 6). *A*

J. W. F. Dorleijn: Electrical conduction in ferromagnetic metals.
Philips Res. Repts. **31**, 287-408, 1976 (No. 4). *E*

H. Dormont: Généralités sur l'utilisation des propriétés statistiques des signaux.
Acta Electronica **19**, 233-244, 1976 (No. 3). *L*

M. J. C. van Gemert & H. van Tongeren: Stralend verval van geëxciteerde atomen in de afterglow van een Na-Ne-Ar-ontlading.
Ned. T. Natuurk. **41**, 103-105, 1975 (No. 9). *E*

R. Genève: From colour television to digital television.
Acta Electronica **19**, 185-213, 1976 (No. 3). *(Also in French.)* *L*

Y. Genin & Y. Kamp: Algebraic properties of two-variable orthogonal polynomials on the hypercircle.
Philips Res. Repts. **31**, 411-422, 1976 (No. 5). *B*

A. Heidemann (Technische Hochschule München & Institut Laue-Langevin, Grenoble), **D. Richter** (Kernforschungsanlage Jülich) **& K. H. J. Buschow:** Investigation of the hyperfine fields in the compounds $LaCo_{13}$, $LaCo_5$, YCo_5 and $ThCo_5$ by means of inelastic neutron scattering.
Z. Physik B **22**, 367-372, 1975 (No. 4). *E*

F. Hottier: Contribution to the study of the vicinal surfaces of GaAs; application to homoepitaxy.
Philips Res. Repts. **31**, 466-479, 1976 (No. 5). *L*

J. P. Klozenberg: Theory of periodic modulation in a thermal imaging system.
Infrared Phys. **16**, 487-488, 1976 (No. 4). *M*

A. J. R. de Kock, S. D. Ferris*, L. C. Kimerling* & H. J. Leamy* (* Bell Laboratories, Murray Hill, N.J.): Investigation of defects and striations in as-grown Si crystals by SEM using Schottky diodes.
Appl. Phys. Letters **27**, 313-315, 1975 (No. 6). *E*

B. J. Mulder: Repetitive, extensive motion in ultra-high vacuum systems through the shape-memory of nickel-titanium alloys.
Vacuum **26**, 31-32, 1976 (No. 1). *E*

K. van Oostrum: Colourful use of the electron microscope.
New Scientist **65**, 712-713, 1975 (No. 941). *E*

J. G. J. Peelen: Influence of MgO on the evolution of the microstructure of alumina.
Sintering and catalysis, editor G. C. Kuczynski, publ. Plenum Press, New York 1975, pp. 443-453. *E*

P. M. Petroff (Bell Laboratories, Murray Hill, N.J.) & **A. J. R. de Kock:** Characterization of swirl defects in floating-zone silicon crystals.
J. Crystal Growth **30**, 117-124, 1975 (No. 1). *E*

R. J. van de Plassche: A wide-band monolithic instrumentation amplifier.
IEEE J. **SC-10**, 424-431, 1975 (No. 6). *E*

P. J. Rijnierse & U. Enz: Photomagnetism.
Physics Bull. **26**, 15, 1975 (Jan.). *E*

B. Schiek, J. Köhler & W. Schilz: A modulated subcarrier technique with instantaneous amplitude and phase information.
IEEE Trans. **IM-25**, 128-131, 1976 (No. 2). *H*

W. Schilz: Radartechnik in der Industrie.
VDI-Z **118**, 525-528, 1976 (No. 11). *H*

J. M. Shannon: Control of Schottky barrier height using highly doped surface layers.
Solid-State Electronics **19**, 537-543, 1976 (No. 6). *M*

T. Thalhammer: Opslag van energie.
Ned. T. Natuurk. **41**, 177-181, 1975 (No. 12). *E*

G. E. Thomas, E. E. de Kluizenaar, L. W. J. van Kollenburg & L. C. Bastings: Thin film analytical technique based on sputtering.
Anal. Chem. **47**, 2357-2360, 1975 (No. 14). *E*

E. P. G. T. van de Ven (Philips Elcoma Division, Eindhoven) & **H. Koelmans:** The cathodic corrosion of aluminum.
J. Electrochem. Soc. **123**, 143-144, 1976 (No. 1). *E*

H. J. Vink: Defects and defect transport in solids; industrial applications.
Ber. Bunsen-Ges. phys. Chemie **79**, 957-970, 1975 (No. 11). *E*

P. Wiedijk (Philips Lighting Division, Eindhoven): Simultaneous microdetermination of water and oxygen in metal halides by reductive fusion in an inert gas.
Anal. chim. Acta **81**, 105-110, 1976 (No. 1).

Contents of Philips Telecommunication Review **34**, No. 4, 1976:

F. A. Kluizenaar: Private Automatic Branch Exchange EBX 800 (pp. 145-155).
M. Bergsten & W. G. Bax: Test results of a 60 MHz coaxial system in Sweden (pp. 156-168).
M. Stein: The SEMATRANS range of data modems (pp. 170-183).
M. M. Jung & J. de Boer: Cyclic overflow of calls between subgroups in a full-availability group of lines (pp. 184-194).

Contents of Electronic Applications Bulletin **34**, No. 2, 1976:

D. Arentsen & G. P. J. van Schaik: The effect of base-current waveform on the turn-off behaviour of high-voltage switching transistors (pp. 52-60).
Pro Electron — order out of chaos (p. 61).
A. Boekhoudt: A low-distortion 50 W h.f. amplifier for s.s.b. using transistors (pp. 66-76).
G. J. Johnson: Mean power or rms power? *(Correspondence)* (pp. 76-77).
A self-regulating horizontal deflection circuit for b/w TV receivers (pp. 78-89).

Contents of Mullard Technical Communications **14**, No. 132, 1976:

J. A. Garters & J. S. Malcolm: The TDA1071 radio IC in communications receivers (pp. 54-62).
D. R. Armstrong: Zero-crossing detector circuits (pp. 63-68).
C. R. Hewitt: The TDA1050 IC in car radio a.m. receivers (pp. 69-76).
D. R. Armstrong & D. R. Hyde: Simple temperature sensing circuits using thermistors (pp. 77-82).
Zinc oxide VDRs for transient suppression (pp. 83-84).

Volume 37, 1977, No. 4 pages 77-108 Published 14th October 1977

PHILIPS TECHNICAL REVIEW

VOLUME 37, 1977, No. 5/6

Lithium niobate as a material for holographic information storage

H. Kurz

The availability of the laser and holography in the sixties was a strong stimulus to the development of ideas for optical storage devices, and set the pattern that was to be followed for some years. Hopes at that time were high: main memories were envisaged with bit densities of the order of 1 Gbit/mm³. Since then various possible systems — both holographic and localized — have been investigated in various parts of the world, and these studies are still continuing. The invariable conclusion has been that performance targets would have to be less ambitious — though they were still worth aiming at — owing mainly to limitations connected not with the optical part of the system but with the storage material. Thin films of a suitable magneto-optic garnet are now expected to give the best results for localized storage, and ferroelectric crystals whose refractive index can be changed locally and reversibly by irradiation offer the best prospects for holographic memories at Philips GmbH Forschungslaboratorium Hamburg. The article below deals with an investigation of iron-doped lithium niobate as a potentially very useful storage material for three-dimensional phase holograms. In a subsequent issue we shall publish an article on a device developed for magneto-optic memories at the Hamburg laboratories.

Introduction

Three main things are necessary for an optical memory: a material for storing the information, a light source for read-in and read-out, and an optical system to guide the light to the intended position.

In many cases the most suitable light source is the laser, since it approximates closely to an intense monochromatic point source. Now that lasers of many different types have become available, optical information storage has come in for a great deal of attention in recent years. Great advances have been made in the development of optical subsystems, such as modulators, beam deflectors and detector arrays [1].

The most difficult problem in making an optical memory is usually the material in which the information is stored. The material is required to have a high bit density, a long life, to take little optical energy for reading and writing, to allow stored information to be erased and new information to be written in, and to have a low cost per stored bit. In these respects optical memories have to compete with existing systems, which are mainly magnetic. The great virtue of optical memories is that they are able to handle large quantities of information in parallel operation.

Dr H. Kurz is with Philips GmbH Forschungslaboratorium Hamburg, Hamburg, West Germany.

Optical memories may be divided into localized and holographic types. In localized memories each bit is separately stored at a small location on the memory surface. We shall not be concerned with this type of memory system here [2].

In holographic memories the information is written in groups of bits on a larger surface, on which the separate bits can no longer be localized. The principle of a holographic memory is illustrated in *fig. 1.* Here again a laser is used as the light source. The laser beam is divided into a reference beam and an object beam. The object beam illuminates a semitransparent plate on which the information to be stored is contained in the

[1] See for example M. Balkanski and P. Lallemand (eds.), Photonics, Gauthier-Villars, Paris 1973.

[2] See the article by H. Heitmann *et al.* to appear shortly in this journal.

form of an image or a coded pattern (e.g. a punched card or a passive display). The two beams are made to converge on a small block of a suitable material, and it is here that a hologram of the information package is formed. The hologram can be read out later by illuminating the block with the reference beam alone. The resultant beam diffracted by the hologram is a faithful reproduction of the object beam modulated by the information. A lens produces an image of the information pattern on a detector, which may be a camera tube or an array of semiconductor detectors.

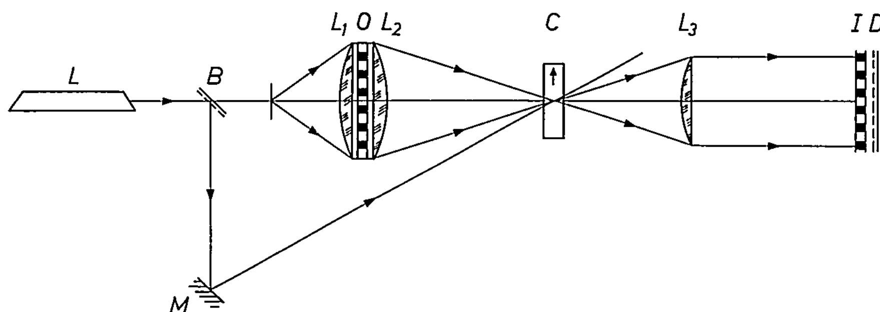

Fig. 1. Optical diagram of a holographic memory. The beam produced by the laser L is divided into two beams by means of a beam-splitter B. One beam illuminates the object O; this beam is focused by the lenses L_1 and L_2 in a block C of a suitable material. The other beam is projected on to C through the mirror M. Interference between the two beams produces a hologram in C. The hologram can be read out by illuminating the crystal by the reference beam BMC. The diffracted wave is identical with the object wave during the recording. An image of the reconstructed object I is produced on the detector D by the lens L_3.

On read-out a complete package of information becomes available at once. In addition, each bit is spread out over a relatively larger part of the storage medium than in localized storage, so that the information is less vulnerable. These features distinguish the holographic memory from the localized memory. But there is another difference that makes the holographic memory an attractive proposition.

When the thickness of the recording medium, the block of storage material, is large compared with the period of the interference patterns that form the hologram, several holograms can be recorded one above the other and read out again separately. This can be done by means of the Bragg effect: a three-dimensional diffraction grating only diffracts the light effectively when it is incident at a particular angle. For a grating or hologram formed by the interference between an object beam and a reference beam, the direction and wavelength of the incident beam must be the same at read-out as those of the reference beam. If the volume hologram is sufficiently thick the angle of incidence is sharply defined [3]. By rotating the block of storage material between two exposures different holograms can be stored and read out separately later.

In this article the properties of single-crystal lithium niobate ($LiNbO_3$), doped with iron or other metallic ions, as a storage or memory material are discussed for volume holograms.

Their use for this application is based on the change produced in the refractive index of this material when it is exposed to visible light or ultraviolet radiation.

A reversible change in the refractive index of $LiNbO_3$ and of a number of other ferroelectric and paraelectric substances exposed to laser radiation has been discovered as a side-effect in experiments concerned with nonlinear optics and optical modulation [4]. This effect, originally referred to as 'optical damage', occurs at moderate light intensities. As is so often the case, what was at first regarded as a nuisance turned out later to have a useful application [5]. Three-dimensional modulation of the refractive index, produced by illuminating the crystal by the interference pattern of two beams, results in a phase hologram in the crystal. Phase holograms have a high diffraction efficiency, i.e. the relative power of the part of the read-out beam that is deflected to the detector [3].

The following picture may be put forward to explain the change produced in the refractive index. When the crystal is exposed to illumination, charge carriers are released and these move in a preferred direction because of the asymmetric structure of the crystal. This results in an electric current proportional to the illumination. In addition, a photoconduction current is generated which is proportional to the product of illumination and the electric field-strength in the crystal. When the illumination is spatially modulated, the current follows this modulation and a space-charge field arises in the

[3] R. J. Collier, C. B. Burckhardt and L. H. Lin, Optical holography, Academic Press, New York 1971, particularly chapter 10.
[4] A. Ashkin, G. D. Boyd, J. M. Dziedzic, R. G. Smith, A. A. Ballman, J. J. Levinstein and K. Nassau, Appl. Phys. Lett. **9**, 72, 1966.
[5] F. S. Chen, J. T. LaMacchia and D. B. Fraser, Appl. Phys. Lett. **13**, 223, 1968.

crystal. The total field in the crystal is the sum of the space-charge field and any external field that may be applied. Since lithium niobate is an electro-optic material (this is also related to the asymmetrical structure of the crystal) the refractive index changes by an amount proportional to the total field.

In the next section we shall examine the dynamics of this chain of effects. It is found that the change in refractive index exponentially approaches a saturation value. The time needed to reach a given percentage of the saturation value is inversely proportional to the photoconduction coefficient. As a result of the same photoconductive effect any refractive-index distribution present is erased by illumination. A hologram can thus be erased by homogenous illumination, making the crystal useful as a reversible memory material. This also means, however, that on read-out of the stored information or when a hologram is written in later the information present in the crystal is partly erased. What is more, erasure has the effect of eliminating all the information stored in the crystal; it is not possible to erase a number of stored holograms and to let the others stored in the same volume remain.

The quantity of exposure energy necessary to reduce a refractive-index change to half its value is equal to the energy necessary to reach half the saturation value in writing in the information. Since it is not always necessary to approximate closely to the saturation value to obtain an adequate diffraction efficiency, information can be written in with much less energy than is required for erasure.

The time for which a recorded hologram can be stored in the dark depends on the conductivity caused in that state by thermal excitation of charge carriers. At room temperature lithium niobate is a poor conductor and the storage time is then of the order of some tens of hours.

The next section describes how the diffraction gratings with a period of about 1 μm can be written into the medium by interference between two coherent beams. The diffraction efficiency of such a grating as a function of the energy necessary for writing it in or erasing it is an important indicator of the usefulness of the material in optical memories.

The refractive-index change depends not only on the wavelength of the light but also on the concentration and nature of the metal ions in the crystal. Our investigation of the properties of materials, which is discussed in the third section, has mainly been concerned with iron as the dopant. It is found that charge transfer between divalent and trivalent iron ions causes the photocurrent on which the effect is based.

Erasure during read-out can be avoided by giving the material a thermal treatment during the recording; this method is also described in the third section. Thermally fixed holograms can be used for permanent information storage; the storage time is a few years.

Owing to the erasure effect a non-fixed hologram can only be read out a finite number of times. The number of holograms that can be stored in a crystal is therefore limited to a few hundred. For storing one hologram only a very small area is necessary. The maximum bit density is about 5×10^6 bits per mm^2. In the fourth section expressions will be derived for the number of times a hologram can be read out, for the number of holograms that can be stored and for the minimum energy needed for writing a hologram in. Finally, there is a description of some experiments with reversible and permanent information storage in digital and analog form.

The main results of the experiments with diffraction gratings and holograms are presented in *Table I*. These results show that reversible and permanent information storage is possible in $LiNbO_3$ crystals with a very

Table I. Properties of $LiNbO_3$ as a memory material.

	Reversible	Fixed
Resolution	$> 10^4$ lines/mm	not known, but lower
Efficiency:		
for a single hologram	95%	95%
for storage of more than one hologram	0.01-1%	up to 1%
Minimum writing energy	0.1-10 mJ/cm^2	2-13 J/cm^2 [14]
Number of read-outs	10^5-10^7	10^{10}
Erasure energy	1-100 J/cm^2	not applicable
Number of superimposed holograms	100-500	> 500
Capacity	10^6-5×10^6 bits/mm^2	$> 5 \times 10^6$ bits/mm^2
Storage time at room temperature	15 min-300 days	2-3 years

high bit density and a reasonable read-write sensitivity.

Apart from their use in optical memories, $LiNbO_3$ and related optical materials (for example $KNbO_3$ and $BaTiO_3$, all of them ferroelectric) also have potential uses in many other electro-optic components such as waveguides, modulators, variable beam-splitters, holographic filters, optical coding, scanners and colour holograms. These applications will not be dealt with in this article.

Dynamic behaviour of the refractive index during irradiation

The way in which an $LiNbO_3$ crystal doped with iron or copper oxide behaves under uniform illumination is illustrated in *fig. 2*. When the end c-faces of the crystal are short-circuited, a photocurrent proportional to the intensity of the illumination flows in the direction of the c-axis.

Until the crystal has reached equilibrium, there is a progressive change in the permanent dipole moment, and this change sets up an induced current. This pyroelectric current component [6], which also occurs when the illumination is switched off, will not be taken into account in the discussion.

The current in the z-direction is given as a function of the incident radiant intensity $I(z)$ — for convenience we assume that this depends only on the coordinate z in the direction of the c-axis — and the electric field $E(z,t)$ by [7]:

$$j_z(z,t) = K_0\alpha I(z) + K_1\alpha I(z)E(z,t) + \sigma_D E(z,t), \quad (1)$$

where α is the absorption coefficient and K_0 and K_1 are constants that depend on the wavelength of the incident radiation and on the concentration and nature of the dopant. *Fig. 3* gives a graph of the measured photocurrent values as a function of an external e.m.f.

The last term in (1) is also found when there is no irradiation; σ_D is the conductivity of the unilluminated crystal. Lithium niobate is an extremely good insulator: the third term in (1) may be regarded as negligible compared with the other two when the intensity of the incident radiation is moderate.

The second term in (1) is a photoconduction current and as such is nothing out of the ordinary: there are plenty of materials that become conductive upon irradiation. The first term in (1) also gives a current when there is no field, for example with uniform illumination and the end faces of the crystal short-circuited. D. von der Linde and A. M. Glass [8] explain this current by a photovoltaic volume effect. This could arise from the presence of substitutional lattice defects (e.g. Fe^{2+} ions) which give rise to anisotropic excitation and transport of charge carriers. A complete explanation of the effect on a microscopic scale has not yet been given. It has, however, been established that impurities (in particular iron ions) play an essential part; more will be said about this later.

The rest of this section will be confined to a description of the effects, taking eq. (1) as our starting point. When the magnetic field is neglected, Maxwell's equations give the following relation between current and field:

$$j_z(z,t) + \varepsilon\varepsilon_0 \frac{\partial E}{\partial t} = j_0(t). \quad (2)$$

Here $\varepsilon\varepsilon_0$ is the dielectric constant and $j_0(t)$ is the external current, which depends on the circuit to which the crystal is connected.

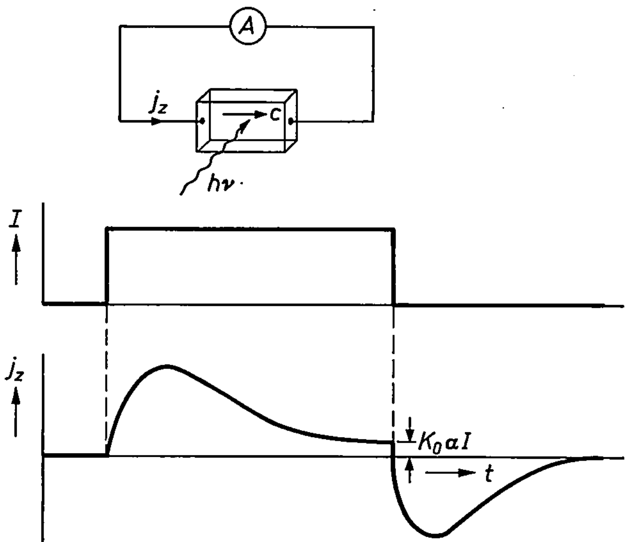

Fig. 2. The current j_z in a short-circuited $LiNbO_3$ crystal as a function of time t when a uniform illumination I is switched on and off. The switching peaks are due to the pyroelectric effect; the current takes a certain time to reach the steady-state value $K_0\alpha I$. In the diagram the arrow indicates the direction of the c-axis and the saturation field; A is a sensitive current indicator.

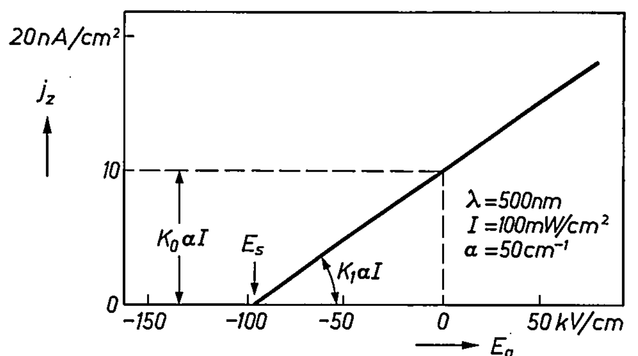

Fig. 3. The photovoltaic current j_z as a function of an external field E_a during homogeneous illumination at a given intensity and wavelength. The value of the current for $E_a = 0$ is given by $K_0\alpha I$, the slope of the characteristic by $K_1\alpha I$. When α and I are known it is possible to determine K_0 and K_1.

From (1) and (2) we obtain a differential equation for $E(z,t)$, which can be solved after determining the boundary conditions $j_0(t)$ imposed on the crystal. We shall now try to show that in practical cases j_0 may be taken as very nearly constant.

When the crystal is connected to a current source, j_0 is at once established. An open-circuit, for which $j_0 = 0$, is a special case of current control. When the crystal is connected to a voltage generator, the average field is equal to the e.m.f. of the generator divided by the length of the crystal. From eq. (2) we see that in this case j_0 is equal to the average of $j_z(z,t)$ over z. A short-circuited crystal is a special case of voltage control, with the external current j_0 approximately equal to $K_0\alpha I_0$, where I_0 is the mean of $I(z)$, as follows from (1). The approximation is valid for a small modulation depth of $I(z)$.

The solution of equations (1) and (2), if j_0 is constant, may be written as:

$$E(z,t) = E(z,0)e^{-I(z)t/U} + E(z,\infty)(1 - e^{-I(z)t/U}), \quad (3)$$

where $U = \varepsilon\varepsilon_0/K_1\alpha$. The field at the time $t = 0$, $E(z,0)$, does not necessarily have to be zero or even homogeneous: an external e.m.f. may have been applied, and as a result of a previous illumination a space-charge field may have remained in the crystal.

For prolonged illumination the field tends towards a saturation value $E(z,\infty)$ given by:

$$E(z,\infty) = \frac{j_0 - K_0\alpha I(z)}{K_1\alpha I(z) + \sigma_D}. \quad (4)$$

For an open-circuit $E(z,\infty)$ is approximately equal to $-K_0/K_1$. For a short-circuit and a small modulation depth of $I(z)$, $E(z,\infty)$ is given by:

$$E(z,\infty) = \frac{K_0}{K_1} \cdot \frac{I_0 - I(z)}{I_0}, \quad (5)$$

where σ_D is assumed to be negligible compared with $K_1\alpha I_0$. We see that for a short-circuit the saturation field is proportional to the modulation index of the interference pattern. As long as the modulation depth is small, the crystal therefore behaves as a linear storage medium.

From (3) and (4) it follows that the parameters K_0/K_1 and U determine the dynamics of the field distribution. The constant K_0/K_1, which will be called E_s from now on, has the dimension of a field and determines the magnitude to which the saturation field can grow. The constant U has the dimension of an energy density and determines the rate at which the saturation is reached during constant illumination. The orders of magnitude of E_s and U are 100 kV/cm and 100 J/cm^2.

Equations (1) to (5) constitute a simple model for the dynamics of the field in the crystal. Owing to the presence of this field the crystal lattice is locally deformed and the refractive index for light perpendicularly incident on the z-axis is changed. In lithium niobate this change can be quite considerable, owing to the polar asymmetry of the crystal.

The refractive index change Δn caused by a field in the z-direction is given by:

$$\Delta n(z,t) = \tfrac{1}{2}n^3 r_{33}E(z,t), \quad (6)$$

where n is the refractive index and r_{33} is an element of the electro-optical tensor [9].

The way in which irradiation brings about a change in the refractive index has been shown. When the illumination is switched off, equations (1) and (2) indicate that the field distribution decays exponentially with a relaxation time $t_D = \varepsilon\varepsilon_0/\sigma_D$. The quantity t_D is called the storage time, which may range from many hours to days, depending on the dopant concentration.

To erase a refractive-index change rapidly, the crystal has to be shorted and uniformly illuminated. From (5) we see that the existing refractive-index distribution is then driven to zero. This takes place exponentially with a relaxation time U/I_0:

$$\Delta n(z,t) = \Delta n(z,0)e^{-I_0 t/U}. \quad (7)$$

The parameter U is one of the factors that determines the capacity of reversible memories in which the storage medium is $LiNbO_3$. We shall return to this subject presently.

Write-in and read-out from a diffraction grating

Write-in

The change brought about in the refractive index by irradiation can be measured by illuminating the crystal with two coherent beams (see *fig. 4*). A three-dimensional diffraction grating is then produced in the crystal; the intensity of the light diffracted by this grating during illumination is a function of the parameters of interest in the storage of information. Since a hologram is also a kind of diffraction grating, the measurement made in this way gives a good indication of the usefulness of the material as a storage medium for holograms.

Interference between the incident waves gives rise to an intensity distribution of the form

$$I(z) = I_0(1 + m \cos Kz) \quad (8)$$

---

[6] C. Kittel, Introduction to solid state physics, 4th edition, Wiley, New York 1971, page 477. See also E. T. Keve, Philips tech. Rev. 35, 247, 1975.
[7] H. Kurz, Ferroelectrics 13, 291, 1976.
[8] D. von der Linde and A. M. Glass, Appl. Phys. 8, 85, 1975.
[9] J. F. Nye, Physical properties of crystals, Oxford University Press, London 1957.

in the crystal. The modulation depth m depends on the ratio of the intensities of the interfering beams, the wave number K on the angle between their directions of propagation. If we insert (8) in our model (1)-(5) we can calculate the change in refractive index at the

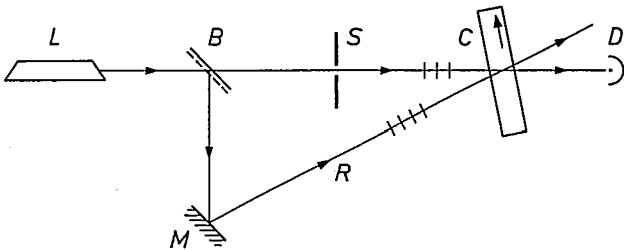

Fig. 4. Experimental arrangement for write-in and read-out of diffraction gratings. The beam from the laser L is divided into two beams by means of a beam-splitter B. One beam is projected on to the crystal C through a mirror M, the other beam is passed through a shutter S. The polarization of the beams is parallel to the plane through the directions of propagation and the c-axis of the crystal. On read-out the shutter S is closed and the crystal is illuminated with the beam R; the diffracted light is received by the detector D.

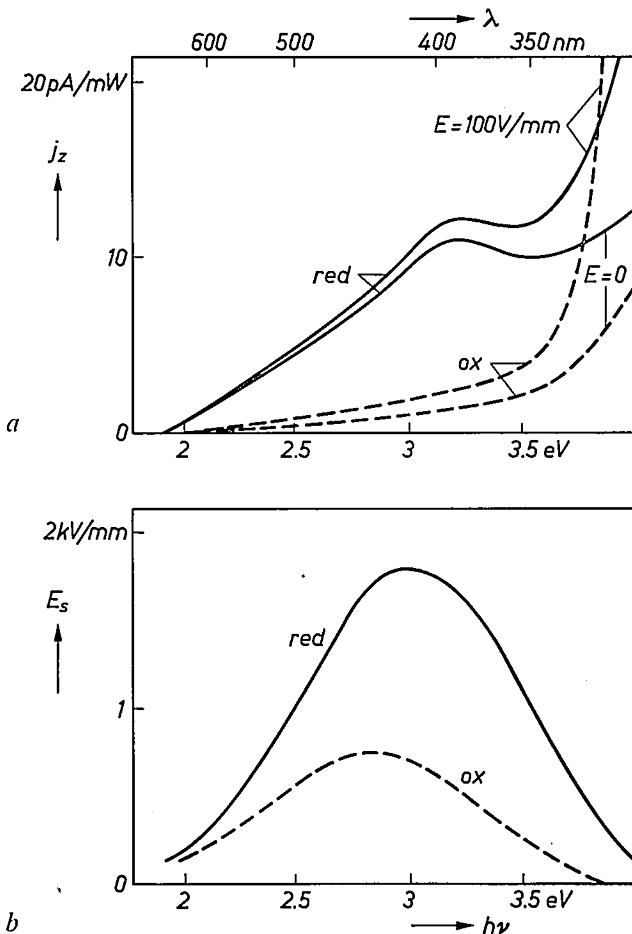

Fig. 5. The current j_z and the saturation field E_s for reduced and oxidized crystals as a function of the wavelength λ of the illumination (the photon energy $h\nu$ is also indicated). The intensity of the illumination was 100 mW/cm² in all cases. The difference between the characteristics at an external field $E = 0$ and at $E = 100$ V/mm is proportional to the product $K_1\alpha$.

position z. From (5) it follows that the saturation value is:

$$\Delta n(z,\infty) = \Delta n_s \, . \, m \cos Kz, \qquad (9)$$

where $\Delta n_s = \frac{1}{2}n^3 r_{33} E_s$. We have assumed here that the crystal was short-circuited. From (3) we see that for a previously unilluminated crystal the refractive index is given as a function of time by

$$\Delta n(z,t) = \Delta n(z,\infty)(1 - e^{-I(z)t/U}). \qquad (10)$$

In our investigation of materials, described in the next section, we measured the writing sensitivity S. This is defined as the derivative of the amplitude of the refractive-index distribution with respect to the illumination $I(z)t$ in the limit for small values of $I(z)t$. From (9) and (10) we find:

$$S = \frac{m\Delta n_s}{U}. \qquad (11)$$

The quantity S is the illumination necessary to obtain a given refractive-index modulation $m\Delta n_s$. It follows from (7) that the illumination necessary for erasure must always be a few times greater than U.

Read-out

When a crystal containing a diffraction grating is illuminated by a beam of the same wavelength and direction as one of the beams used for writing in the grating, light is diffracted in the direction of the other writing beam. The power of the diffracted beam is a function of the amplitude of the refractive-index distribution $\Delta n(z,t)$ in the crystal. The ratio η_1 of the diffracted and incident power is called the efficiency. For a crystal of absorption coefficient α and thickness d, where the refractive index is modulated by an amplitude Δn_1, the efficiency is given approximately by [10].

$$\eta_1 = R e^{-\alpha d/\cos\theta} \sin^2\left\{\frac{\pi\Delta n_1}{\lambda\cos\theta} \cdot \frac{1 - e^{-\alpha d}}{\alpha}\right\}, \qquad (12)$$

where θ is the angle between the bisector of the beams and the normal to the crystal surface. In the following we shall use the approximation $\cos\theta \approx 1$. The factor R is a correction for reflection losses at the front and rear faces of the crystal. These are considerable, since the refractive index is fairly high (about 2.5). In addition, unwanted multiple reflections may occur. These side effects can be substantially reduced by means of vapour-deposited antireflection layers. The maximum efficiency is then approximately equal to $e^{-\alpha d}$, that is to say the light that is not absorbed is diffracted.

In formulating eq. (12) the exponential decay of the refractive-index modulation along the direction of propagation of the light was taken into account. If the

argument of the $\sin^2$ function is equal to $\pi/2$, the efficiency is at a maximum. In practice, the maximum efficiency can be obtained with a crystal about 0.2 mm thick. At a wavelength of 500 nm we then have a refractive-index modulation with an amplitude of about 10^{-3}.

Resolution

In the derivation of our model (1)-(5) it was assumed that the current depends only on the illumination and the local field. This is not strictly true, since the charge carriers are displaced because of the presence of potential and concentration gradients. This may give rise to a displacement and a decrease of contrast in the diffractive grating produced. In lithium niobate both the diffusion length and the drift length of the charge carriers are less than 10 nm, so that the effect is negligible with a grating period of the order of 1 μm.

The constants K_0 and K_1 are based on transport lengths, which are proportional to the product of the mobility and lifetime of the charge carriers. If the writing or erasure sensitivity, which depend on K_0 and K_1, were to be made greater, the resolution might deteriorate.

Materials and treatment of materials

In the previous section we saw that the exposure energy U necessary for obtaining the maximum refractive-index change depends on the photoconduction constant K_1 and the absorption coefficient α. The maximum amplitude of the refractive-index modulation is proportional to E_s $(= K_0/K_1)$. The material constants K_1, α and E_s are functions of the wavelength; they also depend on the nature and concentration of the impurity in the crystal, and can therefore be controlled by treatment of the material. The other constants that play a part in the writing in are not readily accessible to control. Their values are therefore given for a wavelength of 500 nm:

$$\varepsilon = 32,$$
$$n = 2.55,$$
$$r_{33} = 2.2\times 10^{-9}\ \mathrm{cm/V},$$
$$\tfrac{1}{2}n^3 r_{33} = 1.7\times 10^{-8}\ \mathrm{cm/V}.$$

The absorption spectrum of iron-doped lithium niobate has characteristic bands at photon energies of 1.1 eV and 2.6 eV. Strong absorption occurs at photon energies higher than 3.1 eV. The two bands at 1.1 and 2.6 eV are correlated with the presence of Fe^{2+} ions. This has been confirmed both theoretically and experimentally in a study that also included EPR and Mössbauer spectroscopy [11]. At a given concentration of Fe ions in the crystal, determined by addition of Fe_2O_3 during growth, the concentration of Fe^{2+} ions can be varied by reduction or oxidation.

It has been found that the writing sensitivity S of the crystal, which from (11) is proportional to the ratio of Δn_s to U, and hence is proportional to $K_0\alpha$, first increases with rising relative Fe^{2+} concentration and then decreases. It might be deduced from this that K_0 is proportional to the concentration of Fe^{3+} ions. Little is to be noticed of the presence of Fe^{3+} ions in the absorption spectrum in the visible region — apart from a few weak bands at 2.55 and 2.95 eV, which are attributed to Fe^{3+}. Evidence that K_0 depends on the Fe^{3+} concentration is therefore somewhat indirect.

The values of $K_0\alpha$ and $K_1\alpha$ can be determined not only from optical measurements but also from the current under homogeneous illumination at a given external field. Eq. (1) shows that the current is linear in both intensity and field-strength. *Fig. 5a* shows the results of measurements of the photocurrent as a function of wavelength at constant intensity, both with and without external field [12]. The current when the crystal is short-circuited is proportional to $K_0\alpha$, and the difference between this and the current found when an external field is applied is proportional to $K_1\alpha$. A high field (100 V/mm) has to be applied to observe any appreciable difference between the two values in the visible region: the photoconductive effect is clearly weak compared with the photovoltaic effect. Fig. 5*b* shows the spectral distribution of the constant E_s, which determines the saturation value of the change in refractive index. There is a marked difference between the two figures: the values of K_1 and α clearly increase considerably in the near ultraviolet, whereas K_0 is large only in the visible region. The increase in the absorption coefficient α is so large that the writing sensitivity S, which is proportional to $K_0\alpha$, increases strongly in the near ultraviolet.

The effect of oxidation and reduction is also shown in fig. 5: reduction can cause a considerable increase in the visible region both in the photocurrent and in the saturation value of the refractive index. It can also be seen that the photoconduction current in the near ultraviolet is greatly increased by oxidation. Since U is proportional to $1/K_1\alpha$, an increase in this current component is connected with a greater erasure sensitivity. Reduction causes a very marked increase in the absorption coefficient α. In an untreated crystal after growth, α is of the order of 10 cm^{-1}; after heating in an argon atmosphere, α can rise to 100 cm^{-1}.

The conclusion that we may therefore draw is that diffraction gratings or holograms can best be written

[10] N. Uchida, J. Opt. Soc. Amer. **63**, 280, 1973.
[11] See H. Kurz, E. Krätzig, W. Keune, H. Engelmann, U. Gonser, B. Dischler and A. Räuber, Appl. Phys. **12**, 355, 1977.
This study was undertaken by Philips Forschungslaboratorium Hamburg in cooperation with the University of the Saarland at Saarbrücken and the Institut für Angewandte Festkörperphysik at Freiburg im Breisgau, West Germany.
[12] E. Krätzig and H. Kurz, Ferroelectrics **13**, 295, 1976.

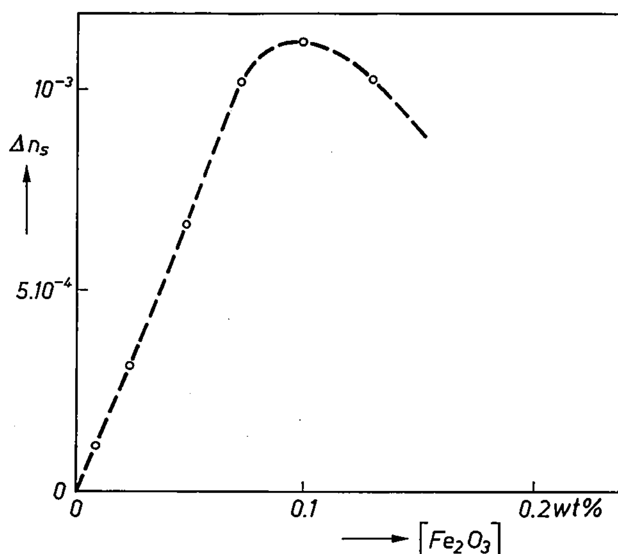

Fig. 6. Maximum refractive-index modulation Δn_s as a function of the Fe_2O_3 concentration.

and read in visible light (e.g. with an argon-ion laser) and in a reduced crystal, whereas oxidation and ultraviolet light (Kr laser) are better for erasure.

So far it has been assumed that the concentration of iron ions (irrespective of the valency) is constant in the crystal. If this concentration is varied in crystals that have undergone the same thermochemical treatment, we can see the following [11]. The writing sensitivity S, which is proportional to $K_0\alpha$, first increases as the square of the concentration, and then linearly. Since the absorption coefficient α increases linearly with concentration, we conclude that K_0 tends towards a saturation value. The saturation value Δn_s of the change in refractive index, which is proportional to K_0/K_1, has a maximum at a concentration of 0.1 wt % of Fe_2O_3. Since K_0 is approximately constant in that range, K_1 must therefore pass through a minimum. A concentration of about 0.1 wt % of Fe_2O_3 is therefore satisfactory for the rapid writing and frequent reading of information, but erasure is difficult. As an illustration a graph of Δn_s as a function of the Fe_2O_3 concentration is shown in *fig. 6*. The experiments mentioned above lend support to the explanation of the effects noted by Von der Linde and Glass [8]. More study is required before the mechanism can be described in detail.

One thing is certain, however: in iron-doped lithium niobate the Fe^{2+} ions are the donors from which the charge carriers originate that give the photocurrent. From the fact that in a short-circuited crystal the external current tends towards a saturation value, it follows that the Fe^{3+} ions act as acceptors for the charge carriers. Otherwise, of course, charge-carrier depletion would occur.

To conclude this section, *Table II* shows some representative values for the constants K_0 and K_1 and for the parameters Δn_s and S that may be derived from them. The values of α and of the storage time are also given, since they are relevant to holographic memories. It can be seen that oxidation has the effect of drastically increasing the storage time.

Table II. Material parameters (λ = 514 nm).

Concentration	Chemical treatment	Optical absorption α (2.6 eV) cm^{-1}	Photo-voltaic constant $K_0 \times 10^9$ Acm/W	Photocon-ductivity constant $K_1 \times 10^{14}$ $cm^2/\Omega W$	Sensitiv-ity [*] $S \times 10^4$ cm^2/Ws	Refractive-index change $\Delta n_s \times 10^4$	Storage time t_D in days
wt % Fe_2O_3							
0.1	None	18	2.0	1.66	0.27	3.0	0.5
0.1	Reduced	54	1.66	1.3	0.66	3.2	—
0.1	Strongly reduced	134	1.11	1.6	1.13	1.66	—
0.015	None	1	1	4	0.04	1.0	10
0.015	Oxidized	—	0.2	2	—	0.4	100
wt. % CuO							
0.25	None	1	0.3	3	0.004	0.4	50

[*] Eq. (11) shows that the sensitivity is proportional to the modulation depth m of the illumination. In our experiments we kept to m = 0.4.

Thermal fixing of the refractive-index distribution

The erasure of stored information during read-out can be prevented by fixing the refractive-index distribution. In this section we shall consider a method in which the refractive index is thermally fixed by recording the hologram at an elevated temperature and then cooling the crystal to room temperature [13]. This method has the incidental advantage that where several

Fig. 7. Reconstruction of holograms during the various stages of thermal fixing. *a*) Direct image of the object, seen through the crystal. *b*) Reconstruction during recording at 150 °C. *c*) Reconstruction after fixing.

holograms are superimposed there is no interference from earlier recorded information. This avoids the formation of mixing products between the superimposed gratings as would follow from eq. (3), which applies to the normal method of recording at room temperature.

When the refractive-index distribution is recorded in a ferro-electric crystal at higher temperatures ($>$ 100 °C) the mobility of the ionic defects in the crystal is high, whereas the electrons are relatively much less mobile. The ionic defects then move in a few seconds to places where the highest electron charge is located, so that the charge distribution of the electrons is almost completely compensated by that of the ions. The amplitude of the internal field has now fallen almost to zero, and so has the change in refractive index. If the crystal is now cooled, the ion distribution is 'frozen in'. This gives an ion-field distribution that is more or less identical with the original distribution of the space-charge field during the recording. The modulation depth will decrease slightly owing to ion diffusion during the recording. Illumination of the crystal now gives rise to a space-charge field of opposite sign to the ion field in the limit $I_0 t \to \infty$. This space-charge field is not removed by subsequent illumination, which means that a hologram can be read out as frequently as required. Erasure is possible only by heating above 300 °C, which has the effect of setting the electrons and ions in motion again. For this method it is useful if the photoconductivity is highly temperature-dependent. The hologram can then easily be recorded at a high temperature, so that at a low temperature it no longer changes. The required temperature dependence can be obtained by doping with manganese [14].

Fig. 7 shows reconstructions of holograms made during the various stages of the fixing process. There is little loss of quality to be detected; the interference fringes due to multiple reflections in the crystal, which degrade the pictures shown here, can be suppressed by means of antireflection filters.

The lifetime of thermally fixed diffraction gratings and holograms is determined by the stability of the frozen ion distribution. The activation energy of the ions is about 1.4eV [14], and the storage time at room temperature is therefore of the order of years.

Thermal fixing is important in memories containing information that is required to change very little with time (compilers, translation programs, archives).

Holographic information storage

The main properties that determine the usefulness of an optical storage medium were mentioned in the introduction to this article. In this section it will be shown how these properties depend on the parameters Δn_s and U and on the sensitivity of the detectors, as well as on the volume of the crystal. Some experiments with reversible and permanent information storage will then be described.

Writing, reading and erasure

The energy required for reading out a hologram depends on the diffraction efficiency of the hologram and on the minimum energy that the detector requires to produce a read-out signal. The detector we have used is a silicon JFET type, developed at Philips Research Laboratories, Eindhoven [15]. This has 25 image elements, requiring 10^{-12} J per element.

[13] D. L. Staebler and J. J. Amodei, Ferroelectrics **3**, 107, 1972.
[14] D. L. Staebler and W. Phillips, Appl. Optics **13**, 788, 1974.
[15] J. Lohstroh, 1974 IEEE Int. Solid-State Circuits Conf. Dig. tech. Papers, p. 34.

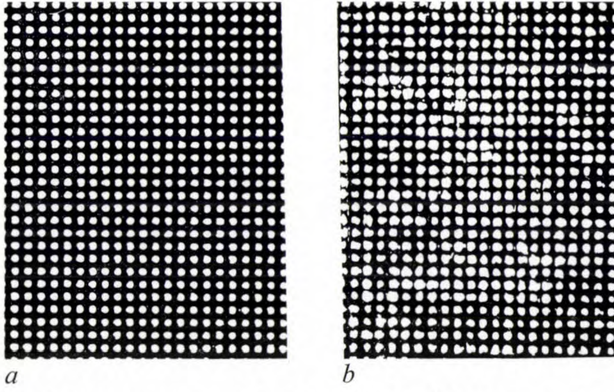

Fig. 8. Reconstruction of a thermally fixed hologram with a minimum area (1 mm^2). *a*) Direct image seen through the crystal. *b*) Reconstruction of a thermally fixed hologram.

Since the hologram is gradually erased by the reference beam, the diffraction efficiency decreases during read-out. This means that with a given initial value of the refractive-index modulation the number of times the information can be read out is limited. If the information is to be read out once only, then the minimum value of refractive-index modulation has to be written in; this determines the minimum writing energy.

The number of possible read-outs for the maximum refractive-index modulation where the writing requires an illumination U will now be calculated. From eq. (7) the curve of the refractive-index modulation Δn_1 can be found as a function of the illumination $I_0 t$ during read-out.

The number of possible read-outs M is now given by the integral of the efficiency over the exposure and the surface of the crystal, divided by the minimum detector energy required, W_0. Proceeding from eq. (12) for the efficiency and eq. (7) we then find:

$$M = cUA/W_0, \qquad (13)$$

where A is the surface area of the crystal and c is a numerical factor that depends on the optical density αd and on the initial phase modulation $2\pi\Delta n_1(0)d/\lambda$. With $\alpha d = 1$ and a phase modulation π it follows that $c = 0.15$. An absorption coefficient of 50 cm^{-1} then results in a thickness d of 0.2 mm and a refractive-index modulation $\Delta n_1(0)$ of the order of 10^{-3}. UA is the energy necessary to erase the hologram. For writing a hologram with refractive-index modulation 10^{-3} an energy of the same order of magnitude is necessary. We know from the previous section that U is of the order of 100 J/cm^2. For a hologram of 1 mm^2 and a detector with 10^4 image elements, giving a value of about 10^{-8} J for W_0, the number of possible read-outs is more than 10^7.

The energy required for writing a hologram that has to be read out once only can be found by equating the integrated efficiency with W_0. For a hologram with a surface area of 1 mm^2, an optical density $\alpha d = 1$ and with $W_0 = 10^{-8}$ J, we find that an initial phase modulation of about 10^{-3} is required. At a thickness d of 0.2 mm and a wavelength in the visible region, this gives an initial refractive-index modulation of the order of 10^{-7}. For writing this in, an exposure energy of 10^{-4} U is sufficient, i.e. about 0.1 mJ/mm^2. This exposure energy can be delivered by a laser with an output power of 100 mW in 1 ms over a surface area of 1 mm^2.

Consideration of the material parameters and the detection sensitivity shows that a wide variety of systems can be built. The writing sensitivity and the number of read-outs are complementary parameters in this respect: both cannot be made large at the same time.

The energy density necessary to write a hologram that can be read out a large number of times is comparable with the erasure energy U. If the number of read-outs is small, the energy density required for writing is correspondingly smaller.

Memory capacity

If a number of holograms N are written in one on top of the other, and the crystal is rotated between the exposures so that the holograms can be read out separately, each hologram is partly erased by each subsequent illumination. The hologram that was first written in is of course the one that suffers most. The number of superpositions that can be stored will now be calculated, for the minimum requirement that each hologram can be read out once only. It is assumed that the average exposure for each hologram is identical. From equations (3) and (12) the maximum refractive-index modulation is reached when the total exposure is equal to U. For a single grating the refractive-index modulation must then be equal to $m\Delta n_s/eN$. We must now insert this value in the expression for the efficiency. Given reasonable values of Δn_s and $N \gg 1$ the efficiency is now small. In this case it follows that instead of (13) we can write:

$$MN^2 = cUA/W_0, \qquad (14)$$

where c has the same significance as in (13) when $m\Delta n_s/e$ is substituted for $\Delta n_1(0)$. Equation (14) describes the connection between the number of stored holograms and the number of read-out cycles. The numerator on the right-hand side is the product of two constants that are characteristic of the material and the crystal surface area; the denominator is the sensitivity of the detector.

To calculate the capacity of the memory it is also necessary to know the number of image elements per hologram. The area of the hologram increases in proportion to the number of bits stored. The number of image elements of the detector is equal to the number

of bits stored. Taking L bits, we find that the area A of the hologram is equal to A_iL, where A_i is the minimum area per bit.

If we want to read each hologram at least once, the number of read-outs M must be at least equal to N. Instead of (14) we can now write:

$$N^3 < cUA_iL/W_0. \qquad (15)$$

Here W_0/L is the energy required for a single detector element, about 10^{-12} J [15]. Given $U = 100$ J/cm^2, $c = 0.15$ and $A_i = 10^{-4}$ mm^2 we find that the number of holograms N must be less than 500. (This applies to reversible information storage; in the case of thermally fixed holograms, of course, the recorded information is not affected by being read out.)

The number of holographic superpositions is limited not only by the diffraction efficiency of the holograms and by the sensitivity of the detector but also by the angular sensitivity upon read-out [3]. In the case of a crystal with optical density equal to 1 and phase modulation equal to π, the minimum rotation between two recordings is about 0.3°. In fact not many more than a few hundred holograms can be stored, even when the holograms are thermally fixed. With thermal fixing the number of holograms that can be stored in a single crystal is greater if a thicker crystal is used.

The memory capacity of the crystal is given by LN. We have seen above that N is limited to about 500; L is proportional to the surface area A. A sufficiently thick crystal with a surface area of 1 mm^2 has a capacity of 5×10^6 bits.

Reversible information storage

For this application it is useful if the erase energy is not unduly high, but a small value of U limits the number of read-outs and the number of holograms that can be stored in a crystal (eq. 12). For this reason we have stored the holograms *side by side* on small pieces of the crystal. The storage of holograms side by side has the advantage that they can be selectively erased by irradiating the part of the crystal that corresponds to the hologram. Fairly thin crystals, giving a lower angular and spectral selectivity, can also be used [3]. When the interference patterns are approximately perpendicular to the front face of the crystal, the reduced wavelength selectivity then permits read-out with a longer wavelength, so that the information will not be affected by the reading process.

A thin crystal has the advantage of allowing a high absorption coefficient. To make K_1 greater for writing with short-wavelength radiation the crystal is oxidized, and values up to 5×10^{-14} cm^2/ΩW have been reached. With an external field of 2×10^4 V/cm an illumination of 10 J/cm^2 is sufficient to achieve the maximum refractive-index modulation. For holograms where the number of bits L is 10^4 the minimum area of the hologram must be 1 mm^2 [3]. This implies an illumination of 10 mJ per hologram for an efficiency of 1% and cycle times between 20 and 100 ms when commercially available UV lasers are used. A memory of such a type is attractive because of the large number of bits that can be processed per unit time.

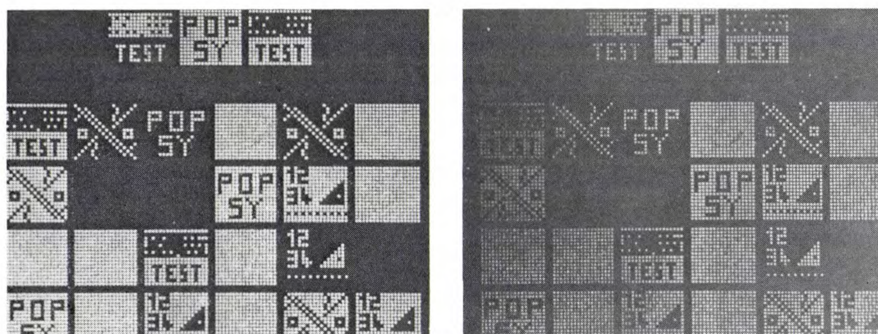

Fig. 9. Reconstruction of thermally fixed holograms recorded on a crystal of surface area 10 mm^2. *Left:* Reconstruction of the first recorded hologram. *Right:* Reconstruction of the hundredth hologram.

Permanent information storage

The thermal fixing of holograms makes it possible to store a large quantity of information permanently.

In the first experiments we took a black-and-white pattern with 10^4 bits that was stored in a hologram with an area of less than 1 mm^2 in a crystal 1 mm thick. *Fig. 8a* shows the direct image of the object, imaged through 1 mm^2 of the crystal. The image quality gives an indication of the optical quality of the crystal. The reconstruction of a thermally fixed hologram (fig. 8*b*) shows that the image quality and the signal-to-noise ratio deteriorate slightly as a consequence of fixing. The experiment demonstrates the limits of what can be achieved in the storage of a single hologram.

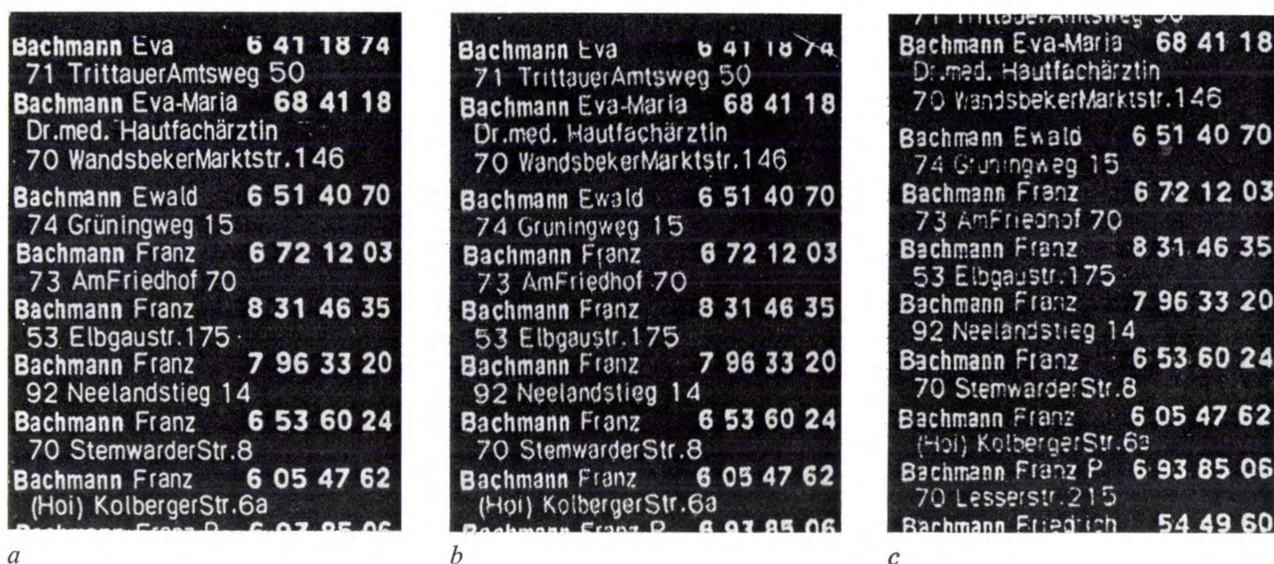

Fig. 10. Reconstruction of images with high information density. *a*) Object. *b*) Direct image seen through the crystal. *c*) Reconstruction of a thermally fixed hologram, recorded at 150 °C. Area of crystal 50 mm², thickness 5 mm.

In our second experiment we set out to determine the maximum number of holograms that can be stored in one crystal. Between the exposures the crystal was rotated by 0.3° after each hologram, with the angle between object beam and reference beam fixed. The recordings were made at a temperature of 150 °C. To increase the image quality we used a crystal with a surface area of 10 mm². *Fig. 9* shows the reconstruction of the first and the hundredth recorded hologram. The results indicate an attainable memory capacity of 10^6 bits/mm².

The results of our experiment with the storage of black-and-white patterns were compared with the results of experiments with the storage of text and images with an information content of about 10^6 bits per cm². For these experiments we used a crystal with a surface area of 50 mm². The image quality was now mainly determined by the optical quality of the crystal. *Fig. 10a* shows the object, fig. 10*b* the direct image recorded through a crystal 5 mm thick. Fig. 10*c* shows the reconstructed image of a thermally fixed hologram.

The conclusion to be drawn is that iron-doped lithium-niobate crystals, provided they are thermally fixed, are ideally suitable for the permanent storage of information.

Summary. In some ferroelectric and paraelectric substances, such as $LiNbO_3$, a space-charge field can be induced by spatially modulated illumination, resulting in three-dimensional modulation of the refractive index. This allows volume holograms to be recorded in such crystals. If the thickness of the crystal is large compared with the period in the hologram, read-out by means of the Bragg effect is only possible if the light is incident in a closely determined direction. By rotating the crystal through a small angle between each pair of exposures several hundred holograms can be recorded. In the iron-doped material studied and developed at the Philips Hamburg laboratories the change in the refractive index is the result of a photocurrent caused by charge transfer between divalent and trivalent iron ions; this current contains both a photovoltaic and a photoconduction component. The rate at which the refractive index changes depends on the photoconductivity. If the crystal is a poor conductor in the dark, a hologram can remain undegraded for several days at room temperature. The stored information can be erased by homogeneous illumination of the crystal. An existing hologram is to some extent erased when the next one is written in. The erasure energy is however 10^4 to 10^6 times greater than the minimum writing energy (1-100 J/cm² as against 0.1-10 mJ/cm²). The capacity of the $LiNbO_3$ is 1-5 Mbit/mm². When a hologram is recorded at an elevated temperature (150 °C), so that the ionic defects are displaced, and the crystal is then cooled down to room temperature, the charge distribution is 'frozen in'. The hologram cannot then be erased by subsequent irradiation, and can therefore be read out an almost unlimited number of times. These 'thermally fixed' holograms remain intact for several years.

Determination of zinc-diffusion profiles in gallium phosphide and gallium arsenophosphide with the aid of radioactive isotopes

Zinc is widely used in semiconductor technology as an acceptor in group III-V compounds. Important representatives of these compounds are GaP, GaAs and their mixed forms, which can be used as the starting material for the manufacture of light-emitting diodes (LEDs). For good efficiency light-emitting diodes should have the *P-N* junction situated close to the surface, which implies that the *P*-type dopant — in this case zinc — should not extend very far into the *N*-type material, preferably to a depth of no more than 5 to 10 μm. The zinc is diffused into the *N*-type material at high temperature.

Little is known about the profile of the zinc concentration from the surface to such a shallow *P-N* junction; until now it has only been possible to measure thick diffused layers (50 to 500 μm). The usual method is to lap or etch away the doped material in steps and to determine the zinc content of the successively removed material, with the thickness of the removed layer generally determined by weighing. Such methods are not suited for sufficiently accurate analysis of submicron layers 0.1 μm thick, which is necessary when the total layer thickness is 5 μm.

The principle of our new method is twofold. The gallium compounds are anodically oxidized giving a thin layer of uniform thickness, and this oxide layer is selectively dissolved by an etchant [1]. Accurate measurements of the oxidized material and the zinc content are carried out by means of a 'double tracer technique', using the radioactive nuclides ^{32}P and ^{65}Zn. The thickness of the layers removed by etching is determined from the measured quantity of ^{32}P, and the zinc present in the material is determined from the quantity of ^{65}Zn.

In principle this method can also be used for determining doping profiles in other semiconductor matreials. A condition is that the half-life of the nuclides used should not be too short and it must also be possible to discriminate one radiation from the other. From now on we shall only consider GaP.

The specimens for measurement are prepared from a GaP substrate on which an *N*-type epitaxial layer of GaP or $GaAs_{0.1}P_{0.9}$ has been formed. Radioactive ^{65}Zn is diffused into the epitaxial layer at 675 °C for 2.5 to 16 hours (^{65}Zn has a half-life of 244 days and a gamma-radiation energy of 1.115 MeV). The diffusion source is an alloy of 70 wt% Zn, doped with ^{65}Zn, and 30 wt% Ga (specific activity 4 GBq/g; 1 Bq = 1 becquerel ≙ 1 disintegration/second). The diffusion takes place in silica capsules with a volume of 10 cm³. At 675 °C the zinc pressure is about 2700 Pa (20 torr).

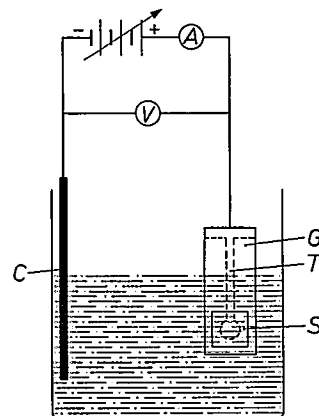

Fig. 1. Arrangement for the anodic oxidation of a specimen *S*. *G* glass plate. *T* conducting track. *C* platinum cathode.

After diffusion, the layer is removed from the edges and from the substrate side, and the specimen is then placed for 5 minutes in a neutron flux of about 5×10^{13} neutrons/cm²s. From the gallium radioactive ^{72}Ga is formed (half-life 14.1 hours) and from the phosphorus radioactive ^{32}P (half-life 14.3 days). The specific activity of the ^{65}Zn changes by less than 0.1% under this irradiation, a change that may be considered negligible. To permit the quantities of material to be calculated correctly, two reference specimens of undoped GaP are irradiated at the same time.

After a waiting period of about 280 hours (i.e. about 20 half-lives) the ^{72}Ga activity has decreased to a negligible level compared with the ^{32}P activity. The specimen to be measured can then be anodically oxidized. The method is illustrated in *fig. 1*. The specimen *S* is provided with a non-rectifying contact layer on the substrate side and is then attached to a glass plate *G* on which a conducting track *T* has been formed. The track *T* makes contact with the contact layer. To prevent *T* from coming into direct contact with the

[1] J. C. Verplanke and R. P. Tijburg, J. Electrochem. Soc. **124**, 802, 1977.

anodizing bath [2] it is coated with adhesive wax. The cathode C is of platinum. During oxidation the voltage V is held to a value such that the current is no more than a few mA per cm² of specimen surface. However, V must not exceed 150 V [3], otherwise the surface will be irregularly oxidized. After 3 minutes at this voltage a layer of GaP 0.10 µm thick is converted into oxide. (For $GaAs_{0.1}P_{0.9}$ the thickness is 0.14 µm.)

The oxide layer thus formed is next dissolved selectively, i.e. without attacking the underlayer, in hot phosphoric acid at a concentration of 10%.

Once a layer of the desired thickness has been removed, which may require repetition of the process, the anodizing and the etching baths are both analysed. This is done because ^{65}Zn and ^{32}P are dissolved in the anodizing bath as well as in the etching bath. Calculated in terms of total amounts of removed material, it is found that 5% of the ^{32}P and 70% of the ^{65}Zn are dissolved in the anodizing bath. The layer thickness is determined by measuring the ^{32}P activity by means of the Cerenkov radiation excited in the two baths because of the high velocity of the emitted β-particles. The intensity of the Cerenkov radiation is determined with a liquid scintillation spectrometer. From the ^{32}P activity, originating from the reference specimens, and the mass of the reference specimens, it is possible to calculate the conversion factor to be used for the determination of the quantity of dissolved specimen material. The quantity of radioactive zinc is determined from the emitted gamma-radiation (energy 1.115 MeV) by a Ge(Li) detector connected to a 2048-channel gamma spectrometer (1 keV per channel). This method of measurement is particularly suitable for ^{65}Zn concentrations that are so low that the fluctuations of background radiation become significant. For higher ^{65}Zn concentrations, measurements using an NaI(Tl) scintillation detector in the range from 1.00 to 1.25 MeV are more accurate because of the high absorption coefficient of the detector for gamma radiation. Conversion of the ^{65}Zn activity into the quantity of zinc is carried out in the same way as for the ^{32}P.

It has been found that the accuracy of the thickness measurement is about 3%; the accuracy of the zinc determination is 5% for quantities of zinc greater than 10^{-11} g. The results obtained are so good because none of the removed material escapes measurement. A good check on the accuracy of the thickness determination is to add the molar fractions of the group-III element and those of the group-V element in both baths and to compare the results; since the ratio of Ga to P in GaP is 1:1, this should also be found in the baths.

Figs. 2 and *3* show a zinc-diffusion profile (dashed line) measured by this method in GaP and in $GaAs_{0.1}P_{0.9}$. In the first 50 nm the zinc concentration

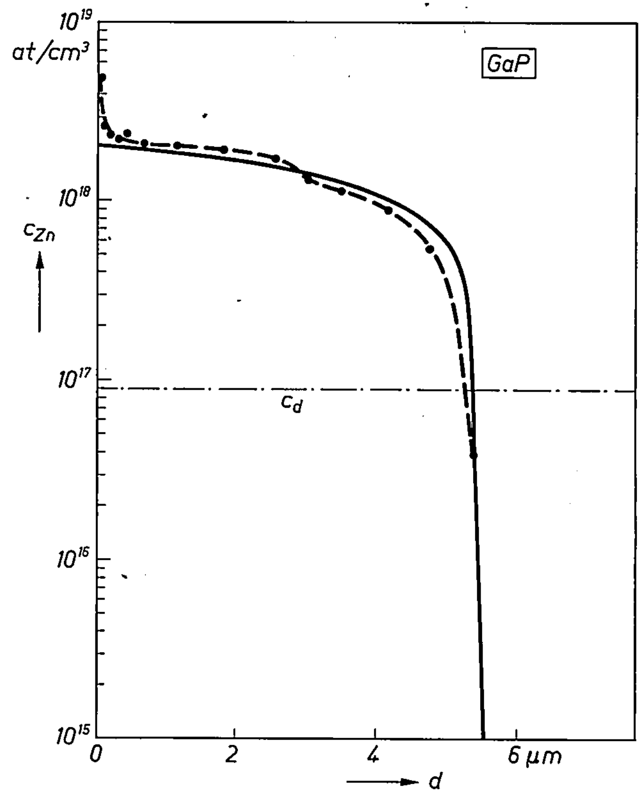

Fig. 2. The concentration c_{Zn} of zinc atoms diffused in GaP (dashed line) as a function of the depth d under the surface. The donor concentration c_d in the material is 9×10^{16} at/cm³; the P-N junction thus lies at a depth of about 5.5 µm. The solid line is a calculated doping profile.

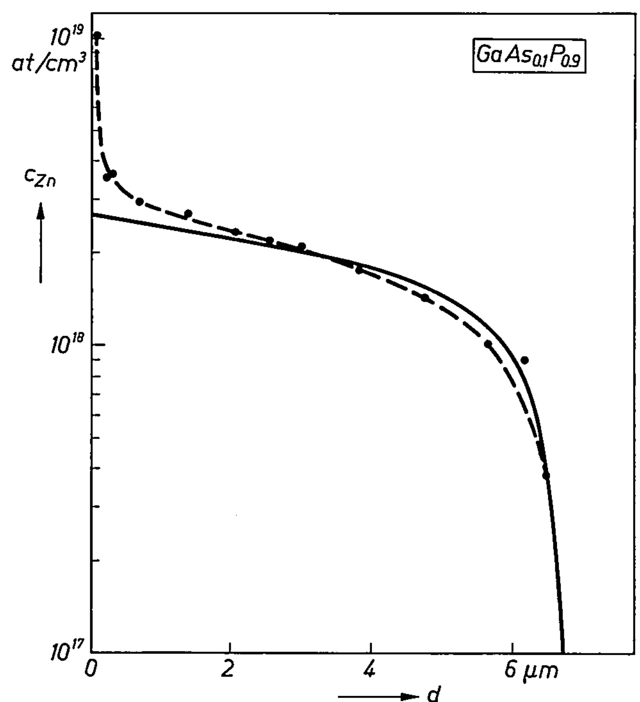

Fig. 3. As in fig. 2, but now for $GaAs_{0.1}P_{0.9}$. The P-N junction here lies at a depth of about 7 µm.

is very much higher than elsewhere, an effect which has not yet been fully explained. At a depth of about 3 μm there is a kink in the curve in fig. 2; this kink is not attributable to inaccuracy in the measurement. It can be explained qualitatively as due to the diffusion of gallium vacancies. The curve in fig. 3 also has a slight kink. The *P-N* junction in fig. 2 lies at a depth of about 5.5 μm (the donor concentration c_d is 9×10^{16} at/cm^3) and in fig. 3, where $c_d = 1.8 \times 10^{16}$ at/cm^3 (outside the figure), it lies at a depth of 7 μm. The solid line represents a calculated doping profile, based on the theory that the zinc-diffusion coefficient is not constant but increases with the square of the zinc concentration [4]. This is connected with the fact that a zinc atom may arrive at a substitutional or an an interstitial lattice site where it may act as an acceptor or a donor. It follows from the curves that the surface diffusion coefficient D_0 is 4.3×10^{-12} cm^2/s for GaP and 6.5×10^{-12} cm^2/s for $GaAs_{0.1}P_{0.9}$. Normalized to a concentration c_{Zn} of 10^{18} at/cm^3 at the surface this gives a diffusion coefficient of 1.1×10^{-12} cm^2/s and 8.9×10^{-13} cm^2/s respectively. The curves also confirm the interstitial nature of the diffusion.

From the diffusion profile in fig. 2 we calculated a concentration gradient of 1.1×10^{22} at/cm^4 near the *P-N* junction [5]. This value agrees well with the value of $(1.3 \pm 0.3) \times 10^{22}$ at/cm^4 determined by measuring the capacitance as a function of the voltage across the *P-N* junction.

J. C. Verplanke
R. P. Tijburg

[2] The composition of the anodizing bath is described in H. Hasegawa, K. E. Forward and H. Hartnagel, Electronics Letters **11**, 53, 1975.
[3] R. A. Logan, B. Schwartz and W. J. Sundburg, J. Electrochem. Soc. **120**, 1385, 1973.
[4] L. R. Weisberg and J. Blanc, Phys. Rev. **131**, 1548, 1963.
[5] C. van Opdorp, Solid-State Electronics **11**, 397, 1968.

Ing. J. C. Verplanke and R. P. Tijburg are with Philips Research Laboratories, Eindhoven.

Philips tech. Rev. 37, 124-130, 1977, No. 5/6

A channel-plate image intensifier for hard X-rays

V. Chalmeton

In industrial radiography the objects usually give greater absorption than in medical X-ray diagnostics. For this reason it is often necessary to use higher supply voltages for the X-ray tube in industrial applications than in medical applications. A higher tube voltage has two advantages here; the X-rays generated have a shorter wavelength and thus a greater penetrating power, and a higher radiation intensity is generated for the same dissipated power. To satisfy the requirements for radiation protection at the higher voltages the X-ray tube and the object under investigation are placed in a cage that has to be locked during irradiation and whose walls are lined with lead. If the information is not to be recorded on X-ray film — which does not give immediate results and uses raw materials such as silver, which is becoming extremely expensive — then the information must be obtained in a suitable form for display outside the cage on a closed-circuit television system. An X-ray image intensifier has been designed for this purpose and optimized for a tube voltage of 400 kV, a voltage that is used in industrial radiography for a number of special applications (e.g. in pipelines and spacecraft).

An X-ray image intensifier for use in some types of industrial radiography has to be optimized to operate at a tube voltage of about 400 kV, a supply voltage now available for industrial radiography. The intensification of the brightness (luminance) must also be variable over a wide range to allow for marked variations in the thickness of an object, and hence in its absorption. It is also desirable that the image intensifier should cause as little optical distortion as possible. Since these requirements differ somewhat from those imposed on an image intensifier for medical X-ray diagnosis, a medical X-ray intensifier [1], which is designed to operate at tube voltages between 100 and 150 kV, is not suitable for all industrial applications.

In the X-ray spectrum emitted at a tube voltage of 400 kV the average energy of the X-ray quanta is about 200 keV. As can be seen in *fig. 1*, the intensity reduction that the primary X-ray beam undergoes in this case in passing through an object is largely due to Compton scattering, especially in materials with a low atomic number. The scattered radiation produces a continuous background in the X-ray image and hence reduces the contrast. Since, however, the Compton-scattered quanta have less energy than the primary quanta, it is possible in principle to reduce the background by means of selective detection of the quanta of primary energy. We have in fact accomplished this by using as the input screen of the image intensifier a metal foil of the kind long used for certain applications as an intensifying screen for X-ray film [2].

Dr V. Chalmeton, Ing. E.S.E., is with the Laboratoires d'Electronique et de Physique Appliquée (LEP), Limeil-Brévannes (Val-de-Marne), France.

A metal foil as the input screen for an image intensifier

The operation of a metal foil as the input screen of an image intensifier for relatively high quantum energies is partly based on Compton scattering, partly on photoelectron emission. These two effects convert the intensity distribution in the X-ray beam into a distribution of the intensity of the electrons emitted by the foil. The brightness of the resultant electron image can then be intensified electrically. The difference in energy between the primary and the Compton-scattered quantum is converted into kinetic energy of an electron. If the scattering medium is a thin foil, the electron may leave the foil at the other side (*fig. 2*). Absorption of X-rays in a metal foil also gives rise to photoelectric effects. Photoelectron energy differs from the X-ray quantum energy by an amount equivalent to the ionization energy for an electron in the K shell of the atoms of the foil. The extent to which both effects contribute to the electron yield depends on the X-ray quantum energy and the atomic number of the foil metal. At an X-ray-tube voltage of 400 kV Compton-scattered elec-

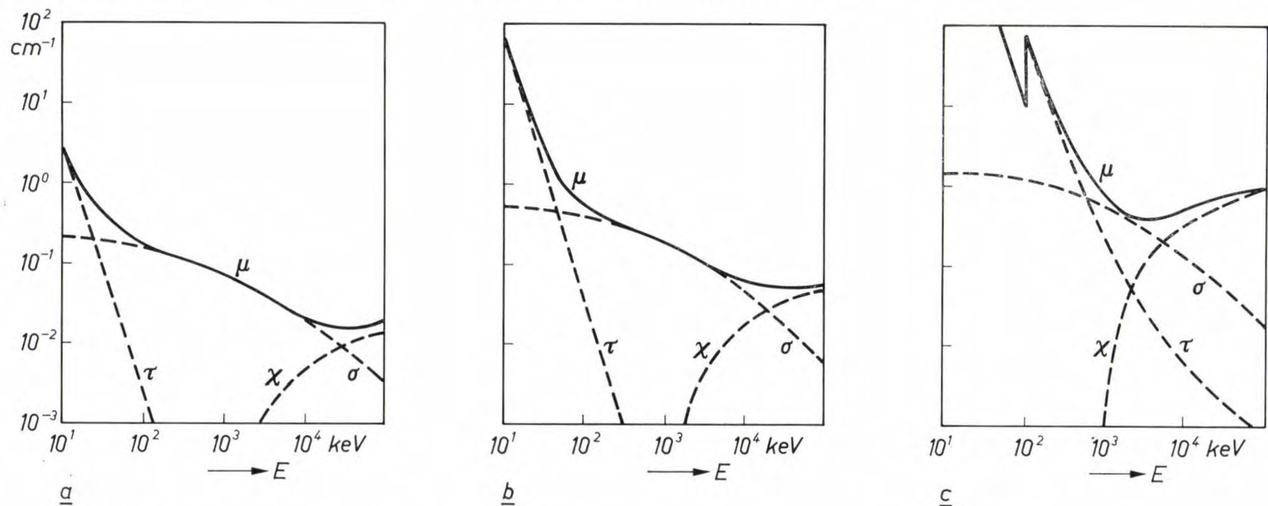

Fig. 1. The solid lines give the total attenuation coefficient μ as a function of the X-ray quantum energy E *a*) for water, *b*) for aluminium and *c*) for lead. The dashed lines give the proportions of Compton scattering (σ), absorption (τ) and pair formation (χ) in the total attenuation.

trons and photoelectrons have comparable energies (about 100 keV).

In this conversion of an X-ray image into an electron image there are two reasons why the high-energy quanta have the advantage over the quanta of lower energy. To begin with, the absorption coefficient for high-energy quanta is lower than that for quanta of lower energy, which means that beyond a certain depth in the foil only high-energy quanta will be present and produce electrons. Secondly, the higher the energy of a primary quantum the greater will be the energy of the electron released by the scattering, so that it will have a greater range inside the foil. Electrons resulting from the scattering of the higher-energy quanta will therefore have a higher probability of leaving the foil. With a foil of an appropriate thickness, both steps in the conversion of the X-ray image into an electron image will give an optimum discrimination between quanta of the primary X-ray beam, which carry the information about the object, and the quanta of less energy, which result from scattering in the object, and yield no information but only a blurring background.

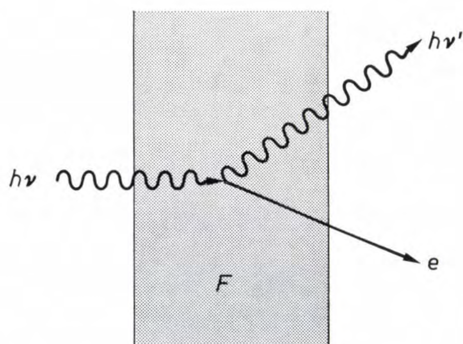

Fig. 2. Compton scattering of an X-ray quantum $h\nu$ in a foil F. The scattered quantum $h\nu'$ has lower energy than $h\nu$. The energy difference between the two quanta is transferred to the electron e. This electron may leave the foil, depending on the position of the scattering and the energy of the electron.

The optimum thickness of a metal foil used as an input element depends on the depth of penetration of the X-ray quanta and the 'escape depth' for the electrons. The optimum thickness of a metal foil will be less than that of a fluorescent screen used on the input side of an image intensifier for medical applications. For metal foils used as an intensifying screen in combination with an X-ray film the literature [3] mentions optimum thicknesses of 30-50 μm, whereas the caesium-iodide fluorescent screens nowadays used are about 200 μm thick. The smaller thickness of the metal foil permits better resolution of details in the X-ray image. This smaller thickness also results in smaller detection efficiency; but this is of less importance in industrial radiography where the X-ray dose that the object may receive is limited only by economic considerations.

The optimum foil thickness

The optimum foil thickness is a compromise between the absorption of X-radiation (and hence the production of electrons) in the first part of the foil thickness, and the absorption of the electrons in the remaining part of the foil. Calculations of the optimum thickness only give very approximate results, since a rather simplified model has to be used for the scattering process.

[1] W. Kühl, J. Soc. Photo-Opt. Instr. Engrs **56**, 80, 1975.
W. Kühl, Medicamundi **14**, 132, 1969.
W. Kühl and J. E. Schrijvers, Acta Electronica **20**, 41, 1977.

[2] R. C. McMaster (ed.), Nondestructive testing handbook, Ronald Press, New York 1959, page **16**.24.
R. Halmshaw (ed.), Physics of industrial radiology, Heywood, London 1966, page 12.
H. E. Seemann, J. appl. Phys. **8**, 836, 1937.

[3] See for example the books [2] by McMaster (pp. **15**.29 and **16**.24) and Halmshaw (p. 168).

Depending on the model used, and given an X-ray-tube voltage of 400 kV, the optimum thickness found is 10-15 μm for gold foil [4] and 25 μm for lead foil [5]. In practice it is necessary to bear in mind for the optimization process that the channel plate itself is sensitive to X-radiation [6] and that the electron multiplication in the channels depends on the energy of the incident electrons [7]. The optimum thickness must consequently be determined experimentally.

We therefore verified our calculations by carrying out measurements on a large number of combinations of metal foil and channel plate. Scaled-down experimental image intensifiers were made and foils of different metals used, a number of foils of different thickness being mounted in each tube. The results, which agreed reasonably well with the calculations, are listed in *Table I*. The calculated conversion efficiency in a gold foil as a function of foil thickness is given in *fig. 3*. Since the optimum is fairly broad, it is possible to use commercially available foils of standard thickness. Partly because of the mechanical properties of the foils, a gold foil 12.5 μm thick and a tantalum foil 20 μm thick were good choices.

We also determined the optimum foil thickness for a tube voltage of 150 kV. In this case it was found that a tantalum foil 7.5 μm thick should be used.

Table I. The optimum thickness of foils of various metals, determined experimentally, for the conversion of an X-ray image into an electron image at an X-ray-tube voltage of 400 kV and the quantum efficiency of the conversion.

Metal	Optimum thickness	Quantum efficiency
Tantalum	17 μm	2.5%
Tungsten	25	1.7
Gold	12.5	2.5
Lead	17.5	2.0

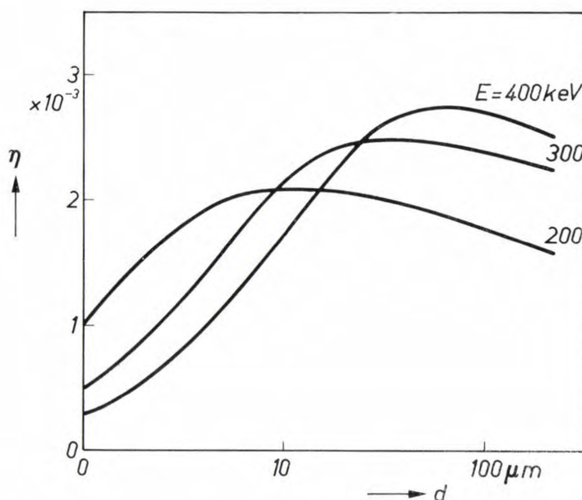

Fig. 3. Conversion efficiency η of a gold foil calculated as a function of the foil thickness d for a number of quantum energies E.

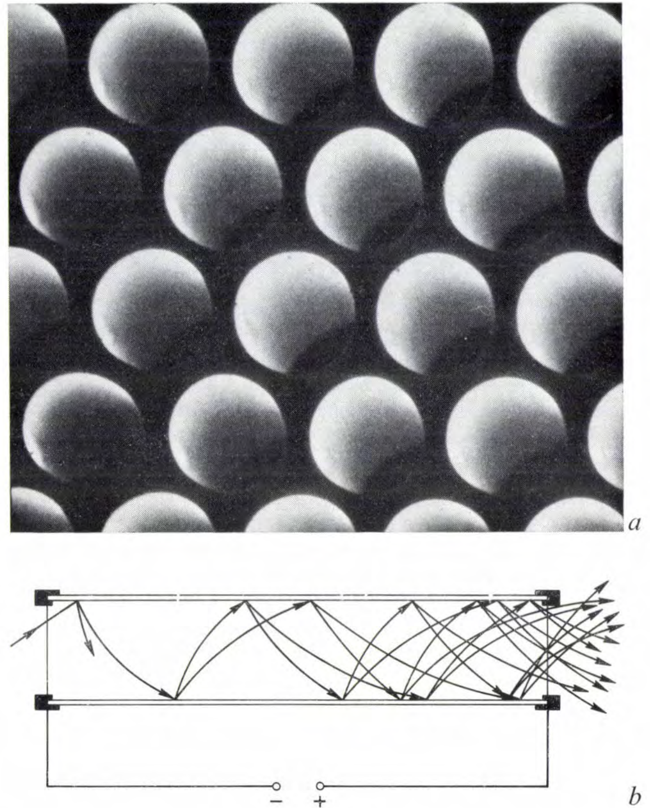

Fig. 4. *a*) Scanning electron photomicrograph of a microchannel plate. *b*) Principle of an electron-multiplier channel. A voltage of about 1 kV is applied across a capillary of semiconducting glass. An electron that strikes the inside wall of the capillary near the negative end produces secondary-electron emission. The secondary electrons are accelerated by the potential gradient in the capillary, strike the wall in their turn and likewise produce secondary emission. If the potential gradient along the wall is steep enough, the electrons reach a velocity such that the secondary-emission coefficient becomes greater than unity, so that for every electron entering at one end a large number leave the capillary at the other.

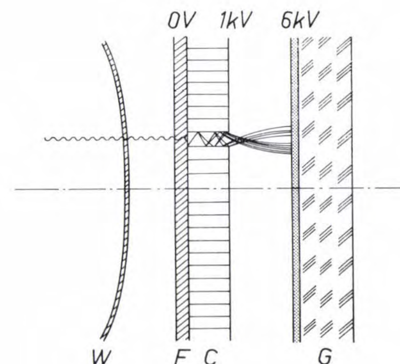

Fig. 5. Cross-section of an X-ray image intensifier with metal conversion foil and a channel plate for electron-intensity amplification. *W* titanium foil (thickness 0.2 mm) which forms the wall of the vacuum chamber at the input side. *F* conversion foil of an appropriate metal. *C* channel plate. *G* glass plate with fluorescent layer, which forms the output window of the image intensifier. The electrical potential differences between the conversion foil and the various other surfaces in the image intensifier are indicated.

Construction of the image intensifier

The average energy of the electrons emitted through the foil is about 100 keV, with considerable spread in the energy. For this reason the electrostatic lenses used in medical X-ray image intensifiers [1] are not suitable for the further processing of the electron image. A very suitable device for this is the microchannel plate, as earlier used in an image intensifier for neutron radiography [8]. The channel plate (*fig. 4*) receives the relatively fast electrons from the foil, multiplies them and produces an electron image of low-energy electrons [9]. To prevent loss of resolution in the transition between the two elements, the foil is mounted in direct contact with the channel plate.

The electrons leaving the channel plate arrive at a fluorescent screen, causing the electron image to be converted into a visible image. A potential difference of about 5 kV between channel plate and screen gives a faithful image and ensures that the electrons strike the screen with sufficient energy. *Fig. 5* gives a cross-section of our image intensifier.

All the components of the image intensifier are contained inside a vacuum chamber. The flat glass plate carrying the fluorescent screen forms the output side of the chamber. At the input side the chamber is closed by a titanium window with a thickness of 0.2 mm designed to minimize the X-ray absorption. Because of the difficulty of completely outgassing the channel plate, a getter-ion pump is included in the assembly to remove the residual gas, which is mainly released at high X-ray intensities. *Fig. 6* gives a picture of the X-ray image intensifier.

The channel plate has a useful area of 120 mm in diameter. The diameter of the individual channels is 40 μm and their length/diameter ratio is 60. With a voltage of 1300 V across the channel plate the amplification at a tube voltage of 400 kV is about 1700 (cd/m^2)/(R/s). This amplification can be varied over a wide range by varying the voltage across the channel plate. The quantum efficiency is then about 2.5%.

Fig. 6. An X-ray image intensifier with metal conversion foil and electron-intensity amplification by means of a channel plate. The photograph shows the glass output window with the fluorescent layer. The getter-ion pump, which remains permanently connected, removes the residual gases released from the channel plate during operation. In this construction there is no room to incorporate a conventional absorption getter of sufficiently large capacity.

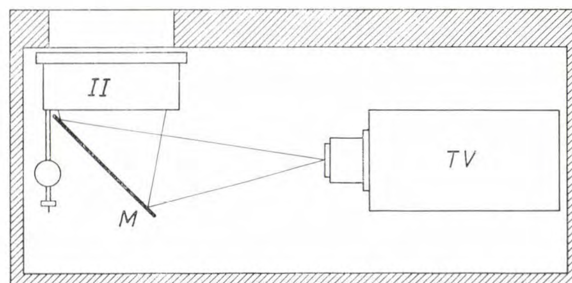

Fig. 7. Construction of our X-ray camera, which forms the input element of the image-transfer system. *II* image intensifier. *TV* television camera. *M* mirror. The elements are enclosed in an aluminium box lined with lead: 20 mm thick at the front, 5 mm thick on the other sides.

The image-transfer system

To enable the output screen of the image intensifier to be viewed outside the shielded cage, we use an 875-line television system. A reduced image of the output screen of the image intensifier, which has the same diameter as the input screen, is produced on the input window of the television camera tube. The camera is protected against direct X-radiation by means of the arrangement illustrated in *fig. 7*. The television camera is incorporated in a lead-lined box, and the image intensifier is mounted in front of a circular aperture in a wall of the box. The camera sees the output screen of

[4] V. Chalmeton, Acta Electronica **20**, 53, 1977.
[5] U. Shimoni, B. Sheinfux, A. Seidman, J. Grinberg and Z. Avrahami, Nucl. Instr. Meth. **117**, 599, 1974.
[6] J. Adams and I. C. P. Millar, Acta Electronica **14**, 237, 1971.
[7] Acta Electronica **14**, numbers 1 and 2 1971; and **16**, No. 1, 1973.
[8] V. Chalmeton, 7th Int. Conf. on Nondestructive testing, Warsaw 1973, Vol. III, B-42.
V. Chalmeton, Acta Electronica **16**, 73, 1973.
[9] A. J. Guest, Acta Electronica **14**, 79, 1971.
J. Adams and B. W. Manley, Philips tech. Rev. **28**, 156, 1967.

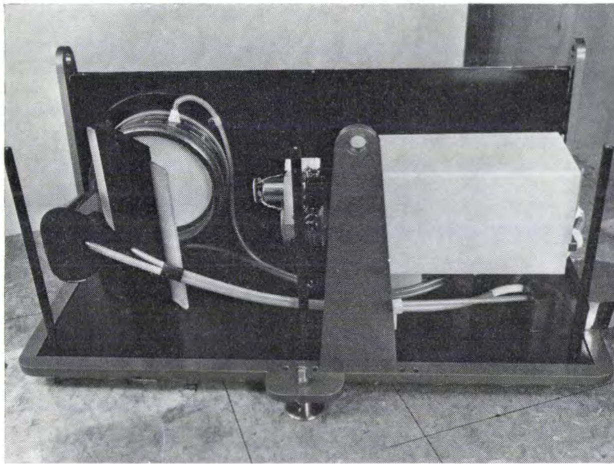

Fig. 8. Interior of the X-ray camera.

the image intensifier via a plane mirror, in such a way that both the imaging lens and the camera tube remain outside the direct X-ray beam. *Fig. 8* shows a photograph of the X-ray camera with the side walls removed.

A silicon vidicon camera tube was used to obtain sufficient sensitivity for the very small quantity of light that reaches the camera tube in this way when the object is highly absorbent. Because of the high sensitivity of the camera tube the shielding enclosure has to be made light-tight to prevent stray light from reaching the camera tube.

The radiant flux delivered by the X-ray tube we used at a tube voltage of 400 kV is about 0.2 R/s at one metre from the focus. Assuming an attenuation of 200 times in the object, we find that the luminance of the output screen is 1.7 cd/m^2. With an optical coupling system of numerical aperture 0.95, the luminous flux at the input window of a camera tube gives an illuminance of about 1 lux at optimum coupling. Only a silicon vidicon is sensitive enough for such low light intensities.

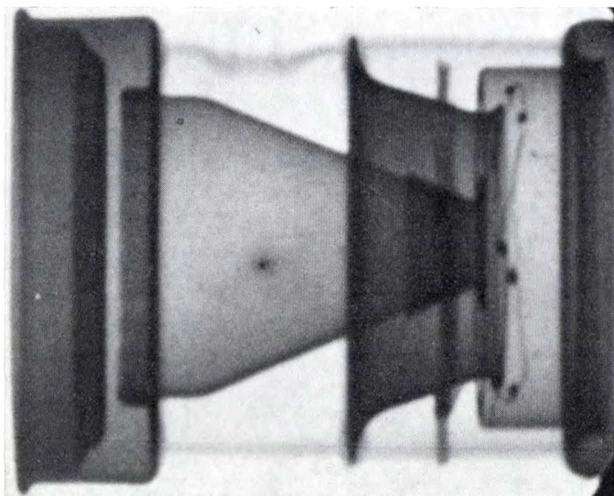

Fig. 9. X-ray picture of an electron-optical image-intensifier tube, obtained with the channel-plate intensifier described here.

System performance

Fig. 9 illustrates what can be achieved with the image intensifier described here. To have a more objective yardstick of performance, however, we have used a number of test objects [10] designed and built at SNPE [11].

One of the applications for which we designed the image intensifier was for X-ray screening of blocks of solid rocket fuel. These blocks have to be examined for the presence of small cavities and cracks. Test objects of this rocket fuel were therefore made, both with cavities of different sizes and with cracks of different width (*fig. 10*). Similar test objects were also made of aluminium. Since narrow fissures in relatively thick material are only observable if they run parallel to the X-ray beam, we arranged for all the test objects to rotate in the beam.

Figs. 11 and *12* show the results of measurements of the perceptibility of cavities and cracks in test objects both of rocket fuel and of aluminium at an X-ray-tube voltage of 400 kV. It is evident that it is useful to rotate the object to observe cavities as well. The cavities that are only just perceptible in a rotating object are only half as deep as in a stationary object.

To assess the image intensifier for an X-ray-tube voltage of 150 kV we used 'wire penetrameters', which are widely used for this purpose. A stationary test object is used that consists of a block of material with

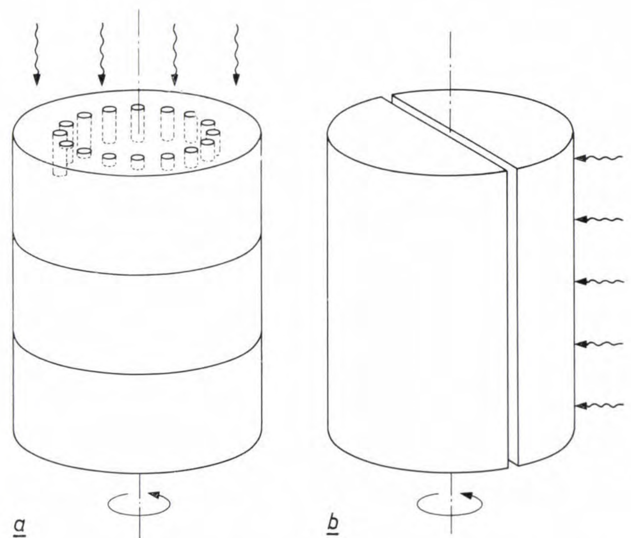

Fig. 10. Test objects for evaluating the performance of the image-transfer system. *a*) A disc of material 38 mm thick in which 16 holes have been drilled with a diameter of 6 mm and with depths increasing from 0.4 to 11.6 mm. A number of solid discs 50 mm thick can be added to increase the total irradiated thickness. The assembly can be rotated in the X-ray beam. The axis of rotation and the direction of radiation are indicated. *b*) A divided cylinder; the width of the gap between the two halves is adjustable. This cylinder can also be rotated in the X-ray beam. The axis of rotation and the direction of radiation are again indicated. Extra plates of material can be added in the X-ray beam to increase the total irradiated thickness.

wires of different diameter fixed to it. The effective thickness of the block is varied by adding extra plates to it, and measurements are made to determine which wire is only just visible at each thickness. The diameter of this wire is then expressed as a percentage of the plate thickness. *Fig. 13* gives the results of these measurements. The wire diameter only just perceptible is plotted as a function of the plate thickness, both for aluminium and for iron. During the measurements the wires were placed one by one on the plate in arbitrary positions unknown to the observer.

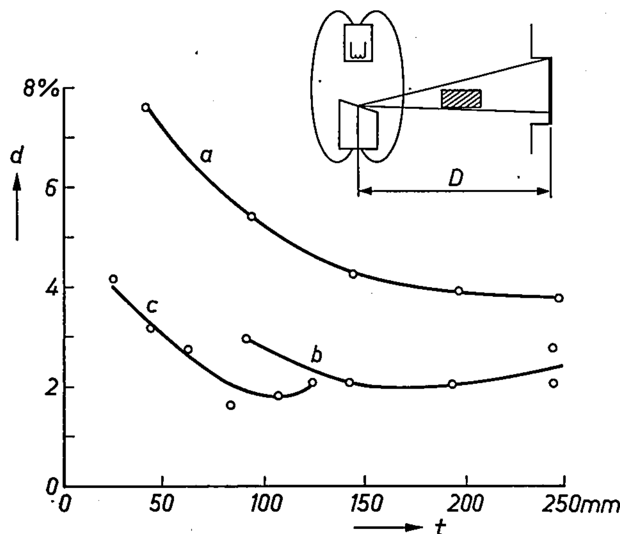

Fig. 11. The smallest observable cavity depth d in the test object in fig. 10a, expressed as a percentage of the total irradiated object thickness t as a function of this thickness. The supply voltage for the X-ray tube was 400 kV. Curve a was measured for a stationary test object of rocket fuel; the distance D between the focus of the X-ray tube and the input window of the image intensifier was 1 m, and the test object was locted midway between tube and image intensifier. Curve b was measured on a rotating test object of rocket fuel; D was again 1 m. Curve c was measured on a test object of aluminium; the distance here D was 70 cm.

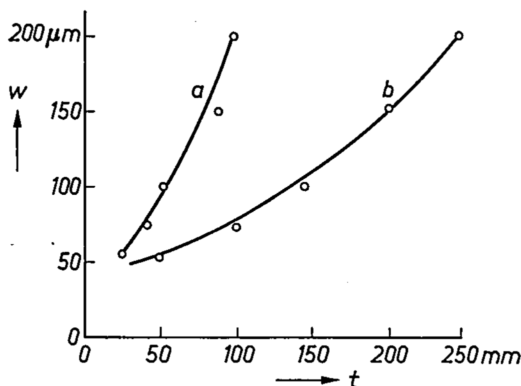

Fig. 12. The gap width w, only just observable, as a function of the total irradiated thickness t, measured with a test object as in fig. 10b at a supply voltage of 400 kV for the X-ray tube. Curve a was measured with an aluminium cylinder of 15 mm diameter, curve b with a cylinder of rocket fuel of 25 mm diameter. The distance from the focus of the X-ray tube to the input window of the image intensifier was 1 m in both cases.

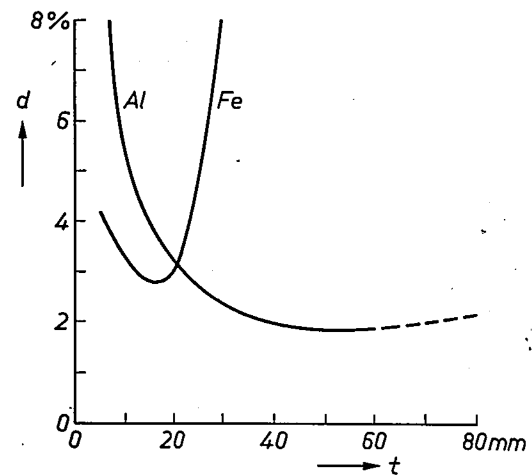

Fig. 13. The wire thickness d, only just observable for a total irradiated thickness t, expressed as a percentage of the thickness t, as a function of t and measured for both iron (Fe) and aluminium (Al). The measurements were carried out at an X-ray-tube voltage of 150 kV and with a distance of 80 cm between the tube focus and the input window of the image intensifier.

The performance of the image intensifier was also studied by measuring the modulation transfer. This was done with the aid of a grid consisting of lead strips 50 µm thick of varying widths and distance between them (pitch). Where the width of the strips and the pitch was such that there were 2.9 line pairs per mm, the intensity modulation in the picture on the television monitor had fallen to 5% of the maximum value.

Estimate of the effect of scattered radiation

When the X-ray beam is collimated a smaller part of the object is irradiated, which means that there is less material that can scatter the radiation. As a result any background in the picture due to scattered radiation will decrease in intensity and there will be an improvement in the perceptibility of details in the rest of the picture. An evaluation of the effect of scattered radiation can be obtained by investigating the extent to which collimating the X-ray beam affects the perceptibility of details.

Fig. 14 shows the results of wire-penetrameter measurements carried out with a collimated beam on the image intensifier for an X-ray-tube voltage of 150 kV. Collimation is seen to have hardly any effect on the quality of the picture. The slight reduction in the perceptibility of the wires when the beam aperture is very small is attributable to the very small dimensions of the area observed; because of this the full length of the wires does not always fall within this area and the intensity fluctuations are large.

[10] V. Chalmeton, C. Patanchon and C. Mesnage, 8th World Conf. on Nondestructive testing, Cannes 1976, 3E 13.
C. Patanchon and C. Mesnage, Acta Electronica **20**, 65, 1977.

[11] SNPE: Société Nationale des Poudres et Explosifs, 33160 Saint-Médard-en-Jalles, France.

At an X-ray-tube voltage of 400 kV, collimating the X-ray beam was found to have just as little effect on detail perceptibility.

It may be concluded from these observations that the sensitivity to scattered radiation is so small with this image intensifier that scattered radiation has no noticeable effect on image quality.

Finally, it should be noted that the image intensifiers described here can be used over a wide range of X-ray intensities. Apart from the control facilities in the closed-circuit television system, the image intensifier protects itself against overloading. At high radiation intensities the channel plate takes more current, with the result that the voltage across the plate falls and so does the electron multiplication in the channels.

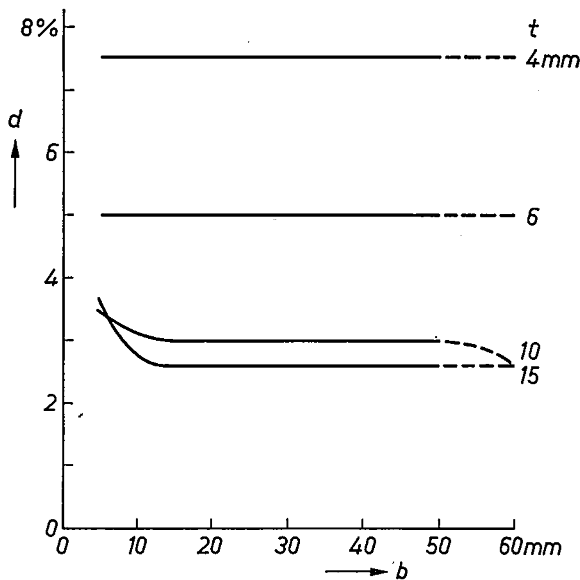

Fig. 14. The same measurements as in fig. 12, but now carried out only on iron, with the X-ray beam collimated to a diameter *b* just in front of the object. The almost horizontal nature of the curves indicates the very low sensitivity of the image intensifier to scattered radiation.

Life tests on an experimental tube have shown that the characteristics remained unchanged after 600 hours of continuous operation at maximum load with 3 cd/m² for 10 nA/cm² at the screen; after 1000 hours the luminance had decreased by a factor of two owing to ageing of the output screen.

For some possible applications it may be desirable to increase the resolution and the intensification factor still further. The intensification can be increased by using a channel plate with longer channels or bent channels to increase the electron multiplication. Extensive measurements have shown that improvement in resolution is most likely to be found in the closed-circuit television system, since the limiting resolution of the intensifier itself is significantly better than that of the complete system.

Summary. The X-ray image in the image intensifier described here is converted into an electron image with the aid of a thin metal foil. The electron image is intensified by means of a channel plate and then converted into a visible image by a phosphor screen. The electrons that form the electron image originate from Compton scattering of the X-ray quanta at the atoms in the metal foil and from photoelectric absorption in the foil. The foil thickness is chosen in such a way that the high energy quanta in the X-ray beam are preferentially converted. The radiation due to Compton scattering in the object, which causes a blurring continuous blackground in the X-ray image, is thus largely suppressed. This suppression of the background due to scattered radiation is particularly important in industrial radiography for the examination of objects containing mainly elements with a low atomic number, and for examinations of thick objects for which a high X-ray-tube voltage is necessary to obtain a sufficiently high radiation intensity behind the object. The sensitivity of the radiographic system at 400 kV corresponds to a minimum flux of 1 mR/s at the input window of the converter for a correct image. The resolution of the system is about 2.9 line pairs/mm and is limited mainly by the television system.

Liquid crystals for numerical displays

W. H. de Jeu and J. van der Veen

The atoms of a crystal form a regular lattice in which they take up fixed positions in relation to one another. The name 'liquid crystal' is therefore a contradiction in terms. Nevertheless it has remained in use since it was first introduced in 1900 by Otto Lehmann to describe organic compounds in states in which, while possessing the mobility of a liquid, they show more resemblance to crystals than to ordinary liquids in the fascinating colour and other optical effects they exhibit under the polarizing microscope. These are states, or phases, that lie on the temperature scale between the solid and the isotropic liquid state of the compound. In the sixties these phases aroused growing interest when it become apparent that there were useful applications for liquid crystals, for example for digital displays in pocket calculators and watches. The article below is mainly concerned with the relations that exist between the properties of the liquid crystal and its molecular structure, and with the consequences of these relations on the selection and the synthesis of the organic compounds for such applications.

Introduction

Liquid crystals combine the mobility of a liquid with an anisotropy in their optical, electrical and other properties that is otherwise only found in crystals. Because of this combination of properties striking optical effects can easily be produced in thin layers of these substances; for example, by applying a potential of a few volts, they can be switched from transparent to opaque. Effects of this type are nowadays used for numerical displays in pocket calculators and digital watches. In these applications the liquid crystal modulates incident light. They therefore use hardly any power, which often gives them a significant advantage over indicators that emit light themselves (miniature electric lamps, neon tubes, LEDs). In another respect the two kinds of indicator supplement one another. Miniature lamps and tubes can be seen in dark spaces but not so well in sunlight, whereas the opposite applies to liquid-crystal displays.

Scientific research on liquid crystals dates from the end of the previous century. Prominent among the many workers in this field were Otto Lehmann (1855-1922), the pioneer; G. Friedel (1865-1933), who made a classification which is still useful today, and Daniel Vorländer (1867-1941), under whose supervision numerous organic compounds with a liquid-crystalline phase were synthesized. Research on these compounds was greatly intensified in the 1960s because of the emergence of possible applications, and again many new compounds were synthesized. In fact the new interest was in compounds with a strongly anisotropic dielectric constant in the liquid-crystalline phase, and with this phase occurring in a convenient temperature range. The classic liquid crystals cannot be used for most applications because their temperature range is far above room temperature.

In this article we shall pay particular attention to the relationship between the molecular structure and the temperature range of the liquid-crystalline phase as well as the dielectic properties, and we shall show how this knowledge can enable us to synthesize compounds suitable for practical applications. To enable us to formulate the practical requirements, we shall first look more closely at liquid crystals in general, at their anisotropic properties, and at the effects that are used in practice [1].

Since the name 'liquid crystal' is really a contradiction in terms, liquid-crystalline phases are sometimes referred to as 'mesomorphic phases' or 'mesophases'. Apart from this, the nomenclature in this field is often confusing, partly because the term 'liquid crystal' is sometimes understood to refer to the compound even when it is not in the liquid-crystalline state. Following

Dr Ir W. H. de Jeu and Dr J. van der Veen are with Philips Research Laboratories, Eindhoven.

[1] A general treatment of liquid crystals is given in E. B. Priestley, P. J. Wojtowicz and P. Sheng (eds), Introduction to liquid crystals, Plenum Press, New York 1974/75, and P. G. de Gennes, The physics of liquid crystals, Clarendon Press, Oxford 1974.

the example of many publications, we shall refer to these compounds as 'mesogenic compounds'. We shall take a liquid crystal to be a mesogenic compound in the liquid-crystalline phase.

Nature, classification and properties of liquid crystals

Nature and classification

The liquid-crystalline phase lies on the temperature scale between the crystalline-solid and isotropic-liquid phases. The transitions, at the melting point T_m and the 'clearing point' T_c, are both of the first order, which appears from the existence of a latent heat and a step in the density. At T_c, however, these quantities are much smaller than at T_m. The transition at T_c is clearly visible with the naked eye: the initially opaque liquid becomes clear.

The molecules of mesogenic compounds are always elongated; this is illustrated in *fig. 1* with three familiar examples [2]. The liquid-crystalline phase is characterized by long-range order *in the orientation but not in the position* of the molecules. This is different from the solid phase, in which both forms of order exist, or the isotropic liquid phase in which neither exists. Owing to the thermal motion of the molecules, the orientational order is never perfect. The 'order parameter' S — which would be 1 for perfect order and 0 for complete disorder — falls in practice from at the most 0.8 at T_m to a value between 0.3 and 0.5 at T_c.

A distinction is made between nematic, cholesteric and smectic liquid-crystalline phases (*fig. 2*). These can best be characterized by considering a 'liquid single crystal', i.e. a region over which the long-range order is ideal (apart from the thermal fluctuations).

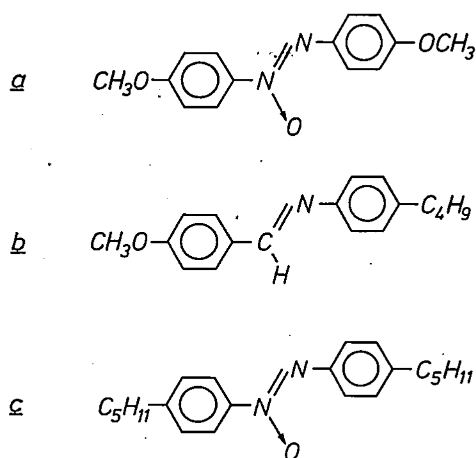

Fig. 1. The molecular structure of three mesogenic compounds.
a) PAA (*p*-azoxyanisole); temperature range 116-135 °C.
b) MBBA (N-(*p*-methoxybenzylidene)-*p*-butylaniline); temperature range 22-47 °C.
c) PENTAB (*p,p'*-dipentylazoxybenzene); temperature range 24-67.5 °C.
PAA is one of the classic mesogenic compounds; the other two have been synthesized since 1960. Characteristic features are the two (or more) aromatic rings, connected by a bridging group and the presence of end substituents, giving the elongated shape [2].

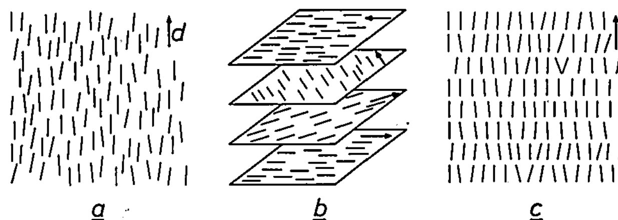

Fig. 2. Molecules, represented by dashes, in a nematic (*a*), in a cholesteric (*b*) and in a smectic liquid (*c*). The unit vector in the (local) mean orientation is called the *director* (*d*). In *a* and *b* there is orientational order, but no positional order of the molecules. In *c* there is partial positional order in addition to orientational order: the molecules are arranged in layers. Because of thermal motion the orientations of the molecules differ from that of the director. Cholesteric phases have a helical structure; this is illustrated by showing the molecules in several planes one above the other. For clarity the thermal deviations have been omitted here.

In the *nematic* phase the long axes of the molecules — again apart from the thermal fluctuations — are parallel; there is no correlation over long distances between the centres of mass (fig. 2*a*). The average direction of the long molecular axes is indicated by the unit vector in that direction, called the director (*d*). There is uniaxial symmetry about the director. Reversal of the director has no physical significance, since a molecule has no preference for being directed with its 'head' or with its 'tail' in either of the two directions. In reality the nematic liquid is not usually a 'liquid single crystal'. The director then indicates the *local* mean of the directions of the long molecular axes, and varies continuously over distances that are large compared with the molecules. In thin layers under a polarizing microscope filamentary structures can be seen (Greek νῆμα means 'wire' or 'filament'). The filamentary structures are 'disclinations', discontinuities in the variation of the director (*fig. 3*).

The *cholesteric* or *chiral-nematic* phase is a variant of the nematic phase that occurs in optically active compounds. The liquid is locally nematic, but the director pattern in a liquid single crystal has a helical structure over larger distances (fig. 2*b*). Here again, there is no long-range correlation between the centres of mass. When light is incident along the helical axis, and its wavelength is equal to the product pn of the pitch p of the helix and the refractive index n, one of the two circularly polarized components is completely reflected. If this wavelength pn is in the visible region, striking colour effects are observed. The pitch p may also be highly temperature-dependent. Liquids in which both these effects are found are suitable for thermography.

Smectic phases (fig. 2*c*), which occur in various forms, have mechanical properties reminiscent of soap

(from the Greek σμῆγμα for soap or salve). In these phases one finds in addition to orientational order a *partial* positional order: the molecular centres are arranged in equidistant planes.

In the following we shall only consider the nematic phase. The examples in fig. 1 show that the molecules themselves are not axially symmetric. We assume nevertheless that in the nematic phase the molecules are effectively axially symmetric as a result of rotation about the long axis, as is suggested by the representation of the molecules by dashes in fig. 2a.

The various kinds of order discussed above are related to long-range correlations between the molecules. Short-range correlations between the molecules are always present, even if there is no long-range order at all. Just as in isotropic liquids there are short-range correlations between the centres of mass and the orientations, in the nematic phase there are short-range correlations between the centres of mass in addition to the long-range correlations in orientation.

Physical properties

Owing to the uniaxial symmetry of a nematic liquid crystal about the director, the various properties are usually anisotropic. We shall briefly discuss here the anisotropy of the dielectric constant ε, the diamagnetic susceptibility χ and the refractive index n. The anisotropy of ε or χ permits the director pattern to be manipulated by means of electric or magnetic fields. The effect of this on incident light is due to the anisotropy of n.

The dielectric constant along the director ($\varepsilon_{||}$) in general differs from that perpendicular to the director ($\varepsilon_{\perp}$). The difference $\Delta\varepsilon$ ($= \varepsilon_{||} - \varepsilon_{\perp}$) is positive in some compounds and negative in others. If the polarization of the material is pure induced polarization, then $\Delta\varepsilon$ is positive, because the polarizability of the molecule in the longitudinal direction is much greater than in the transverse direction. However, if the molecule has a permanent dipole moment, the orientational polarization will generally predominate; $\Delta\varepsilon$ can then be much greater than in the first case, and positive or negative depending on whether the dipole lies more in the longitudinal direction or more in the transverse direction of the molecule. Because of the anisotropy of ε the director tends to orient itself in an electric field E, and it does so in the direction of the field if $\Delta\varepsilon$ is positive and perpendicular to the field if $\Delta\varepsilon$ is negative. These are the orientations in which the free electrical energy, $-\frac{1}{2}\Delta\varepsilon E^2$, is at a minimum.

Most nematic substances are diamagnetic. The greatest contribution to the anisotropy of the diamagnetism comes from the occurrence of circular currents in the aromatic rings (see fig. 1) when a magnetic field is applied. Since this effect is greatest when the fields are perpendicular to the director, the 'perpendicular susceptibility' ($\chi_{\perp}$) is greatest in absolute value. Diamagnetic susceptibilities, however, are negative, so that $\Delta\chi$ ($= \chi_{||} - \chi_{\perp}$) is in general positive. In a magnetic field the director is in general aligned preferentially in the direction of the field.

A uniaxial (liquid) single crystal has two principal refractive indices, n_o and n_e. The first, n_o, holds for a linearly polarized light wave whose electrical vector $\boldsymbol{e}$ oscillates at right angles to the director $\boldsymbol{d}$; the second,

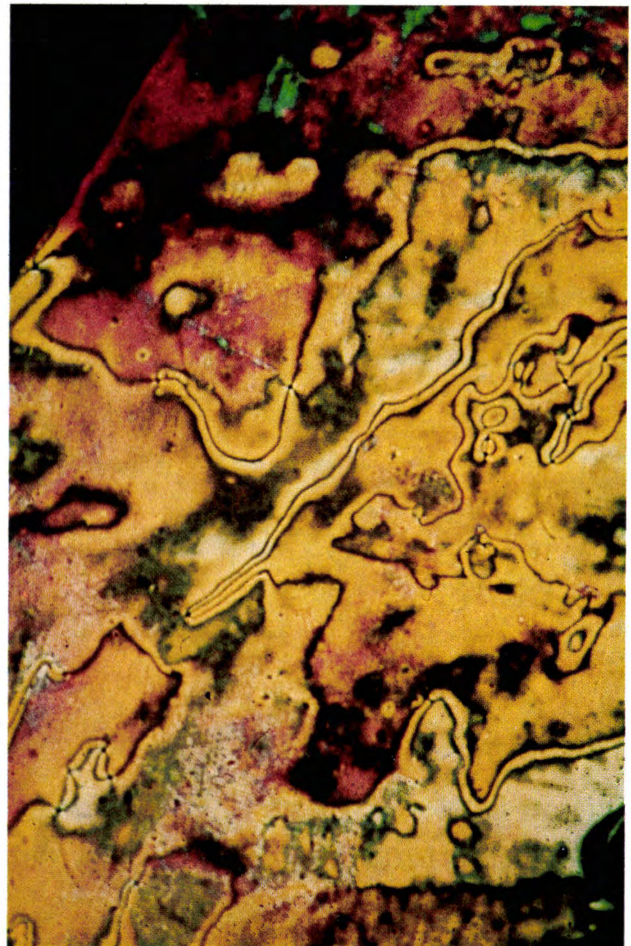

Fig. 3. A thin layer of a nematic liquid seen through a polarizing microscope. The 'filaments' are discontinuities in the director pattern.

n_e, holds for a wave where $\boldsymbol{e}$ is parallel to $\boldsymbol{d}$. For an 'ordinary ray' the refractive index is always n_o, for an 'extraordinary ray' it lies between n_o and n_e; see *fig. 4*. By analogy with the convention used above, we shall write $n_{\perp}$ for n_o and $n_{||}$ for n_e. In liquid crystals $n_{||}$ is always much greater than $n_{\perp}$, which is directly related to the strong polarizability of the molecules in the

[2] See D. Demus, H. Demus and H. Zaschke, Flüssige Kristalle in Tabellen, VEB Verlag, Leipzig 1974.

longitudinal direction. (Permanent dipoles and orientation polarization no longer play any part at optical frequencies.) The difference Δn ($= n_{\parallel} - n_{\perp}$) is about 0.2 or 0.3, which is thus much higher than for example in a well known birefringent material like quartz ($\Delta \approx 0.01$). The temperature dependence of Δn (*fig. 5*) reflects the decrease of order with rising temperature.

In a nematic liquid the director will vary from position to position and from moment to moment if no special precautions are taken. This leads to marked variations in refractive index and hence to light scattering, so that the liquid is cloudy. The textures seen in thin layers between crossed polarizers (fig. 3) give a direct impression of the director variations. In addition to the disclinations, dark bands or striae ('schlieren') are observed, where the continuously varying director lies exactly in the plane of polarization or in a plane perpendicular to it.

Apart from the uniaxial symmetry and hence anisotropy of various properties, the tendency of the molecules towards orientational order also appears macroscopically as an *elasticity* of the liquid, which tends to make neighbouring director orientations the same. This elasticity is described by three constants, K_{11}, K_{22} and K_{33}, which indicate respectively how strongly the liquid opposes 'splay', 'twist' and 'bend' of the director pattern; see *fig. 6*. K_{11}, K_{22} and K_{33} are the coefficients in the expression for the free elastic energy per unit volume of the nematic phase, F_d:

$$F_d = \tfrac{1}{2}\{K_{11}(\mathrm{div}\,\boldsymbol{d})^2 + K_{22}(\boldsymbol{d}\,.\,\mathrm{curl}\,\boldsymbol{d})^2 + K_{33}(\boldsymbol{d}\times\mathrm{curl}\,\boldsymbol{d})^2\}. \quad (1)$$

Note that this type of elasticity only corrects directions and not relative changes of position, as is the case with the ordinary elasticity in the solid state.

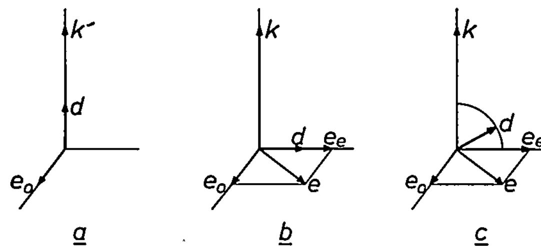

Fig. 4. Propagation of light in a (liquid) uniaxial crystal; $\boldsymbol{k}$ direction of propagation of the light wave, $\boldsymbol{d}$ director (optical axis), $\boldsymbol{e}$ electrical vector of the light wave. *a*) If the light propagates parallel to the axis there is only an 'ordinary ray' ($\boldsymbol{e}_o \perp \boldsymbol{d}$, refractive index $n_{\perp} \equiv n_o$). *b*) If the light propagates perpendicular to the axis, there is an extraordinary ray as well ($\boldsymbol{e}_e \parallel \boldsymbol{d}$, refractive index $n_{\parallel} \equiv n_e$). As a result of the strong polarizability of the molecules in the longitudinal direction, $n_{\parallel}$ is always much greater than $n_{\perp}$. *c*) In the general case ($\boldsymbol{k}$ skew with respect to $\boldsymbol{d}$) the light again consists of an ordinary ray ($\boldsymbol{e}_o \perp \boldsymbol{d}$) and an extraordinary ray ($\boldsymbol{e}_e$ in the plane through $\boldsymbol{k}$ and $\boldsymbol{d}$). For the extraordinary ray the refractive index now lies between $n_{\perp}$ and $n_{\parallel}$.

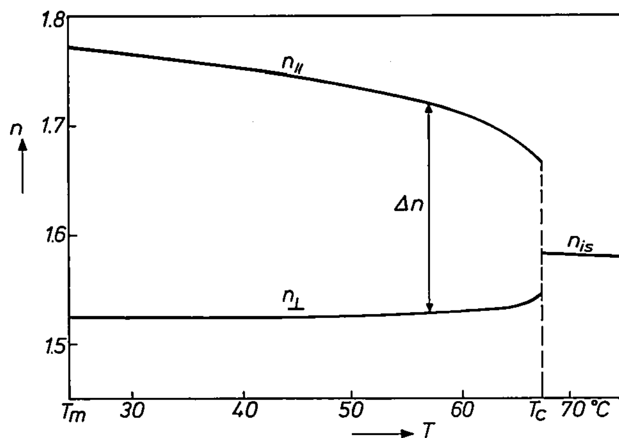

Fig. 5. Refractive indices of PENTAB as a function of temperature. The variation of Δn with temperature reflects the variation of the order parameter.

Thin layers; boundary conditions

For research and applications it is necessary to have liquid crystals possessing a uniform director pattern (single crystals). A pattern of this kind can be obtained in thin layers through the interaction with the glass walls enclosing the liquid. Certain chemical or mechanical treatments of the surface of these walls will give the director a strong preferred orientation at the wall. As a result of the elasticity the director then takes up this direction everywhere in the layer. As the thickness of the layer decreases the influence of the boundary conditions becomes greater and the response to disturbances introduced in the pattern becomes more rapid. Thin layers are therefore generally to be preferred.

We have *homeotropic layers*, in which the director is perpendicular to the wall, and *uniform-planar layers*, in which the uniform director pattern is parallel to the wall (*fig. 7a* and *b*). Uniform-planar layers can be made

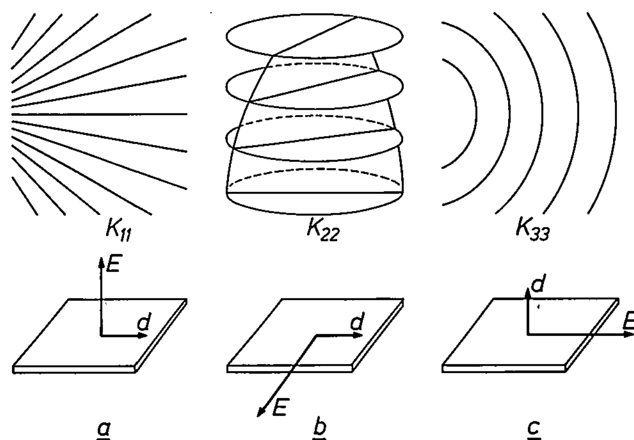

Fig. 6. *Above:* deformations of the director pattern: 'splay', 'twist' and 'bend', from left to right. The extent to which the liquid opposes these deformations is given by the elastic constants K_{11}, K_{22} and K_{33} respectively. *Below:* the configurations in which these constants can be determined by measuring a threshold field (see page 136).

by rubbing the surfaces in one direction with polishing agents or by depositing a thin layer of silica on them by oblique evaporation. The *twisted-planar layer* in fig. 7*c* is obtained from a uniform-planar layer by rotating one of the glass plates through 90° in its own plane. Because of the elasticity of the liquid this rotation is uniformly distributed over the director pattern, so that this acquires a quarter of a helical turn. It is assumed here that the boundary conditions are *rigid*, that is to say that the director at the interfaces remains fixed under all circumstances. The twisted-planar layer is very important in the applications because of the following property: when incident light is polarized linearly in the direction of the director on the incident side, or perpendicular to it, the polarization plane *rotates with the director in the layer*. Between crossed polarizers the layer therefore transmits light.

It is assumed that the pitch p of the twist is much greater than the wavelength λ of the light. There is no longer any question of 'rotating with the director' if the director makes so many turns in a layer that p becomes comparable with λ, which is often the case in cholesteric liquids. In particular, if p is equal to λ/n, then one of the two circularly polarized components is completely reflected, as already mentioned.

The use of liquid crystals for displays

There are various effects in liquid crystals that are put to practical use for displays. In the first place there are the *Frederiks transitions*, in which the orientation of the director, whose alignment is initially determined by the boundary conditions, changes when an electric field is applied. In an appropriate combination with polarizers the initially absorbing layer then becomes transparent. Two configurations in which Frederiks transitions occur can be seen in *fig. 8a* and *b*. Frederiks transitions can also be produced by magnetic fields.

Another effect is *dynamic scattering*. For this to occur the liquid has to possess some (anisotropic) conductivity. A typical example is the configuration shown in fig. 8*c*. The director is already in the alignment favoured by the field, so that a Frederiks transition cannot occur. Above a certain threshold value of the field-strength, however, the liquid becomes hydrodynamically unstable, and starts to flow. When the field-strength is increased further the flow gradually becomes turbulent; the resultant dynamic scattering makes the liquid opaque.

Finally, we should mention the use of a nematic liquid to which a small amount of cholesteric material has been added. This results in a cholesteric liquid crystal with a large pitch. This can be put to use in two ways. When $\Delta\varepsilon$ is positive, the pitch can be so greatly enlarged by applying an electric field that effectively there is a *transition from cholesteric to nematic*. Secondly, when $\Delta\varepsilon$ is negative, a *memory effect* is obtained, in which the dynamic scattering is 'frozen in' when the field is switched off.

A Frederiks transition in a twisted-planar layer is at present the most important effect for displays. We shall only consider Frederiks transitions from now on [3].

In practice the liquid crystal is confined to a layer about 10 μm thick between two glass plates. These are provided with patterns of transparent electrodes (stannic or indium oxide), which permit patterns to be generated in the liquid crystal. The various problems concerned with establishing fixed boundary conditions, filling and sealing the cells, applying the electrodes, etc., will not be discussed here.

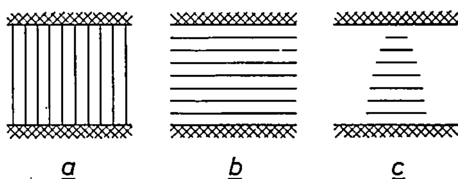

Fig. 7. *a*) A homeotropic layer, *b*) a uniform-planar layer, *c*) a twisted planar-layer. In *a* and *b* the director pattern is shown, in *c* the director itself is shown at points on a vertical line; a shorter dash indicates 'perspective shortening', a rotation of *d* in a plane perpendicular to the paper.

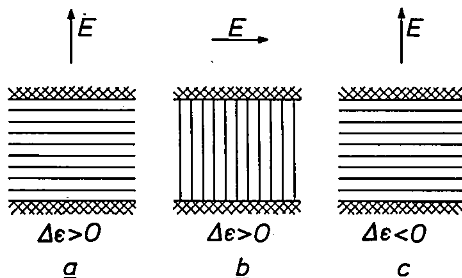

Fig. 8. *a*, *b*) Examples of configurations in which Frederiks transitions occur with increasing field. *c*) A configuration in which Frederiks transitions cannot take place. This configuration is characteristic of the occurrence of 'hydrodynamic instabilities'; for this to occur the liquid must have some anisotropic conductivity.

Frederiks transitions

Let us consider the configuration in fig. 8*a*, with fixed boundary conditions. When the field increases in the direction indicated, there is a gradual change in the director pattern once E exceeds a threshold value E_c (*fig. 9*). At any field-strength the stable equilibrium state can be found by minimizing the total free energy with respect to variations in the director pattern. For $E < E_c$ this is the state shown in fig. 9*a* (director everywhere horizontal). For $E > E_c$ this situation has become an *unstable* equilibrium state; at the slightest

[3] A general review of the effects in liquid crystals used for information display is given in L. A. Goodman, J. Vac. Sci. Technol. 10, 804, 1973.

fluctuation the system jumps to one of two stable states, b or d in fig. 9. In practice the system chooses b in the one domain and d in the other; the transitions between such domains ('domain walls') are clearly visible under the polarizing microscope. The angle ϕ between the director in the middle of the layer and the horizontal varies from 0 to $\pm$ 90° if E increases from E_c without restriction (fig. 9a, b, c, ... or a, d, e, ...). The critical field E_c is given by [4] [5]:

$$E_c = \frac{\pi}{l}\sqrt{\frac{K_{11}}{\Delta\varepsilon}}, \qquad (2)$$

where l is the layer thickness. The critical field-strength is thus high when the liquid strongly opposes deformation (K large), when the boundary conditions are important (l small) and when the field cannot readily manipulate the liquid ($\Delta\varepsilon$ small). The critical *voltage* V_c depends only on the properties of the liquid and not on the geometry:

$$V_c = lE_c = \pi\sqrt{\frac{K_{11}}{\Delta\varepsilon}}. \qquad (3)$$

The constant K_{11} can in principle be determined by measuring the critical voltage. With other configurations K_{22} and K_{33} can be determined in an analogous way (see fig. 6). In practice, it is desirable to make such measurements in a magnetic field to avoid any unwanted effects due to conduction.

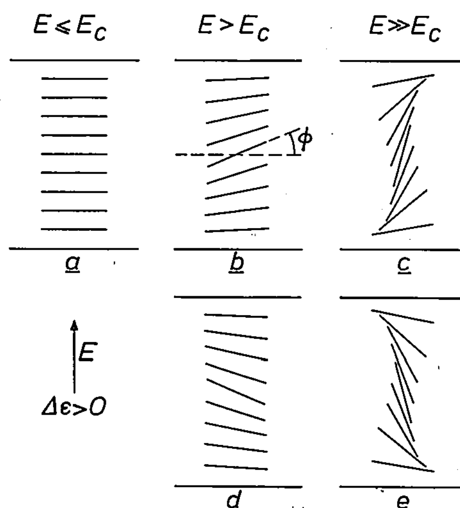

Fig. 9. Frederiks transition. The configuration a is stable as long as E is lower than a certain critical field E_c. If E becomes greater than E_c, then a is no longer stable, and the system changes to the state b or d, which gives c or e if the field is increased further.

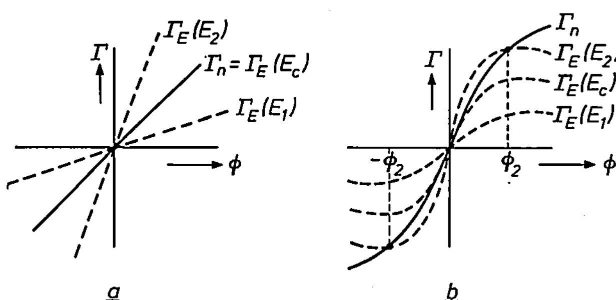

Fig. 10. Torques acting on the director in the centre of the patterns of fig. 9, as a function of ϕ. *Solid line*: the stabilizing elastic torque Γ_n; *dashed lines*: the destabilizing electric torque Γ_E for three values of the field-strength, $E_1 < E_c$, E_c and $E_2 > E_c$. *a*) For small values of ϕ. For $E < E_c$ (e.g. E_1) the stabilizing torque is dominant, for $E > E_c$ (e.g. E_2) the destabilizing torque is dominant. *b*) At greater values of ϕ the torques are no longer proportional to ϕ. As a result points of intersection occur that determine the equilibrium values of ϕ for $E > E_c$ (e.g. $\pm\,\phi_2$ at $E = E_2$). The curves are only qualitative.

Minimizing the free energy, i.e. the sum of the free electrical energy per unit volume, $-\frac{1}{2}\Delta\varepsilon E^2$, and the free elastic energy per unit volume, F_d of equation (1), integrated over the volume of the layer under given boundary conditions, is mathematically a complicated problem. The existence of a threshold value in the field can however be explained in a simple way. Let us consider a *non*-equilibrium situation, i.e. one in which the director pattern is not the equilibrium pattern at the given field-strength E. Only patterns of the type in fig. 9, characterized by a single parameter, the angle ϕ, are taken into account. There then acts on the liquid a stabilizing, elastic torque Γ_n and a destabilizing electrical torque Γ_E, proportional to E. If only small values of ϕ are considered, the problem is a linear one: Γ_n and Γ_E are both proportional to ϕ (*fig. 10a*). Then either the stabilizing or the destabilizing torque in fig. 10a predominates; these two cases are illustrated by $E = E_1$ and $E = E_2$. In the first case $\phi = 0$ is the stable state, in the second case the system tries to get away from this state. The boundary line lies at $E = E_c$.

The stable equilibrium states at a value of E that is greater than E_c are determined by the nonlinear part of the problem. At any value of $E > E_c$ there are two stable solutions for ϕ ($\neq 0$), i.e. patterns where the destabilizing and the stabilizing torques compensate each other (fig. 10b).

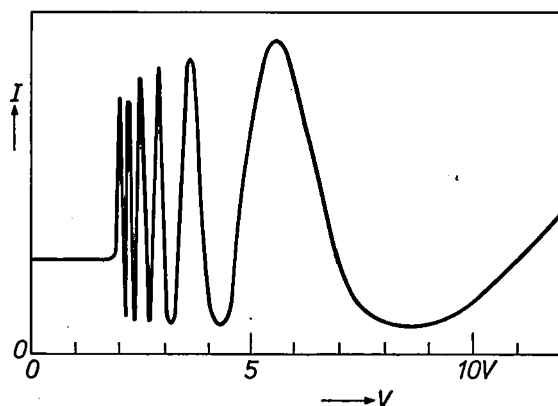

Fig. 11. Intensity I of the transmitted light as a function of the voltage V across the layer in the configuration of fig. 8a between crossed polarizers for monochromatic light. The polarizers are at angles of 45° to the director.

Optical effects

Let us consider the configuration of fig. 8a — a uniform planar layer with positive $\Delta\varepsilon$ in an orthogonal

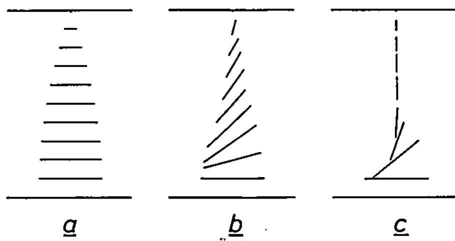

Fig. 12. Director in the twisted-planar layer (E orthogonal, $\Delta\varepsilon > 0$); *a*) for $E < E_c$; *b*) for $E > E_c$; *c*) for $E \gg E_c$. A shorter dash again indicates 'perspective shortening' of the director.

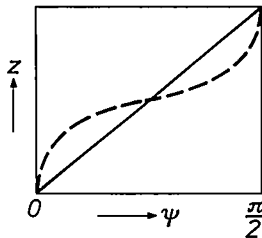

Fig. 13. The angle of twist ψ of the director in a twisted-planar layer as a function of the vertical coordinate z. *Solid curve*: $E < E_c$; for values of E greater than E_c, $\psi(z)$ is represented by curves like the dashed one.

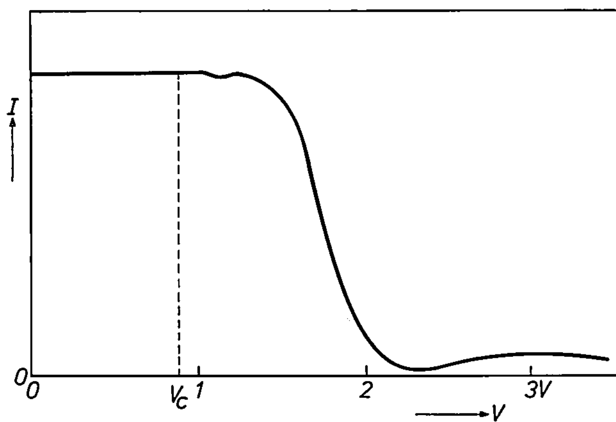

Fig. 14. Intensity I of the transmitted light as a function of the voltage V across a twisted-planar layer with a thickness of 12 μm.

field — between crossed polarizers at 45° to the director. For the ordinary ray (see fig. 4c) the refractive index is always $n_\perp$. For the extraordinary ray the layer has an effective refractive index n_{eff} that, for $E < E_c$, is equal to $n_{||}$, but for $E > E_c$ is dependent on E; if E increases without limit n_{eff} tends towards $n_\perp$. The phase difference between the ordinary and extraordinary rays after passage through the layer thus depends on E, and so therefore does the transmission; see *fig. 11*. The minima in fig. 11 lie at the values of E given by

$$(n_{\text{eff}} - n_\perp)l = k\lambda,$$

where l is the layer thickness and k is an integer. For $E < E_c$ ($n_{\text{eff}} = n_{||}$) the transmission depends on the value of $n_{||} - n_\perp$; for $E \gg E_c$ ($n_{\text{eff}} \rightarrow n_\perp$) the transmission tends to zero. All this applies to monochromatic light; with white light there are colour variations.

This effect is not particularly suitable for applications. Since it is very sensitive to the thickness l, for a fixed value of the field-strength variations in light intensity or colour shifts can easily occur over the plane of the layer. In addition the result is highly temperature-dependent through Δn (see fig. 5).

A more suitable effect for application is that of an orthogonal field on a twisted-planar layer with $\Delta\varepsilon > 0$ between crossed polarizers (*fig. 12*). If the field-strength is zero, the system transmits light (see page 135); the twist ψ of the director as a function of the vertical coordinate z is then linear (solid curve in *fig. 13*). If the field-strength is now increased above the critical field E_c for this situation, the director then also assumes an angle to the horizontal plane; this angle is greatest in the middle. This makes the twisting easier, so that the variation in ψ takes place mainly in the middle (fig. 12*b*; fig. 13 dashed curve). For $E \gg E_c$ the director is vertical, except near the interfaces (fig. 12*c*). There is then no longer any question of a gradual twist — the orientations above and below are 'decoupled' — and with crossed polarizers the layer no longer transmits light. The intensity I of the transmitted light as a function of the voltage across the layer is shown in *fig. 14*.

The critical voltage for a twisted-planar layer with a twist ψ_m between the glass plates is found by replacing K_{11} in eq. (3) by the expression

$$K_{\text{eff}} = K_{11} + (K_{33} - 2K_{22})\,\psi_m^2/\pi^2.$$

When the voltage is switched between zero and a value much higher than V_c (see fig. 14), no colour or thickness effects are produced. In practice V_c is 1 to 2 V. The switching voltages are about three times higher. In the application of liquid crystals for displays this effect is currently the most important. It is used on a large scale in digital watches and to an increasing extent in pocket calculators.

When the field is turned off from the 'decoupled' situation of fig. 12*c*, then the quarter turn that again arises might be either clockwise or anticlockwise. The addition of only a small quantity of a cholesteric compound gives the liquid a natural preference for one of the directions, and thus avoids the occurrence of domain walls.

[4] The equations given in this article are intended for use with the International System of Units (SI). The quantity ε is the product of the relative dielectric constant ε_r and the dielectric constant of free space $\varepsilon_0 = 8.854 \times 10^{-12}$ F/m. The equations given here can be modified for use with the c.g.s. system by substituting $\varepsilon_0\varepsilon_r$ for ε and $1/4\pi$ for the ε_0's.

[5] H. Gruler, T. J. Scheffer and G. Meier, Z. Naturf. **27 a**, 966, 1972.

Molecular structure and clearing point

Many of the well known mesogenic compounds have the configuration shown in *fig. 15a* as the basic molecular structure: two aromatic rings connected by a bridging group X and with two end substituents R and R′, which give the molecule its elongated shape [2]. In this article we shall consider four types of compound, shown in fig. 15*b* to *e*, that differ from each other in the bridging group: these are azobenzenes, azoxybenzenes, Schiff's bases and stilbenes. The terminal or end substituents considered here are non-branched alkyl chains ($-(CH_2)_m-CH_3$) or alkoxy chains ($-O-(CH_2)_m-CH_3$) or groups that only consist of a few atoms. The spatial structure or 'conformation' of the molecules of these compounds is closely dependent on the bond angles and bond lengths in the bridging group. For example, azobenzenes and stilbenes generally have a planar conformation, whereas the two aromatic rings in the azoxybenzenes and Schiff's bases do not usually lie in the same plane.

In the following sections we shall also consider substituents other than end substituents (substituents located at the *para-* position). End substituents do not usually have any effect on the steric orientation of the aromatic rings in relation to one another. This is also usually true for substituents introduced at the neighbouring *meta-* position. However, if substituents are introduced at the *ortho-* position, which lies one position further on, this often does affect the relative orientations of the aromatic rings: these are then rotated in relation to each other (twisted) in such a way that space is made for the *ortho*-substituents ('steric hindrance').

A characteristic feature of mesogenic compounds is the high polarizability, which is a result of the non-localization of the π-electrons of the aromatic rings. Since the bridging group also contains double bonds — and is therefore more or less rigid — conjugation occurs: the π-electron systems of the constituent parts combine to form one single elongated system. The result of this is that the polarization is also strongly anisotropic.

In the explanation for mesogenic behaviour that has been given by W. Maier and A. Saupe [6] the anisotropic polarizability is essential. The basic idea in their approach is that the Van der Waals attraction between the molecules is therefore also anisotropic. This attraction is attributed to the fact that neighbouring molecules can reduce the energy of the system by 'polarizing one another'. In the case of anisotropic polarizabilities the energy gain is largest for such cross-polarization in the 'easy' direction; as a result these directions tend to become parallel. This approach therefore indicates a relationship between the molecular structure and the clearing point: the greater the anisotropy of the polarizability, the higher the clearing point. A relatively high clearing point would thus be expected for molecules with a planar conformation, since the conjugation is greatest in planar molecules.

Maier and Saupe's model leads to the following relation between the clearing point T_c and the longitudinal and transverse polarizabilities α_l and α_t of the molecule [4]:

$$kT_c = \frac{0.0084(\alpha_l - \alpha_t)^2 I}{\varepsilon_0^2 V^2}. \qquad (4)$$

where k is Boltzmann's constant, I an energy representing the jumps in molecular energy that arise on polarization, and V is the molar volume. I is often identified with the ionization potential. Some of the theoretical background to this formula, which only gives a qualitative description of nematic behaviour, is given in Appendix A.

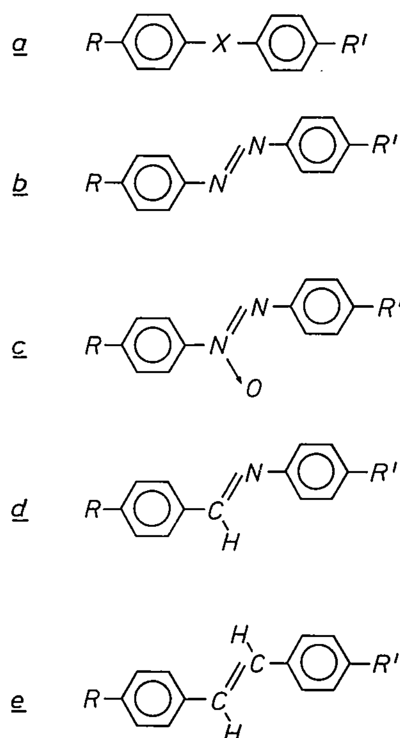

Fig. 15. *a*) The basic structure of many mesogenic compounds: two aromatic rings are connected by a bridging group X and have end substituents R and R′. In (*b*), (*c*), (*d*) and (*e*) the molecular structure of the four types of compound considered in this article are given: azobenzenes, azoxybenzenes, Schiff's bases and stilbenes, which all have different bridging groups.

Maier and Saupe only take into account the anisotropy of the polarizability; they do not consider factors such as anisotropy in the shape of the molecules; their model relates to anisotropically polarizable *spherical* molecules. If the *elongated shape* is also taken into account, then in the first place there are important modifications to the analysis of the Van der Waals forces. In the second place, and quite independently of this, there is the tendency of hard elongated bodies to align themselves parallel to one another, rather like matches. Here the *repulsive* forces, which prevent the hard bodies from penetrating one another, play an essential part.

We shall now start by looking at the effect of the length of the end substituents on the clearing point T_c. In *fig. 16a, b* and *c* the clearing point T_c is shown as a function of the number of carbon atoms m in the end substituent for a number of azobenzenes with non-branched alkyl and alkoxy groups as end substituents. Since the oxygen atom in the alkoxy group makes about the same contribution to the length of the molecule as a carbon atom, this oxygen atom is counted as a carbon atom. What we are ultimately interested in is the *entire* temperature range, and therefore this figure also gives the melting point T_m (dashed curve). This will be discussed in more detail later. A similar curve for T_c is obtained when corresponding azoxybenzenes, Schiff's bases and stilbenes are considered.

is interrupted by kinks with different directions. At the same time the chain becomes more flexible, especially at higher temperatures. This is clearly observed in compounds with a relatively high clearing point (fig. 16c). Both the increasing number of kinks and the greater flexibility reduce the difference in the increment of $\alpha_l - \alpha_t$ as m increases [7].

Fig. 16 also clearly shows that the oxygen atom of the alkoxy group gives an additional contribution to $\alpha_l - \alpha_t$, resulting in marked increases of T_c. An alkoxy group makes a greater contribution to $\alpha_l - \alpha_t$ than an alkyl group of similar length because of the easy incorporation of the non-bonded electron pair of the oxygen atom into the π-electron system (mesomeric interaction, which is also a form of conjugation).

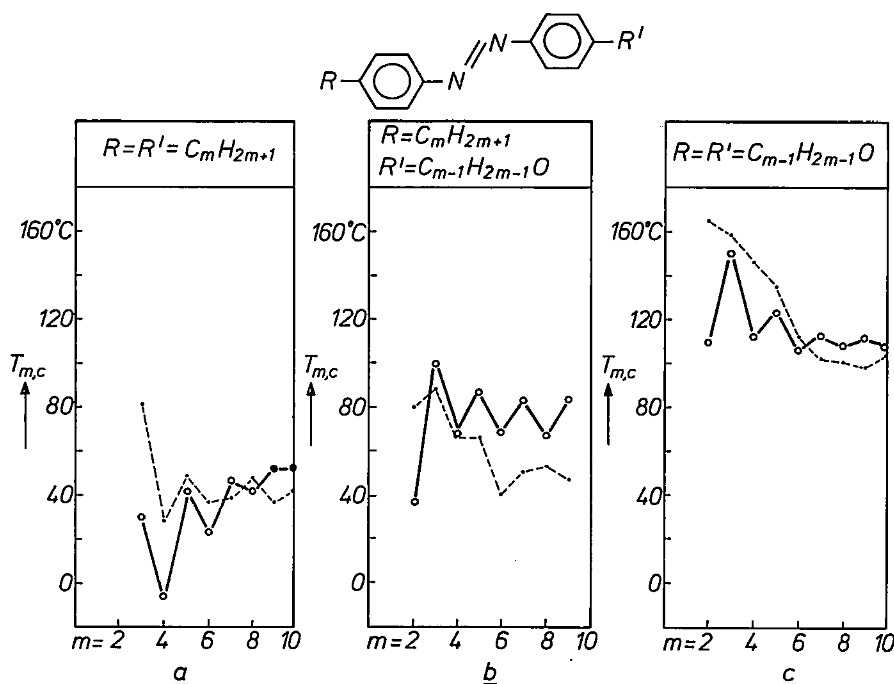

Fig. 16. Measured clearing points T_c (open circles) and melting points T_m (points) as a function of the number of carbon atoms m in the end substituent of the azobenzenes shown in the figure. Where the melting point lies above the clearing point the mesophase is supercooled. Where a smectic phase occurs, the clearing point is indicated by a filled circle.

It is interesting to note the marked alternation of the clearing points with changing m in fig. 16, especially at small values of m. Although the same alternation is indeed maintained at larger m-values, it is somewhat less pronounced. The alternation is explained from the fact that the carbon chain of the end substituent makes alternately larger and smaller contributions to the anisotropy of the polarizability because of its zigzag shape. We attribute the less pronounced alternation to the fact that the longer the carbon chain becomes, the more often the continuation of the normal zigzag shape

This is connected with the observation that in compounds where T_c at small m has a high value (fig. 16c) T_c tends to decrease with increasing m, whereas in compounds where T_c is initially low (fig. 16a) it tends to rise. This effect has also been observed in the three other types of compound considered.

A qualitative explanation of this effect can be based on the assumption that for the complete molecule the

[6] W. Maier and A. Saupe, Z. Naturf. **14 a**, 882, 1959, and **15 a**, 287, 1960.
[7] See W. H. de Jeu and J. van der Veen, Mol. Cryst. liq. Cryst. **40**, 1, 1977.

factor $(\alpha_l - \alpha_t)^2/V^2$ from eq. (4) is an average of the contribution from the various groups that constitute the molecule. In the first type of compound the contribution originating from the central part of the molecule is large compared with the contribution from a CH_2 group, so that an increase in the length of the end substituent leads on average to a decrease in T_c. In the second type of compound this ratio is probably reversed. In the case illustrated in fig. 16 it is in fact the oxygen atom of the alkoxy group, with its non-bonded electron pair, that makes the factor $(\alpha_l - \alpha_t)^2/V^2$ relatively large for the central part of the molecule.

In a more quantitative study [8] of the relation between $\alpha_l - \alpha_t$ and T_c we have synthesized a number of Schiff's bases of the type:

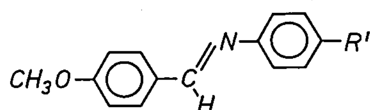

with the groups -F, $-CH_3$, -Cl, $-NO_2$ and -CN as the end substituent R′. In this sequence the contribution from the C-R′ bond to $\alpha_l - \alpha_t$ increases in value from 0.6 to 4.8×10^{-40} Fm^2.

If we can assume that the polarizability of the whole molecule can be obtained by adding the polarizabilities of the different groups that make up the molecule, then we can write:

$$\alpha_l - \alpha_t = (\alpha_l - \alpha_t)_C + (\alpha_l - \alpha_t)_{R'}, \tag{5}$$

where the two terms on the right-hand side relate to the non-varied part of the molecule and to the end substituent R′ respectively. According to Maier and Saupe, T_c is proportional to $(\alpha_l - \alpha_t)^2$, and hence from (5) the quantity T_c is proportional to $(\alpha_l - \alpha_t)_C{}^2 + 2(\alpha_l - \alpha_t)_C(\alpha_l - \alpha_t)_{R'} + (\alpha_l - \alpha_t)_{R'}{}^2$. If we neglect the last term, because $(\alpha_l - \alpha_t)_{R'}$ is much smaller than $(\alpha_l - \alpha_t)_C$, we may then expect a linear relation between T_c and $(\alpha_l - \alpha_t)_{R'}$ for the whole series, in which $(\alpha_l - \alpha_t)_C$ is a constant, and in which the molar volume V does not vary greatly. *Fig. 17* shows that such a relation holds approximately.

It would be interesting to know more about the influence of the bridging groups on T_c. However, there is not enough quantitative information about the degree of conjugation still possible when there are deviations from the planar conformation to form any definite conclusions here.

Even in cases where the necessary information is available, results are sometimes found that do not correspond to Maier and Saupe's equation (4). For example, dialkoxystilbenes have higher T_c values than corresponding dialkoxyazobenzenes, although the $(\alpha_l - \alpha_t)$ value for the bridging group of the dialkoxystilbenes is certainly no higher than that for the compounds of the second kind. Since both bridging groups give a planar conformation, and both bridging groups are also non-polar, this difference in T_c cannot be attributed to differences in these factors. We assume that these discrepancies between theoretical prediction and experimental findings arise, at least in part, because Maier and Saupe's model does not take the repulsive forces into account, as mentioned on page 138.

Molecular structure and dielectric anisotropy

Let us now consider the relation between the molecular structure and the dielectric constant. Onsager's theory for the dielectric properties of isotropic liquids [9] has been extended by W. Maier and G. Meier to nematic liquids [10]. They consider molecules with longitudinal and transverse polarizabilities α_l and α_t and a permanent dipole μ at an angle β to the longitudinal axis, and arrive at the following relations between the macroscopic dielectric constant ε and the molecular quantities α_l, α_t and μ:

$$\bar{\varepsilon} - \varepsilon_0 = NhF\left\{\bar{\alpha} + F\frac{\mu^2}{3kT}\right\}, \tag{6}$$

$$\Delta\varepsilon = NhF\left\{\alpha_l - \alpha_t + F\frac{\mu^2}{2kT}(3\cos^2\beta - 1)\right\} S. \tag{7}$$

Here $\bar{\varepsilon}$ is the mean dielectric constant, $\bar{\alpha}$ is the mean polarizability, N is the number of molecules and S the

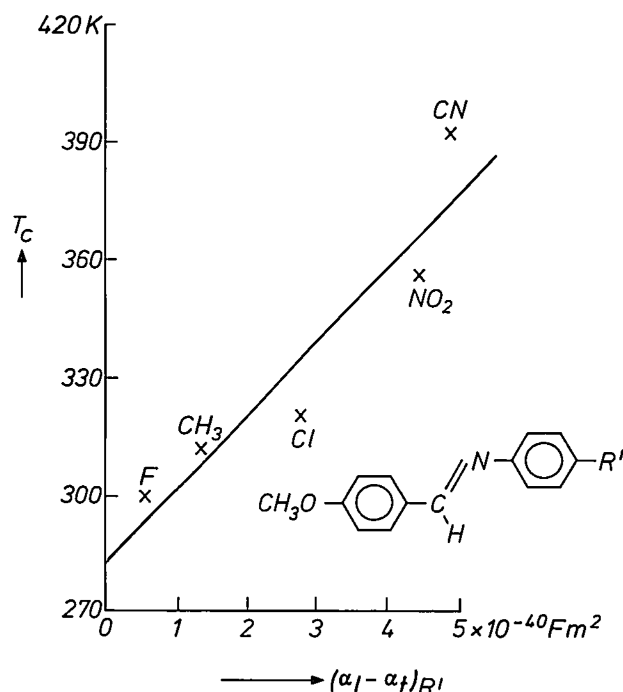

Fig. 17. The clearing point T_c as a function of the contribution $(\alpha_l - \alpha_t)_{R'}$ of the bond between end substituent R′ and aromatic ring to the total anisotropy of the polarizability, for the compound given in the figure with the end substituent R′: -F, $-CH_3$, -Cl, $-NO_2$ and -CN.

order parameter. The theoretical background to these equations and the definitions of h and F are given in *Appendix B*. The last term between curly brackets in eq. (7) gives the contribution of the permanent dipole moment to $\Delta\varepsilon$. It can be seen that this changes sign at a particular value of β ($\beta \approx 55°$).

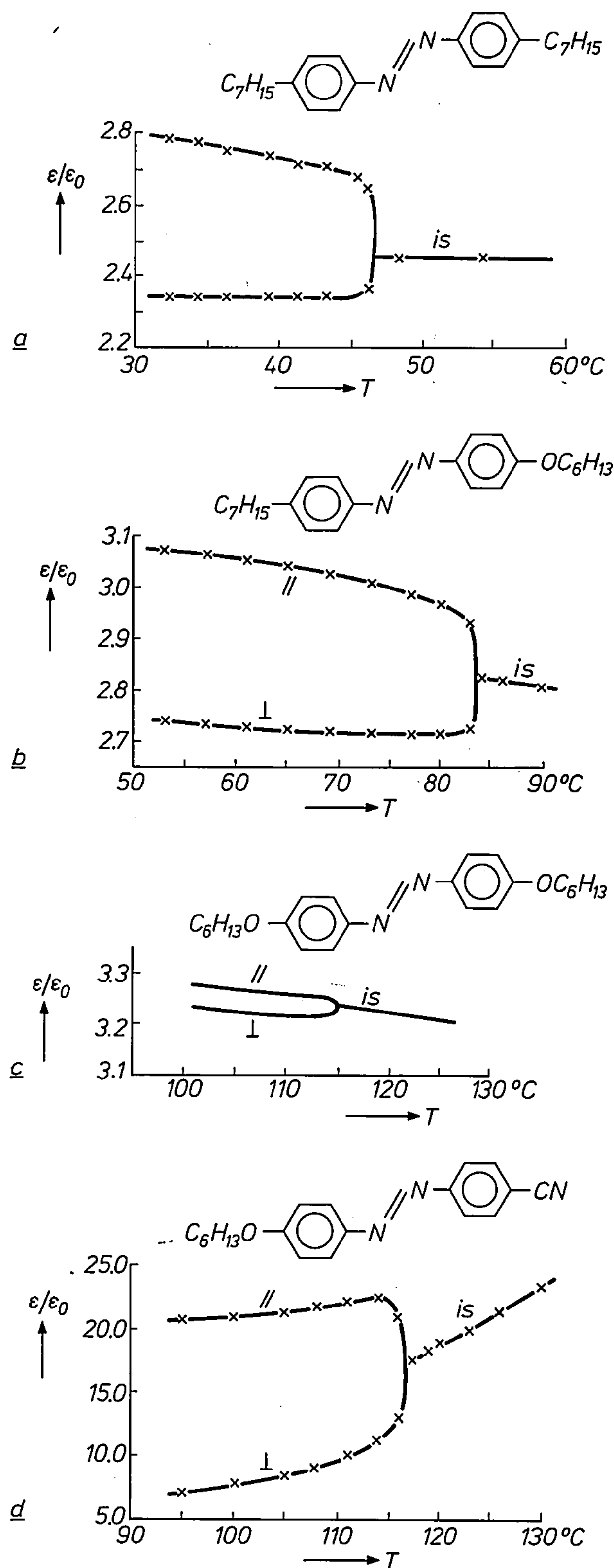

Fig. 18. The relative dielectric constants $\varepsilon_{||}/\varepsilon_0$, $\varepsilon_{\perp}/\varepsilon_0$ and $\varepsilon_{is}/\varepsilon_0$ (parallel or perpendicular to the director and the value above the clearing point) as a function of temperature T for the azobenzenes shown in the figure.

We have tested the above expressions mainly for the effect of the end substituent. The effect of the bridging group is more difficult to investigate, largely because not enough is known about the direction of the permanent dipole moment of the various bridging groups.

The main compounds we have studied are azobenzenes and azoxybenzenes with alkyl, alkoxy and cyano groups (-CN) as end substituents. Azobenzenes and azoxybenzenes are interesting to compare, because although they are both closely related chemically, the bridging group of the azobenzenes is non-polar whereas that of the azoxybenzenes is polar. The alkyl groups used as end substituents have a — relatively small — permanent dipole moment in the direction of the long molecular axis. The symmetrical dialkylazobenzenes do not therefore have a permanent dipole moment in the molecule as a whole and are therefore suitable as a 'reference'. The cyano group is interesting because of its relatively large dipole moment (13.5×10^{-30} Cm).

In *fig. 18* the measured relative values of $\varepsilon_{||}$ and $\varepsilon_{\perp}$ are plotted as a function of temperature T [11]. At the clearing point T_c the difference between these two quantities has of course disappeared; beyond this point the dielectric constant is then denoted by ε_{is}.

If we consider a larger number of dialkylazobenzenes, we find that $\Delta\varepsilon$, like T_c, alternates with increasing length of the end substituent, as would be expected since both quantities depend on $\alpha_l - \alpha_t$. We also find that if an alkyl group is replaced by an alkoxy group of the same length, both $\varepsilon_{||}$ and $\varepsilon_{\perp}$ increase in value (fig. 18*a* and *b*), but that the increase in $\varepsilon_{\perp}$ is rather larger, so that $\Delta\varepsilon$ decreases slightly in value. The substitution of a second alkoxy group for an alkyl group leads to a further reduction in $\Delta\varepsilon$ to nearly zero (fig. 18*c*).

The explanation is as follows. When an alkoxy group is substituted for an alkyl group as end substituent the molecule acquires a permanent dipole moment of 4.3×10^{-30} Cm at an angle of 72° to the axis between the two *para-* positions of the benzene ring on which the substitution is made. This axis is at an angle of about 10° to the long molecular axis, about which the molecule rotates, so that the angle between the permanent dipole moment and the long molecular axis varies between 62° and 82°. This therefore leads

[8] A more detailed description is given in J. van der Veen, J. Physique 36, Cl-375, 1975.
[9] Onsager's theory is discussed in C. J. F. Böttcher, Theory of electric polarization, 2nd edition, Vol. I, Elsevier, Amsterdam 1973.
[10] W. Maier and G. Meier, Z. Naturf. 16 a, 262, 1961.
[11] A more detailed treatment is given in W. H. de Jeu and Th. W. Lathouwers, Z. Naturf. 29 a, 905, 1974.

to a relatively large contribution to $\varepsilon_\perp$. However, as long as the order parameter is not equal to unity, the component of the dipole moment perpendicular to the long molecular axis also contributes to $\varepsilon_{||}$. In addition, the mesomeric effect of the alkoxy group increases the polarizability along the molecular axis (as reflected in the increase of T_c) and these two effects together cause $\varepsilon_{||}$ to increase, but less than $\varepsilon_\perp$. The result is thus a reduction in $\Delta\varepsilon$. When the second alkoxy group is substituted for the alkyl group, both alkoxy groups, freely rotating, contribute to $\varepsilon_\perp$ while the parallel components of their dipole moments now cancel out, so that $\Delta\varepsilon$ falls to almost zero.

If we now look at the effect of substituting a cyano group as end substituent, we see that the large dipole moment of this group, which has about the same direction as the long molecular axis, is dominant over all the other contributions, thus giving a high positive value of $\Delta\varepsilon$.

Let us now use *fig. 19a* and *b* to compare a dialkylazobenzene with a corresponding dialkylazoxybenzene [11]. The azoxybenzenes differ from the azobenzenes in the presence of a permanent dipole moment of magnitude 5.7×10^{-30} Cm in the bridging group. It is usually assumed that this dipole moment is directed along the N-O bond. Comparing the azoxybenzenes with the azobenzenes, we then find that both $\varepsilon_\perp$ and $\varepsilon_{||}$ increase in value, but the increase in $\varepsilon_\perp$ is somewhat greater. As we have seen in the azobenzenes, substitution of two alkoxy groups for the alkyl groups makes a much greater contribution to the value of $\varepsilon_\perp$ than to that of $\varepsilon_{||}$, with the result that $\Delta\varepsilon$ in dialkoxyazoxybenzenes is negative (fig. 19*c*).

It is also interesting to consider the situation in asymmetrically substituted azoxybenzenes, e.g. with an alkyl group as one end substituent and an alkoxy group as the other. The synthesis of such azoxybenzenes produces a mixture of two isomers in which the end groups are interchanged with one another. A mixture of this type is generally difficult to separate into its components.

Fig. 20 gives the dielectric constant of a mixture of the two asymmetrically substituted azoxybenzenes *I* and *II* shown in the figure. Fig. 20*a* gives the value of $\Delta\varepsilon$ for the mixture formed under the usual conditions of synthesis, and consisting of 62% of isomer *I*. Fig. 20*b* gives the value for a mixture in which this percentage has risen to 88%. It can be seen that $\varepsilon_\perp$ hardly changes at this increase, whereas $\varepsilon_{||}$ decreases. Fig. 20*c* gives the value of $\Delta\varepsilon$ for isomer *II* as calculated from fig. 20*a* and *b*, proceeding from the assumption that the dielectric constant of the mixture can be obtained by adding the values of the separate isomers. It can be seen that $\Delta\varepsilon$ for isomer *II* has a positive value [12].

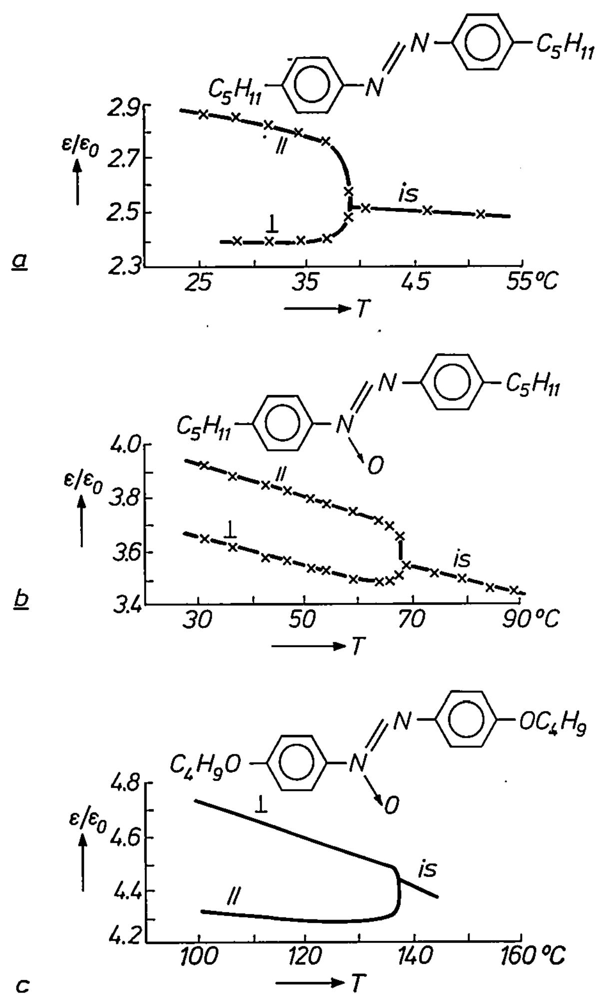

Fig. 19. As in fig. 18, for the azobenzene (*a*) shown in the figure, a corresponding azoxybenzene (*b*) and an azoxybenzene with two alkoxy groups instead of alkyl groups as end substituent (*c*).

The reason why $\varepsilon_\perp$ does not change much when the ratio of the isomers changes is that, provided the alkoxy group rotates freely, interchanging the end groups has little or no effect on the transverse components of the dipoles. This is not so for the longitudinal components. If we can assume that the permanent dipole moment of the CH_3O group is approximately perpendicular to the long molecular axis, and hence has little effect in the longitudinal direction, then the dipole moment of the C_4H_9 group in isomer *I* will have the opposite direction to that of the longitudinal component of the dipole moment of the azoxy group, so that these moments will partly compensate each other. In isomer *II* these dipole moments add, however, giving a high value for the longitudinal component of the dipole moment and hence for $\varepsilon_{||}$.

The temperature dependence of $\Delta\varepsilon$ as expressed in figures 18, 19 and 20 can be understood with the aid of eq. (7). We see from this equation that in non-polar molecules ($\mu = 0$) the dielectric anisotropy $\Delta\varepsilon$ depends only indirectly on the temperature, through the order

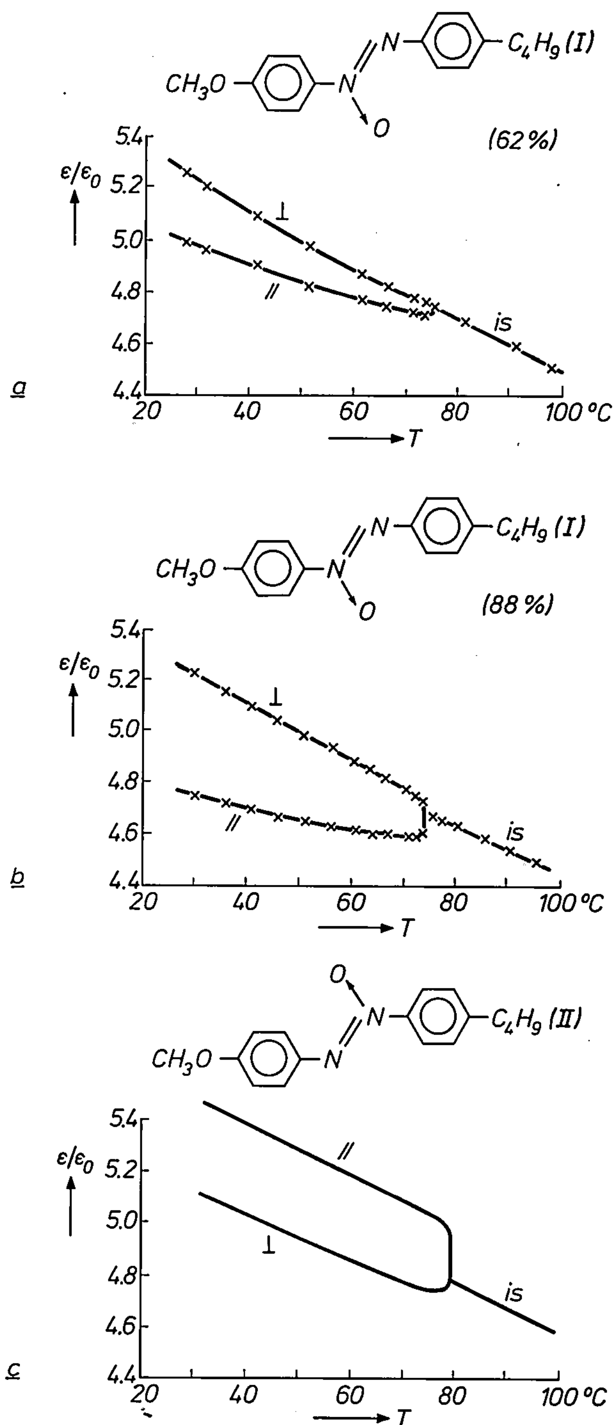

Fig. 20. *a*) and *b*) The values of the relative dielectric constants as a function of temperature for a mixture of two isomers *I* and *II*, shown in the figure, consisting of 62% and 88% of isomer *I*. In (*c*) the values are given for the relative dielectric constants of isomer *II*, calculated from the data from (*a*) and (*b*).

parameter S; in polar molecules the temperature is also directly involved.

In the non-polar dialkylazobenzenes (figs. 18*a* and 19*a*) we see that $|\Delta\varepsilon|$ does indeed increase with decreasing T and hence with increasing S, with the most marked increase near T_c, where the increase in S is also greatest. On decreasing the temperature further, S tends to saturate, making the variation of $|\Delta\varepsilon|$ small.

What can we expect from equation (7) if the molecules are polar? Since the effect of the permanent dipole moment μ is generally much greater than that of the anisotropy of the polarizability $\alpha_l - \alpha_t$, the factor S/T will determine the temperature dependence. Here again, $|\Delta\varepsilon|$ will increase with decreasing T, as can be seen in figures 18*d*, 19*c* and 20*a* and *b*, but in this case $|\Delta\varepsilon|$ goes on increasing, even if the temperature is decreased further.

In the special case where the dipole contribution is about the same as the contribution from the anisotropy of the polarizability — either because the value of $(1 - 3\cos^2\beta)$ is very small, i.e. at a β of about 55 °, or because the dipole moment μ itself is so small — the situation is different. The effect of S is greatest at a temperature just below T_c, and $|\Delta\varepsilon|$ increases with decreasing T. At lower temperatures the factor S becomes practically constant, but the opposite effect of the factor S/T remains, so that the total effect is that $|\Delta\varepsilon|$ remains practically constant with decreasing T (figs. 18*c* and 19*b*) or even becomes smaller.

Suitable compounds

The theoretical work discussed in the two previous sections served as a guide in the search for compounds suitable for practical applications. The search was directed more especially at finding compounds with an appropriate temperature range and possessing a large $|\Delta\varepsilon|$. For a twisted-planar layer, which is important for practical applications, and for the case of a transition between a cholesteric phase and a nematic phase, it is desirable to have a large *positive* $\Delta\varepsilon$. For applications based on dynamic scattering (e.g. the memory effect) it is important to have a large *negative* $\Delta\varepsilon$. In looking for suitable compounds the emphasis was sometimes on the required temperature range and sometimes on a high value of $|\Delta\varepsilon|$, but the aim was of course always to find compounds that combine both properties.

In practical applications there are obviously other requirements to be met, such as a low threshold voltage, chemical and photochemical stability, the absence of toxicity and of colour, but it is beyond the scope of this article to deal with the various ways and means used for meeting these requirements.

The main problem in obtaining a suitable temperature range is usually the melting point (see fig. 16). As we have seen, the melting points of the classic liquid crystals are too high for most applications. One way of lowering the melting point is to remove permanent

[12] A more detailed treatment is given in W. H. de Jeu and Th. W. Lathouwers, Chem. Phys. Lett. 28, 239, 1974.

dipoles. In other respects the behaviour of the melting point on a change in molecular structure is difficult to predict; research on low-melting-point materials is still largely empirical. In practice it is common not only to remove permanent dipoles, but also to investigate molecules that do not have a planar conformation (thus reducing T_c), in the hope of finding a low-melting-point compound. To obtain a suitable temperature range, *eutectic mixtures* are also used; these often have a lower melting point than the corresponding melting points of the components, whereas the clearing point is not much lower (*fig. 21*).

In the following we shall see how a number of compounds have been synthesized to give liquid crystals with useful properties. We shall classify these compounds in terms of the various substitutions used in these syntheses.

One of the main objects of a substitution at an *ortho*-position or in the bridging group is to obtain a low melting point. The value of T_c is reduced by the rotation of the aromatic rings in relation to one another (the twist) — often caused by such a substitution — and also, in the case of an *ortho*-substitution, by the broadening of the molecule. Up to a certain point this is acceptable provided it is offset by a marked decrease in the melting point, which can result from the rotation of the rings.

The *para*- position is frequently a suitable position for the introduction of a substituent with a large permanent dipole moment in the direction of the long molecular axis, so as to obtain a high positive $\Delta\varepsilon$. The bridging group is particularly suitable for the introduction of a substituent with a permanent dipole moment perpendicular to the long molecular axis.

Some of the more interesting chemical aspects of this work are briefly mentioned in the final section of this article dealing with actual syntheses.

Ortho-substitution

As can be seen in *Table I*, substitution of a methyl group at the *ortho*- position of certain Schiff's bases does in fact produce changes in the required direction. Thus, the octyloxy compound ($m = 9$) has the acceptable T_c value of 68 °C, while the melting point is lowered by no less than 50 °C with respect to the non-substituted compound [13].

An even greater reduction in the melting point can be obtained by substitution of a hydroxyl group at the *ortho*- position of azo- and azoxybenzenes [14]. When the OH group is introduced in azo- and azoxybenzenes an intramolecular hydrogen bond is formed (*fig. 22*). Instead of the *ortho*-substitution causing steric hindrance, the *ortho*-substituted OH group is found to stabilize the molecule in a planar form by the formation of the six-membered rings shown. This substitution gives an extra contribution to the anisotropy of the polarizability. Some of the azo-compounds are found to have the desired low melting point (27°, 23° and even 8 °C), as well as a fairly high T_c.

Para-substitution

Azo- and azoxybenzenes with alkoxy groups at the *para*- position as end substituent were already well known [15] when we began our work on synthesis in this field. In particular, we found that the synthesis of azo- and azoxybenzenes terminally substituted by alkyl groups was a fruitful line of investigation. As can be seen in *Table II*, we obtained a fairly large number of compounds that combine a sufficiently high clearing point with a low melting point [16].

A high positive $\Delta\varepsilon$ was mostly obtained by substituting a cyano group at the *para*- position [17], since this group has a relatively large permanent dipole moment (13.5×10^{-30} Cm). We also thought that the isothiocyanato group (-NCS) might be a suitable substituent. Although the permanent dipole moment of

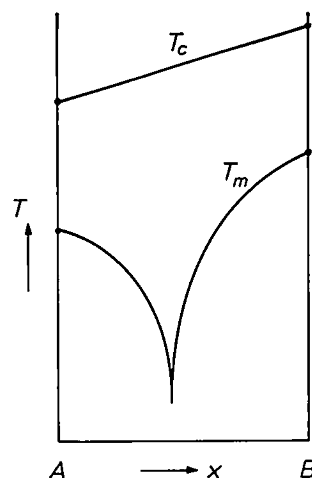

Fig. 21. To obtain a good temperature range it may be advantageous to use a mixture if this forms a eutectic with a relatively low melting point, as illustrated here. The clearing point T_c and the melting point T_m are shown as a function of the mixture ratio x of the components A and B.

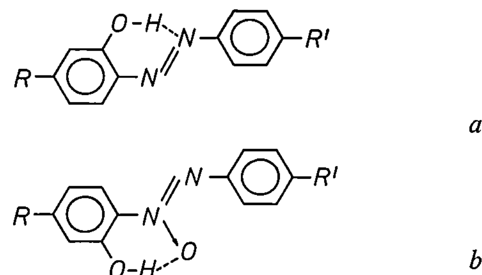

Fig. 22. The structure of an azobenzene (*a*) and an azoxybenzene (*b*) substituted with a hydroxyl group at the *ortho*- position. The dashed lines represent hydrogen bonds.

this group (9.6×10^{-30} Cm) is smaller than that of the cyano group, we hoped that the greater $\alpha_l - \alpha_t$ of the isothiocyanato group, compared with that of the cyano group, would give a good temperature range for the mesophase. This did not prove to be the case, however, and we obtained compounds with somewhat lower T_c values than that of corresponding cyano compounds[18]. This is probably because the isothiocyanato group has a larger molar volume than the cyano group (the sulphur atom in particular is rather large), and this, as can be seen from expression (4), leads to lower values of T_c.

Table I. Melting points T_m and clearing points T_c (in °C) of a number of Schiff's bases and azo- and azoxybenzenes, both substituted and non-substituted at the *ortho*- position, with the following molecular structures:

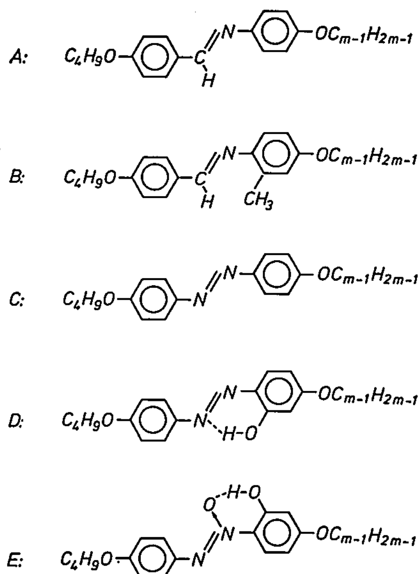

m	*A*		*B*		*C*		*D*		*E*	
	T_m	T_c	T_m	T_c	T_m	T_c	T_m	T_c	T_m	T_c
4					67	68	54	62	68	82
5					65	75	40	83	66	93
6					43	66	36	74	60	88
7	105	119	70	—	44	74	8	82	57	93
8	99	116	78	—			23	79	53	91
9	101	117	51	68			27	81	59	93

Table II. Melting points T_m and clearing points T_c (in °C) of a number of symmetrical dialkylazo- and azoxybenzenes, with the following structures:

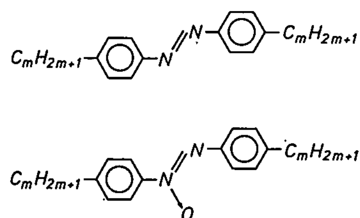

The clearing points indicated by an asterisk are transitions from the smectic to the isotropic phase.

m	Azobenzenes		Azoxybenzenes	
	T_m	T_c	T_m	T_c
3	81.5	30.5	65	60.5
4	28.5	−5	22	32
5	48.5	42	24	67.5
6	37	24	24	54.5
7	40	47	34	71
8	47.5	41.5	39	67
9	37	52.5*	45	76.5*
10	42	53 *	50	76 *

Substitution in the bridging group

The bridging group is a suitable position for the introduction of substituents with a large permanent dipole moment perpendicular to the long molecular axis, since substitution at this position does not generally broaden the molecule very much.

Schiff's bases, which have a hydrogen atom in the bridging group, seemed in principle to be suitable for a substitution of this type. However, the results of introducing a cyano group in this way were not very satisfactory [19]. This is because the permanent dipole moment of the cyano group is to a large extent compensated by that of the bridging group of the Schiff's base.

This result suggested that compounds such as the stilbenes, which have a non-polar bridging group with two hydrogen atoms, could be of interest [20]. We have in fact succeeded in synthesizing compounds in this category with a large negative $\Delta\varepsilon$ [21]. A promising compound, for example, is:

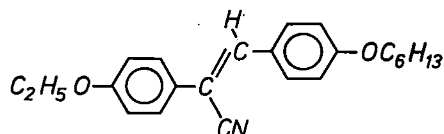

This compound has a $\Delta\varepsilon$ of −5.5, and admixture with a compound of the same type having C_4H_9O and C_7H_{15} as end substituents yields a temperature range of 8-42 °C.

[13] Further details are given in J. van der Veen and A. H. Grobben, Mol. Cryst. liq. Cryst. 15, 239, 1971.
[14] Further details are given in J. van der Veen and Th. C. J. M. Hegge, Angew. Chemie 86, 378, 1974.
[15] See H. Arnold, Z. phys. Chemie **226**, 146, 1964, and R. Steinsträsser and L. Pohl, Z. Naturf. **26 b**, 577, 1971.
[16] A more detailed treatment can be found in J. van der Veen, W. H. de Jeu, A. H. Grobben and J. Boven, Mol. Cryst. liq. Cryst. 17, 291, 1972. See also J. van der Veen, W. H. de Jeu, M. W. M. Wanninkhof and C. A. M. Tienhoven, J. phys. Chem. 77, 2153, 1973.
[17] See G. W. Gray, K. J. Harrison and J. A. Nash, Electronics Lett. 9, 130, 1973.
[18] Further details are given in J. van der Veen, J. Physique **37**, C3-13, 1976.
[19] See also J. van der Veen and W. H. de Jeu, Mol. Cryst. liq. Cryst. 27, 251, 1974.
[20] See W. R. Young, A. Aviram and R. J. Cox, J. Amer. Chem. Soc. 94, 3976, 1972.
[21] See also W. H. de Jeu and J. van der Veen, Phys. Lett. **44A**, 277, 1973.

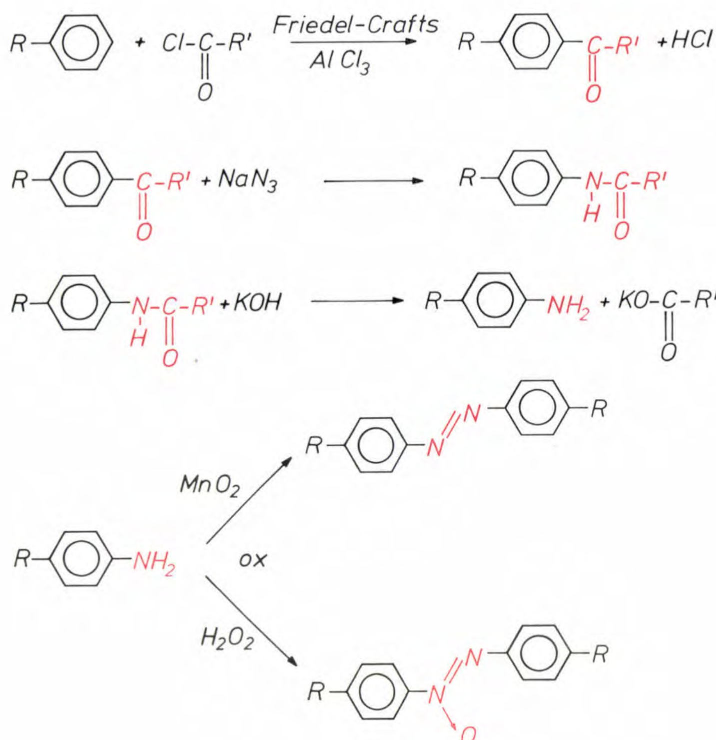

Fig. 23. Reaction scheme for the synthesis of dialkylazo- and azoxybenzenes, with each newly substituted or newly formed group indicated in red.

Chemical aspects of some syntheses

Ortho-substitution

In the synthesis of azoxybenzenes the problem of *selectivity* enters into the picture. A synthesis is selective when the desired compound alone is produced, free from other substances such as isomers. In syntheses of the type described above various types of undesired isomers can be produced. When it is desired to substitute a molecule at the *para-* position *ortho-* or *meta-*substituted molecules may also be produced. In asymmetric molecules like the azoxybenzenes, an isomer may also be formed whose end substituents are interchanged with respect to the (asymmetric) bridging group.

The undesirability of the occurrence of isomers has already been illustrated by the example in fig. 20. To obtain the maximum positive $\Delta\varepsilon$ it would have been necessary to synthesize the isomer *II* selectively.

Azoxybenzenes are generally synthesized by oxida-

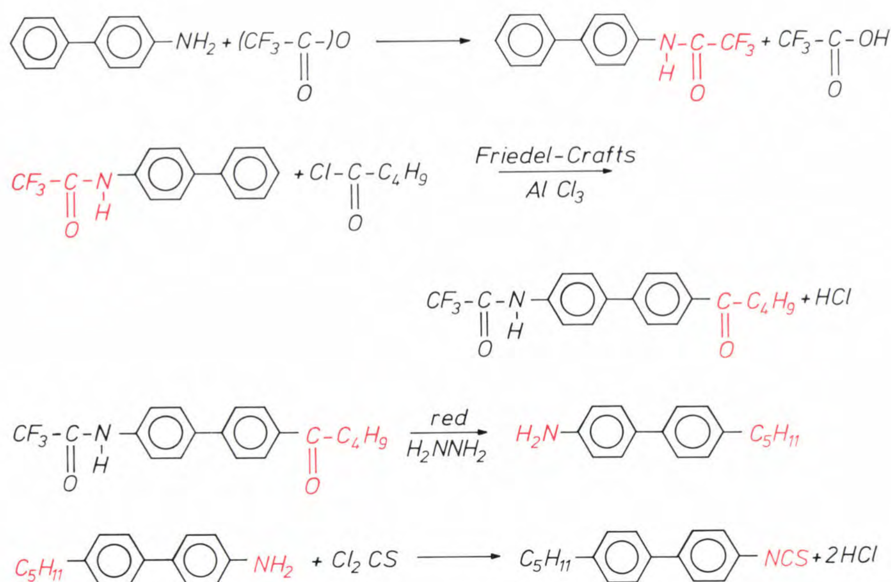

Fig. 24. Reaction scheme for the synthesis of *p*-pentyl-*p*′-isothiocyanatobiphenyl.

tion of the corresponding azobenzenes. In this process the oxygen atom of the azoxy group may attach itself to either of the two nitrogen atoms of the azo group:

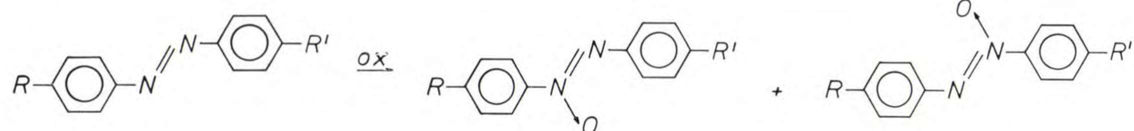

giving in effect two compounds for which the end groups are interchanged.

Compounds with a hydroxyl group substituted at the *ortho-* position represent a special case (fig. 22*b*). The hydrogen atom here has the effect of screening off one of the nitrogen atoms, so that the oxidation can only take place at the other nitrogen atom and the synthesis is completely selective.

Para- substitution

To synthesize the symmetrical dialkylazo- and dialkylazoxybenzenes (Table II) the obvious method is to start with aniline ($C_6H_5NH_2$), then to substitute the desired alkyl group at the *para-* position of aniline, and finally to obtain the required azobenzene or azoxybenzene by oxidation:

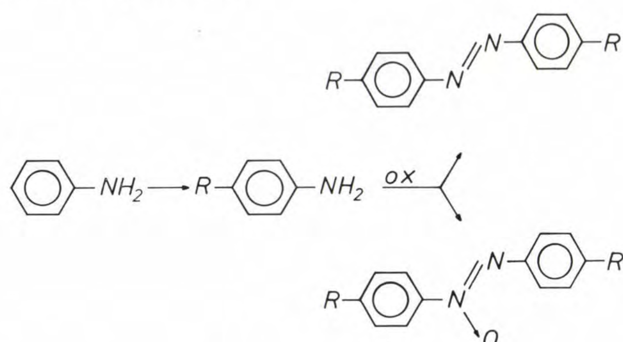

There are two difficulties here. The first, and the less serious, is that in addition to the desired alkylation at the *para-* position, there would also be alkylation at the *ortho-* position. There is a standard method of avoiding this unwanted side-effect, and that is to use the Friedel-Crafts method of acylation [16]; see fig. 23.

The second difficulty in introducing the alkyl substituent is the presence of the highly reactive NH_2 group in the molecule, which would also be substituted if no special precautions were taken. In cases like this the required substitution would therefore have to be preceded by steps to screen off the reactive group. We shall give below an example of a synthesis with this temporary screening.

In the synthesis that we carried out, illustrated in *fig. 23*, we adopted a different approach, which avoided the need for screening by initially excluding the reactive NH_2 group. There is then no great problem in carrying out the desired substitution of the alkyl group. The NH_2 group is then subsequently introduced with the aid of the compound sodium azide (NaN_3).

Also of interest is the last step of the synthesis. Depending on the oxidizing agent used, hydrogen peroxide (H_2O_2) or activated manganese dioxide (MnO_2), the azo- or the azoxybenzene is obtained. In this case no selectivity is required for the oxidation to azoxybenzene, since we are concerned here with symmetrically substituted compounds.

Fig. 24 gives the reaction scheme for a compound that we have synthesized with a *para*-substituted isothiocyanato group: *p*-pentyl-*p'*-isothiocyanatobiphenyl. In this synthesis the presence of the reactive NH_2 group makes temporary screening with a $COCF_3$ group necessary. Here again the Friedel-Crafts method of acylation was used to obtain exclusively *para*-substituents.

Substitution in the bridging group

Finally, *fig. 25* gives an example of a very simple and completely selective substitution in the bridging group, consisting in the introduction of a cyano group into the bridging group of a stilbene.

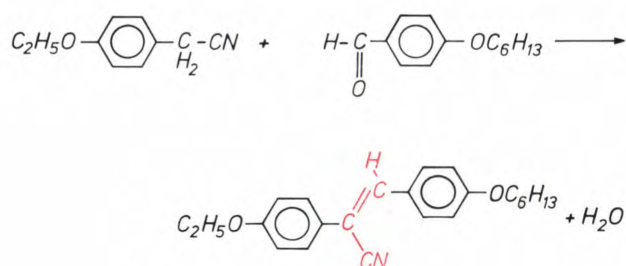

Fig. 25. Reaction scheme for the synthesis of *p*-ethoxy-*p'*-hexyloxy-α-cyano-*trans*-stilbene.

Appendix A. Maier and Saupe's theory on the nematic phase

The theory due to W. Maier and A. Saupe [6] starts from the assumption that the nematic order is based on the dispersion forces or London-Van der Waals forces between the molecules, i.e. the forces that exist between two molecules because they are able to 'polarize one another' (*fig. A1*). The tendency towards orientation is then a consequence of the fact that the energy gain is greatest on polarization in the 'easy' (longitudinal) direction. In this theory there is assumed to be no other cause of orientation. No account is taken of the elongated shape of the molecules, which certainly does have an effect in reality. In discussing this

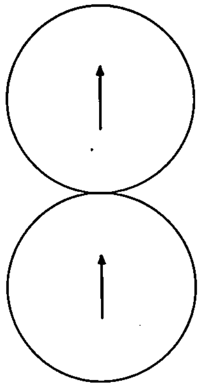

Fig. A1. Two molecules that polarize each other. This leads to the well known London-Van der Waals attraction, but in the case of anisotropic polarizabilities it also leads to a tendency towards orientational order.

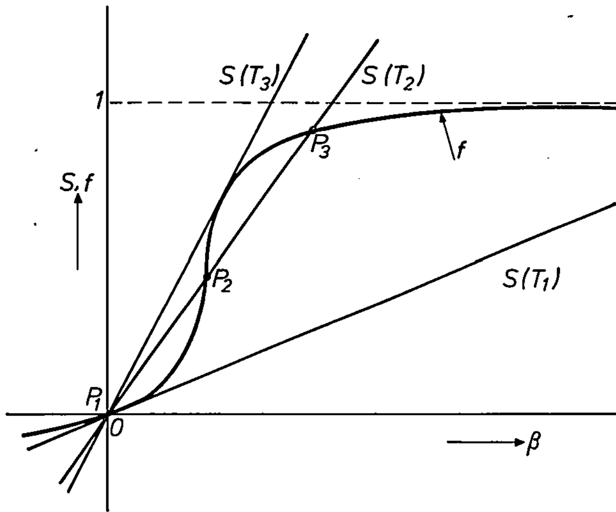

Fig. A2. The curve $f(\beta)$ and the straight lines $S(\beta) = (kT/A)\beta$ for various temperatures; $\beta = AS/kT$. At the temperature T_2 the solution P_1 corresponds to the isotropic phase, P_3 to the nematic phase; P_2 is not stable. Below T_1, where the straight line is tangential to the curve at P_1, the isotropic phase is no longer stable; above T_3, where the straight line is tangential to the curve at the upper bend, the nematic solution no longer exists.

theory it is appropriate to think of spherical molecules with an anisotropically polarizable centre. The 'axis' of a molecule is considered to be the direction of greatest polarizability.

As in the Weiss theory of ferromagnetism the influence of the surrounding molecules on the molecule is described by a 'molecular field'. This field is due to the order of the environment; its strength is proportional to the order parameter S, defined as

$$S = \langle \tfrac{3}{2}\cos^2\theta - \tfrac{1}{2} \rangle. \qquad \text{(A1)}$$

Here θ is the angle between the long axis of a molecule and the director; the brackets indicate averaging over the molecules. Defined in this way, S is indeed equal to zero in the absence of orientational order (isotropic phase, $\langle\cos^2\theta\rangle = \frac{1}{3}$) and equal to 1 for the hypothetical case of perfect order ($\langle\cos^2\theta\rangle = 1$). The potential energy W_i of the molecule i in the 'molecular field' is:

$$W_i = -AS(\tfrac{3}{2}\cos^2\theta_i - \tfrac{1}{2}). \qquad \text{(A2)}$$

W_i has a minimum for $\theta_i = 0$. In orientation, the molecule i is thus situated in a 'potential well' of depth proportional to S. (We shall come back to the factor A later.) The statistical behaviour of molecule i thus depends on S. Conversely, S can be calculated from the statistical behaviour of molecule i, since statistically all the molecules behave identically. To be more exact, S must be equal to the statistical mean of $\frac{3}{2}\cos^2\theta_i - \frac{1}{2}$ over the states of molecule i during its thermal motion in the potential well (A2), for a given value of the parameter S. Calculation of this statistical mean amounts in effect to weighting the *a priori* probability of each orientation by a Boltzmann factor $\exp(-W_i/kT)$. The variable θ_i disappears in the averaging process, and the result is a function of AS/kT only:

$$\langle \tfrac{3}{2}\cos^2\theta_i - \tfrac{1}{2} \rangle = f(\beta), \quad \beta = AS/kT.$$

The quantity $f(\beta)$ plotted as a function of β is S-shaped; this is shown greatly exaggerated in *fig. A2.* This reasoning leads to an implicit equation for S

$$S = f(AS/kT).$$

For a given temperature the value of S is thus found in fig. A2 by taking the intersection of the curve $f(\beta)$ with the straight line $S = (kT/A)\beta$, whose slope is proportional to T. The solution is stable only if the straight line is steeper than the curve at the point of intersection. At the temperature T_2 we therefore find an isotropic phase (P_1, $S = 0$) and a nematic phase (P_3, $S \neq 0$); the solution P_2 is not stable. Stable solutions are only possible in the temperature range from T_1 to T_3 (see fig. A2); below this range the isotropic phase is not stable, above it the nematic phase is not a solution of the problem.

Of the two solutions in the temperature range $T_1 \rightarrow T_3$, the one for which the free energy, $F = U - T\Sigma$, is smallest is the *thermodynamically stable* solution, and the clearing point T_c lies where $F_{\text{nematic}} - F_{\text{isotropic}}$ is zero. The internal energy $U (= \langle W_i \rangle)$ and the entropy Σ for both phases, and hence T_c as well, can be calculated in this model. The result is:

$$kT_c = 4.54A, \quad S(T_c) = 0.43. \qquad \text{(A3)}$$

Assuming that the dispersion forces between the molecule i and all the surrounding molecules are responsible for the 'molecular field', we find the following approximate value for the constant A in (A2) by a quantum-mechanical calculation [7]:

$$A = \frac{1}{540}\,\frac{(\alpha_l - \alpha_t)^2}{\varepsilon_0^2 V^2}\,I. \qquad \text{(A4)}$$

It is assumed in this calculation that the centres of mass of the molecules lie in a spherically symmetrical distribution around the molecule being considered. It is also assumed that the jumps in molecular energy that are relevant to the polarizations lie in a single narrow band (at the value I). These are the main approximations used in the calculation. The factor V^2 in the denominator is directly connected with the marked decrease in the dispersion forces ($\propto R^{-6}$) with increasing distance (R) between the polarizable centres.

Substituting (A4) in (A3) gives equation (4) on page 138.

Appendix B. Maier and Meier's theory on the dielectric constant

The theory due to W. Maier and G. Meier is an extension to nematics of the Lorentz-Debye-Onsager theory [9] for the polarization of isotropic matter. In the Lorentz-Debye-Onsager theory the molecules surrounding a given molecule are represented by a continuum of dielectric constant ε; the molecule considered is situated in a spherical cavity in the continuum. The quantities h and F in equations (5) and (6) are directly related to the fields encountered in this cavity under various conditions.

We shall first consider polarizable molecules with no permanent dipole moment ($\alpha \neq 0$, $\mu = 0$). The polarization is

$$P_\alpha = N\alpha E_i, \qquad \text{(B1)}$$

where E_i is the 'internal field' to which the molecule is subject in the cavity, i.e. the field found in the cavity when the charge distribution of the surroundings is first fixed and the molecule is then

removed (*fig. B1a*). This Lorentz field, as it is called, is given by:

$$E_{\mathrm{i}} = \frac{\varepsilon + 2\varepsilon_0}{3\varepsilon_0} E. \tag{B2}$$

It differs from the 'cavity field' E_c that is found when the surrounding environment is allowed to readapt after the molecule has been removed (fig. B1*b*). This field E_c is given by:

$$E_{\mathrm{c}} = hE, \quad h = \frac{3\varepsilon}{2\varepsilon + \varepsilon_0}. \tag{B3}$$

On applying the formal relation

$$P = (\varepsilon - \varepsilon_0)\, E, \tag{B4}$$

equations (B1) and (B2) give the Clausius-Mossotti equation:

$$\frac{\varepsilon - \varepsilon_0}{\varepsilon + 2\varepsilon_0} = \frac{N\alpha}{3\varepsilon_0}. \tag{B5}$$

If the molecule also has a permanent dipole moment μ, the situation is much more complicated. The mean contribution of a molecule to the polarization now consists of two parts. First there is the mean *induced moment:*

$$p = \alpha E_{\mathrm{i}}, \tag{B6}$$

where E_i is again the field found in the cavity when the charge distribution of the surroundings is first fixed and the whole molecule then removed (*fig. B2a*). The second part, the mean *permanent dipole moment*, is determined by Boltzmann statistics for a permanent dipole in the field to which it is subjected:

$$\overline{\mu} = \frac{\mu^2}{3kT} E_{\mathrm{d}}. \tag{B7}$$

L. Onsager showed that E_d in (B7) should not be identified with the internal field E_i, since E_i contains a component that is not relevant to the Boltzmann statistics of the dipole. This part of the field is known as the *reaction field* R, the field that the dipole itself excites in the cavity through its polarization of the surrounding environment; it is always parallel to μ and does not therefore have any orientational effect on μ.

Direct calculation of the reaction field R of a non-polarizable dipole in a spherical cavity of radius a gives:

$$R = f\mu, \quad f = \frac{1}{4\pi\varepsilon_0 a^3}\,\frac{2\varepsilon - 2\varepsilon_0}{2\varepsilon + \varepsilon_0}. \tag{B8}$$

For the reaction field of a polarizable dipole we must have

$$R = f(\mu + \alpha R),$$

and therefore

$$R = fF\mu, \quad F = (1 - f\alpha)^{-1}. \tag{B9}$$

The internal field is therefore composed of the mean reaction field and the 'directing' field E_d in (B7):

$$E_{\mathrm{i}} = E_{\mathrm{d}} + \overline{R} = E_{\mathrm{d}} + fF\overline{\mu}. \tag{B10}$$

The directing field E_d can be determined by a hypothetical experiment in which the permanent dipole in fig. B2*a* is removed and the environment and the induced dipole are allowed to readapt (fig. B2*b*). The reaction field is thus removed and E_d remains. If the induced dipole is now removed as well and the environment is again allowed to readapt (fig. B2*c*), then the cavity field E_c is obtained (B3). It follows that the difference between E_d and E_c is the reaction field of the induced dipole αE_d of fig. B2*b*:

$$E_{\mathrm{d}} = E_{\mathrm{c}} + f\alpha E_{\mathrm{d}},$$

and hence

$$E_{\mathrm{d}} = FE_{\mathrm{c}} = FhE. \tag{B11}$$

The equations (B6), (B7), (B10) and (B11) can now be combined to give an expression for the total polarization $N(p + \overline{\mu})$ in terms of E. Together with (B4) this yields Onsager's result:

$$\varepsilon - \varepsilon_0 = NhF(\alpha + F\frac{\mu^2}{3kT}). \tag{B12}$$

The quantities h and F are themselves combinations of ε and α, while in addition F contains the radius a of the cavity. This radius is usually chosen in such a way that the volume of the cavity is equal to the volume available per molecule:

$$4\pi a^3/3 = 1/N. \tag{B13}$$

Maier and Meier's theory for anisotropic molecules [10] links up closely with that of Onsager. Here again it is assumed that the molecule is contained in a spherical cavity in a continuum. In addition the anisotropy of ε and α is not taken into account in the correction factors h, f and F. The general pattern of the calculation is as follows.

Let us consider a molecule whose longitudinal axis l (the direction of easy polarization) makes an angle θ with the director (along the z-axis); see *fig. B3*. We assume that a field E acts on the molecule in the z-direction. To find the *induced dipole moment* in the z-direction we first have to resolve E into its components along the l- and t-axes, and the components in the z-direction of the resultant induced moments must then be summed. This gives:

$$< p_{||} > = (\alpha_l \cos^2\theta + \alpha_t \sin^2\theta)\, E.$$

Taking the mean over the orientation of all the molecules gives

$$p_{||} = [\overline{\alpha} + \tfrac{2}{3}(\alpha_l - \alpha_t)S]E, \tag{B14}$$

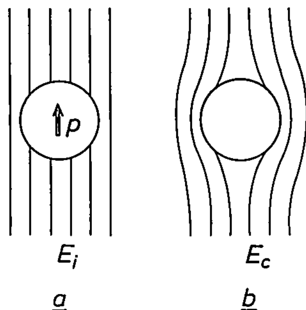

Fig. B1. Internal field E_i and cavity field E_c. *a*) E_i is the field that is found in the cavity when first the charge distribution of the environment is fixed and the molecule is then removed; E_i determines the induced dipole moment. *b*) When the environment is allowed to readapt after removal of the molecule, the 'cavity field' E_c arises.

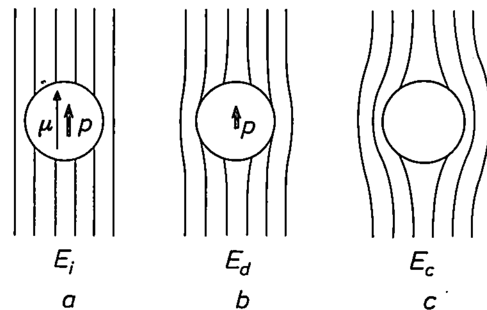

Fig. B2. Internal field E_i, directing field E_d and cavity field E_c. *a*) E_i is obtained by first fixing the environment and then removing the molecule. *b*) E_d is obtained by first removing the permanent dipole, then fixing the environment and finally removing the molecule. *c*) Readaptation of the environment to the empty cavity again gives E_c.

where

$$\bar{\alpha} = \tfrac{1}{3}(\alpha_l + 2\alpha_t).$$

Equation (A1) has been used here to express $\langle\cos^2\theta\rangle$ and $\langle\sin^2\theta\rangle$ in terms of S.

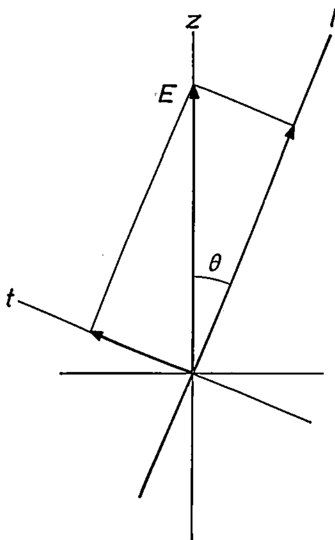

Fig. B3. The long axis l of the molecule is assumed to be at an angle θ to the preferred direction z. To calculate $\varepsilon_{||}$ an electric field $\boldsymbol{E}$ is applied in the z-direction.

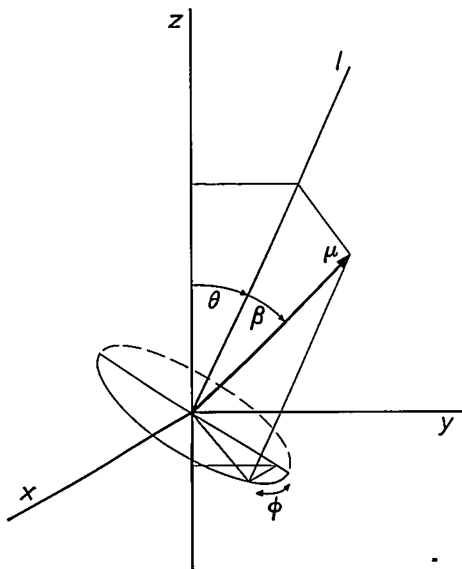

Fig. B4. Calculation of the component in the preferred direction z of the permanent dipole $\boldsymbol{\mu}$; β is the angle between the permanent dipole and the long axis l.

For the contribution of the *permanent dipole moment* of the molecule in a particular orientation (see *fig. B4*) to the dipole moment in the z-direction we find:

$$\mu_{||} = \mu\cos\beta\cos\theta + \mu\sin\beta\sin\phi\sin\theta.$$

We must now calculate the mean value of $\mu_{||}$ in the presence of both the electric field as well as the 'nematic potential' W (eq. A2). The first averageing process is indicated, just as in the isotropic case, by a bar, and the second, as in Appendix A, by brackets. For the potential energy U of the dipole in the electric field we have: $U = -\boldsymbol{\mu}.\boldsymbol{E}$. In the usual linear approximation:

$$\exp\{-(U + W)/kT\} = (1 - U/kT)\exp(-W/kT),$$

we find:

$$\langle\bar{\mu}_{||}\rangle = \langle\mu_{||}(1 + \mu_{||}E/kT)\rangle = \langle\mu_{||}^2\rangle\, E/kT. \qquad \text{(B15)}$$

With $\langle\sin^2\phi\rangle = \tfrac{1}{2}$, and again using (A1), we find:

$$\langle\mu_{||}^2\rangle = \tfrac{1}{3}\mu^2\,[1 + (3\cos^2\beta - 1)S].$$

Now bearing in mind, as in Onsager's approach, that the field in (B14) is an internal field and that the field in (B15) is a directing field, we find:

$$\varepsilon_{||} - \varepsilon_0 = NhF\left[\bar{\alpha} + \tfrac{2}{3}(\alpha_l - \alpha_t)S + F\frac{\mu^2}{3kT}\{1 + (3\cos^2\beta - 1)S\}\right],$$

and, similarly:

$$\varepsilon_{\perp} - \varepsilon_0 = NhF\left[\bar{\alpha} - \tfrac{1}{3}(\alpha_l - \alpha_t)S + F\frac{\mu^2}{3kT}\{1 - \tfrac{1}{2}(3\cos^2\beta - 1)S\}\right].$$

With $\bar{\varepsilon} = \tfrac{1}{3}(\varepsilon_{||} + 2\varepsilon_{\perp})$ and $\Delta\varepsilon = \varepsilon_{||} - \varepsilon_{\perp}$ the equations (5) and (6) then follow.

Summary. In the liquid-crystalline phase exhibited by many organic compounds with elongated molecules ('mesogenic' compounds) — which lies on the temperature scale between the solid and the isotropic-liquid phase — the compound is liquid but also anisotropic in quantities such as the dielectric constant ε and the refractive index n. In *nematic* liquid crystals, the main subject of the article, neighbouring molecules have their long axes parallel, except for deviations due to thermal fluctuations; the director gives the mean local direction. By setting appropriate boundary conditions thin 'homeotropic' and 'uniform-planar' layers, with a uniform director pattern, and also 'twisted-planar' layers can be obtained. Because ε is anisotropic a voltage applied across the layer can change the director pattern ('Frederiks transition'), resulting for example in a change from transparent to opaque of a twisted-planar layer between crossed polarizers. For digital displays in watches and pocket calculators this is currently the most important effect.

Our research on liquid crystals has been aimed primarily at establishing relations between the molecular structure of a mesogenic compound and its physical properties. The article above deals in particular with the effect of the molecular structure on the clearing point and the dielectric properties of the nematic phase. Mesogenic compounds of four types — azo- and azoxybenzenes, Schiff's bases and stilbenes — are taken to illustrate how the theoretical knowledge obtained has made it possible to synthesize compounds suitable for practical applications. Some interesting chemical aspects of some of the syntheses are also discussed.

Recent scientific publications

These publications are contributed by staff of laboratories and plants which form part of or cooperate with enterprises of the Philips group of companies, particularly by staff of the following research laboratories:

Philips Research Laboratories, Eindhoven, The Netherlands	*E*
Philips Research Laboratories, Redhill, Surrey, England	*M*
Laboratoires d'Electronique et de Physique Appliquée, 3 avenue Descartes, 94450 Limeil-Brévannes, France	*L*
Philips GmbH Forschungslaboratorium Aachen, Weißhausstraße, 51 Aachen, Germany	*A*
Philips GmbH Forschungslaboratorium Hamburg, Vogt-Kölln-Straße 30, 2000 Hamburg 54, Germany	*H*
MBLE Laboratoire de Recherches, 2 avenue Van Becelaere, 1170 Brussels (Boitsfort), Belgium	*B*
Philips Laboratories, 345 Scarborough Road, Briarcliff Manor, N.Y. 10510, U.S.A. (by contract with the North American Philips Corp.)	*N*

Reprints of most of these publications will be available in the near future. Requests for reprints should be addressed to the respective laboratories (see the code letter) or to Philips Research Laboratories, Eindhoven, The Netherlands.

J. R. A. Beale & J. A. G. Slatter: The f_T of bipolar transistors with thin lightly doped bases.
Solid-State Electronics **19**, 549-556, 1976 (No. 7). *M*

L. K. H. van Beek: Special properties of physical development processes.
Photogr. Sci. Engng. **20**, 88-91, 1976 (No. 2). *E*

N. M. Beekmans & L. Heyne: Correlation between impedance, microstructure and composition of calcia-stabilized zirconia.
Electrochim. Acta **21**, 303-310, 1976 (No. 4). *E*

V. Belevitch: Dissipative two-ports with small attenuation.
Arch. Elektronik & Übertragungst. (AEÜ) **30**, 153-156, 1976 (No. 4). *B*

C. Belouet: Crystal defects and electro-optical properties of D-KDP.
Rev. Phys. appl. **11**, 253-262, 1976 (No. 2). *L*

L. Benguigui (Technion-Israel Institute of Technology, Haifa) **& K. Bethe:** Diffused phase transitions in $Ba_xSr_{1-x}TiO_3$ single crystals.
J. appl. Phys. **47**, 2787-2791, 1976 (No. 7). *H*

R. Bernard*, W. Rey, H. Vainsel*, M. Demeester*, E. Musoglu* & B. Douny* (* Hôpital St. Pierre, Brussels): Orientations de l'informatique dans l'unité coronarienne.
Ann. Cardiol. Angéiol. **25**, 7-11, 1976 (No. 1). *B*

F. Berz & H. K. Kuiken: Theory of lifetime measurements with the scanning electron microscope: steady state.
Solid-State Electronics **19**, 437-445, 1976 (No. 6). *M*

R. N. Bhargava, P. M. Harnack, S. P. Herko, P. C. Mürau & R. J. Seymour: Thermally stimulated current measurements in Cu and O-doped GaP.
J. Luminescence **12/13**, 515-519, 1976. *N*

M. Binet, B. Kramer & M. Parisot: Characterization and applications of gallium arsenide MESFETs.
Microwave Syst. News **6**, No. 2, 82-83, 85-86, 88-89, 1976. *L*

G. Bioul, M. Davio & J. J. Quisquater: A computation scheme for an adder modulo $(2^n - 1)$.
Digital Processes **1**, 309-318, 1975 (No. 4). *B*

D. Bois: Dispositif pour la mesure de l'absorption optique à 10,6 μm.
Rev. Phys. appl. **11**, 293-298, 1976 (No. 2). *L*

P. Bonhomme, A. Beorchia, B. Meunier (all with Faculté des Sciences, Rheims), **F. Dumont & D. Rossier:** Incoherent reading light tests of a Pockels-effect imaging device used in an 'in-line' optical processor of microscopical electron images.
Optik **45**, 159-167, 1976 (No. 2). *L*

R. Boom, F. R. de Boer (both with University of Amsterdam) **& A. R. Miedema:** On the heat of mixing of liquid alloys, I, II.
J. less-common Met. **45**, 237-245, 1976 (No. 2), & **46**, 271-284, 1976 (No. 2). *E*

J. van den Boomgaard, A. M. J. G. van Run & J. van Suchtelen: Magnetoelectricity in piezoelectric-magnetostrictive composites.
Ferroelectrics **10**, 295-298, 1976 (No. 1/2/3/4). *E*

O. Boser: The influence of Zener pairs on the temperature dependent component of the critical flow stress of silver based solid solution crystals.
Acta metall. **24**, 439-443, 1976 (No. 5). *N*

G. Bouchier (Faculté de chirurgie dentaire de Paris V) **& V. Chalmeton:** Expériences préliminaires de radioscopie télévisée en odontologie.
Rev. Odonto-stomatologie **5**, 119-125, 1976 (No. 2). *L*

P. W. J. M. Boumans: Einige Überlegungen zur Situation der simultanen Multielementanalyse von Lösungen.
Z. anal. Chemie **279**, 1-16, 1976 (No. 1). *E*

P. W. J. M. Boumans: Corrections for spectral interferences in optical emission spectrometry with special reference to the RF inductively coupled plasma.
Spectrochim. Acta **31B**, 147-152, 1976 (No. 3). *E*

J.-P. Boutot & J.-C. Delmotte: Photomultiplicateurs multianode à microcanaux pour localisation et comptage de photons.
Onde électr. **56**, 59-68, 1976 (No. 2). *L*

A. Bril & A. W. de Jager-Veenis: Quantum efficiency standard for ultraviolet and visible excitation.
J. Electrochem. Soc. **123**, 396-398, 1976 (No. 3). *E*

J. W. Broer: Een experiment in confereren.
Ned. T. Natuurk. **42**, 19, 1976 (No. 2). *E*

H. H. Brongersma & T. M. Buck (Bell Laboratories, Murray Hill, N.J.): Neutralisation behavior in scattering of low energy ions from solid surfaces.
Nucl. Instr. Meth. **132**, 559-564, 1976. *E*

H. H. Brongersma, N. Hazewindus, J. M. van Nieuwland, A. M. M. Otten & A. J. Smets: Angular-dependent Ne^+-ion scattering from a solid Au target.
J. Vac. Sci. Technol. **13**, 670-675, 1976 (No. 3). *E*

H. H. Brongersma & J. B. Theeten: The structure of oxygen adsorbed on Ni(001) as determined by ion scattering spectroscopy.
Surface Sci. **54**, 519-524, 1976 (No. 2). *E*

P. C. M. N. Bruijs (Philips Lighting Division, Eindhoven): Detectie en meting van lekken in hermetisch gesloten voorwerpen met krypton-85.
Ned. T. Vacuümtechniek **14**, 1-9, 1976 (No. 1).

A. L. J. Burgmans & J. P. Woerdman: Selective reflection from sodium vapour at low densities.
J. Physique **37**, 677-681, 1976 (No. 6). *E*

K. H. J. Buschow & M. Brouha: Narrow Bloch walls in the RCo_5-type rare-earth–cobalt compounds.
J. appl. Phys. **47**, 1653-1656, 1976 (No. 4). *E*

K. H. J. Buschow & A. M. van Diepen: Effect of hydrogen absorption on the magnetic properties of YFe_2 and $GdFe_2$.
Solid State Comm. **19**, 79-81, 1976 (No. 1). *E*

K. H. J. Buschow & W. W. v. d. Hoogenhof: Magnetic properties and phase relationships of gadolinium-gallium compounds.
J. less-common Met. **45**, 309-313, 1976 (No. 2). *E*

K. H. J. Buschow, F. A. Kuijpers, A. R. Miedema & H. H. van Mal: Hydrogen in rare earth intermetallics.
Proc. 11th Rare Earth Res. Conf., Traverse City, Michigan, 1974, Vol. 1, pp. 417-429. *E*

K. H. J. Buschow & C. J. Schinkel (University of Amsterdam): Magnetic properties of GdMg.
Solid State Comm. **18**, 609-612, 1976 (No. 5). *E*

K. L. Bye: High birefringence PLZT materials for low voltage displays.
Ferroelectrics **10**, 29-33, 1976 (No. 1/2/3/4). *M*

K. L. Bye, P. W. Whipps, E. T. Keve & M. R. Josey (Mullard Ltd., Southampton): Triglycine sulphate/selenate solid solutions for pyroelectric applications.
Ferroelectrics **11**, 525-534, 1976 (No. 3/4). *M*

T. A. C. M. Claasen: Quantisation-noise analysis of digital filters with controlled quantisation.
Electronics Letters **12**, 46-48, 1976 (No. 2). *E*

T. A. C. M. Claasen, W. F. G. Mecklenbräuker & J. B. H. Peek: A survey of quantization and overflow effects in recursive digital filters.
Proc. 1976 IEEE Int. Symp. on Circuits and systems, Munich, pp. 621-624. *E*

M. G. Collet: The influence of bulk traps on the charge-transfer inefficiency of bulk charge-coupled devices.
IEEE J. **SC-11**, 156-159, 1976 (No. 1). *E*

J. P. M. Damen: Measurement of growth rate and nucleation temperature of flux-grown $YbFeO_3$.
J. Crystal Growth **33**, 266-270, 1976 (No. 2). *E*

J. E. Davies: The surface tension of Bi_2O_3-based fluxes used for the growth of magnetic garnet films.
J. Mat. Sci. **11**, 976-979, 1976 (No. 5). *M*

P. Delsarte: Association schemes and *t*-designs in regular semilattices.
J. combin. Theory A **20**, 230-243, 1976 (No. 2). *B*

A. M. van Diepen, F. K. Lotgering & J. F. Olijhoek: Effect of small variations of the Fe/Cr ratio on the ^{57}Fe Mössbauer spectra of $FeCr_2S_4$.
J. Magnetism and magn. Mat. **3**, 117-119, 1976 (No. 1/2). *E*

J. A. W. van der Does de Bye: Dependence of recombination in *p*-type GaP(Zn,O) on dopant concentrations.
J. Electrochem. Soc. **123**, 544-551, 1976 (No. 4). *E*

R. J. Dolphin, F. W. Willmott, A. D. Mills & L. P. J. Hoogeveen: Column switching techniques in the liquid chromatographic analysis of organochlorine pesticides in milk.
J. Chromatogr. **122**, 259-268, 1976. *M, E*

E. Dormann (Technische Hochschule Darmstadt) **& K. H. J. Buschow**: A comparative study of the hyperfine fields in ferromagnetic GdRh and GdZn.
J. appl. Phys. **47**, 1662-1667, 1976 (No. 4). *E*

J. P. Dougherty & S. K. Kurtz: A second harmonic analyser for the detection of non-centrosymmetry.
J. appl. Cryst. **9**, 145-158, 1976 (No. 2). *N*

C. Ducot: Utilisation domestique des énergies solaire et terrestre.
Revue 2000 No. 35, 52-54; 1976. *L*

H. Duifhuis (Institute for Perception Research, Eindhoven): Cochlear nonlinearity and second filter: possible mechanism and implications.
J. Acoust. Soc. Amer. **59**, 408-423, 1976 (No. 2).

H. Durand: L'Europe de la recherche serait-elle en train de se faire?: I. La genèse, II. L'adolescence.
Revue Andès No. 15/16, 2-7, 1975, & No. 17/18, 24-30, 1976. *L*

H. Durand: L'enveloppe-recherche.
Revue Andès No. 17/18, 1, 1976. *L*

H. Durand, J. Michel, J.-J. Hunzinger & C. Hily: Periodically adjustable concentrators adapted to solar cell panels.
Rev. int. Héliotechnique 1er semestre 1976, 39-48. *L*

K. Eckrich, E. Dormann, A. Oppelt (all with Technische Hochschule Darmstadt) **& K. H. J. Buschow:** The hyperfine fields in ferromagnetic rare-earth zinc compounds with CsCl structure.
Z. Physik B **23**, 157-171, 1976 (No. 2). *E*

L. D. J. Eggermont: A single-channel PCM coder with companded DM and bandwidth-restricting digital filtering.
IEEE 1975 Int. Conf. on Communications (ICC75), San Francisco, Vol. III, pp. 40.2-40.6. *E*

J. B. A. A. Elemans (Kamerlingh Onnes Laboratory, Leiden) **& K. H. J. Buschow:** Magnetic structures of $Th(Fe_{1-x}Co_x)_5$ and Th_2Fe_{17}.
Phys. Stat. sol. (b) **57**, K 155-157, 1973 (No. 2). *E*

J. B. A. A. Elemans (Kamerlingh Onnes Laboratory, Leiden) **& K. H. J. Buschow:** The magnetic structure of Tm_2Fe_{17}.
Phys. Stat. sol. (a) **24**, K 125-127, 1974 (No. 2). *E*

J. B. A. A. Elemans (Netherlands Reactor Centre, Petten) **& K. H. J. Buschow:** Comment on the crystal and magnetic structures of $CaCu_5$-type compounds of Th with Fe, Co, and Ni.
Phys. Stat. sol. (a) **34**, 355-359, 1976 (No. 1). *E*

J. B. A. A. Elemans (Netherlands Reactor Centre, Petten), **P. C. M. Gubbens** (Inter-university Reactor Institute, Delft) **& K. H. J. Buschow:** On the interpretation of Mössbauer-effect and diffraction measurements on rare earth - iron compounds of the type R_2Fe_{17}.
J. less-common Met. **44**, 51-62, 1976. *E*

G. Eschard, A. Pelissier, J. Paulin & J. F. Bonnal: Experimental studies of a linear strip cesium contact ion thruster.
J. Spacecraft & Rockets **13**, 193-197, 1976 (No. 4). *L*

H. A. van Essen: I^2L and its application in a digital data transmitter.
Proc. 1976 IEEE Int. Symp. on Circuits and systems, Munich, pp. 735-738. *E*

V. H. C. M. Evers: ANS on-board software: functional integration as a key to unattended spacecraft operation.
J. Brit. Interplanetary Soc. **29**, 255-272, 1976 (No. 4). *E*

V. H. C. M. Evers: Operational experience with the ANS on-board computer.
J. Brit. Interplanetary Soc. **29**, 417-427, 1976 (No. 6). *E*

E. Fabre, Ngo-Tich-Phuoc, G. M. Martin & F. Ortega: γ-ray detection stability under total depletion in CdTe surface barrier detectors.
IEEE Trans. **NS-23**, 182-184, 1976 (No. 1). *L*

E. Fischer: Axial segregation of additives in mercury–metal-halide arcs.
J. appl. Phys. **47**, 2954-2960, 1976 (No. 7). *A*

E. Fogarassy, G. M. Martin & E. Fabre: Thermally stimulated current measurements on vapour-grown HgI_2.
Appl. Phys. **10**, 93-95, 1976 (No. 1). *L*

R.C. French: Radio propagation in London at 462 MHz.
Radio and electronic Engr. **46**, 333-336, 1976 (No. 7). *M*

R. C. French: Mobile radio data transmission in the urban environment.
IEEE 1976 Int. Conf. on Communications (ICC76), Philadelphia, pp. 27.15-27.20. *M*

G. Frens: Measurements with colloids.
Progr. Colloid & Polymer Sci. **59**, 27-32, 1976. *E*

P. Geittner, D. Küppers & H. Lydtin: Low-loss optical fibers prepared by plasma-activated chemical vapor deposition (CVD).
Appl. Phys. Letters **28**, 645-646, 1976 (No. 11). *A*

J.-M. Goethals: Nonlinear codes defined by quadratic forms over GF(2).
Information and Control **31**, 43-74, 1976 (No. 1). *B*

P. C. M. Gubbens (Inter-university Reactor Institute, Delft) **& K. H. J. Buschow:** Mössbauer effect study of $Tm_2Fe_{17-x}Co_x$ and $Tm_2Fe_{17-x}Ni_x$ compounds.
Phys. Stat. sol. (a) **34**, 729-735, 1976 (No. 2). *E*

F. E. L. ten Haaf & M. L. Verheijke: An improved gamma well counter for radioactive tracer applications.
Int. J. appl. Rad. Isot. **27**, 79-84, 1976 (No. 2). *E*

S. H. Hagen & A. W. C. van Kemenade: On the role of boron in the luminescence of silicon carbide doped with nitrogen and boron.
Phys. Stat. sol. (a) **33**, 97-105, 1976 (No. 1). *E*

J. Hasker: A new class of efficient low-pressure gas discharges with high radiation output per unit volume.
Appl. Phys. Letters **28**, 586-588, 1976 (No. 10). *E*

E. E. Havinga: Why are the close-packed structures of the noble metals cubic?
Physica **82B**, 277-287, 1976 (No. 2). *E*

N. Hazewindus: Toepasbaarheid van een computer-managed instructiesysteem in geïntegreerde vormen van voortgezet onderwijs.
Pedagog. Studiën **53**, 57-61, 1976. *E*

J. H. C. van Heuven: A new integrated waveguide-microstrip transition.
IEEE Trans. **MTT-24**, 144-147, 1976 (No. 3). *E*

B. Hill, J.-P. Krumme, G. Much, D. Riekmann & J. Schmidt: Fully operational write-read-write and random-access optical store.
J. appl. Phys. **47**, 3697-3701, 1976 (No. 8). *H*

B. Hill & K. P. Schmidt: The realization and technology of interfaces between optics and electronics in holographic memories.
Laser 75 Opto-electronics, Proc. Conf. Munich 1975, pp. 255-259; 1976. *H*

B. Hoekstra: Evidence for the stratification of epitaxial films of $Y_{2.85}La_{0.15}Fe_{3.75}Ga_{1.25}O_{12}$ from microwave resonance measurements.
Solid State Comm. **18**, 469-471, 1976 (No. 4). *E*

W. K. Hofker*, H. W. Werner, D. P. Oosthoek* & N. J. Koeman* (* Philips Research Labs., Amsterdam Division): Redistribution effects associated with sequential implantations.
Applications of ion beams to materials 1975, Proc. Conf. Coventry (Inst. Phys. Conf. Ser. No. 28), pp. 13-17; 1976. *E*

E. P. Honig: D.C. conduction in Langmuir-Blodgett films with various electrode materials.
Thin Solid Films **33**, 231-236, 1976 (No. 2). *E*

H. Howden & J. A. Clarke: Refracting replica aspheric optics.
Opt. Engng. **15**, 197-201, 1976 (No. 3). *M*

G. Jacob, R. Madar & J. Hallais: Optimized growth conditions and properties of *n*-type and insulating GaN.
Mat. Res. Bull. **11**, 445-450, 1976 (No. 4). *L*

H.-G. Junginger & R. Strunk: Latent image changes during electrophotographic development.
J. appl. Phys. **47**, 3021-3027, 1976 (No. 7). *A*

D. Kasperkovitz & R. J. M. Verbeek (Philips Telecommunication Industries, Hilversum): A low-power circuit block for digital telephone exchanges.
Microelectronics and Reliability **15**, 163-170, 1976 (No. 2). *E*

E. T. Kève: Structure-property relationships in PLZT ceramic materials.
Ferroelectrics **10**, 169-174, 1976 (No. 1/2/3/4). *M*

A. M. Kiemeneij & J. G. Kloosterboer: Rapid photochemical decomposition of organic mercury compounds in natural water.
Anal. Chem. **48**, 575-578, 1976 (No. 3). *E*

E. Klotz & H. Weiss: X-ray 3-D coded aperture imaging: displaying the heart.
Appl. Optics **15**, 1913-1918, 1976 (No. 8). *H*

W. L. Konijnendijk & J. M. Stevels: The structure of borosilicate glasses studied by Raman scattering.
J. non-cryst. Solids **20**, 193-224, 1976 (No. 2). *E*

W. L. Konijnendijk (Philips Lighting Division, Eindhoven) **& J. M. Stevels** (Eindhoven University of Technology): Density and refractive index of borosilicate glasses in relation to their structure.
Verres Réfract. **30**, 223-225, 1976 (No. 2).

E. Krätzig & H. Kurz: Spectral dependence of the photorefractive recording and erasure process in doped $LiNbO_3$.
Ferroelectrics **10**, 159-162, 1976 (No. 1/2/3/4). *H*

D. J. Kroon: Automatisch meten van luchtverontreiniging.
Extern **5**, 113-131, 1976 (No. 2). *E*

J.-P. Krumme, P. Hansen & K. Witter: Thermomagnetic switching of ferrimagnetic garnet films at their compensation temperature.
J. appl. Phys. **47**, 3681-3689, 1976 (No. 8). *H*

F. E. J. Kruseman Aretz: Concurrent Pascal, een taal van P. Brinch Hansen.
Math. Centre Syllabus **25**, XII, 219-236, 1976. *E*

H. K. Kuiken: Theory of lifetime measurements with the scanning electron microscope: transient analysis.
Solid-State Electronics **19**, 447-450, 1976 (No. 6). *M*

W. Kwestroo & H. A. M. van Hal: Hydrates of lanthanide triiodides.
J. inorg. nucl. Chem. **38**, 1019-1022, 1976 (No. 5). *E*

J. P. L. Lagerberg: A high density static master slave shift register in I^2L.
First Eur. Solid State Circuits Conf. (ESSCIRC), Canterbury 1975 (IEE Conf. Publn No. 130), pp. 16-17. *E*

P. R. Lloyd: Quantisation error in area measurement.
J. Brit. Cartogr. Soc. **13**, 22-25, 1976 (No. 1). *M*

J. Lohstroh: Active recharging of bipolar phototransistors in the charge storage mode.
First Eur. Solid State Circuits Conf. (ESSCIRC), Canterbury 1975 (IEE Conf. Publn No. 130), pp. 50-51. *E*

J. Lohstroh: Dynamic behavior of active charge in I^2L transistors.
1976 IEEE Int. Solid-State Circuits Conf. Dig. tech. Papers, pp. 94-95. *E*

A. W. Ludikhuize & J. Th. Schrama: Monolithic PIN-attenuator IC with reduced cross-modulation at VHF-UHF.
First Eur. Solid State Circuits Conf. (ESSCIRC), Canterbury 1975 (IEE Conf. Publn No. 130), pp. 95-96. *E*

H. H. van Mal: The activation of a lanthanum-nickel-five hydrogen absorbent.
Hydrogen energy, editor T.N. Veziroğlu, publ. Plenum Press, New York 1975, Part A, pp. 605-610. *E*

G. Marie: Light valves using DKDP operated near its Curie point: Titus and Phototitus.
Ferroelectrics **10**, 9-14, 1976 (No. 1/2/3/4). *L*

G. M. Martin, E. Fabre, E. Fogarassy, C. Belin & Ngo-Tich-Phuoc: Deep levels and compensation in *p*-CdTe material for γ-ray detection.
IEEE Trans. **NS-23**, 154-158, 1976 (No. 1). *L*

G. M. Martin, E. Fogarassy & E. Fabre: Deep-level energy spectroscopy in *p*-type CdTe using TSC measurements.
J. appl. Phys. **47**, 264-266, 1976 (No. 1). *L*

P. L. A. Chr. M. van der Meer, L. J. Giling (both with University of Nijmegen) **& S. G. Kroon** (Philips Semiconductor Development Laboratory, Nijmegen): The emission coefficient of silicon coated with Si_3N_4 or SiO_2 layers.
J. appl. Phys. **47**, 652-655, 1976 (No. 2).

R. Metselaar, J. P. M. Damen, P. K. Larsen & M. A. H. Huyberts: Investigation of colour centres in gadolinium gallium garnet crystals.
Phys. Stat. sol. (a) **34**, 665-670, 1976 (No. 2). *E*

R. Metselaar & P. K. Larsen: Diffusion of oxygen vacancies in yttrium iron garnet investigated by dynamic conductivity measurements.
J. Phys. Chem. Solids **37**, 599-605, 1976 (No. 6). *E*

A. R. Miedema: On the heat of formation of solid alloys, II.
J. less-common Met. **46**, 67-83, 1976 (No. 1). *E*

A. R. Miedema: On the valence state of europium in alloys.
J. less-common Met. **46**, 167-173, 1976 (No. 1). *E*

A. E. Morgan & H. W. Werner: Quantitative analysis of low alloy steels by secondary ion mass spectrometry.
Anal. Chem. **48**, 699-708, 1976 (No. 4). *E*

C. Mulder (Philips Data Systems Division, Apeldoorn) **& H. E. J. Wulms:** High-speed I^2L.
First Eur. Solid State Circuits Conf. (ESSCIRC), Canterbury 1975 (IEE Conf. Publn No. 130), pp. 28-29. *E*

P. C. Mürau & R. N. Bhargava: Oxygen gettering in green GaP:N LED's grown by overcompensated LPE.
J. Electrochem. Soc. **123**, 728-733, 1976 (No. 5). *N*

F. L. van Nes (Institute for Perception Research, Eindhoven): Analysis of keying errors.
Ergonomics **19**, 165-174, 1976 (No. 2).

H. Ontrop: A monolithic clipping amplifier for digital application up to 1 GHz.
First Eur. Solid State Circuits Conf. (ESSCIRC), Canterbury 1975 (IEE Conf. Publn No. 130), pp. 80-81. *E*

W. J. Oosterkamp: Benefit/risk comparisons in diagnostic radiology.
Medicamundi **21**, 2-6, 1976 (No. 1). *E*

A. van Oostrom: Application of AES to the study of selective sputtering of thin films.
J. Vac. Sci. Technol. **13**, 224-227, 1976 (No. 1). *E*

J. A. Pals: On the detectibility of spin-triplet pairing superconductivity with the aid of the Josephson effect.
Physics Letters **56A**, 414-416, 1976 (No. 5). *E*

D. W. Parker, R. G. Pratt & R. Stevens: A television IF acoustic surface wave filter on bismuth silicon oxide.
Proc. IEEE **64**, 677-681, 1976 (No. 5). *M*

H. L. Peek: Twin-layer PCCD performance for different doping levels of the surface layer.
IEEE J. **SC-11**, 167-170, 1976 (No. 1). *E*

P. Piret: Notes on cyclic convolutional codes.
Information theory, new trends and open problems, editor G. Longo, publ. Springer, Vienna 1975, pp. 283-292. *B*

P. Piret: Structure and constructions of cyclic convolutional codes.
IEEE Trans. **IT-22**, 147-155, 1976 (No. 2). *B*

P. Piret: Some optimal AMC codes.
IEEE Trans. **IT-22**, 247-248, 1976 (No. 2). *B*

R. J. van de Plassche: Dynamic element matching for high-accuracy monolithic D/A converters.
1976 IEEE Int. Solid-State Circuits Conf. Dig. tech. Papers, pp. 148-149 & 240. *E*

J. Polman: Recent developments in low pressure gas discharge research.
Physica **82C**, 125-140, 1976 (No. 1). *E*

W. Puschert & H. Scholz: γ-ray spectra detected with HgI_2 at room temperature.
Appl. Phys. Letters **28**, 357-359, 1976 (No. 6). *A*

W. Rey: Mean life estimation from censored samples.
Biométrie-Praximétrie **15**, 145, 159, 1975. *B*

W. Rey: On the upper bound of the probability of error, based on Chebyshev's inequality, in two-class linear discrimination.
Proc. IEEE **64**, 361-362, 1976 (No. 3). *B*

A. Rijbroek (Philips Telecommunication Industries B.V., Huizen): Design approaches for a PCM-codec per channel.
Proc. 1976 IEEE Int. Symp. on Circuits and systems, Munich, pp. 587-590.

F. G. Rüdenauer, W. Steiger (both with Österreichische Studiengesellschaft für Atomenergie, Vienna) **& H. W. Werner:** On the use of the Saha-Eggert equation for quantitative SIMS analysis using argon primary ions.
Surface Sci. **54**, 553-560, 1976 (No. 3). *E*

W. Schäfer, G. Will (both with University of Bonn) **& K. H. J. Buschow:** The magnetic structure of the rare earth tetraborides ErB_4 and DyB_4.
J. chem. Phys. **64**, 1994-1997, 1976 (No. 5). *E*

H. Scholz, W. Bauhofer* & K. Ploog* (* Max-Planck-Institut für Festkörperforschung, Stuttgart): Preparation of lanthanum hexaboride by electrolysis and measurements of the Raman-active phonons.
Solid State Comm. **18**, 1539-1542, 1976 (No. 11/12). *A*

J. Schröder: Thermal energy storage and control.
Trans. ASME B (J. Engng. Ind.) **97**, 893-896, 1975 (No. 3). *A*

M. F. H. Schuurmans: Spectral narrowing of selective reflection.
J. Physique **37**, 469-485, 1976 (No. 5). *E*

G. B. Scott & D. E. Lacklison: Magnetooptic properties and applications of bismuth substituted iron garnets.
IEEE Trans. **MAG-12**, 292-311, 1976 (No. 4). *M*

B. Singer & J. Lalak: Pyroelectric vidicon with improved resolution.
Ferroelectrics **10**, 103-107, 1976 (No. 1/2/3/4). *N*

C. H. Smedema: Real-time concepts and Concurrent Pascal.
Proc. 1975 IFAC-IFIP Workshop on Real-time programming, Boston/Cambridge, Mass., pp. 31-38; 1976. *E*

C. H. Smedema: 1975 IFAC/IFIP Real-time Programming Workshop.
J. Physics E 9, 252-253, 1976 (No. 4). *E*

J. L. Sommerdijk & A. Bril: On the position of the $^5D_0$ level of Eu^{3+} in $AMgF_3$ (A = K, Rb, Cs).
J. Luminescence **12/13**, 669-673, 1976. *E*

R. Spitalnik: On the large-signal behavior of transferred-electron amplifiers with a cathode notch.
IEEE Trans. **ED-23**, 58-59, 1976 (No. 1). *L*

A. L. N. Stevels: Recent developments in the application of phosphors.
J. Luminescence **12/13**, 97-107, 1976. *E*

A. Thayse: Difference operators and extended truth vectors for discrete functions.
Discrete Math. **14**, 171-202, 1976 (No. 2). *B*

A. Thayse & J. P. Deschamps: Logic properties of unate and of symmetric discrete functions.
Proc. 6th Int. Symp. on Multiple-valued logic, Logan, Utah, 1976, pp. 79-87. *B*

J. B. Theeten & H. H. Brongersma: Rétrodiffusion d'ions de gaz rares de faible énergie par la surface d'un solide: mécanismes fondamentaux et application à la détermination des structures cristallines de surface.
Rev. Phys. appl. **11**, 57-63, 1976 (No. 1). *L, E*

G. E. Thomas & E. E. de Kluizenaar: The effect of adsorption of Cs and coadsorption of Cs and O_2 on bombardment-induced light emission from Cu and Al surfaces.
Nucl. Instr. Meth. **132**, 449-452, 1976. *E*

C. van Trigt: Analytically solvable problems in radiative transfer, IV.
Phys. Rev. A **13**, 726-733, 1976 (No. 2). *E*

C. van Trigt: Complete redistribution in the transfer of resonance radiation.
Phys. Rev. A **13**, 734-751, 1976 (No. 2). *E*

J. van der Veen: Liquid crystalline isothiocyanates.
J. Physique **37**, C3/13-15, 1976 (Colloque C3). *E*

J. van der Veen & H. B. Haanstra: Fine structure in a smectic stepped drop.
J. Physique Lettres **37**, L 43-44, 1976 (No. 3). *E*

C. H. F. Velzel: A general theory of the aberrations of diffraction gratings and gratinglike optical instruments.
J. Opt. Soc. Amer. **66**, 346-353, 1976 (No. 4). *E*

J. M. P. J. Verstegen (Philips Lighting Division, Eindhoven): New fluorescent materials for reprographic lamps.
4. Int. Kongreß für Reprographie und Information 1975, pp. 15-17; 1976.

J. M. P. J. Verstegen (Philips Lighting Division, Eindhoven): Entwicklungstendenzen bei Leuchtstofflampen.
Elektrotechn. Z. etz.b **28**, 88-89, 1976 (No. 4).

M. J. Vliegenthart: Het omzetten van teksten in braillekortschrift met behulp van een rekenautomaat.
Thesis, Delft 1976. *E*

J. Vlietstra, H. A. Klamet & J. S. Sullivan (Philips Central Development Bureau, Eindhoven): Computer-aided design: an industrial view.
First Eur. Solid State Circuits Conf. (ESSCIRC), Canterbury 1975 (IEE Conf. Publn No. 130), pp. 1-4.

J. O. Voorman: The adaptive gyrator.
Proc. 1976 IEEE Int. Symp. on Circuits and systems, Munich, pp. 34-37. *E*

L. Vriens: Light scattering from excited hydrogen atoms.
Physics Letters **55A**, 331-332, 1976 (No. 6). *E*

J. H. N. van Vucht & K. H. J. Buschow: The crystal structure of La_2Ni_3.
J. less-common Met. **46**, 133-138, 1976 (No. 1). *E*

W. F. van der Weg (Philips Research Labs., Amsterdam Division), **N. H. Tolk*, C. W. White* & J. M. Kraus*** (* Bell Laboratories, Murray Hill, N.J.): Optical excitation during ion bombardment of copper under channeling conditions.
Nucl. Instr. Meth. **132**, 405-410, 1976.

K. Weiss: Koelen naar extreem lage temperaturen.
Natuurk. Voordr. Diligentia Nieuwe Reeks No. 53, 103-124, 1975. *E*

H. W. Werner & A. E. Morgan: Charging of insulators by ion bombardment and its minimization for secondary ion mass spectrometry (SIMS) measurements.
J. appl. Phys. **47**, 1232-1242, 1976 (No. 4). *E*

M. V. Whelan & J. G. de Groot: 100-element resistive MOS-gated line scanner.
First Eur. Solid State Circuits Conf. (ESSCIRC), Canterbury 1975 (IEE Conf. Publn No. 130), pp. 115-116. *E*

H. E. J. Wulms: Base current of I^2L transistors.
1976 IEEE Int. Solid-State Circuits Conf. Dig. tech. Papers, pp. 92-93. *E*

P. Zandveld: Some properties of ion-implanted *p-n* junctions in silicon.
Solid-State Electronics **19**, 659-667, 1976 (No. 8). *E*

H. Zijlstra: Permanent magnets.
Phys. in Technol. **7**, 98-107, 1976 (No. 3). *E*

D. J. Zwanenburg & Th. A. M. M. Maas: The reactions between 3′-methyl-6-nitrospiro[2*H*-1-benzopyran-2,2′-benzothiazolines] and 1,1-bis[4-(dimethylamino)-phenyl]ethylene and the reactions of salicylaldehydes with 1,1-bis[4-(dimethylamino)phenyl]propene. A striking effect of an extra methyl group; photochromic chromenes.
Recueil Trav. chim. Pays-Bas **95**, 97-98, 1976 (No. 5). *E*

W. K. Zwicker, J. P. Dougherty, M. Delfino & J. Ladell: Growth of high quality lead germanate crystals for pyroelectric applications.
Ferroelectrics **11**, 347-350, 1976 (No. 1/2). *N*

Volume 37, 1977, No. 5/6 pages 109-156 Published 20th January 1978

PHILIPS TECHNICAL REVIEW

VOLUME 37, 1977, No. 7

Ferroxdure

C. A. M. van den Broek and A. L. Stuijts

Permanent magnets are found everywhere in our modern civilization. In toys, cupboard catches, electric clocks, cassette recorders, loudspeakers and television receivers; in windscreen wipers, fans, tachometers and ammeters; in ore separators, cranes, milling and grinding machines, relays and precision motors. The materials for these magnets may be divided into two groups: the magnetically hard alloys which, like the Philips product Ticonal, were introduced in the thirties, and the magnetically hard ferrites of the fifties. Unlike the alloys, the ferrites contain no scarce and expensive materials such as nickel or cobalt. This is the main reason for their economic success; in about 1970 the ferrites took the lead over the alloys in world production measured in tonnes per annum. Some minor deviations apart, the chemical composition of these ferrites is either barium hexaferrite or strontium hexaferrite. Carefully controlled ceramic processing is essential to give the products the desired properties. At the time of their discovery and development these materials were given the name Ferroxdure. It is now 25 years since Philips first introduced Ferroxdure with a publication in this journal and an exhibition of the first applications at the Hanover Trade Fair. We think this is a proper occasion for drawing attention once again to the research on this material and its technology.

Introduction

In 1952 mention was made for the first time of a group of new materials, called 'Ferroxdure' [1]. These materials, ceramically processed ferromagnetic oxides, are magnetically hard and are therefore suitable for permanent magnets. The opinion expressed at the time was that these new materials were of great economic importance. That opinion has been fully confirmed: the total world production of magnetically hard ferrites — which, in composition and crystal structure, all belong to the same group — is now estimated at about 70 000 to 80 000 tonnes a year, with a value of some 200 million dollars. *Fig. 1* shows how these ferrites have acquired an ever increasing share of the world production of permanent magnets, measured in tonnes per annum.

Compared with other materials for permanent magnets, Ferroxdure was characterized by an *exceptionally high coercivity*, combined with a remanence which, though not very high, is valuable for practical purposes. With such a material, it became possible to produce magnets of shapes such that they would have almost completely demagnetized themselves if made of a different material. Typical cases were flat ring magnets, magnetized perpendicular to the plane of the ring, or transversely magnetized rods with many north and south poles closely adjacent to each other (*fig. 2*). Ferroxdure is also highly resistant to external demagnetizing fields, as encountered in d.c. motors, for example. These novel properties were exploited on a large scale, e.g. for making flat loudspeakers and compact d.c. motors.

Let us examine these properties in somewhat more detail. A magnetic material is often rated in terms of its 'maximum energy product' $(BH)_{max}$, the maximum of the BH product along the demagnetization curve (B is the magnetic flux density, H the magnetic field).

Ir C. A. M. van den Broek is with the Ceramics Laboratory of the Philips Elcoma Division, Eindhoven. Prof. Ir A. L. Stuijts, is a Scientific Adviser with Philips Research Laboratories, Eindhoven, and is Professor Extraordinary in the Technology of Inorganic Materials at Eindhoven University of Technology.

[1] J. J. Went, G. W. Rathenau, E. W. Gorter and G. W. van Oosterhout, Philips tech. Rev. 13, 194, 1951/52.

Ferroxdure does not, in fact, have a particularly high *BH* product (*fig. 3*), and indeed a particular field-strength in a given air gap can be obtained with a smaller volume of other materials. But Ferroxdure does have the special feature of a *broad* demagnetization curve. After it has been magnetized to saturation, a magnet arrives at the operating point *P* (*fig. 4*). This is the point where the demagnetization curve intersects the load line *l*, which is determined by the shape of the magnetic circuit. With the high and narrow demagnetization curves of the older materials a steep load line, i.e. a long and thin magnet, is necessary if the magnet is to be left with any significant flux; a 'short and thick' magnet (load line *l'* in fig. 4) is irreversibly demagnetized. This is not the case with Ferroxdure. An 'optimum circuit' — a circuit whose operating point coincides with the point of maximum *BH* — can be much more compact with Ferroxdure, 'squarer', than with a material such as Ticonal. The historical development of the slope of the optimum load line, i.e. the development of magnets from long and thin to short and thick, is illustrated in *fig. 5*.

The great economic success of Ferroxdure is due in the first place, however, to the low price per unit of available magnetic energy (*fig. 6*). It is, therefore, mainly used not so much as a technical improvement but more as a substitute for more expensive components, such as Ticonal magnets in loudspeakers or stator coils of windscreen-wiper motors. Ferroxdure is inexpensive because it does not contain any rare materials such as nickel or cobalt, and it is relatively easy to manufacture: it is only necessary to 'mix a few cheap oxides' and to 'bake them to the right shape'. Nevertheless, this process has some interesting aspects, and we shall return to these presently.

Finally, Ferroxdure — an oxide — has a high electrical resistivity, so that there are hardly any eddy-current losses. This is an important advantage in radio-frequency applications and also in certain types of electric motor. A disadvantage is the relatively high temperature coefficient of the remanence and the coercivity. This makes the material less suitable for certain professional applications.

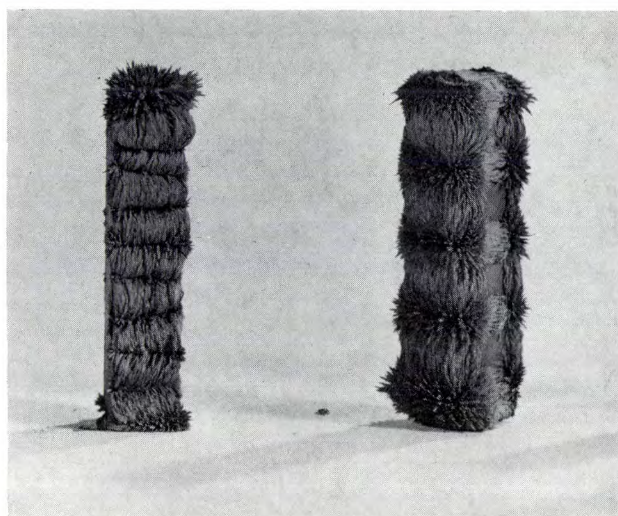

Fig. 2. Transversely magnetized Ferroxdure rods with (*left*) ten and (*right*) five north and south poles side by side [1].

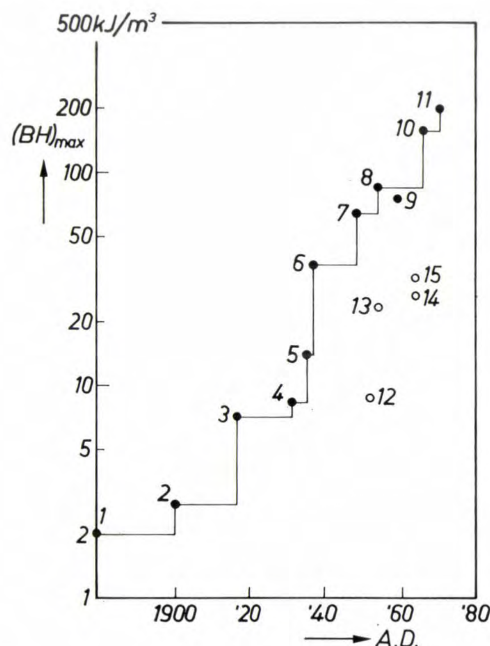

Fig. 3. The values of $(BH)_{max}$ attained since 1880; *filled circles:* steels and alloys; *open circles:* Ferroxdure [3].

1 C steel	*5* Ticonal II	*9* PtCo	*12* FXD 100
2 W steel	*6* Ticonal G	*10* $SmCo_5$	*13* FXD 300
3 Co steel	*7* Ticonal GG	*11* $(Sm,Pr)Co_5$	*14* FXD 330
4 Fe-Ni-Al alloy	*8* Ticonal XX		*15* FXD 360

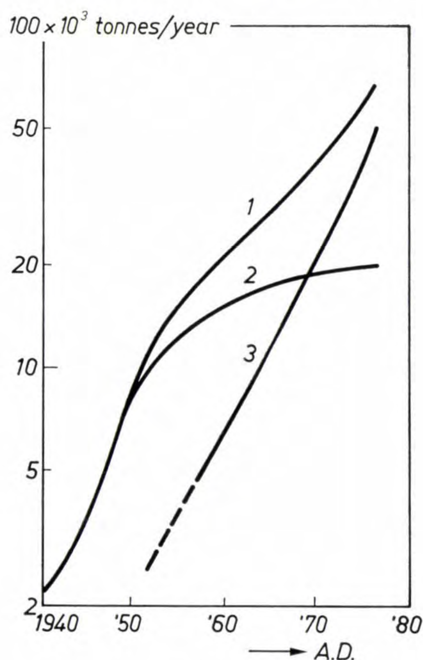

Fig. 1. Estimate of the world production of permanent magnets. *1* total, *2* alloys, *3* ferrites [2].

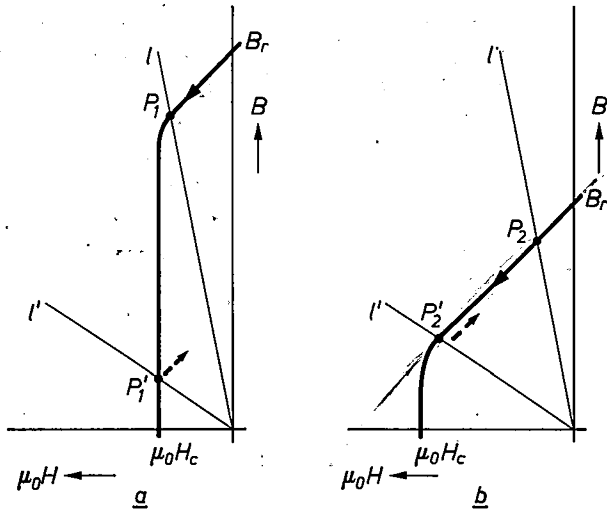

Fig. 4. Demagnetization curves in the B-μ_0H diagram: *a*) for a magnetic alloy, e.g. Ticonal, *b*) for Ferroxdure (schematic, not drawn to scale for clarity). B_r remanence, H_c coercivity. The operating point P is the point where the demagnetization curve cuts the load line l, which is determined by the magnetic circuit. The classical alloys call for long thin magnets (steep load line l, operating point P_1); in short thick magnets (l') demagnetization occurs (P_1'), which is irreversible: when H decreases again, the material follows the dotted arrow. With the same load line there is no irreversible demagnetization in Ferroxdure. In this figure, and in the text of the article, H represents the value of the demagnetizing field, i.e. a field which, at positive H, is opposite to the original magnetizing field.

Ferroxdure is manufactured either in solid ceramic form or in the form of ceramic particles dispersed in a plastic. Both forms can be *isotropic* or *anisotropic.* Anisotropic material has to be magnetized in a particular direction, and it has better magnetic properties in that direction than isotropic material. The isotropic material is more suitable for multipole magnets, and is cheaper. The solid form is hard and brittle, so that magnets of this material can only be finished by grinding. The 'plastoferrite' is of lower magnetic quality, but it can be stamped and cut and can be produced in the form of flexible sheets. *Table I* shows some typical applications of the various types [4].

The properties of each of these types can be varied quite considerably by variations in the method of preparation. As an example *fig. 7* shows the demagnetization curves of some varieties of sintered anisotropic Ferroxdure. The good use that can be made of this freedom may be summarized very schematically as follows. We assume that the demagnetization curves in the J-μ_0H diagram are rectangular, where J is the magnetic polarization (*fig. 8a*). We further assume that the saturation polarization is a fixed quantity, given by

[2] G. W. Rathenau, Proc. 3rd Eur. Conf. on Hard magnetic materials, Amsterdam 1974, p. 7.
[3] H. Zijlstra, Philips tech. Rev. 34, 193, 1974.
[4] More details of the properties and applications of Ferroxdure are given in Philips Data Handbook, Components and Materials, Part 4b.

Table I. Applications of Ferroxdure.

Anisotropic Ferroxdure	Isotropic Ferroxdure	Anisotropic plastoferrite	Isotropic plastoferrite
Loudspeakers Windscreen-wiper motors Fan motors Industrial motors Magnetic holding (catch) systems Magnetic separators Clocks Relays	Small electric motors (toys, recorders) Correction magnets for television tubes Holding magnets Rotors for cycle dynamos	Small electric motors	Refrigerator-door magnets Correctionr magnets fo television tubes

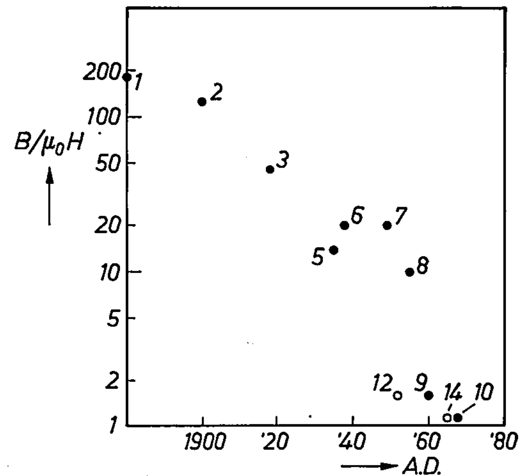

Fig. 5. The slope (B/μ_0H) of the optimum load line — for which the operating point coincides with the point of maximum BH — for the materials in fig. 3 [2]. A low slope allows short thick magnets to be made.

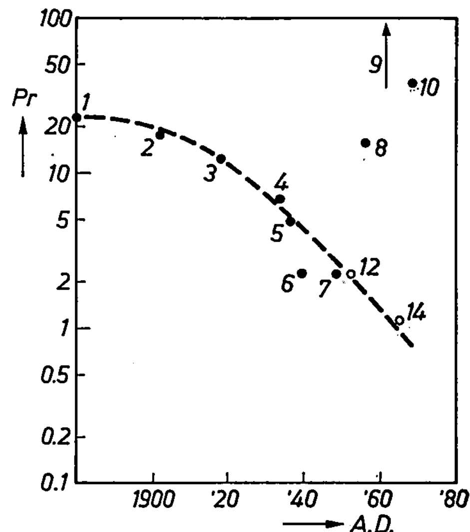

Fig. 6. Comparison of the price per unit of available magnetic energy (Pr) for the materials in fig. 3 [2].

the number of atomic magnetic moments per unit volume, and that the coercivity can always be increased, depending on the expense and trouble involved. A simple calculation then shows that the optimum operating point for demagnetization curves of type *1* in fig. 8*b* ($\mu_0 H_c < \frac{1}{2}B_r$) lies at the 'knee' P_1, but that for curves of type *2* ($\mu_0 H_c > \frac{1}{2}B_r$) it lies at P_m ($\mu_0 H = B = \frac{1}{2}B_r$). With increasing H_c, $(BH)_{max}$ increases until H_c reaches the value $\frac{1}{2}B_r/\mu_0$; it then remains constant. There is therefore no point in making H_c larger than $\frac{1}{2}B_r/\mu_0$, if it is assumed that the only criterion is the highest possible $(BH)_{max}$. Nevertheless, H_c generally has to be made higher, because the operating point must never fall beyond the knee (fig. 8*c*). Two things that might bring this about are a temperature reduction, which will produce a decrease of H_c, at least in the case of Ferroxdure (fig. 8*d*), and strong fluctuations in the demagnetizing field (e.g. in motors). These effects might be cumulative, as when switching on the motor of a frozen windscreen wiper at a temperature of −30 °C. The requirement that the stator magnet should remain fully magnetized even under such extreme conditions led to the development of the type FXD 270 (see fig. 7).

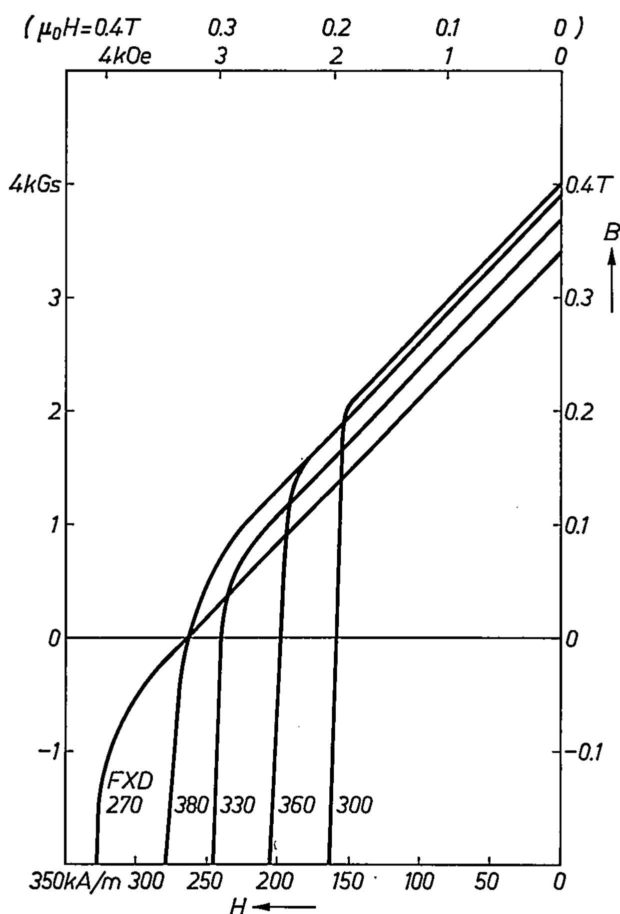

Fig. 7. Demagnetization curves at 25 °C for varieties of solid-sintered anisotropic Ferroxdure.

After the discovery of Ferroxdure — the discovery of a 'stubborn' kind of magnetism in a new oxidic powder — it was very soon developed into a viable permanent-magnetic material. This could be done because ferrites and permanent-magnet steels and alloys were the subject of intensive research at Philips Research Laboratories at the time of the discovery. Among the results of this research were the soft 'Ferroxcubes' and the alloy Ticonal. In these circumstances rapid progress could be made in grasping the physical and chemical fundamentals of the new ferrite and determining the desired microstructure for the ceramic product.

In this article, after summarizing the knowledge of the crystal chemistry, magnetic and microstructural aspects gained by about 1954, we shall discuss a number of investigations and developments that have taken place since that time. They will be divided, somewhat arbitrarily, into two categories: 'materials research' and 'technology' [5].

Chemical composition, saturation polarization and anisotropy; the desired microstructure

Except for minor differences necessary for the ceramic process, the composition of Ferroxdure is $MFe^{III}_{12}O_{19}$, where M stands for Ba, Sr or Pb. The composition is often referred to as a 'hexaferrite', since it can be thought of as a compound of MO and Fe_2O_3 in the ratio of 1 to 6. Most of the research has been on the barium compound. The strontium compound is a little more expensive, but is superior if a high coercivity is a prime requirement, as in electric motors. The lead ferrite is not used because of the associated environmental pollution problems and because it is more expensive.

The value of the saturation polarization J_s was satisfactorily explained in 1952 on the basis of the crystal structure, which had been determined in 1938, and by applying the theories of L. Néel and P. W. Anderson on ferrimagnetism [1]. The iron ions are divided among five sublattices. They interact in a 'superexchange' process in such a way that out of the twelve iron ions per formula unit there are eight whose magnetic moments ('spins') have the same orientation and four whose magnetic moments have the opposite sense. Together with the strong 'magnetic dilution' with oxygen, this partial compensation of magnetic moments is responsible for the relatively low values of J_s and B_r. The subject of the (hexagonal) crystal structure and the sublattices will be dealt with presently in a broader context (see fig. 12).

The magnetic hardness of the material depends essentially on the hexagonal, strongly anisotropic crys-

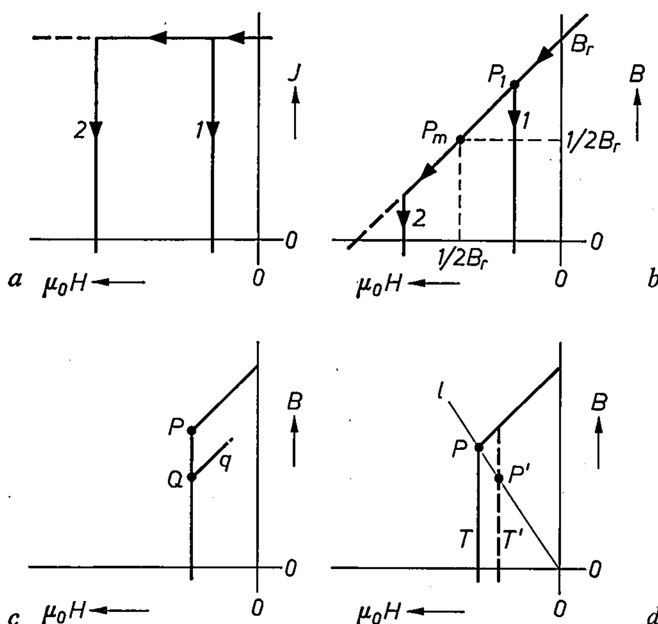

Fig. 8. Schematic situation with rectangular demagnetization curves in the J-$\mu_0 H$ diagram, a fixed saturation polarization and a variable coercivity. *a)* The demagnetization curves in the J-$\mu_0 H$ diagram. *b)* The demagnetization curves in the B-$\mu_0 H$ diagram ($B = -\mu_0 H + J$). In curve *1* the optimum operating point lies at P_1, in curve *2* at P_m. *c)* When the operating point goes from P to Q and the demagnetizing field decreases, the material follows the curve q instead of the old curve; flux has been lost. *d)* With decreasing temperature the coercivity of Ferroxdure decreases ($T' < T$); as a result the operating point may go beyond the knee.

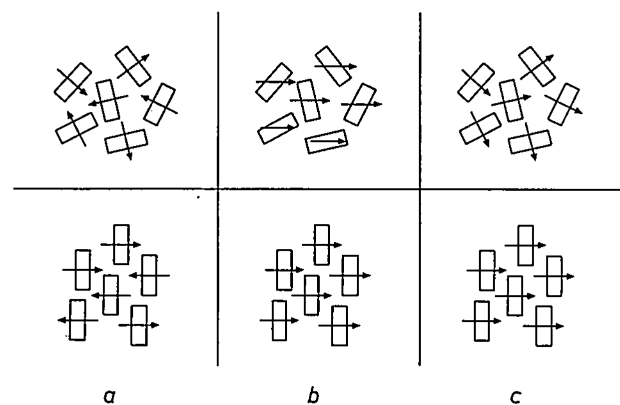

Fig. 9. Ferroxdure with non-oriented crystals (*above*) and with oriented crystals (*below*). *a)* Non-magnetized material, *b)* the material in a saturating field, *c)* the material after saturation without external field. The small rectangles represent cross-sections of the plate-like crystals, the arrows their magnetic moments. These have a preference for the *c*-axis, perpendicular to the platelet.

tal structure; the hexagonal axis (the '*c*-axis') constitutes a strongly preferred (easy) direction for the resultant moment. A measure of this 'intrinsic hardness' is the anisotropy field H_A, the field theoretically required to reverse all the spins as one unit in a saturated single crystal. This is given by:

$$H_A = 2K/J_s, \qquad (1)$$

where K is the anisotropy constant, i.e. the work necessary to rotate the polarization from the easy direction into the direction perpendicular to it. In barium hexaferrite the value of H_A is about 1400 kA/m (17 kOe).

The quantity H_A can be considered an absolute maximum for the coercivity H_c. In practice, however, H_c is always much smaller, mainly because relatively weak fields may often be capable of changing the magnetization through *domain-wall movements* (Bloch-wall shifts). According to C. Kittel's 'single-domain' theory, to obtain a high coercivity the material must therefore be divided into such small particles that each particle consists of only one magnetic domain, and therefore has no Bloch wall. Although this theory does not in fact give a valid explanation for the existence of a coercive field [3], its application was very successful. The critical particle size in barium hexaferrite was calculated to be about 1 μm from this theory, and indeed it is found that at this particle size the value of H_c increases very strongly when an initially coarse powder is more finely ground. The ceramic end-product 'Ferroxdure' must therefore have a microstructure of crystallites no larger than about 1 μm.

The existence of a coercive field is undoubtedly a much more complicated effect than is suggested by the single-domain theory. It is not so much a question of whether Bloch walls are present or not, but more of the ease with which they arise and are displaced when the field changes. Bloch walls occur more easily, for example, in particles with a rough surface than in particles with a smooth surface. It has been found that the coercivity of a powder produced by milling a sintered product can be increased from say 150 to 400 kA/m (2 to 5 kOe) by tempering the powder at 900 to 1000 °C. Bloch walls are also generated more readily at certain types of crystal defect than elsewhere in a crystal. Presumably the success of the single-domain theory is not therefore attributable to the absence of Bloch walls in a subcritical particle, but to the fact that the probability of a crystal defect in such a particle is very small. The magnetic hardness of Ferroxdure would in this respect show some resemblance to the mechanical strength of 'whiskers'.

In 1954 the material was substantially improved by *orienting* the crystallites [6]. In isotropic material the magnetic moments of the crystallites, in zero field after saturation, are randomly distributed over a hemisphere (*fig. 9*). In *anisotropic Ferroxdure*, on the other hand, which is the material now most widely used, the *c*-axes and hence the moments after saturation are approx-

[5] More information on both soft and hard magnetic ferrites is given in: J. Smit and H. P. J. Wijn, Ferrites, Philips Technical Library, 1959, and on hard ferrites in: G. Heimke, Keramische Magnete, Springer-Verlag, Wien/New York 1976.

[6] A. L. Stuijts, G. W. Rathenau and G. H. Weber, Philips tech. Rev. 16, 141, 1954/55.

imately parallel. Consequently the remanence is about twice as great and $(BH)_{max}$ is about four times higher.

At the time it was a surprise that the attempts to produce crystal-oriented Ferroxdure were so successful. It was feared, quite reasonably, that the orientation of the crystallites, achieved with much difficulty in the compacted product, would be lost during sintering. The result exceeded all expectations; the texture was not only preserved but was indeed greatly improved. Eventually it turned out that this was because the grain growth that occurs during sintering is mainly a growth of the well aligned crystals at the expense of the poorly aligned crystals.

The orientation does introduce some slight reduction in the coercivity, however, because the 'pressure' of a demagnetizing field on a Bloch wall is greater in an oriented particle than on a wall in a non-oriented particle; see *fig. 10*. For this reason, if the material is to be subjected to strong demagnetizing fields, as in d.c. motors, a compromise must often be found between high remanence and a large coercivity.

To sum up, the materials technologist has to produce a densely sintered hexaferrite with a microstructure of *small* and preferably *oriented* crystallites. We shall return presently to the associated technological problems.

Materials research since 1954

The steady improvements in the properties of Ferroxdure since 1954 have been mainly technological. Scientific research on the chemistry and physics of the materials has not really led to actual intrinsic improvements since that time. It has, however, led to new, interesting lines of investigation, to a better understanding of the properties of the materials and to a broadening of their technical possibilities. We shall touch here on some highlights of this research.

Related compounds; Ferroxplana; crystal structure

A new line of investigation was initiated by the discovery of a new compound, $BaFe^{II}_2Fe^{III}_{16}O_{27}$ (W in fig. 11), which is closely related chemically and magnetically [7]. This compound turned out to be very difficult to synthesize, however: the balance between the ferric and ferrous ions can be very easily upset if the atmosphere during preparation is slightly too reducing or too oxidizing. Such considerations led to the substitution of Ni^{2+}, Co^{2+}, . . . for the ferrous ion. Similar substitutions in the cubic ferrites had resulted in the successful, magnetically soft Ferroxcubes. As a result of this research, barium-Ferroxdure may be regarded as a member of a family of magnetic ferrites shown in *fig. 11*, the upper part of the ternary diagram for the BaO-MeO-Fe_2O_3 system. Here Me represents a small divalent metal ion: Mn, Fe, Co, Ni, Zn or Mg. The Ferroxcubes are represented by **S**, Ferroxdure by **M**. **B** is the non-ferromagnetic compound $BaFe_2O_4$.

The compounds **W** and **Z** thus produced closely resemble **M**; owing to a strong preferred direction for the moments they are magnetically hard. There is one exception, however: when cobalt is substituted the moments try to avoid the *c*-axis, and prefer to align themselves in the plane perpendicular to it. This marked the discovery of a new class of materials, called 'Ferroxplana' [8]. In the compound **Y**, which is the most important representative of the class, the magnetic mo-

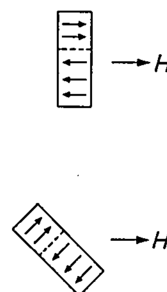

Fig. 10. Crystallite with a Bloch wall (*dashed*) in a demagnetizing field *H*. *Above:* a non-oriented particle, *below:* an oriented particle. The energy gain per centimetre shift of the Bloch wall, and hence the pressure on the Bloch wall, is greater in the oriented particle than in the non-oriented one.

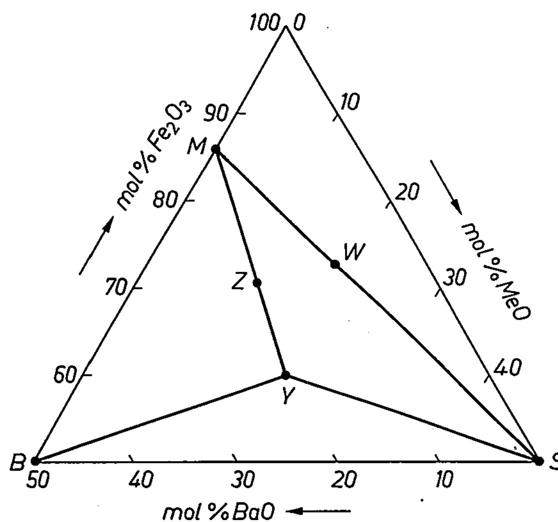

Fig. 11. Upper part of the ternary diagram of compositions in the system BaO-MeO-Fe_2O_3. Me represents the divalent ion of Mn, Fe, Co, Ni, Zn or Mg. **S** Ferroxcube, **M** Ferroxdure. **B** is non-ferromagnetic. In the compounds **Y**, Co-**Z** and Co-**W** ('Ferroxplana') the plane perpendicular to the *c*-axis is the preferred plane for the magnetic moments. As in **M**, the *c*-axis is the easy direction of magnetization in the other **Z** and **W** compounds. Composition of the compounds:
S: $MeFe_2O_4$,
B: $BaFe_2O_4$,
M: $BaFe_{12}O_{19}$,
W: $BaMe_2Fe_{16}O_{27}$,
Y: $BaMeFe_6O_{11}$,
Z: $Ba_3Me_2Fe_{24}O_{41}$.

ments have a preferred *plane* for *all* of the substitutions.

The crystal structures of the compounds in fig. 11 are closely related; they are all close-packed sphere structures of O^{2-} ions in which the Ba^{2+} ions, of about the same size, occupy oxygen sites, and the much smaller Fe^{3+} and Me^{2+} ions occupy the interstices between the O ions. The relationship goes much further than this, however. If we start from the familiar spinel structure (the structure of **S**), we can think of the structures of **M**, **W**, **Y** and **Z** as built up from spinel layers — slabs of the spinel structure four or six oxygen layers thick — with one or two layers with barium between them [9]. *Fig. 12* shows the structure of **M**.

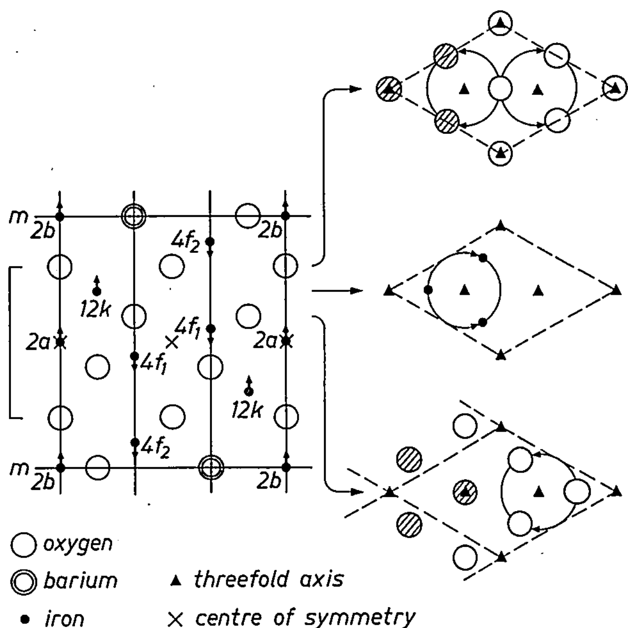

Fig. 12. Crystal structure and magnetic sublattices of Ferroxdure (**M** in fig. 11). The figure on the left shows the atoms in a mirror plane that contains the *c*-axis. From this the whole crystal can be reconstructed by rotations of 120° about the threefold axes (the vertical lines) and reflections in the mirror plane *m*. (The spin states are not reflected.) *Right:* three planes perpendicular to the *c*-axis, demonstrating the ± 120° rotations.

The indications by the iron ions correspond to the sublattices, which are specified in the table below. The table gives the type of site occupied by an iron ion, the coordination (the number of oxygen neighbours, the corners of the site), the number of ions per formula unit and the orientation of the spin. In the figures on the right the six oxygen ions that form the octahedron containing the 12*k* ion in the layer in between are shown hatched.

The square bracket at the left indicates a 'spinel slab', a piece of the spinel structure. The crystal may be regarded as built up from spinel slabs of four oxygen layers joined by barium-containing oxygen layers.

Sublattice	12*k*	$4f_1$	$4f_2$	2*a*	2*b*
Site	Octahedron	Tetrahedron	Octahedron	Octahedron	Trigonal bipyramid
Coordination	6	4	6	6	5
Number of ferric ions per formula unit	6	2	2	1	1
Spin	↑	↓	↓	↑	↑

Substitution research

Fig. 12 also shows how the eight 'spin-up' and the four 'spin-down' ferric ions per formula unit are distributed among the sublattices. The substitution of non-magnetic ions for 'spin-down' ions would increase the saturation polarization J_s and thus intrinsically improve the material. A great deal of experimental work on substitutions was directed towards this, but without success. In the first place, substituted ions often take the place of 'spin-up' ions. But even if they take the place of 'spin-down' ions, as in the case of Zn substitution, the effect on the saturation polarization *at room temperature* is nevertheless negative, because the magnetic structure has been weakened. This is reflected most clearly in a marked decrease in the Curie point.

Substitutions can, however, be used for other purposes. When J_s is reduced, and K remains unchanged, the anisotropy field H_A increases (see eq. 1), and this leads to expectations of an increased coercivity. In practice the relative increase in H_c due to the substitution is often found to be much greater than in H_A. With Al and Cr substitutions, for example, the coercivity could be substantially increased without greatly reducing the remanence [10]. A substitution of this type accounts for the special properties of FXD 270 (see fig. 7). Substitutions are also used in high-frequency applications (e.g. in microwave isolators), for tuning the resonant frequency by varying H_A [10].

Mössbauer spectroscopy

A valuable aid in substitution research is Mössbauer spectroscopy. Here the spectrum of the resonance absorption of gamma radiation by the iron nuclei is determined, with excited iron nuclei from radioactive cobalt forming the radiation source [11]. The Mössbauer spectrum of an absorbing iron ion is strongly affected by its nearest oxygen- and iron-ion neighbours. Since the five sublattices each have different nearest-neighbour environments, *the sublattices can be studied separately*. It is for example possible to follow closely how the Al ions in $BaAl_xFe_{12-x}O_{19}$ first occupy 2*a* sites when x is increased and then, when the 2*a* lattice is full ($x = 1$), take up positions in the 12*k* lattice [12].

[7] H. P. J. Wijn, Nature **170**, 707, 1952.
P. B. Braun, Nature **170**, 708, 1952.
[8] G. H. Jonker, H. P. J. Wijn and P. B. Braun, Philips tech. Rev. **18**, 145, 1956/57.
A. L. Stuijts and H. P. J. Wijn, Philips tech. Rev. **19**, 209, 1957/58.
[9] P. B. Braun, Philips Res. Repts. **12**, 491, 1957.
[10] See for example L. G. Van Uitert, J. appl. Phys. **28**, 317, 1957.
[11] See for example J. S. van Wieringen, Philips tech. Rev. **28**, 33, 1967.
[12] See for example J. G. Rensen, J. A. Schulkes and J. S. van Wieringen, J. Physique **32**, C1-924, 1971.

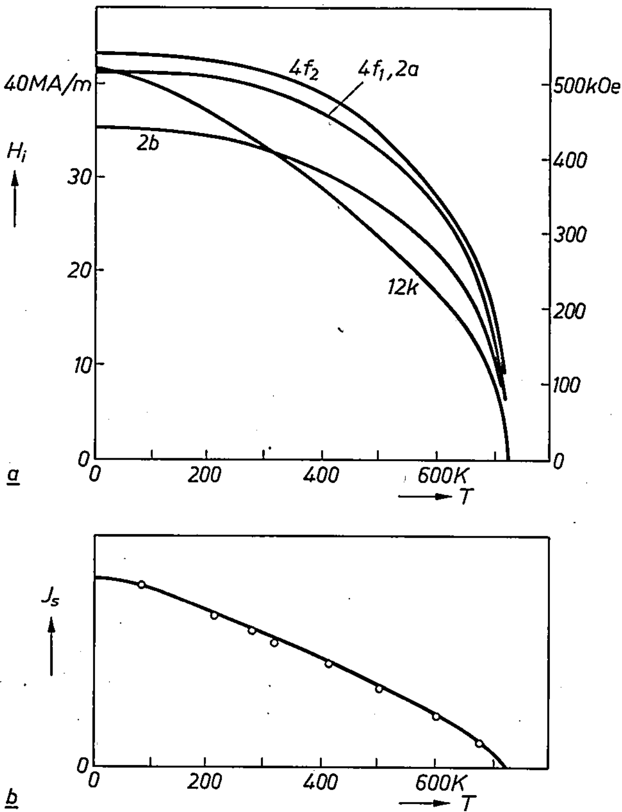

Fig. 13. *a*) The internal field (H_i) of the various sublattices of Ba-Ferroxdure as a function of the temperature T, from Mössbauer measurements. *b*) The saturation polarization J_s of Ba-Ferroxdure as a function of temperature. The solid curve is derived from (*a*), taking into account the number and orientation of the spins in each sublattice, as indicated in the table in fig. 12. The polarization per atom of a sublattice is proportional to H_i. The circles are experimental values; the vertical scale is adapted to give the best match to the curve [11].

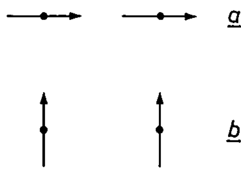

Fig. 14. Anisotropy due to dipole-dipole interaction in a system of two coupled magnetic moments. When the two moments are coupled in parallel (e.g. due to superexchange), they have a lower energy in position *a* than in position *b*, because of their magnetic interaction. By the same principle, large spin systems may also exhibit anisotropy.

The application of Mössbauer spectroscopy to Ferroxdure was an important step in the explanation of the unusual variation of the saturation polarization with temperature. In most magnetic materials this variation approximates to a Brillouin function, but in Ferroxdure it is roughly linear. From Mössbauer measurements it may be concluded that the reason for this anomalous behaviour is to be found entirely in the 12*k* lattice; see *fig. 13*. The unusual form of the polarization of this lattice has a dominant effect on the total polarization, since the 12*k* ions occur in relatively large numbers and in addition the other lattices partially compensate one another.

Origin of the strong anisotropy

A question of scientific interest is the origin of the strong anisotropy of Ferroxdure. The mechanisms that can account for it are *dipole-dipole interaction* and *spin-orbit coupling* [13]. The contribution of dipole-dipole interaction can be calculated accurately for each lattice of magnetic moments (see *fig. 14*). In spin-orbit coupling the spin direction of the ion is coupled to the lattice via the orbit. This effect is difficult to calculate for the ferrite considered here, largely because free ferric ions in the ground state have no orbital moment ($L = 0$), so that the mixing of excited states ($L \neq 0$) into the ground state by 'perturbations' is essential here. The 2*b* lattice is a special one in this connection: the ions in this lattice are strongly 'perturbed' due to the unusual fivefold coordination, and the spin-orbit coupling of these ions might therefore make a considerable contribution to the anisotropy.

Assuming that the spin-orbit coupling is responsible for the difference between the measured anisotropy coefficient K and the calculated dipole-dipole term, it must largely account for the high positive value of the anisotropy constant K in Ferroxdure **M**, since the calculated dipole-dipole term is relatively small. In **Y**, on the other hand, the calculated (negative) dipole-dipole term has a substantially *higher* absolute value than the (negative) experimental value of K; apparently the spin-orbit coupling here compensates part of the dipole-dipole interaction.

The contribution from spin-orbit coupling that is obtained in this way is greater for **M** than for **Y**. The difference may well be due to the contribution from the 2*b* lattice of **M** (see above), since no such lattice is found in **Y** [13]. In the Mössbauer spectrum a perturbation of the ferric ion is manifested in a shift of the absorption lines, and the lines of the 2*b* spectrum are indeed found to be more displaced than the others. However, it should not be inferred from this that the 2*b* lattice has a dominant effect on the anisotropy, since the other lattices — which together contain eleven times as many ions — also exhibit fairly marked line shifts [11].

It is also interesting here to mention the compound $LaFe_{12}O_{19}$ [14]. Because La is trivalent, one out of every twelve iron ions is a ferrous ion. The compound is very strongly anisotropic (at low temperature K is about $2\frac{1}{2}$ times greater than in Ferroxdure). This is undoubtedly due to spin-orbit coupling of the ferrous ion, which does have an orbital moment.

Magnetic bubbles

Finally, we should remember here that the cylindrical magnetic domains now known as 'bubbles' — carriers of a single bit of information in bubble-domain mem-

ory devices [15] — were first extensively studied in single-crystal wafers of barium hexaferrite [16]. The *c*-axis is perpendicular to the plane of such a platelet. Magnetic domains can be made visible by means of the Faraday effect. *Fig. 15* shows three of the domain structures observed at the time; the dark patches in fig. 15*c* are the stable cylindrical domains of opposite magnetization, which were then the subject of extensive theoretical investigation.

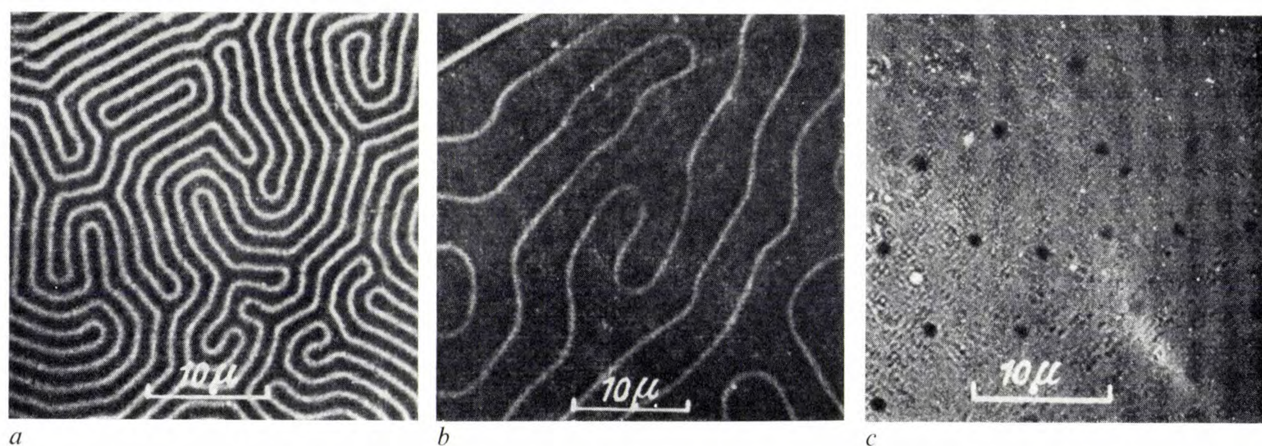

Fig. 15. Domain structures in thin single-crystal wafers of barium hexaferrite in an orthogonal magnetic field H [16]. *a)* $H = 0$ Oe, *b)* $H = 3080$ Oe, *c)* $H = 3500$ Oe. The 'spots' in *c* are stable cylindrical domains of opposite magnetization. Similar domains (in other materials) are now known as magnetic bubbles, carriers of information in bubble-domain memory devices.

Technology

Fig. 16 gives a broad outline of the steps in the manufacture of various types of Ferroxdure. Prefiring produces the hexaferrite by a solid-state reaction between the basic materials $BaCO_3$ or $SrCO_3$ and Fe_2O_3. The clusters of crystallites thus formed are then finely ground in a mill to a powder with a particle size of about 1 μm. During or after this process a dry or wet mass is formed, or a plastic mass after the addition of plasticizing agents. Objects are formed from this mass by various shaping processes: dry pressing, wet pressing and extrusion for Ferroxdure that is subsequently sintered, and extrusion, injection moulding and rolling for plastoferrite. The plastoferrites, after cutting or punching to size or shape, are then ready for use. The shaping of the solid varieties is followed by a high-temperature treatment, in which sintering produces strong, hard objects, which are then ground to the required dimensions. The magnetization is usually left to the user, since the non-magnetized products are easier to handle, e.g. during transport and assembly.

The milling process on the one hand increases the sintering reactivity, as for all ceramics, and on the other — especially for Ferroxdure — it should produce as many single-crystal grains as possible that are sufficiently small and can be oriented. These are obtained by milling larger crystal clusters consisting of crystallites that are not too small. The particles of the anisotropic varieties are oriented in the shaping process. When the material is pressed or moulded *in a magnetic field*, the orientation results because the grains have an axis of easy magnetization that takes on the direction of the field. When the material is extruded through a narrow slit, or is rolled, the orientation results because the particles are of platelet form and tend to settle in the plane of the ribbons or sheets produced. (The easy direction of magnetization is perpendicular to the plane of the platelets.) By far the best orientational effect is obtained by wet pressing in a magnetic field. Products pressed or moulded in a field are demagnetized after shaping, again to facilitate handling.

Grinding objects of sintered Ferroxdure is expensive, but it is usually necessary because the previous ceramic process cannot be controlled sufficiently accurately to ensure that the products meet strict dimensional tolerances without being ground. Since Ferroxdure is so hard it must be ground with a diamond tool. The grinding of Ferroxdure is in itself a major problem and has been the subject of intensive study [17].

In the following we shall briefly discuss some interesting developments and investigations related to powder preparation, shaping and sintering.

---

[13] J. Smit, J. Phys. Radium **20**, 370, 1959.
[14] F. K. Lotgering, J. Phys. Chem. Solids **35**, 1633, 1974. A. M. van Diepen and F. K. Lotgering, J. Phys. Chem. Solids **35**, 1641, 1974.
[15] See for example A. H. Bobeck and H. E. D. Scovil, Sci. Amer. **224**, No. 6, 78, June 1971.
[16] C. Kooy and U. Enz, Philips Res. Repts. **15**, 7, 1960.
[17] A. Broese van Groenou, J. D. B. Veldkamp and D. Snip, J. Physique **38**, C1-285, 1977.

POWDER PREPARATION

SHAPING

mixing raw materials

granulating, prefiring

wet milling

dry milling

drying, deagglomeration

deagglomeration, granulation

plasticizing

mixing with plastic, granulation

wet milling, filtering, drying, annealing, mixing with plastic

dry pressing

wet pressing in field

dry pressing in field

extrusion

extrusion

injection moulding in field

rolling

Fig. 16. Diagram illustrating the manufacture of Ferroxdure.

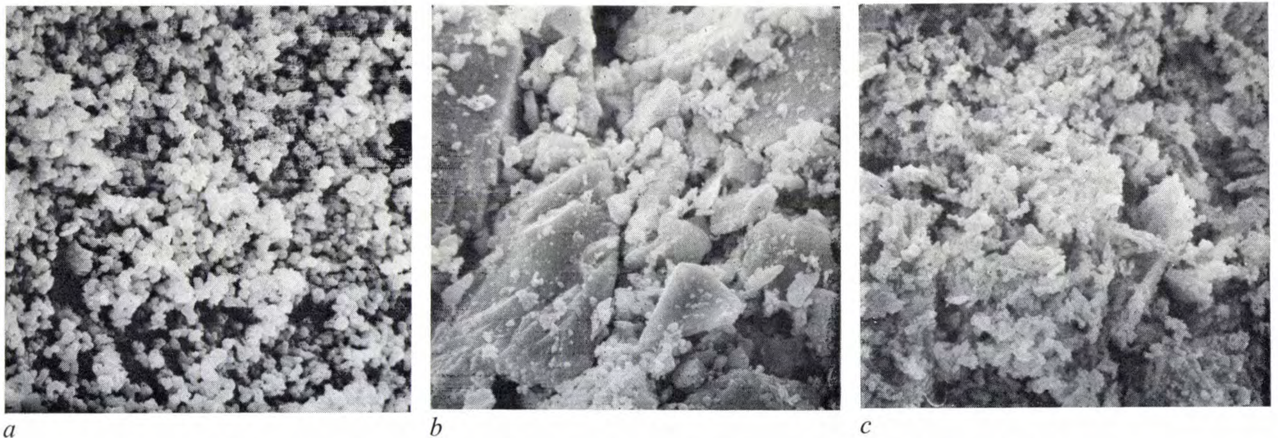

a *b* *c*

Fig. 17. The structure of *a*) synthetic, *b*) mineral and *c*) regenerated iron oxide. The synthetic powder has a well defined grain size. In the mineral powder, obtained by milling and sieving a coarse powder, there is a considerable variation in grain size. The regenerated iron oxide slightly resembles the synthetic type, but the grains form large clusters. Scanning-electron-microscope photomicrographs, magnification 1500 ×.

Powder preparation

Since 1970 there have been developments, relating to the iron oxides used, that have considerably reduced the production costs [18]. It was formerly the practice to use synthetic iron oxide, obtained from the pigment industry. Raw-material costs then accounted for some 20% of the price of the product. This percentage is very much lower since the change-over to cheaper raw materials: mineral iron oxide and iron oxide obtained as a by-product in the regeneration of pickling liquids used in steel rolling mills. As can be seen in *fig. 17*, these raw materials are not so well defined, and may vary appreciably from one source to another; the suppliers do not usually accept exact specifications. However, these materials are satisfactory because the prefiring process is carefully controlled. Crystallites of the

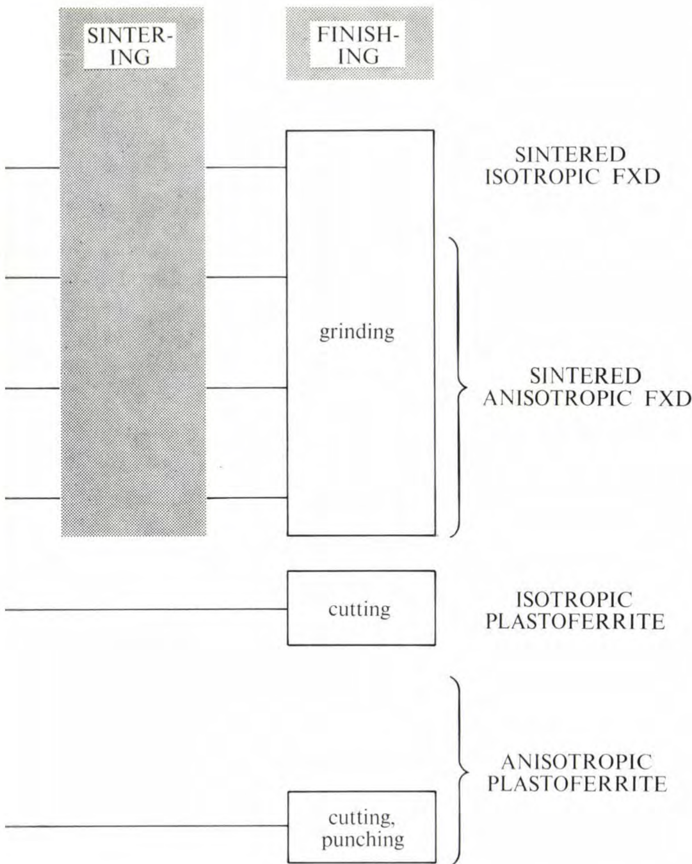

required dimensions are obtained by carrying out this process at high temperature (about 1300 °C) with additives (including the impurities) that ensure that there is also a liquid phase. As shown in *fig. 18*, the raw materials under these conditions lose their original identity; the mixing room has become 'omnivorous'.

Accurate control of the continuous prefiring process depends essentially on a regular flow of the mixture of raw materials through the furnace. The untreated powder mixture is not suitable for this. Formerly the mixture was passed through the furnace in the form of pressed blocks, but a special crushing operation was then necessary afterwards to repulverize the blocks, which became very hard. Nowadays the prefiring takes place in rotary kilns (*fig. 19*), and the feed is in the form of granules with diameters ranging from 3 to 10 mm. *Fig. 20* shows a granulating mill in action.

Powders for the plastoferrites are dry-milled in vibratory mills, and those for sintered Ferroxdure are wet-milled in ball mills to 20 m^3. The milling introduces crystal defects in the particles, which have the effect of lowering the coercivity. In the plastoferrites, however, these defects can be eliminated by annealing after the milling, and in sintered Ferroxdure by the sintering process itself. The milling time will be dealt with later.

Shaping

Dry pressing, extrusion, injection moulding and rolling are familiar shaping methods in the ceramics and plastics industries. We shall confine ourselves here to the technique specific to Ferroxdure: 'wet pressing' (pressure filtration of an aqueous slurry) in a magnetic field; a great deal of development effort has gone into this technique.

Fig. 21 shows a schematic diagram of a pressing cycle. Controlled amounts of the suspension of ferrite particles in water, forming a slurry with a water content of about 40 wt %, are injected by a pump under high pressure (50 to 100 atm) into the compression space (fig. 21*a*, *b*). In this space, formed by a die plate and two punches, a magnetic field is applied. Water is drained off through filters in the punches; the slurry is densified to a water content of about 13 %. The applied field orients the particles. Additional densification is produced by the lower punch moving up a few millimetres (fig. 21*c*), and the compacted product is demagnetized and removed from the die (fig. 21*d*).

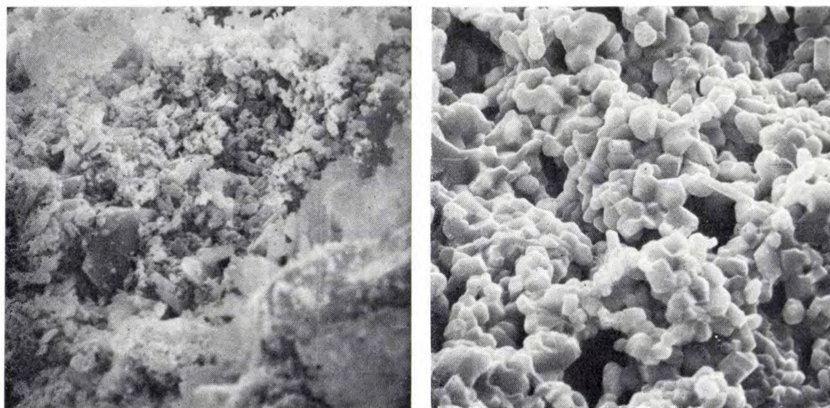

Fig. 18. A mixture of Fe_2O_3 and $SrCO_3$, *left:* before prefiring, *right:* after prefiring. Scanning-electron-microscope photomicrographs, magnification 1500×.

[18] C. A. M. van den Broek, Proc. 3rd Eur. Conf. on Hard magnetic materials, Amsterdam 1974, p. 53, and Ceramurgia Int. 3, 115, 1977.

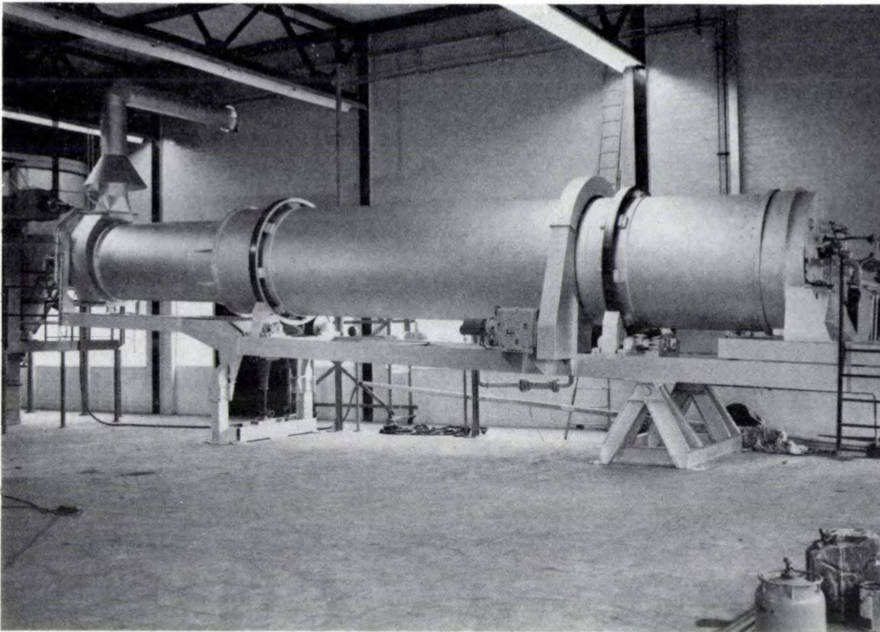

Fig. 19. Rotary kiln in which the mixture of raw materials is converted into the hexaferrite by a solid-state reaction.

Simple shapes such as blocks, discs and rings, and more complicated objects such as ring segments with radial orientation can be produced in this way. Filtration during injection into the die and after-pressing (fig. 21*a*, *b* and *c*) takes from 10 to 25 seconds, depending on the product, and the total cycle lasts from 20 to 40 seconds. Multiple dies have been developed to increase the production rate; these may be very complicated in construction (*fig. 22*). Press-forming methods, such as the high-pressure injection method [19], and punch constructions are often protected by patents. The high cost of the dies makes quantity production desirable to keep down the price of the products. A complete press can be seen in *fig. 23*.

Particle orientability; milling time

Suspensions of specially prepared powders have been studied to determine what happens during the orientation of the particles in a magnetic field [20]. In the zero-field state the particles in the suspension lie in convoluted chains (*fig. 24a*). When a magnetic field is applied, the polarization of the suspension increases sharply at about 40 kA/m (500 Oe). The structure of convoluted chains is apparently broken fairly suddenly to form the structure shown in fig. 24*b*, in which the chains are stretched in the direction of the field. Tests to determine the 'orientability' of the particles (see below) have shown, however, that some hundreds of kA/m (thousands of oersteds) are necessary to ap-

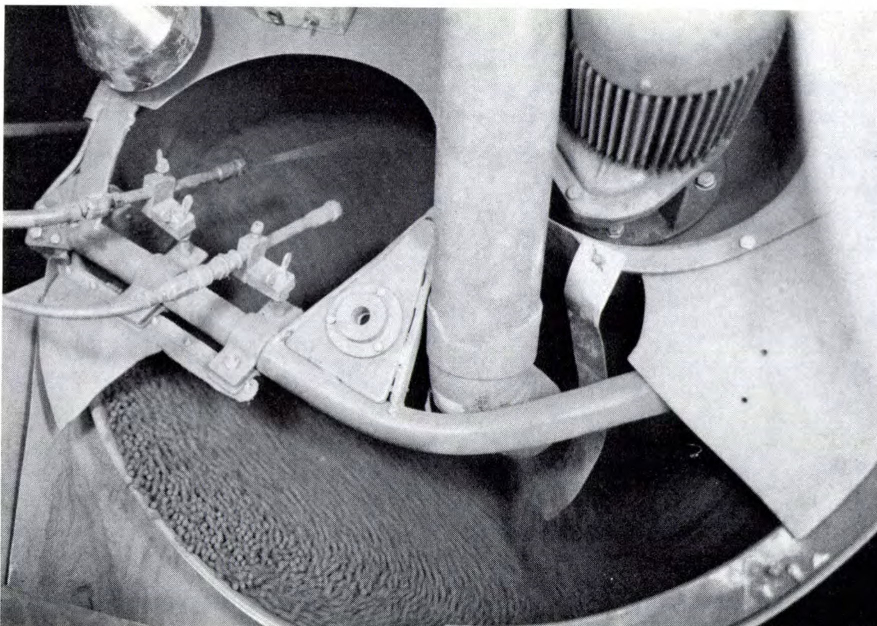

Fig. 20. Granulating mill. Because of the rotary movement and the addition of water, spherical granules are formed from the powder. The largest granules 'float' to the surface where they enter the outlet tube.

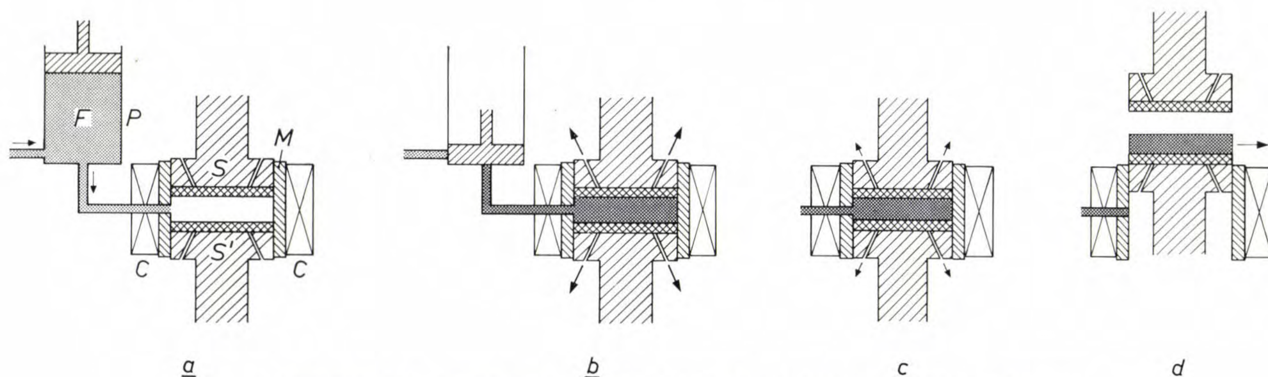

Fig. 21. Diagram of the pressing cycle. *M* die, *S,S'* punches, *P* injection pump, *F* suspension, *C* magnet coil. The punches contain filters and drainage channels for the water. *a*) Before, *b*) after the material is injected into the compression space; the slurry is densified from 40% to 13% water content, and the particles are oriented by the magnetic field. *c*) After-densification by slight upward movement of the lower punch, the amount of the movement depending on the thickness of the product; demagnetization. *d*) Removal of the compacted product.

proach complete orientation of the particles. A detailed picture of the chains of fig. 24*a*, after drying, is given in fig. 24*c*.

For suspensions of particles that can be completely oriented the remanent polarization J_r is equal to the saturation polarization J_s. If the particles cannot be oriented and therefore remain in random orientation, J_r is equal to $\frac{1}{2}J_s$. A good measure of the degree of orientation (r) of the particles is therefore J_r/J_s, a figure between $\frac{1}{2}$ and 1. With the milling procedures used for this study there is a maximum in the orientability as a function of the milling time after about 10 hours of milling (see *fig. 25*). The field does not therefore have an optimum effect if the powder is milled for a shorter or much longer time than 10 hours. In the first case there are apparently still too many particles in the polycrystalline state; in the second case the milling treatment gives rise to new, unyielding clusters of particles that can no longer be oriented.

Texture of the pressed product

The success of the method depends to a great extent on whether the texture of stretched chains (fig. 24*b*) is preserved during the filtration under pressure in the magnetic field. A further study [21] has demonstrated that this is indeed so, at any rate up to a fairly high degree of densification. Thin suspensions of the specially prepared powders mentioned above were filtered under pressure, both in a field parallel to the direction of compression and in a field perpendicular to it (*fig. 26a, b*). Two stages were distinguished: a stage of 'cake formation' — where the pressure required for a particular filtration rate rises relatively slowly — and a 'cake-densification' stage, where the pressure rises steeply (fig. 26*c*). At the pressure P_c at which the cake had just formed, the porosity was always found to be

[19] E. Haes and A. van der Maat, U.S. Patent 3.530.551.
[20] F. Kools, Proc. 3rd Eur. Conf. on Hard magnetic materials, Amsterdam 1974, p. 98, and Ber. Dtsch. Keram. Ges. **52**, 213, 1975.

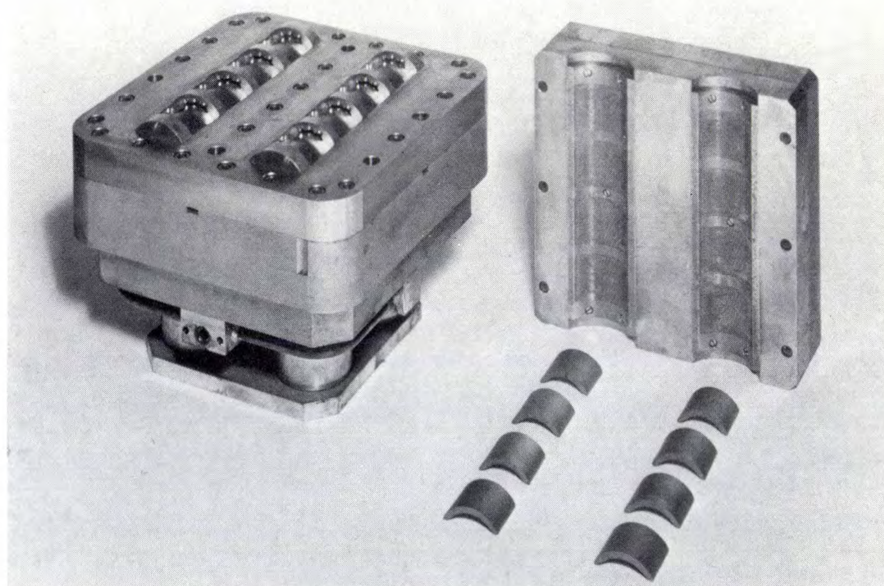

Fig. 22. A die for pressing eight radially oriented segments simultaneously.

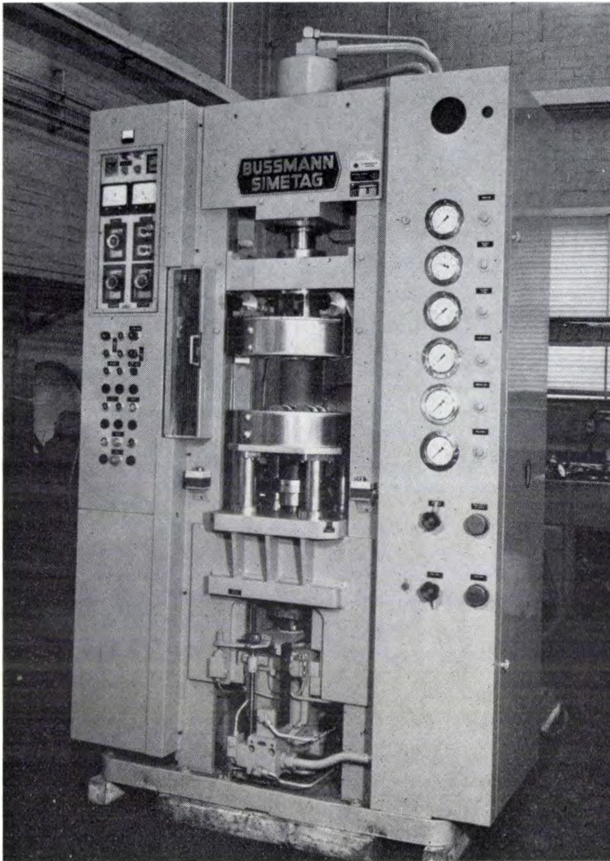

Fig. 23. Press comprising die and punches for producing segments.

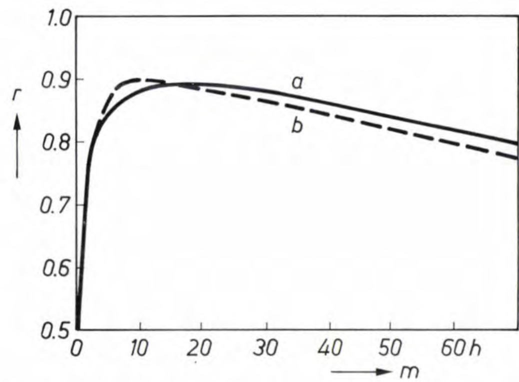

Fig. 25. 'Degree of orientation' r (= J_r/J_s) of the particles in suspension of hexaferrite as a function of the milling time m in *a*) a ball mill and *b*) a vibratory mill. J_r is the remanent polarization of the suspension, J_s the saturation polarization.

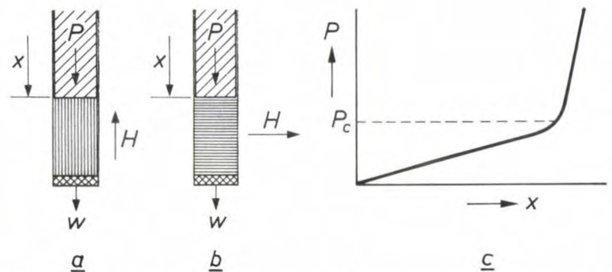

Fig. 26. Filtration under pressure of a suspension with excess of water, *a*) in a magnetic field parallel to the pressing direction, *b*) in a field perpendicular to it. *c*) The pressure P as a function of the punch displacement x at constant filtration rate (constant water flow w). At $P = P_c$ the 'cake-formation' stage changes to the 'cake-densification' stage.

about 60 vol. %. However the permeability p of the cake to water — as calculated from P_c and the filtration rate — was different in the two cases given in fig. 26: at $H > 200$ kA/m (2500 Oe) the value of $p_{\parallel}/p_{\perp}$ was no less than about 2 (*fig. 27*). This is just about the value that was found both theoretically and experimentally for the ratio between the longitudinal and the transverse permeability of stacks of long, cylindrical, parallel particles to liquid.

A further confirmation of the picture thus obtained of the 'cake' — compressed but still oriented chains of particles — is obtained by applying to the chains the

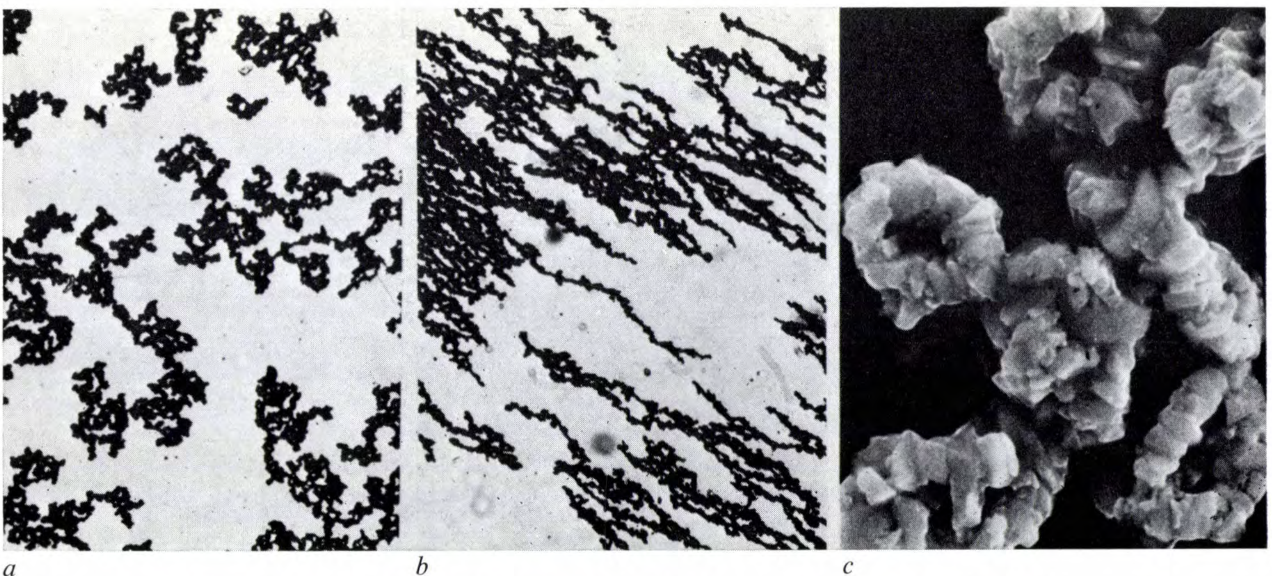

Fig. 24. *a*) Photomicrograph of particles of a specially prepared powder in suspension. *b*) As *a*, but in a magnetic field. *c*) Electron-microscope photomicrographs of particle clusters, after drying. Magnification of (*a*) and (*b*) 110×, of (*c*) 2800×.

theoretical relation between the longitudinal permeability $p_{\parallel}$ of parallel stacked cylinders and the diameter of the cylinders. With the measured values for $p_{\parallel}$ diameters are then found that correspond reasonably well to the diameters of the particles as estimated, for example, from scanning-electron-microscope photomicrographs of the original powder.

As stated earlier, this study related to the structure of a cake with a porosity of about 60 vol. %. Further measurements have shown that the degree of orientation (J_r/J_s) of the product that is *completely* compacted in a parallel field is about 10% lower than that of the original suspension [22].

Sintering

Ferroxdure is sintered by firing it in an oxidizing atmosphere. In the factory this is usually done in electrical or gas-fired furnaces with a capacity of 1000 to 4000 tonnes per year.

For both prefiring and sintering it is essential to have a knowledge of the phase diagram. The phase diagrams of the systems used are now reasonably well known. *Fig. 28* shows part of the diagram for the system SrO-Fe_2O_3.

We shall now discuss the results of a large series of experiments with crystal-oriented Sr-Ferroxdure, which clearly demonstrate the effects of the sintering temperature and the composition on the sintered product [24]. In these experiments a standard sintering programme was used with only one variable, the sintering temperature T_s (*fig. 29*). The powder used in all the experiments was milled to a mean particle size of 1-2 μm.

It has long been known that the sintering reactivity is very low for a stoichiometric composition, and can be greatly increased by an excess of the alkaline-earth ion. This is clearly demonstrated in *fig. 30*. Here n is the molar ratio between Fe_2O_3 and SrO ($n = 6$ for the stoichiometric composition). As can be seen, at $n = 5.90$ the material is far from completely sintered even at 1300 °C, whereas at $n \approx 5.5$ it is already densely sintered at 1150 °C. This effect is generally attributed to an increased diffusion rate due to lattice defects or to the occurrence of a liquid phase. The results of fig. 30, combined with those of fig. 28, suggest that a liquid phase does not occur here: there is dense sintering apparently even below the eutectic temperature (1210 °C).

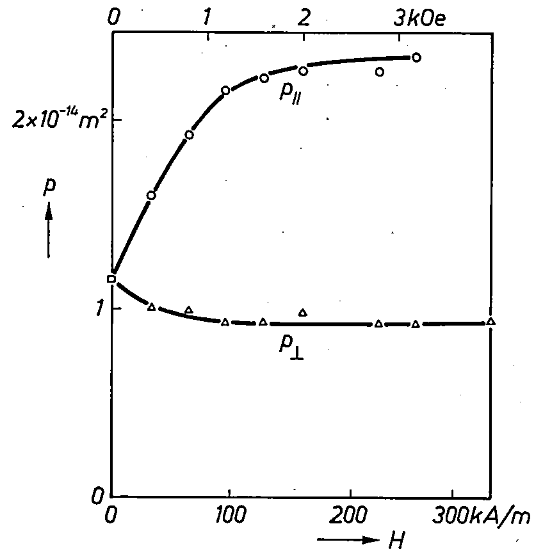

Fig. 27. Permeability to water, p, of a cake just formed ($P = P_c$ in fig. 26) as a function of the strength of the applied magnetic field; $p_{\parallel}$, field parallel to the pressing direction; $p_{\perp}$, field perpendicular to it.

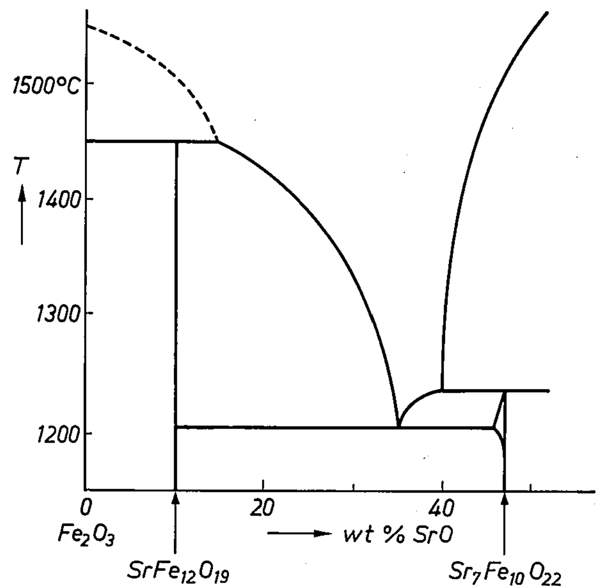

Fig. 28. Part of the phase diagram of the system SrO-Fe_2O_3 [23].

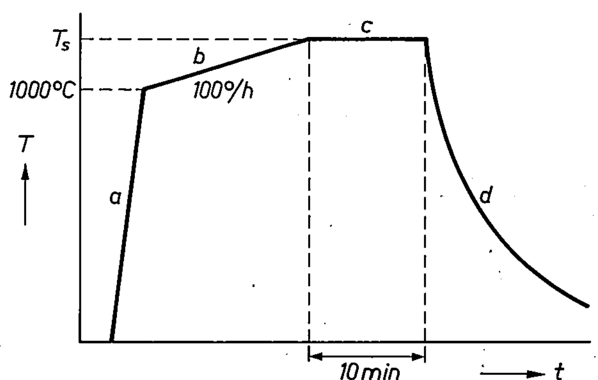

Fig. 29. Normalized sintering programme with one variable, the sintering temperature T_s. *a*) Rapid heating to 1000 °C. *b*) Temperature rise of 100 °C per hour to the desired sintering temperature. *c*) Sintering for ten minutes at the temperature T_s. *d*) 'Free' cooling.

[21] S. Strijbos, Proc. 3rd Eur. Conf. on Hard magnetic materials, Amsterdam 1974, p. 102.
[22] F. Kools, to appear shortly in Ber. Dtsch. Keram. Ges.
[23] P. Batti, Ceramurgia 6, 11, 1976.
[24] This investigation was carried out by Ir G. S. Krijtenburg, of the Ceramics Laboratory of Philips Elcoma Division, Eindhoven. See also Proc. 3rd Eur. Conf. on Hard magnetic materials, Amsterdam 1974, p. 83.

It has also long been known that sintering is associated with grain growth. Because of this the sintering temperature is a compromise: a higher temperature gives a higher density, and by the same token more atomic moments per unit volume and hence a higher remanence, but at the same time it results in larger grains and consequently a lower coercivity. The great importance of a high sintering reactivity is therefore in the first place that it makes high densification possible at temperatures where grain growth is still moderate. The beneficial effect of the excess SrO ceases when the remanence is too greatly reduced as a result of the increasing concentration of the non-ferromagnetic phase $Sr_7Fe_{10}O_{22}$ (see fig. 28). Initially, however, this has little effect (see *fig. 31*), so that the main thing is to choose n sufficiently small, e.g. less than 5.8.

The relation between sintered density and grain size is clearly demonstrated by the straight line A in the B_r-H_c diagram in *fig. 32*. This represents a large number of samples with a 'good' composition ($n \approx 5.5$; the crosses $\times$). Sintering temperature, density and grain size increase from bottom right to top left.

In ceramic technology grain growth is also more directly restrained by means of modifying agents and grain-growth inhibitors. The principal grain-growth inhibitor for Ferroxdure is SiO_2. Its effect is demonstrated in fig. 32 by curve B, which represents samples with $n \approx 5.5$ to which about 1% of SiO_2 was added. In fact, the samples naturally fall into the groups A and B because, with increasing SiO_2 content, the transition $A \rightarrow B$ takes place fairly sharply. *Fig. 33a-d* also shows a difference in microstructure between the A and B samples.

At higher densities (higher temperatures) the grain-growth inhibitor ceases to have any useful effect. The curve B bends over towards A. This is caused by an undesirable effect familiar in sintering technology and called 'discontinuous grain growth', in which some of the grains abruptly grow very large. This effect is the greatest practical limitation to the quality that can be achieved. The theoretical maximum for $(BH)_{max}$ (see fig. 8) at room temperature is 45 kJ/m³ (5.7 MGsOe). The $(BH)_{max}$ of commercial products (fig. 7) is about 28 kJ/m³ (3.5 MGsOe). By optimizing all the steps in the production process, laboratory values of about 40 kJ/m³ (5 MGsOe) have been achieved [25].

Anisotropic shrinkage

During the sintering of ferrites there is very considerable densification; the sintered product is about 20% smaller in linear dimensions than the pressed product. Anisotropic Ferroxdure products not only change in size but also in shape, because the shrinkage is also strongly anisotropic. The shrinkage of Ba-Ferroxdure,

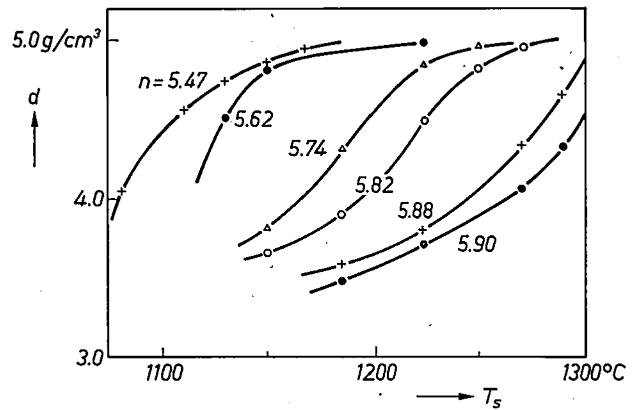

Fig. 30. Density d of the sintered product as a function of the sintering temperature T_s, for various values of the mole ratio n between Fe_2O_3 and SrO. The greater the deviation from stoichiometry, the lower the temperature at which the product is densely sintered. For the stoichiometric composition, n is equal to 6.

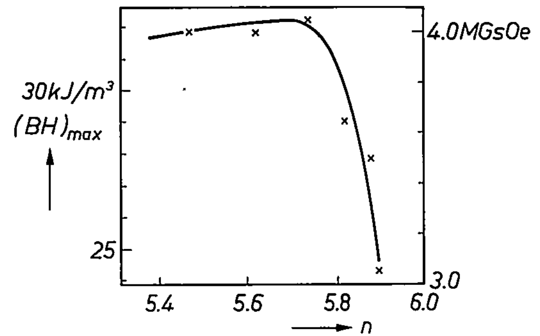

Fig. 31. The 'quality' $(BH)_{max}$ of the sintered product as a function of the composition parameter n. For each composition the sintering temperature was optimized with respect to $(BH)_{max}$.

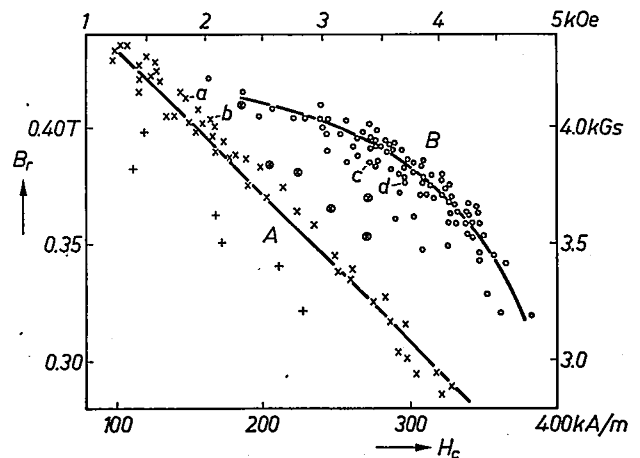

Fig. 32. B_r-H_c combinations for a large number of samples. + Stoichiometry or excess Fe_2O_3 ($n \geqslant 6.0$), $\times$ surplus SrO ($n \approx 5.5$), both with little or no addition of SiO_2 ($m < 0.6$, where m is the mole ratio of the added SiO_2 to the excess SrO). ○ Excess SrO ($n \approx 5.5$) and added SiO_2 ($m > 0.6$). ⊗ $n \approx 5.5$ and $m \approx 0.6$. The sintering temperature increases from lower right to top left; a, b, c and d represent the samples in fig. 33.

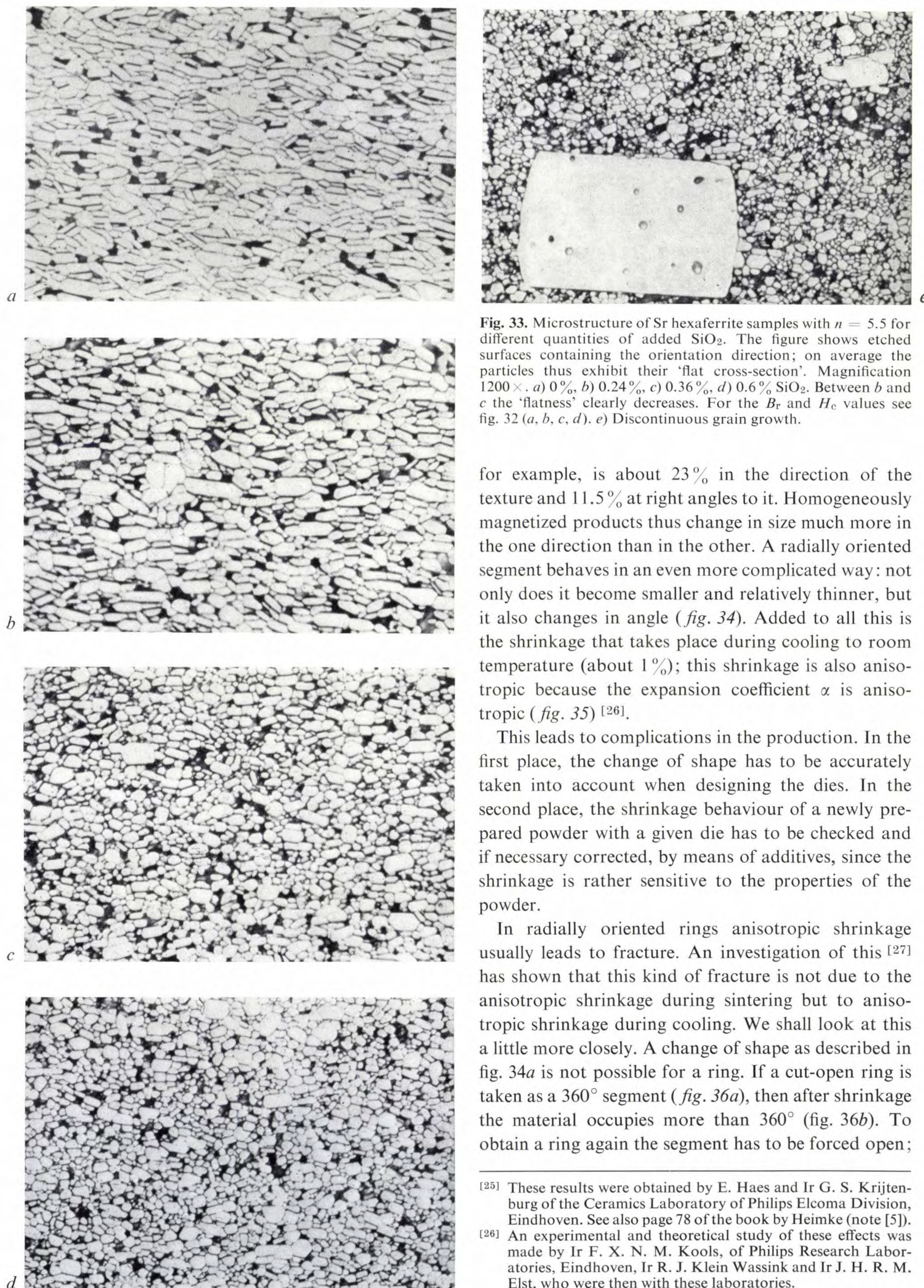

Fig. 33. Microstructure of Sr hexaferrite samples with $n = 5.5$ for different quantities of added SiO_2. The figure shows etched surfaces containing the orientation direction; on average the particles thus exhibit their 'flat cross-section'. Magnification 1200×. *a*) 0%, *b*) 0.24%, *c*) 0.36%, *d*) 0.6% SiO_2. Between *b* and *c* the 'flatness' clearly decreases. For the B_r and H_c values see fig. 32 (*a*, *b*, *c*, *d*). *e*) Discontinuous grain growth.

for example, is about 23% in the direction of the texture and 11.5% at right angles to it. Homogeneously magnetized products thus change in size much more in the one direction than in the other. A radially oriented segment behaves in an even more complicated way: not only does it become smaller and relatively thinner, but it also changes in angle (*fig. 34*). Added to all this is the shrinkage that takes place during cooling to room temperature (about 1%); this shrinkage is also anisotropic because the expansion coefficient α is anisotropic (*fig. 35*) [26].

This leads to complications in the production. In the first place, the change of shape has to be accurately taken into account when designing the dies. In the second place, the shrinkage behaviour of a newly prepared powder with a given die has to be checked and if necessary corrected, by means of additives, since the shrinkage is rather sensitive to the properties of the powder.

In radially oriented rings anisotropic shrinkage usually leads to fracture. An investigation of this [27] has shown that this kind of fracture is not due to the anisotropic shrinkage during sintering but to anisotropic shrinkage during cooling. We shall look at this a little more closely. A change of shape as described in fig. 34*a* is not possible for a ring. If a cut-open ring is taken as a 360° segment (*fig. 36a*), then after shrinkage the material occupies more than 360° (fig. 36*b*). To obtain a ring again the segment has to be forced open;

[25] These results were obtained by E. Haes and Ir G. S. Krijtenburg of the Ceramics Laboratory of Philips Elcoma Division, Eindhoven. See also page 78 of the book by Heimke (note [5]).

[26] An experimental and theoretical study of these effects was made by Ir F. X. N. M. Kools, of Philips Research Laboratories, Eindhoven, Ir R. J. Klein Wassink and Ir J. H. R. M. Elst, who were then with these laboratories.

the inside surface is then put into tension and the outside is put into compression. These are typical of the stresses that occur during cooling. During sintering, on the other hand, the ions are of course highly mobile, and no stress of any significance can therefore occur. The stresses that develop during cooling are greater in thicker rings than in thinner ones. The investigation shows that rings whose inside diameter is greater than 0.85 times the outside diameter always remain intact and that thicker rings always break.

No account has been taken here of the fracture that can easily occur when the pressed ring is being heated up before sintering, as a consequence of the anisotropic expansion combined with low mechanical strength. The strength of the product can be increased and fracture avoided by subjecting the ring to isostatic compression under high pressure after the normal pressing process.

The main application for radially oriented rings would be as stator magnets in d.c. motors. In practice, for reasons connected with the difficulties just discussed, two radially oriented segments of 120° to 163° or four segments of about 70° are usually used.

Finally, there is a further complication that must be taken into account in the production of segments and other shapes; it even occurs with isotropic Ferroxdure, but is less serious in this case because of the greater strength of this material. We refer to the rapid varia-

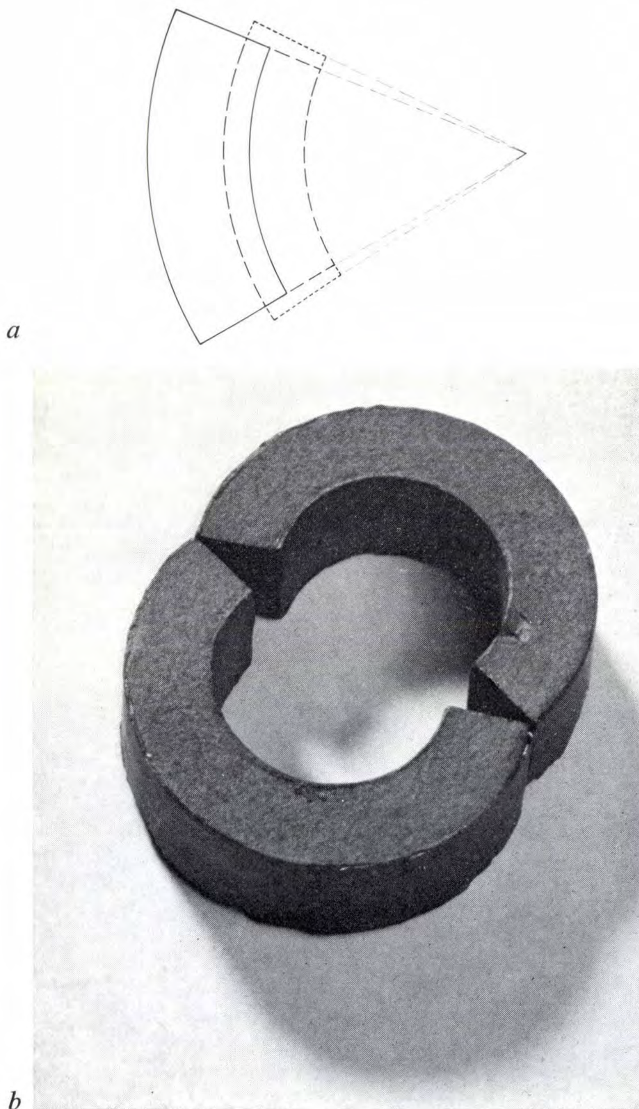

Fig. 34. Change in the shape of a radially oriented segment as a result of anisotropic shrinkage. *a) Solid line:* a segment before sintering. *Dashed line:* the result of isotropic shrinkage. The shape indicated by the dotted line represents the same shrinkage in the radial direction but less in the tangential direction. The angle of the segment has thus increased. *b)* Laboratory demonstration of this effect. A radially oriented ring was cut into two after pressing. The photograph shows the two halves after sintering.

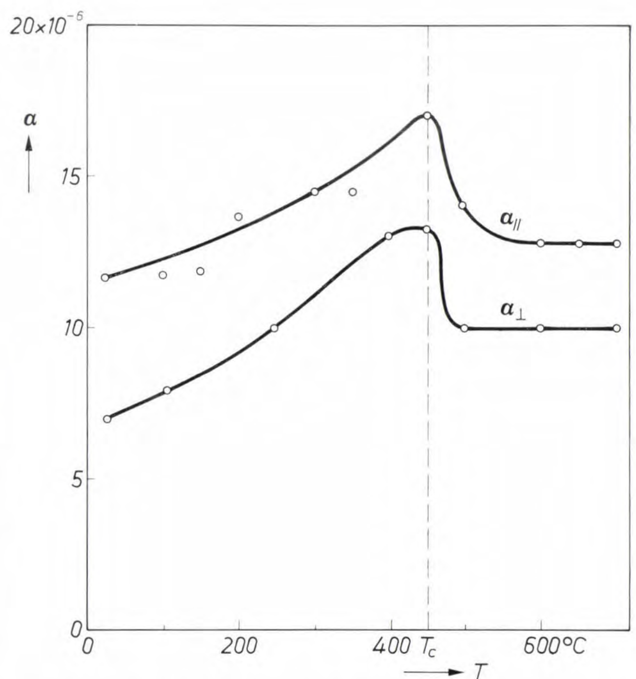

Fig. 35. The expansion coefficient of oriented Ferroxdure (Sr-Ferroxdure 370) in the direction of orientation ($\alpha_{||}$) and perpendicular to it ($\alpha_{\perp}$), as a function of temperature. T_c Curie point (450 °C).

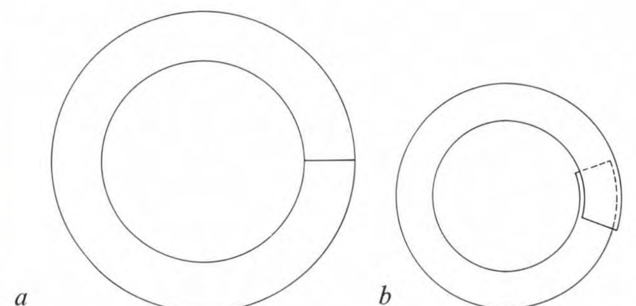

Fig. 36. *a)* Cut-open ring before sintering, regarded as a 360° segment. *b)* The same segment after sintering (see fig. 34), assuming that the illustrated change of shape (the overlapping) is possible, for example because the ring is very thin.

[27] F. Kools, Science of Ceramics 7, 27, 1973.

tion of α at the Curie point (see fig. 35). The temperature gradient in the material during cooling introduces stresses that are proportional to α and to the temperature difference ΔT between the 'hot' inner regions and the 'cold' outer regions. At constant cooling rate there are no marked variations in the temperature difference but, as we saw above, the expansion coefficient does vary. As a consequence the stresses increase by about 30% when the Curie point is passed. In practice this means that the Curie point has to be passed very slowly. In the factory a transitional tunnel at the outlet of the sintering furnace is used, to spread the temperature decrease of the product over a longer time.

* *
*

If we look back over the 25 years of the existence of Ferroxdure, we notice at once that hardly any non-metallic materials have been used for permanent magnets apart from those that were given the name 'Ferroxdure' in 1952. Barium and strontium 'hexaferrite' were the important compounds right from the beginning. They are still important Philips products, processed into ceramic magnets under the name of 'Ferroxdure' or 'Magnadure'. Now that the patent rights have expired they are also produced elsewhere and marketed under other names, as indeed they already had been under licence.

The development from discovery to commercial magnetic materials took place at the beginning of the 1950s. The sixties saw a marked shift from the barium to the strontium ferrite, connected with the large-scale use of this material in small electric motors for the automobile industry. In the last ten years Ferroxdure has become steadily cheaper with the introduction of larger manufacturing centres and the use of cheaper raw materials.

The market for Ferroxdure products is still growing strongly. In addition to the rising demand for products such as Ferroxdure stator magnets for small electric motors in the automobile industry (about 50 W) there is now a growing market for stator magnets for industrial motors up to 10 kW.

Summary. The great success of Ferroxdure, the name given to a group of ceramic magnetically hard ferrites introduced in 1952, is mainly due to the low price per unit of magnetic energy. The broad demagnetization curve leads to 'short thick' magnets. The main constituent is (Ba, Sr)$Fe_{12}O_{19}$. The crystal has five magnetic sublattices which partly compensate each other (ferrimagnetism). The magnetic hardness is connected with the strongly anisotropic crystal structure and also with the microstructure of small crystallites or grains which, in the anisotropic varieties, are magnetically oriented.

Further research led to new materials, notably to Ferroxplana. Substitution of Al or Cr ions for Fe ions can increase the coercivity. The sublattices can be studied separately by means of Mössbauer spectroscopy. 'Spin-orbit coupling' appears to be responsible for the anisotropy. Magnetic 'bubbles' were first observed in $BaFe_{12}O_{19}$.

Developments and research relating to the technology of these materials are discussed, with emphasis on the prefiring process (introduction of cheaper raw materials), wet pressing in a magnetic field (complicated punch-tool constructions; the formation and preservation of oriented chains of particles in the suspension) and the sintering process (dense sintering without grain growth by non-stoichiometry and the addition of SiO_2; complications due to anisotropic shrinkage during sintering and cooling).

Philips tech. Rev. 37, 176-179, 1977, No. 7

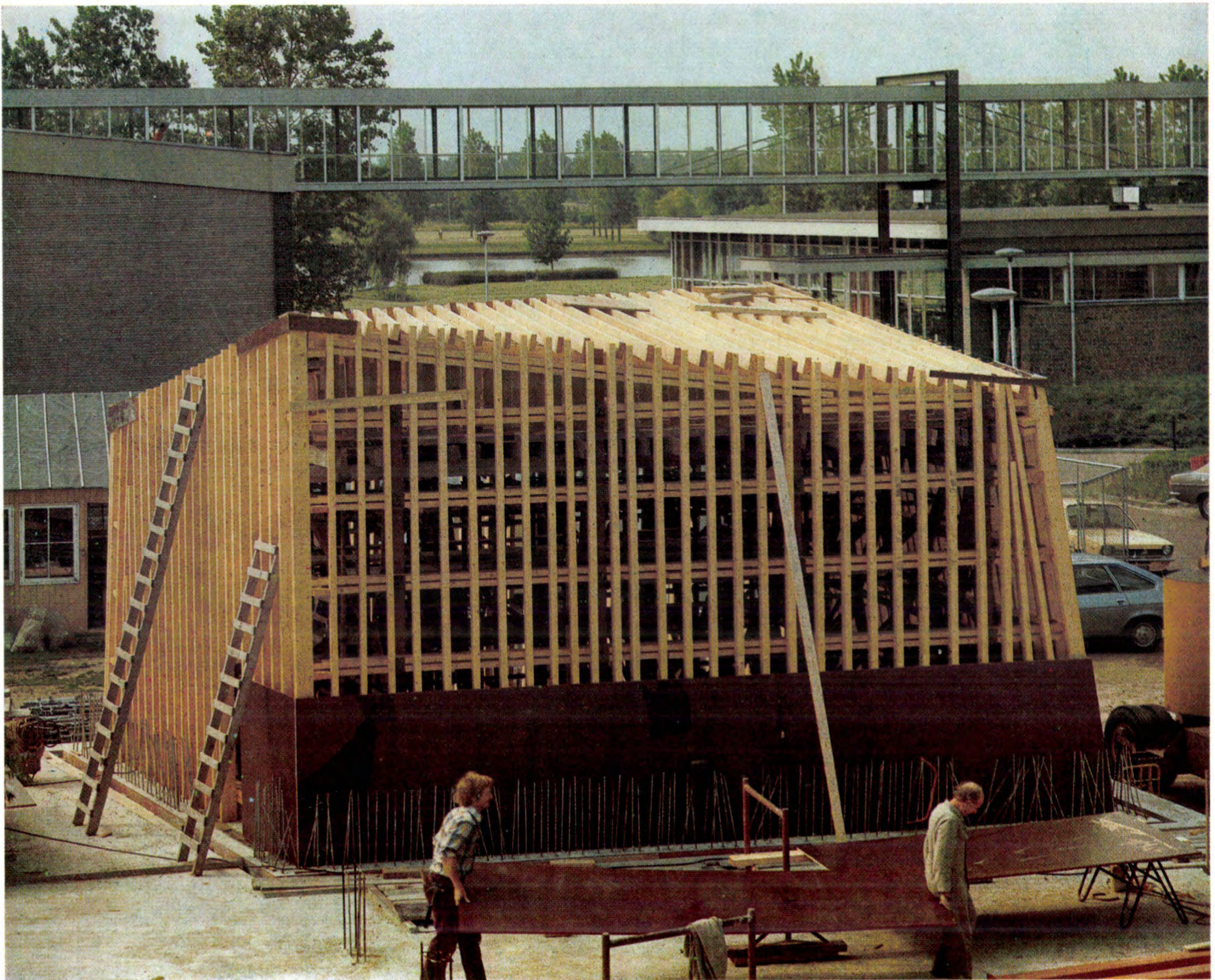

The design and construction of a non-rectangular reverberation chamber

The rather strange structure now taking shape at the Philips Research Laboratories complex in Eindhoven is a reverberation chamber. This is a chamber with hard sound-reflecting walls and is of great value in acoustic measurements. The chamber now being built should be ready by about March 1978; it will be used for investigations connected with noise abatement. These will include measurements on appliances such as vacuum cleaners and washing machines, to help in the design of quieter products, and measurements on production machines, so that noise can be reduced in workshops and factories. A reverberation chamber is also necessary for for testing the quality of sound-absorbent material.

When a reverberation chamber is available it is possible to obtain a quick and reliable measurement of the acoustic power radiated from an acoustic source. In the ideal case an acoustic source in a reverberation chamber produces a homogeneous and isotropic acoustic field, whose level is directly related to the power of the source. The acoustic field is homogeneous and isotropic because a large number of standing-wave patterns are excited simultaneously. As a result of the superposition of all these standing-wave patterns there is no preferential excitation of any one frequency, and no one place or direction is systematically favoured. The result is an almost continuous spectrum of resonant frequencies. Any chamber in the form of a rectangular parallelepiped and with a volume of 200 m^3 corresponds fairly well with this ideal picture at frequencies above about 250 Hz, i.e. at wavelengths shorter than about 1.4 m. For longer waves, however,

the possible number of standing-wave patterns in such a chamber is limited, and the chamber then has a clearly discontinuous spectrum of resonant frequencies.

It has long been known that a better approximation to the ideal behaviour of a reverberation chamber can be obtained at these low frequencies by making the walls oblique in such a way that the chamber is asymmetric in all three dimensions. This has the effect of producing irregular spatial patterns of standing waves. Superposition of the few standing-wave patterns occurring at low frequencies then leads to a more homogeneous acoustic field than in a 'rectangular' chamber. This asymmetry also has the effect of producing the desired uniform distribution of the resonant frequencies over the frequency scale.

The standing-wave patterns and resonant frequencies of a rectangular reverberation chamber can be calculated analytically [1]. This is not possible if the chamber is not rectangular. In the past this was often held to be a major drawback of a non-rectangular chamber. Nowadays, however, the behaviour of a non-rectangular chamber can be calculated numerically by means of the finite-element method [2].

In spite of the greater technical problems, we therefore decided to build a reverberation chamber of irregular shape. In calculating the sound-pressure distribution with the finite-element method the total volume of the chamber is divided into a large number of tetrahedral elements, and the differential equation for the acoustic field in the chamber is replaced by a set of equations for the field at the nodes of the tetrahedral network. The results of such a numerical calculation will be more accurate the finer the meshes of the network. To keep down the amount of calculation required, we only considered the frequency range below 125 Hz; this is the range where the various resonant frequencies are relatively far apart.

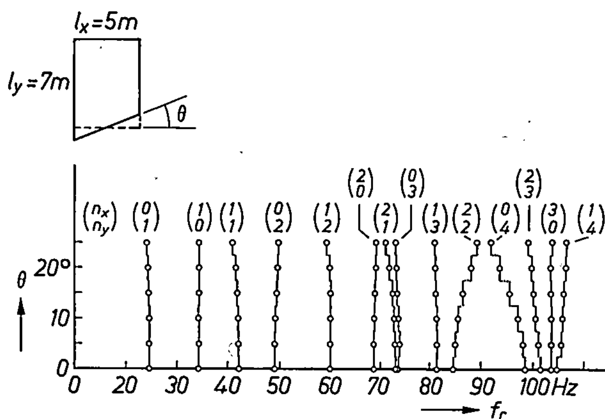

Fig. 1. Behaviour of the resonant frequency f_r of a two-dimensional rectangular chamber of total area 5×7 m², when one of the short walls is rotated through an angle θ. Each of the resonant frequencies is characterized by a pair of numbers $(n_x n_y)$ that indicates the number of half-periods in the standing-wave pattern in the x- and y-directions of the rectangular chamber.

We calculated a number of standing-wave patterns in this frequency range, for both two-dimensional and three-dimensional chambers [3].

The first thing that we noticed during these calculations was that if the angle of one of the walls was changed slightly, the effect on the resonance spectrum was completely unpredictable. *Fig. 1* shows the calculated behaviour of a number of resonant frequencies in a two-dimensional chamber, with a surface area of 5×7 m², as one of the walls is rotated through an angle. The result of changing the angles of two walls cannot be found by superimposing the results of changing the angles of each of the two walls separately. *Fig. 2* shows a number of calculated standing-wave patterns for the two-dimensional rectangular chamber and for a non-rectangular chamber with the same area. At higher frequencies in particular there is hardly any agreement between the pattern in a rectangular chamber and that in a non-rectangular chamber.

The computer time necessary for calculating the acoustic field in a single three-dimensional chamber is considerable, and the geometry of a three-dimensional non-rectangular chamber is determined by a large number of parameters. The method of calculation is therefore not so suitable for calculating the optimum values of all these parameters, and hence the optimum shape of the chamber. It is however possible to calculate the acoustic field in a given chamber. From calculations of this kind it can be seen quantitatively why a non-rectangular chamber is superior to a rectangular one, both in the homogeneity of the acoustic field and in the regularity of the spectrum of resonant frequencies in the low-frequency region.

We arrived in this way at a shape that promised acceptable behaviour even at frequencies lower than 100 Hz, and which has characteristics that come within the limits recommended in the ISO standards [4]. This means that our future measurements will be immediately comparable with measurements made elsewhere in other reverberation chambers constructed to these standards. This basis for intercomparison is particularly

[1] P. M. Morse, Vibration and sound, McGraw-Hill, New York, 2nd edition 1948, chapter VIII.
J. W. Strutt, 3rd Baron Rayleigh, The theory of sound, Vol. II, Macmillan, London, 2nd edition 1896, sections 267 and 299.
[2] The principles of the finite-element method are described in the article by J. H. R. M. Elst and D. K. Wielenga in this volume of Philips tech. Rev., p. 56 (No. 2/3).
[3] J. M. van Nieuwland and C. Weber, to be published shortly.
[4] International Standard ISO 3741-1975: Acoustics — Determination of sound power levels of noise sources — Precision methods for broad-band sources in reverberation rooms.
International Standard ISO 3742-1975: Acoustics — Determination of sound power levels of noise sources — Precision methods for discrete-frequency and narrow-band sources in reverberation rooms.

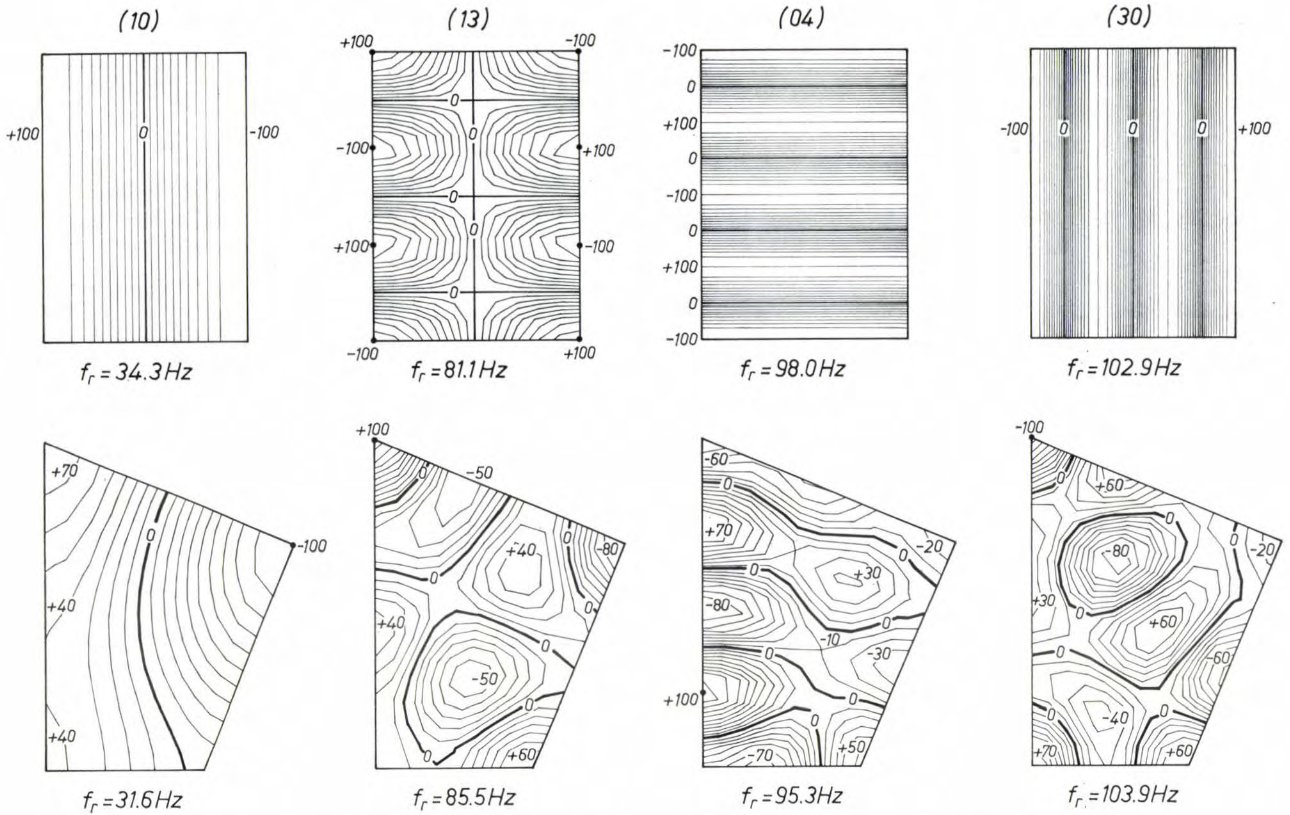

Fig. 2. Calculated sound-pressure distributions in a two-dimensional rectangular chamber and in a non-rectangular chamber of the same area. The calculations were carried out for a number of the lowest resonant frequencies. The resonant frequency f_r is indicated in each case. The nodal lines (zero sound pressure) are the bold contours. The pressure value in relative units is indicated next to the other contours of equal sound pressure. The correspondence in shape between the patterns in the two chambers is soon lost at higher resonant frequencies.

desirable since future recommendations and specifications are expected that will quantify the permitted sound levels from equipment such as domestic appliances.

The shape finally chosen for the reverberation chamber after we had considered the results of our calculations is shown in *fig. 3*. The floor is not rectangular, only two of the four side walls are perpendicular to the floor, and the ceiling consists of two planes that are not parallel to the floor. The volume of the chamber is 227 m^3. To check the calculations we made a model from concrete slabs, at a quarter of full scale, in which

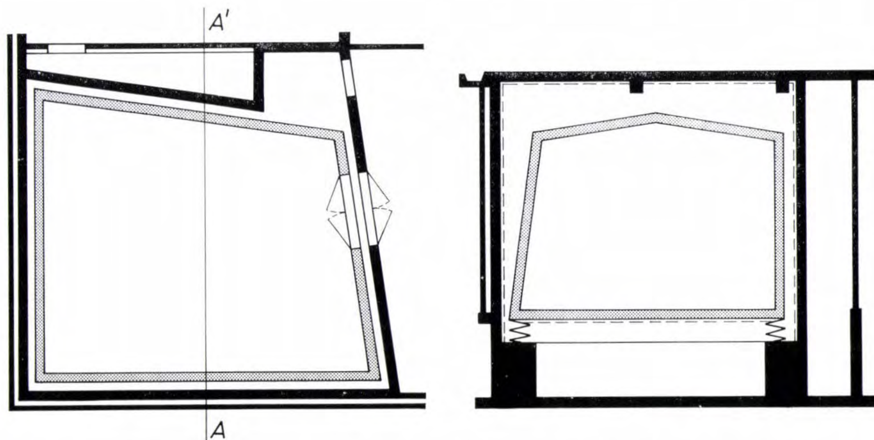

Fig. 3. Plan of the reverberation chamber (*left*) and a vertical cross-section along the line *AA'* (*right*). The concrete wall of the reverberation chamber is shown grey; the sound-insulating brick walls of the enclosure are shown black. To prevent external vibrations from entering the chamber through the floor, the 150-tonne concrete chamber is mounted on 80 steel coil springs.

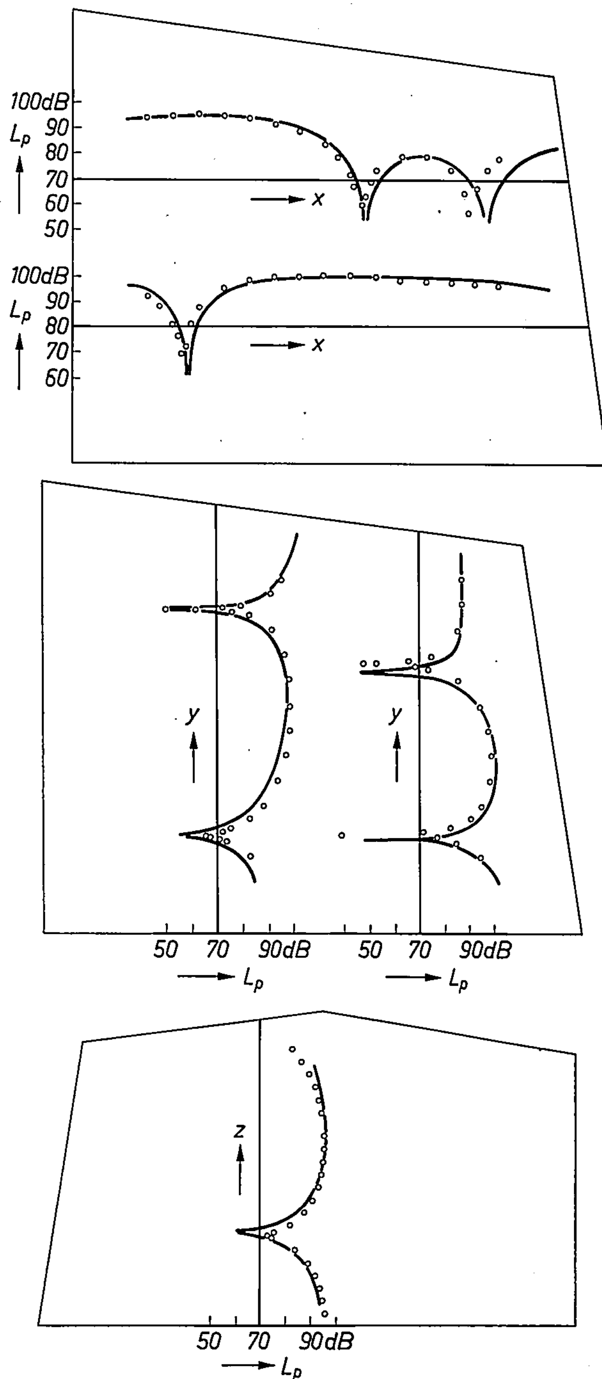

Fig. 4. Distribution of the sound pressure L_p as a function of the x-, y-, and z-coordinate in the final design of our reverberation chamber. The solid lines give the distribution calculated for the full-sized chamber at a frequency of 91.4 Hz, the points give the measurements for the quarter-scale model at a frequency of 365.5 Hz. In the neighbourhood of the nodal lines the difference between measurements and calculations may be relatively large. At these positions small deviations in the location of the microphone used for the measurements result in large errors, and the dimensions of the microphone will also have an effect.

the sound pressure was measured at a large number of locations. As can be seen in *fig. 4*, the results of these measurements are in good agreement with the calculations.

The chamber is built entirely of reinforced concrete. Special precautions were taken to make the inside surface as smooth as possible to give the maximum sound reflection from the walls.

The unpredictable and sometimes drastic effect of a small change in dimensions on the characteristics of the chamber, as mentioned earlier, meant that the dimensions specified in the design had to be adhered to very accurately in the construction. A heavy wooden structure, supported by steel girders, was therefore made for the internal shuttering (formwork) of the concrete chamber, as shown in the title photograph. This wooden structure was later covered with a cladding of special very hard smooth plywood boards. The exterior of the boarded formwork exactly followed the dimensions of the interior of the chamber.

To reduce external interference as much as possible during the measurements the entire reverberation chamber is enclosed inside a space with heavy brick walls. These walls are lined inside with sound-absorbing material to prevent resonances in the gap between the walls and the outside of the chamber. The weight of the chamber will be 150 tonnes, and it will stand on 80 steel coil springs located around the outside edge of the base. The natural frequency of the complete structure is at about 3 to 4 Hz, so that external vibrations at a frequency higher than about 10 Hz will have no noticeable effect on the chamber. Very high frequencies may however be transmitted along the springs; to prevent this, rubber pads are placed between the springs and the foundation. The wall of the reverberation chamber has openings, which can be tightly sealed, for ventilation and for introducing cables. The chamber itself and the surrounding structure are closed with heavy soundproofed doors.

J. M. van Nieuwland
A. Petterson
C. Weber

Dr Ir J. M. van Nieuwland, Ing. A. Petterson and Dr Ir C. Weber are with Philips Research Laboratories, Eindhoven.

Philips tech. Rev. 37, 180-187, 1977, No. 7

An edge-enhancing double-focus camera for image processing

W. G. Baig

In processing pictorial information one of the activities of the human brain is the 'strategic' reduction of data. This is necessary to distinguish essentials from inessentials, and image-processing machines must do something similar if they are to be of any real help. The first step in extracting features from pictures is therefore data reduction. The article below describes a camera in which the amount of data is reduced by means of a double-thresholding technique. The new camera produces information that is remarkably free from noise, and at the same time it gives good spatial resolution.

Image processing

In machines for processing pictorial information the input device is often a camera that converts optical information into electrical signals. The (spatial) resolution necessary for such a camera to be able to accurately localize particular details is so high that much of the output signal consists of information about the point-to-point variations in reflection (the grey scale) from the surface of the object. This information may not be required at all by the image-processing machine, however. In optical character recognition (OCR), for example, it is not necessary to distinguish between the numerous shades of grey. It is then advantageous to reduce the amount of information about the grey scale *before* the recognition procedure is started.

One method for such a reduction of information is to apply a threshold to the output signal from the camera. In this way binary information is produced, i.e. information consisting of black or white picture elements only, depending on whether the output signal exceeds the threshold level or not. The binary form is of particular interest for further processing of the data.

Fig. 1 shows the block diagram of a complete system for image processing. The arrangement includes a camera, which produces analog signals, a 'threshold' unit, which converts the analog signals into binary signals, and a 'recognition' unit, which processes the binary signals. In an OCR application the output signal might be the identity of a number that the camera has observed, whereas in the assembly of mechanical or electronic devices the signal might be the position of a small locating lug or mark on the object.

In this article a new method of image processing, with a double-focus camera, will be discussed. A camera of this type, shown schematically in *fig. 2*, operates with a split beam to give simultaneous scanning with two images; one image is sharp, the other is blurred. The blurred image is used for the *local* determination of a threshold level for the sharp image; this level therefore varies. The essential difference between the new method and others is that in addition to the local-area threshold it simultaneously employs a fixed (or single) threshold. The threshold unit therefore has a double function. The new thresholding procedure allows a high resolution to be maintained, although short-distance variations in reflectance are ignored. When camera and thresholds are properly adjusted the image edges are enhanced whereas noise is suppressed. (For simplicity the term 'camera' will from now on be used to indicate the *combination* of the blocks *CA* and *TB* in fig. 1.)

The performance of the double-focus camera has been investigated by using an OCR system that included this camera to read documents in machine-print and handprint characters. The camera was connected to a minicomputer, via a machine that could sort and position documents. However, it should be emphasized that the argument put forward would be equally valid in all applications where thresholding is employed.

The following section deals with the nature of both kinds of threshold level, in particular the local-area threshold. Details of the camera arrangement are then given, and finally an account is given of the performance of the system with the new camera as applied to the reading of machine-print and handprint text.

W. G. Baig, M.Sc. (Eng.), formerly with Philips Research Laboratories, Redhill, Surrey, England, is now with the University of Petroleum and Minerals, Dhahran, Saudi Arabia.

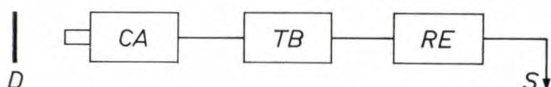

Fig. 1. Block diagram of systems for image processing by machine. *D* object scanned. *CA* camera. *TB* thresholding circuits. *RE* recognition equipment. *S* output signal.

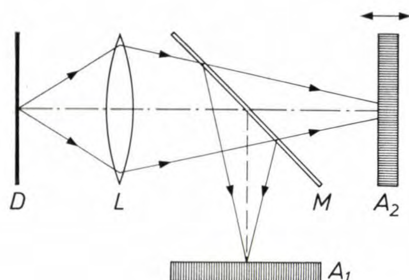

Fig. 2. The arrangement of a double-focus camera for processing pictorial information with the aid of a local-area threshold. *D* document to be processed. *L* imaging lens. *M* semitransparent mirror. $A_{1,2}$ linear arrays of solid-state detector cells. A_1 is placed at the focal plane. The array A_2, which provides the threshold, is placed at an out-of-focus position; it can be adjusted.

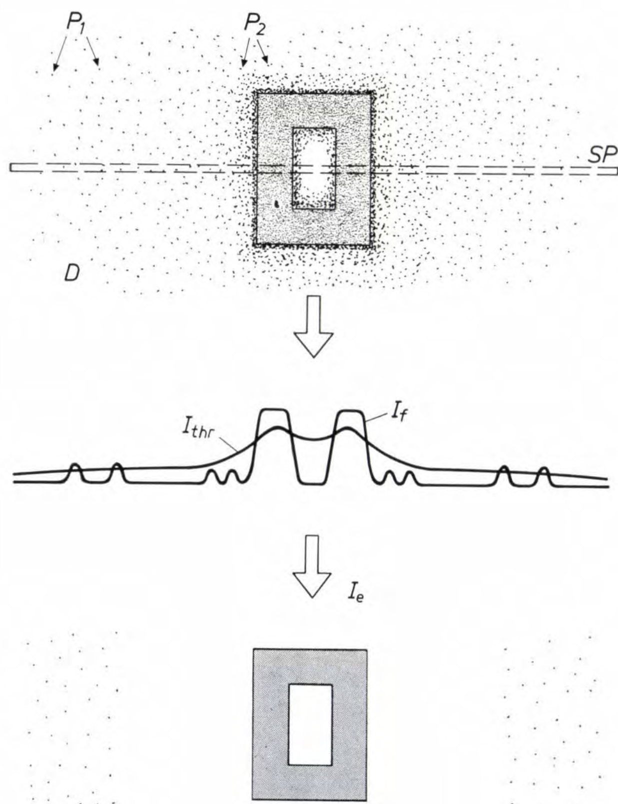

Fig. 3. An example of edge enhancement in optical character recognition (OCR), as obtained with the camera of fig. 2. *D* document to be scanned. *SP* position of scanned line. The focused array, A_1 in fig. 2, then produces the image signal I_f and the defocused array A_2 produces the local-area threshold I_{thr}. The resulting output I_e produces the picture shown, in which noise (points P_2) close to the character edges is eliminated; the noise (points P_1) in the white parts of the document cannot be eliminated.

Thresholding

In image processing the selection of a threshold is in essence the determination of a value, on the grey scale for the object observed, at which the decision between black and white will be made. The choice occurs somewhere between the maximum and minimum values of the video signal.

As was pointed out above, there are two kinds of threshold: the single threshold and the 'local-area' threshold. The single threshold has a constant value for the whole of the object to be processed. The local-area threshold is a level that is determined by the immediate surroundings of the object element involved. When a camera with a local-area threshold is used it labels the element as 'black' only if it is significantly darker than the immediate surroundings. This procedure gives particular enhancement to the edges in the image. Edge enhancement is particularly useful in processing poor-quality pictures, where the edges represent the most useful information.

The single threshold

The single threshold is the more simple of the two: it is a fixed level that in theory should lie between the absolute black level and the absolute white level. In practice there are two possible ways of selecting such a level: in the first the maximum levels of blackness and whiteness on the document are determined and the threshold is set at some intermediate value; in the second the threshold is set at a value between the observed maximum whiteness and the level for absolute black. Both ways of level setting are only suitable for high-contrast characters on a clean background, in other words for good-quality printing.

In processing characters with poor contrast or characters on a noisy background the single threshold is not satisfactory, because the small separation between the peak levels in the black and white areas makes the threshold setting too critical.

The local-area threshold

As we saw above, in local-area thresholding each picture element is compared with its immediate surroundings. The machine must then look for the relatively small changes that occur when a character is present. The small size of the changes may result from poor contrast between the text and the surrounding white or from noise. For most documents the noise, even when it is high, remains fairly constant over the whole area. The noise then makes the background more grey, reducing the contrast with the text.

The operation of local-area thresholding will now be explained with the aid of fig. 2 and *fig. 3*. There is a scanning system with two linear arrays of solid-state

detector cells. Array A_1 is placed in the focal plane of the camera lens and array A_2 in an out-of-focus plane; each cell of A_1 therefore records the image of one individual element (or 'point') of the document, while each cell of A_2 looks at a certain area around that same point.

In white areas free from spurious dark points, the output signals of the two arrays will be equal, but when spurious dark points are encountered the focused array A_1 responds to these, whereas the other array, A_2, is hardly affected. Now, when the white/black boundary is approached, the defocused array A_2, which looks at a larger area, is the first to see the boundary and its output increases. At this instant array A_1 is still looking at the scatter, and therefore its output remains low. As the boundary is crossed the output of A_1 rises sharply until it is considerably above that of A_2 — since the array A_2 is still affected by the white area. When the white area in the centre of the dark region is reached, the output of A_1 falls sharply but that of A_2 falls only slightly.

The output of the defocused array A_2 is used as local-area threshold and the output of the focused array A_1 as read-out signal. In the result obtained points like P_1 will still be present, but points like P_2, which are close to large dark areas, will have disappeared. In the final picture, therefore, character edges will be enhanced, whereas the overall picture will be rather noisy. This noise is a characteristic of most local-area thresholding, and it can be present even when good-quality text is processed.

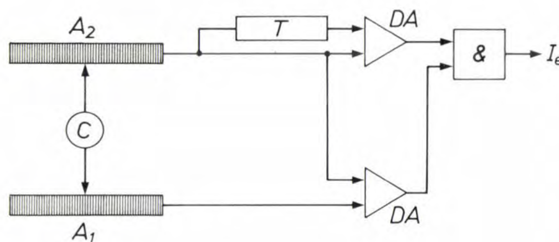

Fig. 4. Schematic diagram of the threshold circuits of the double-threshold camera. $A_{1,2}$ linear detector arrays; A_1 captures the sharp image, A_2 the blurred one (see fig. 2). The output signal of the detector A_2 is compared with the output of A_1 and with a single threshold T. The pictorial output I_e is formed via two comparators DA and an AND gate. I_e represents a black picture element (or '1') only if $A_1 > A_2$ and $A_2 > T$ simultaneously; in all other situations I_e represents a white element (or '0'). The clock circuit C controls the read-out of the arrays.

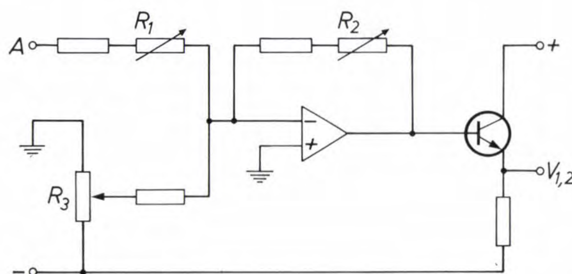

Fig. 5. One of the two gain-correction circuits. A input signal, obtained from the arrays A_1 or A_2 (fig. 2). The corresponding video output signals are V_1 and V_2. The variable resistors correct for any change in the sensitivity of the array. The potentiometer R_3 provides an offset voltage for correction of the zero.

The camera with double threshold

The way in which the two thresholding methods are combined in the new camera is shown in diagrammatic form in *fig. 4*. The output signal from the defocused array of detector cells acts as local-area threshold, and is compared with the output signal from the focused array and with a single threshold level as well. This single threshold level is derived from the maximum blackness level detected on the document and the maximum whiteness level; it lies just above the document background level. The diagram shows that for a point to be labelled 'black' the in-focus output signal must exceed the local-area threshold and that in addition the local-area threshold must be higher than the single one.

The lens of the camera has a focal length of 25 mm and an *f*-number (ratio of focal length to diameter) of 1.9; it is used with the aperture fully open. As the transmission and reflection coefficients of the semi-transparent mirror are not equal, an optical attenuator has been positioned in one ray path; in this way the light falling on the two arrays can be balanced. The array A_2 can be moved along the axis.

As the array A_2 is moved farther from the focal plane the field of view of the individual detector cells continuously increases; the edge-enhancing effect, however, does not increase commensurately. There turns out to be a defocusing distance at which the edge-enhancing effect is at a maximum. At larger distances the actual threshold acts more and more as a single threshold that depends on the peak-black level.

The detector arrays are MOS bucket-brigade devices of an experimental type, but standard arrays can be used. Since each array is composed of 64 photodiodes, 64 elements in line can be scanned at the same time. With the focused array each photodiode is independently affected by a single element (a point) of the document; with the defocused array several photodiodes are affected simultaneously. The detected signals are available sequentially, via a shift register. The output signals from the two arrays are each fed into a correction circuit (*fig. 5*). These circuits produce the video signals V_1, corresponding to the focused-array output, and V_2, corresponding to the defocused-array

output, which are corrected for differences in sensitivity. The signals V_1 and V_2 are fed into two comparator circuits (*fig. 6*), together with the single-threshold signal T.

The output signals from the comparators, together with a timing signal, are fed via a NAND circuit to a bistable circuit at the appropriate time during the clock cycle. The final thresholded pictorial output information is produced at the terminal $\bar{Q}$ of the bistable circuit.

The single-threshold signal T is given by:

$$T = W + m(B - W),$$

where W is the maximum whiteness level of the document and B is the maximum blackness level; the coefficient m is set to some value between 0 and 1. The signals W and B are derived from the 'peak-white' and the 'peak-black' follower circuits (*fig. 7*). These follower circuits consist of a comparator whose output controls the discharging or charging, as appropriate, of a small capacitor by means of an MOS switch. The capacitor is connected to a source follower, whose output represents the actual peak value of the incoming signal. The output of the source follower forms one of the inputs to the comparator. The initial conditions for the two capacitors are 'absolute black' for the peak-white signal and 'absolute white' for the peak-black signal, as determined by the auxiliary signal DP ('document present'). DP is 'high' when the document is not present and 'low' when it is present.

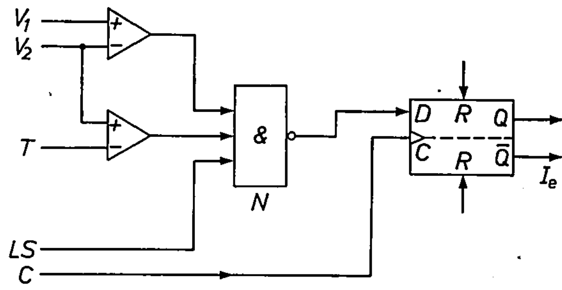

Fig. 6. Circuit of the comparators (DA in fig. 4). Comparisons are made between the video output signals V_1 and V_2 (fig. 5) and between V_2 and the single threshold T (fig. 4). LS line-scan signal, '1' only during scanning. C actuating clock signal (fig. 4). The NAND circuit N produces a '0' at D only if $V_1 > V_2$ during a line scan and at the same time $V_2 > T$. The pictorial output signals I_e ('1' for black element, '0' for white element) appear at the $\bar{Q}$ terminal of a D-type bistable circuit. R condition-input terminals for presetting and clearance.

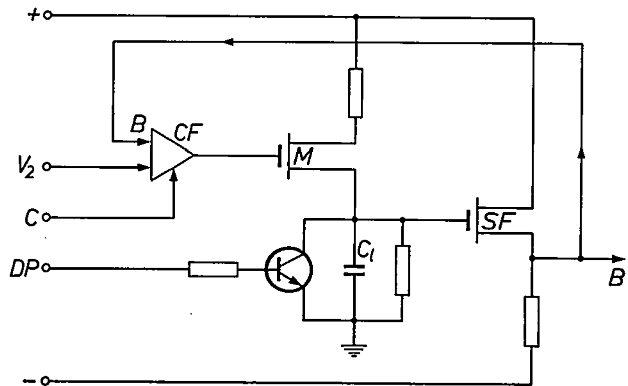

Fig. 7. Circuit of a peak-black follower. V_2 video output signal (fig. 5). B signal representing the maximum blackness level in the dark areas of the document being scanned. C_1 capacitor whose charge determines B via the source follower SF. The MOS switch M controls the charging (and discharging) of C_1. The comparator circuit CF is triggered by the clock signal C (fig. 4). DP signal that sets the initial condition of C_1 (e.g. '0' if document present). A similar circuit is used to determine the maximum whiteness level in the light areas of the document.

Performance

To assess the qualities of the new camera in OCR, two sets of characters were processed. The first set contained examples of machine-print characters and the second set examples of handprint characters in pencil; both groups contained examples at different levels of quality. The two sets have also been processed, for reasons of comparison, by an OCR machine (Philips X-1300) that uses a single-array camera with a single threshold based on the peak-white level; the recognition in this machine is by the well known procedure of 'mask-matching' [1].

Reading machine-print characters

Fig. 8 shows the results for the machine-print examples. The single threshold in the camera was set to a level corresponding to 15% of the difference between the peak-black and the peak-white levels, as detected by the defocused array.

The results of fig. 8 indicate that an OCR machine fitted with the new camera will adequately process a set of good-quality characters followed by a set of poor-quality characters of the low-contrast type or vice versa, without any manual intervention. On the other hand, after processing good-quality characters it is not immediately possible to process automatically a set of poor-quality characters of the 'heavy' type such as those obtained with a fresh carbon in a typewriter. In such a case the single threshold has to be raised slightly for acceptable results. *Fig. 9* shows the results obtained with the X-1300 machine, for the same set of machine-print characters as used for fig. 8. A comparison of figs. 8 and 9 shows that the camera with the double threshold is better for processing poor-quality characters of the low-contrast type, as clearly revealed by the G, M, N and Q. The X-1300 machine, on the other hand, is better for processing poor-quality characters

[1] L. Uhr, Pattern recognition, learning and thought, Prentice-Hall, Englewood Cliffs 1973, chapter 2.

△

Fig. 8. The output pictures obtained with a set of machine-print characters of good quality (*a*), poor quality of low-contrast type (*b*), poor quality of 'heavy' type (*c*), all processed by an OCR machine that included a camera with a double threshold. The material for figs. 8*b* and 8*c* was also processed by an X-1300 machine (fig. 9).

▷

Fig. 9. The output pictures obtained from a set of machine-print characters of poor quality of low-contrast type (*a*) and poor quality of heavy type (*b*), both processed by the X-1300 machine. Comparison shows that the results of fig. 8*b* are better than those of fig. 9*a*, whereas the results of fig. 9*b* are better than those of fig. 8*c*.

of the heavy type. With such characters the high resolution of the new camera is a disadvantage. It accentuates the irregular shape of the characters — they are fairly broad and surrounded by noise — so that odd marks along the edges tend to join together and ill-defined pieces of white inside characters tend to become bridged.

Both systems produce clear unbroken characters when scanning good-quality documents, and the results are then very similar.

Reading handprint characters

In processing handprint characters the new system does not always produce output that can be successfully read by the present character-recognition procedure for handprint. With both sharp and blunt pencils there are more errors than with the X-1300 system [2]. The main reason for the larger number of rejects or errors with sharp pencils is that the camera gives a very detailed reproduction of the edges of the characters. Small irregularities at the corners and junctions are

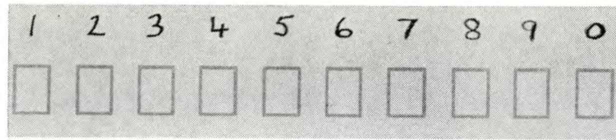

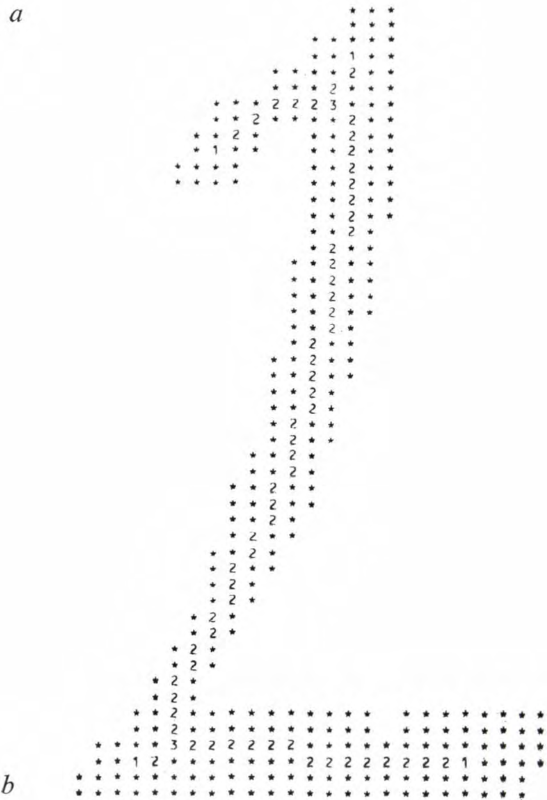

Fig. 10. *a*) An example of handprint. The numbers 1, 2, . . . , 9, 0 were written with a sharp pencil under heavy pressure. *b*) The number 2 as reproduced by an OCR machine with the new camera. This picture was rejected by the recognition procedure because of the highly detailed peculiarities at the edges of the figure.

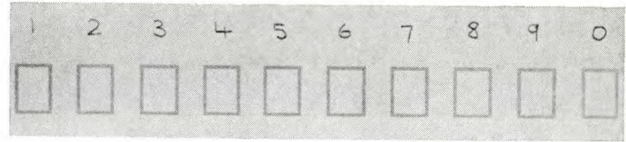

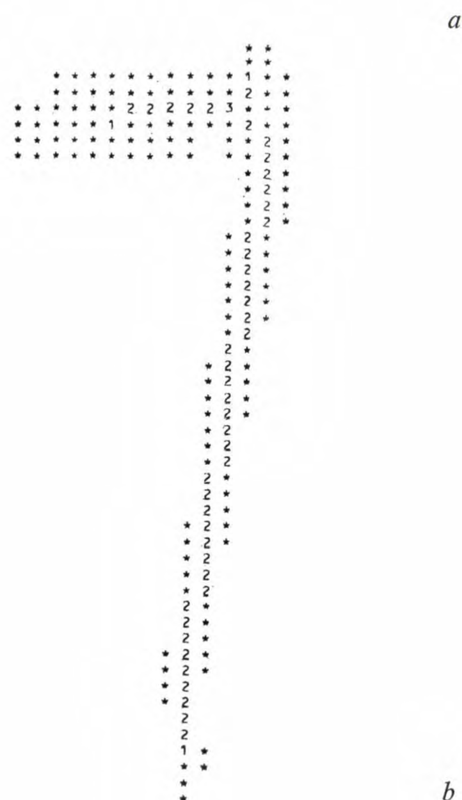

Fig. 11. *a*) Another example of handprint. The numbers 1, 2, . . . , 9, 0 were written with a sharp pencil under light pressure. *b*) The number 7 as reproduced by an OCR machine with the new camera. This picture was incorrectly read by the recognition procedure.

accentuated by the local-area threshold of the camera and reproduced as 'projections' or 'tails' attached to the boundaries of the binary picture. Part of the recognition procedure searches for the number of ends and junctions in a character and therefore the projections may result in the character being rejected or incorrectly read.

Two examples of the processing of handprint by the new camera are shown in *fig. 10* and *fig. 11*. The original documents are shown in fig. 10*a* and fig. 11*a*. The characters as reproduced by the machine with the new camera are shown in fig. 10*b*, rejected by the recognition procedure, and fig. 11*b*, which was read incorrectly.

The high reject or error rates for the handprint characters written with a blunt pencil are caused primarily by the increased width of character limbs. This increased width does not suit the field of view of the defocused array of detector cells. The effect of this can be that the output of the defocused array is raised above that of the focused array, which gives a displacement of the centre in the final picture (*fig. 12*).

The field of view of the defocused array has a width corresponding to five cells, the optimum value found from applying the system to machine-print characters. Black areas of 7×7 cells, however, are not uncommon for characters written with a blunt pencil, particularly at the corners and junctions of limbs. The defocused array cannot then see any background, and this affects the local-area threshold. The effect can be corrected by increasing the field of view of the defocused array. This is not without its problems, however, since it lowers the sensitivity of the camera and leads to difficulties in establishing the threshold for characters of poor contrast.

[2] Modified thresholding, in a variable-level system devised by D. M. Connah of Philips Research Laboratories, Redhill.

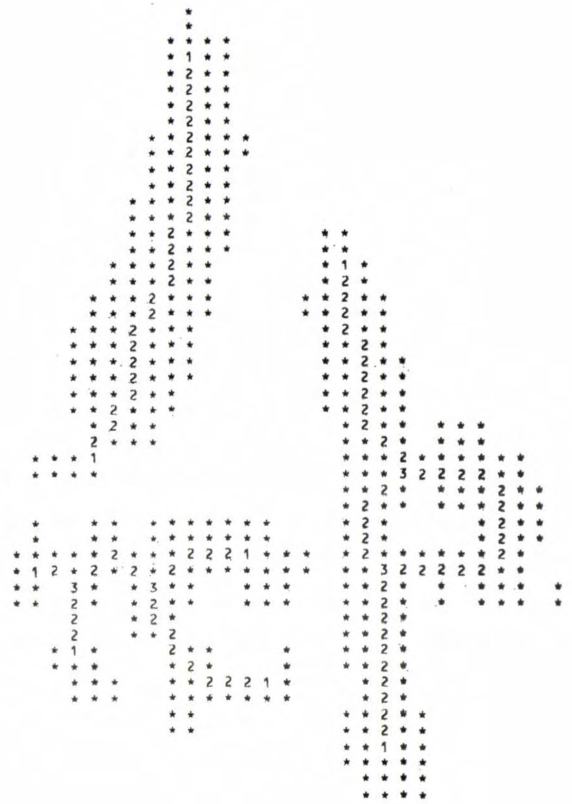

Fig. 12. An example of severely mutilated handprint output. The original, the number 4 written with a blunt pencil under heavy pressure, had limbs so wide that the defocused array (fig. 4) could not see the background in some locations. Increasing the field of view of the defocused array could overcome this difficulty, but the sensitivity of the camera would then decrease.

For the results from the handprint characters to be seen in the proper light, it should be realized that the camera discussed here and the recognition procedure are *not* perfectly matched to one another. The recognition procedure was in fact developed during an earlier stage of the work, and the training material consisted of characters obtained with the camera of the X-1300 system.

Although the assessment of the camera has been limited to OCR, the main conclusion to be drawn is that the method with the double threshold is highly useful wherever small low-contrast characters or marks have to be detected. The new method therefore has potential applications in equipment for other functions. An example is shown in *fig. 13*. The main features of the method are that it is sensitive to edges or 'white/grey' boundaries, but insensitive to large variations in

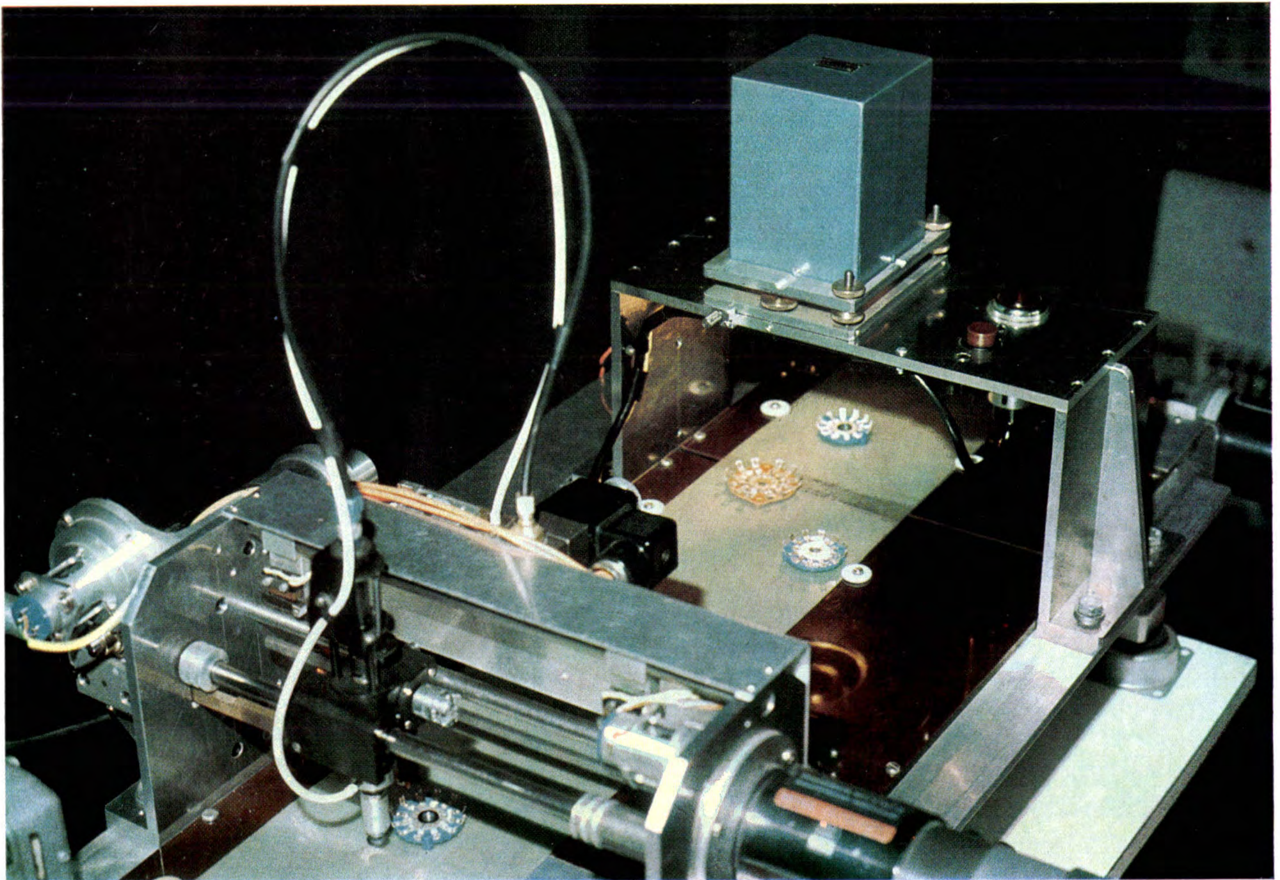

Fig. 13. Image processing in an assembly line for wafer switches. The input camera produces signals that will provide all the orientational information for passing the spindle of the switch through the correct hole in the central terminal ring.

illumination; we have found the overall performance of the camera unaffected by variations of 50% or more in the illumination.

In conclusion, we should note that the output signals of the camera with the threshold system discussed here do not produce analog pictures, but binary sequences of black and white picture elements. It is however possible to obtain an edge-enhanced analog picture. This can be done by gating the signal of the focused array of detector cells by the binary sequences.

Summary. The construction and performance of a double-focus camera for image processing are described. Local-area thresholding and single-level thresholding have been combined to retain high resolution and edge enhancement, while redundant information is suppressed. The camera operates with a 'split-beam geometry and two solid-state line scanners — one focused, the other defocused — and produces a binary output. The performance has been tested by reading machine-print characters. Good-quality characters followed by poor-contrast characters can be processed without manual readjustment of the thresholding; poor-quality characters of 'heavy' type, such as typewritten copy from a new carbon, cannot. The reading of handprint characters is still liable to include rejections. The system is best suited to processing low-contrast characters and marks; it is sensitive to edges or white/grey boundaries. Changes in illumination by ± 50% do not affect performance.

Recent scientific publications

These publications are contributed by staff of laboratories and plants which form part of or cooperate with enterprises of the Philips group of companies, particularly by staff of the following research laboratories:

Philips Research Laboratories, Eindhoven, The Netherlands	*E*
Philips Research Laboratories, Redhill, Surrey, England	*M*
Laboratoires d'Electronique et de Physique Appliquée, 3 avenue Descartes, 94450 Limeil-Brévannes, France	*L*
Philips GmbH Forschungslaboratorium Aachen, Weißhausstraße, 51 Aachen, Germany	*A*
Philips GmbH Forschungslaboratorium Hamburg, Vogt-Kölln-Straße 30, 2000 Hamburg 54, Germany	*H*
MBLE Laboratoire de Recherches, 2 avenue Van Becelaere, 1170 Brussels (Boitsfort), Belgium	*B*
Philips Laboratories, 345 Scarborough Road, Briarcliff Manor, N.Y. 10510, U.S.A. (by contract with the North American Philips Corp.)	*N*

Reprints of most of these publications will be available in the near future. Requests for reprints should be addressed to the respective laboratories (see the code letter) or to Philips Research Laboratories, Eindhoven, The Netherlands.

P. Baudet, M. Binet & D. Boccon-Gibod: Submicrometer self-aligned GaAs MESFET.
IEEE Trans. MTT-**24**, 372-376, 1976 (No. 6). *L*

V. Belevitch: Theory of the proximity effect in multiwire cables, Part I.
Philips Res. Repts. **32**, 16-43, 1977 (No. 1). *B*

O. Boser: Determination of the activation energy for solute diffusion from critical flow stress measurements.
Scripta metall. **10**, 563-564, 1976 (No. 6). *N*

F. J. A. den Broeder & H. Zijlstra: Relation between coercive force and microstructure of sintered $SmCo_5$ permanent magnets.
J. appl. Phys. **47**, 2688-2695, 1976 (No. 6). *E*

E. Bruninx: X-ray fluorescence analysis by means of crystal dispersion and a position-sensitive counter.
Spectrochim. Acta **31B**, 221-223, 1976 (No. 4). *E*

M. Davio & G. Bioul: Fast parallel multiplication.
Philips Res. Repts. **32**, 44-70, 1977 (No. 1). *B*

H. Dimigen, H. Lüthje, H. Hübsch & U. Convertini: Influence of mask materials on ion-etched structures.
J. Vac. Sci. Technol. **13**, 976-980, 1976 (No. 4). *H*

M. J. C. van Gemert, S. C. Lincolne & J. Heuvelmans: Afterglows of an ac-operated Na-Ne-Ar low-pressure discharge.
Philips Res. Repts. **32**, 8-15, 1977 (No. 1). *E*

B. K. Herbert: A circuit for stabilizing the electron current to the anode of a hot-filament device.
Vacuum **26**, 363-369, 1976 (No. 9). *M*

W. L. Konijnendijk (Philips Lighting Division, Eindhoven) **& J. M. Stevels** (Eindhoven University of Technology): The linear expansion of borosilicate glasses in relation to their structure.
Verres Réfract. **30**, 371-377, 1976 (No. 3).

D. Küppers, J. Koenings & H. Wilson: Codeposition of glassy silica and germania inside a tube by plasma-activated CVD.
J. Electrochem. Soc. **123**, 1079-1083, 1976 (No. 7). *A*

E. J. Millett: Digital techniques in laboratory automation.
J. Physics E **9**, 794-802, 1976 (No. 10). *M*

A. G. van Nie: Electroless NiP processing for hybrid integrated circuits.
Microelectronics and Reliability **15**, 221-226, 1976 (No. 3). *E*

J. J. Opstelten & L. B. Beijer (Philips Lighting Division, Eindhoven): Specification of colour rendering properties of light sources for colour television.
Lighting Res. Technol. **8**, 89-102, 1976 (No. 2).

J. A. Pals & L. H. J. Graat: The simultaneous occurrence of Josephson effects and series resistance in $Nb\text{-}U_6Fe$ point contacts.
Physics Letters **56A**, 487-488, 1976 (No. 6). *E*

M. Steers & A. Mircea-Roussel: A novel electro-optic storage mode in smectic A liquid crystals.
J. Physique **37**, C3/145-148, 1976 (Colloque C3). *L*

L. Vriens & F. A. S. Ligthart: Energy balance and Coulomb relaxation in low-pressure gas discharges.
Philips Res. Repts. **32**, 1-7, 1977 (No. 1). *E*

Volume 37, 1977, No. 7 pages 157-188 Published 21st March 1978

PHILIPS TECHNICAL REVIEW

VOLUME 37, 1977, No. 8

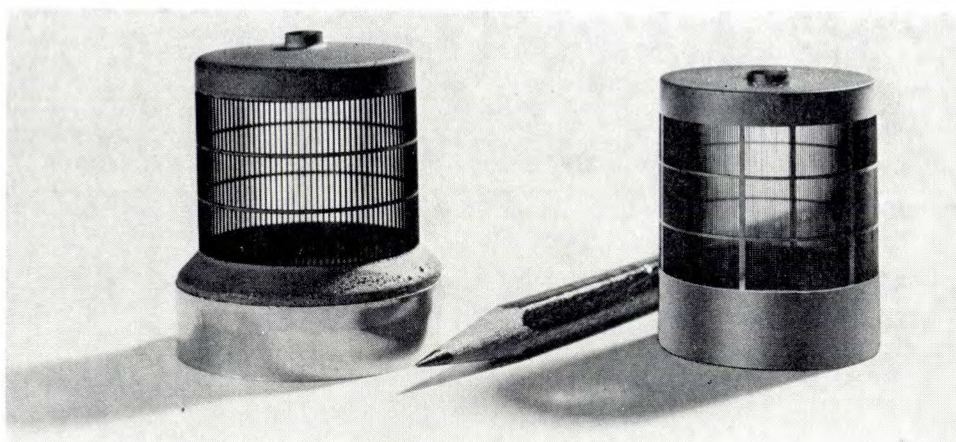

Products of pyrolytic graphite

W. F. Knippenberg, B. Lersmacher and H. Lydtin

The old competition between carbon and certain of the high-melting-point metals such as tungsten will be well known to anyone familiar with the history of the rivalry between the carbon-filament lamp and the metal-filament lamp in about 1910. Although it has long been clear that the metal-filament lamp was the victor, the carbon-filament lamp has nevertheless been the subject of recent investigations [*]. *It will not perhaps be so well known that competition between such apparently dissimilar materials has also been of significance in transmitting valves. In the forties electrographite was used for the control and screen grids of transmitting valves, but this material was later completely superseded in this application by tantalum, tungsten and molybdenum. Whereas in carbon-filament lamps the main difficulty was that the filament material evaporated rapidly at the operating temperature, it was the more limited scope for design with electrographite grids that decided the issue in favour of the metal grids. The article below describes recent developments in the manufacture of pyrolytic-graphite products by chemical vapour deposition that may yet give carbon the opportunity of an extended role in transmitting-valve technology.*

In existing technology 'pyrolytic graphite' has mainly been made and used in the form of thin layers adhering to a substrate [1]. The layers are formed by chemical vapour deposition (known as the CVD method) in which carbon layers are deposited from a carbon-containing gas subjected to pyrolysis. Now, however, our knowledge and control of the method of preparing pyrolytic graphite have advanced to a stage at which it is now possible to make 'self-supporting' objects with very thin walls with this material.

In this article we shall demonstrate the possibilities of the method by discussing the manufacture of grid electrodes 0.1 to 1 mm thick for experimental trans-

Dr W. F. Knippenberg is with Philips Research Laboratories, Eindhoven; Dr B. Lersmacher and Dr H. Lydtin are with Philips GmbH Forschungslaboratorium Aachen, Aachen, West Germany.

[*] See W. J. van den Hoek and W. A. Klessens, Philips tech. Rev. **35**, 316, 1975.

[1] See for example W. F. Knippenberg, B. Lersmacher, H. Lydtin and A. W. Moore, Philips tech. Rev. **28**, 231, 1967.

mitting valves for high frequencies and high powers.

We shall first give a brief recapitulation of our knowledge of the formation of carbon deposits on substrates by pyrolysis of a carbon-containing gas, and a description of the two fundamentally different methods used in practice, the hot-wall and cold-wall methods.

Deposition of carbon from gaseous hydrocarbons

Pyrolytic graphite is a form of graphitic carbon that is deposited from certain gases at temperatures above about 2000 °C. The original development of the method was very largely empirical, but at a later stage thermodynamic calculations and kinetic studies provided a clearer understanding of the method. These studies were mainly concerned with gas/solid-carbon systems produced by heating hydrocarbons of low molecular weight such as methane (CH_4), ethane (C_2H_6), propane (C_3H_8), ethene (C_2H_4), propene (C_3H_6), etc. The calculations show that the 'solubility' of carbon in these gas systems has a minimum value between 1000 and 2500 °C, depending on the pressure (*fig. 1*). The solubility of carbon is here taken to be the ratio C/H of the number of carbon atoms present in the gas phase (whether or not in bound form) to the number of other atoms present (in this case always H atoms). The occurrence of a reduction in the solubility on increasing the temperature may be understood from the fact that the molecules present in the initial state (e.g. CH_4) are more readily converted at temperatures above 1000 °C into hydrogen and molecules that contain proportionally more carbon atoms (e.g. C_2H_2, C_2H, etc.), while some of the carbon is deposited. At temperatures above 3500 °C all the hydrocarbons dissociate to form carbon and hydrogen; see *fig. 2*.

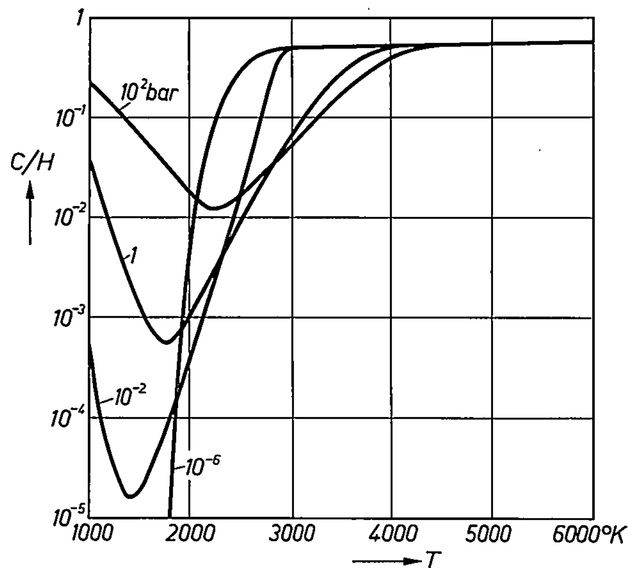

Fig. 1. The thermodynamically calculated 'solubility' C/H of carbon in the gas phase as a function of the temperature T to which methane gas (CH_4) is subjected at pressures of 10^{-6}, 10^{-2}, 1 and 10^2 bars when it is in equilibrium with solid carbon. The solubility is expressed here as the ratio of the numbers of carbon and hydrogen atoms in the gas phase. There is a distinct minimum in the solubility.

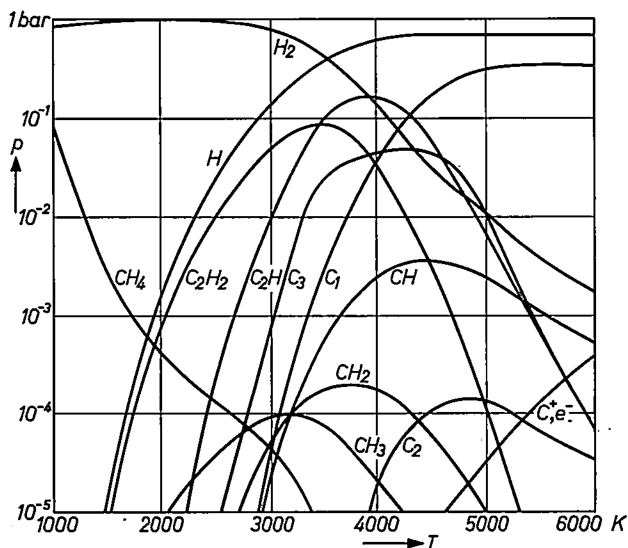

Fig. 2. Composition of the system C-H as a function of temperature, as produced on heating hydrogen in equilibrium with solid carbon at a total pressure of 1 bar. (Courtesy of R. Kuthe, Interne Mitteilung des Instituts für Chemische Technologie der Technischen Hochschule Braunschweig.)

The different sign of the gradient of the carbon-solubility curves on either side of the minimum indicates that the carbon in the equilibrium systems considered here can be deposited in two different ways by a chemical transport reaction [2]: either on a substrate at a *higher* temperature than the temperature corresponding to the local gas/solid-carbon equilibrium, or by deposition on a substrate at a *lower* temperature.

In practice the methods used are not based on chemical *equilibria*; but instead, purely and simply to obtain the desired deposition rate, CVD methods are used in which the gas system throughout is in a state that differs considerably from the equilibrium.

The CVD methods can be carried out in two ways, with temperature gradients of opposite sign at the location of the substrate. In both methods the substrate is placed in the centre of a reaction vessel (*fig. 3*). The essential difference is in the position of the source of heat. In the one case the substrate itself is heated and therefore becomes hotter than the wall of the reaction vessel; in the other case the substrate is surrounded by a heating element and the wall is hotter than the substrate. This is why the names 'cold-wall' and 'hot-wall' are used in the descriptions of the two methods. The contribution to the deposition resulting from the difference in solubility at differing temperatures is very

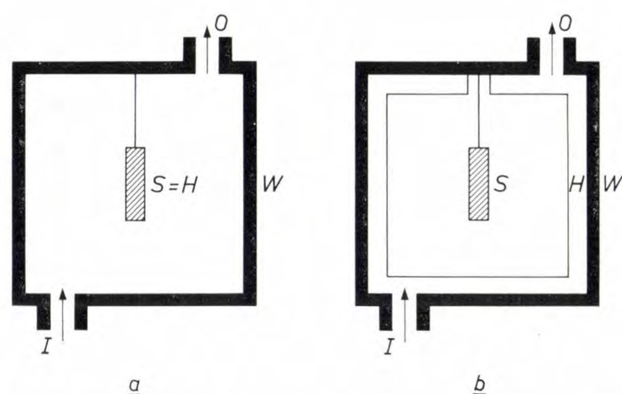

Fig. 3. Diagram of the equipment for the cold-wall method (*a*) and the hot-wall method (*b*). *W* wall of reaction vessel. *I* and *O* input and output for the gas mixture to be pyrolysed. *S* substrate and also heating element in method (*a*), consisting of electrographite. *H* heating element.

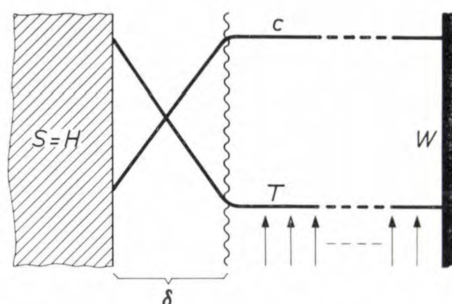

Fig. 4. Temperature *T* as a function of concentration *c* (mol CH_4/l) in the peripheral zone δ around the substrate where the diffusion processes and reactions take place. This zone, in which there is no flow, is very narrow (about 1 mm) compared with the total space in which the gases are supplied and removed.

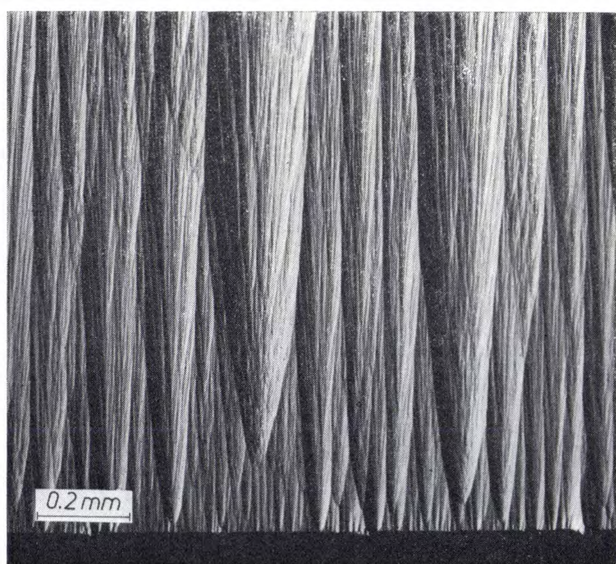

Fig. 5. Polarized-light photomicrograph of pyrolytic graphite made by the cold-wall method. It can be seen that most of the nucleation centres, which can initiate the growth of carbon 'bundles', are concentrated on the surface of the substrate; hence the term 'substrate-nucleated pyrolytic graphite'.

small compared with the deposition resulting from a large 'forced' supersaturation; we shall return to this shortly.

In looking at the advantages and disadvantages of these two methods, we have to remember that in both of them the carbon is deposited in a gas system whose state is very different from an equilibrium in a wide region, and not just at the location of the substrate. The initial reagents with compositions corresponding to a C/H ratio of 0.25 to 1 are supplied at a pressure of 10^{-3} to 10^{-1} bar (1 to 100 mm Hg), while the deposition on the substrate takes place at a temperature from 1600 to 2200 °C. This combination of conditions implies, as can be seen from fig. 1, that the solubility is so low (C/H is 10^{-3} to 10^{-2}) that it gives a high degree of supersaturation of carbon in the gas phase where it has acquired these temperatures. The quantity of carbon that can be transported to the substrate in this way is many times greater than the quantity that would in practice be transported by chemical transport reactions based on equilibrium states. In such a case it would only be possible to cause the transport by creating a very large temperature difference across a very short distance, which is an extremely difficult combination of experimental conditions.

We shall now look at the consequences of the high supersaturation for the two different methods of carbon deposition.

Comparison of the cold-wall and the hot-wall methods

In the cold-wall method the substrate is heated by passing an electric current through it or by induction heating. At the flow rate at which the gas for pyrolysis is supplied (about 50 m/s), it is in a turbulent state, and the temperature and concentration (e.g. for CH_4 in mol/l) behave in the manner shown in *fig. 4*. The temperature decreases rapidly and the concentration rises rapidly in a relatively narrow zone around the substrate — this is where the method differs essentially from the hot-wall method. All the diffusion processes and reactions that lead to the deposition of carbon on the substrate take place in this peripheral zone, which is a few millimetres wide. At the temperature of the surface of the substrate (1600 to 2200 °C) the mobility of the molecules supplied is so great that the carbon atoms arriving at the substrate can arrange themselves in the pattern of the ideal graphite lattice. This ordering takes place on a number of simultaneously formed nuclei that act as traps, each with its own radius of action, so that a 'bundled' structure is produced instead of a single-crystal structure (*fig. 5*). The pyrolytic graphite formed in this way is called 'substrate-nucleated pyrolytic graphite'.

[2] See for example A. Rabenau, Philips tech. Rev. **26**, 117, 1965.

The pressure of the gas feed is one of the factors that determines the degree of nucleation in both the solid phase and the gas phase, and it is the degree of nucleation in the gas phase that determines the probability of 'cluster' formation, i.e. the formation of carbon agglomerates of varying magnitude that can be trapped inside the growing graphite layer and act there as new growth centres (*fig. 6*). The nuclei form anywhere in the peripheral zone, in which the temperature is higher than the dissociation temperature and the carbon is present in a high degree of supersaturation. In the method described here the formation of the clusters can be fairly easily controlled in such a way that the grown layer has a high degree of perfection without this having too great an effect on the growth rate of the layer.

There are three factors that make this possible. Firstly, the number of clusters is not very large, because of the narrowness of the zone; secondly, clusters once formed encounter a rising temperature as they approach the substrate, so that they are dissolved again provided they have not exceeded a critical magnitude; thirdly, such clusters also tend to drift away from the substrate by thermal diffusion owing to the direction of the temperature gradient. This fortunate combination of factors enables us to obtain a virtually perfect graphite layer at a growth rate of about 10 μm/min.

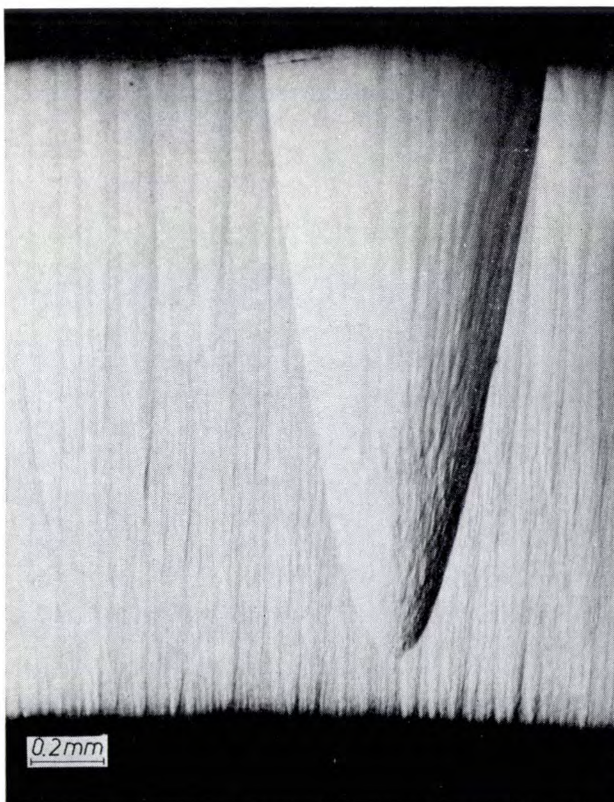

Fig. 6. Polarized-light photomicrograph of carbon growth that has started at some distance from the substrate in a trapped 'cluster'.

The disadvantages of the cold-wall method are connected with the necessity for keeping the surface temperature of the substrate uniform and constant during the deposition of the carbon. Whether this temperature control depends on inductive heating or on the use of direct electrical heating with appropriate adjustment of the energy supply during the growth of the graphite layer, the desired goal can only be reached if the substrate is a body that has rotational symmetry; this means that it is very difficult to cover a large number of substrates uniformly at the same time. What is more, in both methods of heating there is a temperature gradient in the growth direction during the deposition of the carbon, and with direct electrical heating this gradient may be as much as hundreds of degrees per millimetre. This introduces stresses during the growth of the graphite layer; during the cooling these stresses are much increased because of anisotropic shrinkage. The result is that the layer formed will crack or crumble unless it is thinner than about 10 μm and very strongly attached to the substrate, or if the layer is thicker than 0.5 to 1 mm. This means that the cold-wall method is not suitable for making self-supporting objects with wall thicknesses between those values, because in the production of thin-walled objects of pyrolytic graphite it is necessary to remove the layer of deposited graphite in its entirety from the substrate by the use of controlled cooling.

In the hot-wall method this problem is far less serious. Here the substrate is heated by a surrounding element (fig. 3*b*), and the substrate surface is easily kept at a uniform and constant temperature during the deposition by radiation and heat conduction, even when the substrate does not have cylindrical symmetry, or when several substrates are being processed simultaneously. Stresses only occur during the cooling of the products, but if the cooling is suitably controlled the stresses can be kept below a level at which they introduce unwanted effects.

In the hot-wall method, however, the fact that the carbon in the gas system is in a highly supersaturated state is a much greater disadvantage than it is in the cold-wall method. This is because in the hot-wall method the entire volume of gas is heated to above the dissociation temperature (*fig. 7*), so that nuclei can now form anywhere in the volume of the gas and also on other parts of the system, such as the heating element. An added difficulty is that the direction of the temperature gradient at the substrate is the opposite to that in the cold-wall method, so that clusters do not tend to redissolve. Furthermore, these clusters now move towards the substrate because of thermal diffusion. The risk of clusters forming — or even of 'sooting up' — is therefore so great that much lower

gas pressures have to be used than in the cold-wall method, and this considerably reduces the rate of deposition. In practice a pressure is used at which the formation of clusters is just invisible. We are then able to produce very dense graphite layers, at a rate of 0.1 to 1 μm/min, but with growth centres distributed uniformly *throughout the entire volume*. This product is known as 'continuously nucleated pyrolytic graphite'; see *fig. 8*.

The growth centres in the pyrolytic graphite formed in this way reduce the electrical and thermal conductivities, though only to a slight extent, but on the other hand they improve its mechanical strength. We thus have a second factor that makes the hot-wall method particularly suitable for producing self-supporting objects with wall thicknesses between 10 μm and 1 mm.

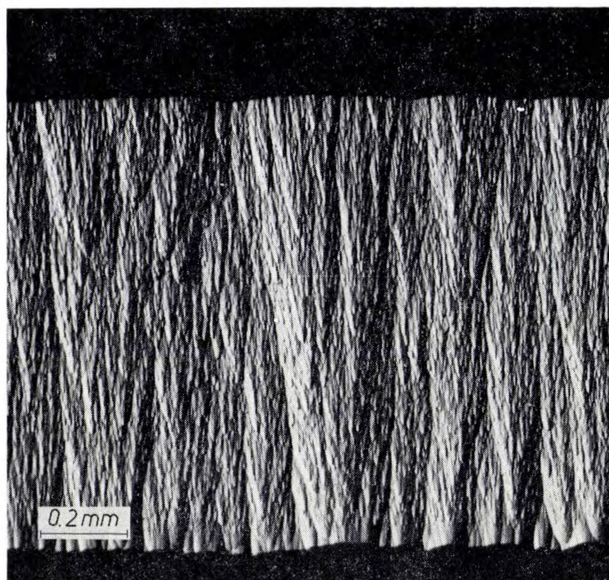

Fig. 8. Polarized-light photomicrograph of pyrolytic graphite made by the hot-wall method. Nucleation centres are clearly seen throughout the entire volume, hence the term 'continuously nucleated pyrolytic graphite' for this material.

The hot-wall method in general terms; properties of substrate and material produced

In producing thin-walled objects of pyrolytic graphite, with which we shall mainly be concerned here, it is necessary to be able to detach the deposited graphite layer from the substrate in one piece by cooling. This means that the coefficient of expansion of the substrate in the direction of the surface should be greater than that of the deposited pyrolytic graphite. In addition, it is usually preferable for the substrate to be made from an easily machinable and thermally stable material that does not react too strongly with the deposited graphite at the high deposition temperatures employed. Electrographite [3] is a substrate material that fully meets all these requirements; another material that can sometimes be used is tantalum.

Electrographite meets the second condition because it is chemically identical with pyrolytic graphite. To return to the first requirement, the coefficient of expansion of pyrolytic graphite, which is strongly anisotropic, is smaller in the direction of the surface on which the material is deposited than it is perpendicular to the surface. The expansion coefficient of electrographite, which is virtually isotropic, is an average of these values, and therefore does indeed have the magnitude required. If the deposited layer is thicker than about 10 μm, it separates spontaneously from the substrate on cooling to room temperature.

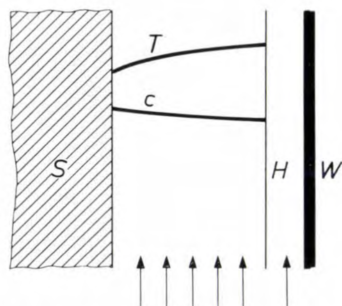

Fig. 7. Temperature T as a function of concentration c (mol CH_4/l) in the hot-wall method. In this case the various reactions take place in the entire gas volume. The shape of the concentration profile in the peripheral flow zones adjoining the substrate and the heating element is the same as in fig. 4.

The improvement that we referred to earlier in the mechanical strength of pyrolytic graphite made by the hot-wall method is also important for the further treatment received by the detached product, and for the various operations that may be necessary in producing the final shape of the product or for connecting it to other components.

In making thick-walled objects of pyrolytic graphite there are usually no great problems in obtaining the required mechanical strength. The problems here are mainly those related to the production of the desired shape within the desired tolerances.

Other properties that make pyrolytic graphite so attractive for various applications are its high resistance to chemical attack or mechanical effects at high temperatures, its high thermal and electrical conductivities (in the direction of the surface, at any rate), and above all its high thermal-radiation coefficient and its high thermionic work function. Properties such as these make the material suitable for the manufacture of

[3] Electrographite itself was used as a material for the control and screen grids of transmitting valves in the forties. However, the increasingly difficult requirements placed on transmitting valves could not be met when this material was used. A comparison of the properties of electrographite with those of pyrolytic graphite can be found in the article of note [1], and in W. F. Knippenberg and B. Lersmacher, Philips tech. Rev. 36, 93, 1976, particularly pages 93 and 95.

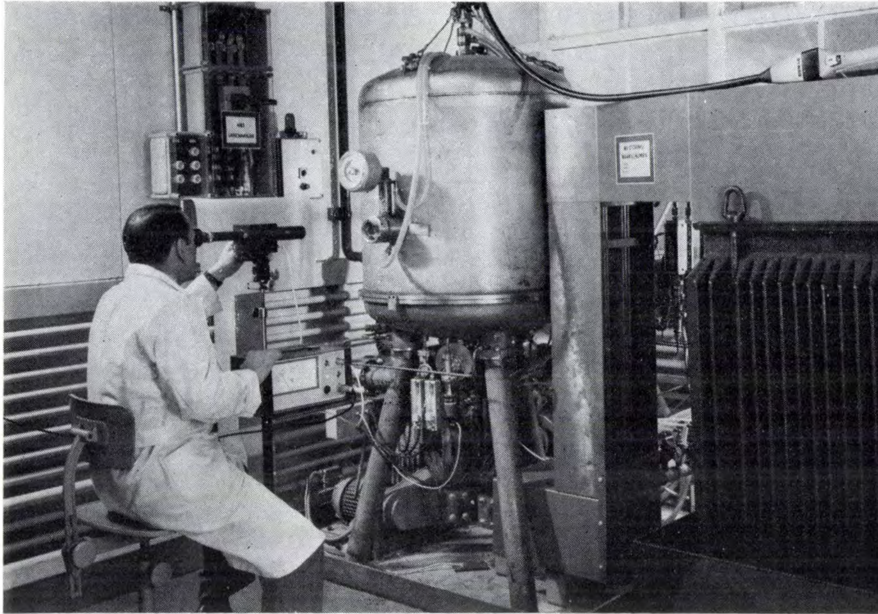

Fig. 9. General view of the equipment for pyrolysis by the hot-wall method. The technician is measuring the temperature of the substrate with a pyrometer.

the example we have taken here: control and screen grids for high-power r.f. transmitting valves.

Although the products considered here as examples are cylindrical, other shapes can also be produced with this method, e.g. by using composite substrates.

Grids for high-power r.f. transmitting valves

As the design frequency for a transmitting valve increases, the spacing required between the grids and the other electrodes decreases and a finer mesh is required for the grids. Also, as the power that the valve is required to handle is increased, the temperatures to which these grids are subjected increase. The heat produced can only be removed by conduction to other parts of the valve and by radiation, and this means that the grid material must have both a good thermal conductivity and a good thermal radiation coefficient. Another and very important requirement is for high mechanical stability at the high temperatures encountered: there must be no deformation that could allow the grids to touch each other or the other electrodes. To minimize parasitic currents it is also necessary that the primary and secondary electron emission from the grids should be as low as possible. This indicates that the thermionic work function should be high.

Until recently metals such as tantalum, tungsten and, most commonly, molybdenum have been the basic materials used in making control and screen grids for frequencies from 500 to 1000 MHz. These metal grids are made from wire, using a rather laborious spot-welding technique. To improve the radiation and primary and secondary emission from the surface, the metal is often coated with carbon or with certain carbides.

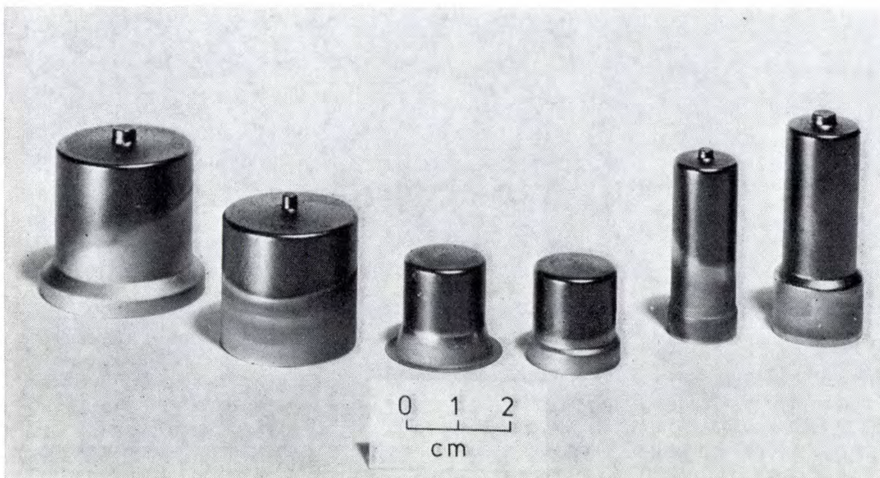

Fig. 10. Hollow cylinders of pyrolytic graphite, detached from the substrate by cooling.

The main weakness of these grids is their mechanical instability at high operating temperatures. This problem is particularly troublesome when it is desired to use higher operating frequencies, since grids with an even finer mesh are then required [4].

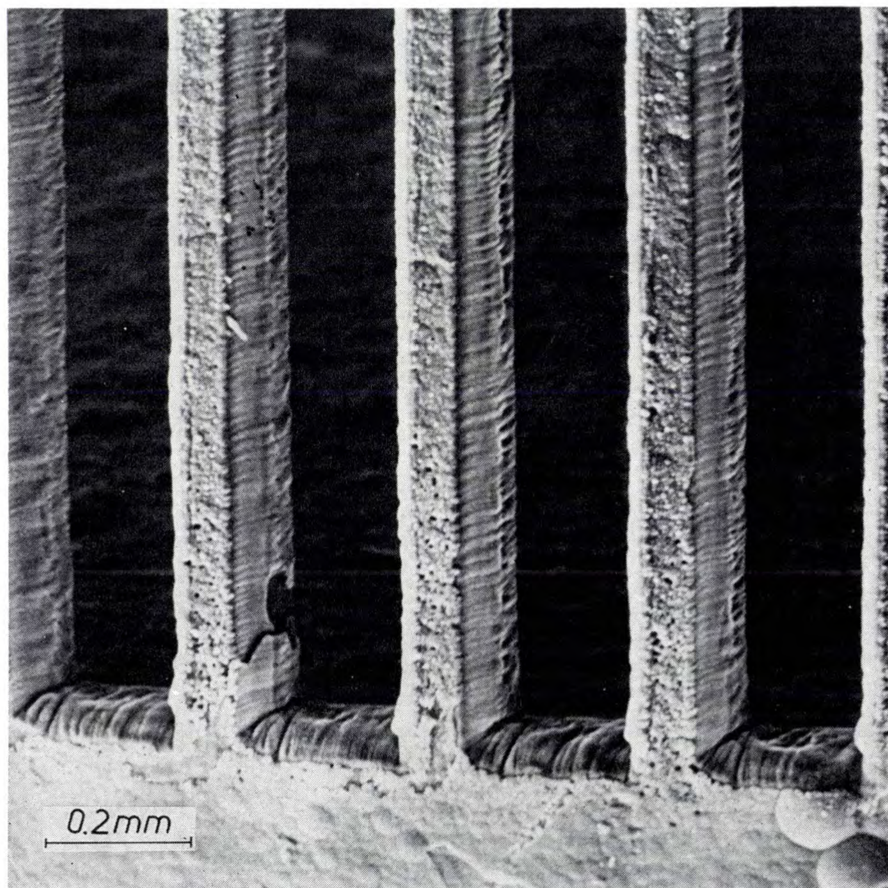

Fig. 11. 'Windows' cut by a laser beam in a hollow cylinder as in fig. 10.

Making control and screen grids from pyrolytic graphite with a 0.1-mm wall

At the Philips Aachen laboratories and at the development laboratory for transmitting and microwave valves in Eindhoven, experimental grids are being made entirely from pyrolytic graphite with thicknesses from 100 μm to 1 mm.

A number of cylindrical pieces of electrographite are simultaneously coated over their complete surface with a thin layer of pyrolytic graphite by the hot-wall method in a pyrolysis equipment like the one illustrated in *fig. 9*. After cooling the cylinders and sawing off one of the ends it is a simple matter to detach from the substrate a thin-walled hollow cylinder of pyrolytic graphite of the desired length and closed at one end (*fig. 10*). If a coarse-meshed grid is then required, it can be produced by operations such as milling, drilling and grinding. Fine-meshed grids are made by methods such as sandblasting, electrochemical treatment, spark machining and cutting with an electron or laser beam.

We have found laser-beam cutting the most satisfactory for making control and screen grids. A fixed laser beam is focused on the workpiece, which is then shifted by means of numerical control in such a way that windows of the required dimensions are cut out of the material (*fig. 11*). The cutting operation is usually carried out in air, so that the desired cut is obtained through both evaporation and oxidation.

Cutting with the laser beam is associated with the formation of spherical carbon condensates. These are difficult to remove mechanically. We have developed a more satisfactory method in which the cut workpiece is briefly annealed in an oxygen-containing atmosphere at about 900 °C. This after-treatment both removes the unwanted carbon condensates by combustion and also removes the sharp points and edges formed during the cutting process. This reduces the risk of electrical

[4] See also P. Gerlach and P. Graf, Fernmelde-Praxis **53**, 171, 1976.

Fig. 12. Part of an experimental high-power r.f. triode with a control grid of pyrolytic graphite.

breakdown during the operation of the finished product. For the same reason the grid is also subjected to a second pyrolytic carbon-deposition process to cover it with a pyrolytic-graphite layer 3 to 5 μm thick.

The grid produced in this way (see the title photograph) is either screwed, clamped or soldered to the other components of the valve. The best solders for this application are alloys of Zr and Mo with Ni, Co or Fe, because they are resistant to high temperatures and have suitable values for the thermal expansion coefficient. To obtain a good bond with the solder it is often desirable to apply a localized coating of tungsten or molybdenum to the grid.

Part of an experimental r.f. triode with a pyrolytic-graphite grid made by the method described in this article is shown in *fig. 12*.

Summary. Pyrolytic graphite can be made by two different processes: the cold-wall method and the hot-wall method. In the cold-wall method the substrate on which the carbon is deposited is the heat source; it is heated by passing a current through it or by r.f. heating. In the hot-wall method the substrate is heated by means of a heater element surrounding it. The first method is mainly limited to the production of objects that have rotational symmetry, and the objects cannot be removed from the substrate without crumbling or cracking if the wall thickness is between 10 μm and 1 mm. This limitation is overcome when the other method is used, although the thermal and electrical conductivities are then slightly lower. The scope of the hot-wall method for producing self-supporting objects is demonstrated by a description of the method used for producing 0.1-mm thick cylindrical control or screen grids for high-power r.f.transmitting valves.

MOPS, a magneto-optic storage wafer of the discrete-bit type

H. Heitmann, B. Hill, J.-P. Krumme and K. Witter

Work has been going on for some time at Philips GmbH Forschungslaboratorium Hamburg on the development of certain garnets, intended as a material for magneto-optic memories of the discrete-bit type. The digital laser deflector now available — it was described in No. 5 of our last volume — makes possible in principle the construction of a fast optical backing store (about 10^8 bits), with completely non-mechanical addressing. The work on thin garnet films discussed here forms a promising complement to the work on lithium niobate, a material for a holographic memory, as discussed in a recent issue.

Optical memories and ferrimagnetic garnets

The work on optical memories is based on two completely different kinds of system: holographic systems and local or discrete-bit systems. A materials study made in connection with a holographic system has already been described in an earlier issue of this journal [1]. In the present article we shall discuss a study of certain ferrimagnetic garnets intended for use in the form of thin wafers as storage elements in discrete-bit memories [2].

The basic idea in the use of light in these memories is the addressing of the individual storage cells in a bistable magnetic film by means of a focused beam of laser light; the addressing is then followed by the thermomagnetic writing or reading of data. The reading depends on a magneto-optic effect, Faraday rotation. The writing is done by thermomagnetic flux reversal; 'thermomagnetic' means that the desired reversal of the directions of magnetization is achieved by heating the material in the presence of an external magnetic control field. In principle, the heating could be provided by the focused laser light. However, so that a laser of only moderate power could be used, we applied a thin photoconducting layer to the storage material. The thermal energy required for switching a storage cell is generated in the photoconducting layer as Joule heat, which penetrates to the cell by thermal conduction. The laser beam for addressing thus merely switches on the electrical heat source at the desired address. Reading requires much less energy; the (polarized) laser beam is itself sufficiently powerful to provide signals of high magneto-optic contrast.

In addressing by means of a laser beam there is no electrical contact to individual storage cells, nor is there any requirement for complicated electrical circuits — two significant advantages. The main motivations for the development of a magneto-optic storage wafer, however, are the very high packing densities and short access time that should be obtainable. Laser beams in the visible part of the optical spectrum can be focused to a spot with a diameter of a few microns; with such a small spot size a packing density of more than 10 kbit/mm^2 can be achieved. A short and uniform access time can also be achieved now that the PFH digital laser deflector is available [3]. This will deflect a laser beam to any one of more than a quarter of a milion ($2^9 \times 2^9$) positions within less than 0.5 μs. If passive beam-splitters are added to the deflector [4] the addressing capacity can be increased by a factor of 1000. The original single laser beam is multiplied by the beam-splitters to form a collection of up to 1000 'fingers' that simultaneously record or retrieve a word

Dipl.-Phys. H. Heitmann, Dr B. Hill and K. Witter are with Philips GmbH Forschungslaboratorium Hamburg, Hamburg, West Germany; Dr J.-P. Krumme, formerly with these laboratories, is now with Philips Research Laboratories, Eindhoven.

[1] H. Kurz, Lithium niobate as a material for holographic information storage, Philips tech. Rev. 37, 109-120, 1977 (No. 5/6).
[2] B. Hill, U. J. Schmidt and H. J. Schmitt, Optical memories, J. appl. Sci. Engng. A 1, 39-48, 1975. See also B. Hill, Optische Speichersysteme, paper read at the Conference on Digital Storage, Stuttgart 1977.
[3] U. J. Schmidt, Electro-optic deflection of a laser beam, Philips tech. Rev. 36, 117-132, 1976 (No. 5).
[4] B. Hill, J.-P. Krumme, G. Much, R. Pepperl, J. Schmidt, K. P. Schmidt, K. Witter and H. Heitmann, Polycube optical memory: a 6.5×10^7 bit read-write and random access optical store, Appl. Optics 14, 2607-2613, 1975.

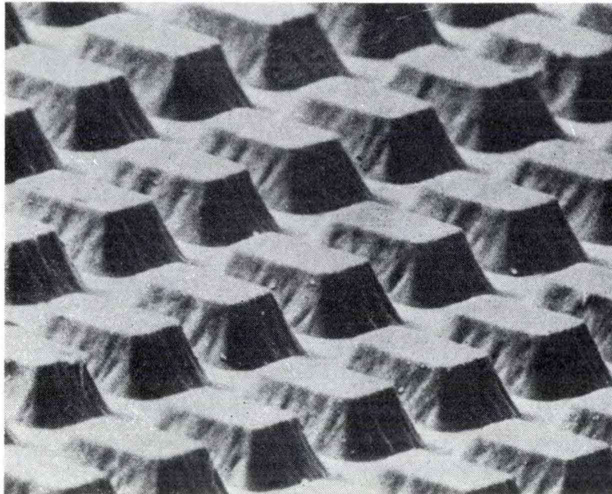

Fig. 1. Photograph made by scanning electron microscope of part of a prototype MOPS (Magneto-Optic Photoconductor Sandwich) storage wafer. Each 'island', composed of a ferrimagnetic garnet material, functions as a single-bit storage cell. The islands protrude about 3 μm above the substrate. In the finished wafer there is a photoconducting layer on the islands; the photograph was taken before this layer was applied.

of up to 1000 bits. The number of fingers is equal to the word length in writing and reading; we shall return to this presently.

The storage wafer that has been developed (*fig. 1*) consists of small islands (about 8×8 μm) of single-crystal gadolinium iron garnet, containing a few per cent of bismuth and gallium, on a substrate that is paramagnetic. Each island is an individual storage cell with uniaxial magnetic anisotropy; the free space between the islands provides thermal and magnetic isolation. Interference at neighbouring cells during writing is thus minimized. The photoconducting layer is located between transparent electrodes on top of the islands. The wafer is therefore a kind of five-layer sandwich, which has been given the name MOPS, standing for Magneto-Optic Photoconductor Sandwich [5]. The construction of the wafer is shown in *fig. 2*. The substrate is a rigid layer with a thickness of 0.5 mm. The other layers have a total thickness of about 5 μm.

Manufacture

The MOPS wafers are made [6] by using well known planar technology. The problem in the materials studies has been that of finding the optimum choice of substituents for the storage film and for the photoconducting layer. The 'molecular architecture' of the material is of importance, as we shall see later, to make sure that the best temperature for storage operation is in fact room temperature and that at the same time there is sufficient Faraday rotation and an adequate recording sensitivity.

The material for the storage film is grown by liquid-phase epitaxy to a thickness of 2 to 3 μm [7], on a (111) plane of the substrate, a gadolinium gallium garnet, which is paramagnetic. The substrate is partly substituted with calcium and zirconium to give better matching of the lattice constants of film and substrate [8]. The uniaxial magnetic anisotropy appears in the film during the growth; the mechanism responsible for it is not as yet fully understood. We shall return to this later, and also to the matching of the lattice constants.

The next stage in the manufacture is the production of the island structure. This is done by sputter-etching at radio frequencies, in an argon/oxygen plasma. The mask material is titanium. Titanium masks do not crumble away during sputter-etching, since titanium has a smaller etching rate than the garnet, so that thin masks can be used. The resolution of grooves to be etched into the garnet via titanium masks is of the same order of magnitude as the groove depth in the garnet film; this sets a limit to the packing density of cells made by the present technology. In fact, the MOPS concept would also work well with smaller islands and channels.

Finally, the islands are subjected to a series of evaporation and sputtering operations for the deposition of the remaining layers (fig. 2).

The ferrimagnetic properties

The net magnetization in a gadolinium iron garnet ($Gd_3Fe_5O_{12}$) can be interpreted as the sum of the magnetic moments of two Fe^{3+} sublattices with antiparallel alignment and the Gd^{3+} sublattice [9].

The three sublattice moments are all spontaneously aligned in the direction normal to the plane of the thin film — this direction is the easy axis induced by the growth process mentioned above. The antiferro-

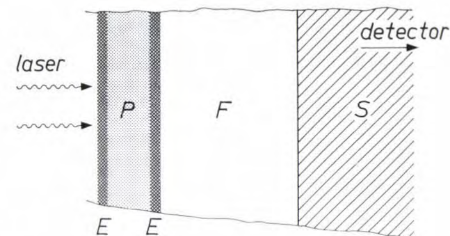

Fig. 2. Cross-section of a storage wafer. *S* paramagnetic substrate. *F* ferrimagnetic garnet film. *P* photoconducting layer. *E* planar electrodes. The photoconducting layer is about 3 μm thick and consists of CdS doped with a trace of Cu to give sufficient photoconductivity at the wavelength of the laser radiation (632.8 nm). The layers *E* are transparent, like the other layers of the 'sandwich', and consist of In_2O_3 doped with SnO_2; the electrical leads (not shown) are evaporated-aluminium strips.

magnetic ordering of this type associated with the sublattice moments is called ferrimagnetism.

A characteristic feature of gadolinium iron garnets is that the three sublattice moments have different temperature dependence. Because of this there is a 'compensation point', that is to say a temperature T_{comp} at which the resultant of the magnetic moments of the sublattices is zero. The material is still magnetically ordered, i.e. the compensation point lies below the Curie point. The compensation point is chosen as the operating temperature for storage and retrieval, since external magnetic fields cannot then easily destroy the data content — because the net magnetization in the material is then zero. At temperatures above the compensation point, however, an external magnetic field can switch an addressed cell from its existing direction of magnetization to the desired one (writing of '0' or '1'). The value of T_{comp} for the garnet films for MOPS has been chosen such that it approximately coincides with room temperature.

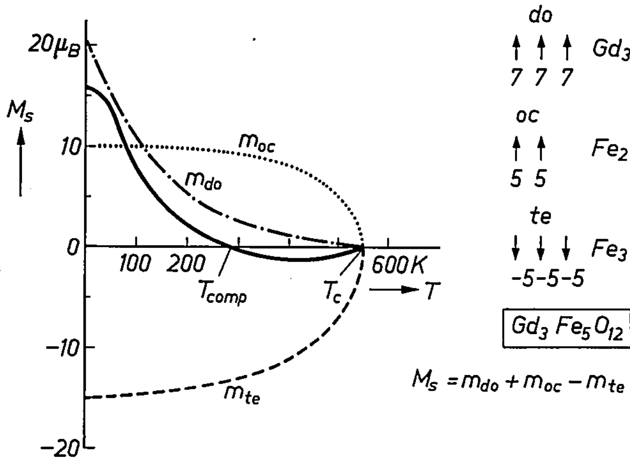

Fig. 3. The saturation magnetization M_s, in Bohr magnetons, as a function of the temperature T in a gadolinium-iron-garnet film. M_s is the sum of the magnetic moment m_{oc} arising from the Fe^{3+} ions at the octahedral sites, m_{te} from the Fe^{3+} ions at tetrahedral lattice sites, and m_{do} from the Gd^{3+} ions at the dodecahedral lattice sites. T_{comp} compensation point. T_c Curie point. The easy axis of magnetization is in the direction normal to the film owing to the growth process; the compensation point is the temperature at which M_s passes through zero.

Fig. 3 shows how the net magnetization in a thin film of gadolinium iron garnet, partly substituted as described above, depends on the temperature. Above and below the compensation point the polarity of the net magnetization has opposite values, unless an external magnetic field is applied.

Fig. 4 shows the magnetic field-strength that is necessary to switch the direction of magnetization of a storage cell, as a function of $T - T_{comp}$. The net magnetization — and hence each of the magnetic moments of the sublattices — can be rotated, provided that the applied field is sufficiently strong to override the coercivity of the material. When the temperature increases, the coercivity will decrease sharply. For the material of fig. 4 a field-strength of about 10 kA/m is sufficient if the temperature rises to about 20 degrees above T_{comp}. Switching only occurs in the cell that is heated; the applied field is however too weak to switch any other cells, as can be appreciated from the strongly negative temperature gradient in fig. 4.

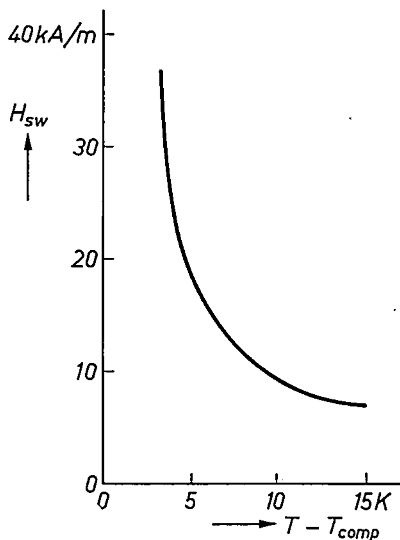

Fig. 4. The field-strength H_{sw} necessary to switch a storage cell of the film of fig. 3, as a function of the temperature T. The compensation point T_{comp} is taken as the zero. To obtain maximum selectivity in switching, the slope of this curve should be as large as possible; a high slope is associated with a relatively small anisotropy.

About 0.1 μJ is necessary per cell for the required increase in temperature. When the material has cooled to the compensation point again, the new direction pattern will remain 'frozen in'. The material can therefore store data permanently without the need for any energy input. (A memory with this special feature is called 'non-volatile'.) The Faraday rotation at the compensation point is positive or negative depending on the stored bit; as we said earlier, it is this effect that makes reading possible.

[5] J.-P. Krumme, B. Hill, J. Krüger and K. Witter, A highly sensitive reversible and nonvolatile hybrid photoconductive/magneto-optic storage material, J. appl. Phys. **46**, 2733-2736, 1975.
[6] J.-P. Krumme, H. Heitmann, D. Mateika and K. Witter, MOPS, a magneto-optic-photoconductor sandwich for optical information storage, J. appl. Phys. **48**, 366-368, 1977 (No. 1).
[7] W. Tolksdorf, Growth and properties of garnet films for storage application, IEEE Trans. **MAG-11**, 1074-1078, 1975.
[8] D. Mateika, J. Herrnring, R. Rath and Ch. Rusche, Growth and investigation of $\{Gd_{3-x}Ca_x\}[Ga_{2-y-z}Zr_yGd_z](Ga_3)O_{12}$ garnets, J. Crystal Growth **30**, 311-316, 1975.
[9] J. Smit and H. P. J. Wijn, Ferrites, Philips Technical Library 1959.
[10] B. Hill, I. Sander and G. Much, Magneto-optic memories, Optica Acta **24**, 495-504, 1977 (No. 4).

System design

Fig. 5 shows a design for a magneto-optic memory system that incorporates MOPS wafers as storage elements [5]. The inset is an enlarged part of the wafer with four individual cells (the islands) in cross-section. The magnetic alignment of the sublattices, which correspond to the ferrimagnetism in the material, is indicated by the three small arrows in each cell; the patterns represent either a stored '0' or a stored '1.

The positioning is carried out by two electromechanical loudspeaker systems. The storage capacity would be about 10^7 bits, with random access times of a few ms.

A third potential application is in a device for storing images. Here each storage cell functions as a 'black' (or 'white') point of an extremely small raster. This collection of points is projected on a screen to produce an enlarged image that can be read or examined by an observer. A device such as this could be used for the storage of (erasable) alphanumeric information in a format comparable with microfilm.

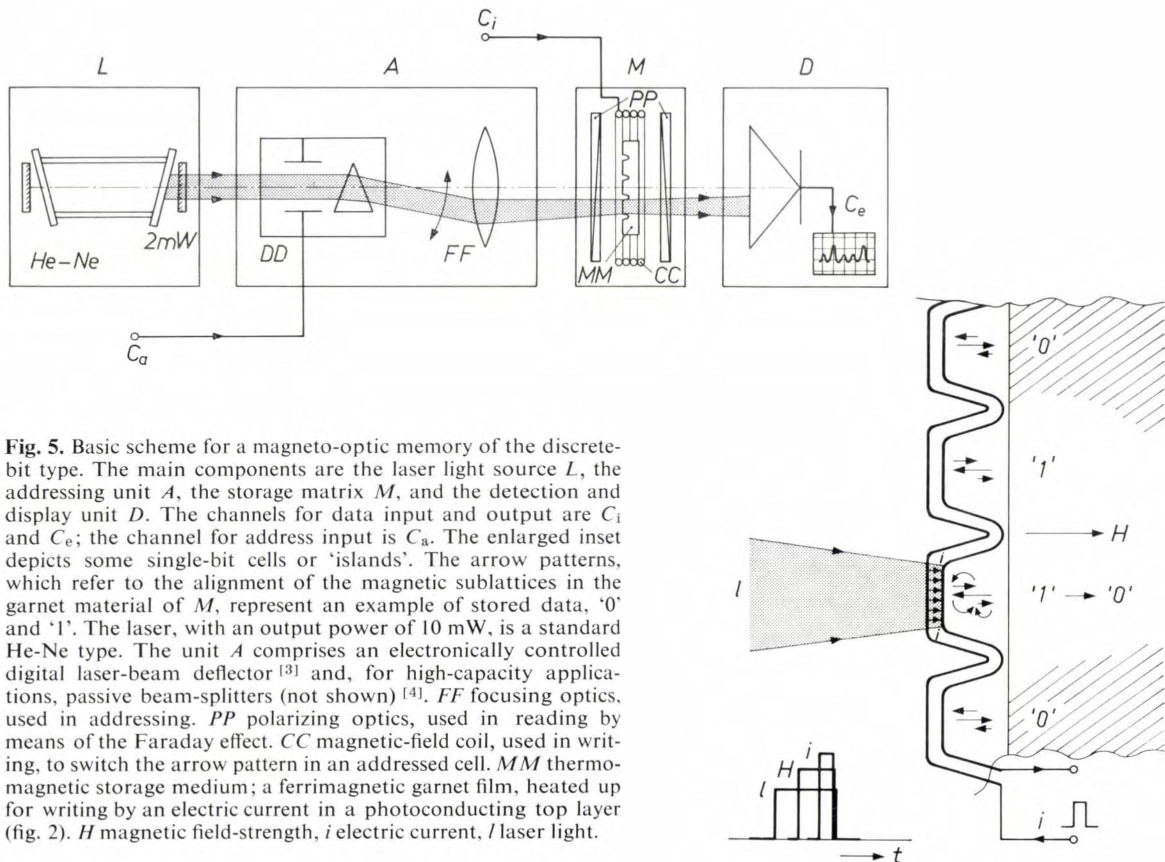

Fig. 5. Basic scheme for a magneto-optic memory of the discrete-bit type. The main components are the laser light source *L*, the addressing unit *A*, the storage matrix *M*, and the detection and display unit *D*. The channels for data input and output are C_i and C_e; the channel for address input is C_a. The enlarged inset depicts some single-bit cells or 'islands'. The arrow patterns, which refer to the alignment of the magnetic sublattices in the garnet material of *M*, represent an example of stored data, '0' and '1'. The laser, with an output power of 10 mW, is a standard He-Ne type. The unit *A* comprises an electronically controlled digital laser-beam deflector [3] and, for high-capacity applications, passive beam-splitters (not shown) [4]. *FF* focusing optics, used in addressing. *PP* polarizing optics, used in reading by means of the Faraday effect. *CC* magnetic-field coil, used in writing, to switch the arrow pattern in an addressed cell. *MM* thermomagnetic storage medium; a ferrimagnetic garnet film, heated up for writing by an electric current in a photoconducting top layer (fig. 2). *H* magnetic field-strength, *i* electric current, *l* laser light.

The design for a 'polycube' optical memory (POCOM [4]) is a good example of an application of the MOPS wafers in a system for backing storage; it incorporates a digital laser-beam deflector with a passive 'polycube' beam splitter. The storage capacity is comparable with that of a magnetic disc store. The (random) access time, however, is rather smaller: it is of the order of 100 μs. POCOM has a completely non-mechanical method of addressing.

Another (inexpensive) backing-storage system that can be considered employs mechanical addressing by *x-y* positioning of the storage plane with respect to a light source — or more than one light source, if desired.

In the remaining sections of this article we shall first discuss the place that the MOPS wafers can occupy as a component of a large storage system. This will give the characteristic features the greatest emphasis. We shall then pay some attention to the solid-state physics of the storage film, the substrate, and the photoconducting layer. Finally, we shall give some results of the work on switching cycles in a recent version of a MOPS wafer. A batch of samples has now been made with a diameter of about 2 cm; this version will give packing densities of up to 5 kbit/mm^2.

The MOPS wafer as system component

The performance of a magneto-optic storage wafer with regard to information processing and the associated limitations to its operation in a memory system are best expressed by certain figures of merit [11]. These figures are characteristic of the reading efficiency, the magneto-optic contrast and the (optical) recording sensitivity. The recording sensitivity relates to writing, the other two parameters to the reading of data. Before discussing these figures of merit, let us first have a closer look at the writing and reading operations.

The individual cell: writing and reading

The writing of data into a particular individual cell is performed under the control of three variables (fig. 5): laser light, which illuminates the cell (addressing); electric current in the photoconducting layer, which provides the energy for heating up the cell addressed; field-strength of the applied magnetic field, which switches the magnetizations of the sublattices into one of the two stable directions.

Some of the heat developed in the cell that has been addressed will eventually reach the neighbouring cells. Precautions against cross-talk must be taken by ensuring that the temperature increase does not exceed a certain maximum when the magnetic field is still applied. The electric field at the photoconductor is therefore only switched on for a limited time to restrict the thermal input to the cell addressed [11]. The magnetic field only has to be switched on during a short period around the instant at which the temperature in the addressed cell is at a maximum.

The maximum pulse duration τ can be estimated from the relation for heat flow

$$\Delta x = (D\tau)^{\frac{1}{2}},$$

where D is the mean diffusion constant of the medium through which the heat is being transported and Δx is half the distance across an island (about 4 μm). On applying the equation above we find that τ should not exceed a few μs.

After switching the cell cools to the ambient temperature again, and the stored data can then no longer be affected by external magnetic fields, since the compensation point of the material approximately coincides with the ambient temperature.

The polarization-optics system for reading the information contained in an individual cell is also shown in fig. 5. The laser beam in the system first passes through a linear polarizer before striking the storage film. Behind the film there is an analyser and a photodetector. (In practice the polarizer and the analyser take the form of thin sheets of dichroic plastic attached to the MOPS wafer.) The transmission direction of the analyser is oriented in such a way with respect to the transmission direction of the polarizer that the light emerging from a cell whose content represents a '0', say, is strongly absorbed, whereas the light from a cell whose content represents a '1' is partly transmitted. The photodetector transforms the corresponding difference in transmitted light intensity into a difference in electrical-signal level.

Reading and writing; some figures of merit

The reading efficiency η represents the difference in the detected radiant fluxes Φ_1 and Φ_0 in reading a '1' and a '0', expressed as a percentage of the power Φ_e delivered to the storage cell in question by the laser beam, so that

$$\eta = \frac{\Phi_1 - \Phi_0}{\Phi_e} 100\,\%.$$

It will be clear that both radiant fluxes, and hence their differences, depend on the setting of the polarization optics — in practice on the angle between the directions of transmission of the polarizer and the analyser. When this angle is exactly equal to 90° both signals are transmitted at equal strength; it is impossible to distinguish between '1' and '0' ($\eta = 0$). At slightly higher values η increases approximately linearly with the angle (*fig. 6*).

The magneto-optic contrast C, i.e. the ratio Φ_1/Φ_0, also depends on the same angle. Fig. 6 shows that C has a maximum value as a function of the angle. To obtain a clear distinction between '0' and '1' it is important to make the contrast as high as possible. The reason for this is twofold: the optical properties of the material will vary to some extent from cell to cell, and the output power of the laser will never be absolutely constant. A setting with C equal to about 5 is an acceptable choice. The associated reading efficiency for the film of fig. 6 is about 0.5%.

A third kind of noise that limits the operating characteristics is shot noise from the photodetector itself. (Other sources of noise, such as statistical fluctuations in the number of light quanta and noise in the load resistor of the photodetector can be neglected [12].) To obtain some idea of the values involved, it can be assumed that the noise from a reasonable photodetector corresponds to a power of about 10 nW. The weaker reading signal, which corresponds to reading a '0', requires a signal-to-noise ratio of at least 1 for reliable detection; this in turn implies that the time constant of the photodetector should be at least 100 μs (the avail-

[11] J.-P. Krumme and H. J. Schmitt, Ferrimagnetic garnet films for magnetooptic information storage, IEEE Trans. **MAG-11**, 1097-1102, 1975.

[12] R. P. Hunt, Magnetooptics, lasers, and memory systems, IEEE Trans. **MAG-5**, 700-716, 1969.

able signal-to-noise ratio increases as the square root of the time constant). The period of 100 μs has therefore also been used as the (minimum permissible) cycle time for the POCOM memory system. The only other time constants in the system with a value anywhere near 100 μs are the rise and decay times of the heating current induced in the photoconducting layer of the actual wafers during writing. Their values (about 50 μs) limit the cycle time to about the same value.

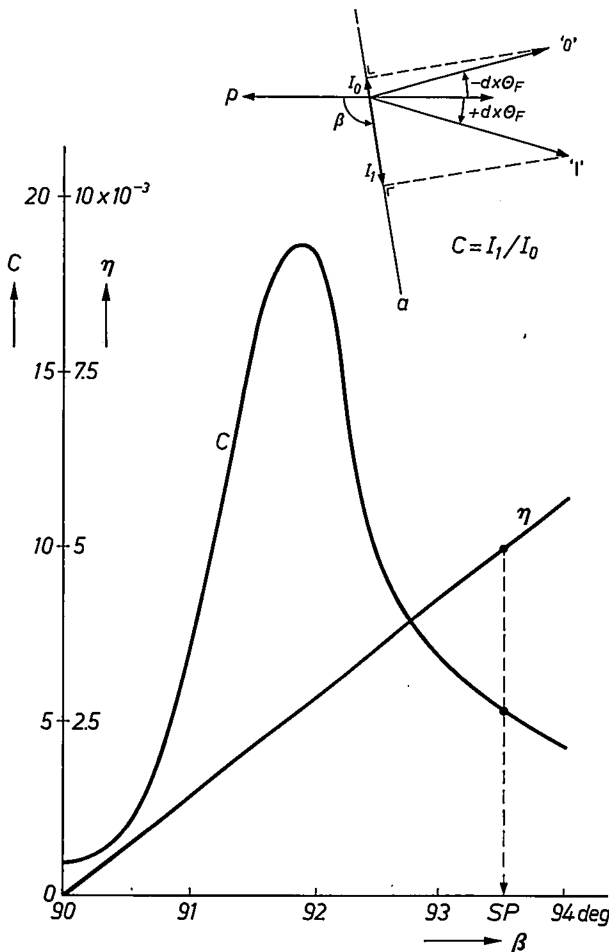

Fig. 6. The reading efficiency η and the magneto-optic contrast C for a MOPS storage wafer, both calculated as a function of the azimuth angle β, the angle between the planes of maximum transmission of the fixed polarizer p and the adjustable analyser a; the components p and a belong to the polarization optics in fig. 5. The Faraday rotation employed for reading data is equal to $d\Theta_F$, the product of layer thickness d (5 μm) and the specific Faraday rotation (3000 degrees/cm). Curve C is valid for a typical MOPS prototype wafer, at $\lambda = 632.8$ nm. The maximum of C occurs at about $d\Theta_F$. *SP* operating point.

The storage system of fig. 5 can be brought to one of its sensitivity limits if the addressing unit is extended by adding passive beam-splitters that produce a thousandfold spatial division of the laser beam by a multiplexing operation. A system extended in this way could reach a maximum reading rate of 10 Mbit/s, with a cycle time of 100 μs. The reading rate is then a word of 1000 bits per cycle. A laser with a power of 20 mW could then simultaneously transmit 2 μW to each of 1000 storage cells (it is assumed that 90% of the laser power is dissipated in the addressing unit). For reading the magnetic state of lower transmission 10 nW is then available (at $\eta = 0.5\%$), which is equal to the equivalent power level of the detector noise. The requirements for an acceptable signal-to-noise ratio and a sufficiently high magneto-optic contrast are then completely satisfied. (In anticipation of the next section we ought to mention here that it is readily possible to make material with a stronger Faraday rotation.)

The third figure of merit is the (optical) recording sensitivity. This is the minimum amount of energy necessary for switching one bit of information, or in other words the minimum amount of energy required for switching a storage cell. The energy that the laser can produce is 2×10^{-10} joule per bit — as in reading — which is 500 times less than the amount required for the increase in temperature. The photoconducting layer of the addressed cell bridges this 'energy gap', as was stated earlier; in this way the presence of the layer increases the recording sensitivity by a factor of 500, if the laser beam is taken as the power input in the usual way.

Application in backing systems

In memories of a 'multichannel type' intended for backing systems, simultaneous illumination by means of passive beam-splitters can be extensively applied, as we saw earlier. There are however certain limitations here, which are connected with the existing technology and also with the developments in backing systems in general. We shall have more to say about this at the end of this section.

All the MOPS wafers, which together form such an optical backing system, are addressed by a multiplexed laser beam. As we noted before, three parameters are available for switching the separate cells, and the laser light is already used for the addressing; the magnetic field or the electric field must therefore be used in such backing systems for differentiation between the writing of a '0' or a '1' in the addressed cells. Which of the two fields is chosen depends very much on the technology [10]. The generation of the magnetic field (about 10 kA/m) requires 'macroscopic' coils, whereas the voltage for the electric field can be applied with evaporated electrodes that satisfy integrated-circuit standards. Where a large number of wafers have to be combined it is therefore preferable to distribute the electric field rather than the magnetic field. The writing of a word then requires a two-stage procedure: firstly, all the 'zeros' are written, giving the common magnetic

field the corresponding direction; secondly, all the 'ones' are written with the magnetic field reversed.

Fig. 7 shows how a storage plane can be combined with a coil for a magnetic field. The coil is located in grooves in two base-plates on either side of the wafer. The geometry of the coil minimizes its inductance, so that the field can be generated in the form of pulses of no more than μs duration and of high repetition rate, as required for fast access in backing systems.

should exceed about 3000 degrees per cm (at a wavelength of 632.8 nm). This lower limit implies a difference in rotation of the plane of polarization of about 2 degrees for the two opposite directions of magnetization. This difference allows the information contents '0' and '1' to be distinguished from one another (*fig. 8*). The addition of Bi^{3+} ions is particularly effective for increasing the Faraday rotation. For the composition quoted above the rotation is about 5000 degrees per cm.

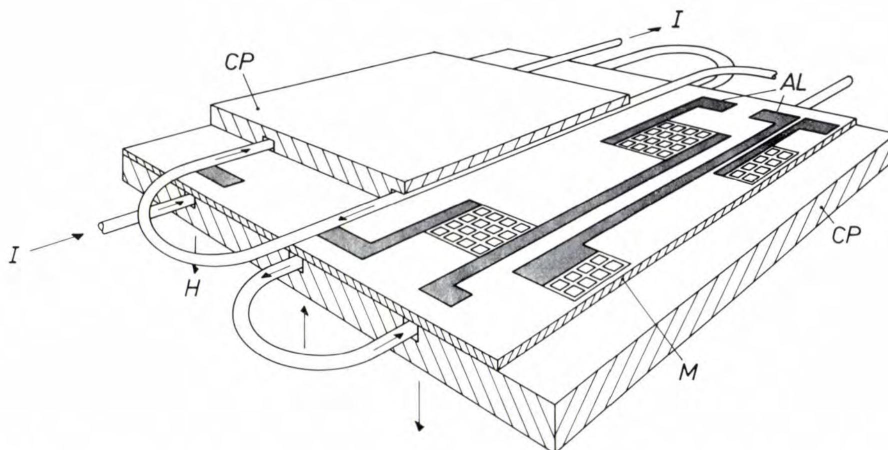

Fig. 7. Geometry of the coil for the external magnetic field *H*, which determines whether a '0' or a '1' is written in the storage cells addressed. *CP* transparent carrier plates, in which the field coil is mounted. *M* MOPS storage wafer (fig. 10). *AL* aluminium electrode leads. *I* current in the field coil.

Materials studies

The storage film and the substrate

The main purpose of the 'molecular engineering' in the development of the storage wafer has been to find the optimum quantities of diamagnetic substituents for incorporation in the storage film [7] [11]. These substituents are Bi^{3+} and Ga^{3+} (or Al^{3+}) ions, which take up some of the positions of the Gd^{3+} and Fe^{3+} ions in the garnet lattice. These substituents are added to satisfy two important conditions. The first has been stated earlier: the compensation point should approximately coincide with room temperature. In such a situation stabilization of the temperature, if necessary, will not introduce so many problems. The diamagnetic substituents have been found to affect the compensation point considerably, but to have only a small effect on the Curie point. The composition used at present, $(Gd_{2.8}Bi_{0.2})(Fe_{4.8}Ga_{0.2})O_{12}$, has a compensation point of 26 °C.

The second condition is that the specific Faraday rotation, the angle of rotation per unit film thickness,

In designing the composition of the material attention must of course be paid to the optical absorption. The best way of doing this is to use another figure of merit: the ratio $2\Theta_F/\alpha$, where α represents the optical absorption coefficient of the film and Θ represents the specific Faraday rotation. This ratio has the dimensions of an angle; it is strongly dependent on the optical wavelength and is related to the signal-to-noise ratio in reading (see the part of the previous section that deals with the other figures of merit). For storage cells of adequate quality in POCOM it is required that $2\Theta_F/\alpha$ should be more than 2 degrees. In the present case the value is more than twice the lower limit. (This applies for room temperature and for light at a wavelength of 632.8 nm.) The optimum thickness for the film, i.e. the thickness for the maximum signal-to-noise ratio, is about 10 μm. In practice, however, a smaller value has been chosen because it gives better resolution and heat transport.

An increase in the percentage of Bi^{3+} does not only increase the Faraday rotation, but also gives a stronger uniaxial anisotropy. This anisotropy is responsible for the bistability of the material. It would therefore seem desirable in every way to increase the Bi^{3+} content; on the other hand, however, when the anisotropy in-

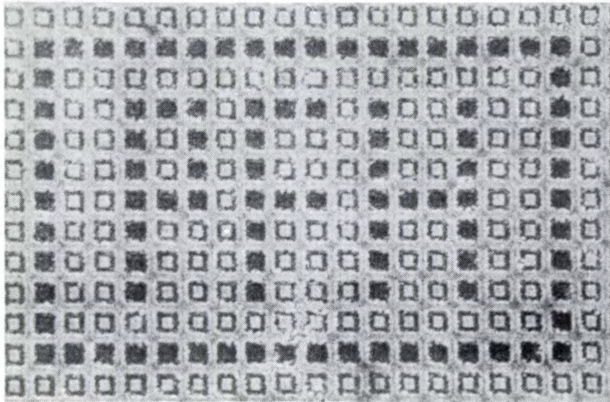

Fig. 8. Part of a MOPS wafer, in which the letters PFH are written thermomagnetically. The single-bit cells show up either dark ('1') or light ('0'), a distinction which arises from using polarization microscopy (the Faraday effect).

creases the recording sensitivity decreases, which means that more heat is necessary for switching a memory cell at a given value of the magnetic field-strength. The reason for this is that for writing the rotation of the magnetic moments — away from the easy axis — requires a quantity of magnetic-field energy that is of the order of the anisotropy energy. This anisotropy energy, calculated per unit volume, should remain below a few hundred joules per m^3.

Until an independent and accurate way of controlling the uniaxial anisotropy has been found, some sort of compromise for the Bi^{3+} content will therefore have to be adopted.

It seems probable that the trade-off between recording sensitivity and reading efficiency is connected with certain boundary conditions of a chemical nature that arise during the growth of the crystalline layer. As indicated earlier, the exact origin of the growth-induced magnetic anisotropy is still not well understood.

The relation between the amount of Bi^{3+} substitution and the degree of anisotropy is not straightforward. Theory indicates that uniaxial anisotropy may arise from an ordering process during the growth of the layer and that the anisotropy increases with the growth rate. On the other hand, the addition of Bi^{3+} as a substituent is the more successful the more oversaturated the melt, which implies a higher growth rate — which is in turn associated with greater anisotropy [13].

The magnitude of the uniaxial anisotropy is also affected by lattice stress in the magnetic film [14]. Depending on the kind of stress in the material — tensile or compressive — and on the sign of the magnetostriction constant, the uniaxial anisotropy is either reinforced or weakened. In our garnets, which have a negative magnetostriction coefficient, the anisotropy is weakened by a compressive stress. Complete compensation of these high anisotropies by magnetostriction would require too great a mismatch between the (free) lattice constants of the substrate and the film, which would make epitaxial growth impossible. The substrate is therefore partly substituted by calcium and zirconium, which makes its lattice constant no more than 0.01 to 0.1% smaller than that of the growing film [8]. In this way an acceptable compressive stress can be incorporated into the storage cells, and a higher Bi^{3+} content is permissible. Since substitution of Bi^{3+} and Ga^{3+} or Al^{3+} ions affects the lattice constant of the film, it provides a fine control of the mismatch between the film and the substrate.

The localized heating that occurs during writing causes local thermal expansion. This increases the compressive stress, and the uniaxial anisotropy in the storage cell is further reduced via the magnetostriction. On the other hand, a gradual and uniform heating up of the entire storage layer has only a small effect on the switching sensitivity, since the total anisotropy of these stressed films is not very large in the temperature range of interest (another factor that helps to decrease the accuracy required in stabilizing the temperature of the film [14]).

The photoconducting layer

The substitution of copper into the CdS film causes a considerable increase in the photosensitivity in the wavelength region above 600 nm (*fig. 9*), where the helium-

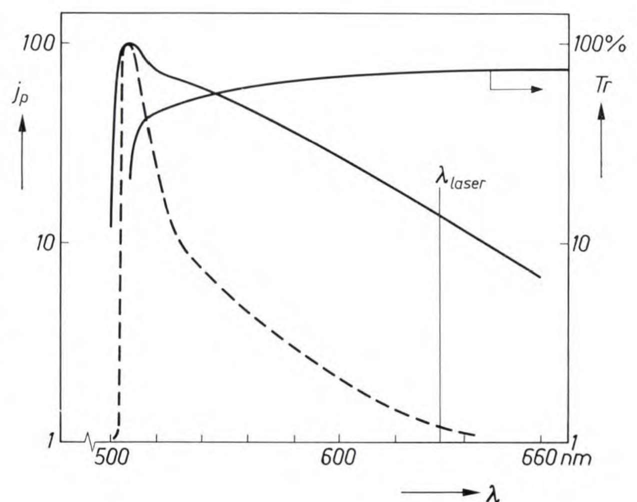

Fig. 9. Example of a measured spectral response of a CdS (Cu) layer — the photoconducting upper layer of a MOPS storage wafer (fig. 2). *Tr* optical transmission and j_p normalized photoelectric current, both plotted against wavelength. The copper reduces the dark current and it extends the photosensitivity into the red part of the spectrum, where the laser operates (fig. 5). The dashed curve is the photoelectric current in single-crystal CdS with no Cu dopant. The shape of the curve for j_p is not as good as it would be under normal operating conditions (one of the differences is the light intensity; in the storage system it would be at least 1000 times as large).

neon laser operates. Pure CdS only has a substantial photosensitivity near 510 nm, associated with an 'absorption edge'. An increase in the photoelectric response due to doping with copper implies an effective increase in the optical recording sensitivity of the MOPS wafers.

The thickness of the CdS(Cu) layer should of course be such that the laser beam is not too strongly attenuated. The CdS powder that we have used for vapour deposition of the photoconductor contains some chlorine as a dopant; the chlorine acts as a 'coactivator' in the photoconduction process. On the other hand, the chlorine also introduces donor levels that increase the dark current [6]. This undesirable effect is counteracted by the copper doping. However, too much copper leads to recrystallization of the CdS film accompanied by a general deterioration of the optical properties. The optimum concentration of the copper dopant is of the order of a hundred ppm. In photoconducting CdS films of this type the ratio of the resistances of the dark and illuminated states is greater than 10^4, at 632.8 nm wavelength and typical laser-power levels in POCOM.

For approximately rectangular laser pulses, the rise and decay times of the induced photocurrent are shorter than 50 μs. The decay time is not determined by the electrical characteristics of the cell, but by its thermal characteristics, as absorption measurements have shown.

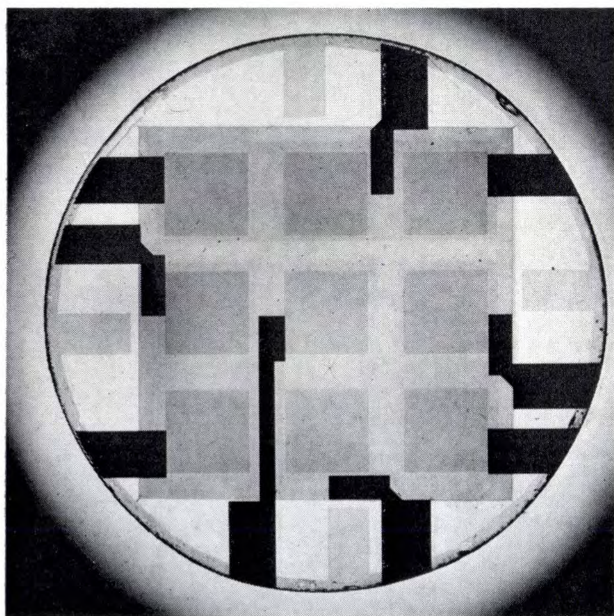

Fig. 10. A MOPS prototype wafer consisting of 9 (= 3 × 3) groups of 128 × 128 single-bit storage cells. The cells, made from a ferrimagnetic garnet material, lie like 'islands' (fig. 1) on a thin paramagnetic disc 18 mm in diameter. The large square is the photoconducting layer, CdS with Cu, between transparent electrodes; the nine black regions are aluminium connecting leads to the individual upper electrodes of the photoconducting layer.

Prototypes and their performance

The technology described here has been used in making a number of prototypes of the storage wafer; see *fig. 10*. The garnet layer of this prototype is divided into 3 × 3 subpatterns, each consisting of more than 16 000 cells. Each subpattern has a separate upper electrode, with a vapour-deposited aluminium lead and

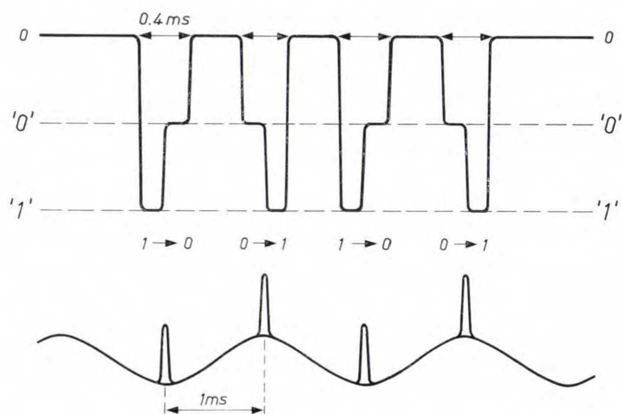

Fig. 11. Oscillogram of four switching cycles, '1' → '0', '0' → '1', etc., induced in a storage cell of a MOPS wafer (fig. 10). The upper signal is from the photodetector, obtained by means of Faraday rotation. Switching occurs when three signals coincide: a laser pulse (duration 400 μs), an extreme value of the external magnetic field (the sine wave, lower trace, half-period 1 ms), and the electrical pulse (the spikes on the lower trace, duration 30 μs). With the field-coil geometry of fig. 7 the magnetic field could also be pulsed, with the advantage of shorter cycle time and lower energy dissipation. The laser pulse duration is made long here to give good visibility to the detail of the oscillogram; the contrast, here about 2 : 1, would in practice have another value.

is addressed by only one partial beam. This arrangement allows each subpattern to be switched individually, whether or not storage cells in the other subpatterns are illuminated at the same time. Each individual storage cell of MOPS can therefore be switched selectively.

The prototypes of the storage wafers, as shown in fig. 10, have been closely investigated [6]. A study was made of the behaviour during a limited number of reading and writing cycles, and also of the long-term behaviour. An example of the results from the long-term study is that more than 10 million switching cycles of randomly selected storage cells did not give any deterioration or change in any of the characteristics. No cross-talk between adjacent storage cells was observed during these tests.

Table I lists the operating conditions used in testing the individual writing and reading cycles. The external

[13] J.-P. Krumme, G. Bartels, P. Hansen and J. M. Robertson, Control of the growth-induced magnetic anisotropy in ferrimagnetic garnet films grown by liquid-phase epitaxy, Mat. Res. Bull. **11**, 337-346, 1976 (No. 3).
[14] J.-P. Krumme, P. Hansen and K. Witter, Thermomagnetic switching of ferrimagnetic garnet films at their compensation temperature, J. appl. Phys. **47**, 3681-3689, 1976 (No. 8).

magnetic field was pulsed or varied sinusoidally. *Fig. 11* shows several switching cycles for the case of a sinusoidally varying field and also the output signals when the recorded information is read. Switching for writing can only occur when the magnetic field assumes an extreme value. The contrast ratio between reading a '1' and a '0' is at least 2. This ratio is not entirely satisfactory for the intended application in backing stores; a reduction in the optical scattering at the edges and increased Faraday rotation will considerably improve this ratio.

Table I. The operating conditions used in thermomagnetic switching single-bit cells of a MOPS wafer.

Laser (He-Ne)	Wavelength	632.8 nm
	Focus	6 μm diameter 2 μW intensity (per bit)
	Energy density (writing and reading)	6 μJ/mm², pulsed
Cycle time		about 100 μs
External field		10 kA/m pulsed (50 μs duration) or sinusoidal
Electric field		5V, pulsed (30 μs duration)

Summary. A magneto-optic storage wafer of the discrete-bit type is described. These wafers are potential building elements for optical backing stores (about 10^8 bits) and for certain image-processing equipment working at two levels (large-scale projection and erasable microstorage), all non-volatile. Prototype wafers consist of a dense (5 kbit/mm²) 'open island' structure with 1.5×10^5 single-bit storage cells, on a paramagnetic substrate, and allow fast random access (cycle time about 100 μs) by a laser beam (λ = 632.8 nm, 2 mW). The cells consist of a bistable ferrimagnetic garnet film $(Gd, Bi)_3(Fe, Ga)_5O_{12}$, and a photoconducting top layer, of CdS(Cu) sandwiched between $In_2O_3(SnO_2)$ electrodes, which increase the optical recording efficiency by a factor of 500. The writing of data corresponds to the alignment of the sublattice magnetizations in the addressed cell with a control field (about 10 kA/m) at about 20 °C above the compensation point of the material. The addressing laser beam triggers the required heating up (0.1 μJ/bit) locally in the photoconductor. The reading of data depends on Faraday rotation, using a (linearly polarized) laser beam of the same power. The transmission (i.e. the reading efficiency) of the wafers is about 0.5%. 'Molecular engineering' has been applied successfully in adjusting the compensation point to room temperature, raising the specific Faraday rotation to about 5000 degrees per cm, and obtaining a better match between the photoconductor sensitivity curve and the wavelength of standard helium-neon lasers. A trade-off between recording sensitivity and reading efficiency is discussed. Some results of long-term tests and also of single write/read cycles are given for prototype wafers.

Speaker recognition by computer

E. Bunge

We all know from experience that people can be easily recognized by their voices. This comes about not just from their individual habits of speech, but from the endless variety of the acoustic parameters of the vocal tract throughout the population — it is almost impossible to find two voices that are perfectly identical. The voice may therefore serve as a passport, provided there are technical means of distinguishing the individual voices from one another with a sufficiently high degree of reliability. This is where the techniques for speech analysis come in. These were developed years ago for resolution and resynthesis of the speech signal to condense the information so that speech could be transmitted in narrower frequency bands; now they have been turned to the more general applications of man-machine communication by voice. As might have been expected, computers have come to play a large part in this. Whereas the prospect of a free and fluent conversation between man and machine still seems to be a long way off, the simpler task of recognizing a person by his voice has been proved to be well within the capabilities of a machine and high reliability has been obtained. Research projects on this subject are going on in several places in the world. One of these is a government-sponsored project called AUROS at Philips Forschungslaboratorium Hamburg, in West Germany.

Introduction

When listening to somebody who is talking, a human listener perceives *what* is said, *who* is speaking and *how* it is said. The human brain is capable of splitting up the complex information contained in the speech signal to answer simultaneously questions about the meaning of what is said, the identity of the speaker and his emotional state. Investigations have been going on for some time to see whether the artificial intelligence available in computers can be employed to perform at least part of this task.

Speech recognition by computers — i.e. computers understanding *what* is said — still seems to be a very difficult problem and to give valuable results only with restricted vocabularies and restricted groups of speakers. On the other hand, speaker recognition — the identification of *who* is speaking — seems to have made considerable progress and to be nearly ready for practical application.

The value of a device for speaker recognition is obvious. It would be highly efficient if a simple voice utterance was sufficient in all those cases where a person's identity has to be established or verified. The human voice is very specific to the individual speaker; it cannot be lost or stolen, it cannot easily be imitated [1], and it can be transported over long distances at low cost. For all these reasons the human voice would provide an ideal 'acoustic passport'. This passport could be used to supplement existing systems to increase their security, or by itself, e.g. to allow authorized access to money from banks and to confidential information from data banks and government authorities. A second application is in crime investigation, where recorded voices of blackmailers and kidnappers have to be compared with the voices of suspects.

Systems for speaker recognition have one or more speech-input terminals, connected to a central computer. The connection may be made via the public telephone system. The voice is analysed in the computer and compared with stored voice-patterns.

Dr E. Bunge, formerly with Philips GmbH Forschungslaboratorium Hamburg, Hamburg, West Germany, is now with Bundeskriminalamt, Wiesbaden, West Germany.

[1] B. S. Atal, Automatic recognition of speakers from their voices, Proc. IEEE 64, 460-475, 1976.
A. E. Rosenberg, Automatic speaker verification: a review, Proc. IEEE 64, 475-487, 1976.

Speaker identification has to be distinguished from speaker verification. In speaker verification an unknown speaker claims to be a certain person X, and by comparing his voice data with that of speaker X the system decides whether he really is speaker X or an impostor. For speaker identification, an unknown voice is compared with a stored voice-pattern library and the system finds out if the voice is present in the library, and if so, who it belongs to.

The greater part of this article is a description of an experimental speaker-recognition equipment called 'AUROS' (AUtomatic Recognition Of Speakers), which has been designed at Philips Forschungslaboratorium Hamburg, in West Germany, for a government-sponsored research project at PFH. The system has been set up to enable us to compare the merits of different speaker-identification and verification procedures. Attention is given to the error rates in experiments with larger groups of subjects, and also to the computer time required and the complexity of the equipment, which is quite different for different procedures. The experiments already made — which will be reported in the last section — indicate that the error rates are of the order of one per cent for procedures of average complexity [2].

In speaker recognition by computer there are two fundamental problems: first, all speech utterances are unique and not exactly reproducible, and, secondly, the amount of data to be processed in short time intervals is extremely large. Let us look more closely at these two problems and at the procedures that they compel us to adopt.

The non-reproducibility of human speech

No-one can pronounce a sentence twice in an identical manner. Each repetition yields a different acoustic representation. *Fig. 1* shows three curves of sound pressure as a function of time for three utterances of the vowel 'a' pronounced by the same speaker. The differences between the three curves are evident although the speaker tried hard to produce identical utterances.

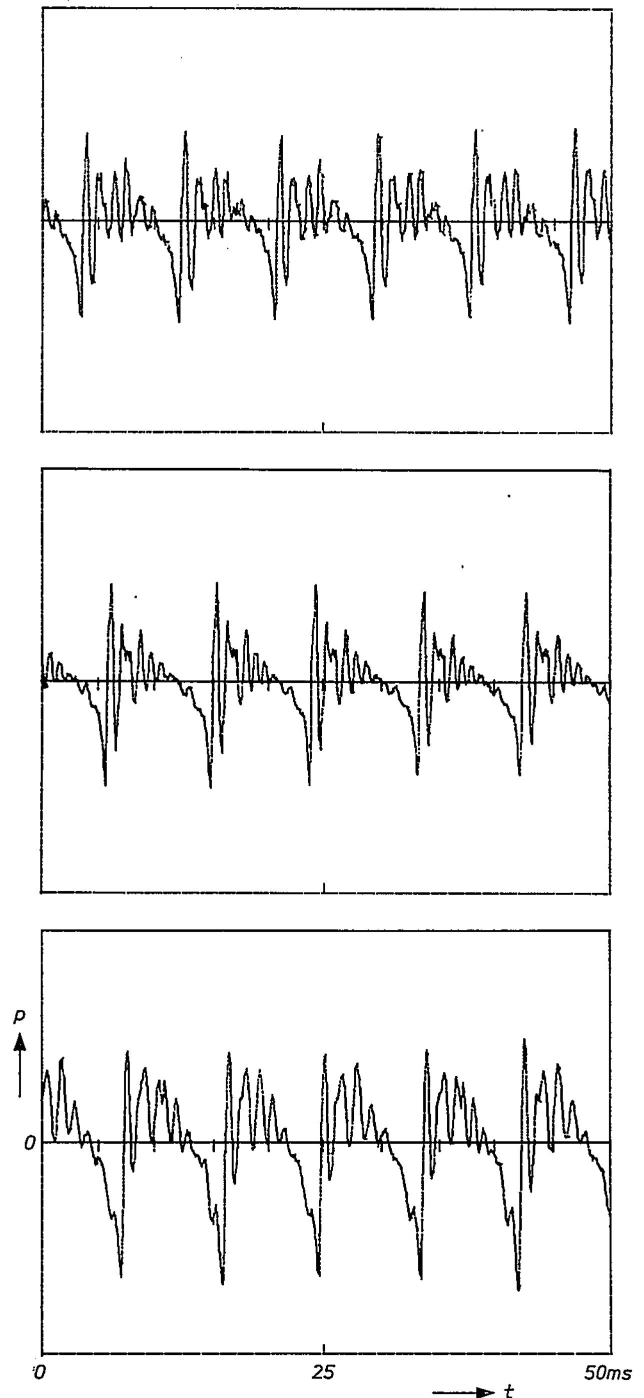

Fig. 1. Sound pressure p as a function of time t for three utterances of the vowel 'a' by the same speaker. The different curve shapes demonstrate that human speech is not exactly reproducible; this constitutes a problem in speaker recognition by computer.

The non-reproducibility also holds for any feature extracted from the original time function. *Fig. 2* shows as examples the Fourier spectra and the 'cepstrum' functions of the three versions of the vowel 'a'. This function is obtained by computing the power spectrum of the logarithm of the Fourier spectrum. The Fourier spectrum has periodic ripples corresponding to the harmonics of the speech signal; the frequency spacing between these ripples is equal to the fundamental frequency of the speech. The cepstrum, which is again a time-domain function, will have a peak corresponding to the periodicity of the Fourier spectrum, and indicating the fundamental pitch period of the speech [3].

It follows that the voice of a speaker cannot be described by one single utterance, because other utterances produce different data. Instead, it is necessary to process a set of utterances statistically to determine the characteristic features of a voice. This can be done systematically by pattern-recognition techniques.

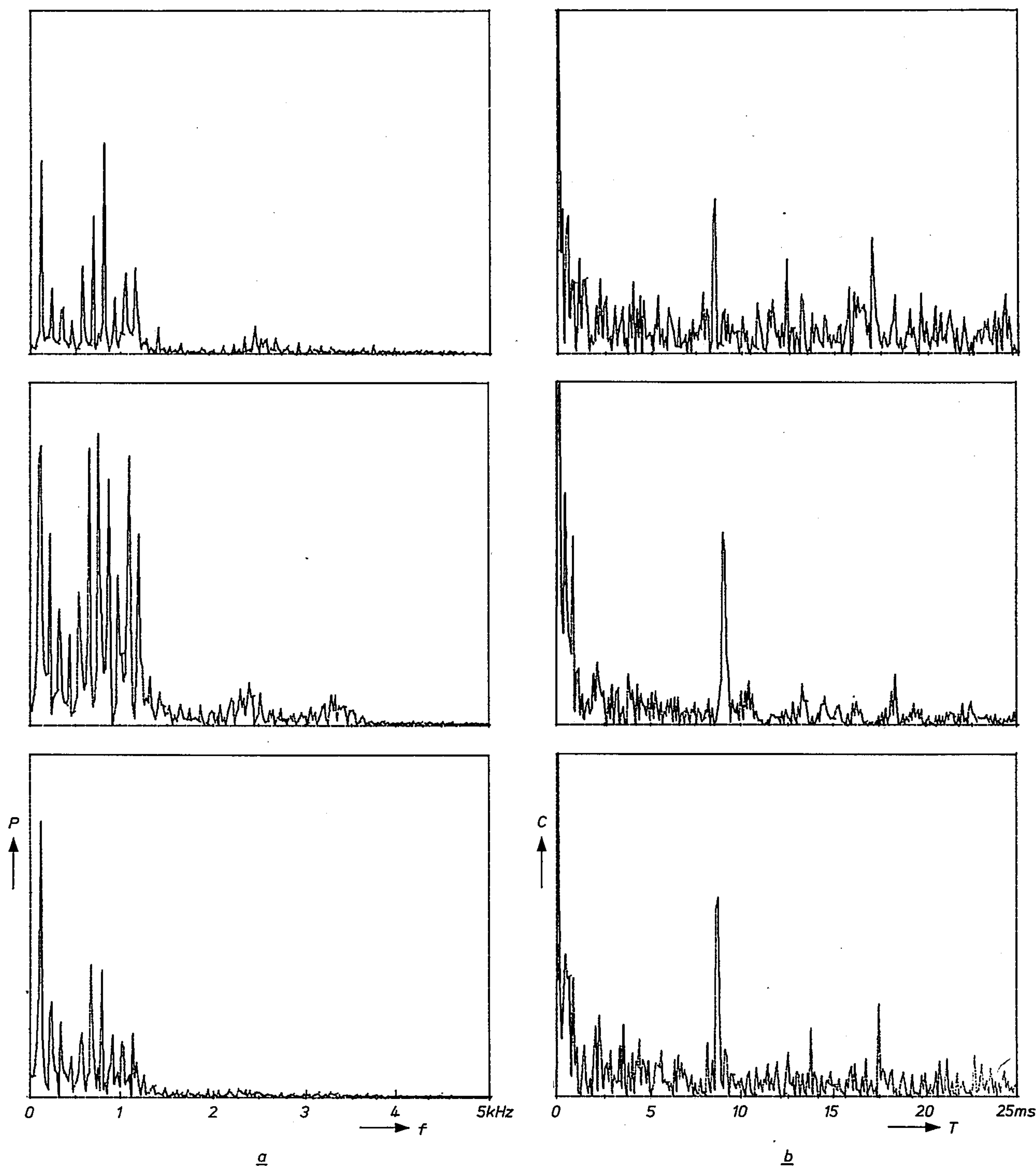

Fig. 2. Fourier spectra (*a*) and cepstra (*b*) for the three utterances of vowel 'a' represented in fig. 1. Spectrum and cepstrum functions also appear not to be reproduced exactly. *P* power density. *f* frequency. *C* cepstrum function. *T* pitch period.

The large amount of data to be processed

The sampling theorem shows that with an upper limiting frequency of 5 kHz, 1 second of human speech can be represented by a string of 10 000 samples. With a dynamic range of 48 dB, each sample can be coded as an 8-bit computer word. Under these circumstances — which correspond to those in our experiment —

[2] E. Bunge, Automatic speaker recognition system AUROS for security systems and forensic voice identification, Proc. 1977 Int. Conf. on Crime Countermeasures — Science and engineering, Oxford 1977, pp. 1-7.
E. Bunge, Vergleichende systematische Untersuchung zur automatischen Identifikation und Verifikation kooperativer Sprecher, dissertation, Darmstadt 1977.

[3] A. M. Noll, Short-time spectrum and 'cepstrum' techniques for vocal-pitch detection, J. Acoust. Soc. Amer. 36, 296-302, 1964.

the amount of information contained in 1 second of human speech is equal to 80 kilobits. Since many seconds of speech by many different speakers have to be stored and processed, problems of amount of storage and computer time are inevitable. Fortunately, the speech signal has high redundancy; the same characteristic features are encountered over and over again. These features can be extracted by specially developed processors, which is preferably done in real time. Instead of the speech signal it is only necessary to store these voice-specific features in the computer, to form the reference with which newly arrived speech utterances are compared in a manner similar to the procedures used in optical-pattern recognition by computers. The term 'pattern recognition' will therefore be used here.

General description of the AUROS equipment

A meaningful approach to the speaker-recognition problem is to combine real-time speech-analysis techniques with statistical pattern-recognition methods. But there is no *a priori* knowledge that indicates which combination of analysis and pattern-recognition methods will give the highest recognition rates for large populations. The AUROS equipment allows the merits of different combinations to be assessed. It consists of a general-purpose computer for pattern recognition and a set of the signal-analysis processors referred to above. These have been specially designed by us for this application; the voice features resulting from the signal analysis are stored in the computer memory. A dedicated computer for simulation is also available.

Most of the processors perform an analysis in real time on consecutive time segments of the speech signal. Each segment is described by a set of numbers representing quantities such as the output voltages of a filter bank used to measure the frequency spectrum. These numbers are considered as the components of a multidimensional vector. The probability-density distribution over the vector space, or a mean vector, is calculated from the consecutive vectors.

A second set of analysis procedures is based on linear transformations such as the fast Fourier transform, the Walsh-Hadamard transform and inverse filtering. They are used off-line to obtain pitch contours and cepstrum functions, and the frequencies and bandwidths of the higher-order speech resonances (the formants).

An explanation of the three linear transformations mentioned here is perhaps appropriate. The *fast Fourier transform* is simply a computer algorithm enabling us to carry out the complicated computations — implying several multiplications — of the Fourier coefficients in a reasonable time. The repeated computation of Fourier spectra required in some applications has only become feasible thanks to this algorithm [4].

Like the Fourier transform, the *Walsh-Hadamard transform* is used to compute a frequency spectrum. In place of the sine and cosine functions, however, it uses square-wave functions for the set of orthogonal functions required for the signal decomposition [5]. The square-wave functions only have the values +1 and —1; their use simplifies digital implementation.

Inverse filtering, finally, is based on the observation that the frequency spectrum of the human voice, characterized by the frequencies and bandwidth of the formants, derives mainly from the acoustic resonances of the vocal tract; the excitation by the glottis — which sets up a pulse train — has in itself a rather flat frequency spectrum. If we succeed in filtering the speech signals in such a way that a flat spectrum is again obtained, then the filter has a transfer function that is the inverse of the acoustic transfer function of the speaker's vocal tract. The parameters of the inverse filter are therefore characteristic of the speaker [6].

In the AUROS system the analysis data, obtained either in real time or by the more time-consuming linear transformations mentioned above, is fed to the general-purpose computer for statistical evaluation and 'classification', i.e. assignment to a known speaker. A large set of pattern-recognition methods is available.

A supervisory program allows a special analysis procedure and a pattern recognition method to be selected and combined for special experiments. The input to the system takes the form of voice signals, which can either be received from microphones in an on-line experiment or recorded on magnetic tape for off-line experiments with large data bases. The output of the system takes the form of statistical data describing voices, recognition rates, error rates and rejection rates.

The procedure followed in speaker recognition can generally be described by three phases:
— preprocessing the speech signal,
— 'training' the system, and
— testing its reliability.

Each of these three phases will now be dealt with in more detail. This provides a natural opportunity to present an outline of several speech-analysis procedures and classification algorithms.

[4] J. W. Cooley and J. W. Tukey, An algorithm for the machine calculation of complex Fourier series, Math. of Comp. **19**, 297-301, 1965.
[5] A good introduction is given by W. K. Pratt, J. Kane and H. C. Andrews, Hadamard transform image coding, Proc. IEEE **57**, 58-68, 1969.
[6] J. D. Markel, Digital inverse filtering — a new tool for formant trajectory estimation, IEEE Trans. **AU-20**, 129-137, 1972.

Preprocessing phase

As was stated earlier, the acoustic speech signal contains information concerning *what*, *who* and *how*, and the most suitable approach is therefore not to use the redundant speech signal for the recognition procedure, but to describe it by a set of features that are typical of the speaker's identity. This is what has to be done in the preprocessing phase. In speaker recognition there are three general ways of feature extraction. One way is to rely on the analysis of one short preselected time segment of the speech utterance. Another method is to measure contours such as those of pitch or energy content, during a specific utterance. The third way is to compute the mean (or the probability-density distribution) of the feature vectors characterizing successive time segments. Each of the three methods was studied by means of the AUROS system.

Short-time analysis of a preselected segment

The idea behind the procedure of analysis of a single preselected segment is that the speaker-specific information is already contained in a segment of a few tens of milliseconds of speech. So, using a segmentation algorithm, a special segment of this length, e.g. a few pitch periods of a nasal sound, is selected from the acoustical signal. The same segment is selected from the same 'code word' for all the speakers. Operations such as a Fourier transform, a Walsh-Hadamard transform or a cepstrum transform are performed on this segment. The coefficients of these transforms are the components of feature vectors used in the pattern-recognition procedure. *Fig. 3* shows four examples of an analysis of a 20-ms segment of vowel 'a'.

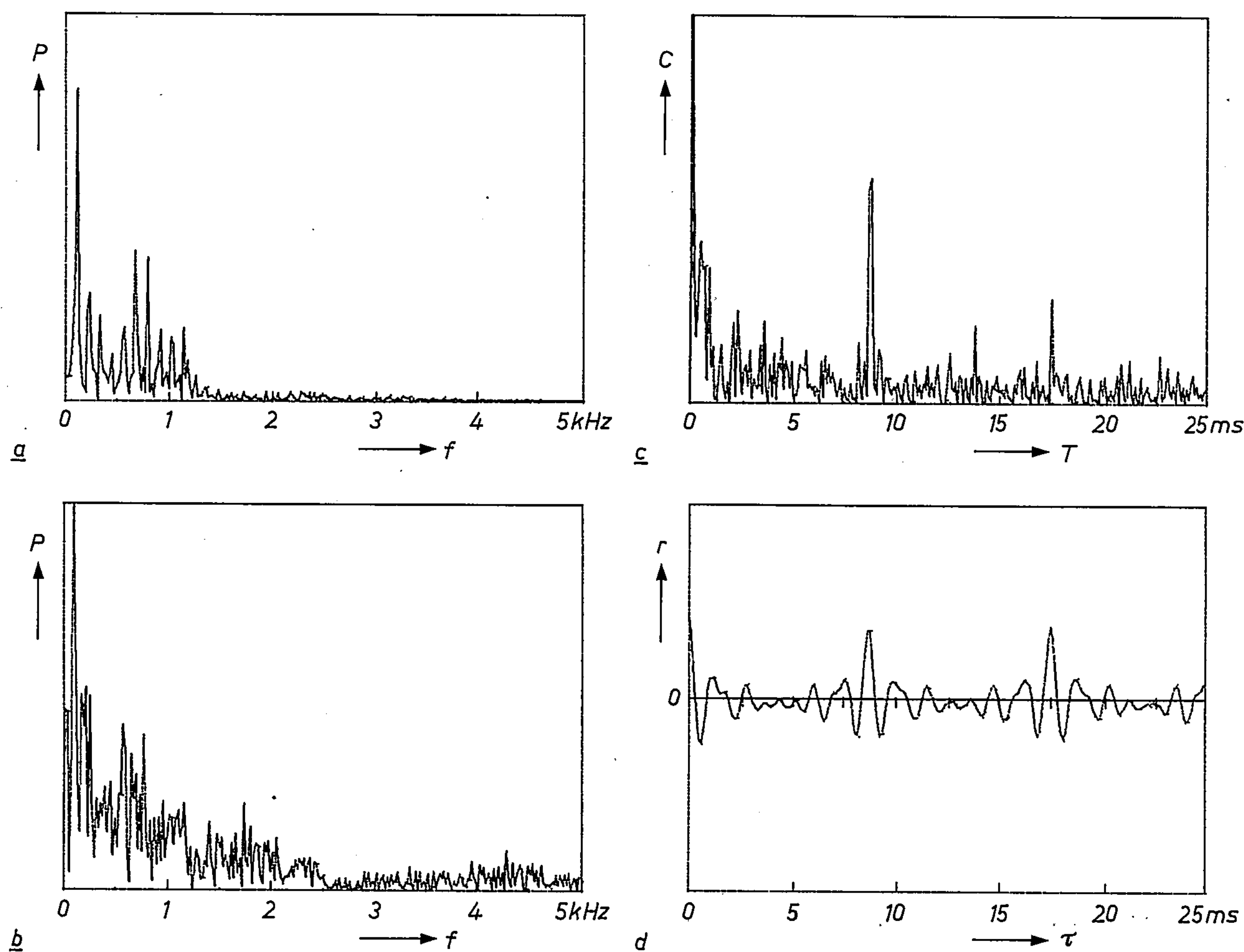

Fig. 3. Four analyses of a 20-ms segment of vowel 'a'. Even in such a short segment the speech data is characteristic of the individual speaker and can provide sufficient data for voice patterns to be recognized by a computer. *a*) Fourier power spectrum. *b*) Power spectrum derived by the Walsh-Hadamard transform. *c*) Cepstrum function. *d*) Autocorrelation function. r correlation coefficient. τ time shift.

The problem in short-term feature extraction is the accuracy of the preceding segmentation algorithm. If

the defined segment in the acoustic signal is not located exactly, the following steps are not meaningful since representations of physically different events are being compared.

Contour analysis

Contour analysis describes the temporal structure of an utterance. The acoustic signal is segmented equidistantly. For each segment only a single feature, e.g. the pitch period or the energy, is evaluated. The sequence of these segment features forms the resulting contour curve. *Fig. 4* shows as an example the pitch contour of the sentence 'My name is Nemo' which was obtained by applying cepstrum analysis and peak detection to the segments (about 100) of this speech utterance.

The results can be combined to form a feature vector of a dimensionality equal to the number of segments. The consequence of this is that if a given sentence is spoken slowly the dimensionality will be high (because many segments are produced), and if it is pronounced rapidly a low dimensionality will result. However, since the pattern-recognition algorithms assume equal dimensionality for each speaker, complicated time-normalization methods have to be applied to the contour vectors to stretch them for fast speakers and to compress them for slow speakers. These time-normalization or time-warping methods are complicated and require a great deal of computer time [7].

The use of contour analysis for feature extraction in speaker recognition entails a restriction to code-word-related recognition, as with the previous method. Text-independent recognition is not possible because the time-normalization methods are adapted to a given code word.

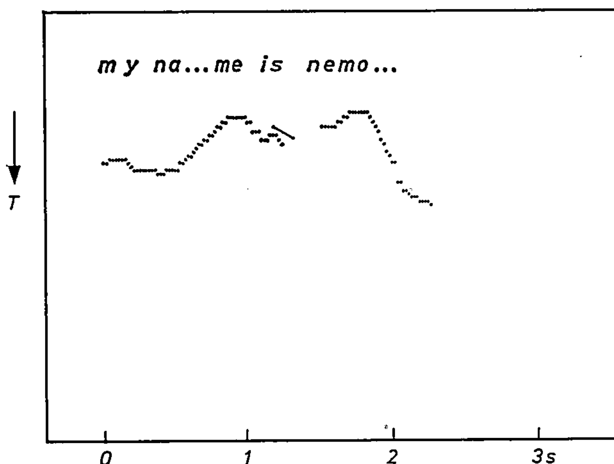

Fig. 4. Contour analysis describes the temporal structure of an utterance. Here the value of the pitch period T has been evaluated for each 20-ms segment, and the sequence of pitch values is combined to the pitch contour curve of the sentence 'My name is Nemo'. These contour curves differ from speaker to speaker and can function as specific features in a recognition procedure.

Statistical speech-signal analysis

The speech signal is divided into a sequence of 20-ms segments by equidistant segmentation. A set of coefficients is evaluated for each segment by one of the available methods of analysis; these include its linear transformations mentioned earlier and also the determination of the autocorrelation function. As mentioned earlier, a feature vector is combined from the sequence of these sets of coefficients, either by evaluating the mean-value vector or by approximating probability densities of event groups.

This kind of statistical feature extraction will give speaker recognition without the condition that all the speakers speak the same prescribed text; however, we found that the processed speech signal should last at least 10 seconds. There are no segmentation or time-normalization problems. These advantages turn out to be of considerable importance, which is why, in the course of our investigations, we have come to prefer this statistical method in our research project. As an example of this technique, *fig. 5* shows the averaged long-term Fourier spectrum, the long-term Walsh-Hadamard transform, the long-term cepstrum, and the long-term autocorrelation function. All of these have been evaluated from the same text.

Training phase

To characterize the voice of a speaker it is necessary to combine the analysis results of a few utterances (at least ten) to a typical voice reference. Because of the poor reproducibility of human speech a single utterance does not contain a sufficient amount of information. It is in the training phase that a reference 'pattern' for each voice is stored in the system.

Each feature vector generated by preprocessing the speech signal can be mapped as a pattern point in an N-dimensional feature space, where N is a quantity such as the number of Fourier coefficients. Each utterance of a speaker produces a new point in this space. The entirety of all the pattern points of the training phase forms a 'cloud' in the N-dimensional space.

Different methods can be followed to find out whether a pattern point produced by an utterance from an unknown speaker must be assumed to belong to a given speaker or not. It depends on the method which further operations the voice data will have to undergo while training the system. One method is to evaluate the distance from the point to the centre of gravity of the cloud of pattern points belonging to the known speaker. Another method establishes whether the new point lies inside the (hyper)sphere enveloping the cloud. A third method divides the N-dimensional space into subspaces and determines the probability for each

subspace that a point in it will belong to any of the given speakers. The operations performed during the training phase on the points in the N-dimensional space in the first case consist in the evaluation of the centre of gravity of the cloud of points, in the second case in the construction of the (hyper)sphere, in the last case in the determination of the probabilities for the individual subspaces.

Minimum-distance classificator

The centre of gravity of the cloud of pattern points is evaluated independently for each speaker and stored as reference vector. An unknown pattern point is classified by evaluating the distances from this point to the centres of gravity of each cloud. This point is then associated with the cloud whose centre of gravity is the nearest.

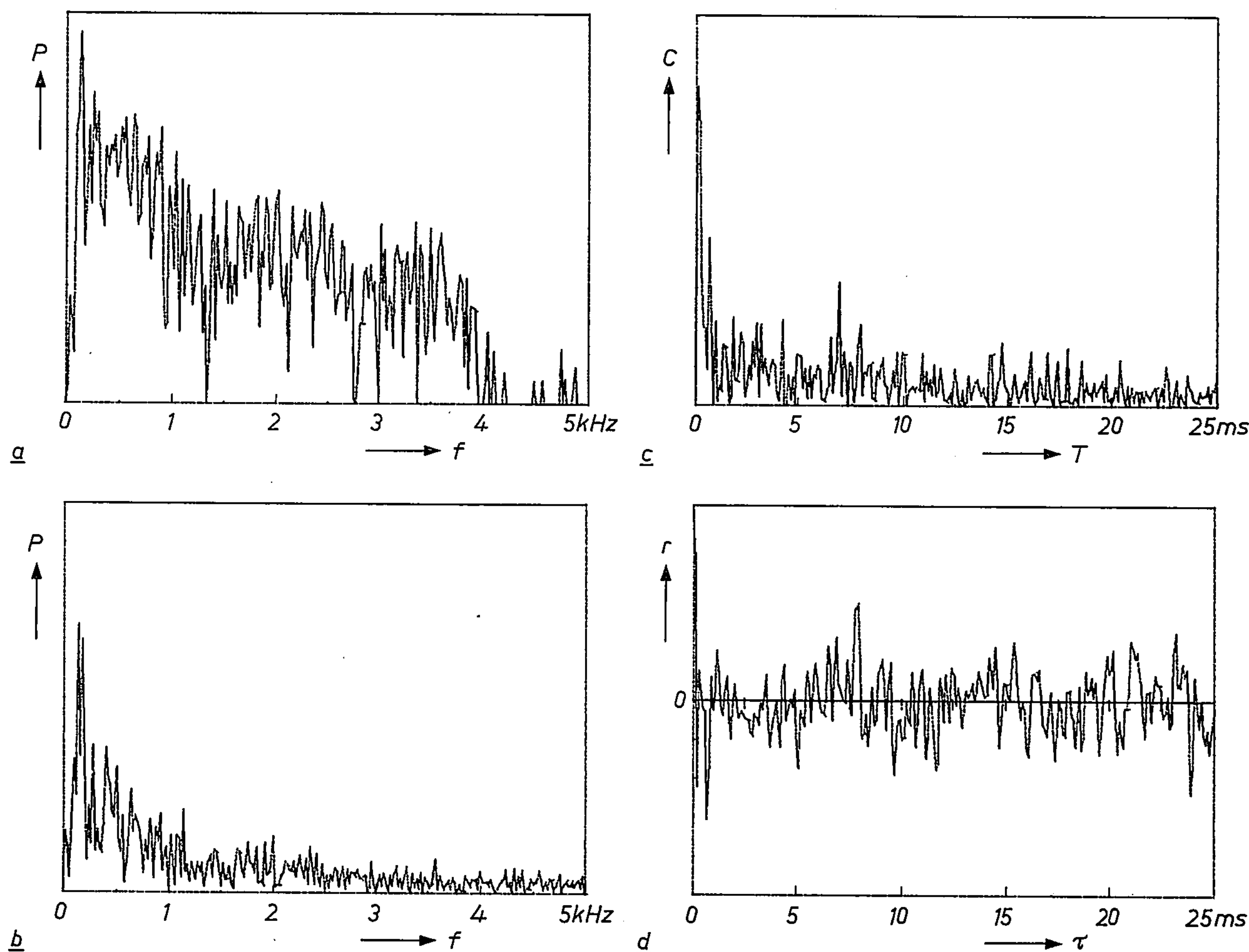

Fig. 5. Long-term averages over an utterance about 10 s long of Fourier spectrum (*a*), Walsh-Hadamard spectrum (*b*), cepstrum function (*c*), and autocorrelation function (*d*). The statistical feature-extraction method avoids the problems of segmentation and time normalization and permits text-independent speaker recognition.

We have used the three methods outlined here in speaker-recognition experiments. There were many modifications for measurements of distance, data normalization and probability-density approximation. These methods will now be described in some more detail. The assignment of a point to a given speaker is called 'classification', which is related to the term 'class' used for the array of pattern points of a speaker; the algorithm performing the assignment is called a 'classificator'.

The distance measure used for defining the proximity of points may be the usual Euclidean distance. The distance measure may also be based on the correlation between the two corresponding feature vectors. The correlation is at a maximum when the two vectors coincide; the distance may be defined as the amount by which the correlation falls short of this maximum.

[7] G. R. Doddington, A computer method of speaker verification, dissertation, Madison 1970.

Let the feature vectors be X and Y with components $(x_1, x_2, \ldots, x_N)$ and $(y_1, y_2, \ldots, y_N)$. The Euclidean distance is

$$d_E(X,Y) = \sqrt{\sum_{i=1}^{N} (x_i - y_i)^2}. \tag{1}$$

The correlation between the two vectors is expressed by the correlation coefficient, whose maximum value is 1. By subtracting the true correlation coefficient from 1 we obtain the distance measure

$$d_c(X,Y) = 1 - \frac{\sum_{i=1}^{N} x_i y_i}{\sqrt{\sum_{i=1}^{N} x_i^2 \sum_{i=1}^{N} y_i^2}}. \tag{2}$$

Both distance measures can be altered by weighting each dimension by the inverse of its variance between different utterances of the same speaker, to base the decision mainly on the parameters of the feature vector with the highest reliability.

Distribution-free tolerance-region classificator

The region occupied in multidimensional space by a cloud of pattern points can also be taken as its prime characteristic, regardless of the distribution of the points over this region. This region may be demarcated by evaluating an enveloping hypersphere of the cloud of pattern points in a manner that avoids intersections between different classes. The mathematical equation of this hypersphere defines the tolerance region inside which a point must fall to be classified with the corresponding speaker, and thus represents his voice characteristics. To classify an unknown pattern point a check is made for each class to see whether the point lies within its hypersphere or not. If the point cannot be found in any tolerance region, it will be rejected.

Minimum-risk classificator

With the minimum-risk classificator, the N-dimensional pattern space is subdivided into subspaces of equal volume. For each subspace a conditional probability is approximated by counting the number of pattern points in this volume independently for each speaker. This conditional probability indicates the likelihood that a pattern point, given that it belongs to a certain speaker, will lie in that subspace. For classification of a pattern point a check is made to find out which subspace it lies in, and the values of the corresponding conditional probabilities for this subspace are compared. The unknown point is then classified with the speaker having the highest conditional probability. In this way the risk of loss due to a wrong classification is minimized. *Fig. 6* shows the principle for the one-dimensional case.

Reliability-test phase

During the reliability-test phase, utterances that have not been used for training are offered to the system for classification. In a speaker-identification test the utterance belonging to one of the speakers entered into the system may be either correctly classified, or wrongly classified, or rejected as unclassifiable. The wrong classifications and rejections together determine the typical error rate for the system performance. Wrong classifications cause speaker confusion; by counting the number of confusions the probability of confusion of each pair of speakers can be represented in a 'confusion matrix'.

In speaker verification the system only has to decide between the alternatives of acceptance or rejection. An error may be either the false rejection of a customer or the false acceptance of an impostor. *Fig. 7* shows a simplified speaker-verification experiment with real data. Speaker X spoke a test sentence 15 times. A long-term spectrum was evaluated for each utterance. Fig. 7*a* shows a plot of these 15 spectra. The non-reproducibility is clearly seen. In a 'model' training phase, a tolerance region was constructed in form of a mask by connecting all the minimum and maximum values (fig. 7*b*); no consideration was given to the distribution of the values between the maximum and minimum. For verification, the speaker X repeated the same text, and the result of the analysis was compared with the reference. It was accepted, as this long-term spectrum was within the tolerance region (fig. 7*c*). When speakers Y and Z claimed to be speaker X, they were rejected, because their curves did not fit the tolerance-region template (fig. 7*d*).

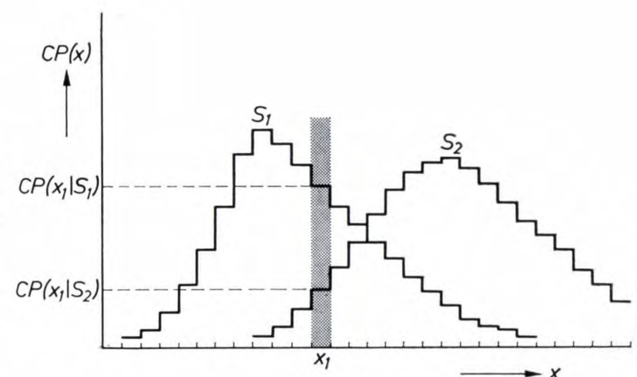

Fig. 6. Principle of the minimum-risk classificator shown for a one-dimensional case. One-dimensional space (the abscissa x) is subdivided into equal lengths for each of which the number of points belonging to the different classes is counted (two classes S_1 and S_2 are shown). From these numbers it is possible to calculate the conditional probability $CP(x)$ that a point, given its class membership, will lie in the subspace with abscissa x. An unknown point in subspace x will be assigned to the class with the highest conditional probability $CP(x)$ in that subspace. In the figure for abscissa x_1 this is class S_1. The risk of a wrong classification is then at a minimum.

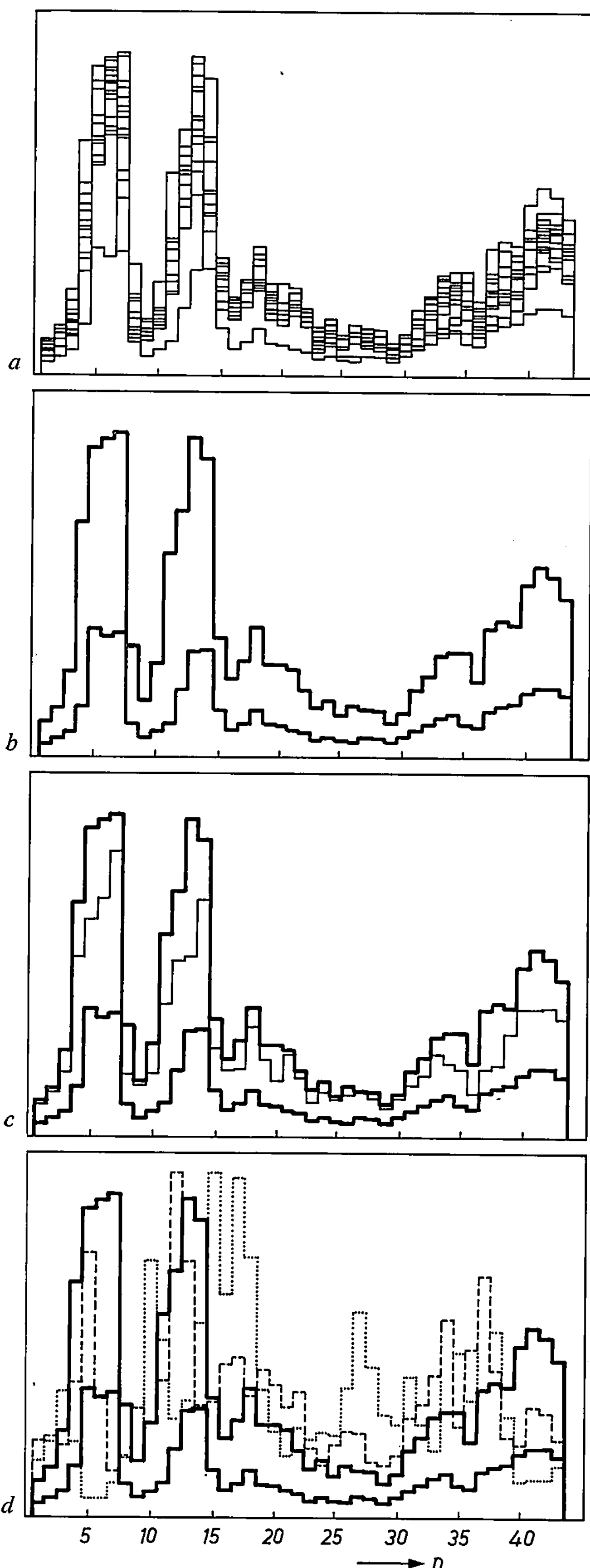

Fig. 7. Example of a speaker-verification experiment with real data. *a*) Speaker X speaks a sentence fifteen times. The long-term spectrum is evaluated each time. *n* number of frequency channel. *b*) From the fifteen long-term spectra a speaker-specific template is constructed by connecting all the minimum and maximum values. *c*) A new long-term spectrum from speaker X fits the template, and he is accepted. *d*) Long-term spectra from speakers Y and Z do not fit the template. These speakers are rejected.

Test results obtained with the AUROS system

A number of classification procedures have been tested using the AUROS system, each of them employing several kinds of voice features, some of which have been mentioned above. In experimenting with different kinds of voice features the advantages of long-term spectra — the absence of segmentation and time normalization — turned out to be very important, as was the possibility of text-independent voice-feature extraction. We therefore found it preferable to use the long-term spectra for our most important tests; the results of these tests will now be reported.

In the AUROS system the long-term spectra are derived in real time, and this is very important for any practical application. Spectral analysis is performed by a 43-channel filter bank covering the frequency band from 100 Hz to 6 kHz; each filter has a bandwidth of nearly 10 per cent of the centre frequency. Equidistant segmentation is carried out by scanning the filter outputs every 20 ms. The short-term spectra are averaged by a special digital multiplex integrator, which also performs a rough energy normalization. For a comparative study 5000 utterances of 82 male and 18 female subjects have been processed. *Fig. 8* shows long-term spectra of a 12-s utterance of two men (*a*) and two women (*b*). The absence of energy in the first three channels for the women indicates the higher pitch of their voices.

It turns out that for a given data base the variations in the recognition rate with the chosen pattern-recognition algorithm are considerable. Each algorithm only operates in the optimum fashion when a set of *a priori* assumptions is satisfied, e.g. concerning the kind of distribution of the features or the correlation and covariance of the data of each individual speaker (which may be expressed by a correlation and a covariance matrix). For that reason, investigation of the statistics of the data base is necessary to adapt the pattern-recognition algorithm to the data structure.

From the correlation matrix of the 43 frequency parameters averaged over 2500 long-term spectra (see *fig. 9*) it can be seen that the 43 parameters of the feature vector are not statistically independent but correlated. The average correlation coefficient is 0.4. This correlation has to be taken into account when designing an appropriate pattern-recognition algorithm.

For optimum performance of most of the pattern recognition algorithms it is assumed that the components of the feature vectors are not cross-correlated. It can be shown from vector analysis that this, if it is

indeed possible, is only the case in one particular position of the system of basic vectors of the vector space. The basic vectors are brought into this position by rotations in accordance with data provided by the covariance matrix mentioned above. In this way decorrelated, 'whitened' feature vectors are obtained. Applying the minimum-distance classificator with Euclidean distance to the whitened data corresponds to 'Mahalanobis classification' [8]; in our tests this yielded error-free identification for all the speakers tested. minimum-risk classificator (with histogram approximation) were considerably faster and required far less storage capacity, while the recognition rates did not drop below 98.5%.

Speaker identification

For the recognition experiments the 5000 processed utterances have been divided into two data bases of 2500 utterances each. This allowed code-word-related recognition and text-independent recognition to be in-

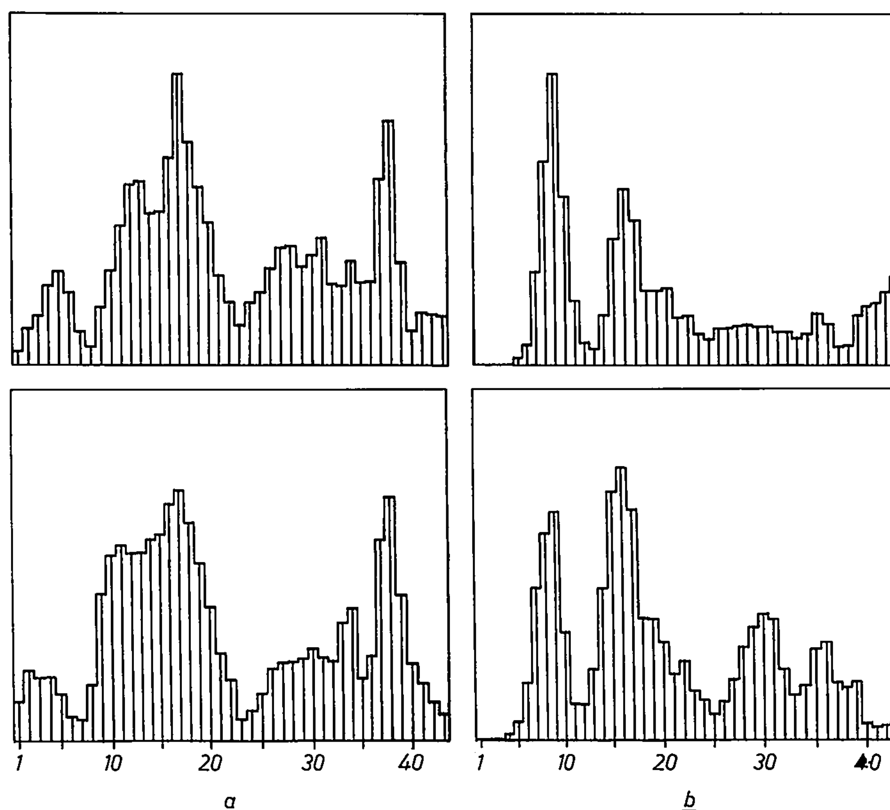

Fig. 8. Long-term-averaged frequency spectra of two male voices (*a*) and two female voices (*b*). The spectra, which cover frequencies between 100 Hz and 6000 Hz, are obtained by scanning a 43-channel filter bank 50 times a second and adding the output voltages for every separate filter in a multiplex digital integrator. Because of their higher pitch the female voices do not give energy in the lowest three frequency channels.

Whenever recognition rates are being compared, it is necessary to consider all the assumptions and boundary conditions. In speaker-identification tests the Mahalanobis classificator achieved recognition rates of 100% for 2500 utterances of 50 speakers; the utterances were the same apart from the name of the speaker given in each utterance. However, the Mahalanobis classificator is a rather 'expensive' algorithm in storage capacity and computer time. 'Economical' classificators like the minimum-distance classificator or

vestigated separately. The speaker-identification tests were performed with 'economical' pattern recognition algorithms. All the speakers tested were known to the system and the system was made to classify any utterance presented; rejection as 'unclassifiable' was not allowed. Recognition rates of 99.5% were achieved for both data bases, code-word related as well as text-independent. For training the classificators 10 to 20 utterances seem to be necessary to obtain this high recognition accuracy.

Speaker verification

While in speaker identification only one rate — that for correct classification — has to be considered, a speaker-verification experiment is characterized by two error rates; the rate for false acceptation (mix-up) and the rate for false rejection. There is a functional relation between these two error rates, given by the decision threshold. During the training phase of speaker verification, in addition to the reference pattern, this threshold is evaluated. If a pattern with a claimed class membership has to be verified, it is compared with the reference of that class using the classificator-typical similarity measure. If the similarity exceeds a given threshold the claimed class membership is confirmed and the speaker is accepted; otherwise the speaker will be rejected.

The relation between the threshold value and the error rates for false acceptance and false rejection is easily seen: if the threshold value is too low, many speakers will be falsely rejected because of the variability of their utterances. On the other hand, if the threshold value is too high, speakers with similar voices will be falsely accepted and thus be mixed up with the real speakers. So the value of the threshold is a trade-off between security of the system (low false-accept rate) and customer convenience (low false-reject rate). The interdependence of these three variables is shown in *fig. 10* for a minimum-distance classificator.

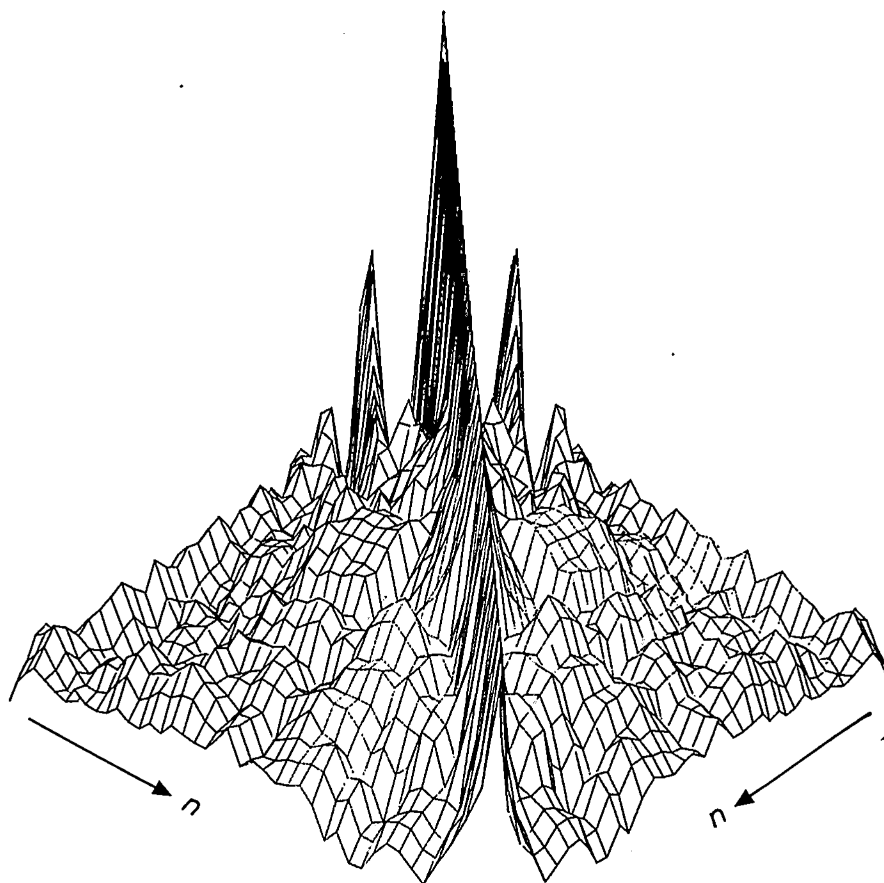

Fig. 9. Cross-correlation between the frequency channel outputs of the filter bank is expressed by vertical deviation in the figure; n is the channel number. The figure is the average for 2500 long-term spectra. The highest correlation is between adjacent channels.

Various methods for decision-threshold evaluation by the computer have been compared. The most effective method is to evaluate the mean of the distance measure determined by the absence of correlation (see above, p. 213). First, the mean is taken within each class, for the distance between each pair of points, and then the results are averaged over all the classes.

[8] K. Fukunaga, Introduction to statistical pattern recognition, Academic Press, New York 1972.

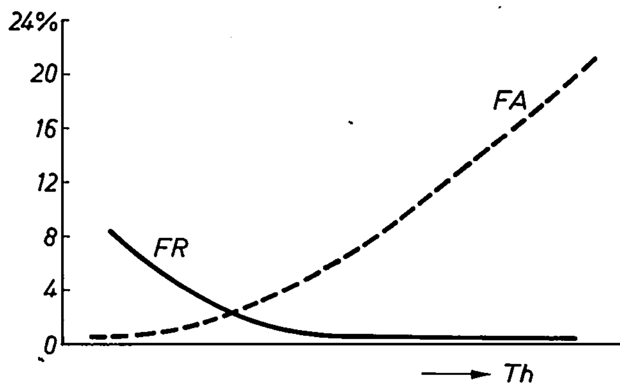

Fig. 10. The dependence of false-accept rate (curve *FA*) and false-reject rate (curve *FR*) on threshold level *Th* in a speaker-verification system. A higher threshold value *Th* means that a greater distance is permitted between the pattern point of the speaker claiming to be speaker X and the centre of gravity of speaker X's cloud of pattern points.

The distance measure referred to here is d_c, expressed by eq. (2). The threshold value obtained by averaging d_c is

$$Th_{NN} = \frac{R}{S}\sum_{k=1}^{S}\frac{1}{M-1}\sum_{j=1}^{M-1}\frac{1}{M}\sum_{l=j+1}^{M}\left(1-\frac{\sum_{i=1}^{N} x_{ijk}\,x_{ilk}}{\sqrt{\sum_{i=1}^{N} x_{ijk}^2 \sum_{i=1}^{N} x_{ilk}^2}}\right), \quad (3)$$

where S is the number of speaker classes and M the number of utterances per class. R is a scaling factor allowing the threshold value to be shifted along the horizontal axis in fig. 10 to obtain the desired false accept/false reject ratio. Generally $R = 1$; in particular cases, however, R is adjusted by hand to another value.

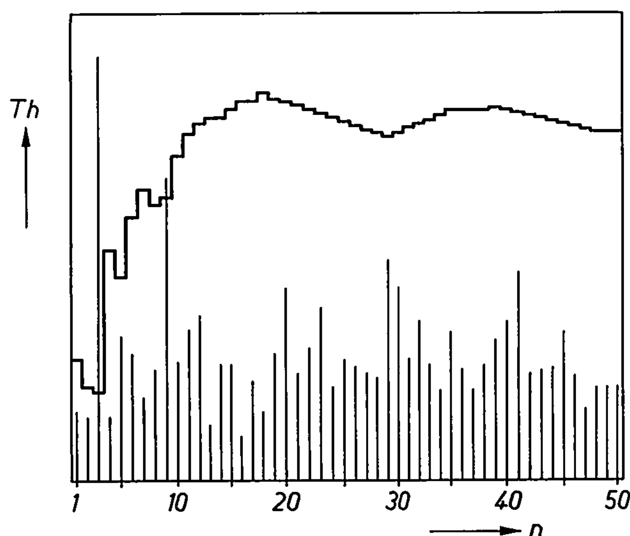

Fig. 11. During the training phase with a growing number n of samples offered to the speaker-verification system the similarity-threshold level *Th* gradually approaches a steady value that is high enough to make false rejections extremely unlikely. Some 20 samples appear to be required to reach a steady level.

It is important to know how many speech samples have to be used for training to establish a suitable threshold value. *Fig. 11* shows the threshold value as a function of the sample size of the training phase. The threshold was initially evaluated using two samples and the third sample of the same class was verified. Then this third sample was included for training, a new threshold was evaluated and the fourth sample was verified, and so on up to 49 samples for training. The threshold value is drawn as a stepped curve, while the actual distance for verification is plotted as a bar. As long as the bar is below the threshold, the sample is correctly accepted, otherwise it is falsely rejected as in the case of the third bar. By adding this sample to the training phase the threshold, which was obviously too small, is increased, and the following samples are classified correctly. After another correction by the ninth bar, the threshold adapts almost asymptotically to a value at which no false rejects occur. For this picture the false accepance rate was 0%.

In general, the verification experiments showed that 10 to 20 samples for the training phase seem to be necessary to obtain reliable results.

Applying the verification system to the two voice-data bases of 2500 samples yielded error rates of about 1% for false accept and false reject in both cases, code-word related as well as text-independent.

The effects of transmission by telephone line

For commercial application of a speaker-recognition system it is important to know how telephone transmission of the speech signal affects the security.

Transmitting speech over a telephone channel means freqency-band limitation from 300 Hz to 3500 Hz. The transfer characteristic in this frequency range is not flat but changes its shape depending on the line selected by dialling. The spectra available from telephone lines are therefore band-limited and also multiplied by a transfer function of unknown shape. As a first step it could be shown that band-limiting the long-term spectra to telephone quality did not affect the recognition rate significantly. However, weighting the spectra by arbitrary transfer functions made recognition based on long-term-averaged spectra unreliable because in some cases the effect of the transfer function on the spectra outweighed the voice characteristics. To overcome this difficulty a novel feature set has been introduced to eliminate the effect of the unknown transfer functions. These features, which we call the modified standard-deviation profiles (MSP), are a function of the voice characteristics only and are not affected by the channel transfer function.

The j-th component S_{bj} of this novel feature vector is expressed by

$$S_{bj} = \frac{\sum_{i=1}^{I}\left| a_j x_{ij} - \frac{1}{I}\sum_{i=1}^{I} a_j x_{ij}\right|}{\frac{1}{I}\sum_{i=1}^{I} a_j x_{ij}}. \quad (4)$$

In the numerator a modified standard deviation of the j-th spectral component of the i-th short-term spectrum is evaluated,

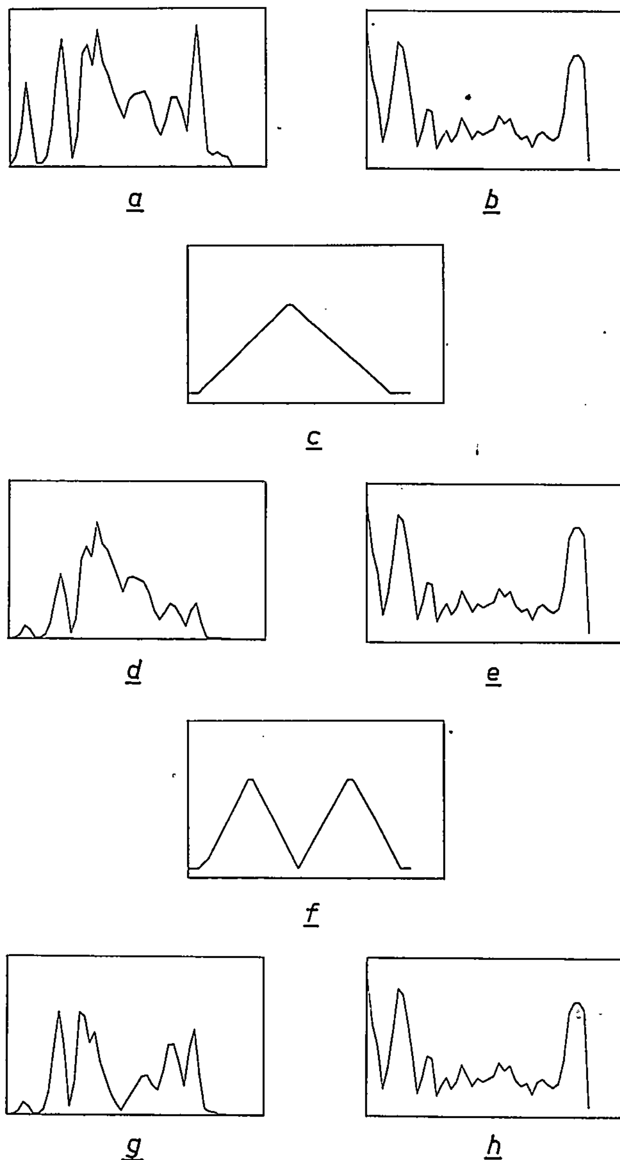

Fig. 12. The effect of a hypothetical, erratic telephone-line transfer function (*c* or *f*) on a long-term spectrum (*a*) is shown by (*d*) and (*g*) respectively, the effect on the modified standard-deviation profile (*b*) is shown to be non-existent (*e*, *h*). First recognition experiments using the modified standard-deviation profile as a feature vector yield promising results.

where I is the number of spectra taken. A large value of the numerator points to a high short-term variability of the speech signal. The numerator still contains the frequency-weighting factor a_j of the unknown transfer function. The average in the denominator, on the other hand, describes the long-term properties of the voice on which the unknown line characteristic is superimposed. Since the unknown weighting factor a_j occurs in both numerator and denominator it vanishes and in this way the effect of the unknown transfer function is eliminated. *Fig. 12* shows a long-term spectrum (*a*) and an MSP vector (*b*). Simulating a telephone line by a characteristic like that in fig. 12*c* or *f* changes the long-term spectrum to the curve in fig. 12*d* or *g* respectively, while the MSP vector remains unchanged (*e*, *h*). First recognition experiments with these MSP vectors and related functions yield promising results.

The work described was sponsored by the German Federal Ministry for Research and Technology under contract No. 0812014 Kap. No. 3004 Titel 68301. Responsibility for the contents of this publication rests with the author.

Summary. AUROS, an experimental system for speaker recognition by computer, has been developed at Philips Forschungslaboratorium Hamburg, in West Germany, in a government-sponsored research project. The system comprises several speech-signal processors which extract different characteristic features from the signal in real time, and can also use procedures such as the fast Fourier transform, the Walsh-Hadamard transform, and computation of the autocorrelation and cepstrum functions. A general-purpose computer is programmed to compare the features with the stored data from a group of known speakers; 5000 utterances from 100 speakers are stored in a data base. Several different measures of similarity are being tried. Some of these are more economical than others in computer time and storage capacity, but yield slightly higher error rates. In speaker-identification experiments using economical classificators recognition rates of 99.5 % have been obtained. Experiments where a speaker's claimed identity is verified yield error rates of about 1 % for false acceptance and false rejection.

Recent scientific publications

These publications are contributed by staff of laboratories and plants which form part of or cooperate with enterprises of the Philips group of companies, particularly by staff of the following research laboratories:

Philips Research Laboratories, Eindhoven, The Netherlands *E*
Philips Research Laboratories, Redhill, Surrey, England *M*
Laboratoires d'Electronique et de Physique Appliquée, 3 avenue Descartes, 94450 Limeil-Brévannes, France *L*
Philips GmbH Forschungslaboratorium Aachen, Weißhausstraße, 51 Aachen, Germany *A*
Philips GmbH Forschungslaboratorium Hamburg, Vogt-Kölln-Straße 30, 2000 Hamburg 54, Germany *H*
MBLE Laboratoire de Recherches, 2 avenue Van Becelaere, 1170 Brussels (Boitsfort), Belgium *B*
Philips Laboratories, 345 Scarborough Road, Briarcliff Manor, N.Y. 10510, U.S.A. (by contract with the North American Philips Corp.) *N*

Reprints of most of these publications will be available in the near future. Requests for reprints should be addressed to the respective laboratories (see the code letter) or to Philips Research Laboratories, Eindhoven, The Netherlands.

W. J. Bartels, L. Blok & C. W. Th. Bulle: X-ray topography and diode efficiency of vapour grown $GaAs_{1-x}P_x$ layers.
J. Crystal Growth **34**, 181-188, 1976 (No. 2). *E*

V. Belevitch: Theory of the proximity effect in multiwire cables, Part II.
Philips Res. Repts. **32**, 96-117, 1977 (No. 2). *B*

C. Belin: On the growth of large single crystals of calcite by travelling solvent zone melting.
J. Crystal Growth **34**, 341-344, 1976 (No. 2). *L*

C. H. J. van den Brekel (I, II) & J. Bloem (II): Characterization of chemical vapour-deposition processes, Parts I and II.
Philips Res. Repts. **32**, 118-133, 134-146, 1977 (No. 2). *E*

A. M. van Diepen: The B-site Mössbauer linewidth in Fe_3O_4.
Physics Letters **57A**, 354-356, 1976 (No. 4). *E*

C. T. Foxon, B. A. Joyce & S. Holloway (University of Leicester): Instrument response function of a quadrupole mass spectrometer used in time-of-flight measurements.
Int. J. Mass Spectrom. Ion Phys. **21**, 241-255, 1976 (No. 3/4). *M*

M. Gleria & R. Memming: Novel luminescence generation by electron transfer from semiconductor electrodes to ruthenium-bipyridil complexes.
Z. phys. Chemie neue Folge **101**, 171-179, 1976 (No. 1-6). *H*

H. Hieber: Aging properties of gold layers with different adhesion layers.
Thin Solid Films **37**, 335-343, 1976 (No. 3). *H*

A. Humbert, L. Hollan & D. Bois (I.N.S.A. Lyon, Villeurbanne): Influence of the growth conditions on the incorporation of deep levels in VPE GaAs.
J. appl. Phys. **47**, 4137-4144, 1976 (No. 9). *L*

A. J. R. de Kock: Characterization and elimination of defects in silicon.
Festkörperprobleme **16**, 179-193, 1976. *E*

W. Lems, H. Kinkartz & W. Lechner: Incandescent lamp filaments: facet-cooling, failure mechanisms.
Philips Res. Repts. **32**, 82-95, 1977 (No. 2). *A*

A. Milch: Etch polishing of GaP single crystals by aqueous solutions of chlorine and iodine.
J. Electrochem. Soc. **123**, 1256-1258, 1976 (No. 8). *N*

C. Mulder & H. E. J. Wulms: High speed integrated injection logic (I^2L).
IEEE J. **SC-11**, 379-385, 1976 (No. 3). *E*

J. M. S. Schofield: The physics of gas discharge cells within d.c. memory display panels.
4th Int. Conf. on Gas discharges, Swansea 1976 (IEE Conf. Publn No. 143), pp. 397-400. *M*

A. L. N. Stevels: On the luminescence of CsI:Mn and CsBr:Mn.
Philips Res. Repts. **32**, 77-81, 1977 (No. 2). *E*

A. L. N. Stevels & A. D. M. Schrama-de Pauw: Eu^{2+} luminescence in hexagonal aluminates containing large divalent or trivalent cations.
J. Electrochem. Soc. **123**, 691-697, 1976 (No. 5). *E*

R. P. Tijburg & T. van Dongen: Selective etching of III-V compounds with redox systems.
J. Electrochem. Soc. **123**, 687-691, 1976 (No. 5). *E*

Recent United States Patents

Abstracts from patents that describe inventions from the following research laboratories that form part or cooperate with the Philips group of companies:

Philips Research Laboratories, Eindhoven, The Netherlands	*E*
Philips Research Laboratories, Redhill, Surrey, England	*R*
Laboratoires d'Electronique et de Physique Appliquée, 3 avenue Descartes, 94450 Limeil-Brévannes, France	*L*
Philips GmbH Forschungslaboratorium Aachen, Weißhausstraße, 51 Aachen, Germany	*A*
Philips GmbH Forschungslaboratorium Hamburg, Vogt-Kölln-Straße 30, 2000 Hamburg 54, Germany	*H*
MBLE Laboratoire de Recherches, 2 avenue Van Becelaere, 1170 Brussels (Boitsfort), Belgium	*B*
Philips Laboratories, N.A.P.C., 345 Scarborough Road, Briarcliff Manor, N.Y. 10510, U.S.A.	*N*

4 052 340

Method for reproducing a voltage dependent resistor and a voltage dependent resistor obtained therewith

R. K. Eijnthoven *E*
J. T. C. van Kemenade

Voltage dependent resistor obtained by sintering a body of a mixture of ZnO and other metal oxides in an atmosphere which contains bismuth.

---

4 052 605

Interpolating non-recursive digital filter

L. D. J. Eggermont *E*

An interpolating non-recursive digital filter for generating output signal samples which occur at a given output sampling frequency and which are related in a predetermined way to a sequence of input signal samples has an output sampling frequency which is an integer multiple of the frequency of the input signal samples. In order to make more efficient use of the storage capacity of a storage device in the filter, multiplying coefficients representative of the difference between two samples of the impulse response which belong to different sets but to the same sampling period are used.

---

4 052 633

Restorable cold cathode in a gas discharge electron gun

T. M. B. Schoenmakers *E*

Restorable cold cathode in a gas discharge electron ion gun in which the eroded material in the active surface of the cathode is restored by supplying new material in the form of a wire which is moved through a hole in the cathode body by means of a screw spindle.

---

4 052 681

Gas-discharge laser

K. Bulthuis *E*
B. J. Derksema
H. T. Dijkstra
J. van der Wal

A gas-discharge laser having a Brewster window near at least one of the reflectors which is secured directly to the laser tube. The Brewster window is secured to a surface of the laser tube and a normal to the window makes an angle equal to the Brewster angle with the axis of the laser tube. The surface may be a slot in the laser tube or a recessed end face of the laser tube near a reflector. An advantage is that the Brewster window may have any convenient diameter and that the laser tube need not be drilled to form a cavity.

---

4 052 683

Microwave device

J. H. C. van Heuven *E*
F. C. de Ronde

A microstrip waveguide transition where the substrate is arranged in a symmetry plane of waveguide and is situated parallel to the field lines of the electrical field and the longitudinal axis of the waveguide. The asymmetric microstrip conductor structure is coupled, via a symmetrical-asymmetrical transformer, to symmetric band line provided on the substrate. To be conductive for RF energy, the individual conductors of the band line are connected to opposite walls of the waveguide via broadening conductors.

---

4 052 707

Magnetic device having domains of two different sizes in a single layer

W. F. Druyvesteyn *E*
H. M. W. Booij

A magnetic device comprising at least one thin layer of a magnetizable material having a preferred direction of magnetization which is approximately perpendicular to the surface of the layer in which magnetic domains are generated, maintained and possibly annihilated in the layer. A domain guiding structure which with a given magnetic field substantially in the preferred direction enables the occurrence of two types of magnetic domains. The area of the largest domain is at least 15% and at most 125% larger than that of the other domains. The device also has means which convert one type of domain into the other type of domain.

---

4 052 747

Device for the magnetic domain storage of data having a shift register filled with coded series of domains

J. Roos *E*

A magnetic bubble domain device for recording information on a magnetizable recording medium including a shift register filled with a series of bubble domains coded in accordance with the information to be recorded, the whole bubble domain pattern being printed, in combination with a magnetic transfer field, in one time on a recording medium, new information replacing the old information by shifting of the bubble domains in the register.

4 052 748

Magnetoresistive magnetic head

K. E. Kuijk *E*

A magnetic head for detecting information-representing magnetic fields on a magnetic recording medium and comprising an elongate magneto-resistive element of a magnetically anisotropic material which at its ends has contacts for connection to a current or voltage source. In order to linearize the playback characteristic of the element, the easy axis of magnetization coincides with the longitudinal direction of the element and means are present which force the current to travel at an angle of minimum 15° and maximum 75° with the longitudinal direction. These means consist in particular of equipotential strips provided on the element.

---

4 052 853

Hot-gas reciprocating machine comprising two or more working spaces, provided with a control device for the supply of working medium to the said working spaces

J. H. Abrahams *E*

A hot-gas reciprocating machine involving a plurality of cycles having a mutually different phase, during each crank shaft revolution working medium from a source of pressurized working medium being successively supplied to each cycle separately, via a control device, comprising one or more slides which are controlled exclusively by the variable cycle pressures.

---

4 053 207

Electro-optic devices

E. T. Keve *R*
K. L. Bye

An electro-optic device having a platelet of PLZT material, the birefringence of which depends on an electric field. The thickness of the platelet preferably is smaller than the thickness of one grain. As a result of this the sensitivity is large and this permits a low operating voltage in the device.

---

4 053 796

Rectifying circuit

R. J. van de Plassche *E*

A rectifying circuit for balanced input currents, of which the two components are applied to a first and a second point of a selective current mirror circuit respectively, either the first point constituting the input and the second point the output, or the first point constituting the output and the second point the input of the selective current mirror circuit, depending on and under control of the polarity of the difference between the two components. As a result, the selective current mirror circuit follows either the greater or the smaller of the two components of the balanced input current. The first and the second point are each connected to the output terminal of the rectifying circuit via a current circuit. These current circuits each have a reverse direction and each comprise the main current path of a transistor for transferring the difference between the output current of the selective current mirror circuit and the component of the balanced input current which is applied to the relevant output to the output terminal in a voltage decoupling manner.

---

4 053 806

Pyroelectric detector comprising nucleating material wettable by aqueous solution of pyroelectric material

A. A. Turnbull *R*
H. Sewell

A pyroelectric detector employing a substrate supporting a thin, i.e., 0.5 to 5 μm thick, solid layer of pyroelectric material with an intermediate layer of nucleating material, i.e., a material which is wettable by a solution of the pyroelectric material so that an adherent continuous layer is formed thereon. The pyroelectric layer may be in the form of a mosaic of islands separated by an electrically conductive material covered with an electrically insulating material.

---

4 053 887

Doppler radar system

K. Holford *R*

A Doppler radar system for controlling portable traffic signals in response to on-coming traffic. Each of two channel amplifiers of the system is fixed at high gain and passes both noise signals and Doppler signals to a phase detector. A threshold element provides a control signal when the average level of the phase detector output between high and low levels changes sufficiently, due to the presence of Doppler signals, from a mean level which is due to noise alone.

---

4 055 961

Device for liquefying gases

P. S. Admiraal *E*

A liquefactor includes a refrigeration stage for cooling a compressed gaseous body, and a first duct containing a first Joule-Thompson valve for connecting the refrigeration stage to a collecting container for use when the gaseous body comprises a single gas. A second duct parallelly connects the refrigeration stage to the collecting container and contains a second Joule-Thompson valve for use when the gaseous body comprises a mixture of two gases to be separated.

---

4 056 810

Integrated injection logic memory circuit

C. M. Hart *E*
A. Slob

A new integrated circuit in which bias currents are supplied by means of a current injector, a multi-layer structure in which current is supplied, by means of injection and collection of charge carriers via rectifying junctions, to zones to be biased of circuit elements of the circuit, preferably in the form of charge carriers which are collected by the zones to be biased themselves from one of the layers of the current injector. By means of said current injector circuit arrangements can be realized without load resistors being necessary, while the wiring pattern may be very simple and the packing density of the circuit elements may be very high. In addition a simple method of manufacturing with comparatively few operations can in many cases be used in particular upon application of transistors having a structure which is inverted relative to the conventional structure.

---

4 055 953

Hot-gas reciprocating engine

A. M. Nederlof *E*

A hot-gas reciprocating engine in which the tubular connection members interconnect a heater duct inside the heat pipe with the engine's expansion space and regenerator, each connection member extends transverse of the center line of the relevant unit, and is connected to the heat pipe wall with a flexible sealing member.

---

4 056 832

Servo system for controlling the position of a reading head

J. de Boer *E*
A. Walraven

A servo system for controlling the position of a magnetic reading head relative to the center of a selected information track. During recording a long-wave positioning signal is recorded below the

data signal in the tracks. Upon reading out, the head not only reads the information of the selected track but, as result of cross-talk, also the positioning signals of the adjacent tracks. After filtering out and processing the positioning signals, a control signal for controlling the head is obtained.

---

4 057 063

Device for sterilization by transuterine tube coagulation

A. C. M. Gieles *E*
G. H. J. Somers

A device for sterilizing human females by transuterine fallopian tube coagulation wherein the substantial increase in impedance of the tissues during coagulation is used to signal for termination of treatment.

---

4 057 725

Device for measuring local radiation absorption in a body

W. Wagner *H*

A device for measuring the spatial distribution of radiation absorption in a body wherein a multiplicity of radiators are regularly distributed about a circle surrounding the body, each radiator emitting a wedge-shaped beam of radiation in the plane of the circle toward a different arc portion of the circle between two other radiators, a multiplicity of adjoining detectors in each arc portion measuring radiation from the radiator emitting radiation to that arc portion, the spatial distribution of radiation absorption being calculated from the measured radiation values of all the detectors.

---

4 057 728

X-ray exposure device comprising a gas-filled chamber

K. Peschmann *A*
H.-G. Junginger

An x-ray exposure device comprising a flat and plane rectangular chamber containing an ionizable gas and having walls provided with electrode structures which generate a potential distribution corresponding to that of two concentric spherical electrodes, an insulating foil on which charge carriers resulting from ionization of the gas by the x-radiation and displaceable in the longitudinal direction of the chamber being arranged therewithin.

---

4 057 796

Analog-digital converter

A. Hoogendoorn *E*
R. E. J. van de Grift
T. J. van Kessel

An analog-digital converter in which a capacitor is charged or discharged by a reference current with the aid of transistor switches, a continuous current flows through the capacitor which is determined by an input difference voltage. One side of the capacitor is connected via a comparator to a flip-flop, to which flip-flop a clock signal is applied and which flip-flop drives the transistor switches. The other side of the capacitor is connected to the first input of a differential amplifier, which differential amplifier forms part of a negative feedback loop which maintains the voltage at the first input of the differential amplifier equal to the voltage which is applied to the second input of the differential amplifier.

4 057 831

Video record disc manufactured by a process involving chemical or sputter etching

B. A. J. Jacobs *E*
J. van der Wal
G. B. Gerritsen

A mother for manufacturing long-playing video records is provided by (1) selectively exposing a photoresist disposed as the outer layer on a substrate comprising a disc-shaped plate, a thin layer of base material, e.g., an oxide or nitride, adhering to the plate and a thin metal layer, e.g., chromium, silver, nickel or titanium, coating the base material layer, (2) removing non-activated sections of the photoresist layer and (3) sputter or chemically etching the thin metal and base material layers in sections corresponding to the removed sections of the photoresist layer.

---

4 057 833

Centering detection system for an apparatus for playing optically readable record carriers

J. J. M. Braat *E*

An apparatus as described for reading a record carrier on which information, for example video and/or audio information is stored in an optically readable track-shaped information structure. A deviation between the center of a read spot which is projected on the information structure and the center line of a track to be read can be detected with the aid of at least two detectors which are disposed in the far field of the information structure in different quadrants. With the aid of the same detectors a reference signal is obtained which is used for deriving a control signal for correcting the position of the read spot relative to the track to be read.

---

4 058 382

Hot-gas reciprocating machine with self-centered free piston

J. Mulder *E*

A hot-gas reciprocating machine having a free piston, one face of which varies the volume of a working space while its other face bounds a buffer space of constant pressure. A control mechanism maintains a constant nominal central piston position by momentarily connecting the working space and the buffer space.

---

4 058 743

Pulse generating circuit

D. R. Armstrong *R*

A pulse is generated in an output transformer and this pulse is used to provide a spark across a spark gap for the purpose of igniting any gas/air mixture present. The circuit operates from a 1.5 volt d.c. source.

A blocking oscillator is energized by a two position switch which is operated to a first position, and this charges a capacitor. The capacitor is then discharged through an output transformer to produce the spark when the switch is returned to its original rest position. The winding used to charge the capacitor from the blocking oscillator is also used in the discharge path for the capacitor and this inductive loading provides a slower discharge and a more controlled lower energy spark which is found to be better for gas ignition.

PHILIPS TECHNICAL REVIEW

VOLUME 37, 1977, No. 9/10

The behaviour of phosphors with aluminate host lattices

J. L. Sommerdijk and A. L. N. Stevels

The ultraviolet radiation from the low-pressure mercury discharge in a fluorescent lamp is converted into visible light with the aid of phosphors. The aim is to combine the maximum luminous efficacy with a good colour rendering. With the conventional halophosphate phosphors the maximum luminous efficacy is in the region of 80 lm/W; any improvement in colour rendering is usually obtained at the expense of the luminous efficacy. It is however possible to achieve good colour rendering with a high luminous efficacy by using three phosphors that give blue, green and red luminescence in the correct intensity ratio, each within a relatively narrow spectral range. Among the phosphors developed for such lamps, the blue and green phosphors have an aluminate host lattice. The article below gives some results of an investigation into the fundamentals of the behaviour of these new aluminate phosphors. The investigation has provided an improved general understanding of the quantum efficiency and energy transfer between the various centres in phosphors of this type.

Introduction

In a new type of fluorescent lamp, which combines good colour rendering with a high luminous efficacy, there are three phosphors: one emits red light, another emits blue light, and the third emits green light [1]. The red phosphor is an yttrium oxide activated with trivalent europium — a phosphor widely used in colour-television picture tubes. The blue and green phosphors, developed by the Philips Lighting Division, are based on the luminescence of rare-earth ions incorporated in an aluminate lattice [2]. Some aluminate phosphors of this type are particularly suitable for use in fluorescent lamps; they emit the right colour, they are resistant to the corrosive effects of the mercury discharge in these lamps and they give a high light output under the conditions that exist in these lamps.

Our investigation was mainly concerned with the fundamentals of the behaviour of Eu^{2+} and Ce^{3+} ions in aluminate lattices, either by themselves, or combined with Tb^{3+} or Mn^{2+} ions. *Fig. 1* illustrates some of the possibilities that these phosphors offer in the conversion of ultraviolet radiation into visible light.

The structure of the aluminate lattice has been found to have a considerable influence on the properties of the phosphors. We shall therefore start by describing

Fig. 1. Some of the phosphors dealt with in this article, irradiated by an ultraviolet lamp. From left to right: two blue phosphors, $Sr_{0.9}La_{0.1}Mg_{0.1}Al_{11.9}O_{19}:Eu^{2+}$ (i.e. Sr-La-Mg aluminate activated with divalent europium) and $BaMgAl_{10}O_{17}:Eu^{2+}$, the red phosphor: $La_{0.68}Eu_{0.21}Mn_{0.60}Al_{11.52}O_{19.11}$, the blue-green phosphor: $(Ca,La)Al_{12}O_{19}:Eu^{2+},Mn^{2+}$ and the two green phosphors: $BaMgAl_{10}O_{17}:Eu^{2+}$, Mn^{2+} and $Ce_{0.67}Tb_{0.33}MgAl_{11}O_{19}$.

Dr J. L. Sommerdijk and Dr Ir A. L. N. Stevels are with Philips Research Laboratories, Eindhoven.

[1] M. Koedam, J. J. Opstelten and D. Radielović, J. Illum. Engng. Soc. **1**, 285, 1972.
See also: J. J. Opstelten, D. Radielović and J. M. P. J. Verstegen, Philips tech. Rev. **35**, 361, 1975.

[2] J. M. P. J. Verstegen, J. Electrochem. Soc. **121**, 1623, 1974.

the structure of two types of aluminate that act as the host lattice for the phosphors we shall discuss here. This will be followed by a discussion of some phosphors and the background to their behaviour [3].

In an aluminate lattice the Eu^{2+} ion usually gives a blue luminescence band. It is in fact an Eu^{2+}-activated Mn^{2+}, sometimes red as well. We shall take a closer look at the properties of the combination Ce^{3+}-Tb^{3+}, which is used in the green phosphor for the fluorescent lamp mentioned above. It is found that a very reasonable explanation can be given for the behaviour of this combination.

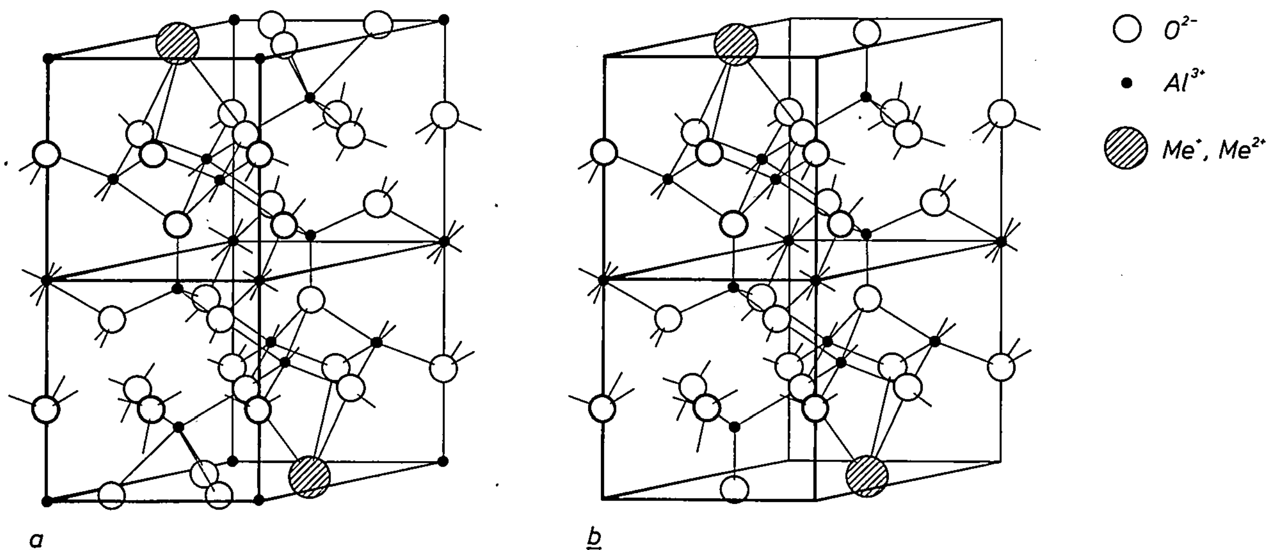

Fig. 2. The crystal structure of magnetoplumbite (*a*) and of *β*-aluminium oxide (*b*). In both cases half a unit cell is shown; the complete cell is obtained by mirror reflection of this part from a lower or an upper plane. (Taken in part from C. A. Beevers and M. A. S. Ross, Z. Kristallogr. 97, 59, 1937.)

aluminate phosphor that is used for the blue component in the fluorescent lamp mentioned above. In one particular host lattice, however, Eu^{2+} can also give luminescence in the ultraviolet. As a rule, Ce^{3+} ions in an aluminate lattice give ultraviolet luminescence, but in some cases blue emission is also observed. In dealing with the Eu^{2+} and Ce^{3+} phosphors we shall examine the factors that determine the colour of the luminescence, and also examine the dependence of the efficiency of the luminescence on temperature and concentration.

The energy that Eu^{2+} and Ce^{3+} ions absorb when subjected to ultraviolet radiation can be given up not only by luminescence but also by the transfer of energy to other ions deliberately incorporated in the lattice, which can then luminesce in their turn. Energy can also be transferred to non-radiative centres, a process that is obviously most undesirable. An interesting case is the energy transfer to Tb^{3+} or Mn^{2+} ions, which are not themselves sufficiently capable of absorbing ultraviolet radiation. There is then competition between the intrinsic luminescence of Eu^{2+} or Ce^{3+} ions and the energy transfer to Tb^{3+} or Mn^{2+} ions, which in their turn both give green luminescence or, in the case of

Crystal structure of the host lattices

The phosphors we have investigated have two types of host lattice. One has the general formula $Me^{2+}Me^{3+}_{12}O_{19}$, the other $Me^{+}Me^{3+}_{11}O_{17}$. The Me^{2+} and Me^{+} ions are comparable in diameter with the O^{2-} ions. The Me^{3+} ions are mainly aluminium ions, which are much smaller and are located in the interstices between the oxygen ions.

When ions of a different valency are substituted for the monovalent or divalent large cations, this must be compensated by other substitutions. A deviation in the stoichiometry may also occur to compensate such a marked deviation in the charge of the large cations. This would then imply a deviation from the ideal structure of the crystal lattice.

The crystal structure of the aluminates with the formula $Me^{2+}Al_{12}O_{19}$ is known as the *magnetoplumbite* structure, from the mineral magnetoplumbite, $PbFe_{12}O_{19}$, in which this structure was first found. $Me^{+}Al_{11}O_{17}$ crystallizes in the *β*-aluminium-oxide structure, first found in $NaAl_{11}O_{17}$. This is a mineral that was originally thought to be a modification of aluminium oxide. Both these structures are also found in ferrites [4]. Experience with X-ray-diffraction

studies of these ferrites [5] has proved of great value in determining the structure of the phosphors described here.

As can be seen in *fig. 2*, the unit cell in both structures consists of blocks with a spinel structure, in which oxygen and aluminium ions occur, alternating with thinner intermediate layers. The differences between the two structures are due entirely to the different arrangement of the ions in these intermediate layers. In the magnetoplumbite structure the intermediate layer consists of a close-packed arrangement of oxygen ions and large cations, with the large cations forming a hexagonal pattern in the layer. The intermediate layer also contains some aluminium ions. In the β-aluminium-oxide structure the intermediate layer is relatively empty, in each unit cell it contains only one large cation and one oxygen ion.

The rare-earth ions incorporated as activators in the phosphors may be built into the intermediate layers of the aluminate lattice at the sites of the large cations. The Mn^{2+} and Mg^{2+} ions, which come into our considerations, are located at aluminium sites. The Al^{3+} sites in the aluminates we have studied are of different types. The luminescent properties of the Mn^{2+}-containing phosphors depend to a great extent on which of these sites is occupied by the Mn^{2+} ion.

As noticed earlier, the valency of the large cations may in practice be higher than in the ideal structure. In compensating the excess charge by the incorporation of Mg^{2+} ions, these ions take up positions at the Al^{3+} sites in the lattice. For compensation by the addition of O^{2-} ions, these extra ions are incorporated at the sites of large cations in the intermediate layer. The various possible ways of compensation are summarized in *Table I*.

An example of a combination of modes of compensation is barium aluminate, which has the β-aluminium-oxide structure. The compensation for the divalence of the barium ion is brought about in principle by the creation of aluminium vacancies: $BaAl_{10.67}O_{17}$. The existence region of the β-aluminium-oxide phase for Ba aluminate is fairly broad, and compensation can also be effected by incorporating O^{2-} ions at large-cation sites, for example $Ba_{0.75}Al_{11}O_{17.25}$. In this way a great variation in composition is possible without the formation of a different crystal structure. This is not the case for La and Ce aluminate. Both these compounds have the magnetoplumbite structure, and the existence region, corresponding to the formulae $(La_{0.86}O_{0.14})Al_{11.9}O_{19}$ and $(Ce_{0.86}O_{0.14})Al_{11.9}O_{19}$, is fairly narrow. These formulae show that compensation for the trivalence of La and Ce takes place here through the occurrence of both Al vacancies and oxygen ions at the sites of large cations. A study of

Table I. Various possible reactions to compensate for a too high valency of the large cations in the aluminates discussed here. Each 'reaction equation' for the compensation process is accompanied by an example.

Equation	Example
$Me^{2+} + Al^{3+} \rightarrow Me^{3+} + Mg^{2+}$	$CeMgAl_{11}O_{19}$
$Me^{+} + Al^{3+} \rightarrow Me^{2+} + Mg^{2+}$	$BaMgAl_{10}O_{17}$
$Me^{+} \rightarrow Me^{2+} - \frac{1}{3}Al^{3+}$	$BaAl_{10.67}O_{17}$
$Me^{+} \rightarrow \frac{3}{4}Me^{2+} + \frac{1}{4}O^{2-}$	$Ba_{0.75}Al_{11}O_{17.25}$

luminescence data indicates that we can assume that the presence of oxygen ions at the large-cation sites causes a regrouping of the neighbouring oxygen ions and the aluminium ions in the intermediate layer. As a result the structure may be so deformed that the aluminium ions originally surrounded by five oxygen ions in the intermediate layer are now tetrahedrally surrounded. These tetrahedrally surrounded ions are situated at a short distance from the large cations. The consequence of this for the luminescence of some aluminate phosphors will be discussed later on in this article.

In general, aluminates with monovalent large cations are only found to have the β-aluminium-oxide structure, and aluminates with trivalent large cations only have the magnetoplumbite structure. In the case of divalent large cations the structure is determined by the cation diameter. Where the cations are relatively small, like Ca^{2+}, only the magnetoplumbite structure is found, but where they are relatively large, like Ba^{2+}, only the β-aluminium-oxide structure is seen. The cations Sr^{2+} and Eu^{2+} occupy an intermediate position: the structure that occurs now depends on the small cations. In spite of the very close similarity between the two structures, their miscibility is nevertheless small. Phase separation occurs, as in the system $SrAl_{12}O_{19}$—$SrMgAl_{10}O_{17}$.

The solubility of the various activator ions in both types of aluminate lattice is really a direct consequence of the foregoing. Eu^{2+} can be taken up in both host lattices. Ce^{3+} has a marked preference for the magnetoplumbite structure and is not readily soluble in β-aluminium-oxide phases. Tb^{3+} is small and while it can be taken up in a magnetoplumbite lattice it can hardly be incorporated at all in a β-aluminium-oxide lattice. Mn^{2+} has a preference for the β-aluminium-oxide lattice. Mn^{2+} ions only fit into a magnetoplumbite lattice when sufficient trivalent large cations are present.

---

[3] A general introduction to the luminescence mechanisms in phosphors is given in: G. Blasse and A. Bril, Philips tech. Rev. **31**, 304, 1970. We shall refer to various pages of that publication.

[4] See for example the article by C. A. M. van den Broek and A. L. Stuijts in this volume of Philips tech. Rev., p. 157 (No. 7).

[5] P. B. Braun, Philips Res. Repts. **12**, 491, 1957.

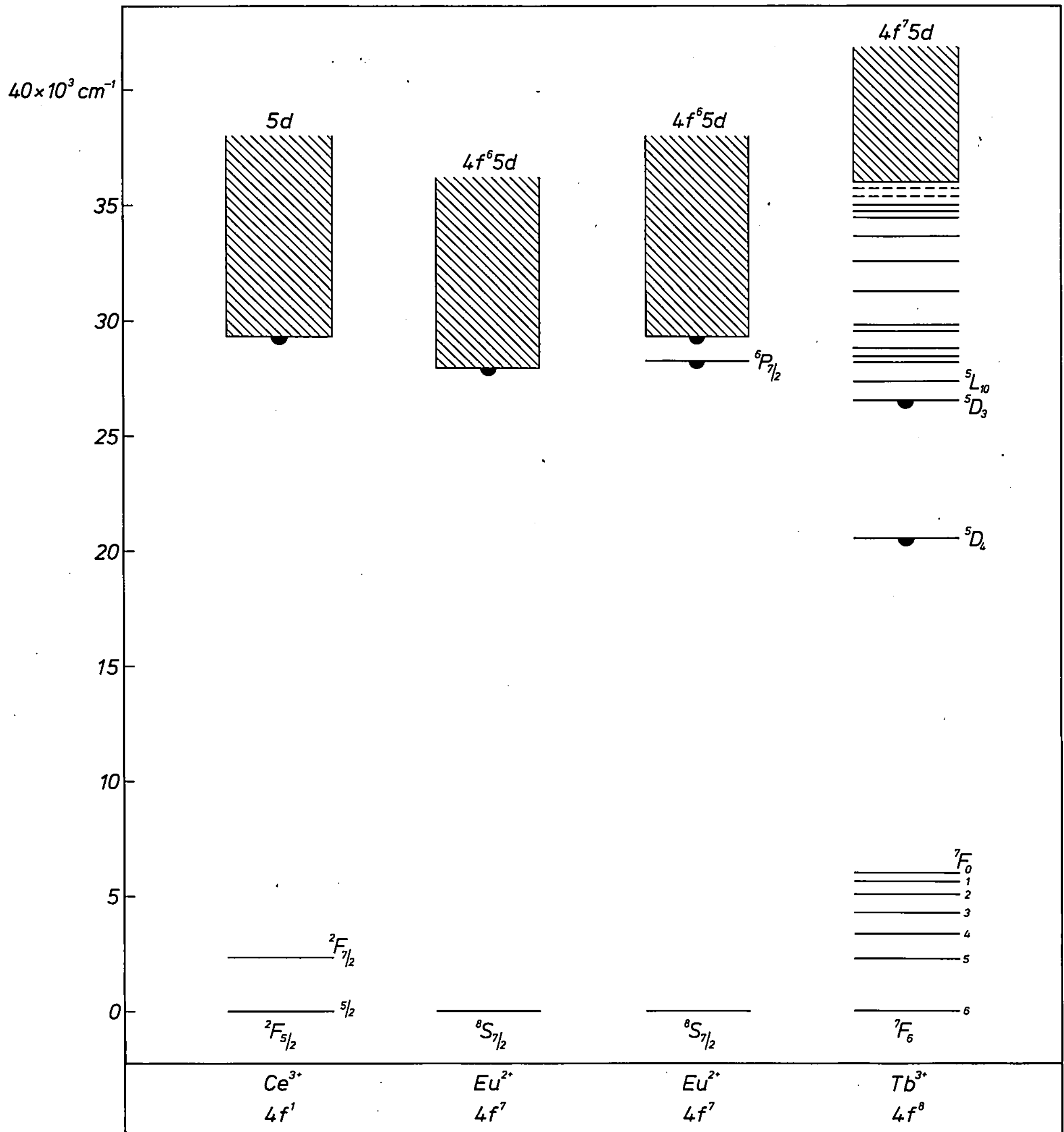

Fig. 3. Energy-level diagrams of Ce^{3+}, Eu^{2+} and Tb^{3+} in oxidic host lattices; the energy is plotted on the vertical axis in cm^{-1}. The horizontal lines represent the sharp 4f levels and the hatched areas represent bands formed by the $4f^{n-1}5d$ states. The levels on which a filled semicircle is drawn are the levels from which luminescence is observed. For Eu^{2+} two situations are shown: the case in which a luminescence band is observed, originating from the transitions $4f^65d \rightarrow 4f^7$ and the case in which emission lines are observed in addition, originating from the $^6P_{7/2}$ level. The second case is encountered when the crystal field is such that the bottom of the $4f^65d$ band is higher than the $^6P_{7/2}$ level.

Luminescence of Eu^{2+} and Ce^{3+}

In nearly all cases the luminescence of Eu^{2+} and Ce^{3+} ions stems from a transition from a 5d orbit to a 4f orbit (*fig. 3*). The 5d orbits lie on the outside of the ions and are strongly affected by the immediate environment. Because of this the position of the associated energy levels varies quite considerably. Thermal vibrations of the surrounding ions and local variations in the lattice structure therefore have the result that the luminescence spectra have no sharp lines but relatively

broad bands. Owing to differences in the crystal field between the various host lattices, the location of these bands is closely dependent on the host lattice.

As we stated earlier, the luminescence of Eu^{2+} in aluminates is mostly blue and that of Ce^{3+} is mostly in the long-wave ultraviolet. If the light output is sufficiently high, the Eu^{2+} emission is directly usable for lighting. Ce^{3+}, on the other hand, can only be used for lighting as a sensitizer in combination with appropriate activator ions, which deliver visible light via a process of energy transfer. In addition to this 'ordinary' emission from Eu^{2+} and Ce^{3+}, another emission is found in some aluminates. For instance, in one particular host lattice the Eu^{2+} ion emits lines in the long-wave ultraviolet. In other host lattices a very strong interaction appears to take place between Eu^{2+} or Ce^{3+} ions and neighbouring oxygen ions. In the case of Eu^{2+} this gives green and in the case of Ce^{3+} blue luminescence.

The ordinary luminescence bands

The spectra given in *fig. 4* show how the structure of the host lattice and the diameter of the large cations affect the location of the luminescence bands.

There are two factors of influence here: the first is the strength of the crystal field at the sites of the luminescing ions, and the second is the degree of covalence of these ions, i.e. the extent to which they share the electrons in their outermost shell with the surrounding oxygen ions. The action of the crystal field splits the 5d level into sublevels, the luminescence always taking place from the lowest sublevel. In a stronger crystal field there is more splitting, causing this lowest sublevel to shift to a lower energy, so that the luminescence appears at a longer wavelength. The degree of covalence determines the location of the centre of mass of the collective sublevels; with stronger covalence all 5d levels shift to a lower energy, which also means that the luminescence shifts to a longer wavelength.

In addition to the luminescence spectra, as shown in fig. 4, another aid to the study of phosphors is given by the excitation spectra, where the light output is given as a function of the wavelength of the exciting ultraviolet radiation. In our case these excitation spectra make it possible to study the split 5d level in a more direct way. In nearly all cases the excitation wavelength is shorter than the wavelength at which the ensuing luminescence takes place. The effect is known as the Stokes shift [6].

From the luminescence spectra, and with the results of the excitation measurements, we can draw a number of conclusions [7]. It is found, for example, that covalence has relatively little influence in the case of Eu^{2+} and is almost the same for all host lattices. The observed differences in luminescence are thus mainly a

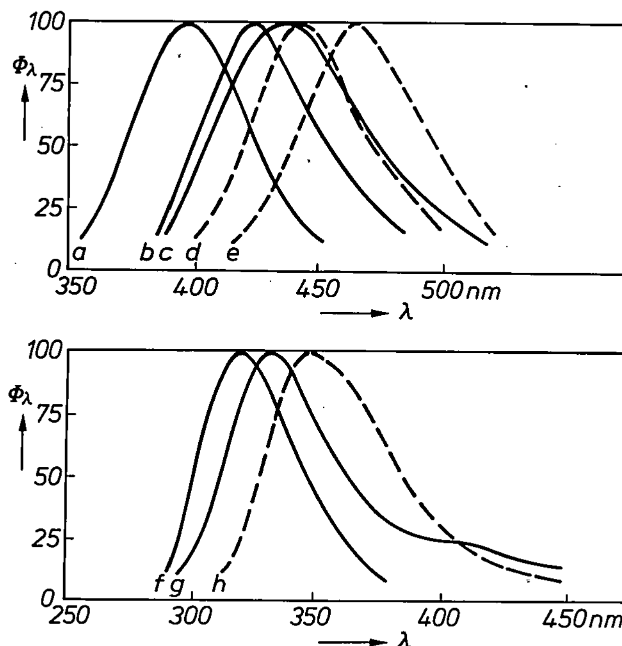

Fig. 4. The intensity Φ_λ, in arbitrary units, of the emission of Eu^{2+} (*above*) and Ce^{3+} (*below*) in a number of aluminates as a function of the wavelength λ. The curves of host lattices with the magnetoplumbite structure are drawn as solid lines, the curves for host lattices with the β-aluminium-oxide structure are shown as dashed lines.
a) $SrAl_{12}O_{19}:Eu^{2+}$.
b) $CaMgAl_{11}O_{18.5}:Eu^{2+}$.
c) $La_{0.86}Al_{11.9}O_{19.14}:Eu^{2+}$.
d) $BaAl_{10.67}O_{17}:Eu^{2+}$.
e) $SrMgAl_{10}O_{17}:Eu^{2+}$.
f) $SrAl_{12}O_{19}:Ce^{3+}$.
g) $La_{0.86}Al_{11.9}O_{19.14}:Ce^{3+}$.
h) $BaAl_{10.67}O_{17}:Ce^{3+}$.

consequence of differences in the crystal field. Apparently Eu^{2+} gives more crystal-field splitting in a β-aluminium-oxide lattice than in a magnetoplumbite lattice. The reason for this difference is that in the β-aluminium-oxide structure the arrangement of the oxygen ions around the Eu^{2+} ion is strongly asymmetrical. If $BaMgAl_{10}O_{17}$, which has the β-aluminium-oxide structure, is activated with Eu^{2+}, this phosphor then emits exactly the right wavelength (450 nm) for the three-phosphor lamp mentioned in the introduction.

The lanthanum aluminates $La_{0.86}Al_{11.9}O_{19.14}$ and $LaMgAl_{11}O_{19}$, as host lattices for Eu^{2+} phosphors, occupy a position midway between the magnetoplumbite and the β-aluminium-oxide structure. The crystal structure resembles that of the magnetoplumbite lattices, but the behaviour of the luminescence spectra more closely resembles that of phosphors with a β-aluminium-oxide structure. The explanation for this is that Eu^{2+} in the lanthanum aluminates occupies the site of a trivalent ion. Because the positive charge of the Eu^{2+} ion is too small, the 5d orbits are enlarged, with the result that the crystal field around the ion exerts a stronger influence. The effect of this is that there is

[6] See the article by Blasse and Bril [3], pages 314-316.
[7] A. L. N. Stevels and A. D. M. Schrama-de Pauw, J. Electrochem. Soc. 123, 691, 1976.

more splitting of the 5d levels in the excitation spectra, so that the luminescence has a longer wavelength than would at first sight be expected.

The emission spectra also show that the diameter of the large cations affects the wavelength of the Eu^{2+} luminescence. With an otherwise identical crystal structure, the largest cations give luminescence with the shortest wavelength, as a result of a relatively weak crystal field at the location of the Eu^{2+} ions. The effect of the cation diameter is clearly less than that of structural differences. Indeed, the influence of the large-cation diameter does not show up at all in the excitation spectra. This is not entirely unexpected, since the influence of the structure is also relatively small in these spectra.

In the phosphors activated with Ce^{3+} the two types of host lattice differ in much the same way as in the Eu^{2+} phosphors [8]. Here, however, the crystal-field splitting is on the whole smaller than with the Eu^{2+} phosphors. This is a consequence of the higher charge of the Ce^{3+} ion, which draws the 5d orbits closer to the nucleus so that they are less affected by the crystal field.

The excitation spectra of the Ce^{3+} aluminates show that the degree of covalence in the bond between these ions and the host lattice has a distinct effect on the location of the centre of mass of the 5d levels. In 'magnetoplumbite' phosphors with Ca or Sr, where the covalent interaction is small, it lies about 41 000 cm^{-1} above the 4f level; in the Ce^{3+}-activated lanthanum aluminate this interaction is relatively strong and the distance is consequently smaller, about 38 000 cm^{-1}.

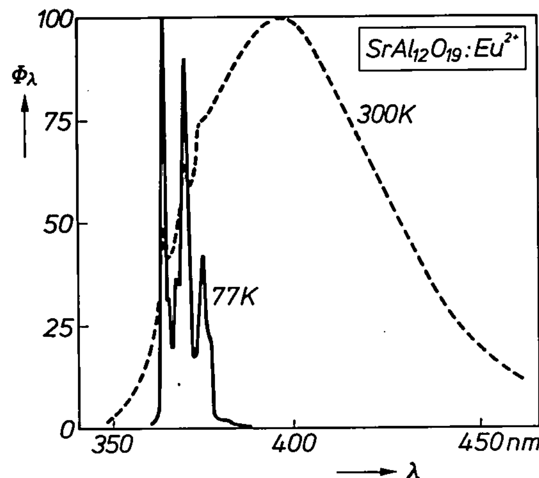

Fig. 5. The luminescence spectrum of $SrAl_{12}O_{19}$ activated with Eu^{2+}, measured at 300 K (*dashed*) and at 77 K (*solid curve*).

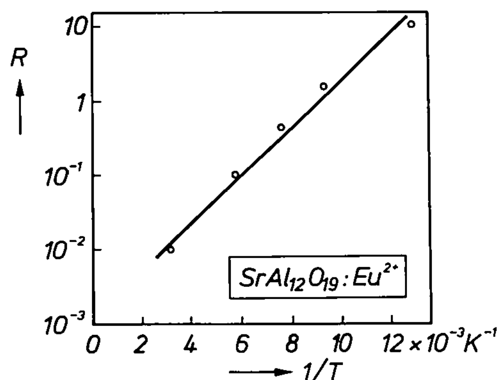

Fig. 6. The ratio R of the line intensity to the band intensity of $SrAl_{12}O_{19}$ activated with Eu^{2+}, as a function of the reciprocal of the temperature T.

Luminescence lines of Eu^{2+}

Recent work has revealed that, in addition to the luminescence band of Eu^{2+} described above, which is due to a $4f^65d \rightarrow 4f^7$ transition, this ion can also emit lines when it is incorporated in certain host lattices. These lines appear to arise from the transition from an excited $4f^7$ state to the $4f^7$ ground state. The electron orbits to which these states correspond are both located entirely in the interior of the ion, as we saw earlier, and are therefore little affected by the crystal field in the host lattice. Because of this the luminescence lines are narrow. The decay time of this luminescence is relatively long: a few milliseconds as against a few microseconds for the band emission. The reason for this is that the luminescence lines originate from 'forbidden' transitions, and the screening of the orbits makes it more difficult for the crystal-field effects to counteract this prohibition.

Among the aluminates so far investigated, $SrAl_{12}O_{19}$ is the only host lattice in which the line emission of Eu^{2+} has been observed [9]. As shown in *fig. 5*, some structure is already to be seen at room temperature on the short-wave edge of the broad luminescence band; at 77 K the band has just about disappeared and only the lines are left. The lines can only be observed in $SrAl_{12}O_{19}$ and not in other aluminates because the crystal field in $SrAl_{12}O_{19}$ is relatively weak. Because of this there is little crystal-field splitting of the $4f^65d$ level, and the bottom of the corresponding band in the energy-level diagram lies just above the excited $4f^7$ level. In all other aluminates the crystal-field splitting is so much stronger that the $4f^7$ level is overlapped by the $4f^65d$ band, and since the band transition has a much greater probability than the line transition, the lines vanish.

---

[8] A. L. Stevels, J. Electrochem. Soc. 125, 588, 1978.
[9] J. M. P. J. Verstegen, J. L. Sommerdijk and A. Bril, J. Luminescence 9, 420, 1974.

The ratio R of the line intensity to the band intensity in the temperature range of interest can be described by

$$R = (r_l/r_d) \exp(\Delta E/kT),$$

where r_l and r_d are the probabilities of the radiative line transition ($4f^7 \rightarrow 4f^7$) and the band transition ($4f^65d \rightarrow 4f^7$). ΔE is the difference in energy between the lowest $4f^65d$ state and the $4f^7$ emission state, k is Boltzmann's constant and T the absolute temperature. Measurement of the ratio R as a function of T gives a value of about 500 cm^{-1} for ΔE and the ratio r_l/r_d is found to be about 10^{-3} (see *fig. 6*).

Luminescence of Ce^{3+} and Eu^{2+} in very strong interaction with oxygen

In aluminates activated with Ce^{3+} a blue band is observed in addition to the luminescence band in the ultraviolet described earlier. *Fig. 7* shows this effect for $La_{0.86}Al_{11.9}O_{19.14}$:$Ce^{3+}$. The blue band may be attributed to the very strong interaction between the Ce^{3+} ions and oxygen ions at neighbouring large-cation sites, an interaction we shall refer to here as 'associate formation', to distinguish it clearly from the other interactions that take place in phosphors. At low Ce concentrations about 16% of the total number of quanta are emitted as blue luminescence, irrespective of this concentration. This indicates that the distribution of Ce among the available sites is completely random and that associate formation does indeed occur with all Ce ions close to a large-cation site occupied by oxygen. At high Ce^{3+} concentrations the energy transfer from excited free Ce^{3+} ions, emitting in the ultraviolet, to the Ce-O associates appears to be so efficient that the blue luminescence is dominant and the luminescence in the ultraviolet is completely quenched (see fig. 7). Apparently the presence of Mg^{2+} ions in a sample hinders the formation of associates, since Ce aluminates containing Mg do not give a blue luminescence.

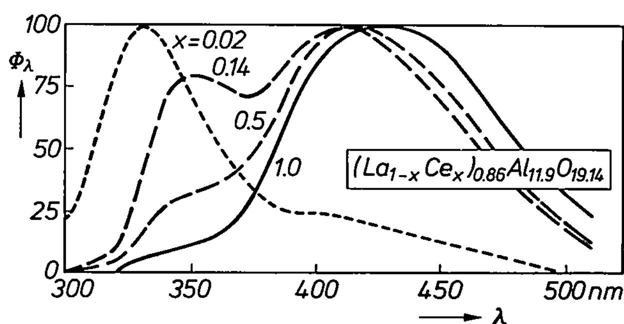

Fig. 7. Luminescence intensity Φ_λ, in arbitrary units, as a function of the wavelength λ of $(La_{1-x}Ce_x)_{0.86}Al_{11.9}O_{19.14}$ for four values of the parameter x. At low Ce concentrations there is only luminescence in the ultraviolet, characteristic of the Ce^{3+} ions. At higher concentrations a blue emission band appears, which is a result of very strong interaction between the Ce^{3+} ions and neighbouring oxygen ions, causing the ultraviolet luminescence to disappear completely, owing to efficient energy transfer to the blue luminescing centres.

Ce^{3+} phosphors in which there are no oxygen ions at large-cation sites do not give blue luminescence from Ce-O associates. Oxygen ions can, however, be incorporated at the large-cation sites by adding an excess of Al_2O_3 during the preparation of such phosphors; blue fluorescence is then produced in addition to the usual ultraviolet fluorescence (see *fig. 8*).

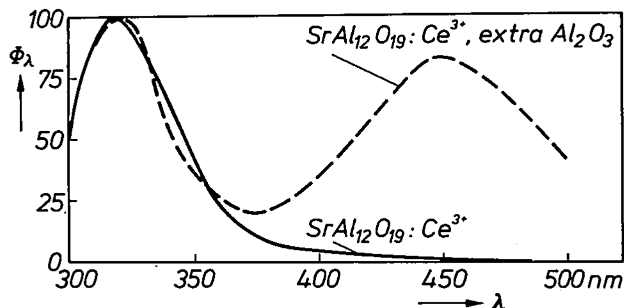

Fig. 8. Emission spectra of two Ce^{3+}-activated Sr aluminates. The compound that gives the solid curve contains no oxygen ions at large-cation sites. In the preparation of the compound that gives the dashed curve an excess of Al_2O_3 has been added; this causes oxygen ions to appear at large-cation sites. The compound corresponding to the dashed curve therefore gives a blue luminescence band in addition to the characteristic Ce^{3+} emission. This blue band is due to very strong interaction between Ce^{3+} and neighbouring oxygen ions.

A similar fluorescence band in the green, also attributable to associate formation, is found in phosphors activated with Eu^{2+}. The only difference from the Ce^{3+} situation is that the green band has a much lower intensity, because the energy transfer from free Eu^{2+} ions to Eu-O associates is much less than with Ce.

Efficiency of the luminescence

As we have seen, luminescence colours varying from green to ultraviolet can be obtained with Eu^{2+} and Ce^{3+} in aluminate host lattices. It is even possible to select a host lattice such that the wavelength is accurately defined. In practice, however, the colour is not the only important quantity. To make a good lamp the phosphors must give a high light output, which means that the ultraviolet absorption and the quantum efficiency of the luminescence must both be high. The host lattice in which the activator is incorporated has a marked effect on the light output, as does also the activator concentration. Another point is that the light output of a phosphor generally decreases with rising temperature; this again evidently depends on the host lattice.

We shall now consider in somewhat more detail the various factors that have an effect on the quantum efficiency of a phosphor.

Table II. Approximate values for the quantum efficiency (in %) of a number of phosphors activated with Eu^{2+} or Ce^{3+}, on excitation by radiation at a wavelength of 250-270 nm.
—: Sample was not homogeneous or showed no luminescence.
*: Sample in which all available sites are occupied by activator ions (differing from the contents stated at the head of the table).

Host lattice	Quantum efficiency on activation with 2% Eu^{2+}	Quantum efficiency on activation with 14% Ce^{3+}
Magnetoplumbite		
$CaAl_{12}O_{19}$	50	50
$CaMgAl_{11}O_{18.5}$	—	50
$SrAl_{12}O_{19}$	55	70
$EuAl_{12}O_{19}$	20*	—
As above, with large trivalent cations		
$Ce_{0.86}Al_{11.9}O_{19.14}$	—	60*
$La_{0.86}Al_{11.9}O_{19.14}$	50	55
$CeMgAl_{11}O_{19}$	—	60*
$LaMgAl_{11}O_{19}$	60	60
β-aluminium oxide		
$SrMgAl_{10}O_{17}$	65	—
$EuMgAl_{10}O_{17}$	45*	—
$BaAl_{10.67}O_{17}$	70	50
$BaMgAl_{10}O_{17}$	70	60

Effect of the host lattice

Table II gives some approximate figures for the quantum efficiencies of various phosphors activated with Eu^{2+} and Ce^{3+} and excited by radiation with a wavelength of 250-270 nm, the wavelength range that includes the emission of a low-pressure mercury discharge. These efficiencies can be said to be fairly high, certainly if it is remembered that in some cases the excitation spectra show an optimum excitation wavelength higher than 270 nm.

In the β-aluminium-oxide lattice of $BaMgAl_{10}O_{17}$ the luminescence band of Eu^{2+} lies at 450 nm, which is the appropriate wavelength for the three-phosphor lamp, as we saw earlier. The quantum efficiency of this phosphor is high and is not very sensitive to impurities, nor is it much affected by temperature.

Concentration quenching

The quantum efficiency of the Eu^{2+}-activated phosphors decreases noticeably at higher Eu^{2+} concentrations; this effect is known as concentration quenching. The Ce^{3+}-activated phosphors do not give this quenching effect, or if they do, only slightly. The explanation for concentration quenching with Eu^{2+} is that with increasing Eu concentration the energy transfer between the activator ions steadily improves, so that the excitation energy is transported over larger distances through the lattice before luminescence can occur. This means that lattice defects where a non-radiative transition can occur are more easily reached. The energy transfer between Eu^{2+} ions in aluminates is found to be so good that in some cases the quantum efficiency is governed by the number of lattice defects, even at low Eu concentrations. For Ce^{3+} the energy exchange between the activator ions is apparently much less effective, since little or no concentration quenching occurs with this activator.

When small amounts of Mg^{2+} ions are incorporated at Al^{3+} sites in $SrAl_{12}O_{19}:Eu^{2+}$, defects are produced that strongly quench the luminescence. The resultant reduction in efficiency is again greatest at higher Eu^{2+} concentrations, where the energy transfer between the Eu^{2+} ions becomes significant. The addition of Mg is probably responsible for the introduction of oxygen vacancies as a result of the reduced positive charge caused by this addition. An argument in support of this is that when the creation of oxygen vacancies is prevented by adding an equal quantity of La^{3+} ions as well as Mg^{2+}, the efficiency is again almost equal to that of $SrAl_{12}O_{19}:Eu^{2+}$.

Fig. 9 shows that $SrAl_{12}O_{19}:Eu^{2+}$ must also contain natural defects, in view of the strong concentra-

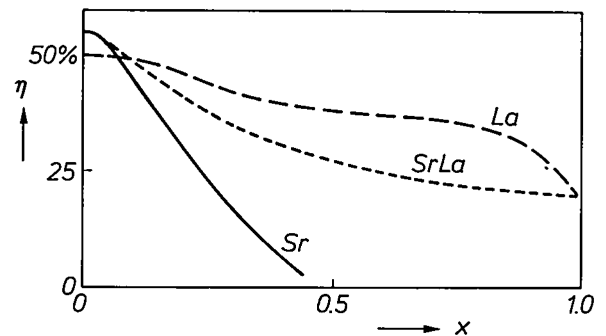

Fig. 9. Quantum efficiency η of a number of Eu^{2+}-activated aluminates, as a function of the europium content x. Pure $SrAl_{12}O_{19}:Eu^{2+}$ exhibits strong concentration quenching. The addition of lanthanum causes a marked decrease in the concentration quenching, because of its effect on the defect situation in the crystal lattice.

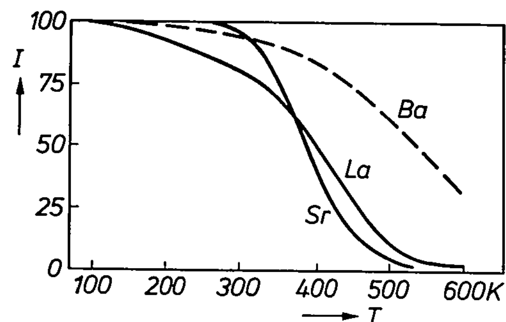

Fig. 10. The total luminescence intensity I, in arbitrary units, as a function of the temperature T for a number of Eu^{2+}-activated aluminates. The solid curves relate to phosphors whose host lattice has the magnetoplumbite structure; the dashed curve was measured on a phosphor whose host lattice has the β-aluminium-oxide structure.

tion quenching of this phosphor. This is also to be expected from the good transfer of energy, since the defects where non-radiative transitions occur are reached more effectively. The addition of a little lanthanum is sufficient to reduce the concentration quenching quite considerably, and when the host lattice is $La_{0.86}Al_{11.9}O_{19.14}$ hardly any quenching is observed. It has therefore been possible here to improve the defect situation of the host lattice by changing the composition. This is a very exceptional situation for oxidic phosphors in general. Usually the existence region of a phase suitable as a host lattice is too narrow to allow any essential change in the defect situation. Fig. 9 also shows that there is a marked difference in the defect situation in Sr aluminate and in La aluminate. It seems as if the additional oxygen atoms contained in the intermediate layers in La aluminate are able to prevent the occurrence of lattice defects that adversely affect the efficiency.

Since La and Ba aluminates contain Al vacancies, the incorporation of Mg^{2+} ions will not lead to oxygen vacancies. The addition of Mg to these aluminates will not therefore cause any drop in efficiency. On the contrary, La aluminate gives a slightly higher efficiency after the addition of Mg. The reason for this is that phosphors activated with Eu^{2+} give a somewhat lower efficiency when oxygen ions occupy large-cation sites, and the addition of Mg to $La_{0.86}Al_{11.9}O_{19.14}$ partly eliminates these oxygen ions.

Table III. Thermal quenching in a number of Eu^{2+}-activated phosphors, characterized by the temperature T_{50} at which the efficiency has dropped to 50% of its value at 77 K.

Host lattice	T_{50} (K)
Magnetoplumbite	
$CaAl_{12}O_{19}$	380
$CaMgAl_{11}O_{18.5}$	380
$SrAl_{12}O_{19}$	385
$EuAl_{12}O_{19}$	370
As above, with large trivalent cations	
$La_{0.86}Al_{11.9}O_{19.14}$	400
$LaMgAl_{11}O_{19}$	410
β-aluminium oxide	
$SrMgAl_{10}O_{17}$	575
$EuMgAl_{10}O_{17}$	565
$BaAl_{10.67}O_{17}$	535
$BaMgAl_{10}O_{17}$	610

Thermal quenching

In most cases the luminescence intensity of the phosphor decreases with rising temperature, an effect known as thermal quenching. This quenching is caused by the activation at higher temperatures of non-radiative processes, which at very high temperatures eventually predominate over the luminescence. If a phosphor is to be of practical use, thermal quenching should not occur at the normal operating temperature. We have studied the thermal-quenching effect mainly with reference to the luminescence of Eu^{2+}. It is found that this effect is also dependent on the host lattice. *Fig. 10* shows, for example, that the thermal quenching of the luminescence of Eu^{2+} in a host lattice with the β-aluminium-oxide structure becomes significant at much higher temperatures than in a host lattice with the magnetoplumbite structure.

For thermal quenching a model has been given that is based on the 'configuration coordinate' for an active ion [10]. This model shows that the stronger the bond between the activator and the environment, the higher the temperature at which quenching occurs. In a host lattice with the β-aluminium-oxide structure the bond of an Eu^{2+} ion with the nearest-neighbour oxygen ion is much stronger than in a lattice with the magnetoplumbite structure. In the first case quenching is therefore expected at a much higher temperature than in the second. *Table III* again shows that this is in fact the case. The quenching is characterized here by T_{50}, the temperature at which the efficiency has dropped to 50% of the value at 77 K (the temperature of liquid nitrogen). It also appears from the table that the difference in structure, and hence in bond strength, has a much greater influence than a difference in diameter of the other large cations. In its thermal-quenching behaviour, a lanthanum-aluminate host lattice is most closely related to the magnetoplumbites. The Eu^{2+} ion replaces a trivalent La ion here, and two opposing effects come into play. On the one hand T_{50} must be high on account of the high bond strength in a lattice containing a large number of trivalent large cations substituted for divalent cations. On the other hand, as we saw earlier, the Eu^{2+} ion is greatly expanded by its effective negative charge, which must lead to a lower bond strength and hence to a lower quenching temperature.

Eu^{2+} and Ce^{3+} as sensitizers

It is known from the literature that Eu^{2+} and Ce^{3+} ions can act as sensitizers for the luminescence of activator ions that are not themselves sufficiently capable of absorbing ultraviolet radiation. This is also found to be the case in the aluminate lattices dealt with here. The energy transfer from the sensitizer ions to the activator ions can be very good, particularly in the combinations Ce^{3+}-Tb^{3+}, Ce^{3+}-Mn^{2+} and Eu^{2+}-Mn^{2+}. The Mn-activated phosphors emit a green fluorescence band, which makes them useful in xerography. The phosphors activated with the Ce-Tb combination emit a number of luminescence lines, mainly green. This combination is used for the green-emitting phosphor in the fluorescent lamp mentioned in the introduction. We shall consider here the combinations Ce-Tb and Eu-Mn.

[10] See the article by Blasse and Bril [3], pages 314-320.

It was noticed at quite an early stage that the Ce-Tb phosphor had to contain a fairly large amount of the rather expensive Tb to give green Tb^{3+} emission with a high efficiency. This alone made it worthwhile to study the behaviour of this very interesting phosphor.

In the combination Eu-Mn and Ce-Mn the Eu^{2+} and Ce^{3+} ions are situated in the intermediate layers that separate the spinel blocks from each other. The Mn ions, on the other hand, are usually situated in the spinel blocks, unlike the situation in all the phosphors so far considered, where the active ions are only found in the intermediate layers. This means that the effect of the structure of the host lattice on the luminescent properties of the Eu-Mn and Ce-Mn phosphors is far more complicated.

The combination Ce^{3+}-Tb^{3+}

A very useful phosphor, with high quantum efficiency and light output, is based on the combination Ce^{3+}-Tb^{3+}. The composition of the compound, which combines a low-intensity ultraviolet emission from the Ce^{3+} with a high-intensity green emission from the Tb^{3+}, is found to be approximately $Ce_{0.67}Tb_{0.33}MgAl_{11}O_{19}$. This phosphor contains a large number of activator ions (Tb^{3+}), compared with most other phosphors where energy transfer is significant. An activator content of a few per cent is usually sufficient to give an optimum quantum efficiency. A knowledge of the crystal structure and the energy-transfer mechanisms enables an explanation to be given for the different behaviour of this Ce-Tb phosphor [11].

Let us first consider the geometry of the Ce-Tb phosphor. The active ions are situated in the intermediate layers in the magnetoplumbite structure of the host lattice. As can be seen in *fig. 11*, the large-cation sites form a hexagonal lattice in this layer. The distance between an ion and its six nearest neighbours is 0.56 nm; the distance to the six next nearest neighbours is $\sqrt{3}$ times greater, amounting to 0.97 nm. The distance between large cations in different intermediate layers amounts to half the hexagonal cell constant, i.e.

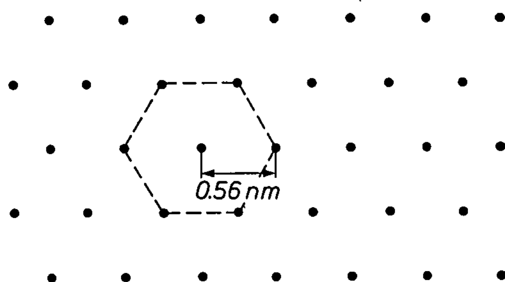

Fig. 11. The hexagonal arrangement of the large cations in the thin intermediate layer of the magnetoplumbite structure of $Ce_{1-x}Tb_xMgAl_{11}O_{19}$. The distance between the nearest rare-earth neighbours is always 0.56 nm, as indicated.

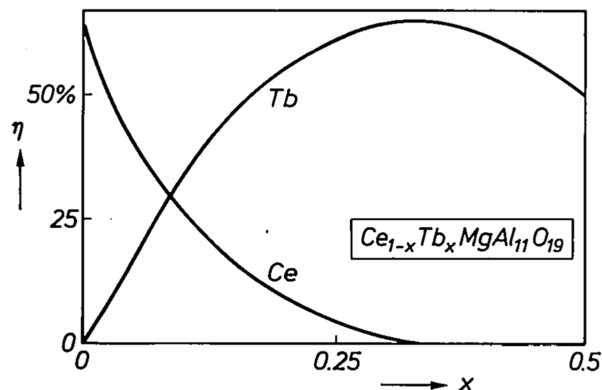

Fig. 12. Quantum efficiency η for the luminescence of Tb^{3+} and Ce^{3+} in $Ce_{1-x}Tb_xMgAl_{11}O_{19}$, as a function of the Tb fraction x.

more than 1.1 nm. We assume that the Ce and Tb ions are randomly distributed among the available sites in the intermediate layers. X-ray diffraction gives no information on this, since the scattering coefficients of Ce and Tb are almost identical. Neutron diffraction, which does permit discrimination between the two kinds of ion, reveals no indications of any regularity in the distribution.

In principle there are two ways in which energy can be transported from a sensitizer to an activator ion: by Coulomb interaction or by exchange interaction. Direct exchange interaction is only reasonably possible over distances up to 0.3-0.4 nm [12]. Since the smallest possible distance between sensitizer and activator ions is 0.56 nm in our case, this transfer mechanism must be regarded as rather unlikely.

Coulomb interaction, in which energy transfer takes place via electric fields, does offer a means of bridging the relatively large distance between a sensitizer and an activator ion. For the radiative transition of Ce^{3+} a dipole transition is the most probable, since it is an allowed transition and has a much higher oscillator strength than the quadrupole transitions of the Ce^{3+} ion. The excitation transition of Tb^{3+} may be either a dipole or a quadrupole transition. The selection rules forbid the dipole transition, so that the oscillator strength is very low and does not differ much from that of the quadrupole transition. Estimates based on the theory show in addition that the probability of a quadrupole transition of Tb^{3+} in the energy transfer from Ce^{3+} to a neighbouring Tb^{3+} ion is much greater than that of a dipole transition of Tb^{3+} [13]. The probability of this energy-transfer process is also greater than the probability of a radiative transition of Ce^{3+} itself. The transfer between Ce^{3+} ions alone is negligible, as appears from the absence of concentration quenching of the fluorescence in phosphors that contain only Ce^{3+}, as mentioned above.

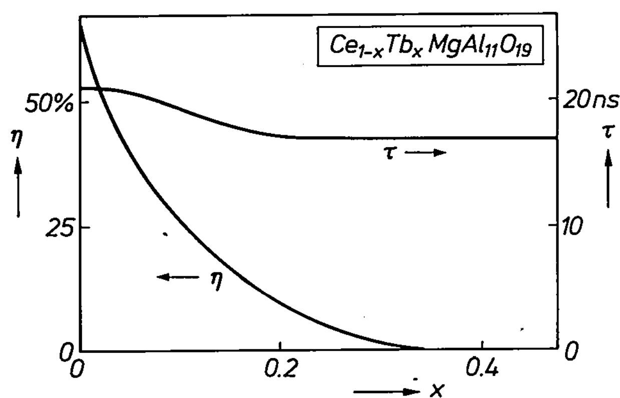

Fig. 13. The decay time τ and the quantum efficiency η of the Ce^{3+} luminescence in $Ce_{1-x}Tb_xMgAl_{11}O_{19}$ as a function of the Tb fraction x.

We can now calculate the manner in which the efficiencies of the Ce and Tb emission of a Ce-Tb phosphor depend on the concentration of Ce^{3+} and Tb^{3+} [11]. The transfer probability in dipole-quadrupole interaction between a Ce^{3+} ion and a Tb^{3+} ion at a distance R apart is proportional to $(1/R)^8$. This means that the energy transfer between next-nearest neighbours in an intermediate layer is $(\sqrt{3})^8$ or 81 times less probable than transfer between nearest neighbours. Transfer between ions in different intermediate layers is even less probable, because of the large distance (1.1 nm). For all these reasons the probability of Ce^{3+} emission in a Ce^{3+}-Tb^{3+} phosphor is determined by the probability that a Ce^{3+} ion will have no Tb^{3+} ion as its nearest neighbour, and the probability of Tb^{3+} emission is determined by the probability that a Ce^{3+} ion will have at least one Tb^{3+} ion as its nearest neighbour. If the amount of Tb^{3+} per formula unit is x, so that $1-x$ is the amount of Ce^{3+}, then these two probabilities are given by $(1-x)^6$ and $1-(1-x)^6$, since each Ce^{3+} ion has six nearest-neighbour sites that may be occupied by Ce or Tb. A plot of these probabilities as a function of x also gives a picture of the quantum efficiencies of the Ce and Tb emission of $Ce_{1-x}Tb_xMgAl_{11}O_{19}$. *Fig. 12* shows a plot calculated in this way of the quantum efficiencies as a function of x; there is good agreement with the experimental findings. Our experiments also show that concentration quenching of the green luminescence by energy transfer between the Tb^{3+} ions alone is of no importance either. The drop in the quantum efficiency of the Tb^{3+} emission at higher x values is due to the limited solubility of Tb^{3+} in the magnetoplumbite lattice.

The behaviour of the decay time τ of the Ce^{3+} emission of $Ce_{1-x}Tb_xMgAl_{11}O_{19}$ as a function of x is shown in *fig. 13*. At first sight it seems strange that τ remains virtually constant whereas there is a marked decrease in the quantum efficiency η of the Ce emission. The efficiency decreases because in addition to the radiative decay of the excited state the competitive possibility arises for non-radiative decay (energy transfer to neighbouring Tb^{3+} ions); as a consequence τ is expected to become smaller [14]. The observed behaviour, however, turns out to be completely in agreement with the model used above to explain the concentration dependence of the quantum efficiencies of the Ce^{3+} and Tb^{3+} emission [15]. To make this clear, we divide the Ce^{3+} ions into two groups; those with at least one Tb^{3+} as nearest neighbour: $^{I}Ce^{3+}$, and those without Tb^{3+} as nearest neighbour: $^{II}Ce^{3+}$. The $^{II}Ce^{3+}$ ions, as we have seen, cannot transfer energy to Tb^{3+} ions, and the only possibility is therefore radiative decay, giving the ultraviolet Ce^{3+} luminescence. The decay time of this luminescence is the same as if there were no Tb^{3+} ions present at all. For the $^{I}Ce^{3+}$ ions the probability of energy transfer to neighbouring Tb^{3+} ions is very much greater than the probability of radiative decay. They therefore give hardly any Ce^{3+} luminescence and consequently have no effect on the decay time of this luminescence. Here again, the constancy of τ reflects the fact that the energy transfer between Ce^{3+} and Tb^{3+} takes place only between nearest neighbours.

The combination Eu^{2+}-Mn^{2+}

It is also found that Mn^{2+} ions, which can occupy an Al^{3+} site in aluminate lattices, can act as activators. From data in the literature it appears that an Mn^{2+} ion at a site tetrahedrally surrounded by oxygen gives a green fluorescence band, and an Mn^{2+} ion at a site octahedrally surrounded by oxygen gives a red fluorescence band. This luminescence corresponds in both cases to a transition between 3d levels; the difference in wavelength is due to a difference in the strength of the crystal field.

The transition between the 3d levels is forbidden by the selection rules, just like the 4f→4f transition in the case of Tb^{3+}. This means that the absorption of excitation energy is small and so also is the luminescence intensity. The light output from the Mn^{2+} phosphors is consequently capable of being improved considerably by the incorporation of sensitizer ions. Both Eu^{2+} and Ce^{3+} ions are suitable for this, because the luminescence bands of these ions sufficiently overlap the excitation band of the Mn^{2+} ion [16]. The result of the

[11] J. L. Sommerdijk and J. M. P. J. Verstegen, J. Luminescence 9, 415, 1974.
[12] See the article by Blasse and Bril [3], p. 327.
[13] J. M. P. J. Verstegen, J. L. Sommerdijk and J. G. Verriet, J. Luminescence 6, 425, 1973.
[14] See the article by Blasse and Bril [3], p. 325.
[15] J. L. Sommerdijk, J. A. W. van der Does de Bye and P. H. J. M. Verberne, J. Luminescence 14, 91, 1976.
[16] A. L. N. Stevels and J. M. P. J. Verstegen, J. Luminescence 14, 207, 1976.

competition between the luminescence of Mn and that of Eu or Ce again depends on the concentrations of the two elements, the distances in the crystal lattice between sensitizer and activator, the absorption and emission spectra and the probabilities of the transitions involved in the transfer. *Fig. 14* shows something of the behaviour of Ba-Mg aluminate phosphors that contain a combination of Eu^{2+} and Mn^{2+} ions. These phosphors exhibit the green emission of Mn^{2+}. At increasing Mn concentrations the intensity of this green emission increases at the expense of the Eu^{2+} emission.

In the β-aluminium-oxide structure of Ba-Mg aluminate the tetrahedrally surrounded sites for an Mn ion — necessary for the green emission — are at a distance of about 0.35 nm from the large-cation sites (*fig. 15*). It appears that at this distance the probability of energy transfer from Eu^{2+} to Mn^{2+} is high and even exceeds that of the radiative transition of Eu^{2+} itself. In the magnetoplumbite structure tetrahedrally surrounded sites for Mn^{2+} are located much farther away from the large-cation sites, and in phosphors with this structure there is consequently no green Mn^{2+} emission. The sites that are octahedrally surrounded by oxygen and are close to the large cation in the magnetoplumbite structure are evidently not occupied by Mn ions, because the red emission characteristic of Mn ions at sites of this kind is not observed either.

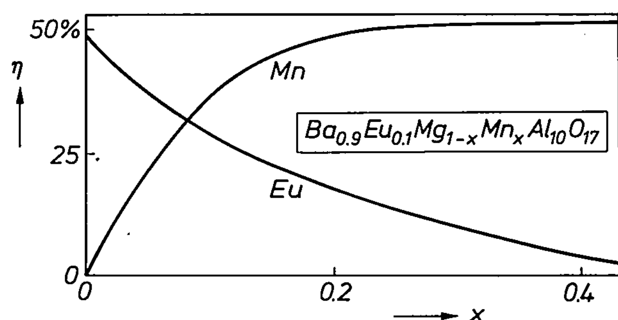

Fig. 14. Quantum efficiency η of the Mn^{2+} luminescence and the Eu^{2+} luminescence of $Ba_{0.9}Eu_{0.1}Mg_{1-x}Mn_xAl_{10}O_{17}$ as a function of the Mn fraction x.

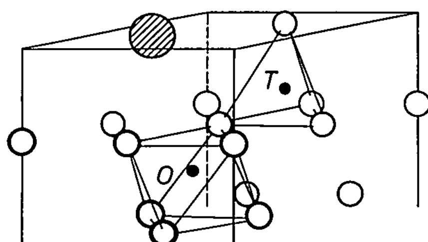

Fig. 15. The surroundings of a large cation in the upper plane of a unit cell with the β-aluminium-oxide structure. In the immediate neighbourhood there are two small-cation sites, which are surrounded tetrahedrally (T) and octahedrally (O) by oxygen atoms. These sites are occupied not only by Al^{3+} but also by any Mn^{2+} that may have been added. The green luminescence indicates that the Mn^{2+} ions preferentially occupy the tetrahedrally surrounded sites.

In lanthanum aluminates, even though the structure closely resembles magnetoplumbite, green emission is nevertheless observed from the Eu-Mn combination. This effect seems to be related to the presence of oxygen ions that occupy a small number of the large-cation sites to compensate for the trivalence of lanthanum. The result is a lattice deformation that leads to sites tetrahedrally surrounded by oxygen in the immediate neighbourhood of positions that can be occupied by Eu^{2+}. *Fig. 16* shows a possible configuration. It can be seen that Mn^{2+} ions prefer to occupy such sites, which are not found in the ordinary magnetoplumbite structure. The Eu-Mn distance in these cases is very small (0.32 nm) and makes possible an energy transfer that is even more efficient than in the β-aluminium oxides. The introduction of some lanthanum in aluminates with nearly ideal magnetoplumbite structure again creates tetrahedrally surrounded sites for Mn (due to oxygen on large-cation sites). The combination La-Eu-Mn, added to $SrAl_{12}O_{19}$ for example, therefore results in a green-emitting phosphor when the La and Mn concentrations are sufficiently high.

In La aluminate there are only a limited number of oxygen ions occupying a large-cation site. Consequently, for Mn^{2+} ions there are relatively few sites close enough to Eu^{2+} ions for green Mn^{2+} luminescence to be possible. As a result, above a particular Mn concentration there is no further increase in the green emission; however, as appears from curve a in *fig. 17* the red luminescence characteristic of Mn^{2+} ions octrahedrally surrounded by oxygen does appear. This band is also related to the occurrence of oxygen on large-cation sites; details will not however be given here. It is found that when the Mn concentration is increased the red band increases in intensity and finally predominates. It is interesting to note that, given suitable Eu and Mn concentrations, a phosphor can be made in this way that emits bands of comparable intensity in the blue (Eu^{2+}), the green (Mn^{2+}) and the red (Mn^{2+}). Curve b in fig. 17 shows the emission spectrum of such a phosphor.

It is also possible to use Ce^{3+} as a sensitizer for the green Mn emission. In lattices with the β-aluminium-oxide structure the behaviour of Ce^{3+} does not differ in this respect from that of Eu^{2+}. In lattices with the magnetoplumbite structure it is an advantage that the Ce^{3+} ions themselves provide for the appearance of the oxygen ions at the large-cation sites, so that suitable sites become available for the Mn^{2+} ions. The addition of lanthanum, as with Eu^{2+}, is not necessary here. The properties of the Ce^{3+}-Mn^{2+} phosphors do not differ fundamentally from those of the Eu^{2+}-Mn^{2+} phos-

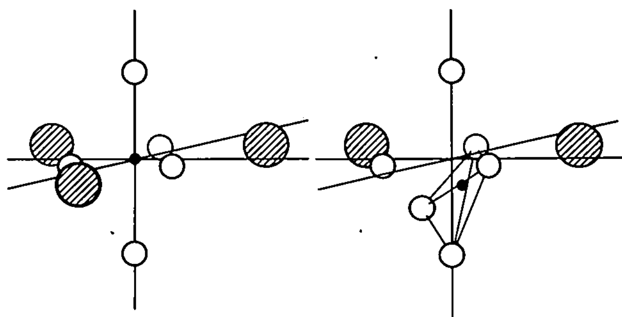

Fig. 16. *Left:* The surroundings of a small cation at a corner of the unit cell of the magnetoplumbite structure. The small cation is surrounded by five oxygen ions and three large cations. *Right:* If an oxygen ion is substituted for one of the large cations, deformation of the crystal lattice may occur, producing a site tetrahedrally surrounded by oxygen ions.

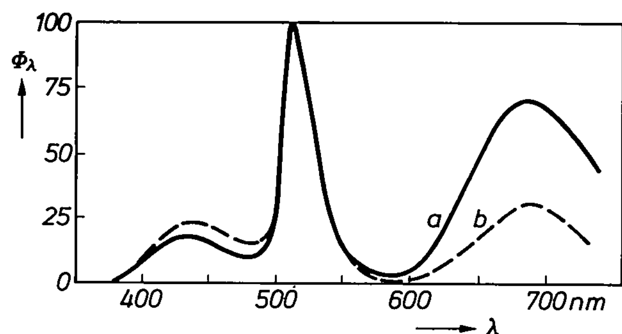

Fig. 17. Luminescence intensity Φ_λ as a function of the wavelength λ for lanthanum aluminate activated with Eu^{2+} and Mn^{2+}. The Mn^{2+} concentration is raised to a level at which, in addition to the green luminescence characteristic of Mn^{2+} ions tetrahedrally surrounded by oxygen, red luminescence also occurs which is characteristic of Mn^{2+} ions octahedrally surrounded by oxygen (curve *a*). Given a suitable choice of Eu and Mn concentration, a phosphor can be obtained which emits blue, green and red luminescence bands, with the intensity of each nearly the same (curve *b*).

phors. Since the energy transfer between Ce^{3+} ions alone is less efficient than that between Eu^{2+} ions, the energy transfer in Ce^{3+}-Mn^{2+} phosphors will in general be less efficient than in the Eu^{2+}-Mn^{2+} phosphors.

The investigation into the luminescent properties of Eu and Ce aluminate phosphors described above was important in two respects. It provided a better understanding of the luminescent properties and of the practical limits of technologically useful phosphors. It also enabled us to study a number of systems that did not promise the development of phosphors of high efficiency, but which were found to be particularly suitable for providing fundamental knowledge relating to luminescence effects.

Summary. A number of phosphors that have been developed for use in fluorescent lamps consist of aluminates, activated with Eu^{2+} or Ce^{3+}, either alone or combined with Tb^{3+} or Mn^{2+}. The colour and efficiency of the luminescence of these phosphors is dependent on the structure of the aluminate lattice. The crystal field at the sites of the luminescing ions and also the interaction between these ions and neighbouring oxygen ions are found to be of importance; other important factors are the dimensions of the other large cations and the difference in valency between the luminescing ion and the ion that it replaces in the lattice. In Eu^{2+} phosphors the efficiency is very dependent on the activator concentration, but in Ce^{3+} phosphors there is very little such dependence, because of the small energy transfer between the Ce^{3+} ions. This also means that the Ce-Tb phosphors have to contain a relatively large amount of Tb to give a strong green Tb luminescence. The energy transfer in Eu-Mn phosphors is more complicated; these phosphors sometimes give red luminescence as well as green.

Philips tech. Rev. 37, 234-236, 1977, No. 9/10

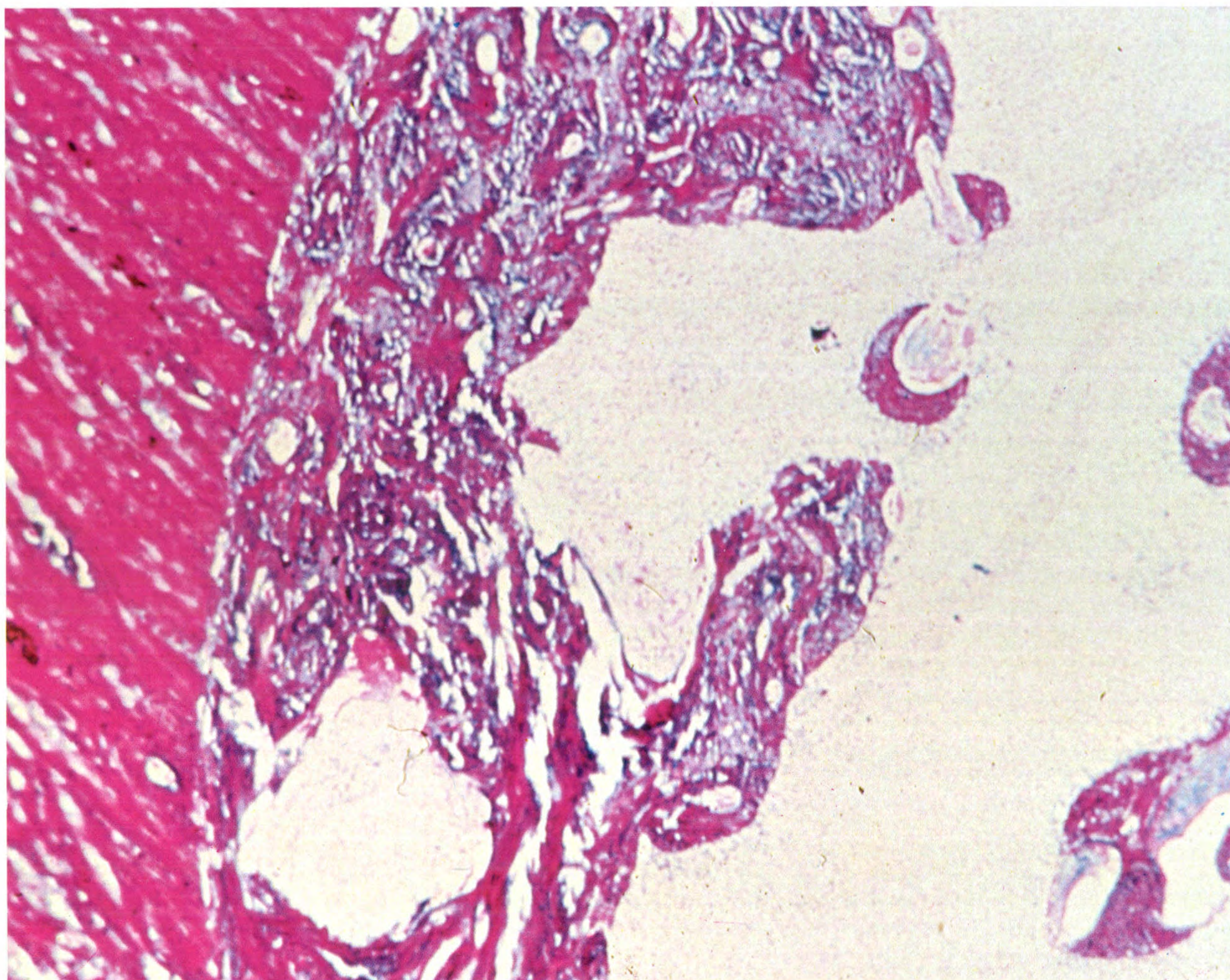

Sintered hydroxylapatite as a bioceramic

Ever since the birth of their profession surgeons have sought a material that could replace missing parts of the human skeleton. Through the centuries many materials have been tried, with varying degrees of success. Although there are now a number of metals, types of ceramic and plastics that are reasonably effective, no material ideal in all respects has been found. We believe, however, that we have found a material that gives a significant step in the right direction.

A material to be used as a substitute for bone in the body has to satisfy three requirements. First of all, it must be biologically compatible. The material must not cause rejection reactions, in which the implant is encapsulated in a layer of connective tissue and rejected by the body. It is an advantage here if the material is biodegradable, i.e. can be broken down by the body and then replaced by new bone, like natural bone tissue. The implant can then take part in the dynamic equilibrium of breakdown and regeneration in which nearly all tissues in the human body participate. A material that meets this requirement is hydroxylapatite, $Ca_5(PO_4)_3OH$, the phosphate found in natural bone tissue. Experiments have been carried out for some years and at various places on this basic material, which can be processed by the usual ceramic-sintering techniques [1].

A second requirement relates to the structure of the material from which an implant is made. It has been found that bone tissue grows successfully into pores of an implant when the pores have a diameter of more than 100 μm [2]. It is necessary for bone tissue to grow into the implant to ensure rapid and firm adherence to the surrounding bone.

The third requirement relates to the mechanical properties. In nearly all applications the implant should ideally have about the same strength as the bone it is to

replace. This requirement rather contradicts the previous one. The strength of sintered hydroxylapatite, like that of any other ceramic, decreases as the porosity increases, and pores of the desired size will in general only occur in very porous material.

Control of the porosity during the sintering of hydroxylapatite is therefore of the utmost importance if the material is to be used as a bone substitute. We have developed a method that results in only two types of pores, the desired 'macropores' and very small pores, called 'micropores' [3]. The total porosity is then not unduly high, so that the material is reasonably strong.

In this method of preparation, hydroxylapatite powder with a grain size of 1-2 μm is mixed with water, and hydrogen peroxide is added to the resultant slurry. The mixture is poured into a mould and heated slowly. As the mixture heats up the hydrogen peroxide decomposes, and small oxygen bubbles, which will become the macropores, are produced homogeneously distributed throughout the slurry. After the material has completely dried out, it is sintered at a temperature of 1100-1300 °C [4].

In a particular case the final material had a macroporosity of 20 vol. %; the pores were interconnected and had a diameter of 150-250 μm. The microporosity was relatively small — it is also 20 vol. % — with pore diameters between 0.5 and 1.5 μm.

The microporosity can be controlled by varying the conditions of the preparation process, e.g. the sintering time and temperature. The hydrogen-peroxide content of the slurry and the heating (drying) rate affect the macroporosity. *Fig. 1* shows the effect of two of these quantities on the total porosity. *Table I* quotes figures relating to the strength of sintered hydroxylapatite prepared as described, compared with figures for human bone. The compressive strength of the sintered hydroxylapatite is substantially better here than has previously been reported in the literature. The values we have measured correspond well to those for bone; as can be seen from *fig. 2*, they depend strongly on the porosity of the material. The impact strength and the bending strength, which are not usually very high for ceramic materials, are two or three times lower for the sintered material than for bone. As *fig. 3* shows for the impact strength, these values are also highly dependent on the porosity. The impact strength and bending strength of bone are better because bone is a composite of hydroxylapatite and collagen. Experiments are now under way that are directed towards the improvement of both the bending strength and the impact strength of sintered material by impregnating it with a suitable biodegradable plastic.

Investigations have been made to determine the biological compatibility of our sintered hydroxyl-

Table I. The strengths of sintered hydroxylapatite compared with those of ordinary human bone. The widely different values given for human bone relate to bone ranging from spongy to compact. Differences in method of preparation account for the variation in the figures for hydroxylapatite.

	Hydroxylapatite	Human bone
Compressive strength	30-170 MN/m²	40-160 MN/m²
Impact strength	0.29 Nm	0.5 Nm
Bending strength	35 MN/m²	100 MN/m²

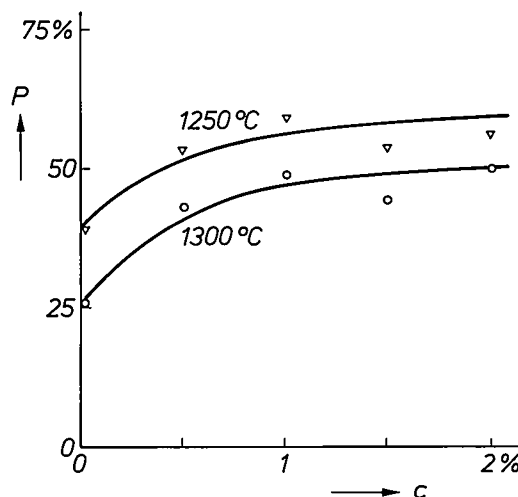

Fig. 1. Total porosity P, expressed in volume percentages, of sintered hydroxylapatite as a function of the hydrogen-peroxide concentration c in the slurry, for two sintering temperatures.

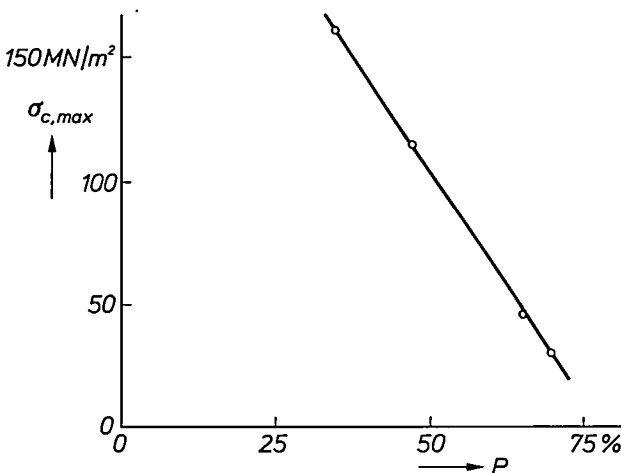

Fig. 2. The compressive strength $\sigma_{c,max}$ of sintered hydroxylapatite as a function of the porosity P.

[1] S. N. Bhaskar, J. M. Brady, L. Getter, M. F. Grower and T. Driskell, Oral Surg. **32**, 336, 1971.
E. Karbe, K. Köster, H. Kramer, H. Heide, G. Kling and R. König, Langenbecks Arch. Chir. **338**, 109, 1975, and **341**, 77, 1976.
M. Jarcho, C. H. Bolen, M. B. Thomas, J. Bobick, J. F. Kay and R. H. Doremus, J. Mat. Sci. **11**, 2027, 1976.
[2] J. J. Klawitter, Ph. D. thesis, Clemson University, Clemson (South Carolina) 1970.
J. J. Klawitter and S. F. Hulbert, J. biomed. Mat. Res., Symp. No. 2, Part 1, 161, 1971.
[3] E. Ryshkewitch, J. Amer. Ceram. Soc. **36**, 65, 1953.
[4] J. G. J. Peelen, B. V. Rejda and K. de Groot, Ceramurgia Int., to be published shortly.

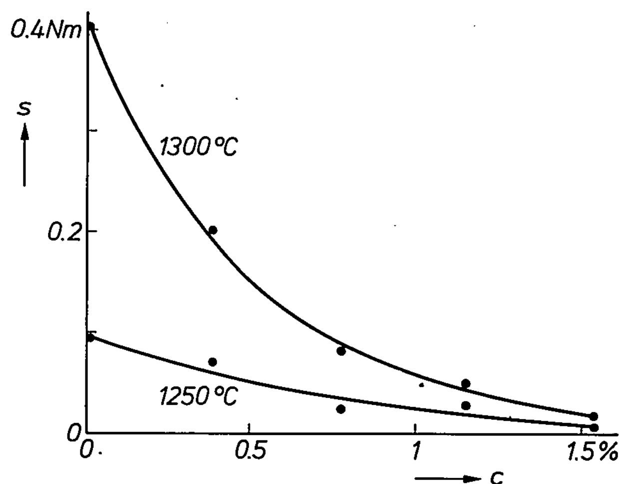

Fig. 3. The impact strength s of sintered hydroxylapatite as a function of the hydrogen-peroxide concentration c in the slurry from which the material is prepared.

apatite [5]. Small cylinders of the material were implanted in the tibia (the shinbone) of young rabbits; one to six months after implantation the rabbits were killed and the implants were removed together with the surrounding bone tissue, fixed and processed into histological specimens for microscopic examination. One month after implantation the implant has become surrounded by loose-meshed scar tissue, which has already been replaced here and there by bone tissue. In the later stages this tissue has disappeared and has been completely replaced by bone tissue. In all cases it was found that the implant was fully accepted by the body. The bone tissue grows into the pores of the ceramic. At the interface the implant is broken down and osteoblasts form new bone. The title photograph is a photomicrograph of the situation after two months. The original bone tissue is on the left; the new bone tissue that has partially replaced the implant in the meantime is in the middle of the picture. At the boundary between those regions — which still shows the implant surface clearly — there are no traces of connective tissue. The light-coloured region on the right is the remaining part of the implant. Pores in this region have been enlarged; they now contain blood vessels and cells that take part in the formation and breakdown of bone tissue. After six months the implanted material has mostly disappeared and new bone has taken its place.

We may therefore conclude that the sintered hydroxylapatite is a highly successful biocompatible implant material. Mechanically it is certainly suitable for use at places where the stresses are mainly compressive. We have in mind, for example, its use for filling jaw cavities caused by the removal of growths, or for filling jaw irregularities after dental extractions. In both cases a reasonably well formed implant can be made from specifications given by the surgeon (dimensional deviations can be kept below five per cent). During implantation the shape can be finished with a conventional dental drill. There is every indication that plastic-impregnated sintered hydroxylapatite, which closely approximates to healthy bone in terms of bending strength, will be of increasing interest as a substitute for bone.

J. G. J. Peelen
B. V. Rejda
J. P. W. Vermeiden

[5] B. V. Rejda, thesis, Free University of Amsterdam 1977.
B. V. Rejda, J. G. J. Peelen and K. de Groot, J. Bioengng. 1, 93, 1977.

Dr J. G. J. Peelen, formerly with Philips Research Laboratories, Eindhoven, is now with the Philips Glass Division, Eindhoven. Dr Ir B. V. Rejda and Dr J. P. W. Vermeiden are with the Dental Subfaculty of the Free University of Amsterdam.

Light-emitting diodes based on GaN

M. Boulou, M. Furtado and G. Jacob

Light-emitting diodes (LEDs) are frequently used today in solid-state light sources. The basic material used in these consists of the III-V semiconductors GaAsP and GaP. The colour of the light emitted from GaAsP and GaP is red, orange, yellow or green; blue cannot be obtained. A blue luminescence can however be obtained from GaN, but until recently this material seemed unsuitable for light sources, since a P-N junction cannot be introduced into it. Nevertheless, investigators at LEP (Laboratoires d'Electronique et de Physique Appliquée, Limeil-Brévannes) have demonstrated that GaN diodes made by using a special method luminesce with a reasonable efficiency.

Introduction

Diodes based on single crystals of III-V semiconductors, such as GaAsP, GaP and also GaN, may emit visible light with reasonable efficiency when an electric current is passed through them [1]. Light-emitting diodes (LEDs) based on GaAsP and GaP are now widely used in applications such as pocket calculators, watches and indicator lamps. The light from these diodes is generated by the recombination of electrons and holes, which are injected from the *N* and *P* layers into the opposite layer by the application of an electric field. The colour of the emitted light depends on the composition of the *N* and *P* layers. For example red, orange and yellow can be obtained with GaAsP and GaP and green can be obtained from GaP. The photon energy, however, can never be greater than the energy difference between the conduction and valence bands of the semiconductor. In GaAsP and GaP this band gap is therefore too small to permit blue emission.

Unlike GaAsP and GaP, the semiconductor GaN has a band gap sufficiently large for it to be used as a blue-emitting light source; the band gap for this material is 3.5 eV. With suitable dopants, any other desired emission colour can be obtained from GaN in addition to blue. Unfortunately, however, it has not yet been possible to produce ordinary diodes consisting of *N*- and *P*-type layers from GaN. This is because no one has yet succeeded in making a *P*-type semiconductor from GaN. Nevertheless, it has been found possible to obtain electroluminescence by substituting a high-resistance layer for the *P* layer [2]. By making this high-resistance layer very thin and preparing it under carefully controlled conditions, we have been able to make a number of GaN diodes that give blue, green or yellow luminescence with reasonable efficiency.

In this article we shall look at the preparation and doping of single-crystal GaN layers. Only Zn dopants will be discussed, since these give the best results and have also been the most widely investigated. We shall then touch briefly on the technology and characteristics of the GaN diodes.

Preparation and doping of GaN layers

The preparation of GaN layers takes place from the gas phase [3]. Hydrogen-chloride gas is passed over liquid gallium metal at 850 °C, so that gaseous GaCl is produced. This gas is brought into contact with am-

Ing. M. Boulou, M. Furtado, M.Sc., and Ing. G. Jacob are with the Laboratoires d'Electronique et de Physique Appliquée (LEP), Limeil-Brévannes (Val-de-Marne), France.

[1] This effect — known as electroluminescence — was first investigated for SiC crystals by O. W. Lossew, Telegrafia i Telefonia **18**, 61, 1923. The *P-N* luminescence of gallium phosphide is described in H. G. Grimmeiss and H. Koelmans, Philips tech. Rev. **22**, 360, 1960/61 and H. G. Grimmeiss, W. Kischio and H. Scholz, Philips tech. Rev. **26**, 136, 1965. More general information on light-emitting diodes can be found in the book by C. H. Gooch, Injection electroluminescent devices, Wiley, London 1973. There have also been two review articles by R. N. Bhargava, one in Philips tech. Rev. **32**, 261, 1971, and the other in IEEE Trans. **ED-22**, 691, 1975. See also the book by J. I. Pankove (ed.), Electroluminescence, Springer, Berlin 1977.

[2] Although light sources based on GaN have no *P* layer, they are referred to for convenience as diodes. They were first reported by J. I. Pankove, e.g. in J. Luminescence **7**, 114, 1973. His diodes worked only at a relatively high voltage (> 10 V) and there was no clear relation between the preparation conditions and the emission colour.

[3] The preparation method used was first described by H. P. Maruska and J. J. Tietjen, Appl. Phys. Lett. **15**, 327, 1969. A detailed description of the preparation of GaN layers can be found in a recent article by R. Madar, D. Michel, G. Jacob and M. Boulou, J. Crystal Growth **40**, 239, 1977.

monia gas at 950 °C to form GaN. The reaction equations are:

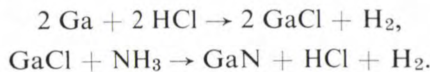

$$2\,\mathrm{Ga} + 2\,\mathrm{HCl} \rightarrow 2\,\mathrm{GaCl} + \mathrm{H_2},$$
$$\mathrm{GaCl} + \mathrm{NH_3} \rightarrow \mathrm{GaN} + \mathrm{HCl} + \mathrm{H_2}.$$

The GaN thus formed is deposited as a hexagonal, single-crystal layer on a sapphire substrate. The material is doped with zinc by adding zinc vapour to the reaction mixture. This vapour is formed by heating the metal to 550 °C in a stream of nitrogen. The nitrogen acts as a carrier for the zinc vapour and also for HCl and GaCl. *Fig. 1* is a diagram of the reactor in which the GaN layers are made.

Undoped GaN is a fairly good electrical conductor. Its resistivity is about 10^{-3} Ωcm, which is very low for a semiconductor. Its surplus of electrons, which makes it an N-type semiconductor, is probably due to partial dissociation through the reaction

$$2\,\mathrm{GaN} \rightarrow 2\,\mathrm{Ga} + \mathrm{N_2}.$$

This produces nitrogen vacancies in the GaN lattice and these can act as electron donors. The number of free electrons in undoped GaN is about 3×10^{19} per $\mathrm{cm^3}$. If the GaN is now doped with Zn, it remains an N-type semiconductor but the number of free electrons decreases. The mobility of these electrons is also reduced, so that the resistivity rises rather steeply. The rise in resistivity is particularly large if there is little or no additional HCl in the reactor during the preparation. We have prepared layers in this way with a resistivity of 10^6 Ωcm; this value is no less than 10^9 times higher than that of the undoped material.

The luminescence of GaN depends critically on the preparation conditions, in particular on the partial pressures of Zn, additional HCl and GaCl. As an example, *fig. 2* shows the change of luminescence with cathode-ray excitation on increasing the partial pressure for zinc. The intensity of the luminescence decreases strongly and the successive emission colours are blue, green, yellow and red. Layers that are good conductors always give a blue emission, whereas layers of high resistivity luminesce blue, green or yellow, depending on the partial pressure of Zn, GaCl and additional HCl during the preparation.

GaN diodes

The diodes we have developed consist of three distinct GaN layers — N^+, N and π — which are deposited in this order on a sapphire substrate (*fig. 3*). The N^+ layer is not doped and thus has a low resistivity. This layer is connected by an indium contact to the negative terminal of the direct-voltage generator. The N layer is doped with Zn but its resistivity is relatively low, 10 Ωcm. The π layer [4] is much thinner than the other two layers and is doped with sufficient Zn to produce a very high resistivity (10^6 Ωcm). This layer is connected to the positive pole of the voltage generator by a gold contact [5].

Fig. 4 is a diagrammatic illustration of the most probable origin of the light emission in such diodes. When an external field of sufficient strength is applied,

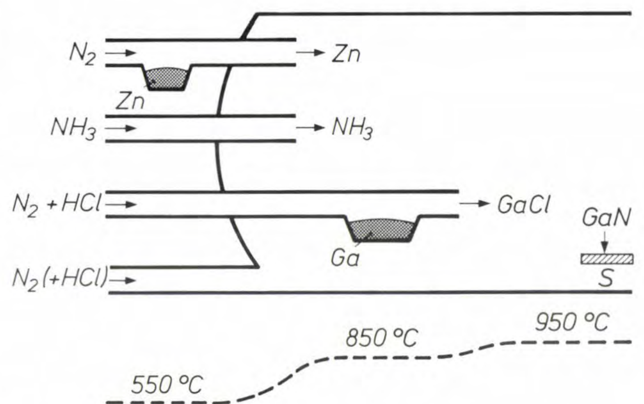

Fig. 1. Reactor for the preparation of single-crystal GaN layers on a sapphire substrate S at a total gas pressure of about 10^5 Pa (1 atm). The temperature profile inside the reactor is shown in the lower part of the figure.

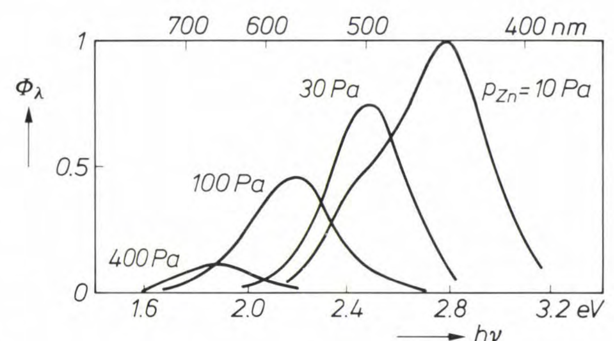

Fig. 2. Emission spectra of GaN on excitation with electrons, as a function of the Zn partial pressure (p_{Zn}) during preparation. The partial pressure of GaCl is 500 Pa and there is no additional HCl. Φ_λ denotes the relative emission intensity in arbitrary units. The maximum of the blue emission is set equal to 1.

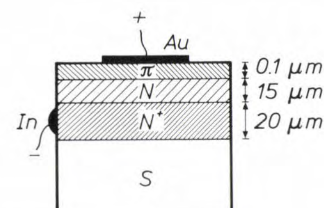

Fig. 3. Diagrammatic section of a GaN diode. N^+ undoped GaN (resistivity about 10^{-3} Ωcm). N Zn-doped GaN with a resistivity of 10 Ωcm. The surface of this layer is flat and transparent, unlike that of the N^+ layer. π GaN doped with sufficient Zn to produce a very high resistivity (10^6 Ωcm). S sapphire substrate. In indium contact. Au gold contact. The area of the diode is about 1 $\mathrm{mm^2}$.

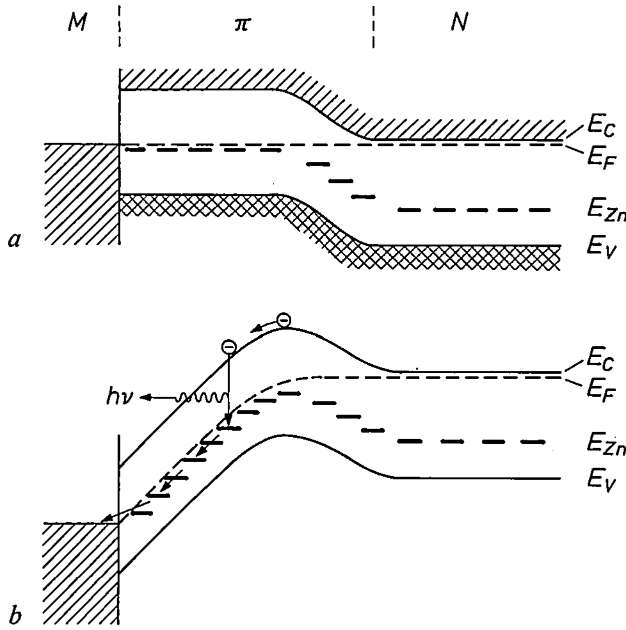

Fig. 4. Schematic diagram illustrating the generation of light in GaN diodes. *a*) Energy-level diagram when no voltage is applied. *M* metal contact. E_V and E_C valence and conduction bands of GaN. E_F Fermi level. E_{Zn} zinc levels. *b*) Energy-level diagram when a voltage is applied. When the electric field is strong enough, electrons from the Zn levels enter the metal. The remaining holes jump in the opposite direction from one Zn atom to another. Electrons originating from the *N* layer recombine with these holes, causing the emission of quanta of visible light.

layer into the π layer will be able to recombine there with the holes, resulting in the emission of visible light. Because the migration of holes in the π layer requires a high electric field, and because the external voltage should not be too high, the π layer must be thin (fig. 3).

It can be shown that the light does indeed originate from the π layer and not from the *N* layer by exciting these layers separately. This can be done by bombarding a diode with electrons. Incident electrons of high energy penetrate so deep into the diode that they mostly excite the *N* layer, whereas electrons of low energy get no further than the π layer. If it is mainly the *N* layer of a green electroluminescent diode that is excited, the emitted light is not green, but blue (*fig. 5*). If, however, the π layer alone is excited, the emission band corresponds almost exactly to that of the electroluminescence. If both are excited simultaneously, both the blue and the green emission bands are observed.

Finally, we shall consider the most important characteristics of the diode for our purposes, i.e. emission colour and the external quantum efficiency defined as the ratio of the number of photons emitted to the number of injected electrons. The emission colour is determined by the composition of the π layer, since the light is generated in this layer. As we noted earlier the emis-

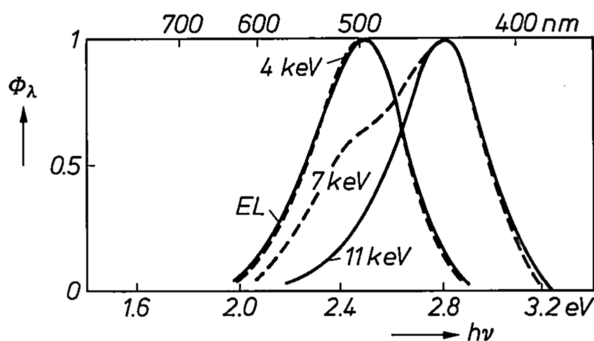

Fig. 5. Emission spectra of the electroluminescence (*EL*) of a GaN diode compared with the emission spectra of the same diode on excitation with electrons of different energy. When the energy of the electrons is low (4 keV), it is mainly the π layer that is excited. In this case the spectrum almost coincides with that of the electroluminescence, corresponding to the model of fig. 4. The maximum of each spectrum is set equal to 1.

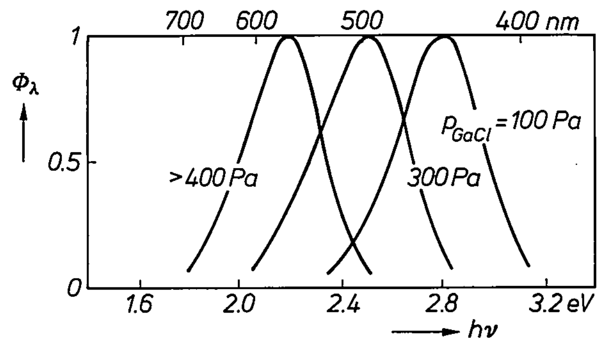

Fig. 6. Emission spectra of the electroluminescence of three different GaN diodes. The π layers of these diodes were prepared with different GaCl partial pressures (p_{GaCl}). The maxima of the spectra are again set equal to 1. The π layers were prepared without additional HCl, the *N* layers with a surplus of HCl at 3000 Pa. The partial pressure of Zn during the preparation of the *N* and π layers was 100 Pa.

electrons go from the N^+ layer to the *N* layer and thence to the π layer. On the other side, electrons can also flow from the π layer into the metal, provided the external field is high enough. These electrons will originate mainly from the Zn atoms, in the proximity of the metal, whose energy levels lie in the forbidden region. The removal of electrons from the Zn atoms may be regarded as an injection of holes into these atoms. The holes can then distribute themselves among the various Zn atoms. Electrons expelled from the *N*

sion colour from such a high-resistivity layer depends on the partial pressures of Zn, GaCl and additional HCl during the preparation. The same dependence is therefore observed in the finished diodes (*fig. 6*). When

[4] The term π layer is used to indicate that this layer takes over the role of the *P* layer in normal *P-N* junction diodes.

[5] Further details, in particular of the electrical characteristics of the diodes, are given in G. Jacob, R. Madar and J. Hallais, Mat. Res. Bull. 11, 445, 1976, G. Jacob and D. Bois, Appl. Phys. Lett. 30, 412, 1977, and G. Jacob, M. Boulou and M. Furtado, J. Crystal Growth 42, 136, 1977.

the π layer is prepared with a relatively low partial pressure of GaCl, the diode gives a blue luminescence. If the partial pressure of GaCl is higher, the luminescence is green or yellow.

The external quantum efficiencies of the diodes emitting green or yellow light are a little better than those of GaAsP and GaP diodes: 10^{-3} to 10^{-2}. However, these GaN diodes require a relatively high operating voltage (5-20 V), which makes them less suitable for practical applications. GaN diodes with blue emission can operate at 3.5 V, which is an acceptably low voltage for practical purposes. Unfortunately the efficiencies of these diodes are relatively low (of the order of 10^{-4}). The efficiencies will have to be improved by at least a factor of 10 if these devices are to be extensively employed.

Summary. GaN is a III-V semiconductor with a band gap large enough to give blue luminescence. Light-emitting diodes based on GaN cannot, however, be produced in the same manner as GaAsP and GaP diodes. This is because a *P*-type semiconductor, and hence a *P-N* junction, cannot be made from GaN. In the GaN diodes described here the place of the *P* layer has been taken by a very thin π layer, which is given a high resistivity by suitable Zn doping. By means of an electric field, holes are injected into this layer through a metal contact and electrons are injected through a contact with a conducting GaN layer. Recombination of these electrons and holes causes the emission of visible light. The luminescence from the diodes is either blue, green or yellow, depending on the preparation conditions. The diodes emitting yellow and green have reasonably high external quantum efficiencies (10^{-3}-10^{-2}) but they require an operating voltage of at least 5 V. The diodes with blue emission operate at only 3.5 V, but their efficiencies (10^{-4}) are not yet high enough for practical applications.

Real-time macro- and microthermography

C. Hily, J. J. Hunzinger, M. Jatteau and J. Ott

Although the basic principle of infrared thermography is the same as for infrared viewing, the great difference is that it is a quantitative and much more rigorous technique. In thermography the image produced must be an accurate reproduction of the local variations of the surface temperature, and the technical means must be available that will permit an accurate analysis of the thermal effects observed. The description 'real-time' implies that changes in the temperature differences are observed immediately, e.g. on a display screen. The thermographic equipment developed earlier at LEP (Laboratoires d'Electronique et de Physique Appliqué), mainly for medical applications, had a minimum focusing distance of about 1 m. Optical devices have now been added to this equipment to bring it within the macro and micro ranges (focusing distances of 150 mm and 12 mm).

In real-time thermography the desired result is a visible image of the exact distribution of the surface temperature of the object at any instant. Such an image is produced by making use of the infrared radiation emitted by each element of the surface. The method requires a number of technical devices for analysing the thermal effects observed. The problems encountered here are those inherent in the passive detection of the weak infrared radiation emitted by the object, and solutions for them have been found in infrared thermography for medical applications [1-3]. In macro- and microthermography, where magnified images of small to very small fields of view have to be produced, similar problems are encountered, in addition to more specific problems. Here again, the thermographic equipment developed at LEP, used with an external optical system for each of these focusing ranges, offers the appropriate technical solutions.

The problems encountered

Very briefly, the operation of infrared thermography is as follows. Some of the infrared radiation emitted from the various surface elements of an object is captured by a detector used in conjunction with optical systems and the resultant spatially varying signal is then converted into visual information. This information can be presented in various ways, depending on the signal-processing method.

The detection of the small differences in the emitted infrared radiation is far from simple [4]. The 'thermal' contrasts corresponding to a deviation of 0.1 °C from room temperature are extremely small, typically no more than a few times 10^{-4}. In addition, the relation between the detected signal and the desired information (e.g. the true temperature) is determined by many factors that are not known exactly, such as the directional dependence of the emissivity and reflectivity, the radiation characteristics of the environment, etc.

In addition to these difficulties there are certain specific problems in both macro- and microthermography, which arise because of the use of optical systems with a very wide aperture, the relatively large field of view and the low value of the transfer function. This means, for example, that owing to the relatively long wavelength of the detected radiation (spectral ranges of the order of 5 μm and 10 μm) the spatial resolution is determined by the diameter of the diffraction ring (10 μm and 20 μm respectively). The thermal resolution is closely related to the product of the picture repetition rate and the number of picture elements that can be discriminated [1]. For example, with an object

Ing. C. Hily, Ing. J. J. Hunzinger, Ing. M. Jatteau and Ing. J. Ott are with Laboratoires d'Electronique et de Physique Appliquée (LEP), Limeil-Brévannes (Val-de-Marne), France.

[1] M. Jatteau, Acta Electronica **12**, 21, 1969.
[2] M. Jatteau, Philips tech. Rev. **30**, 278, 1969.
[3] P. Wurtz, Acta Electronica **12**, 339, 1969.
[4] M. Jatteau, in: Thermography, Proc. 1st Eur. Congr., Amsterdam 1974, p. 9 (published by Karger, Basel 1975).

element of 100 μm² the thermal resolution when a fast scanning microscope (one picture per second or more) is used is no better than 1 °C.

1. With 'fixed-point microscopes' a small area of an object can be viewed while at the same time the infrared radiation from this area is focused on to a point-type

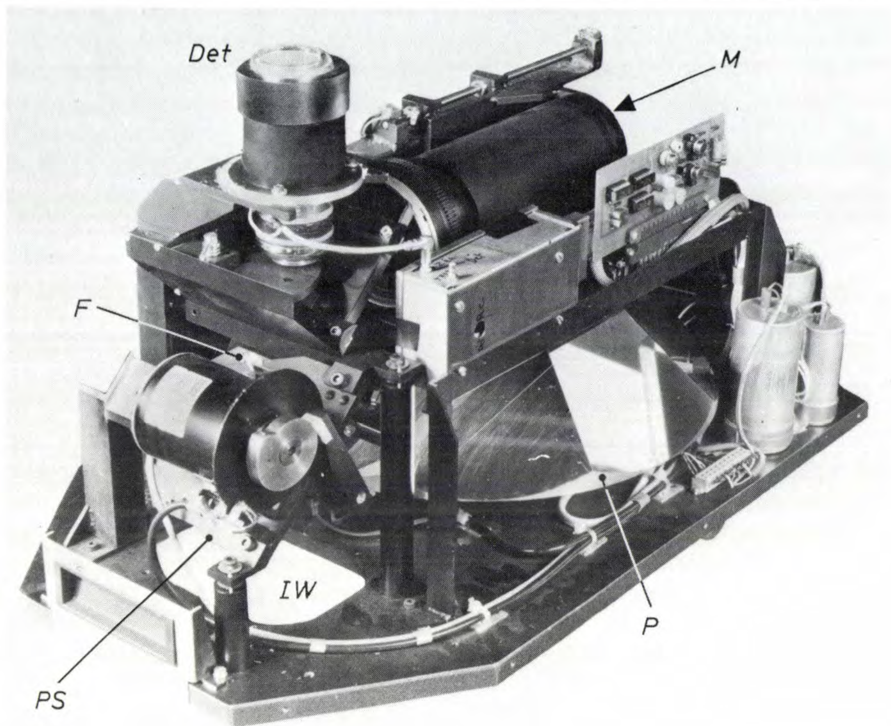

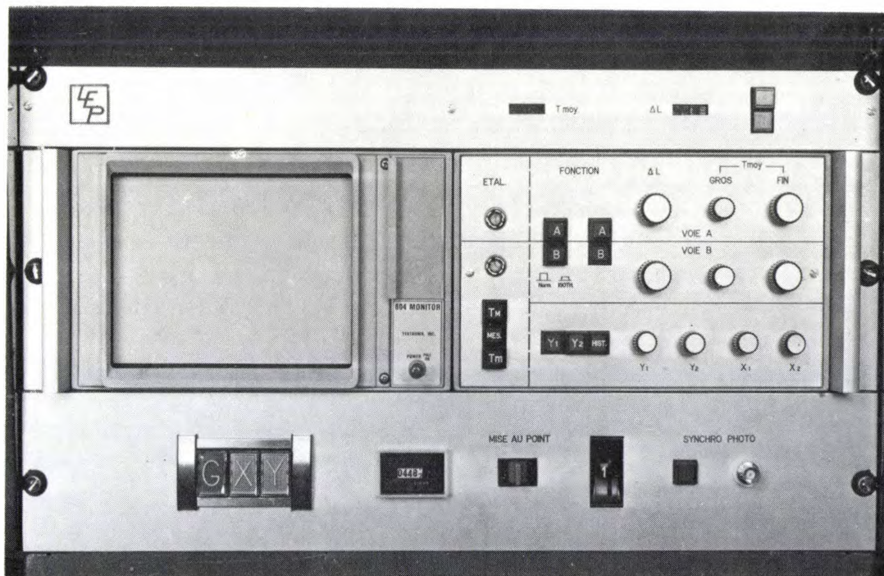

Fig. 1. The infrared camera (*above*) and the signal-processing equipment. *IW* input window. *PS* position sensor. *F* mirror for picture scan. *P* rotating pyramidal drum. *M* focusing mirror. *Det* cooled infrared detector.

Instruments for microthermography

The instruments used for infrared microthermography can be roughly divided into three groups: 'fixed-point microscopes' (1), microscopes with optomechanical scanning systems (2) and infrared cameras with external optical systems (3).

infrared detector. The detector signal is amplified and read off or recorded. Various types of these microscopes are commercially available; the detector is either a thermistor bolometer [5] or a cooled photon detector [6]. With instruments of this type it is possible to cover fields of view ranging from a few centimetres to

10 μm; the thermal resolution is 0.1 °C. Although these microscopes are essentially designed for the thermal study of a fixed object area, they can also be used for drawing a 'thermal map'; this is done by displacement of the object in steps, either by hand or automatically, that are known to an accuracy of better than 1 μm. A serious drawback, however, is that it takes from one to three hours to make such a map. This category also includes thermal monitors of the type in which glass fibres transport infrared radiation from a fixed point on the object to a detector some distance away [7]. These monitors were developed for process control in thermocompression bonding.

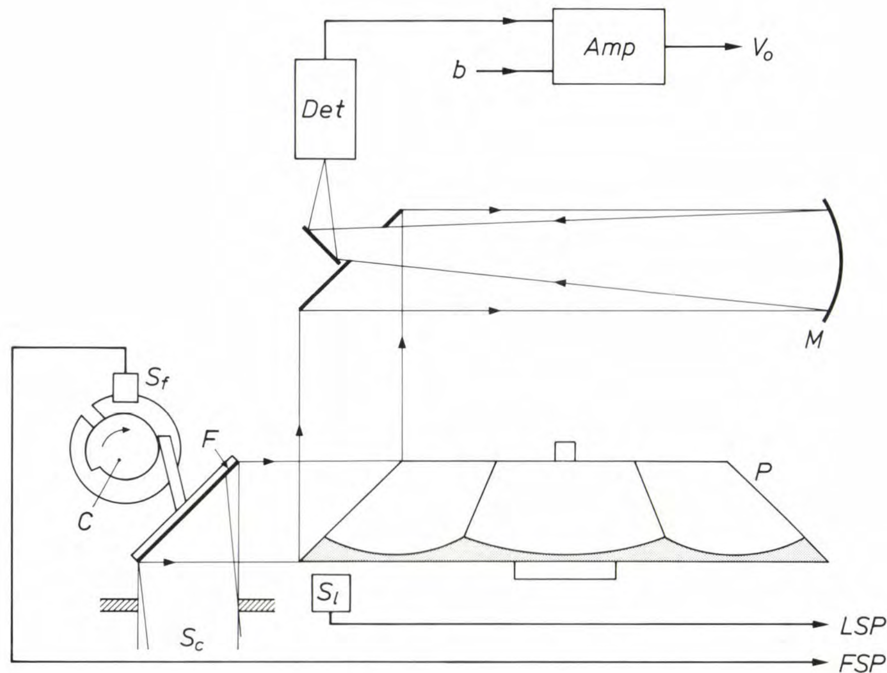

Fig. 2. Diagram of the infrared camera with the optomechanical scanning. *F* planar mirror for the picture scan; the mirror is periodically tilted by the rotating cam *C*. *P* rotating pyramidal drum with eight reflecting planes for the line scan. The infrared beam S_c, originating from the scene, is focused by the mirror *M* and sweeps over the cooled detector *Det*. The sensors S_f and S_l deliver picture- and line-synchronization pulses respectively for the display of the infrared image on the cathode-ray tube screen. *Amp* preamplifier. V_o output signal. *b* Reverse bias for signal processing.

2. By using an infrared microscope in combination with a particular optomechanical scanning system an infrared image can be detected and then displayed on a cathode-ray tube screen. The scanning takes place on the image side of the microscope. Since these optomechanical scanning microscopes were specially designed for microthermography, they are more sensitive than the types mentioned below, but they represent an expensive solution to the problem.

3. General-purpose infrared cameras, fitted with various external optical systems, are a perfectly acceptable compromise for macro- and microthermography. They can be used for a wide range of object dimensions, from large printed circuits to very much smaller integrated circuits. When a camera with optomechanical scanning is used, however, there is the difficulty that some of the arrangements required for optical reasons introduce a degradation of either the sensitivity or the manageability of the combination. In the equipment of this type constructed at LEP such difficulties have been overcome by using a particular arrangement of the optical system.

The LEP equipment for real-time macro- and microthermography

The thermograph is a new and improved version of the medical thermograph constructed earlier by LEP [2] [3] and consists of an optomechanical infrared camera, a monitor and a signal-processing system (see *fig. 1*). The additional optical systems for macro- and microthermography, which will also be described below, were especially designed for the purpose.

[5] R. Vanzetti, IEEE Trans. **IECI-18**, 47, 1971.
[6] T. J. Jarratt, Mullard tech. Comm. **10**, 101, 1968.
[7] A. S. Dostoomian and R. Resta, IEEE Trans. **IECI-18**, 45, 1971.

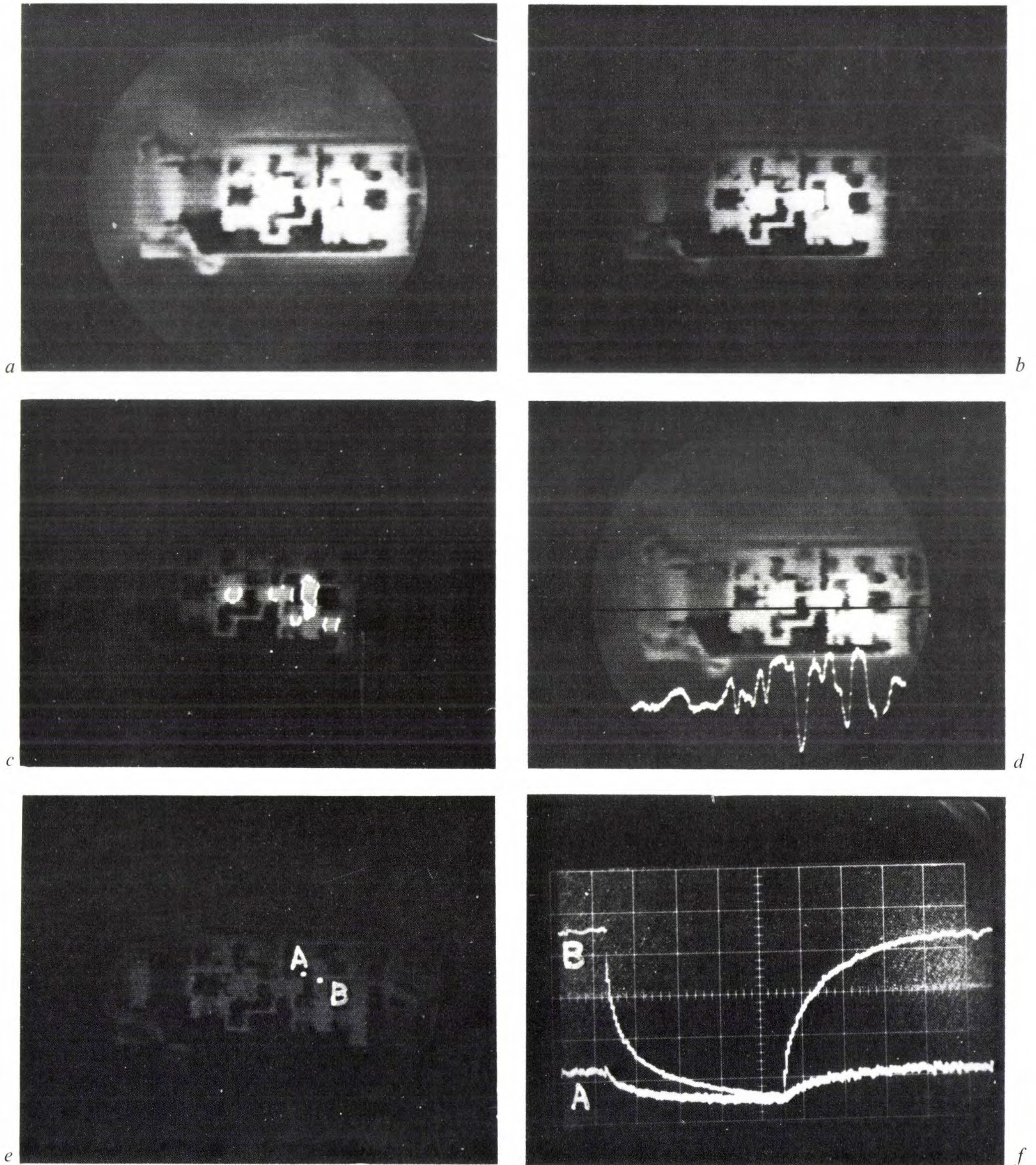

Fig. 3. Thermal investigation of a miniature hybrid amplifier. *a*) Conventional infrared image (thermal map). *b*) Warmest regions, superimposed on a conventional image. *c*) Isotherm, superimposed on a conventional image. *d*) Conventional image, with a thermal profile superimposed on it (the thermal profile is the variation of the temperature along a horizontal line). *e*) Two points (*A* on the substrate, *B* on a transistor) selected for recording comparative histograms. *f*) Histograms for the points *A* and *B* in (*e*), after switching the power off and on again (temperature scale 0.7 °C per scale division, time scale 20 s per division.

The optomechanical camera

In the camera an image of the object is analysed line by line and point by point by means of a dual optomechanical scanning system (*fig. 2*). The picture scan is derived from a planar mirror *F*, which is tilted to and fro at a frequency of 1 Hz, and the line scan is derived from a pyramidal drum *P*, with eight planar mirrors, that rotates at a speed of 25 rev/s (line frequency

200 Hz). Since the scanning takes place before the beam is focused, there is negligible aperture modulation of the beam intensity. This is because focusing can be carried out around the optical axis without geometric aberration, and is not affected by varying shadows and moving mechanical components emitting infrared radiation. The infrared detector has a sensitive area of only 0.2 mm^2 and is made of indium antimonide; it is cooled to the boiling point of liquid nitrogen (77 K). To avoid stray infrared radiation, the detector is fitted with a field-of-view diaphragm that is also cooled. The detector signal is amplified by a low-noise d.c. pre-amplifier.

The monitor and the signal-processing system

There are various ways in which the thermographic equipment may be used for making the infrared image visible and analysing it. The detector signal can be amplified and fed direct to the cathode-ray tube of a monitor so that the image can be displayed in the conventional way (*fig. 3a*). However, a number of image-analysis procedures can be carried out by analog processing, as described below.

The amplification is highly linear, since the detection of small differences in intensity must take place at very different radiation levels.

For plotting *isotherms* very accurately amplitude selection is used, i.e. only the signals between two specific levels (corresponding to the temperatures T and $T + \Delta T$) are passed and amplified. This can be done by applying a direct current of the opposite sense to that of the signal to the amplifier input.

The monitor can show either the warmest regions (fig. 3*b*), or a single isotherm (fig. 3*c*), superimposed on the conventional infrared image. Since there are two amplifier channels, two different isotherms can also be displayed simultaneously by connecting the channels to the cathode-ray tube for alternate one-second intervals; the temperature difference can then be read from one of the small digital panels.

A *thermal profile* is a display of the temperature variations along a horizontal line in the conventional infrared image on the monitor (fig. 3*d*). It is obtained by applying the video signal of the chosen line to the vertical-deflection plates of the cathode-ray tube and not to the grid. The thermal profile is superimposed on the conventional image.

Another aid in the analysis of infrared images is the plotting of *thermal histograms* (temperature as a function of time). Two histograms can be plotted simultaneously, enabling the temperature curve to be compared at any two points of the image; see fig. 3*e*,*f*. The signal for a histogram is obtained by sampling the video signal at the picture frequency.

The optical systems for micro- and macrothermography

The optical system for microthermography is shown in *fig. 4*. The lens system L, consisting of two germanium lenses, and the planar mirror M_1 produce an image of the object (magnification $18\times$) at the focal plane of a concave mirror M_2. The beam reflected from this mirror — which forms an image at infinity — enters the window of the infrared camera. The mirror M_2 produces an inverted image of the exit pupil of the lens L of the same size (magnification $-1\times$) at the entrance pupil of the camera. Careful positioning of the optical system in relation to the mean position of the optical axis of the camera ensures that there is virtually no aperture modulation.

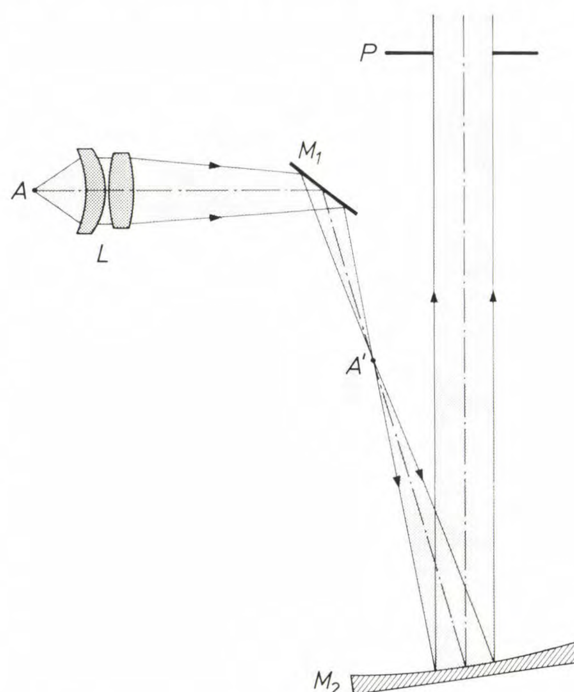

Fig. 4. Diagram of the optical system for microthermography. L objective, consisting of two germanium lenses. M_1 planar mirror, M_2 concave mirror. P image of the exit pupil of L at the entrance pupil of the camera. A object. A' image of the object at the focal plane of M_2.

The field of view of this optical system is a circle with a diameter of 1.5 mm. The worst resolution inside this circle is 25 μm.

The optical system for macrothermography consists of a single germanium lens with a focal length of 154 mm and an aperture of *f*/3. An image of the exit pupil of the lens is again produced at the entrance pupil of the camera. The diameter of the field of view is 25 mm, the resolution 280 μm. *Fig. 5* is a photograph of the two optical systems.

The principal technical data for the equipment are given in *Table I*. *Fig. 6* shows some characterization tests.

Fig. 5. External optical systems for the LEP thermograph for microthermography (*above*) and macrothermography (*below*).

Applications of macro- and microthermography

Infrared thermography can be considered as an ideal method for the study of thermal effects without the need for contact with the object and with negligible perturbation of the observed effects, because only a

Table I. Technical data for the LEP thermograph with external optical systems for macro- and microthermography.

	Conventional thermography	Macro-thermography	Micro-thermography
Focusing distance	1 m-∞	150 mm	12 mm
Field of view	0.22 × 0.28rad	25 mm Ø	1.5 mm Ø
Spatial resolution (modulation-transfer factor 0.7)	1.5 mrad	280 μm	25 μm
Intrinsic thermal resolution	0.1 °C	0.15 °C	2.7 °C
Number of picture elements	200 × 200	100 × 100	60 × 60
Picture frequency	1 Hz	1 Hz	1 Hz

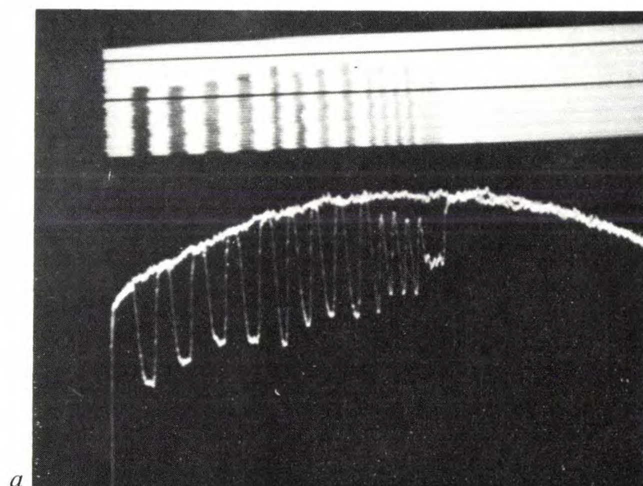

a

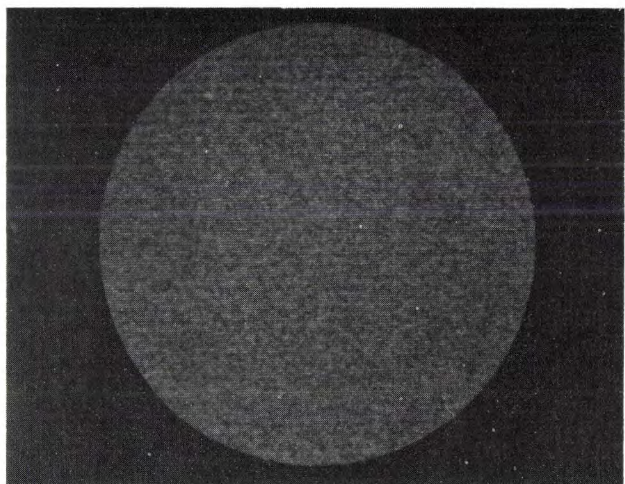

b

c

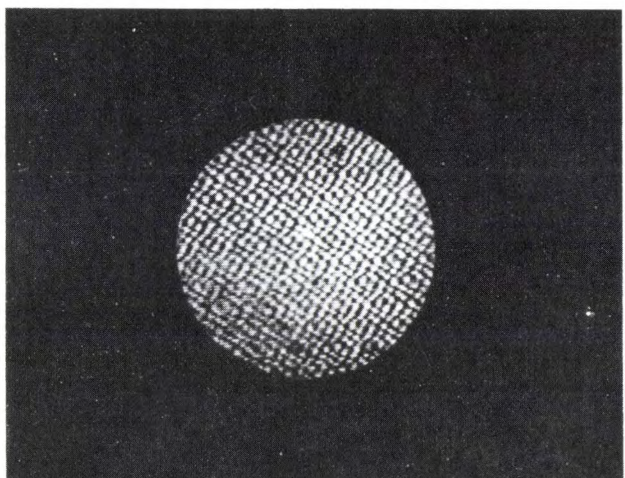

d

Fig. 6. Test images that demonstrate the characteristics of the LEP equipment for macro- and microthermography. *a*) Measurement of the modulation-transfer function of a bar pattern. The contrast factor is 0.75 at an angular resolution of 1.5 mrad ('conventional' thermography). *b*) A check on the uniformity of the response; this amounts to an image of a single isotherm with a width of 0.15 °C. *c*) An indication of the spatial resolution in macrothermography, with the divisions on a ruler used as the 'grating'. *d*) The same for microthermography, with a piece of metal gauze (mesh 51 μm, wire diameter 11.5 μm).

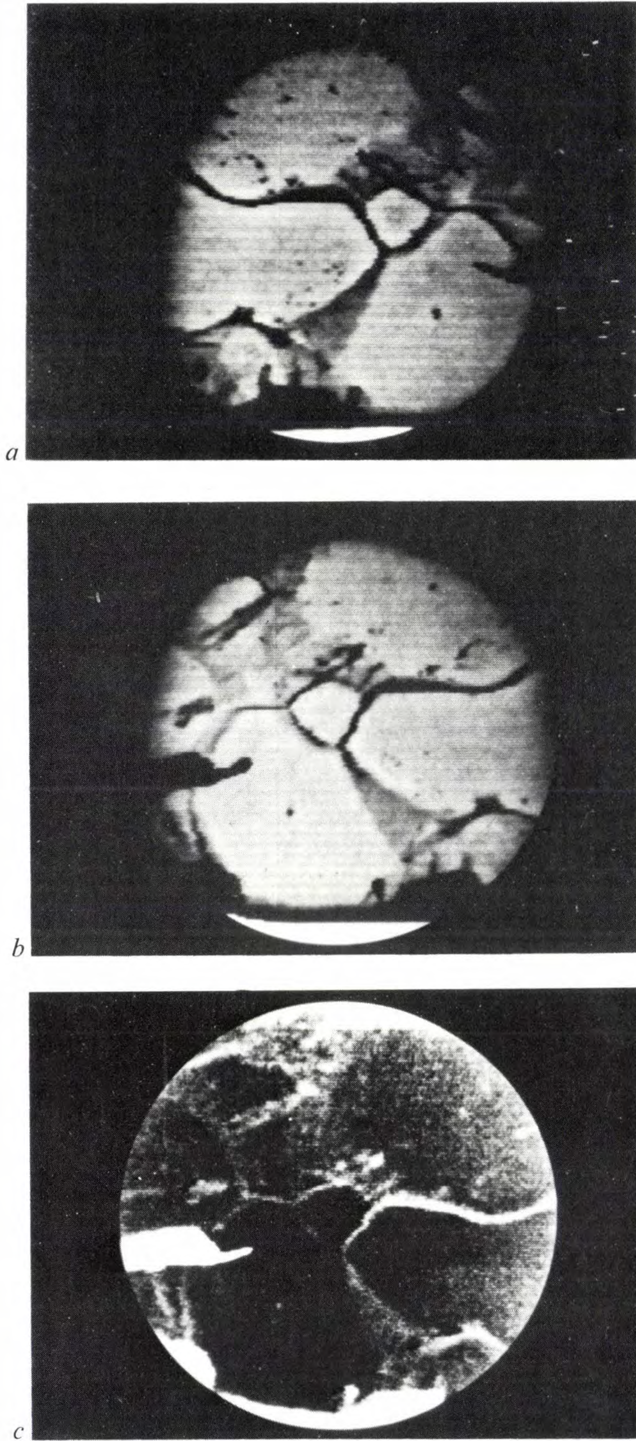

Fig. 7. Inhomogeneities in the infrared absorption of a sample of cadmium telluride (thickness 5 mm). *a,b*) Macrothermograms of the transmitted radiation, seen from both sides of the sample. *c*) Emission image of the sample heated to 40 °C.

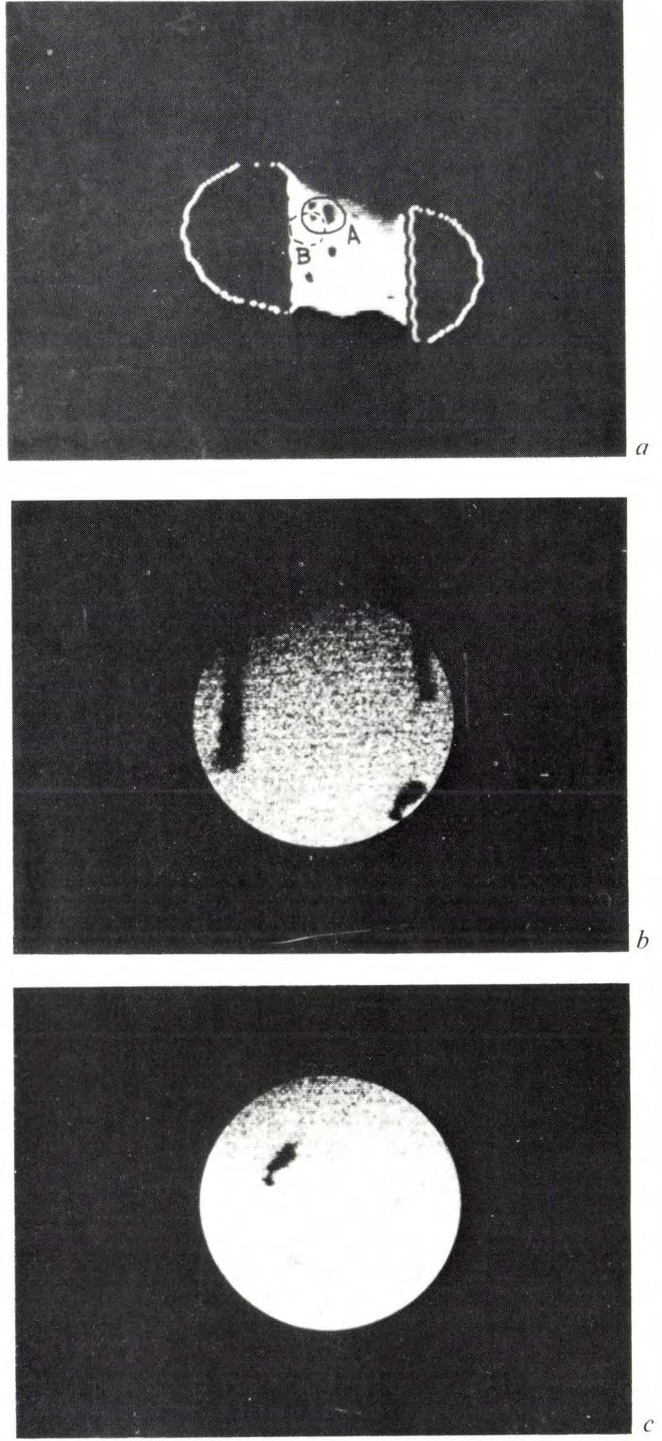

Fig. 8. Inhomogeneities in the infrared absorption of a gallium-arsenide surface. *a*) Macrothermogram. *b*) Microthermogram of the area *A*. *c*) Microthermogram of the area *B*.

very small fraction of the radiated power is used in the detection. Thermography provides a valuable complement to the techniques of pyrometry and radiation thermometry, because the investigator can observe thermal peculiarities within the field of view, because this allows him to make accurate measurements at the correct location and because he can make a study of dynamic thermal effects at the surface of the object.

Real-time macro- and microthermography can be used in a wide temperature range and under very different experimental conditions for many applications; these include non-destructive testing, process control, the investigation of thermal behaviour and fault-finding. Some examples are given below.

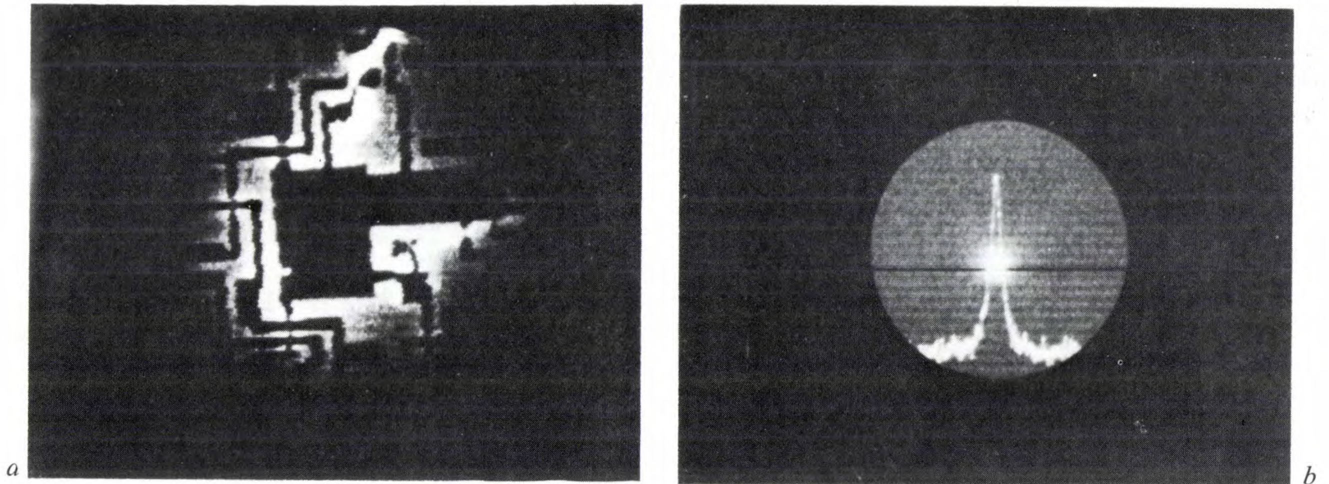

a *b*

Fig. 9. Localization of an insulation fault in an evaporated capacitor. *a*) Macrothermogram of the circuit. *b*) Microthermogram and thermal profile of the area around the electrical breakdown.

Mapping of absorption defects in infrared material

Infrared material for use in optical systems or as laser windows can be investigated for absorption irregularities by means of macro- and microthermography. For example, *fig. 7* shows images from a CdTe sample, made by macrothermography in the 3 to 5.5 μm wavelength band. The absorption defects can be seen in fig. 7*a* and *b*, for each side of the sample, for transmission of infrared radiation from a homogeneous achromatic source; fig. 7*c* was obtained by measurement of the infrared radiation emitted from the sample itself when heated to a uniform temperature of 40 °C. Absorption differences as small as 0.2 % can be observed. It would also be possible to use a dynamic method for tracing thermal deviations by heating the object with a scanning laser beam. The change in absorption would then be observed as a function of temperature until the instant at which the divergent thermal effects began to occur.

Fig. 8 shows absorption defects in a GaAs sample; the effects were made visible by using the infrared transmission method in macrothermography (fig. 8*a*) and in microthermography for studying details of the same area (fig. 8*b* and *c*).

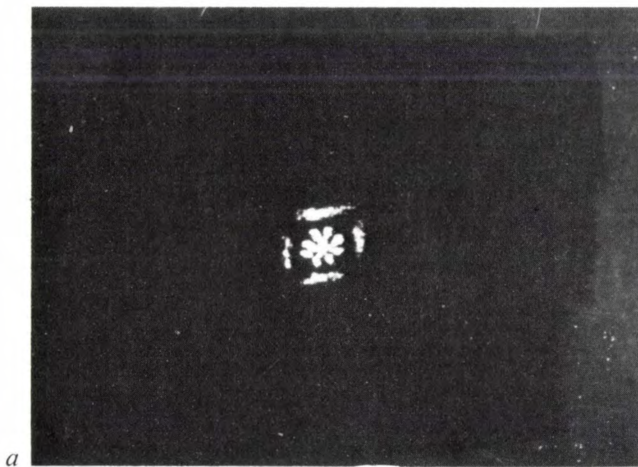

a

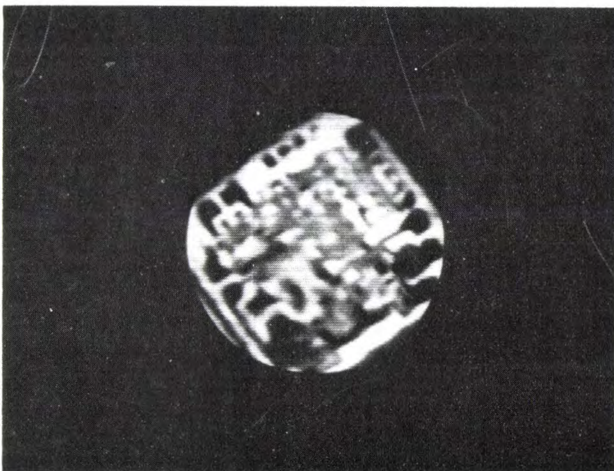

b

Fig. 10. Thermal maps of an LED (*a*), an integrated circuit for an operational amplifier (*b*) and a power transistor (*c*). An electrical breakdown due to a 'hot spot' can be seen in the transistor.

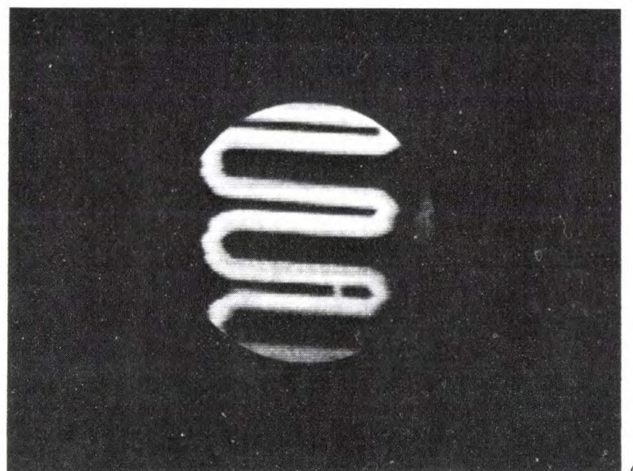

c

Investigation and inspection of miniature circuits, semiconductor elements and integrated circuits

Macro- and microthermography also provide a means of studying the thermal consequences of high component densities, power dissipation and poor-quality bonding and welding in integrated and other small circuits. The final temperature distribution over the circuit can also be determined. Real-time thermography is very useful for rapid inspection during production, since many thermal tests have to be made immediately after a sudden change in the experimental conditions, in a non-equilibrium situation. An example of this has already been seen in fig. 3*e* and *f*. *Fig. 9* shows another example of measurements of this type: the localization of the electrical breakdown in an evaporated capacitor connected to a high voltage.

In *fig. 10a* and *b* conventional thermal maps can be seen of an LED (light-emitting diode) and a recent type of integrated circuit for an operational amplifier. Fig. 10*c*, one of a series of microthermograms made during the thermal testing of a power transitor, shows the location of an electrical breakdown due to a 'hot spot' and the resultant local melting of the substrate.

Medical applications

Infrared thermography is regularly used in hospitals as an investigatory technique complementary to the more conventional clinical methods of prognosis [8], diagnosis and examination. Many medical applications of macro- and microthermography can be thought of, especially in ophthalmology [9] and dermatology, as well as in lesions of peripheral blood vessels. An example of such lesions is shown in *fig. 11*, which shows a macrothermogram of the back of a left hand; the difference in skin temperature at the location of the blood vessels near the surface is clearly visible.

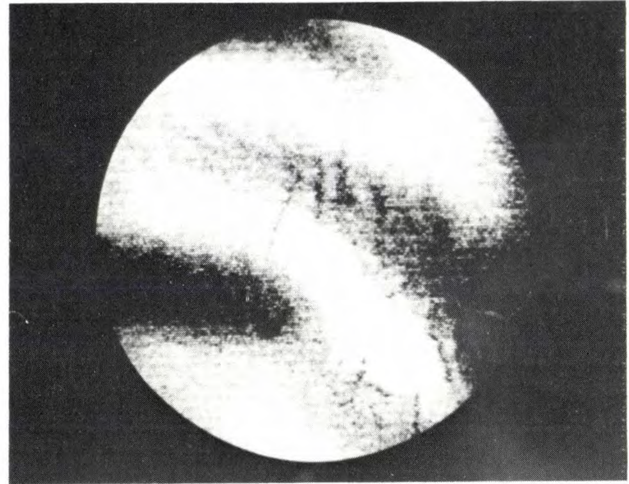

Fig. 11. Differences in skin temperature (on the back of a left hand) near to blood vessels.

The examples given above, although limited in number, indicate that the range of applications of real-time thermography can readily be extended to include macro- and microthermography by combining the thermograph with an external optical system.

[8] N. J. M. Aarts, M. Gautherie and E. F. J. Ring, in: Thermography, Proc. 1st Eur. Congr., Amsterdam 1974, p. 57 (published by Karger, Basel 1975).

[9] P. Sole and D. Rigal, VIme Congrès de la Société Européenne des Ophthalmologistes, Gent 1977, to be published.

Summary. The article deals briefly with the problems encountered in infrared thermography, particularly in macro- and microthermography, where there are limitations on the spatial and thermal resolution. A description of the main features of three groups of instruments for macro- and microthermography is followed by an explanation of the way in which the LEP thermograph has been adapted for these applications by the addition of external optical systems. The potential of this combination is illustrated by a number of examples.

Philips tech. Rev. 37, 250-262, 1977, No. 9/10

Pulling large bismuth-silicon-oxide crystals

J. C. Brice, M. J. Hight, O. F. Hill and P. A. C. Whiffin

The use of acoustic waves on the surfaces of solids has made it possible to replace the present bulky intermediate-frequency filter of a colour-television set by a device of about the same size as a transistor. Such devices offer a considerable saving in space and materials and eliminate the need for i.f. alignment. They are also suitable for many other applications in which exactly tailored passbands and phase responses are required. However, the devices are only economically viable if suitable crystals can be produced. This article describes an investigation into the growth of crystals of a potentially suitable material and illustrates the difficulties experienced in bringing a new material from the initial research stage to a point at which industrial production can be contemplated.

Introduction

Crystals have always played a large part in science and technology. Most of the basic knowledge of solid materials is derived from investigations carried out on crystalline samples. Practical applications of the use of single crystals are gramophone styli, watch bearings and electronic devices, such as transistors, integrated circuits and quartz resonators.

Establishing the suitability of a crystal or class of crystals for application in a device is a long and complex process. It is necessary first to prove that useful devices can be made. Then it must be shown that likely variations in the growth process do not result in unacceptable changes in device properties. Thirdly, it has to be proved that the crystals can be grown in such quantities and sizes that economic device production is possible. All of the first stage and most of the second can be done with laboratory-scale crystals. However, the next stage and establishing the economic viability requires larger crystals to test both the device-production methods and the crystal-growth procedures.

In this article we shall touch upon a number of problems encountered in the growth of such large crystals. Examples include the problem of thermal strain — an analysis of this enables us to predict certain growth conditions that are independent of crystal size — and hydrodynamic effects in the melt which depend on the growth parameters. These effects are described on a semi-quantitative basis for bismuth-silicon-oxide crystals, but many of the results are found to be generally applicable to other crystals. Our examination of the economics of crystal growth show that, subject to some limits, growing bigger crystals does reduce costs in device production and that automation is very desirable. As we shall show, the economic and technological aspects are interlinked.

J. C. Brice, Ph. D., M. J. Hight, B. A., O. F. Hill, M. R. I. C. and P. A. C. Whiffin are with Philips Research Laboratories, Redhill, Surrey, England.

Bismuth-silicon-oxide crystals

The interaction between electrical and mechanical effects can be used to give components which transmit signals at some frequencies and reject all others. These components are usually based on a resonance effect; devices using effects in the bulk of quartz crystals have been known for many years (crystal oscillators). More recently, it has been shown that waves on the surface of crystals can be used in the same way with the advantage that by a simple fabrication it is possible to tailor the passband of frequencies to suit any application [1].

The work to be described here was part of a project to make such devices suitable for use in television receivers, where one component about as large as a transistor can replace a large array of inductors and capacitors, giving a considerable saving of space, materials and time required for manufacture and alignment. It appeared likely that crystals of bismuth oxide would provide a material suitable for this purpose. A number of crystals of the γ-bismuth oxides were grown [2], and it seemed from the measured properties and the relative difficulty in growing the various crystals that $Bi_{12}SiO_{20}$ would be the best material. The correctness of this

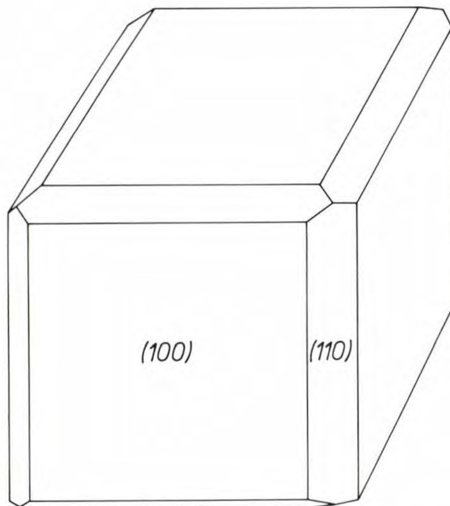

Fig. 1. The 'equilibrium' shape of a crystal of bismuth-silicon oxide (BSO). If the crystal is grown in solution a cube is produced with the planes (100), (010) and (001) as faces. Sometimes the edges are 'chamfered' ((110) planes etc.) When grown from the melt a cylindrical rod is produced.

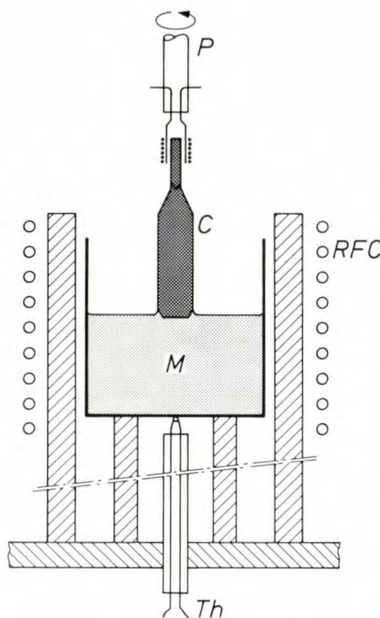

Fig. 2. The apparatus used for pulling small crystals. The assembly was contained in a water-cooled chamber. The crystal *C* is pulled from the melt *M* by a hydropneumatic crystal puller *P*. The thermocouple *Th*, welded to the bottom of the crucible, monitors the melt temperature and can be used to actuate a control system. *RFC* is the radio-frequency coil connected to a power generator.

decision has since been amply demonstrated; technically satisfactory filters for many present and future television applications can be made. These filters are smaller and cheaper than those made from any other currently known material.

The 'equilibrium' shape of $Bi_{12}SiO_{20}$ (BSO) is shown in *fig. 1*. Crystals like this could be produced from solutions or hydrothermally [*] but growth by these methods is slow and the method adopted was the more rapid technique of pulling from the melt. However, in spite of the fact that this was a familiar technique [3], the investigation of the growth of BSO produced some unexpected results and required consideration of aspects which had previously been neglected. This was partly because the properties of BSO differ significantly from those of materials usually grown by this method and partly because of the need to grow large crystals to minimize device costs.

In the following sections of this paper we shall discuss the basic process, the composition of the crystals and its variation, the thermal strain and cracking, hydrodynamic effects during pulling and other technological aspects. The last section deals briefly with the economic aspects of crystal pulling. While the properties of BSO differ from those of other materials, as mentioned earlier, a great deal of knowledge which has been acquired during this study is generally applicable.

Basic pulling technique

In principle, the pulling method is simple. *Fig. 2* shows the essential parts of the system. A melt made from weighed amounts of the component oxides (Bi_2O_3 and SiO_2) is contained in a platinum crucible heated by radio-frequency currents induced in it by the coil, which is connected to an r.f. generator. A seed crystal is brought into contact with the melt and the melt temperature is adjusted so that a small amount of the seed melts. Growth is started by slightly lowering the melt temperature and slowly raising the seed crystal. Material from the melt is pulled upwards and crystallizes. The seed crystal is rotated during growth to improve mixing in the melt and to increase the symmetry of the temperature distribution. The diameter of the crystal is controlled by changing the heat flow into the crystal. The most direct method for doing this is to change the melt temperature: lowering the temperature increases the crystal diameter and vice versa. Small crystals with diameters of about 10 mm could be grown at rates of about 6 mm per hour; the rotation rate was not critical. For larger crystals the conditions had to be adjusted with more care, as will be discussed later. Initially we used very pure starting materials contain-

[1] D. W. Parker, R. G. Pratt, F. W. Smith and R. Stevens, Acoustic surface-wave bandpass filters, Philips tech. Rev. 36, 29-43, 1976.
[2] J. C. Brice, T. M. Bruton, O. F. Hill and P. A. C. Whiffin, The Czochralski growth of $Bi_{12}SiO_{20}$ crystals, J. Crystal Growth 24/25, 429-431, 1974.
[3] See for example J. C. Brice, The growth of crystals from liquids, North-Holland, Amsterdam 1973.
[*] In the hydrothermal method, crystals are grown under very high pressure and at a high temperature, usually from a saturated aqueous solution. See for example A. Rabenau and H. Rau, Philips tech. Rev. 30, 89, 1969.

ing only one or two parts per million of impurities; the crystals were of a pale yellow colour.

When the curved growth face intersects the natural (100) and (110) faces of the crystal, flat regions are formed, the 'facets' (*fig. 3*). The material grown on these facets was slightly different in colour. There is, however, no measurable difference in composition inside and outside the facets. The lattice constant in the facets is at most 0.01 pm (i.e. 0.0001 Å) larger than elsewhere. We shall return to this later. *Fig. 4* shows a BSO crystal obtained by pulling; its diameter is 42 mm.

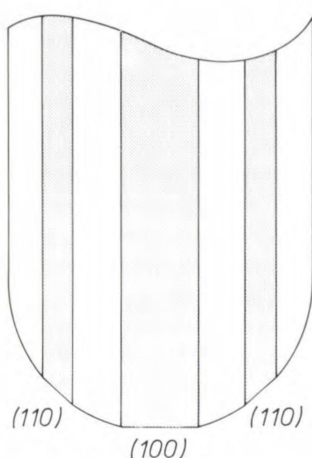

Fig. 3. Diagram of the axial cross-section of a pulled BSO crystal, showing the facets (*shaded*).

Fig. 4. A pulled BSO crystal with a diameter of 42 mm; its weight is 1.4 kg.

Composition of the crystals

Since small variations in the growth process are inevitable, it is important to establish that these have no significant effect on the properties of the devices. Therefore it was necessary to grow crystals under slightly different conditions and with different compositions of the melt. As a starting point, changing the relative amounts of Bi_2O_3 and SiO_2 in the melt should change the relative amounts in the solid. Fortunately this proved to be only a weak effect. If we describe the material as $Bi_xSiO_{1.5x+2}$, we found that the composition in the melt could be varied from $Bi_{10}SiO_{17}$ to $Bi_{14}SiO_{23}$ (x between 10 and 14) without affecting the composition of the crystals produced, provided the growth rate was low. At high growth rates, if x varied significantly from 12 in the melt, inclusions of the excess oxide were found in the crystals. It was found that x in the solid varied very little: the minimum and maximum values were 11.77 and 12.05. These values did not correspond to the minimum and maximum values in the melt. We can therefore conclude that the composition in the melt is not critical.

From the data it is possible to plot the relevant part of the phase diagram which is shown in *fig. 5*. On this diagram the melt composition is labelled *Liq* and the crystal composition is labelled *Sol*. Liquids and solids at the same temperature are in equilibrium, e.g. the melt m_1 is in equilibrium with the crystal having the composition c_1, and melt m_2 gives a crystal having the composition c_2. The compositions c_1 and c_2 are those with the minimum and maximum bismuth contents. If the composition of the melt differs from the composition of the crystal, the composition of the melt will change during the growth of the crystal, since the quantities of Bi and Si removed from the melt are different. However, crystals grown from a melt near the points m_1 and m_2 — the tangent to the curve is vertical there — have compositions which vary only very slightly down their lengths. For other melt compositions, x in the crystal can change by as much as 0.2 if half the melt is used up.

In surface-wave devices we could detect no change in properties when the composition was changed. A melt of composition m_1 or m_2 did however produce crystals which were less strained and therefore more robust.

Traces of impurities had no measurable effect on the surface-wave properties, but did affect the colour of the crystals, some of which were sensitive to light (photochromism): directly after growth the crystals were pale yellow, but some crystals became considerably darker on exposure to daylight.

Crystals were grown from many different batches of starting materials from different suppliers. The impurity contents ranged from less than 10 parts per million (ppm) to about 2000 ppm. Since most impurities fit

[4] J. C. Brice, The cracking of Czochralski-grown crystals, J. Crystal Growth **42**, 427-430, 1977.

badly in the lattice, they are rejected by the growing crystal (see *Table I*) and the crystals typically contained from 2 to 10 ppm of impurities (measured relative to the silicon content). The results of the analyses did not enable the impurity causing the photochromism to be unambiguously identified, but crystals containing significantly less than 1 ppm of both iron and chromium always stayed yellow, while crystals containing more than 1 ppm of either iron or chromium always darkened.

As we mentioned earlier, the lattice constant on the facet is a little larger than in the crystal; see *fig. 6*. This leads to mechanical strain around the facet. On the (100) facets this distortion amounts to about a third of the strain at which the crystal would break. Regions of high dislocation density can therefore be seen outside the facet.

The strain due to the facet is a function of the ratio of the facet area to the total cross-sectional area [4]. Since in general the facet regions are relatively small, the total strain of the crystal is negligible, but crystals with large facets were usually more fragile.

The larger lattice constant cannot be explained by another composition for the facet material. *Fig. 7*

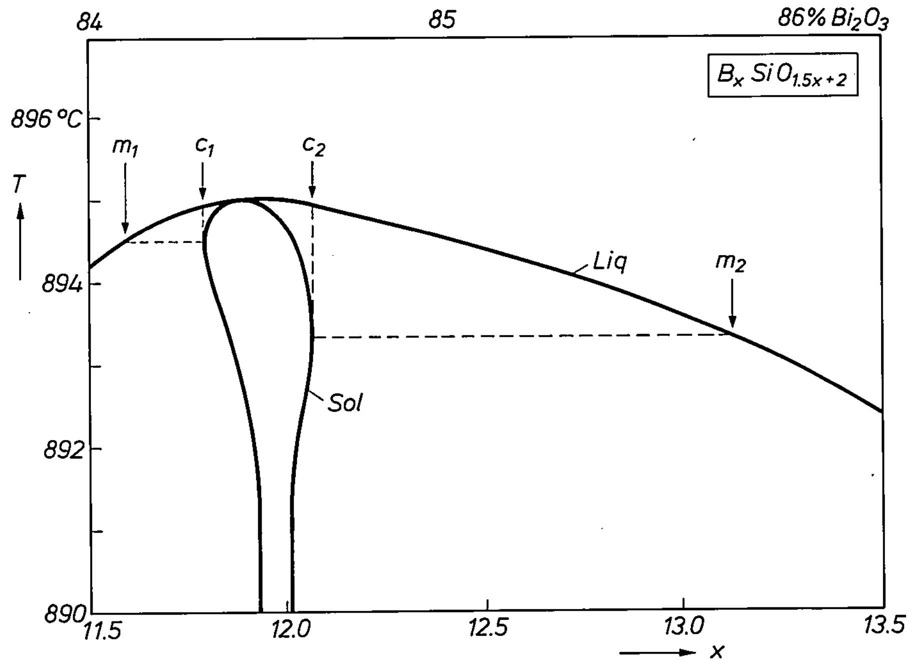

Fig. 5. Part of the phase diagram for the system Bi_2O_3-SiO_2, as derived from existing data. *Liq* composition of the melt. *Sol* composition of the crystal. This diagram applies to crystals grown in air. For crystals grown in different atmospheres the curves are displaced to the left for oxygen or to the right for argon with a trace of oxygen. The combinations m_1, c_1 and m_2, c_2 correspond to the extreme values for x in the crystal. In the neighbourhood of the points c_1 and c_2 large variations of x in the melt only give small variations of x in the crystal.

The facets

The flat parts of the boundary surface where the crystal growth occurs arise because the growth mechanisms on the curved and natural faces are different. The growth on the curved face is due to a random deposition of molecules, while the growth on the natural faces requires the simultaneous deposition of a number of molecules.

The size of the facets increases as the growth face is made less curved. Increasing the rate of rotation of the seed crystal flattens the face and hence makes the facets larger; a similar effect can be produced by increasing the rate of pull. The facetted area in our crystals was typically 1 to 2% of the cross-section. At the greatest rates for stable growth facets were produced that occupied more than 20% of the cross-section.

Table I. The ratio of the concentration in the crystal to the concentration in the melt of $Bi_{12}SiO_{20}$ for 24 impurities.

B	0.2	Cu	0.2
Na	0.1	Zn	0.1
Al	0.7	Ga	0.2
S	0.07	Ge	0.3
K	0.3	Br	0.5
Ca	0.2	Ag	0.02
Ti	0.3	In	0.2
Cr	0.8	Sn	0.2
Mn	0.05	Te	< 1
Fe	0.2	Ba	0.2
Co	0.2	Pt	0.03
Ni	0.2	Pb	0.4

shows the lattice constant of the crystal as a function of the ratio of bismuth to silicon x. To explain a difference in lattice constant of 0.01 pm, x would have to be greater than 12 on the facet. However, chemical analysis of material grown on the facets and close to them showed no difference in the ratio of bismuth to silicon.

No significant difference in impurity content could be detected on and away from the facets, except that silver appeared to be preferentially absorbed on the facet [*]. But even this impurity did not occur in the crystals in sufficient quantity to account for the observed lattice-constant variations; these would have required hundreds of ppm.

It has been suggested [5] that the γ-bismuth-oxide structure can contain some Bi^{5+} ions in addition to the Bi^{3+} ions. If this is the case the lattice will contain some bismuth and oxygen vacancies. It can be postulated that if Bi^{5+} is preferentially incorporated on the facets, its presence would increase the oxygen-ion content there and thus increase the lattice constant in the manner observed.

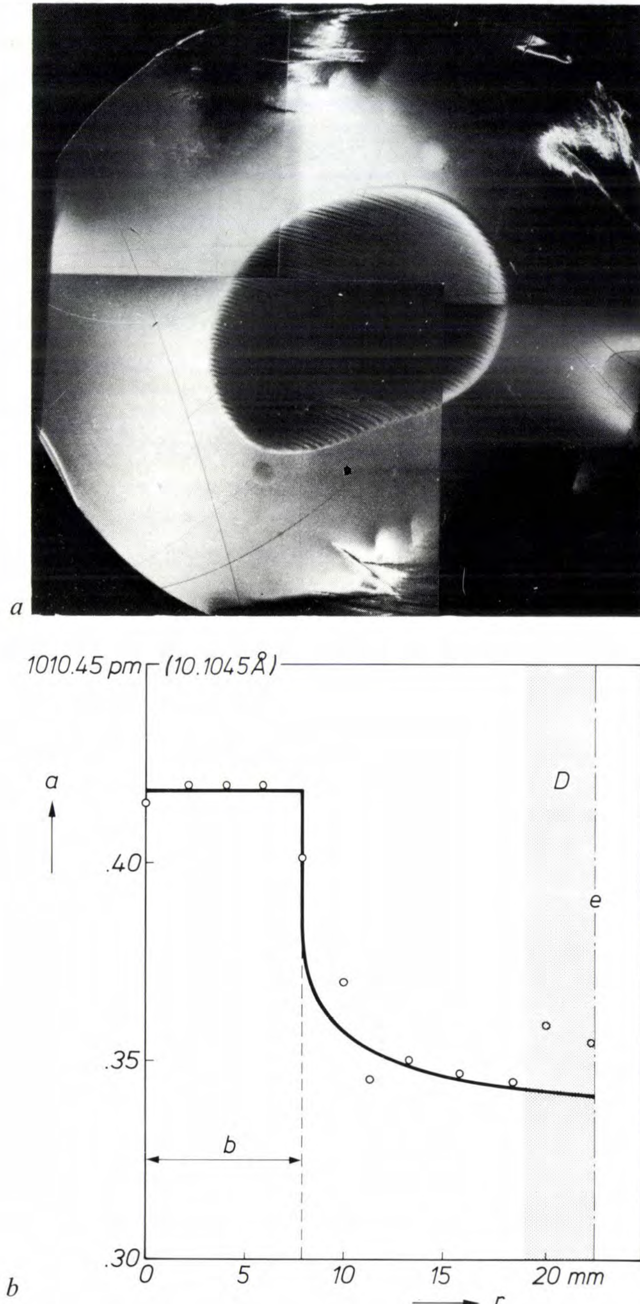

Fig. 6. *a*) Cross-section of a bismuth-silicon-oxide crystal. The photograph was made by a special X-ray technique that shows clearly small differences in lattice constant (X-ray topography). The dark hatched part in the centre is the facet. The even spacing of the interference fringes shows that the material is very homogeneous. *b*) The lattice constant a over the cross-section of the crystal, showing the large difference inside and outside the facet; b is the radius of the facet, e indicates the edge of the crystal. In region D a high dislocation density is observed.

The growth rate

There are three effects that set a limit to the rate at which a crystal can be pulled. In the first place there is the latent heat, which must be removed; secondly, there is the formation of inclusions and the absorption of impurities from the melt, and finally the danger of cracking due to thermal stress. The first two set a limit to the rate at which thin crystals can be pulled; in thick crystals the chief danger is that the crystal may crack. We shall now examine these three limitations in order.

If the crystal grows at a rate of f cm/s the quantity of latent heat evolved at the boundary surface between crystal and melt will be fL joules per cm^2, where L is the latent heat per cm^3. This latent heat is conducted away via the crystal, since this is cooler than the boundary region, which is exactly at the melt temperature T_m, and the molten mass in the crucible is somewhat hotter. The heat flow in the crystal at the growth face is equal to $\lambda_c(dT/dz)_g$, where λ_c is the thermal conductivity of the crystal and $(dT/dz)_g$ is the vertical temperature gradient at the boundary. This temperature gradient depends on the dimensions of the crystal and on the rate at which the crystal can give up its heat to the surroundings. This is proportional to the temperature difference $T_m - T_0$ between the hottest point of the crystal (the boundary) and the surroundings. As is shown in the Appendix, the temperature gradient at the boundary is given by:

$$(dT/dz)_g \approx c(T_m - T_0)/R^{1/2},$$

where R is the radius of the crystal and c is a constant of proportionality that depends on the thermal conductivity of the crystal and the heat-transfer coefficient of its surface.

It can be seen that the heat flow through the crystal does not depend on the pulling rate. This does however determine the contribution of the solidification process

to the heat flow. Conversely, the given heat flow therefore determines the maximum permissible value f_{max} for the pulling rate. If this is exceeded, not all of the latent heat can be conducted away via the crystal and the temperature at the boundary rises; the contact between crystal and melt then fails.

At the rate f_{max} we have for the production and removal of heat

$$f_{max}L = \lambda_c(dT/dz)_g = c\lambda_c(T_m - T_0)/R^{1/2}.$$

The maximum pulling rate is therefore given by

$$f_{max} = c(\lambda_c/L)\,(T_m - T_0)/R^{1/2}. \qquad (1)$$

This rate is clearly proportional to $R^{-1/2}$.

From (1) it would appear that the maximum pulling rate could be increased by reducing the ambient temperature T_0. However, we then encounter some of the effects mentioned above that limit the pulling rate: the chance of formation of inclusions in the crystal and the absorption of impurities from the melt. We shall now examine this more closely.

The transport of material from the melt to the growth face is of course proportional to the growth rate of the crystal. The melt contains impurities, and, as mentioned previously, one of the main components can be present in excess. Since these are not absorbed by the crystal, a high concentration of these substances will be present in the melt near the growth face. These must mix with the melt again by diffusion.

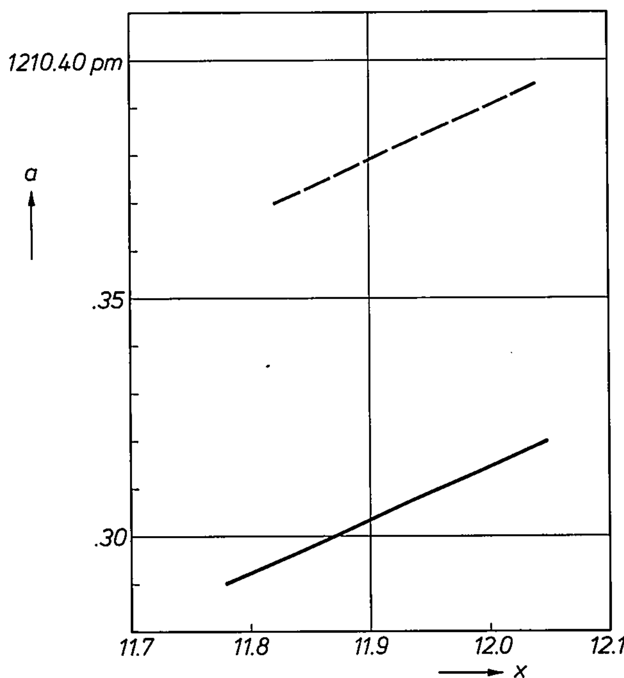

Fig. 7. The variation of lattice constant a with the ratio of bismuth to silicon (x). The solid curve applies to crystals grown in air. The dashed curve is derived from our data for crystals grown in oxygen. All data refer to material grown off the facets.

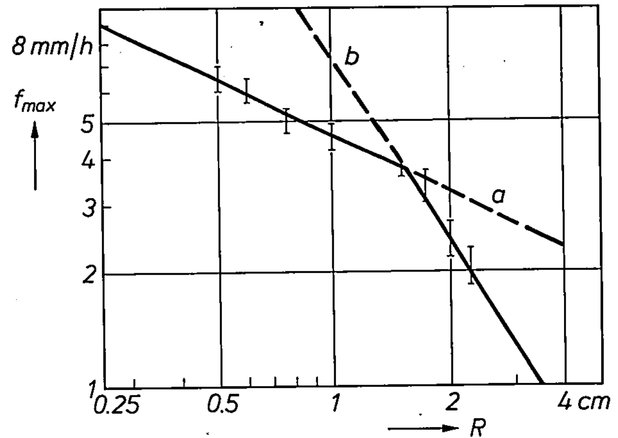

Fig. 8. The maximum permissible growth rate f_{max} as a function of crystal radius R. Line a is proportional to $R^{-1/2}$ and represents the condition for inclusion-free growth. Line b (proportional to $R^{-3/2}$) represents the condition in which the heat loss from the solid must be deliberately limited to prevent cracking.

Since the diffusion rate — and hence the rate of removal — is proportional to the growth rate, the concentration of impurities at the boundary will be proportional to the growth rate. If this concentration exceeds a certain value there is the danger that these substances will be absorbed in the crystal. This process therefore sets a further limit to the growth rate.

For a crystal free from inclusions and impurities, we find a maximum permissible pulling rate that is proportional to $R^{-1/2}$. This is plotted in *fig. 8* and is represented by line a.

In crystals with a radius of more than about 1.5 cm the third limitation has to be taken into account: the danger of cracking due to mechanical stresses arising from the temperature differences inside the crystal.

The strain ε will be greatest at the outskirts of the crystal (radius R). This strain is proportional to R, the expansion coefficient α and the temperature difference $T_m - T_0$:

$$\varepsilon \propto \alpha\, R(T_m - T_0). \qquad (2)$$

Since the lines of cleavage in a cracked BSO crystal lie at 45° to the axis, see *fig. 9*, it can be shown that the stresses along the axis are about the same as those around the circumference.

To prevent ε from becoming too large on increasing R, $T_m - T_0$ should be reduced in proportion to R. Since T_m is fixed, this means that T_0 must be increased.

[*] The analyses were performed by J. B. Clegg, who used solid-source mass-spectroscopic methods with a detection limit of much less than 1 ppm. While the absolute accuracy of the method is uncertain without elaborate calibration, differences of a factor of 1.5 or more are obvious. See for example J. B. Clegg and E. J. Millett, Philips tech. Rev. 34, 344, 1974.

[5] D. C. Craig and N. C. Stephenson, Structural studies of some body-centered cubic phases of mixed oxides involving Bi_2O_3: the structures of $Bi_{25}FeO_{40}$ and $Bi_{38}ZnO_{60}$, J. Solid State Chem. 15, 1-8, 1975.

As we saw above, a reduction in $T_m - T_0$ requires a proportionate reduction in the growth rate f. If ε_b is the maximum permissible value of ε, then by combining (1) and (2) we have an expression for the maximum permissible pulling rate f_{max}:

$$f_{max} \propto \frac{\varepsilon_b}{\alpha} R^{-3/2}.$$

The maximum growth rate is thus no longer proportional to $R^{-1/2}$, as derived for smaller crystals, but to $R^{-3/2}$. This relation is shown as line *b* in fig. 8. This line gives the relation between the radius of the crystal and the maximum growth rate at which the crystal will not crack. For BSO the lines *a* and *b* intersect at a crystal radius of about 1.5 cm.

Cooling

After the crystal has been grown, it has to be cooled to room temperature. If this is done too quickly, the temperature gradients will become too large, and the crystal may crack because of differences in expansion. It is clear that the heat loss through the crystal to its surroundings may be of about the same magnitude as the heat loss during the pulling process. We saw that the temperature difference between the hottest point of the crystal and the ambient temperature, $T_m - T_0$, must be approximately inversely proportional to the radius R. The heat loss w per second and per cm of height is given approximately by

$$w \approx 2\pi R(T_m - T_0).$$

Since $T_m - T_0$ is proportional to $1/R$, the heat loss does *not* depend on the radius of the crystal.

The heat content of the crystal per cm of height is $\pi R^2 cT$, where c is the specific heat per unit volume and T is the mean temperature. Since the heat loss is constant, we should have:

$$\frac{dT}{dz} = \gamma \frac{1}{R^2}.$$

The proportionality constant γ is determined by the specific heat, the thermal conductivity λ, the coefficient of linear expansion α, and the maximum strain before cracking. It is given by:

$$\gamma = 8^{\frac{1}{2}} \frac{\lambda \varepsilon_b}{\alpha c}.$$

Some of the properties of bismuth-silicon oxide are summarized in *Table II* and *fig. 10*. From these it can be shown that the greatest rate of cooling is equal to $74/R^2$ °C/hour at the melting point and twice this value at room temperature. For crystals of radius 2 cm we find, in practice, a maximum rate of 20 °C per

Table II. Some properties of bismuth-silicon oxide.

Quantity	Value
Density, solid	9.206 g/cm^3 at 20 °C
liquid	7.63 g/cm^3 at 950 °C
Linear expansion coefficient	16×10^{-6} °C^{-1}
Volume expansion coefficient	7×10^{-5} °C^{-1} at 950 °C
Specific heat/unit volume,	
solid [*]	2.7 J cm^{-3} °C^{-1}
liquid [*]	3.0 J cm^{-3} °C^{-1}
Thermal diffusivity	See fig. 10
Thermal conductivity	See fig. 10
Viscosity	22 cP at 900 °C
Young's modulus	93 GNm^{-2}
Breaking strain	2×10^{-4}
Latent heat [*]	460 J cm^{-3}
Cooling constant (μ/λ)	0.4 cm^{-1}

[*] The value shown relates to Bi_2O_3; value for BSO is not known.

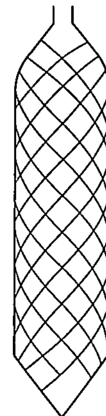

Fig. 9. Diagram of a cracked crystal. Cracks are usually formed at 45° to the axis.

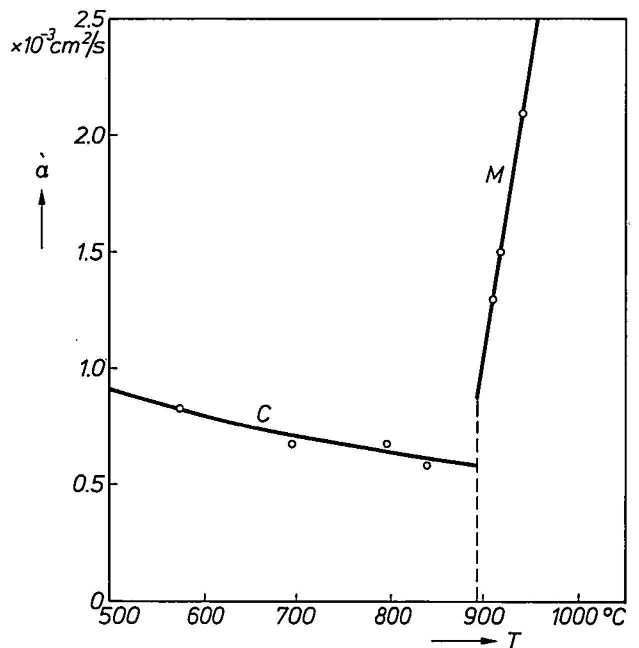

Fig. 10. The variation of thermal diffusivity α with temperature. (From data supplied by Dr T. M. Bruton, formerly with PRL.) The line C applies to the crystal; line M to the melt. The thermal conductivity can be found by multiplying α by the specific heat per unit volume (see Table II).

hour — i.e. within 10% of the predicted value. Nearer to room temperature 35-40 °C per hour is satisfactory, as against a calculated value of about 50 °C per hour. For smaller crystals (R = 1 cm) the rates are found to be about four times higher. These various values indicate that the treatment given above is satisfactory. We have also found these theoretical predictions to be valid for other crystals such as lithium niobate.

rate, the effect could be catastrophic: a large change in the interface shape occurred and the change in heat flow cracked the crystal. Similar effects had been seen in garnets and other investigators have reported the same effect in other materials. An experimental and theoretical investigation [7] showed that the observed effect was the result of a change in the flow pattern from that shown in *fig. 12a* ultimately to that shown in 12*c*.

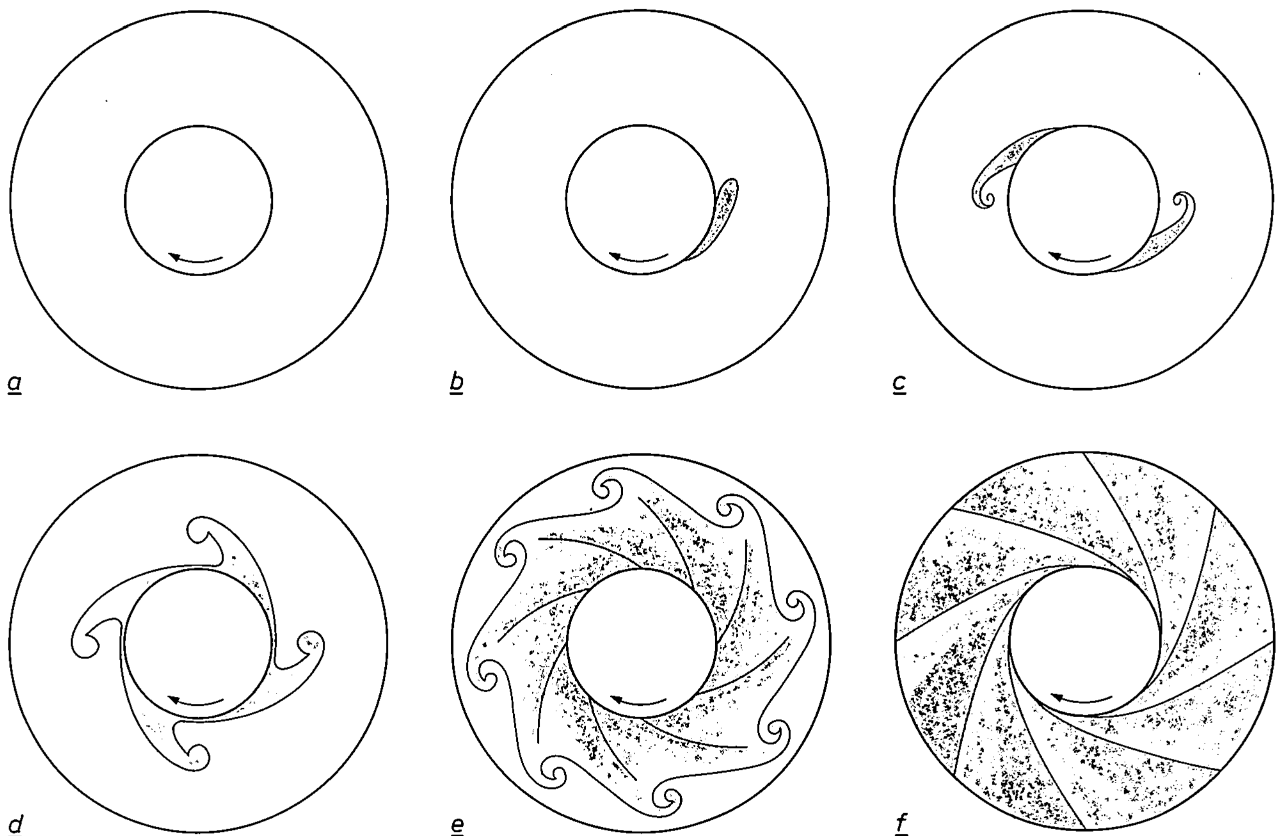

Fig. 11. Swirl patterns observed on the surface of the melt. While these patterns are obvious to a human observer, they are difficult to photograph because they precess and the available viewing angles are not very suitable. (*a*) to (*f*) represent the views seen as the rotation rate increases.

Hydrodynamic effects

In the investigation of the pulling of large BSO crystals it was found that the rate at which the crystal is rotated is also associated with an upper limit. This is related to the fact that the rotation of the crystal does not always bring about a rotation of the complete melt, which can therefore be inhomogeneous. We are not referring here to the well known growth striae [6] — the strains associated with these are small — but to effects that can have more serious consequences.

Our study of melt stirring started from the observation that in some instances dark swirl patterns were observed on the melt surface (*fig. 11*). If these patterns appeared, e.g. due to a change in the crystal rotation

The transition regime 12*b* is difficult to represent because the flow at any point varies with time. Temperature measurements in the transition conditions vary wildly. *Fig. 13* shows the regions in which the various flow regimes exist. In region *a* an axially symmetrical flow occurs. Region *b* corresponds to an asymmetrical flow giving temperature variations with time at a fixed point and in region *c* the flow is again axially symmetrical. Detailed study was only made of the transition from *a* to *b*, so that only these measured

[6] J. C. Brice, Controlling heat transport during crystal pulling, Acta Electronica **16**, 291-301, 1973.

[7] J. C. Brice and P. A. C. Whiffin, Changes in fluid flow during Czochralski growth, J. Crystal Growth **38**, 245-248, 1977 (No. 2).

points are plotted. From the available data and the available theory it is likely that a maximum crystal-rotation rate is to be expected. This rotation rate is a function of the temperature gradient in the melt, the viscosity of the melt, the radius of crystal and crucible and the pulling rate *f*. *Table III* summarizes the data for bismuth-silicon oxide. The same theory can be applied to gadolinium-gallium-garnet production and the predicted and observed crystal-rotation rates are in good agreement [8].

Table III. Temperature gradient, growth rate and critical rotation rate for five combinations of crystal and crucible diameter.

Crystal diameter (cm)	Crucible diameter (cm)	Gradient (°C/cm)	Growth rate (mm/hr)	Critical rotation rate (rev/min)
1.1	3.5	10	6	70
1.7	3.5	10	5	45
2.8	5.0	12	4	25
3.2	6.0	17	3	20
3.7	8.6	20	2.5	15

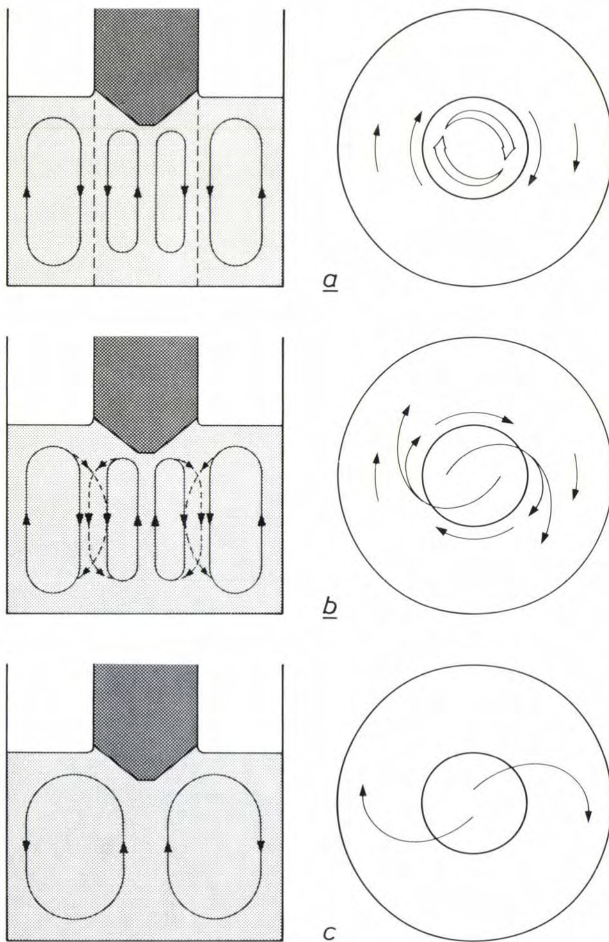

Fig. 12. Elevation and plan views of flow in a crucible at three rates of crystal rotation. In (*a*) the central column under the crystal rotates almost as a solid body and there is little mixing of particles from this column with the outer annulus, but the column is itself well stirred. In (*b*) the flows in the column and annulus mix and in (*c*) the whole melt is stirred.

Automation

The growth rate of large crystals is only a few millimetres per hour, as we saw in fig. 8. The complete process, including cooling down, takes five days for a large crystal like the one shown in fig. 4. This makes an automatic control not only economically desirable but a practical necessity. A number of experiments were carried out to detect the critical parameters to be measured and controlled to obtain a constant growth rate and a constant diameter. Attempts were made to control the process by regulation of the power in the r.f. coil and also by stabilization of the temperature of the melt. Our colleagues in Aachen also developed a laser-reflection system to measure the crystal diameter near the growth face. All systems failed on different points, however. They were not stable enough over long periods of time, not applicable to large crystals or the initial settings of the controls were not reproducible. The alternative approach of using a weighing system was therefore adopted [9].

Fig. 14 is a block diagram of the system. With this system the melt weight is controlled so that it is always very near to a target value produced by a reference source. Since a constant crystal diameter gives a constant rate of reduction of weight, the programmer to produce the target can be a very simple electromechanical system. However, for greater flexibility a numerical technique has been adopted. In the initial phase of the growth, when the crystal is growing from seed to full diameter, the weight of the melt increases nonlinearly with time. The growth pattern is also nonlinear in the final phase, when the diameter of the crystal decreases. In between the weight of the melt increases linearly with time. The necessary digital data can easily be derived from a microprocessor.

This system has produced crystals with diameters within 5% of the target diameter and with variations in diameter of less than 2%. The discrepancy from the target diameter was caused by small variations in the pulling rate and in the crucible diameters; both affect the growth rate of the crystals.

Other technological aspects

The apparatus described at the beginning of this article needed little modification for pulling crystals of larger diameter. The only significant change was to mount the puller on anti-vibration mountings. This was done because our building vibrates at frequencies between 7.5 and 9.5 Hz, and the puller had a resonant frequency of 7.5 Hz. An antivibration mount with a resonant frequency of 4 Hz reduced the vibration on the puller by a factor of about 4. Seed crystals with square cross-sections were used; each side of the

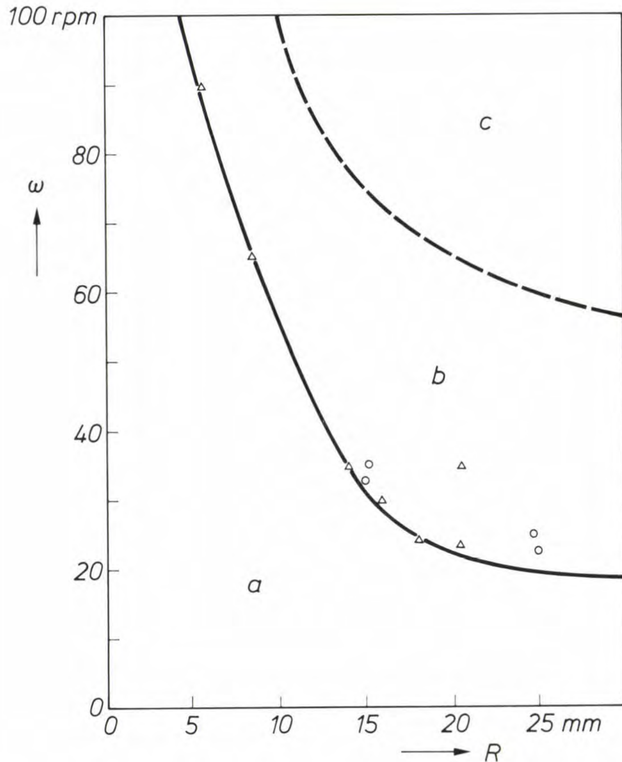

Fig. 13. The regions of the various flows plotted on a diagram showing rotation rate ω as a function of crystal radius. The regions *a*, *b* and *c* correspond to the flows in fig. 12*a*, *b* and *c* respectively.

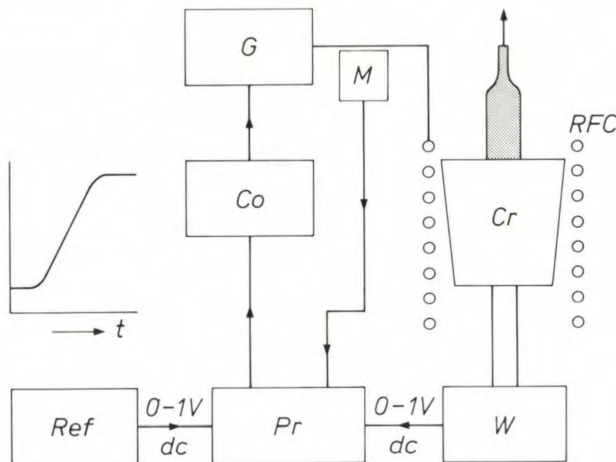

Fig. 14. Block diagram of the control system. The weight of the crucible *Cr* is determined by the weighing cell *W*, which supplies the processor *Pr* with a d.c. signal. The processor combines this signal with the signal from the reference source *Ref* and with a signal proportional to the r.f. current produced in the coil by the power meter *M*. The processor gives a signal to the control amplifier *Co*, which stabilizes the r.f. generator at the desired power level. The voltage of the reference source varies slowly with time (see inset) and the weight of the crucible is controlled to follow the reference source.

square was about a fifth of the crystal diameter. The seed crystals were polished with a fine abrasive powder before use, and a series of grooves were made for the wire used to bind the seed to the V-block holder. This was necessary to eliminate crack-nucleation centres caused by cutting damage. To reduce stresses on the seed crystal, it was wrapped in gold foil before being fastened in place and the holder for the crystal was attached to the pulling shaft by a series of ball-joints so that the system was self-aligning [*]. These measures reduced seed-crystal failure from about 30% to 5%. The crucibles were made from platinum containing less than 200 ppm of rhodium. (A higher rhodium content gave rise to corrosion, which soon led to crucible failure.) The internal heights and diameters of each of the crucibles were the same within ± 20% and we used successively diameters of about 35, 50, 60, 85 and 110 mm. The smaller crucibles had wall thicknesses of 1.5 mm and the bigger ones 2 mm. In use the crucibles distorted by about 5% before we discarded them; usually after about 20 runs. We looked for other materials but our tests showed that most metals, oxides and nitrides are rapidly corroded by the melt.

In order to obtain the temperature distributions necessary to prevent cracking heat shields were required.

Fig. 15 shows the assembly used for 40-mm diameter crystals. *Table IV* lists the sequence of operations, which can be fitted conveniently into a working week.

Table IV. Operational sequence for pulling 40-mm diameter BSO crystals.

Time from start (hrs)	Phase of process
0	Start melt down
2	Put seed crystal into melt
2.5	Start pulling and cooling for expansion
10	Start parallel growth
60	Start tapering in
68	Growth complete
105	Crystal all inside heat shield. Start to cool melt
130	Power off

Economic aspects

Very little has been published on the economic aspects of crystal growing [10]. Probably the reason is that the costs of the crystal production form only a small part of the production costs of a device. In this section we shall make a few comments on the costs of device production: it will appear that larger crystals are more economical than smaller ones, for both growth and processing.

[8] K. Takagi, T. Fukazawa and M. Ishii, Inversion of the direction of the solid-liquid interface on the Czochralski growth of GGG crystals, J. Crystal Growth **32**, 89-94, 1976.
[9] H. J. A. van Dijk, J. Goorissen, U. Gross, R. Kersten and J. Pistorius, Crystal diameter control in Czochralski growth, Acta Electronica **17**, 45-55, 1974.
[10] J. C. Brice, The growth of insulating crystals, Repts. Progr. Phys. **40**, 567-602, 1977 (No. 5).
[*] This attachment system was designed and made by V. E. Cox, of our Laboratories.

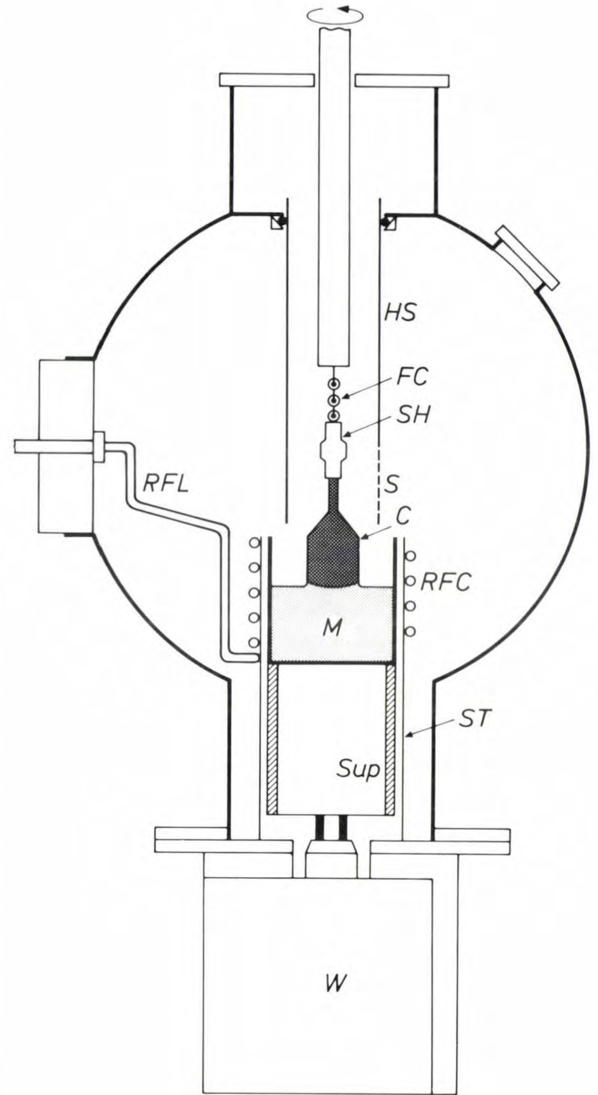

Fig. 15. The pulling apparatus used for growing crystals 40 mm in diameter. *M* melt in platinum crucible. *C* crystal. *SH* holder for seed crystal. *FC* flexible coupling. *HS* heat shield with viewing gaps *S*. *RFC* r.f. heating coil with supply *RFL*. *ST* silica tube that insulates the water-cooled coil *RFC* from the hot crucible. *Sup* support for the crucible. *W* weighing cell.

Table V. The effect of crystal dimensions on the times necessary for various device-fabrication processes. The quantity *L* can be identified with either the length or the diameter of the crystal, since these are in approximate proportion.

Process	Time per device inversely proportional to
Crystal orientation	L^3
Crystal cutting	L
Slice processing	L^2
Device separation	L

After the BSO crystal has been grown there are six further stages necessary for the production of filters. The crystal directions are determined by X-ray methods and slices of known orientation are cut. These are polished, electrodes are evaporated on to them and patterns are etched in the electrodes. Finally, the filter elements are separated from the array on the processed slice. With large crystals the handling costs are lower. *Table V* shows how the time taken for various processes depends on a typical dimension L of the crystal. (It is assumed that length and radius change in proportion, which is usually the case for pulled crystals.) The table suggests that the handling times decrease at least linearly with increasing size and that correspondingly large savings in man and machine time can be made. So even if the price per kilogram of the crystalline material is the same, there are good reasons for spending a great deal of effort to solve the problems of growing large crystals.

However, large crystals can be made more cheaply and more effectively than small ones. For a pulled bismuth-silicon-oxide crystal fig. 8 shows that $fR^{1/2}$ is a constant for smaller crystals and that for larger crystals $fR^{3/2}$ is a constant. The production per hour of single crystals can be calculated from this information. This is plotted in *fig. 16*, which shows the hourly production of a crystal as a function of crystal radius. It is clear that machines pulling larger crystals have a higher hourly output in spite of the lower pulling rate.

The automation, necessary for the long pulling times, gives an additional saving in money. The yield from automated production, in our experience, is 65-75% instead of 40-50% for the manual process. In addition, the predictability of the product from an automated system should not be overlooked.

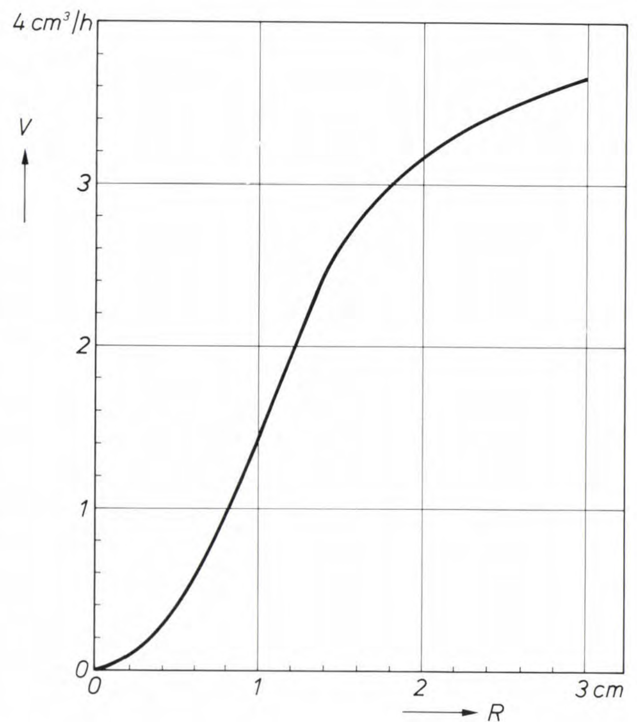

Fig. 16. The volume *V* of single-crystal bismuth-silicon oxide produced per hour, as a function of the radius *R* of the pulled rod.

Device-production processes are most economic with a fixed size of crystal. Exceeding the target radius R by an amount ΔR wastes a fraction $2\Delta R/R$. Hence if an error ΔR can arise, the target must be increased by this amount with the associated wastage. In our case automation at least halved this wastage at $R = 2$ cm. Further reduction in costs would be expected if resistance heating was used instead of radio-frequency heating. Finally, *Table VI* gives a few cost factors and shows how they contribute to the costs per unit volume of crystal pulled.

Table VI. The effect of the pulling rate f and the radius R of the crystal on the cost per cm³ of the crystal produced, for the five most important factors.

Factor	Cost inversely proportional to
Energy	fR
Platinum crucible	R
Manpower	
manual process	fR^2
automated process	R^2
Machine time	
growth	fR^2
cooling	R^2
Materials	No significant dependence [*]

[*] Decrease in the growth rate may allow less pure materials to be used.

Appendix: Calculation of the temperature distribution in a crystal

Let us assume (see *fig. 17*) that a crystal C at the position $z = 0$ is in contact with a melt at the temperature T_m. The diameter of the crystal is $2R$, the thermal conductivity is λ and the heat transferred from the surface of the cylinder to the surroundings (shown here as a heat shield H) is equal to $\mu(T - T_0)$, where μ is a constant determined by the method of cooling, the surface of the crystal, etc., and T_0 is the external temperature. If we also put $\mu R/\lambda = \gamma$, and if $J_0(x)$ is the zero-order Bessel function of argument x, then the temperature of the crystal at the position r,z can be calculated [11]:

$$T(r,z) = T_0 + 2\,(T_m - T_0) \sum_{n=0}^{\infty} \frac{\gamma}{\gamma^2 + \beta_n^2} \times$$

$$\times \frac{J_0(\beta_n r/R)}{J_0(\beta_n)} \exp(-\beta_n z/R). \qquad \text{(A1)}$$

The values of β_n are calculated as solutions of the equation

$$\beta_n J_1(\beta_n) = \gamma J_0(\beta_n), \qquad \text{(A2)}$$

where $J_1(\beta_n)$ is the first-order Bessel function of argument β_n.

For very small values of γ, i.e. for very thin crystals of high thermal conductivity, we only require the first term of this series. Since β_0 is small we can replace the Bessel functions by the first term of their power series. Equation (A2) then gives

$$\tfrac{1}{2}\beta_0^2 = \gamma, \quad \text{so that} \quad \beta_0 = (2\gamma)^{1/2},$$

and equation (A1) is reduced to:

$$T(r,z) \approx T_0 + (T_m - T_0)\frac{1 - \frac{1}{2}\gamma (r/R)^2}{1 - \frac{1}{2}\gamma} \{\exp - (2\gamma)^{1/2} z/R\}.$$

The gradient of the temperature at the growth face is therefore given by:

$$\left(\frac{dT}{dz}\right)_{z=0} = -(T_m - T_0)\frac{(2\gamma)^{1/2}}{R}\,\frac{1 - \frac{1}{2}\gamma (r/R)^2}{1 - \frac{1}{2}\gamma}.$$

Since γ is small and equal to $\mu R/\lambda$, a first approximation for the temperature gradient is

$$\left(\frac{dT}{dz}\right)_{z=0} \approx -(T_m - T_0)\left(\frac{2\mu}{\lambda}\right)^{1/2} \frac{1}{R^{1/2}}.$$

In the case of BSO γ is approximately equal to $0.4R$. A more accurate calculation [12], also valid for larger values of γ, gives:

$$(dT/dz)_{z=0} = -1.3(T_m - T_0)\,(\mu/\lambda)^{0.474} R^{-0.526}.$$

The difference between the accurate and the approximate values is therefore small.

If the temperature distribution is not uniform there will be strain, since the different parts of the crystal do not have the same expansion. The strain ε_θ of a ring of radius r is given by [13]:

$$\varepsilon_\theta = \alpha\left\{\frac{1}{R^2}\int_0^R Tr\mathrm{d}r + \frac{1}{r^2}\int_0^r Tr\mathrm{d}r - T\right\}.$$

If the strain is calculated from the approximate temperature distribution, it is found that the highest permissible temperature gradient at the boundary surface is given by:

$$\left(\frac{dT}{dz}\right)_{max} = \frac{4\varepsilon_b}{\alpha R^{3/2}}\left(\frac{\lambda}{\mu}\right)^{1/2}(1 - \tfrac{1}{2}\gamma),$$

where ε_b is the strain at which the crystal cracks. Since the strains

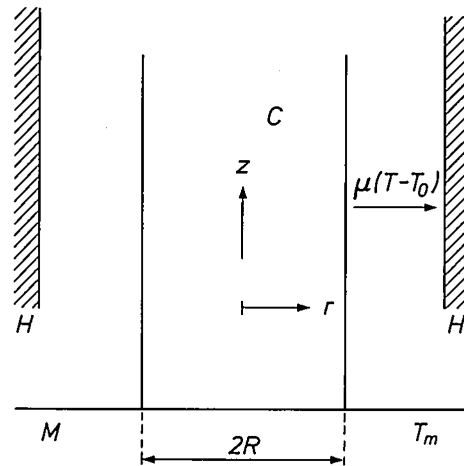

Fig. 17. Calculation of the temperature distribution in a crystal.

Table AI. Calculated and measured values of the maximum permissible temperature gradient $(dT/dz)_{max}$ in the crystal for four values of the crystal radius.

R (mm)	$(dT/dz)_{max}$ (°C/cm)	
	measured	calculated
4	180	279
6	100	145
10	50	61
19	20	18

[11] J. C. Brice, Analysis of the temperature distribution in pulled crystals, J. Crystal Growth 2, 395-401, 1968.
[12] J. C. Brice and D. J. Kroon, to appear in J. Crystal Growth.
[13] S. Timoshenko and J. N. Goodier, Theory of elasticity, 2nd edn, McGraw-Hill, New York 1951.

in the axial and tangential directions are approximately equal (see fig. 7), ε_b is approximately equal to $2^{1/2}\varepsilon_0$.

A more accurate calculation can also be made here; it gives:

$$\left(\frac{dT}{dz}\right)_{max} = 8.7\frac{\varepsilon_b}{\alpha}\left(\frac{\lambda}{\mu}\right)^{0.34}\frac{1}{R^{1.34}}.$$

The maximum permissible growth rate is found by substituting the expression just derived for $(dT/dz)_{max}$ in the relation

$$f_{max} = \frac{\lambda}{L}\left(\frac{dT}{dz}\right)_{max}.$$

Some calculated and measured values of the temperature gradient are summarized in *Table AI.*

Summary. Crystals with the cubic γ-bismuth-oxide structure, such as bismuth-silicon oxide, can be used to make surface-wave filters for TV and other applications. Large crystals of this material weighing several kilograms and with diameters up to 50 mm have been grown at PRL using a pulling technique. To avoid cracking due to thermal strain the maximum permissible axial thermal gradient has to be proportional to $R^{-3/2}$, where R is the crystal radius, whereas for inclusion-free growth the axial thermal gradient has to be proportional to $R^{-1/2}$. The composition of the crystals is found to be highly independent of the composition of the melt. Effective control of the rotation rate is very important to avoid hydrodynamic instabilities. The long pulling times necessary for the growth of large crystals and the reproducibility required made an automated equipment desirable. This system keeps the diameter constant to within 2% and the maximum difference from the desired value is 5%. Devices are cheapest when made from large crystals.

Recent scientific publications

These publications are contributed by staff of laboratories and plants which form part of or cooperate with enterprises of the Philips group of companies, particularly by staff of the following research laboratories:

Philips Research Laboratories, Eindhoven, The Netherlands	*E*
Philips Research Laboratories, Redhill, Surrey, England	*M*
Laboratoires d'Electronique et de Physique Appliquée, 3 avenue Descartes, 94450 Limeil-Brévannes, France	*L*
Philips GmbH Forschungslaboratorium Aachen, Weißhausstraße, 51 Aachen, Germany	*A*
Philips GmbH Forschungslaboratorium Hamburg, Vogt-Kölln-Straße 30, 2000 Hamburg 54, Germany	*H*
MBLE Laboratoire de Recherches, 2 avenue Van Becelaere, 1170 Brussels (Boitsfort), Belgium	*B*
Philips Laboratories, 345 Scarborough Road, Briarcliff Manor, N.Y. 10510, U.S.A. (by contract with the North American Philips Corp.)	*N*

Reprints of most of these publications will be available in the near future. Requests for reprints should be addressed to the respective laboratories (see the code letter) or to Philips Research Laboratories, Eindhoven, The Netherlands.

E. Arnold & J. M. Shannon: Anomalous Hall effect and carrier transport in bandtails at the Si-SiO_2 interface.
Solid State Comm. **18**, 1153-1156, 1976 (No. 9/10). *M*

C. Belouet, M. Monnier, E. Dunia* & J. F. Pétroff* (* Université de Paris VI): X-ray topographic study of dislocations in $KH_{2(1-x)}D_{2x}PO_4$ single crystals.
Mat. Res. Bull. **11**, 903-910, 1976 (No. 8). *L*

A. J. van Bommel & J. E. Crombeen: LEED, Auger electron spectroscopy (AES) and photoemission studies of the adsorption of cesium on the epitaxially grown GaAs(110) surface.
Surface Sci. **57**, 109-117, 1976 (No. 1). *E*

A. J. van Bommel & J. E. Crombeen: Experimental determination of the correlation between the LEED pattern and the Ga-As bond vectors in the surface of GaAs(001).
Surface Sci. **57**, 437-440, 1976 (No. 1). *E*

J. van den Boomgaard & A. M. J. G. van Run: Poling of a ferroelectric medium by means of a built-in space charge field, with special reference to sintered magneto-electric composites.
Solid State Comm. **19**, 405-407, 1976 (No. 5). *E*

M. R. Boudry, J. A. Morice & E. J. Millett: A versatile multi-access computing system for laboratory instrumentation.
On-line computing in the laboratory, editors R. A. Rosner, B. K. Penny & P. N. Clout, Advance Publications, London 1976, pp. 353-361. *M*

P. W. J. M. Boumans, G. H. van Gool & J. A. J. Jansen: A computerised programmable monochromator for flexible multi-element analysis with special reference to the inductively coupled plasma.
Analyst **101**, 585-587, 1976 (No. 1204). *E*

K. H. J. Buschow: Hydrogen absorption and its effect on the magnetic properties of rare-earth iron intermetallics.
Solid State Comm. **19**, 421-423, 1976 (No. 5). *E*

K. L. Bye: Structural dependence of the electro-optic properties of some PLZT ceramics.
Ferroelectrics **12**, 221-223, 1976 (No. 1/2/3/4). *M*

V. Chalmeton: Chaîne de radioscopie 400 kV avec intensificateur à galette de microcanaux.
Acta Electronica **20**, 53-64, 1977 (No. 1). *L*

V. Chalmeton: Principaux éléments d'un système radiographique.
Acta Electronica **20**, 83-87, 1977 (No. 1). *L*

P.-J. Courtois & H. Vantilborgh: A decomposable model of program paging behaviour.
Acta Informatica **6**, 251-275, 1976 (No. 3). *B*

P. A. Devijver: Entropie quadratique et reconnaissance des formes.
Computer oriented learning processes, editor J. C. Simon, Noordhoff, Leiden 1976 (NATO ASI Ser. E 14), pp. 257-278. *B*

J. G. Dil & E. M. Brody (University of Rochester, N.Y.): Brillouin scattering from isotropic metals.
Proc. 3rd Int. Conf. on Light scattering in solids, Campinas, Brazil, 1975, pp. 340-345; 1976. *E*

H. Durand: Transformer le rayonnement solaire en électricité?
Revue Andès No. 19, 24-27, 1976. *L*

D. den Engelsen: Optical anisotropy in ordered systems of lipids.
Surface Sci. **56**, 272-280, 1976. *E*

L. J. M. Esser: Peristaltic charge coupled devices: what is special about the peristaltic mechanism.
Solid state imaging, editors P. G. Jespers, F. van de Wiele & M. H. White, Noordhoff, Leiden 1976, pp. 343-425. *E*

P. C. M. Gubbens, A. M. van der Kraan (both with Interuniversitair Reactor Instituut, Delft) **& K. H. J. Buschow:** Relation between anisotropy and crystal structure in rare-earth (3*d*) transition compounds (R_2M_{17}).
Solid State Comm. **19**, 355-356, 1976 (No. 4). *E*

T. K. Halstead, N. A. Abood (both with University of York) **& K. H. J. Buschow:** Study of the diffusion of hydrogen in $LaNi_{5+x}H_6$ compounds by ^1H NMR relaxation.
Solid State Comm. **19**, 425-428, 1976 (No. 5). *E*

K. H. Härdtl: Physics of ferroelectric ceramics used in electronic devices.
Ferroelectrics **12**, 9-19, 1976 (No. 1/2/3/4). *A*

E. P. Honig & B. R. de Koning: Ellipsometric investigation of the skeletonization process of Langmuir-Blodgett films.
Surface Sci. **56**, 454-461, 1976. *E*

E. Kirchner & J. Leu (C. H. F. Müller, Hamburg): Technical components for the generation of X-rays.
Acta Electronica **20**, 25-32, 1977 (No. 1).

J. L. Kirk & L. E. Cross (both with The Pennsylvania State University, University Park, Pa.) **& J. P. Dougherty:** Pressure and temperature dependence of the dielectric properties and phase transitions of the ferroelectric $Pb_5Ge_3O_{11}$.
Ferroelectrics **11**, 439-443, 1976 (No. 3/4). *N*

F. Kools: Complications in firing oriented hexaferrites due to anisotropic effects. Cracking of radially oriented rings during firing.
Science of Ceramics **7**, 27-44, 1973. *E*

E. Krätzig & H. Kurz: Photo-induced currents and voltages in $LiNbO_3$.
Ferroelectrics **13**, 295-296, 1976 (No. 1/2/3/4). *H*

W. Kühl & J. E. Schrijvers (Philips Elcoma Division, Eindhoven): Design aspects of X-ray image intensifiers.
Acta Electronica **20**, 41-51, 1977 (No. 1).

H. Kurz: Photorefractive recording of volume holograms in doped $LiNbO_3$.
Ferroelectrics **13**, 291-293, 1976 (No. 1/2/3/4). *H*

R. E. van de Leest: Solid-state ion-selective electrodes based on thin ion-selective layers deposited on ionic conductors.
Analyst **101**, 433-438, 1976 (No. 1203). *E*

P. Medema, W. J. Bronnenberg, H. C. Bunt, S. P. J. Landsbergen, R. J. H. Scha, W. J. Schoenmakers & E. P. C. van Utteren: PHLIQA 1: multilevel semantics in question answering.
Amer. J. comput. Linguistics, Microfiche 32, pp. 72-86, 1975. *E*

F. Meyer: Ellipsometric studies of adsorption reactions on clean surfaces.
Surface Sci. **56**, 37-48, 1976. *E*

A. van Oostrom: Auger electron spectroscopy of the surface of a dispenser cathode with barium scandate.
Proc. 5th Italian Vacuum Congress, Perugia 1975, pp. 145-148; 1976. *E*

C. van Opdorp: Methods of evaluating diffusion lengths and near-junction luminescence-efficiency profiles from SEM scans.
Philips Res. Repts. **32**, 192-249, 1977 (No. 3). *E*

G. Piétri: Industrial X-ray control.
Acta Electronica **20**, 8 *(in English)*, 9 *(in French)*, 1977 (No. 1). *L*

H. I. Ralph: Scattering of holes from impurity potentials in the spherical-band approximation.
Philips Res. Repts. **32**, 160-191, 1977 (No. 3). *M*

W. Schilz, R. Jacobson & B. Schiek: Mikrowellen-Entfernungsmeßsystem mit $\pm$ 2,5 mm Genauigkeit.
Mikrowellen-Magazin 2/76, pp. 102-107, 1976. *H*

H. Scholz: Crystal growth by dynamic gradient reversal techniques: I. Consequences of periodic gradient reversals of Gibbs' functions in crystal growth experiments, II. General comments on selection, III. Pure thermodynamic derivation of growth conditions.
Solid State Comm.: **19**, 429-433, 1976 (No. 5); **20**, 195-197, 1976 (No. 3); **20**, 447-448, 1976 (No. 4). *A*

G. Simpson & E. T. Keve: Anomalous ferroelectric behaviour in PLZT.
Ferroelectrics **12**, 229-231, 1976 (No. 1/2/3/4). *M*

J. L. Sommerdijk, A. C. van Amstel & F. M. J. H. Hoex-Strik: On the luminescence of β-Ga_2O_3:Dy^{3+}.
J. Luminescence **11**, 433-436, 1976 (No. 5/6). *E*

J. L. Sommerdijk & A. Bril: Divalent europium luminescence in perovskite-like alkaline-earth alkaline fluorides.
J. Luminescence **11**, 363-367, 1976 (No. 5/6). *E*

J. L. Sommerdijk, A. Bril & F. M. J. H. Hoex-Strik: Luminescence of Dy^{3+}-activated vanadates.
Philips Res. Repts. **32**, 149-159, 1977 (No. 3). *E*

A. L. N. Stevels: New phosphors for X-ray screens.
Medicamundi **20**, 12-22, 1975 (No. 1). *E*

J. B. Theeten & F. Hottier: On the role of chlorine in the vapour phase epitaxy of (100)GaAs as evidenced by LEED and RHEED.
Surface Sci. **58**, 583-589, 1976 (No. 2). *L*

W. Tolksdorf & F. Welz: Verbesserte Tiegelformen zur Herstellung von Yttrium-Eisen-Granat-Einkristallen aus schmelzflüssiger Lösung.
J. Crystal Growth **35**, 285-296, 1976 (No. 3). *H*

E. Zieler (C. H. F. Müller, Hamburg): Possibilities and limits of industrial radiography and radioscopy.
Acta Electronica **20**, 11-24, 1977 (No. 1).

Volume 37, 1977, No. 9/10 pages 221-264 Published 22nd June 1978

PHILIPS TECHNICAL REVIEW

VOLUME 37, 1977, No. 11/12

LSI

In about 1960 there was good reason to say that there had been a revolution in electronics, for in less than ten years the transistor had virtually replaced the thermionic valve in nearly all kinds of application. Today, however, we are in the midst of developments that are even more drastically changing the face of electronics — with no end in sight. When transistor manufacturers changed from the alloy to the planar technology — based on photolithographic processes — it only depended on the nature of the photomasks whether a small, simple circuit was produced or a large, complicated circuit consisting of hundreds of interconnected elements. Now it was possible in principle to make larger and larger integrated circuits. In 15 years integrated-circuit technology has advanced from SSI (small-scale integration; 10 gates per chip) via MSI (medium-scale integration; 100 gates per chip) to LSI (large-scale integration; 1000 gates per chip), and now we are on the threshold of the next great advance (VLSI, very-large-scale integration; 10^4 gates per chip).

This evolution would not have been possible without detailed and extensive research in the large industrial research laboratories, including those of Philips. Readers will probably remember the contributions from Philips Research that have been described in earlier volumes of this journal: the issue on MOS technology, and many articles such as those on the LOCOS process, injection logic (I^2L), and the 'Opthycograph'.

While the full impact of this later and greater revolution in electronics has only penetrated to the user in recent years, the research is by no means at an end. It therefore seemed appropriate to make LSI the subject of this special issue that completes our volume for the year. We start with an introductory article that gives a general picture of the evolution from the simple transistor to the LSI circuit and its repercussions on the designing of electronic circuits. Other articles include contributions on the subject of lithography — including the use of electron beams — and on the computer-aided design of large-scale integrated circuits. Three of the articles deal with specific LSI applications: an N-MOS circuit for telephony, an I^2L circuit for data transmission, and an image sensor based on the charge-transfer principle.

An issue of this size cannot of course given anything like a full picture of Philips activities in the IC field — not even in research. The next volume will therefore contain a few other instances of advances in IC technology or applications. For the present, we will close by noting that developments in integrated circuits are now so rapid that those who are in the front line of the research may regard certain approaches as already out of date even before the work has left the IC development laboratory or has appeared in print.

Manufacturing ever-larger integrated circuits requires continuous improvement in the control of the processes and conditions of production. It is of the utmost importance, for example, that the least possible amount of dust should settle on the wafer during the different operations. At Philips Research Laboratories in Eindhoven all experimental integrated circuits are therefore made in a specially built department that has its own 'clean room'. The number of dust particles of half a micron and larger contained per unit volume of this room is about ten thousand times smaller than in an ordinary laboratory working-space. All the operations necessary for the fabrication of integrated circuits are performed in this room. The equipment is set up in 'lanes'. In the lane on the right of the photograph the silicon wafers are given a coating of photoresist and then illuminated through a mask. In the lane on the left the wafers undergo wet-chemical etching.

Philips tech. Rev. 37, 267-277, 1977, No. 11/12

LSI — a revolution in electronics

H. Bosma and W. G. Gelling

If we take a look at the development that digital integrated circuits have undergone in the last 15 years, we find that the number of gates per chip has increased from less than five to about 10 000, the number of gates per mm² has increased from two to 300, the τD product of the delay time τ and the dissipation D in a gate has decreased from 150 pJ to 0.2 pJ (one pJ is 10^{-12} joules) and the price per gate has fallen from 25 dollars to a tenth of a cent.

This development, towards ever larger circuits and increasing packing densities, has come about through the work of three groups of engineers and scientists. First there are the electronic engineers, who saw the chance of a continued simplification of the elementary circuits for the logic functions, so that these have steadily diminished in size. At the same time they have succeeded in keeping the steadily growing circuits manageable and integrating them to a single and usually very complicated entity.

The second group is formed by the chemists, who continuously study, improve and develop the many processes in the long path from raw material to finished IC. A special place between these two groups is perhaps occupied by the device physicists, who seek for an understanding of the fundamental background to the operation of the separate elements such as diodes, bipolar transistors and MOS transistors. From the knowledge that they amass it is possible to find how best the work should be directed to obtain a particular improvement in performance, for example, and to establish associated physical limits.

We will not consider the economic side of modern IC technology here, with its many and often conflicting aspects. In what follows we shall give a very general picture first of the technological and then of the electronic development. Finally, we shall devote some attention to the development that has taken place in electronic design. The increasing complexity of the circuits makes it increasingly difficult to design them conventionally 'by hand' and to test them after manufacture. The computer, in its present form itself a product of IC technology, has become an indispensible tool here.

Dr Ir H. Bosma and Drs W. G. Gelling are both Deputy Directors of Philips Research Laboratories, Eindhoven.

The silicon starting material

It is now possible to make virtually perfect single crystals of silicon — by pulling from the melt — with a diameter of no less than 10 cm; in about 1960, at the start of the silicon technology, the diameter was 2 cm. The content of undesirable impurities in these crystals is reduced to a value between 1 in 10^5 and 1 in 10^9, depending on the kind of impurity. The 'desirable' impurity content — the doping — which determines the electrical properties, is kept under accurate control. There has also been continued improvement in the methods of sawing the crystals into thin wafers and polishing them. The wafers (sometimes called slices) have a typical thickness of about 0.5 mm; see *fig. 1*.

In the meantime silicon crystals with a diameter of 15 cm have been successfully pulled in the laboratory. Larger wafers can only be processed in the factory after modification of the process equipment and to some extent the actual processes. However, for the development from LSI to VLSI a larger wafer diameter is not as yet essential.

The application of epitaxial layers to the wafers has also undergone a continuous process of development. An epitaxial layer is a single-crystal silicon layer, applied from the gas phase, whose crystal lattice joins that of the wafer substrate in a smooth uninterrupted transition, but the electrical properties differ from those of the substrate because of different doping. Epitaxial layers are necessary for almost all bipolar circuits; on the other hand MOS circuits are almost always made directly in the surface of a wafer of N-type or P-type silicon. As transistors became smaller, it was also necessary to make the epitaxial layer thinner. While IC technology began with epitaxial layers 10 to 15 µm thick, in some extreme cases now layers of only 1 µm are found.

Physico-chemical processing

Oxidation

Integrated-circuit technology would have made far less progress if the element silicon had not had such a unique combination of properties. It is a semiconductor with very good and easily regulated electrical properties;

as we have said, it is very suitable for making large and pure single crystals; and finally it can be oxidized to form a thin, dense and homogeneous layer of oxide that is very strongly bonded to the silicon surface. SiO_2 layers made by thermal oxidation — in oxygen or water vapour at about 1000 °C — are chemically very resistant, have excellent properties as an electrical insulator and protect the underlying silicon from all kinds of environmental effects. It should be noted here that such 'good' oxide layers can only be obtained if the oxidation is carried out in extremely clean furnaces, a condition that also applies for all the other silicon processing in furnaces.

The nearly ideal insulator properties make a layer of silicon oxide very suitable for functioning as a base for the metal interconnection tracks that connect the various components of the IC. Fairly 'thick' oxide layers are usually used for this purpose, from 0.5 to 1.5 μm, or more than 2 μm in extreme cases. The oxide layer was initially applied continuously over the complete wafer, and the various IC components were made by diffusion through windows etched in the oxide (see below). At Philips Research Laboratories a method was found ten years ago for *locally* applying the thick oxide layer that would later serve as the base for the interconnections, so that it was only applied where it was wanted [1]. This technology, known as LOCOS (from LOCal Oxidation of Silicon) is now widely used throughout the world.

A special application that sets very high standards for an oxide layer is its use as the insulating layer between the gate and the channel of an MOS transistor. The oxide layer here must be able to withstand a voltage close to the breakdown value — 10^7 volts per cm for thin layers — without any drift in its properties. The manufacture of these layers, which in the most up-to-date MOS technology are only about 50 nm thick, requires the most careful process control.

Doping

Because of its chemical resistance and impenetrability to certain substances a layer of silicon oxide is also very suitable for use as a doping mask. The 'foreign' atoms are diffused into the silicon surface, through windows etched in the oxide layer, by heating the wafers in a furnace in which the desired dopant is present in a gaseous form. At all the places where the silicon is coated with oxide it is effectively protected against the penetration of foreign atoms. Although silicon oxide is by no means resistant to all foreign substances, it is so for the particular substances that are usually used for doping: phosphorus, arsenic and antimony for obtaining *N*-type silicon and boron to obtain *P*-type silicon.

The mechanism that determines how many atoms penetrate into the silicon and exactly where they reach is very complex. Even with very good control of the furnace temperature it is not very easy to control the concentration profile of the doping at the wafer surface to better than a few per cent. It is also impossible to produce very light doping in this way; in practice the lower limit is in the region of 10^{14} atoms per cm^2. (To give a comparison, a single layer of atoms lying side by side contains about 10^{15} atoms per cm^2, so a doping of 10^{14} atoms per cm^2 is equivalent to 0.1 atomic layers.)

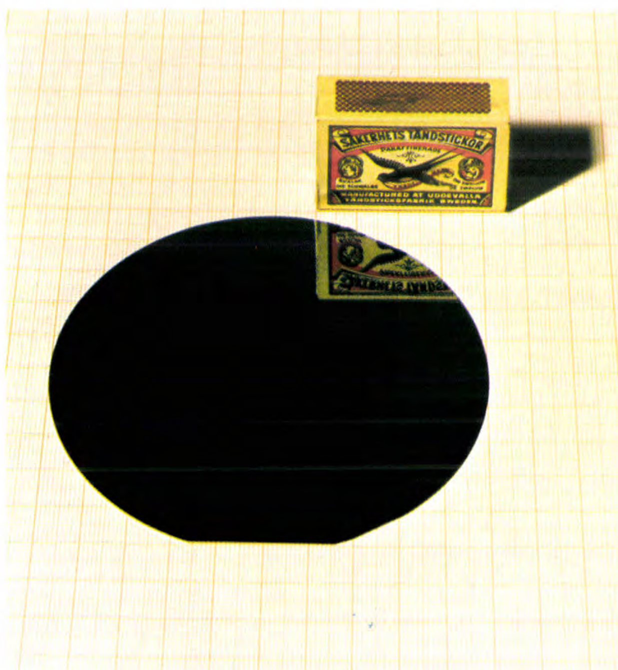

Fig. 1. Polished silicon wafer on which integrated circuits can be made. The wafer is obtained from a cylindrical crystal 10 cm in diameter and is only 0.5 mm thick. After the circuits have been formed the wafer is broken into 'chips', each carrying an IC.

A real revolution took place when silicon was first successfully doped by using 'ion implantation' [2]. In this process the atoms to be introduced into the wafer are ionized, and the ions produced are accelerated in an

[1] J. A. Appels, E. Kooi, M. M. Paffen, J. J. H. Schatorjé and W. H. C. G. Verkuylen, Local oxidation of silicon and its application in semiconductor-device technology, Philips Res. Repts. **25**, 118-132, 1970.
J. A. Appels and M. M. Paffen, Local oxidation of silicon; new technological aspects, Philips Res. Repts. **26**, 157-165, 1971.
E. Kooi, J. G. van Lierop, W. H. C. G. Verkuylen and R. de Werdt, LOCOS devices, Philips Res. Repts. **26**, 166-180, 1971.
See also Philips tech. Rev. **31**, 234 and 276, 1970, and **34**, 19, 1974.

[2] An article by J. Hofker and J. Politiek on this subject will appear in the next volume of Philips Technical Review.

electric field to an energy of 20 to 200 keV. To prevent other kinds of ions from reaching the wafer the ions are sorted by mass in a magnetic field, in the same way as in a mass spectrometer. The unwanted beams are intercepted, while the beam consisting of the desired ions is transmitted and directed towards the surface of the silicon wafer to be doped. Electronic control systems are used which can ensure that the entire surface of the wafer receives a uniform 'sprinkling' of ions, while the amount of the dose can be accurately controlled (to a few per cent) down to the very low values (10^{12} ions per cm, i.e. about 0.001 atomic layers).

Recent improvements in the reproducibility of the chemical deposition of boron and phosphorus may once more enable this method to compete with ion implantation for heavy doping.

In fact the ions are not just 'sprinkled' on the surface; they penetrate a little way into it. This provides more scope: the penetration depth can be varied and the ions can be fired through a thin protective layer, e.g. of SiO_2. Parts of the wafer where no doping is required are masked, e.g. with photoresist. Another advantage of ion implantation is that it will give good results with kinds of atoms that are difficult to deposit by chemical methods, such as arsenic and antimony.

It was ion implantation that enabled the *N*-channel MOS technology to be developed. The application of very small but accurately controlled amounts of boron and phosphorus or arsenic (10^{11}-10^{13} atoms per cm^2) is essential here to prevent the formation of parasitic channels underneath the conductors and to set the threshold voltage of the transistors to the desired values. At the same time the implantation method gives the manufacturer a free choice for the concentration of the boron doping in the silicon wafers, which should ideally be low to keep down the parasitic capacitance between the transistors and the substrate.

The ability to introduce arsenic atoms in an accurately controlled way and in any desired quantity is also very important for another reason. As transistors become smaller, the diffusion depths must also be reduced. For very shallow diffusions (0.2 to 0.4 μm) phosphorus, with its relatively high diffusion rate, cannot be relied upon. Arsenic, which diffuses much more slowly than phosphorus, is a very good replacement here.

The bombardment of the wafer by ions produces some damage in the crystal lattice, but this can be corrected by a heat treatment. The effects arising here have not as yet been explained. Further studies are also necessary of the interaction between different dopings introduced by ion implantation and of the effects that arise for very heavy doping.

Getters

As we mentioned above, all furnace operations must be carried out with the greatest care to ensure the absence of impurities. This is clearly no less true for the cleaning of the silicon wafers before they are processed at very high temperatures. In spite of every precaution it is impossible to completely prevent contamination of the silicon; the starting material contains varying quantities of unwanted atoms, and contamination during the processing cannot be completely avoided. Typical contaminants here are small traces of various metals, such as sodium, iron, copper and gold. These kinds of impurities give rise to higher leakage currents and also to the formation of surface defects during the oxidation of the surface of the wafer. These defects in their turn also give rise to higher leakage and to short-circuits in bipolar transistors with shallow diffusions, and hence to rejects in production. Certain classes of MOS circuits in which very small charges have to be stored for relatively long times in reverse-biased diodes, such as dynamic memories, charge-transfer devices and light-sensitive devices, are very sensitive to leakage current. The achievement of a very low impurity level is an absolute essential for the manufacture of these circuits.

Since in spite of all precautions contamination cannot be completely prevented, methods have been devised in which the undesirable atoms can be removed from the silicon at a late stage in the manufacture. These 'clean-up' treatments, some more effective than others, have the common feature that crystal damage is introduced intentionally, either mechanically or chemically, at some unimportant part of the wafer, such as the back, where it does not matter. The impurity atoms associate themselves preferentially with the crystal defects. If such a wafer with defects is then heated to a temperature at which the impurities can diffuse rapidly, the damaged layer acts as a collection zone for undesirable atoms from the entire wafer.

By analogy with the gas getters used in vacuum work the terms 'gettering' and 'getter treatments' are also used here. The mechanism of the getter operation is perhaps more complicated than has been suggested above and is a subject of investigation, along with the correct method of application in the various IC processes.

Gettering is obviously only effective for impurities that diffuse rapidly. The undesirable metals mentioned above come into this category. Impurities that only diffuse with difficulty, such as oxygen and carbon, cannot be gettered. Manufacturers of silicon wafers continue to devote much attention to this problem.

A treatment that is to some extent related is 'hydrochloric-acid oxidation'. It has been found that the formation of crystal defects directly beneath an SiO_2 layer

during the oxidation can be very effectively suppressed by carrying out the oxidation in an atmosphere of oxygen to which about 1% of hydrogen-chloride gas has been added. The mechanism of this reaction is not as yet understood in all respects.

Lithography

In IC technology the term 'lithography' refers to the collection of operations that are necessary in etching a pattern of small apertures in the thin layers (oxides metals, etc.) applied to the silicon wafers. The basic stages in such a process are: exposure of a light-sensitive coating (photoresist) on the wafer through a photographic negative (the mask), development of the photoresist, followed by the etching away of the exposed parts of the layer underneath. These three operations are performed seven times (or more) on a wafer before it is ready.

The masks are obtained as follows. A photographically produced drawing of the mask for an IC, at ten times full scale, the 'reticle', is projected many times by a special camera in rows and columns on a photographic plate, so that practically all of the plate is covered with the small patterns at the correct scale. Contact copies are made from the master mask obtained in this way, and the copies are used for exposing the silicon wafers.

In the method that has usually been used so far the mask is pressed against the wafer to give a sharp shadow; see *fig. 2*. However, since mask and wafer come into contact it is impossible to avoid damage to the mask, and once such imperfections have been introduced they are repeated on all the following wafers. In practice this effect will strongly reduce the yield, particularly for very large circuits. Contact masks are therefore discarded after they have been used six to ten times. Since a single wafer is exposed seven times or more — with different masks, of course — this means that on average one new mask has to be used for each wafer.

In recent years a breakthrough has been made here, for equipment has been developed that can project a mask on to a wafer by means of a lens or concave mirror. There is no contact between mask and wafer to cause any damage, and the life of the mask is almost unlimited. The masks used in this kind of method can be much more expensive than the contact masks, and more accurate but expensive techniques can be used in their manufacture. It is worth while, for example, to produce the masks directly, without the intermediate stage of a reticle, by 'writing' them with an electron beam. The beam is produced by extremely complex and very accurate (to 0.1 μm) electron-beam pattern generators [3]. These machines are computer-controlled from a magnetic tape carrying all the information about the geometry of the circuit in digital form.

Operation with such an electron-beam pattern generator has various advantages. The time taken from design to completed mask is shorter than with the optical method. The details can also be smaller. The most important advantage, however, is that the number of errors per mask is smaller than with the optical method. This is the feature that makes electron-beam masks and the projection-exposure of silicon wafers a particularly valuable combination for processing very large circuits.

The next phase, probably very close now, in IC fabrication will be lithography in which a special repeating projector (the 'Silicon Repeater') is used to project repeated images of the reticle directly on to the wafer, as described before for the manufacture of the master mask [4]. This is a small step backward in speed, but the great advantage of this method is that each successive pattern can be very accurately aligned again automatically on the previous circuit already present on the wafer — a facility of crucial importance when it becomes necessary to reduce the smallest details in the circuit to about 2 μm.

Accurate positioning with good reproduction of the smallest details can also be obtained by 'writing' directly on the wafer with an electron beam [3], which is already done in the laboratory and on a very small scale in production.

The application of patterns to the photoresist coating is of course only half the story, since it is still necessary to apply the pattern to the layer underneath which usually consists of SiO_2, silicon nitride, metal or polycrystalline silicon.

Until a few years ago all etching treatments were carried out with liquid etchants, usually acids or acid mixtures. These 'wet-chemical' etchants have disadvantages that become more troublesome as the details to be etched become smaller (the difficulties include erosion of the photoresist, capillary penetration beneath the resist and electrochemical effects).

In recent years a completely new etching technology has been developed, plasma etching. In this method the wafers — with photoresist pattern — are placed in a special gas atmosphere in which an electrical discharge is maintained. The discharge has the effect of converting the gas molecules into very reactive particles, which react with the surfaces to be etched [5]. Organic fluorine or chlorine compounds are usually used as etchant gases, mixed with small amounts of other gases. The etching reaction only goes quickly if the fluorides or chlorides formed at the surface are volatile, so that they disappear from the surface. This means that only materials that form volatile reaction products can be etched

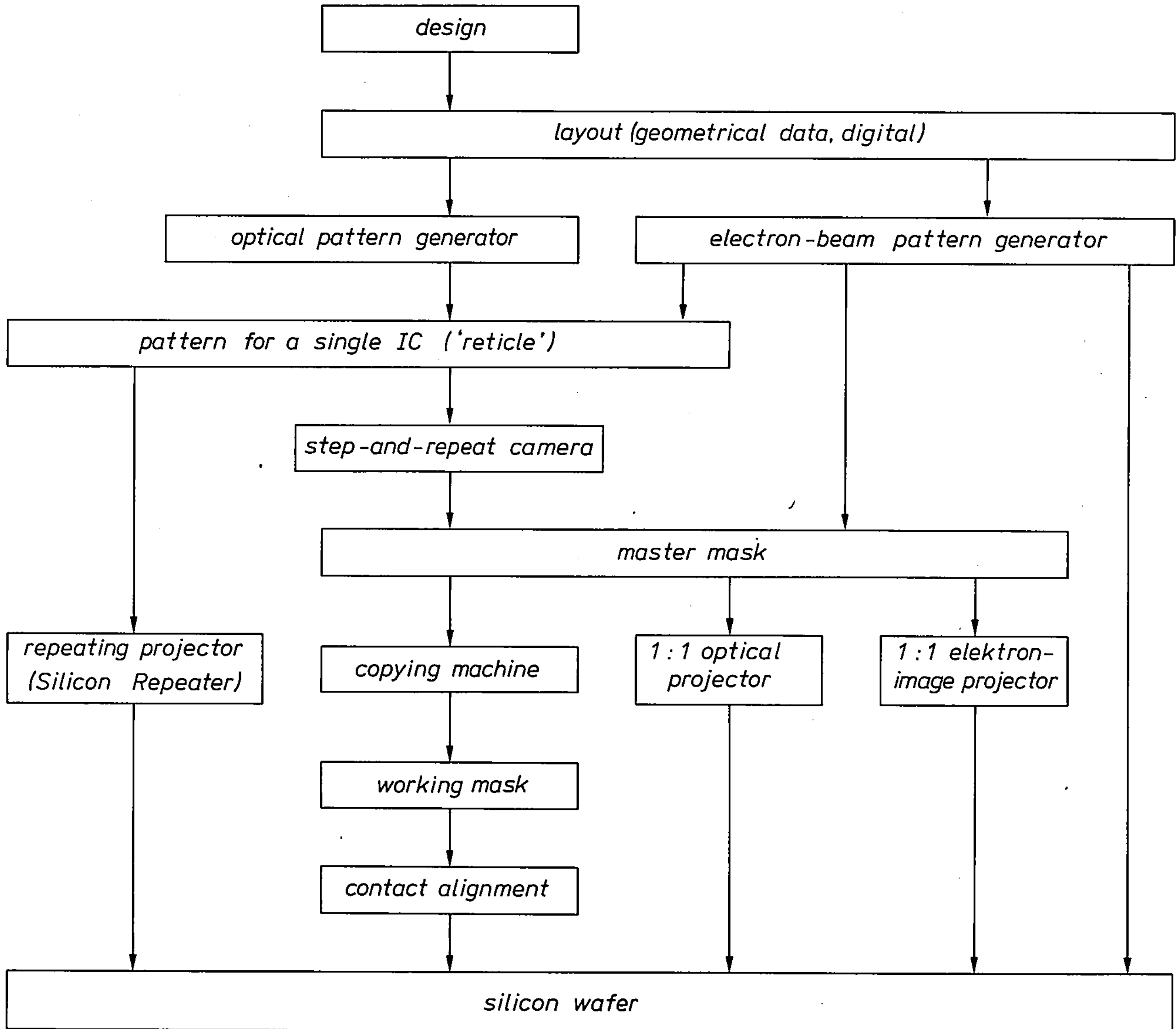

Fig. 2. Diagram showing the various 'lithographic' methods now in use in the production of integrated circuits. The vertical series in the second place from the left has been most generally used until recently, and is still widely employed. On its left is the method in which the single mask drawing ('reticle') is projected by a repeating projector (the 'Silicon Repeater') to give many repeated images forming a matrix on the wafer. *On the right:* the three different ways of working with an electron-beam pattern generator, either by writing directly on the wafer or by using it to make a master mask that is projected on to the wafer by electron-beam or optical methods.

in a plasma. Silicon, silicon nitride, some metals and to a certain degree SiO_2 satisfy this condition. Plasma etching is no universal panacea, but appreciably better results than with wet etching have been obtained for a number of materials.

In conclusion, we should just mention that the reduction of the details to be reproduced, however important, is not sufficient for making ICs with higher packing densities. The dimensions in the vertical direction — the thickness of metal and oxide layers and the diffusion depths — also have to be reduced. From what we have already said it will have become clear that the solution of the associated technological problems is in certain cases an equally difficult exercise.

[3] See for example the article by J. P. Beasley and D. G. Squire, this issue, p. 334.
[4] See for example the article by A. G. Bouwer *et al.*, this issue, p. 330.
[5] An article by H. Kalter and E. P. G. T. van de Ven on this subject will appear in the next volume of Philips Technical Review.

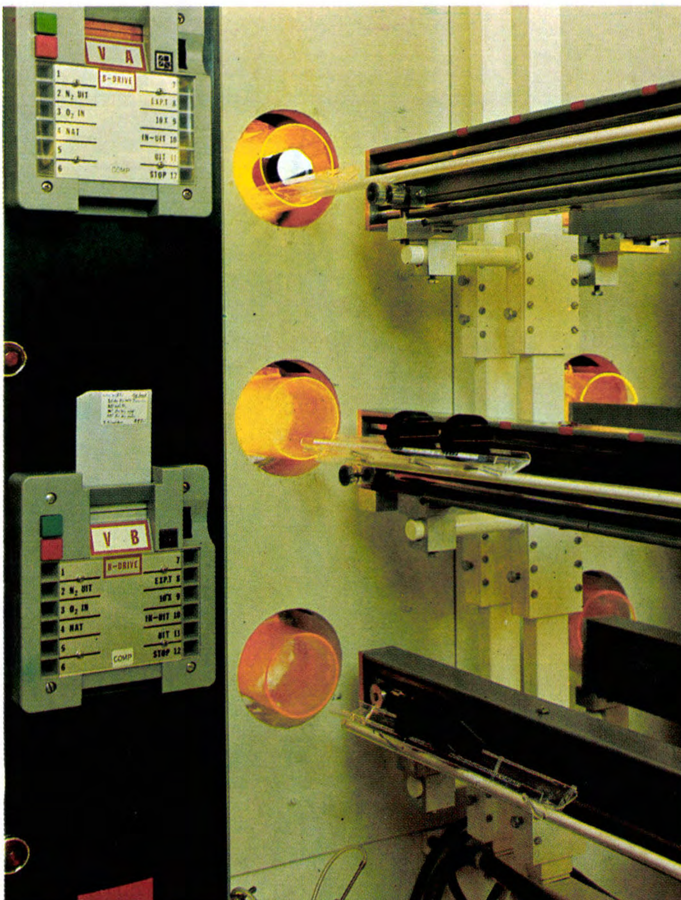

Parts of a clean room at Philips Research Laboratories, Eindhoven (see also page 266), showing slides on which boats carrying silicon wafers are slid into the furnaces. The wafers are coated with an oxide film or given the appropriate doping in the furnaces. For optimum control of temperature and atmosphere the furnaces and the slides are connected to a process computer. The photograph on the left shows three boats with wafers ready to be slid into the furnaces.

Metallization

The metal that is suitable for use as interconnection between the various components of an IC must satisfy a string of conflicting requirements. It must be a good conductor, give good bonding, be corrosion-resistant yet easy to etch and it must be easy to apply. It must also give good contact with *N*-type and *P*-type silicon, without entering into chemical combinations with it, and it must be able to support high current densities.

The metal aluminium has been accepted as the best compromise by practically all semiconductor manufacturers. The weaker points of aluminium are its limited ability to resist corrosion and support high current densities.

In modern integrated circuits the current densities can be very high, because of the continued reduction in dimensions. These high current densities have the effect of displacing the aluminium atoms in the direction of electron flow. This is called electromigration and can eventually give a complete break in the conductor. Pure aluminium conductors will safely carry current densities of 10^5 A/cm^2, but above this value their life-time falls rapidly. The occurrence of electromigration can be effectively prevented by adding a few per cent of copper to the aluminium, but this decreases the corrosion resistance and the ease of manufacture.

After the aluminium pattern has been etched the silicon wafers are heated to 450 to 550 °C to ensure good contact between the silicon and the aluminium. During this treatment a small amount of silicon from the contact windows dissolves in the aluminium. This effect may lead to short-circuits in the transistors, because so much silicon dissolves locally from the contact openings that the aluminium penetrates to the silicon on the other side of the *P-N* junction underneath the contact opening. The remedy for this is to add about 1% of silicon to the aluminium, by applying both materials at the same time. Again, this is an effective measure, but it complicates the production process.

In spite of its weaker points, aluminium has so far maintained its position as an interconnection metal. As the dimensions become smaller, however, it soon becomes more and more difficult to work with aluminium. In the wet-chemical etching methods a relatively large loss in the width of the conductor strips occurs as a result of the metal being etched away laterally under the edges of the photoresist, and in narrow strips this can cause breaks. On the other hand aluminium cannot as yet be successfully etched in a plasma. For these reasons it seems likely that in the future aluminium will be superseded for VLSI applications by another metal, which can be successfully etched in a plasma — e.g. tungsten or molybdenum — but will still require extra precautions to ensure a good contact between metal and silicon. These metals, like many others, do not form good-quality contacts with *P*-type and *N*-type silicon. To overcome this difficulty it is necessary to first apply thin layers of certain metal silicides, such as platinum or cobalt silicide, in the contact windows. These compounds are good conductors and guarantee a good contact with both the silicon and the metal.

'Metallization', which formerly included little more than a relatively simple evaporation and etching of aluminium, is gradually becoming a complicated process. This become even more apparent when we remember that in LSI circuits a single layer of interconnections is hardly ever sufficient. It is usually necessary to cover the first layer of metallization with a layer of high-quality insulation, with contact windows, and to add a second metallization on top of this. Here again conflicting requirements have to be reconciled and good combinations developed, with the ever-present boundary conditions of high production yield and adequate life in all kinds of operational conditions.

* *
*

To summarize, it is the careful control now applied to the starting material, an ever-increasing refinement and control of all the physico-chemical processing stages, the introduction of ion implantation and certainly the immense development in lithography that allow us to succeed in the industrial production of ever larger and more complicated ICs, so that we have gradually come to refer to 'large-scale integration' and even 'very-large-scale integration'. We should also mention that there is increasing use of computer control in the continuous optimization of all the conditions in the complicated equipment necessary for making ICs (see opposite page).

It is clear that the developments we have described in the technology have had and still have a far reaching influence on the layout and design of the electronic circuits.

The evolution of integrated circuits

We shall now indicate in general terms how the nature and the design of the 'monolithic' circuits have changed through the years. The circuits can be divided into two groups: analog circuits and digital circuits, particularly the binary-digital or 'logic' circuits. It is mainly the second group of circuits that have gained considerable importance through IC technology, and we shall therefore give most of our attention to them [6].

[6] A short discussion of various circuits and processes now in use can be found in N. C. de Troye, Digital integrated circuits with low dissipation, Philips tech. Rev. 35, 212-220, 1975.

Logic circuits

The first integrated logic circuits (1962) were built up from a limited number of bipolar transistors and resistors, and contained no more than two to six logic gates per chip. Since fast transistors could not be made at that time the switching times τ in this 'transistor-transistor logic' (TTL) were rather high (40 ns), and to reach this speed a relatively high power D was necessary (10 mW). The τD product for the first TTL circuits was therefore 400 pJ.

In the next few years, with improvement and better control of the technology, the delay time was reduced to about 10 ns for the same power, so that the τD product fell to about 100 pJ ('standard TTL').

TTL circuits are of the type known as saturated logic. In this kind of logic the transistors are driven into saturation, with the maximum current passing through the collector-base junction — the junction is 'completely open' (bottoming) — and with the maximum space charge stored in the base. Switching these currents on and off and transporting these charges in the switching process is expensive in terms of time and power, so that it is difficult to make the τD product small.

With the introduction of Schottky diodes in 1968 it became possible to curb these saturation states, by connecting these diodes in parallel with the collector-base junction. The minimum delay time (10 ns) remained unchanged, but the power required for switching could be reduced to 2 mW (Low-Power Schottky TTL). The τD product was thus reduced to 20 pJ.

In 1963 TTL was joined by ECL (Emitter-Coupled Logic). This logic was of the unsaturated type, and therefore in principle fast. From the start switching times of 4 ns could be obtained, but at a switching power of 35 mW. Improvements in technology enabled the switching times to be reduced to a fraction of a nanosecond, but still at the expense of relatively high powers (up to 50 mW).

The total power dissipated on the chip increases, of course, with the number of transistors in the circuit. If the circuit is not to literally go up in smoke, the total power must be kept below about 1 W. To enable a large number of gates to be put on a single chip — for a high 'degree of integration' — a low switching power per gate is a first requirement.

For these reasons ECL is only suitable for SSI, or at the very best, with careful attention to the removal of the heat produced, for MSI. Low-Power Schottky TTL, on the other hand, is very suitable for MSI.

The breakthrough to LSI for bipolar digital circuits was only made after the invention of integrated injection logic (I^2L) in 1972 [7]. In I^2L circuits the τD product is smaller than 1 pJ. The switching times are still relatively high, up to 10 ns. The packing density of I^2L is fairly high: up to about 200 gates per mm^2, which is about 10 times the density with Low-Power Schottky TTL. As an example, a processor in I^2L on a single chip, with a word length of 16 bits, has since become available; the circuit contains 1800 gates.

As well as the bipolar logic circuits we have so far been discussing, integrated MOS circuits have also been available since 1967. *P*-MOS transistors (with *P*-type channel) with aluminium gates were used at first. Although the τD product was rather high (up to 100 pJ) and switching was somewhat slow (up to 100 ns), this indicated an appreciable improvement over the bipolar circuits then available for the same degree of integration. A further improvement was obtained here with the introduction of a gate electrode of polycrystalline silicon (1970), first in *P*-MOS and then in *N*-MOS circuits, and with greater packing densities resulting from improved lithographic techniques. This brought the τD product down to about 10 pJ and the switching time to 10 ns. With the application of 'dynamic' switching techniques, of growing importance since 1968, the τD product for MOS LSI has since been reduced to about 2.5 pJ. It was only with the invention of I^2L that bipolar techniques became comparable again with MOS in the degree of integration that could be obtained.

* * *

In addition to the improvements in lithographic technology, the more compact construction of the elementary gate circuit and the elementary memory cell have also contributed greatly to the attainment of a higher packing density. It looks as though there are no more spectacular improvements to be expected here, however. Cells with one transistor per bit are now used in memory circuits, while in injection logic (I^2L) the elementary gate and its supplies have been reduced to two closely intertwined transistors.

Further improvement in packing density could be obtained if it were possible to distinguish more than two logic levels per elementary memory cell and elementary gate circuit, and hence process more than one bit at a time per elementary logic circuit. But this means that the reproducibility of voltage and current levels has to be exceptionally high — the very thing that does not matter with two levels. As yet little is known about the likely capabilities of such 'multi-valued logic', but it is quite clear that improvements in reproducibility could be of great significance for compact construction.

---

[7] See for example C. M. Hart and A. Slob, Philips tech. Rev. 33, 76, 1973. An example of an I^2L circuit is described in the article by R. A. van Doorn and N. A. M. Verhoeckx, this issue, p. 291.

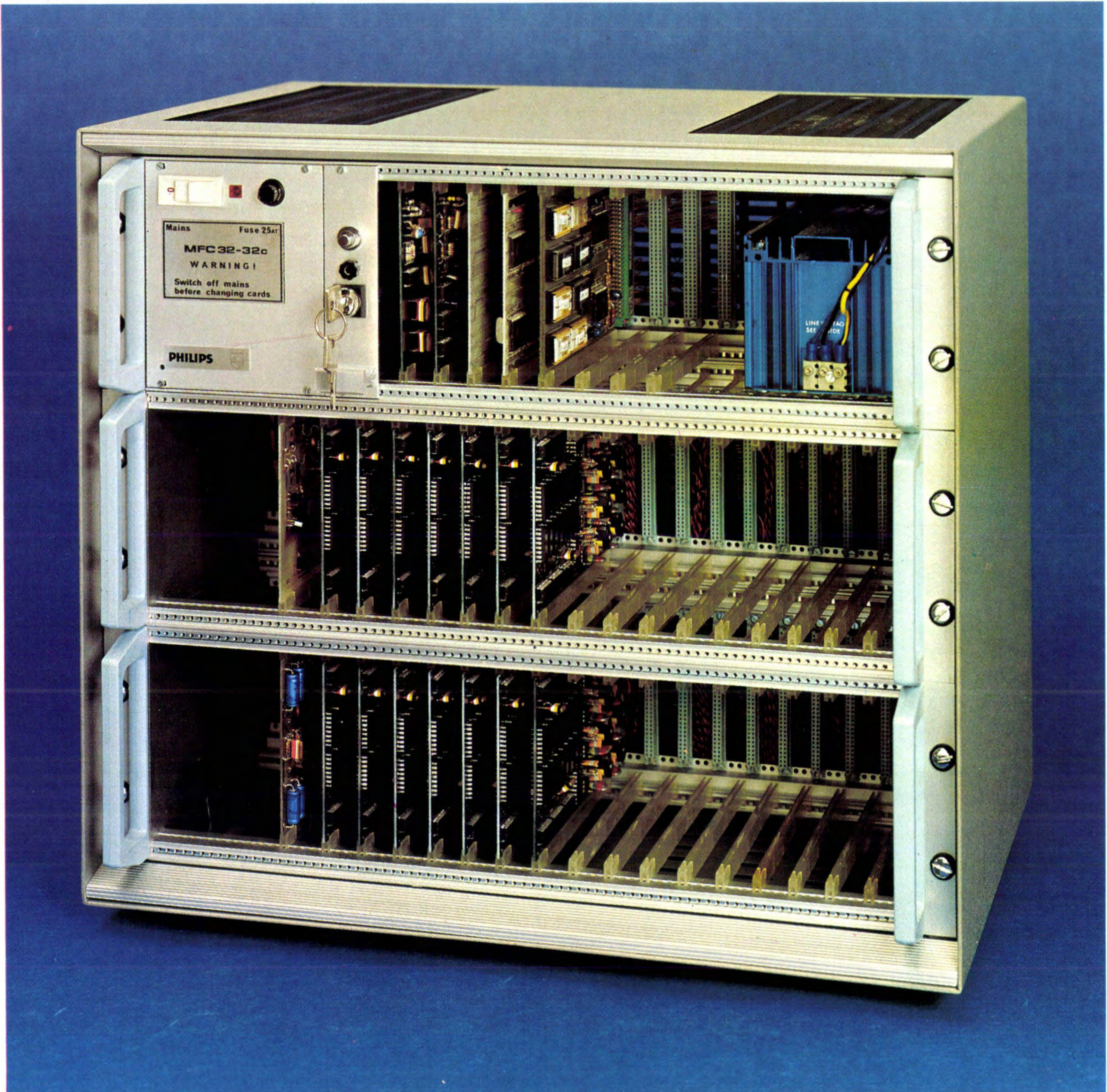

Microcomputers offer the user of an intercom system a number of new facilities. They can give an automatic signal as soon as a station called is no longer engaged, and they also allow the caller to break into a conversation in progress — unless the stations involved have been made inaccessible for interruption. Another facility is automatic transfer to another number if the station called is engaged. In addition a message can be simultaneously passed on to a group of preselected stations. Microcomputers also keep the records of the users' numbers; if the user moves to another location he can keep the same number without any need for changing the wiring. In the Philips MFC 32-32c control unit shown here, for a intercom system with up to 1600 connections, the microcomputer consists of three large-scale ICs, a central processor (CP), a random-access memory (RAM) and a read-only memory (ROM). These are mounted on the boards in the upper compartment. Other ICs arrange the connections to the stations; each of the two lower compartments contains a board for every hundred connections. Boards can be added to extend the system.

Analog circuits

The first analog IC to be applied was an amplifier for a hearing aid; it consisted of three transistors and two resistors. Since then a great variety of analog ICs have appeared, for use in both professional equipment and consumer products: nowadays there are analog circuits for high and low voltages, high and low frequencies, switching and amplification, and many other functions.

In analog circuits the increasing degree of integration is not put to use to give ever more wide-ranging functions, as in logic circuits. Instead, it is used to improve the quality of the functions. Since the number of transistors that could be used in a circuit was no longer a practical limitation, circuits of ever increasing refinement could be constructed. A large number of analog circuit modules are now available, including operational amplifiers, multipliers and log converters, with exceptionally good drift and noise characteristics.

Even though the analog ICs have become larger and more complex with the passage of time, they cannot yet be considered as LSI. Nor can analog LSI circuits be expected in the near future: unquantized signals cannot easily be processed in large systems because the effects of all the error sources are additive if there is no quantization.

Analog ICs are almost all of the bipolar type, since MOS circuits are more susceptible to drift and noise.

Analog-to-digital circuits

Even though completely analog LSI circuits are not to be expected in the near future, increasing numbers of LSI circuits have recently appeared that contain adjacent analog and digital sections. In particular, the knowledge and understanding that is now available in information theory and signal processing has shown how 'analog' functions such as filtering and modulation can be performed digitally, and how analog signals can be put into digital code. This knowledge can also be applied in practice, where appropriate, by using integrated circuits. If discrete circuit elements had to be used to obtain this digital execution of 'analog' functions, digitization would be a clumsy and expensive approach. However, now that large digital circuits can be made, the disadvantages do not usually outweigh the advantages any more. The advantages include greater freedom in design, a programmable and versatile system construction, the virtual absence of difficult tuning and matching procedures and a lower sensitivity to drift effects. The designer can decide for each case whether it is better to use the analog or the digital version of a function.

Another important intermediate stage between the analog and the digital signal processing is provided by the CTD circuits (CTD = charge-transfer device). Samples of the signals are taken in these circuits, but the samples are not quantized.

An important advantage of binary-digital circuits is that it is only necessary to distinguish between two levels when processing binary signals. It is therefore unnecessary to preserve the correct amplitude and shape of the signal throughout, which would require accurately linear amplifiers, equalizers and so on; sufficient correction can be obtained from 'simple' level correctors. In effect, this is the old principle of the telegraph relay as a signal amplifier.

The ability to include an extensive and complex information-processing capacity in an integrated digital circuit, together with the fact that information-bearing signals are often of analog type in the 'outside world', is a great incentive towards the combination of analog and digital functions on a single chip. A great deal of attention is therefore given to the conversion of analog signals into digital and vice versa, which is essential here.

It will consequently come as no surprise that considerable attention has recently been given to problems associated with making analog MOS circuits. For the present it appears that I^2L is the most suitable for combined circuits.

Designing electronic circuits

The rise of the integrated circuit has affected the activities of the electronics designer in many ways. Whereas previously the designer built up an electronic circuit from separate components such as resistors, inductors, capacitors and active elements such as diodes and transistors, he now has to think more in terms of gates, memory cells, shift registers, accumulators and operational amplifiers. There have also been great changes in the design limitations and criteria. While the single component used to be expensive and the connecting wire cheap, there is now no real problem in adding a few more transistors but it is necessary to be economical with the interconnections. Whereas the designer formerly had to be able to design networks, he now has to master switching techniques and Boolean algebra. At the same time he must now have a wider knowledge of the manufacturing processes and the rules that they impose than when the components were available ready-made.

Now that a single chip can carry more functions, which in turn can be more extensive, it is becoming harder to distinguish between the equipment (or system) designer and the component designer. The components are taking on the character of a system and the system is strongly and directly influenced by the technology.

It remains as yet to be seen whether designing and making an integrated circuit will broaden the field of the component maker or involve the system builder more deeply in technology. It is clear, however, that tasks that used to be separate no longer remain so.

As the circuits become larger, it becomes more difficult and takes more time to ensure that they remain manageable and do not get out of hand. Much closer inspection of tolerances, interconnections and many other details will be necessary. In addition, the calculation of the circuit and the simulation of the function is becoming an ever more laborious task. Testing the finished product to ensure that it functions correctly is an exercise that begins to approach the limits of human ingenuity. In all these activities the computer is increasingly used as an aid. Much time and thought are being given to the design of computer programs that can execute many of these tasks more or less automatically [8]. The electronic engineer now finds the computer a tool as indispensable as he once found the soldering iron.

* *
*

And now we have come full circle. For the computer is also an indispensable aid in the supervision and control of the technical and chemical processes discussed at the beginning of the article and in the lithographic techniques — the same computer that brought about the growth in importance of the integrated circuit and which could not have reached its present state of development without the integrated circuit. We are now at the beginning of an era in which the significance of the integrated circuit will be far greater than that of a component for computers.

[8] An example of computer-aided testing is given in W. G. J. Kreuwels, Philips tech. Rev. 35, 261, 1975. The computer-aided design of ICs is discussed in the article by C. Niessen, this issue, p. 278.

Some abbreviations and acronyms relating to IC technology.

ADC	Analog/Digital Converter
CML	Current-Mode Logic
C-MOS, CMOS	Complementary Metal-Oxide-Silicon
DAC	Digital/Analog Converter
DIL, DIP	Dual-In-Line (Package)
DTL	Diode-Transistor Logic
ECL	Emitter-Coupled Logic
FET	Field-Effect Transistor
FPLA	Field-Programmable Logic Array
IC	Integrated Circuit
I^{2}L	Integrated Injection Logic
LOCMOS	Locally Oxidized Complementary Metal-Oxide-Silicon
LOCOS	Local Oxidation of Silicon
LSI	Large-Scale Integration
MOS	Metal-Oxide-Semiconductor
MSI	Medium-Scale Integration
MTL	Merged-Transistor Logic
N-MOS, NMOS	MOS circuit with *N*-type FET channels
P-MOS, PMOS	MOS circuit with *P*-type FET channels
PROM	Programmable Read-Only Memory
RAM	Random-Access Memory
ROM	Read-Only Memory
SSI	Small-Scale Integration
TTL	Transistor-Transistor Logic

Philips tech. Rev. 37, 278-290, 1977, No. 11/12

Computer-aided design of LSI circuits

C. Niessen

Introduction

In the design of LSI circuits the computer is an indispensable aid; the calculation of such a design in the conventional way 'by hand' would be a practical impossibility. For some stages of the design process special computer programs have been developed that drastically reduce the amount of work involved and minimize the chance of errors. The essential feature here is that the computer does not take over from the designer, but becomes a partner — hence the name 'computer-aided design' (CAD). In this article we shall look at a number of such programs that have been developed at Philips; since LSI techniques are mainly used for digital circuits, the emphasis here will be on the computer-aided design of digital LSI circuits.

There are several stages in the process of developing an LSI circuit (*fig. 1*). First, starting from a specification of the function which the circuit is required to fulfil, a circuit design is made. This is followed by a verification procedure to determine whether the circuit does in fact represent the desired function; any corrections required can be made at this stage. Next, a test procedure is devised that can be used after manufacture to make sure that the end-product is functioning properly. This is done at such an early stage because there is no certainty that all the possible faults can be found by testing. If the test procedure reveals that the circuit cannot be fully tested, the design must again be modified, and this of course has to be followed by a further function-verification procedure. Once a design has been produced in this way that meets all the specifications, the layout of the circuit is drawn and the photomasks for the manufacture of the IC can be made. The next stage is the actual production of the IC. Finally, the circuits from the production line are put through the test procedure. The stages of the development process for which CAD programs are now available include design verification, test preparation, layout making and mask making.

Review of CAD

During the *design verification* the operation of the circuit is simulated by computer. Two distinct procedures, for which various programs are available, can be used here: these are *circuit analysis* and *logic simulation.* In circuit analysis the 'analog behaviour' of the circuit is investigated; the principal currents and voltages are treated as continuous variables and their waveforms are calculated. The application of circuit analysis is confined to circuits containing no more than a few hundred components. For larger circuits the memory capacity and computer time required for these calculations would be far too large, and the designer would also find it hard to retain a general picture of the design because of the many details.

Larger circuits can only be calculated by splitting them into subcircuits. To do this two conditions have to be met: it must be possible to calculate the subcircuits without any knowledge of the total system, and it must be possible to join the subcircuits together without detailed knowledge about each of them. These

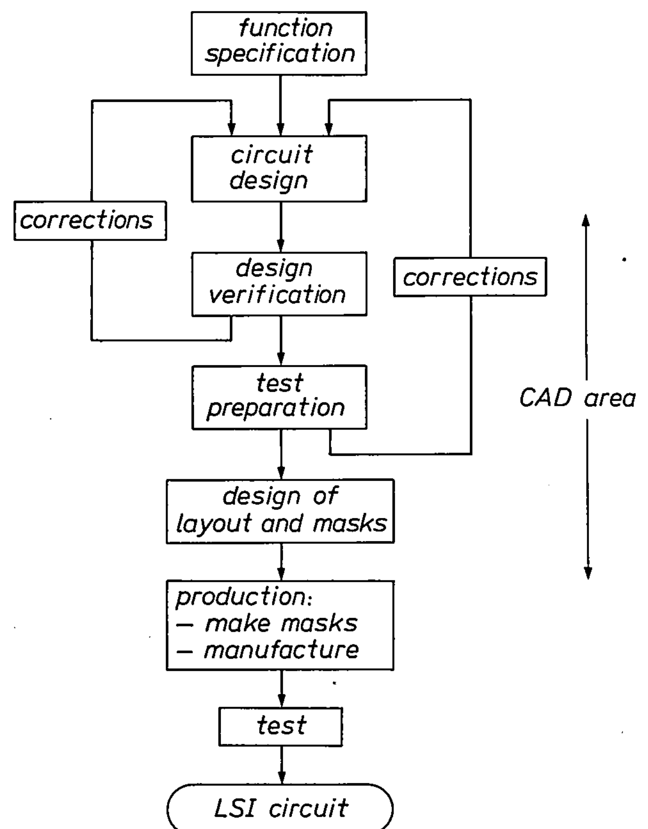

Fig. 1. Diagram of the various stages in the design and manufacture of an LSI circuit. Computer programs are available that the designer can use to verify his design, to prepare tests and to design the layout of the masks for the manufacture of the IC.

Ir C. Niessen is with Philips Research Laboratories, Eindhoven.

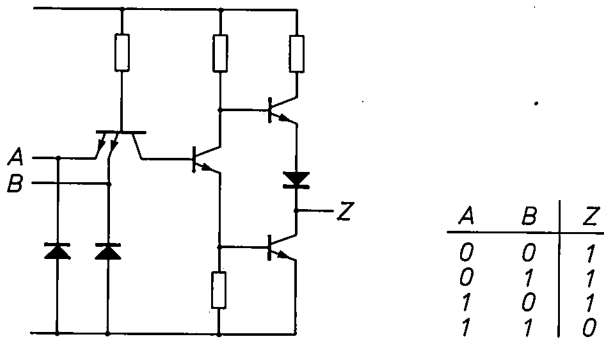

A	B	Z
0	0	1
0	1	1
1	0	1
1	1	0

Fig. 2. NAND gate in 'Transistor-Transistor Logic' (TTL). This circuit is designed with the aid of a CAD circuit-analysis program such that the voltage at the output Z is less than 0.4 V if the voltage at the two inputs A and B is greater than 2 V, while the output voltage is greater than 2.4 V if one of the two inputs has a voltage lower than 0.8 V. If a voltage between 0 V and 0.8 V is taken to correspond to the logic '0' and a voltage greater than 2.0 V to the logic '1', then this circuit is described by the adjacent truth table. The circuit analysis also gives the constraints under which the voltages remain within these limits. When the gate is included in a logic network, for instance, a limit must be imposed on the number of inputs that can be connected to the output (the 'fan-out'). In building a logic network another important consideration is the propagation delay, i.e. the time elapsing before the output voltage responds to a change at the input.

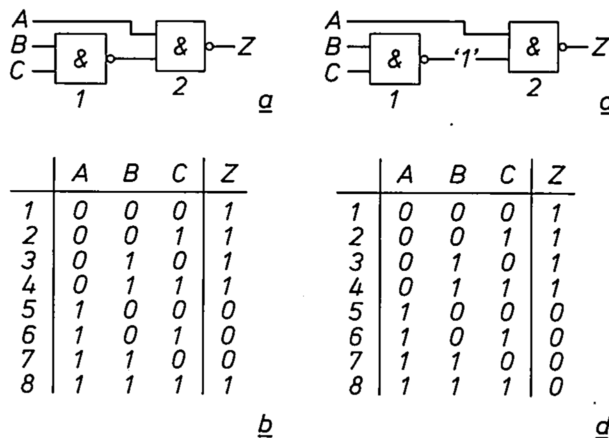

(b)

	A	B	C	Z
1	0	0	0	1
2	0	0	1	1
3	0	1	0	1
4	0	1	1	1
5	1	0	0	0
6	1	0	1	0
7	1	1	0	0
8	1	1	1	1

(d)

	A	B	C	Z
1	0	0	0	1
2	0	0	1	1
3	0	1	0	1
4	0	1	1	1
5	1	0	0	0
6	1	0	1	0
7	1	1	0	0
8	1	1	1	0

Fig. 3. Illustrating the derivation of test patterns. The logic circuit (a), composed of NAND gates of the type in fig. 2, has eight possible states, which are given in the truth table (b). It is now assumed that the output of gate *1* is defective in such a way that this output always gives a '1' (c) irrespective of the state of inputs B and C. In this situation the truth table has the form of (d). Comparison of the two tables shows that the fault at the output is only detectable in state *8*, that is when A, B and C have the value '1'. This is because there are two conditions to be satisfied. Firstly, the required state at the location of the fault must differ from the faulty state. This situation is found when B = '1' and C = '1', in which case the output of gate *1* should then be '0'. Secondly, this fault must be observable at the output and this only happens in state *8*. It is true that in state *4* both B and C are equal to '1', but since A has the value '0', the value of Z is always '1', irrespective of the state of gate *1*. The fault thus comes to a dead end at gate *2*. The combination (1,1,1) is the only test pattern for the fault described here.

requirements are fully satisfied by *digital* circuits, composed of the basic AND, OR, NAND and NOR logic circuits. With circuits of this type it is therefore possible to calculate designs containing many thousands of components; the procedure used for doing this is called *logic simulation*. Large *analog* circuits can sometimes be divided into a number of analog subcircuits, but usually an analog-to-digital conversion is the only possibility of making the circuit calculations. This is why systems of an essentially analog nature are increasingly dependent on the use of digital techniques. In this article we shall therefore be concerned with digital circuits only.

In logic simulation the truth table or Boolean equation is checked to verify whether the circuit will perform the appropriate logic function in practical conditions. A circuit analysis must be carried out beforehand to check the analog behaviour of the basic circuits, so that it is known under what conditions these modules will continue to function as digital circuits; see *fig. 2* and caption. If these requirements are taken into account in the design procedure, the circuit as a whole need only be verified with the aid of logic simulation; no further analysis at the level of currents and voltages will then be necessary.

Testing an integrated circuit is much more difficult than testing a circuit composed of discrete components. The discrete components have already been tested, of course, and there are also many internal measuring points available for testing the circuit. In testing an integrated circuit, on the other hand, it has to be assumed that any component may be faulty; the faults that may occur during manufacture, for example due to mask damage, are completely unpredictable. Moreover, internal points in an IC are not accessible, so that faults can only be detected through the signals that appear at the circuit outputs. In designing a test for an integrated circuit it is therefore necessary to ensure that a combination of input voltages can be found such that any fault will introduce a change in state that can be observed at the output (*fig. 3*). If it is not found possible to arrive at a set of test patterns capable of detecting an acceptable percentage of the possible faults, the only alternative is to change the design. Since it is difficult for a designer to think up such tests and almost impossible for him to assess their quality, various programs have been developed to simplify matters for him [1].

The next step in the development of an IC is to convert the circuit diagram into a drawing of the various components in a plane, showing the appropriate electrical interconnections. This *layout* is then used for making the masks that will be used in the production of the IC. There is no universal program available for designing a layout. However, a layout made by the designer can be described in a computer language; the designer can then use CAD programs to supply

[1] See for example W. G. J. Kreuwels, Structural testing of digital circuits, Philips tech. Rev. 35, 261-270, 1975.

verification drawings for checking whether certain general design rules have been properly observed [2]. After these checks have satisfied the designer that the layout is good and that the description in the computer language is correct, the computer can then supply a punched tape for drawing the photomasks on a numerically controlled drawing machine [3]. The punched tape can also be directly used for controlling an optical pattern generator, such as the 'Opthycograph' [4].

The CAD facilities so far mentioned may be described as passive: the designer makes a design, the computer verifies it and finds out whether the circuit can be tested; the designer makes a layout, the computer makes the necessary checks and produces the control tapes. If the creative steps in the design process are also to be automated, it will be necessary to make programs that will enable the computer to rival the designer's knowledge, inventiveness and repertoire of alternatives. This does not seem to be a practical possibility for the electrical and logic design, but the layout design is something that can be entrusted to the computer.

The programs that have been developed for layout design result in a layout that has a more regular structure than a conventionally produced one, and hence a lower packing density for the components on the chip (the 'layout efficiency'). Whereas optimum layout efficiency was a necessary condition for achieving an acceptable yield in the early days of integrated circuits, nowadays the technological advances made (smaller components, larger chips) allow efficiency to be traded for faster and cheaper layout design. This is particularly important for small production runs, where the production costs are low compared with the design costs. With circuits for mass production, the production costs will be the main consideration, and it will be worth going to the expense of additional development work to reduce the production costs. The layout will then be conventionally designed. An intermediate form, where the layout is partly made by computer and partly by conventional methods, is also occasionally used.

The CAD programs mentioned above, each with their own input language, each deal with an individual aspect of the complete LSI design. A consequence of this is that a designer has to make different design descriptions for one particular problem, e.g. one for the logic simulation and another for the layout. This demands a great deal of work from the designer and also increases the risk of errors in the descriptions. In some cases, for example for LOCMOS [5] and I²L [6], it has therefore been useful to develop programs for linking the various design phases. If these programs are unified ('integrated') in such a way that they are all based on the same circuit description (the 'source information')

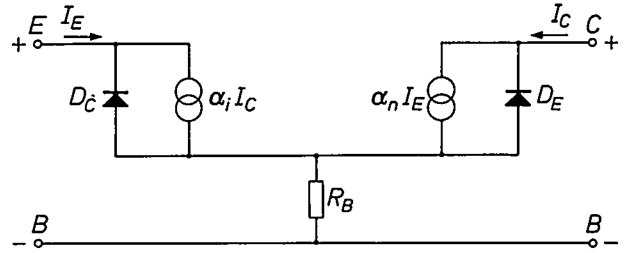

Fig. 4. Ebers-Moll model for an *N-P-N* transistor in the common-base configuration. The current generators represent the gain behaviour of the transistor; α_n and α_i are the current-gain factors in the forward and reverse directions. The diodes D_C and D_E represent the conduction effect of the two *P-N* junctions. R_B is the base resistance. Since this model is composed of ideal elements, it can readily be described in a code suitable for input to a computer. Such models are used in describing an LSI circuit design for verification by a circuit-analysis program.

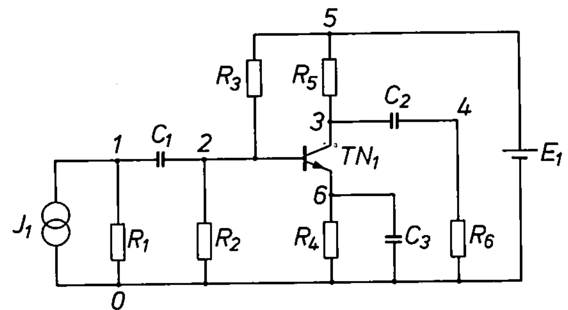

Fig. 5. Diagram of an amplifier stage whose input and output will be shown, by way of example, in the analysis of a pulse response by the PHILPAC circuit-analysis program. The numbers allocated to the nodes of the network are used in the circuit description that serves as the input.

```
TITLE:SINGLE STAGE AMPLIFIERS
CIRCUITS
R1(1,0) 10S R2(2,0) 3K9S R3(5,2) 18KS
R4(6,0) 1.8KS R5(5,3) 10KS R6(4,0) 10KS
C1(1,2) .1US C2(3,4) .1US C3(6,0) .1MLS
E1(5,0) 12S
TN1(3,2,6)'BC108-1X'S
J1(0,1)SINSQ(0,-.5ML,0,7U,36U,7U)S
ENDS
```

Fig. 6. Circuit description in PHILPAC code relating to the circuit of fig. 5. Each component is indicated by an instruction consisting of the name and number of the component, the nodes to which it is connected and its value. For the transistor TN_1 and the current generator J_1 a coded entry refers to a model or a standard function stored in the PHILPAC library.

```
TRANSIENTS
T=AN(0,60U,40)S
PLOT:VN(1),VN(4)S
ENDS
RUNS
```

Fig. 7. Computer instruction in PHILPAC code for a transient analysis of the circuit in fig. 5. The calculation time is stated, and graphs of the input and output voltage are requested.

and always refer back to the result of a previous calculation, we have a *CAD system.*

A number of programs developed at Philips for the various design stages will now be discussed. The program functions will be described and where possible explained with the aid of examples, without going into many of the details required for computer processing. At the end of the article two integrated CAD systems will be described.

Circuit analysis

To calculate the analog behaviour of a circuit, the computer must be supplied with the circuit diagram and at the same time given an instruction describing the nature of the investigation to be carried out, e.g. the determination of the frequency response of an amplifier. Generating a diagram in computer language presents no problems with the interconnections between the components, but the components themselves cannot usually be described by a few simple mathematical equations, because of effects such as parasitic capacitances and leakages. In the documentation of a transistor, for example, this problem is solved by using graphs from which the principal data can be read, but descriptions of this type are quite unsuitable for a computer. For the input of the components *'models'* are therefore used that simulate the behaviour of the components as closely as possible. The model is usually a network containing a few simple elements such as ideal resistances, capacitances and inductances. As an example *fig. 4* shows an Ebers-Moll model of an *N-P-N* transistor; more extensive versions of this model, including cut-off frequencies, are widely used in circuit-analysis programs.

A circuit-analysis program takes the input information and uses it to enter into the computer memory a set of equations that are an equivalent of the circuit. The calculations required are then made from these equations. For example, it is possible to calculate the voltages at the various nodes of the circuit when the supply voltage has been applied. The response to input signals of various kinds can also be calculated, and the voltage waveform can be displayed on a cathode-ray tube screen or an *x-y* plotter, or printed out on a line printer. The circuit-analysis procedure can also include simulated experiments that would be difficult if not impossible to carry out on the actual circuit; for instance, the gain of a transistor can be varied so as to find its optimum value.

A circuit-analysis program widely used at Philips is PHILPAC (PHILips Package for Analysis of Circuits). This can be used for analyses of various types on both bipolar and MOS circuits. The principal analyses relate to d.c. and a.c. behaviour and to transient effects, such as switching transients and pulse responses. It is also possible to carry out various statistical calculations with this program. In the development of PHILPAC much attention was paid to the convenience of the user. The descriptive language for the circuits is simple and its terminology is closely related to that used by the designer. For instance, the value of a resistance of 2700 ohms is fed in as 2K7. Along with the basic elements such as resistances, voltage and current generators, etc., the program has an extensive 'library' with models of commonly used transistors and diodes. The designer can also define his own models if he wishes.

As an example the input and output will be shown for a PHILPAC transient analysis of the amplifier stage of *fig. 5.* To describe the circuit it is first of all necessary to number the nodes of the network. *Fig. 6* shows the network description in the PHILPAC coding. For every element of the circuit this contains an instruction consisting of a code for the kind of element, its name, a list of the nodes to which it is connected and the value of the element. Thus, the instruction 'R2 (2,0) 3K9' means: 'a resistance with the name R_2, connected between the nodes *2* and *0*, and with a value of 3900 ohms' (each instruction ends with the symbol $). The code 'BC 108-1X' as the 'value' of the transistor TN_1 in fig. 6 is a reference to the model of this transistor in the PHILPAC library. The last instruction in fig. 6 defines the current generator J_1; the code 'SINSQ' here refers to a standard function from the PHILPAC library, a pulse train whose repetition frequency, amplitude, rise time, length and decay time must be specified in the instruction (in fig. 6 it relates to a current pulse with an amplitude of 0.1 milliamperes and a total duration of 7 + 36 + 7 μs).

In addition to the network description a calculation instruction must also be fed in; *fig. 7* shows this instruction for the analysis of the amplifier stage. The request is for a transient analysis of the response to the pulse signal from the current generator J_1, during a 60-μs period and calculated in 40 steps (the period of 60 μs corresponds to slightly more than one pulse). It also states that the output should consist of graphs of the voltage waveform at the nodes *1* and *4*, the input and the output.

[2] R. I. Stratford, Computer aided checking of integrated circuit layout constraints, Int. Conf. on Computer aided design, Southampton 1972, pp. 45-50.
[3] C. Niessen and H. E. J. Wulms, Automatic drawing of masks for integrated circuits, Philips tech. Rev. 30, 29-34, 1969.
[4] A. G. Bouwer, R. H. Bruel, H. F. van Heek, F. T. Klostermann and J. J. 't Mannetje, The Opthycograph, Philips tech. Rev. 34, 257-269, 1974.
[5] B. B. M. Brandt, W. Steinmaier and A. J. Strachan, LOCMOS, a new technology for complementary MOS circuits, Philips tech. Rev. 34, 19-23, 1974.
[6] C. M. Hart and A. Slob, Integrated injection logic (I^2L), Philips tech. Rev. 33, 76-85, 1973.

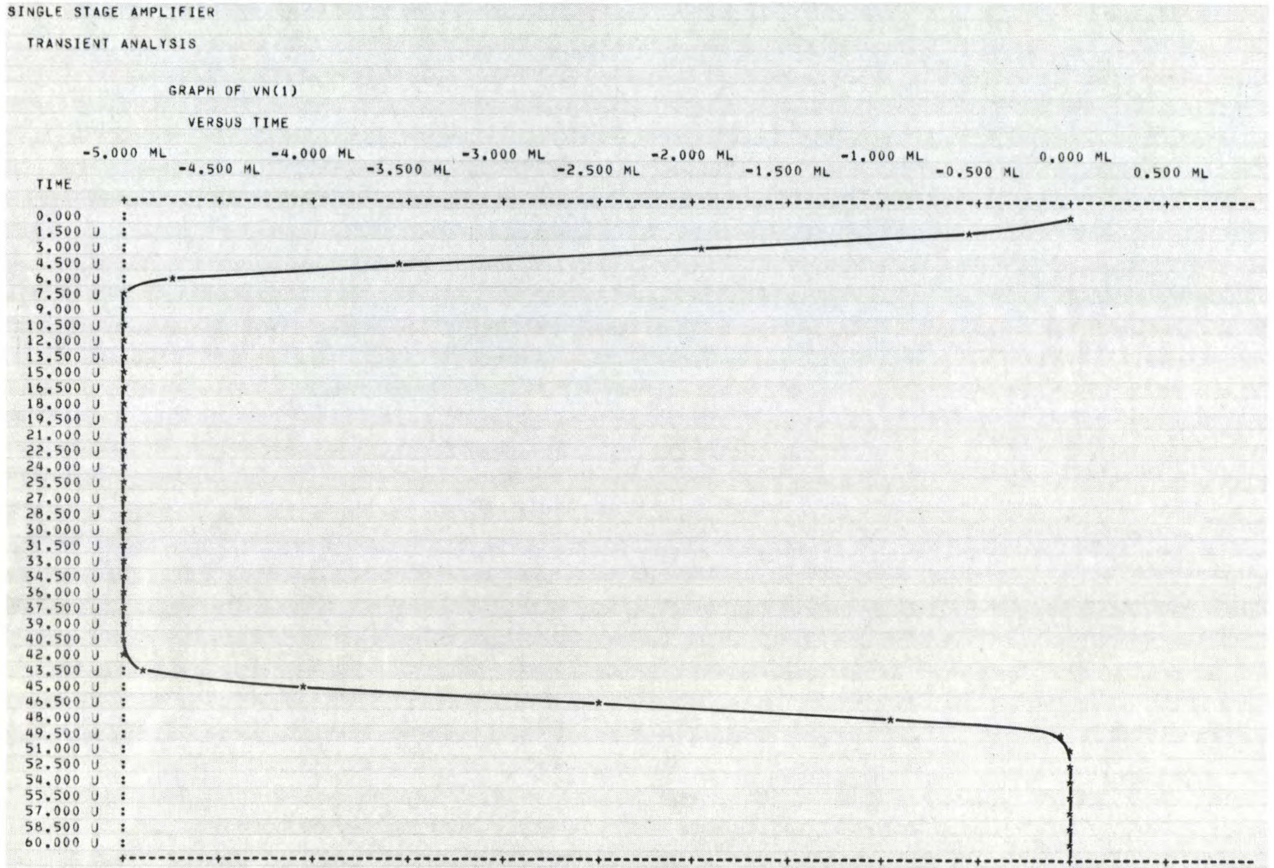

a

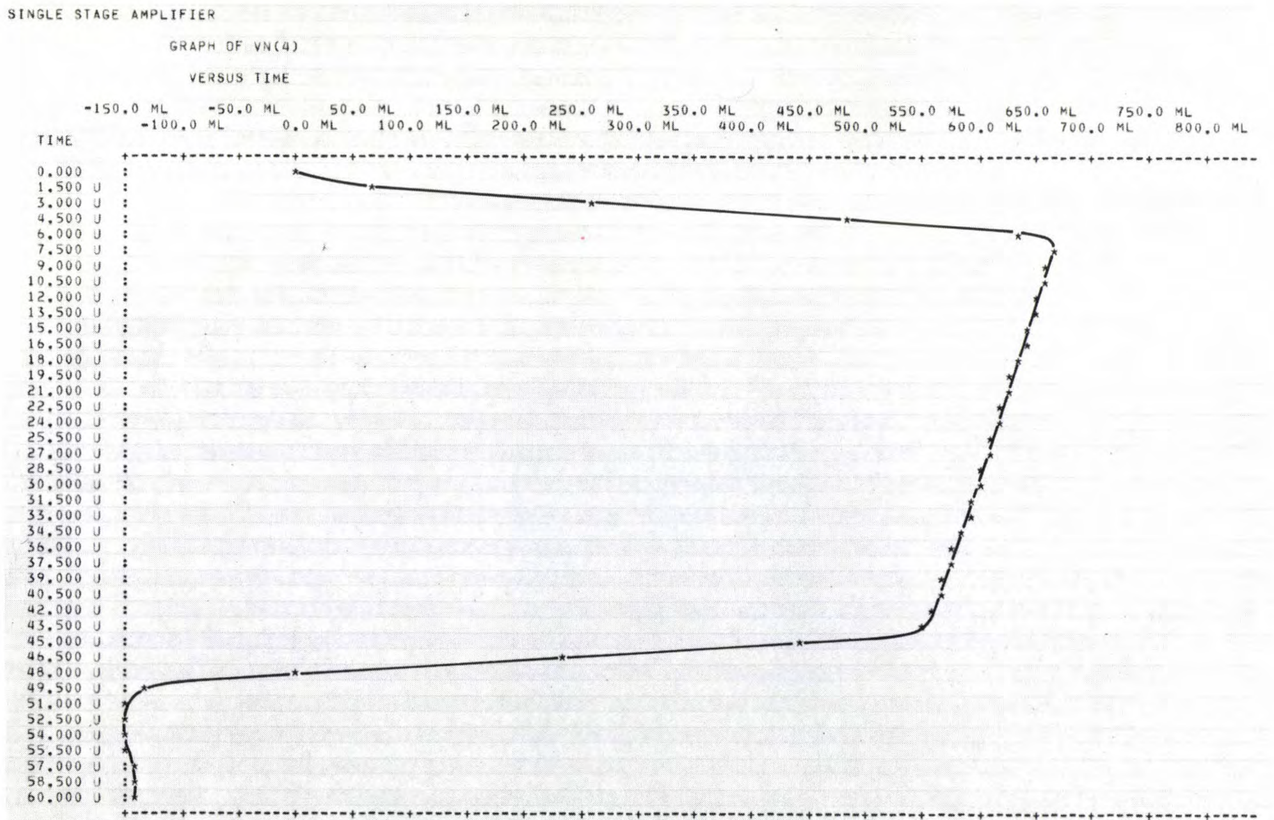

b

Fig. 8. Results of the analysis of fig. 7, produced by a line printer. The graphs indicate the voltage variation at the nodes *1* (*a*) and *4* (*b*) of fig. 5 during the period in which the current generator J_1 delivers one pulse. The time is plotted vertically in 40 steps of 1.5 μs; the voltages are plotted along the horizontal axis in millivolts. The voltage pulse of (*b*) is the circuit response to a voltage pulse with the shape of (*a*) at the input.

After the data have been read in, the computer carries out some checks for faults. It examines, for example, whether all the resistances between two nodes have been connected. The actual analysis then follows, and then the output is printed out on a line printer. *Fig. 8* shows the input and output pulse shapes calculated in this way. The designer can now examine these results to find out whether the circuit meets his requirements and expectations.

The example given demonstrates only a few of PHILPAC's capabilities. There is insufficient space here for a full discussion of all the other facilities it offers. One particular facility deserves a brief mention, however. When a circuit such as that of fig. 5 is designed as an IC, the various components will exhibit deviations from the desired values. A designer obviously wants to know the extent to which his circuit is sensitive to variations of this kind. He can find this out by making a few statistical calculations with PHILPAC. These can be made by adding to the circuit description some data on the spread in the component values; the computer can then calculate, e.g. by means of a Monte-Carlo analysis, their effect on the behaviour of the circuit. (A Monte-Carlo analysis is a series of analyses in which different sets of random component values are chosen within the range of spread.)

Logic simulation

Verification of the design of digital circuits, as discussed in the introduction, takes place in two phases. First, it is necessary to investigate whether the basic units are working properly; since this concerns the analog behaviour of the circuits, this is done with a circuit-analysis program. This analysis also determines the conditions under which the abstraction of analog voltages to the logic levels '0' and '1' remains valid (e.g. the 'fan-out'; see fig. 2 and caption). If these conditions are taken into account when the logic circuit is designed, the complete circuit only needs to be simulated for proper functioning at the logic level. This verification of logic behaviour is done by means of *logic simulation*; in this process the computer investigates systematically the response of the circuit to the combinations of input signals devised by the designer.

The program developed at Philips for performing the logic simulation is known as PHILSIM (PHIlips Logic SIMulator). As an example of how the program works the simulation of a 1-bit adder will be described here. A circuit of this type, usually referred to as a 'full adder', a single section of an adder, for example, in the arithmetic unit of a computer, receives as its input signals two binary numbers A and B and an incoming carry C_{in} from the preceding section. The circuit is required to produce the sum S of these, and also the outgoing carry C_{out} to the next section. This logic behaviour is described in the truth table in *Table I*.

Table I. Truth table for a 1-bit adder. A and B are the binary digits to be added. C_{in} is the incoming carry, S is the sum and C_{out} is the outgoing carry.

A	B	C_{in}	S	C_{out}
0	0	0	0	0
0	0	1	1	0
0	1	0	1	0
0	1	1	0	1
1	0	0	1	0
1	0	1	0	1
1	1	0	0	1
1	1	1	1	1

To design a circuit that works in accordance with the truth table, we first derive from the table the Boolean equations for S and C_{out}:

$$S = C_{in} \cdot (\bar{A} \cdot \bar{B} + A \cdot B) + \bar{C}_{in} \cdot (\bar{A} \cdot B + A \cdot \bar{B}), \quad (1)$$

and

$$C_{out} = A \cdot B + C_{in} \cdot A + C_{in} \cdot B. \quad (2)$$

The operator '·' here denotes the AND function and the operator '+' denotes the OR function; the operator '·' has priority over '+'. Using the rules of switching algebra, we can derive a simpler expression for S from equations (1) and (2):

$$S = C_{in} \cdot A \cdot B + \bar{C}_{out} \cdot A + \bar{C}_{out} \cdot B + \bar{C}_{out} \cdot C_{in}. \quad (3)$$

Equations (2) and (3) indicate directly the composition of the network of AND, NAND and NOR gates that will give S and C_{out} from the signals A, B and C_{in}; see *fig. 9*.

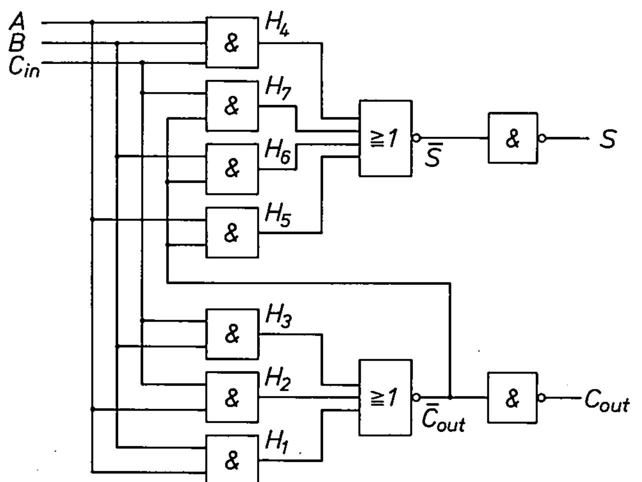

Fig. 9. Diagram of a 1-bit adder (full adder), used as a section of a larger adder. This circuit takes the binary numbers A and B and the incoming carry C_{in} to form the sum S and the outgoing carry C_{out}.

In the PHILSIM program the input, as in PHILPAC, consists of two parts: the network description and the simulation instruction. *Fig. 10* shows the description of the network of fig. 9. It consists of a series of instructions each of which contain the data for one gate: the output signal, the function and the input signals, in that order. For this description a number of internal signals of the circuit are designated by H_1 to H_7.

Although the description in fig. 10 does not mention gate delay times, these are nevertheless taken into account in the simulation. The PHILSIM program also digitizes the time; in the simulation the state of the circuit is calculated from the time zero and after every successive interval of one time unit. For each simulation the designer can assign any value he wishes to this time unit. This implies that events in the network (e.g. changes in input signals) can only take place at integral multiples of this time unit. The gate delay times must also amount to an integral number of time units; this number can be indicated beside each gate in the network description. When, as in fig. 10, no gate delay time is indicated, PHILSIM automatically assumes a delay time of one time unit per gate.

Fig. 11 shows the second part of the input, the simulation instruction. Lines 1 and 2 contain a few indications concerning the output; the subsequent combinations of instructions 'IT' ('initialize to') and 'SU' ('simulate until') give the actual simulation instruction. Thus, line 3 means 'set the time to zero and assign to A, B and C_{in} the value '0'; and line 4 means 'simulate, starting from this situation, the passage of 10 time units'. In the following lines all the possible combinations of input signals are run through systematically. The simulation time required for this network is easily determined: it follows from fig. 9 that forming the sum signal requires a maximum of five time units, i.e. two for forming $\bar{C}_{out}$ and three for determining S. A simulation time of 10 units is thus amply sufficient for all gates to return to the steady state, even in the event of errors in the design or in the network description.

The result of the simulation is printed out in the form shown in *fig. 12*. The left-hand column gives the time axis, on which the time is reset to zero at each 'IT' instruction. In the adjacent columns the calculated values of A, B, C_{in}, S and C_{out} are printed out, but only at the

```
N E T W O R K                 RELEASE 6.0  30/01/78

  1               NETSTART
  2   H1          AND           I(A,B)
  3   H2          AND           I(CIN,A)
  4   H3          AND           I(CIN,B)
  5   CUITN       NOR           I(H1,H2,H3)
  6   CUIT        NAND          I(CUITN)
  7   H4          AND           I(CIN,A,B)
  8   H5          AND           I(CUITN,A)
  9   H6          AND           I(CUITN,B)
 10   H7          AND           I(CUITN,CIN)
 11   SN          NOR           I(H4,H5,H6,H7)
 12   S           NAND          I(SN)
 13               NETEND
 14   /*
```

Fig. 10. Network description in PHILSIM code, relating to the circuit in fig. 9. Instructions *1* to *11*, each for one gate, give the output signal, the function and the input signals. This establishes the form of the network. (The indices here are placed on the line, and the negative sign is replaced by an 'N' after the symbol.)

```
  1        P A,B,CIN,,S,CUIT
  2        PCO
  3        IT 000(A,B,CIN)
  4        SU TIME=*+10
  5        IT 001(A,B,CIN)
  6        SU TIME=*+10
  7        IT 010(A,B,CIN)
  8        SU TIME=*+10
  9        IT 011(A,B,CIN)
 10        SU TIME=*+10
 11        IT 100(A,B,CIN)
 12        SU TIME=*+10
 13        IT 101(A,B,CIN)
 14        SU TIME=*+10
 15        IT 110(A,B,CIN)
 16        SU TIME=*+10
 17        IT 111(A,B,CIN)
 18        SU TIME=*+10
 19        F
 20       /*
```

Fig. 11. Simulation instruction in PHILSIM code for the network of fig. 9. The first two instructions indicate which quantities have to be printed out ('Print A, B, etc.') and also the times: only when a change takes place in one of these quantities ('Print Changes Only'). The simulation is successively carried out for all possible combinations of input signals, and is always started by an 'IT' instruction ('Initialize To'), the time then being reset to zero and the input signals being given their initial values. The instructions in 'SU' ('Simulate Until') always give the time the simulation will take.

```
--------------------------------------------------------------
       ABC SC
         I  U
         N  I
   T        T
   I
   M
   E
--------------------------------------------------------------
      0 000 **
      3 000 00
      0 001 **
      3 001 *0
      5 001 10
      0 010 **
      3 010 *0
      5 010 10
      0 011 **
      3 011 *1
      5 011 01
      0 100 **
      3 100 *0
      5 100 10
      0 101 **
      3 101 *1
      5 101 01
      0 110 **
      3 110 *1
      5 110 01
      0 111 **
      3 111 11

*** SIMULATION TERMINATED AT TIME=          10 ***
```

Fig. 12. Result of the simulation of the network of fig. 9. The left-hand column gives the time (in numbers of time units), and on the right the states of the input and output signals A, B, C_{in}, S and C_{out} are given for these times. Whenever the simulation of a new combination of input signals begins, the time is reset to zero. The signals are only given for the times when a change takes place. The state of the signals marked with an asterisk is not yet known at that time; the actual result is thus given by the lines without asterisks. Comparison of these lines with Table I shows no differences, so that it may be concluded that fig. 9 correctly represents the designed logic function.

times zero and at the times when there is a change in one of these values. An asterisk indicates that the state of the associated output is not known at that moment; as a consequence of the gate delay times the effect of the input signals has not yet made itself felt. As can be seen in fig. 12, first a C_{out} appears, immediately followed by S. Comparing this result with the truth table in Table I, we see that there is complete agreement, so that the simulation shows that the circuit correctly represents the desired function.

In practice the simulation will have to extend over many more time units than in our example. A simulation of a period of 10 milliseconds of 'real time', with a time unit of 10 ns, would require calculations for 1 000 000 time steps, which would require far too much computer time. This difficulty can be overcome to some extent by using 'event simulation'. This kind of simulation is not controlled by times but by events: the circuit is not calculated after every time unit but only at the times when a signal changes state. The consequences of such a change are then administered as future transactions, and the simulation steps from event to event, under the control of this administration, missing out the times when the circuit is in the steady state.

A further simplification that can shorten the simulation time considerably is to change over from an asynchronous to a synchronous circuit. Let us assume that the adder in our example derives its input signals from a logic circuit L_1 (see *fig. 13a*) and passes on the output signals to a logic circuit L_2. In the simulation of circuit L_2 account must then be taken of the delays both in the circuit L_1 and in the adder, because they affect the moment at which the signals S and C_{out} become available. This is no longer necessary when synchronization registers are included between the circuits, as shown in fig. 13*b*. At an instruction from a synchronization pulse, each of these registers takes over the output signals from the preceding circuit and holds them until the next pulse becomes available in the form of input signals from the following circuit. In the intervening period each circuit can then perform its function independently, without being disturbed by the delay effects of the preceding circuits. If the period between the pulses — which is usually constant, hence the term 'clock pulses' — is made long enough to ensure that all gates in the various circuits can return to the steady state during that period, there is no longer any need for the simulation to take the gate delay times into account. Only one calculation per clock pulse then has to be performed for each circuit, and this is much fewer than in the asynchronous case of fig. 13*a*. Synchronous circuits can thus be simulated up to several hundred times faster than asynchronous ones.

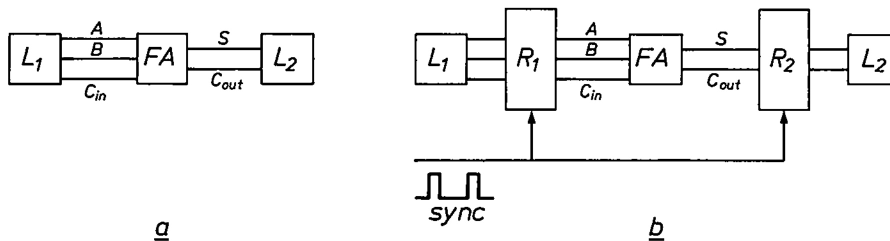

Fig. 13. *a*) Asynchronous circuit, consisting of the full adder of fig. 9 *(FA)* and the logic circuits L_1 and L_2. In simulating each of these subcircuits it is necessary to take into account the gate delays in all the preceding circuits. *b*) The same circuit, but now synchronized by the addition of registers R_1 and R_2. Whenever a synchronization pulse appears at the input *sync* the register takes over the output signals of the preceding circuit and holds them until the next pulse becomes available as input signal for the next circuit. It is now no longer necessary to take the gate delay times into account in the simulation; this represents a time saving by a factor of a few hundred compared with the simulation of an asynchronous circuit.

The 1-bit adder dealt with here will in practice be part of, say, a four-bit adder, and this in turn will be part of a larger system. Since it is convenient for the designer if this structure is expressed in the network description for the simulation, the PHILSIM program is provided with a facility for representing such subcircuits by a single instruction. This consists of the name of the circuit, the input signals and the output signals. The circuit is thus regarded as a 'black box', designated in the PHILSIM code by 'macro'; the contents of a macro are specified in a separate description.

Layout

The IC technology used (e.g. MOS, LOCMOS, I²L) has a considerable influence on the way the layout is arranged. Thus, I²L gates are situated on either side of the injector, the conductor that provides the current supply. In dynamic MOS circuits the gates are arranged in rows to avoid loss of chip area because of bends in the clock lines. Again, the arrangement with a two-layer wiring system will be different from that for single-layer wiring.

So far it has not been found possible to translate the craftsmanship required for making good layouts into

computer strategies that produce equally compact layouts. In spite of the availability of computer programs, layouts are still frequently made in the conventional way. However, programs have been developed to take over the routine work such as the repetition of patterns and checking the layout. DRAW [7] and CIRCUITMASK [8] are examples of such programs. The descriptive language CIRCUITMASK is used for defining all the geometric elements that can be used to form a layout. A number of basic figures are available for this; the most important ones are rectangles and polygons. Circular elements are also available for special purposes. A transistor could be described in CIRCUITMASK as shown in *fig. 14*. This example uses the instruction 'RR' for rectangles and 'PATH' for the U-shaped interconnection tracks of base and collector.

```
      RESOLUTN 0.5
      PATTERN TRANS
    1 RR(DP,190,150)                                   :EILAND
    2 RR(SP,80,100) 55,25                              :BASIS
    3 RR(CO,10,90) 60,30,COPYX 60,1                    :BASIS KONTAKTEN
    4 PATH(IN,65,25,R,0,110,20,R,60,0,10,R,0,-110,20)  :BASIS ALUMINIUM
    5 RR(IN,SN,0,CO,5,20,90) 85,30                     :EMITTER
    6 RR(SN,CO,0,15,100)                               :COLLECTOR
    7 PATH(IN,32.5,20,R,0,137.5,25,R,125,0,15,R,0,-137.5,25) :COLLECTOR ALU
1     END TRANS
      FINISH

THE NUMBER OF DEFINED`PATTERNS IS        1
```

Fig. 14. Description of a transistor in CIRCUITMASK code. The first instruction assigns to this pattern the name 'TRANS'. The lines numbered *1* to *7* contain the description. Each line begins with an indication of the type of figure ('RR' is rectangle, 'PATH' is interconnection track), followed by an indication of the masks these figures have to be placed in (e.g. 'DP' means deep *P*, the isolation diffusion) and also the coordinates where the figures have to be positioned. The final instruction completes the definition of the pattern 'TRANS'.

The correctness of the layout can be checked with the aid of a drawing made on a computer-controlled drawing machine; see *fig. 15*. This can also be done with a graphical display, i.e. a cathode-ray tube connected to the computer; see *fig. 16*. The designer can then immediately correct any faults with a keyboard and a light pen; he does not have to wait for drawings.

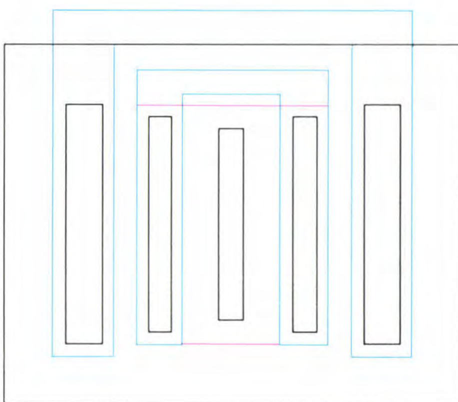

Fig. 15. Drawing of the 'TRANS' pattern made on a computer-controlled drawing machine (plotter) after processing by CIRCUITMASK.

In visual inspection there is always a chance that one or more faults may be overlooked. For this reason various automatic checking methods have been developed that make it possible to determine whether the layout design rules have been observed. For example, the computer can be made to check whether all the interconnection tracks have a specified minimum width and a minimum spacing The instruction

'CHECK GAPS (15,10 IN)'

means 'check whether all the tracks in the mask *IN* (*IN* is the mask for interconnection tracks) are at least 15 μm wide and have a spacing of at least 10 μm'. The faults found by the program can be shown on the graphical display or printed out in the form of coordinate tables by the line printer.

If, after the checks have been completed, the designer finds that the layout is correct, he will then have a control tape made for the mask machine. Since this involves the use of costly precision equipment, the CIRCUITMASK program will arrange the information on the tape in such a way as to minimize the time taken by the mask machine.

Programs that make layouts by automatic methods are nearly always specifically designed for a particular technology. Although all these programs broadly follow the same strategy, differences in technology nevertheless rule out any universal solution. The operations performed by such a program, on the basis of the logie description of the circuit, can be divided into three groups:

— partitioning of the circuit into a number of modules, and broadly allocating the modules a position in the layout;
— positioning the components in the modules, and
— interconnecting the components as required by the logic description.

The partitioning of the circuit is the main and most difficult phase in designing the layout; the aim is to substitute a number of simple problems for the actual problems to be solved. Good partitioning is obtained when the modules have high internal cohesion but few interconnections between modules. A poor choice made during partitioning will result in a large layout, and this makes it important for the designer to be able to intervene at this stage.

Fig. 16. Design and correction of a layout with a graphical display. The light pen is used for indicating and moving figures on the screen; the keyboard (*right*) is used for typing in new values.

In positioning the components in the modules the usual tactic is to arrange the components in rows. As the size of the modules is limited simple iteration procedures can therefore be used. Since the aim is to minimize the area of the circuit, the objective in such a search process could for example be the minimization of the thickness of the interconnection channels.

After positioning of the components the interconnections have to be made. With multilayer wiring this is not so very difficult, but with a single-layer wiring the computer may often only find a partial solution. The designer will then have to do the rest of the work himself.

This account of the mechanical design of a layout may give the impression that there are three autonomous stages. It might seem that it would be sensible to return to a previous stage if it appeared later that a poor choice had been made. In conventional circuit design such interaction does in fact exist between partitioning, positioning and the making of interconnections. In spite of the advantages of such interaction, it is nevertheless seldom used when working with a computer; the computer time required would usually be far too long.

Testing

So that the ICs can be tested after manufacture it is necessary to design a test procedure that will enable all internal faults that can occur in the IC to be measured at a circuit output. The first step in drawing up such a test procedure is therefore to identify all the faults that can possibly occur. For each fault a test pattern must then be produced that will enable the fault to be detected at one of the outputs when the pattern is presented to the inputs. The actual faults in a circuit — breaks, short-circuits, faulty areas — are too complicated to be handled by a computer program. A sim-

[7] See the article mentioned in note [3].
[8] D. B. Jarvis, Design of integrated circuit masks, in: Symp. on Interactive computer graphics, Delft 1970, pp. 95-101.

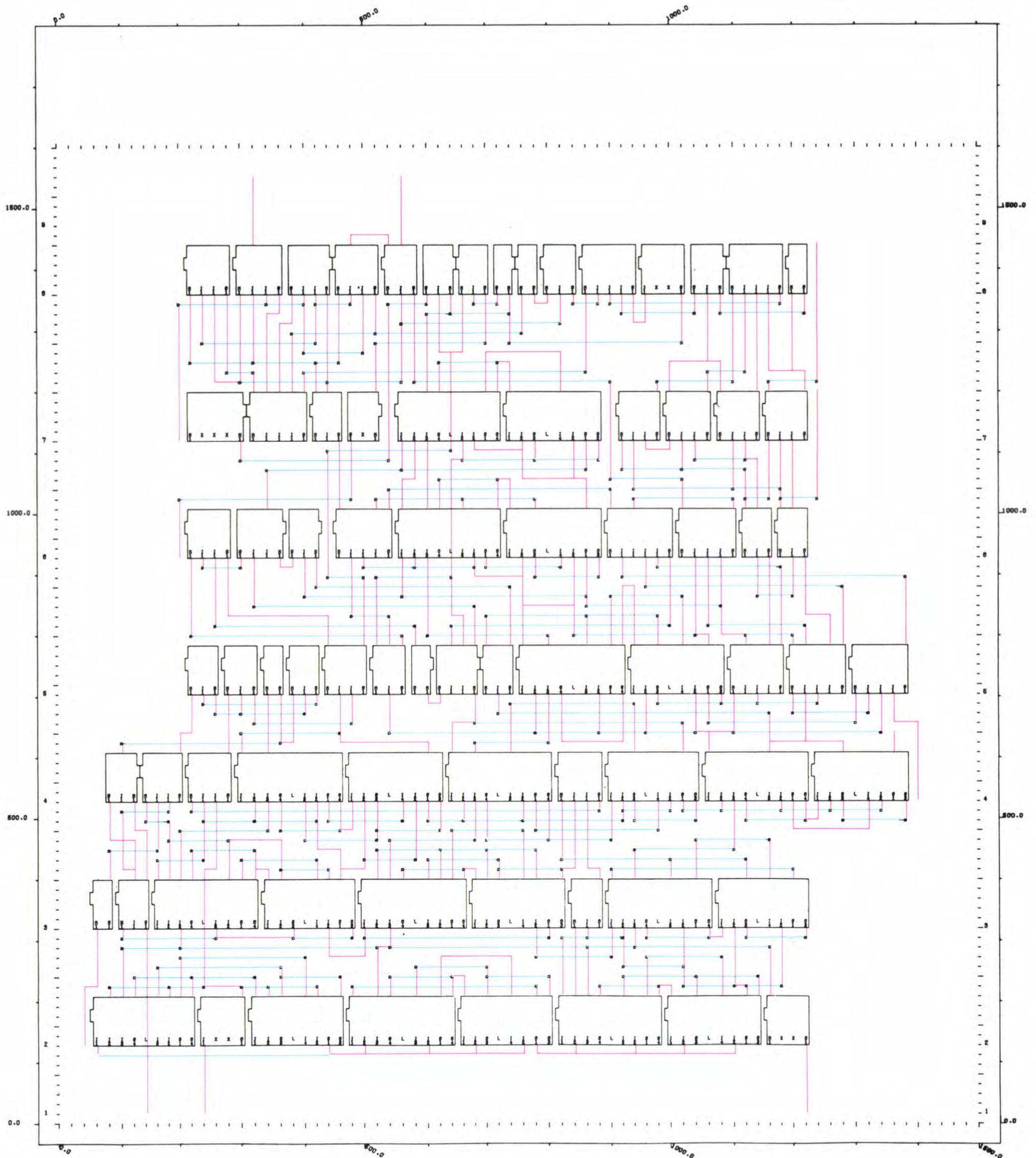

Fig. 17. Part of the layout of a LOCMOS circuit; the black blocks in rows contain the logic modules. The blocks were positioned in the row by the designer. Under each row the modules have been interconnected in two-layer wiring by the computer (red and blue).

plified model is therefore used: faults can only occur in interconnections, and it is assumed that such faults will either make the signal on this interconnection remain at the value corresponding to the logic '0' ('stuck at zero', 'SA 0') or to the logic '1' ('stuck at one', 'SA 1'). As a further simplification it is assumed that the circuit contains no more than one fault. A circuit that passes the test for all possible single 'stuck at' faults is said to be 'good'. The basic consideration is the reasonable, although unproved, assumption that all faults, even multiple ones, can be found in this way. A set of test patterns can be produced in three ways: automatically by means of a computer program, by the designer, or by means of a 'random' generator.

The automatic method uses the knowledge of the circuit structure, and is referred to as 'structural testing'[9].

Although this is in principle a superior test method — a complete test can be generated — the other two are also used. The reason is that the automatic method can require a great deal of computer time, especially for large circuits with many internal memory elements.

In the second method the designer generally uses the patterns he has used for simulation, supplementing them until he considers them sufficient for the test. The amount of work necessary for tracing all the possible faults in this way is impossibly large, however. It has meanwhile become common practice to accept incomplete tests. This method of test designing is the most widely used today.

The determination of test patterns by means of a 'random' generator generally gives disappointing results. In some cases, however, a test made by the designer can be supplemented in this way.

The quality of a test procedure is assessed by means of test-verification programs. For every possible fault in a circuit a verifier performs a simulation at the same time as the simulation of the fault-free circuit. The input for the simulation is the series of test patterns. A fault can be detected if different states appear at the outputs of the two circuits. The result of the verification is a list of detectable and non-detectable faults.

Testing is the most difficult subject for CAD. Since the complexity of LSI circuits may be expected to increase quite considerably, the means at present used will undoubtedly prove to be inadequate. Instead of being a tedious procedure *after* the design, testing will have to become an integral part of the design procedure. Experiments in this direction show promise.

CAD systems

A CAD system contains, in addition to the computer methods required during a design phase, such as logic simulation, a variety of aids that can be used in the transition from one design phase to the next. The interface of the electrical or logic design with the layout is by far the most important of these. This interface may be a constructive connection — so that the layout follows more or less automatically from the design — or a monitoring connection. In the monitoring case the designer still makes the layout, but he receives facilities for proving the correctness of the layout. With the conventional method a compact layout can be made if the designer is prepared to spend a lot of time on it; the automatic method produces a far less densely packed layout with very much less effort. There are also intermediate forms. For example, the automatic method can be 'opened up'; in this case a program proposes a layout, and the designer can then improve on its shortcomings. In such cases the CAD program will usually check whether these improvements are free from faults.

Two CAD systems will now be briefly outlined. In view of their different objectives, the two systems are somewhat different in nature.

CAD systems for LOCMOS circuits

Circuits made with the LOCMOS technology [10] have extremely low dissipation and are capable of reasonably high switching speeds. The range of LOCMOS applications varies from simple standard circuits such as simple gates to complex LSI circuits.

The CAD system for LOCMOS comprises a number of logic modules, whose electrical operation is verified beforehand by means of a circuit-analysis program. The system consists of a method for logic simulation (PHILSIM) and a semi-automatic layout system. It also contains facilities for automatically converting the test procedure made by the designer into a test program for the test equipment. A number of rules have been drawn up for automatically making the layout for LOCMOS circuits. The layout is organized in a number of rows. Each row is divided lengthwise into three parts: the central part contains a number of modules, while the lower and upper parts contain the interconnections between the modules, which contain the logic functions. The layout of these modules has previously been made as compact as possible by hand, and the correctness of the layout has been verified by extensive checks and pilot production.

Designing in LOCMOS amounts to selecting the modules required, allocating them their positions in the layout, making the interconnections between the modules and finally making the connections to the outside world.

Although the allocation of a module to its place in the row can be automated, a 'manual' method has been chosen for this system. The main reason is that the quality of the positioning determines to a great extent the final compactness of the layout. For the time being the designer appears to be more capable of making the right decisions here, as compared with automated procedures.

Making the interconnections between the modules is the most labour-intensive part of the work. This has been fully automated in the CAD system described here, but there is still a facility for the independent specification of interconnections considered to be important, or of proving them under the supervision of the system if the automatic procedures have made less suitable choices. Part of a layout made in this way can be seen in *fig. 17*.

---

[9] See the article mentioned in note [1].
[10] See the article mentioned in note [5].

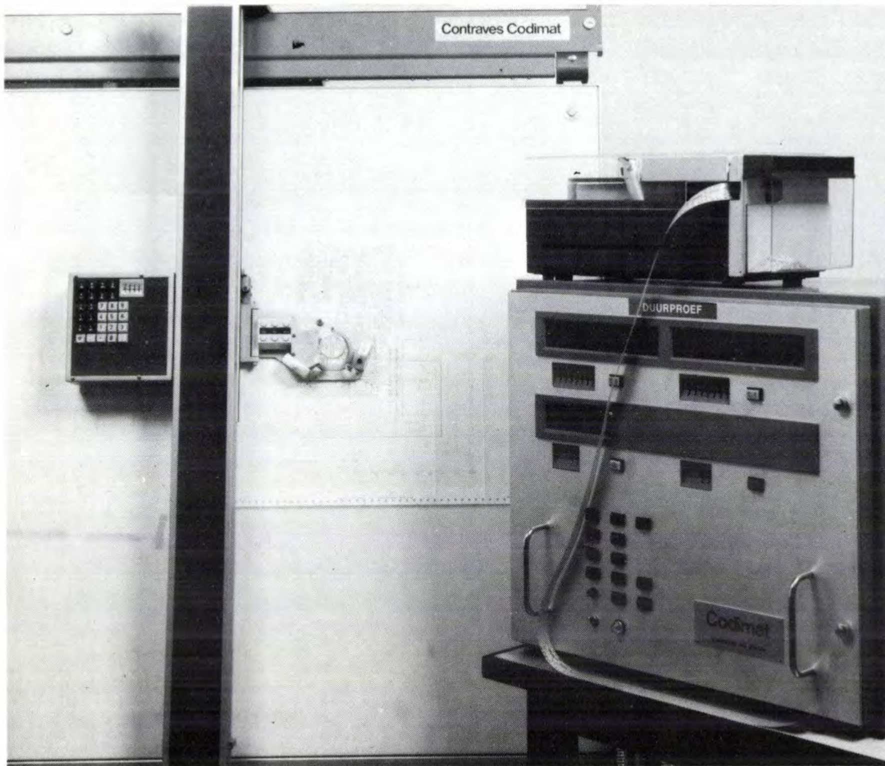

Fig. 18. 'Digitizer' for coding on a punched tape a layout made by the designer (*right*). The layout is held flat against a table; a cross-hair cursor system can be moved across the table in the *x*- and *y*-directions. A magnifying glass can be used for accurate positioning. The various instructions and the coordinates of the points selected on the drawing can be punched in the tape by pressing the appropriate buttons.

CAD system for I²L circuits (CADILL)

Designs for the I²L technology can be made with the CADILL system (Computer Aided Design for Injection-Logic Layouts). CADILL is aimed at the category of designs where no loss of chip area can be tolerated, and where the designer thus wants to make use of all the facilities a technology can offer. In such a case it is not possible to use automated design aids in view of the associated limitations, and so all the work will have to be done by the designer. This type of design will therefore be labour-intensive, and if no special measures are taken there is a serious risk of errors. The CADILL system seeks to facilitate the tracing of errors made during a design without in any way restricting the freedom of the designer. Broadly speaking, designing with CADILL can be described as follows. First, the logic system is checked against the specification in the usual way by means of logic simulation. Next, the designer produces the layout, which is then scanned and coded with the aid of a 'digitizer' (see *fig. 18*). All the coordinates in the layout are then punched on tape in accordance with rules imposed by CADILL. This means that special codes on the kind of information have to be fed in at the same time; these codes, together with the associated data, represent an I²L gate or an electrical interconnection, for example. The punched tape made with the digitizer is then read into a computer. From this tape CADILL can now form a CIRCUITMASK description, which will give a drawing of the layout. Up to this point CADILL does not differ from any other non-automated system. However, since under the CADILL rules some extra data are fed into the punched tape during the digitizing, a logic-network description can also be made from this tape. This description can now be used for a further logic simulation, not to verify the design this time, however, but to check the layout against the specification. CADILL thus offers the designer the means of verifying whether the conventionally made layout is equivalent to the logic design. In addition to this facility, CADILL also possesses a few other less spectacular but particularly useful functions. For example, CADILL can draw attention to obvious faults, such as unconnected inputs, at the stage of making the logic description from the layout. CADILL can also be used for plotting symbolic layouts. A symbolic layout deviates in some respects from the normal technological rules for presenting the circuit in a more readable form; for example, interconnection tracks are shown narrower than they are in reality.

Summary. In the design of LSI circuits it is necessary to have CAD facilities available. Circuit-analysis techniques can be used to verify analog circuits that are not unduly large, such as digital modules. Large LSI circuits cannot be handled in this way, and digital design aids are far more useful here. For this reason, and also because the digital technique is simpler for the designer, LSI circuits will increasingly be made with the aid of digital techniques, even for functions that are essentially of an analog nature. The repertoire of CAD software available includes logic-simulation programs for verifying the correct operation of the circuit, programs that provide help in layout design or that produce the layout completely automatically, and programs that make test procedures for LSI circuits and check their quality. Finally, for a number of widely used technologies there are also CAD systems in which the computer program includes the transition from one design phase to the next

An I²L digital modulation stage for data transmission

R. A. van Doorn and N. A. M. Verhoeckx

Introduction

The telephone network has for many years been used for other purposes besides the transmission of speech signals between subscribers. The main reason for this is that the telephone now extends everywhere; every business firm and the greater number of homes are now connected. However, since the telephone system was originally intended for speech, it does not necessarily meet the requirements for satisfactory transmission of other signals. A good example of this can be found in the signals that are exchanged between a centrally located computer and its remote peripherals, as used by banks, travel agencies and airlines, to name a few examples. The signals here constitute 'data', i.e. information that, unlike speech, is originally presented in the form of a succession of symbols selected from a limited set. In travel reservations and bank transfers the original symbols are the letters of the alphabet and the digits 0 to 9, whereas in communication between computers the original symbols are binary (e.g. 0 and 1). A series of symbols that can assume only a limited number of different values is referred to as a digital signal, and if the signal values (also called 'samples') follow each other at fixed intervals of T seconds, we speak of a digital signal with a sampling rate of $1/T$ Hz. Multivalued digital signals (e.g. of the alphanumeric type) can also be represented with two-valued symbols ('binary digits' or bits). A unique combination ('word'), for example, of eight ones and zeros, is then assigned to each signal value. The reason for doing this is that binary digital signals can easily be processed electronically: the one value ('1') then corresponds, for instance, to a high voltage level for a certain time and the other value ('0') corresponds to a low voltage level.

The term 'data transmission' refers to the electromagnetic transmission of digital signals (often binary) that originate from a data source. Great distances often have to be bridged, sometimes with the aid of international or even intercontinental links. To permit the existing telephone network to be used, the digital data signal has to be converted at the transmitting end into a form that somewhat resembles the output signal from

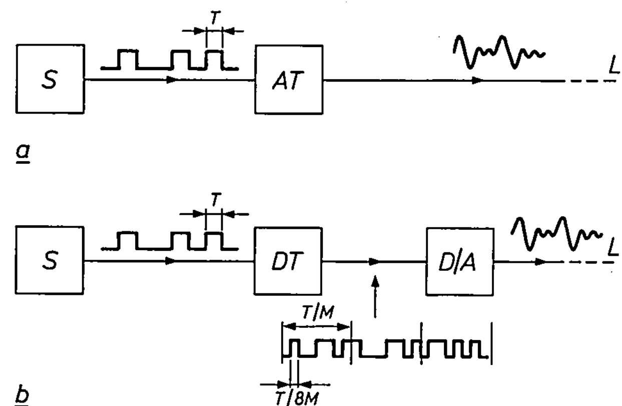

Fig. 1. The signals from a data source S first have to undergo various operations in a data transmitter, such as filtering and modulation, before they can be transmitted via a telephone line L. In a commonly encountered situation the input signal to the data transmitter is a binary data signal, where a high level during the time T represents the symbol '1' and a low level the symbol '0'. In an analog data transmitter AT the required line signal is directly obtained by means of analog circuits (*a*). In a digital transmitter DT digital circuits are used to produce a digital version of the required line signal, and the final analog result is obtained by means of a digital-to-analog converter D/A (*b*). The output signal of the digital transmitter requires many more binary symbols (bits) per second than the input signal. This means that there are more digital words per second (M/T instead of $1/T$), each consisting of a larger number of bits (e.g. eight instead of one).

the microphone of a telephone — in other words, an *analog* signal, in the frequency band from 300 Hz to 4 kHz. This is brought about by means of a variety of electrical operations, such as filtering and modulation (*fig. 1a*). At the receiving end the original data is reconstructed as accurately as possible from the incoming signal. A combined transmitter and receiver is called a data modem (derived from *mo*dulator-*dem*odulator). The amount of information per unit time, expressed in bits per second, that can be transmitted over a telephone link is closely related to the type and complexity of the operations performed in the modem. There are various modulation techniques to choose from [1] and there is also a choice among various forms of equalization [2] at the receiving end. The most commonly

Ing. R. A. van Doorn, formerly with Philips Research Laboratories, Eindhoven, is now with the Philips Audio Division, Eindhoven; Ir N. A. M. Verhoeckx is with Philips Research Laboratories, Eindhoven.

[1] F. W. de Vrijer, Modulation, Philips tech. Rev. 36, 305-362, 1976 (No. 11/12).
[2] F. de Jager and M. Christiaens, A fast automatic equalizer for data links, Philips tech. Rev. 37, 10-24, 1977 (No. 1).

used data-transmission systems have a bit rate of between 200 and 9600 bits/second. The systems with lower bit rates, which are not so complex, are mostly produced with conventional components, such as discrete transistors, inductors and capacitors. In more advanced modems, however, increasing use is made of digital circuits (fig. 1*b*), which have obvious advantages. In the first place, costs can be cut by making the modem from custom-designed integrated circuits (for large production runs), or in the form of general-purpose microprocessors (for smaller production runs). This is closely connected with the versatility that a digital approach permits; by this we mean that one and the same circuit can be used to build systems with entirely different characteristics, such as filter response, modulation method, carrier frequency and transmission rate, simply by replacing a digital storage device — e.g. a 'read-only memory' (ROM). In addition, since tolerances and ageing have virtually no effect, greater reliability and higher accuracy can be achieved. Another advantage of a digital design is greater reproducibility, for one reason because there is no need for filter alignment. In this article we shall describe a digital integrated circuit (IC) that contains, in addition to the digital memory, all the components necessary for filtering and modulating data signals at the transmitting end of a data link [*]. The digital memory has deliberately been left out of this IC to make it more versatile. We have designed our data-modulation stage as an I^2L circuit [3]; this complicated circuit (consisting of some 800 logic gates) can then be arranged in such a way that it requires only about 15 mW of power.

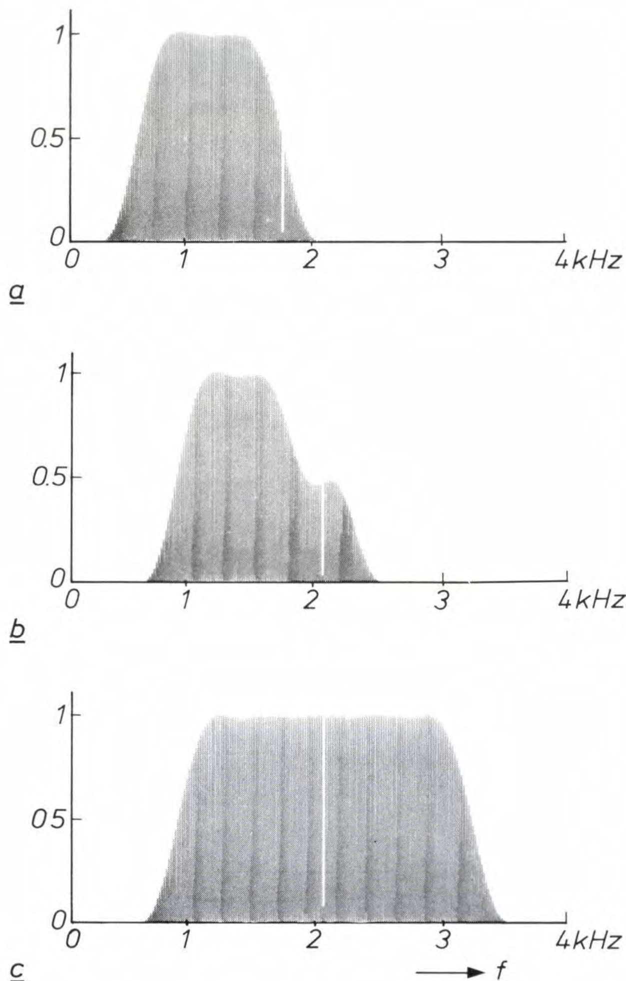

Fig. 2. Some examples of spectra measured at the output of the integrated digital modulation stage (after digital-to-analog conversion). In all three cases the input signal consisted of a periodically repeated pseudo-random binary data signal with a sampling rate of 2.4 kHz. The various spectra were obtained with the same modulation stage simply by replacing the contents of the external digital memory. *a*) Vestigial-sideband-modulated data signal with a carrier frequency of 1800 Hz. *b*) Vestigial-sideband-modulated data signal with a carrier frequency of 2100 Hz with special shaping of the spectrum to facilitate carrier recovery at the receiving end. *c*) Double-sideband-modulated data signal with a carrier frequency of 2100 Hz.

Fig. 2 shows some of the many spectra of modulated data signals that can be generated with our modulation stage. The figure clearly shows how a wide variety of systems can be produced from the same digital circuit merely by changing the contents of the memory.

In this article we shall treat the subject in two parts. In the first part we shall discuss the design of the modulation stage as a digital system, and in the second we shall explain the technology and look more closely at the layout design. In addition we shall touch on various aspects that are not specific to this modulation stage but will also be encountered in the design of other integrated circuits (not necessarily in I^2L).

The linear modulation stage, a versatile circuit module

As indicated above, the output signal from the data source is converted into a signal suitable for transmission via the telephone network by making use of filtering and modulation. For many modulation systems the linear modulation stage shown in *fig. 3a* can be used. This consists of a filter F_1, a carrier generator G_1, and a modulator M in which the output signals from F_1 and G_1 are multiplied. If G_1 supplies a cosine carrier signal, the output signal from the modulation stage is a double-sideband-modulated signal, as shown in fig. 3*b* and 3*c*.

We use the term *linear* modulation stage here because the superposition principle is applicable. If an input signal $u_{ia}(t)$ gives an output signal $u_{oa}(t)$, and similarly a signal $u_{ib}(t)$ gives a signal $u_{ob}(t)$, then an input signal $A.u_{ia}(t) + B.u_{ib}(t)$ corresponds to an output signal $A.u_{oa}(t) + B.u_{ob}(t)$, where A and B are arbitrary constants. A linear modulation stage can be constructed either as an analog or a digital circuit.

If a second filter F_2 is added after the modulator (*fig. 4a*) one sideband can be completely or partly suppressed, and in this way a single-sideband or vestigial-sideband-modulated signal can be obtained. With a double version of the elementary modulation stage (fig. 4*b*), in which G_1 generates a cosine carrier and G_2 a sine carrier, it is also possible to obtain four- or eight-phase modulation or combined phase and amplitude modulation, all widely used in data transmission. (These modulation methods are usually called quadrature or orthogonal modulation.) We see then that the elementary linear modulation stage can be used in a large variety of arrangements. In a digital configuration this facility can be combined with the great versatility inherent in digital systems, giving a module suitable for many applications.

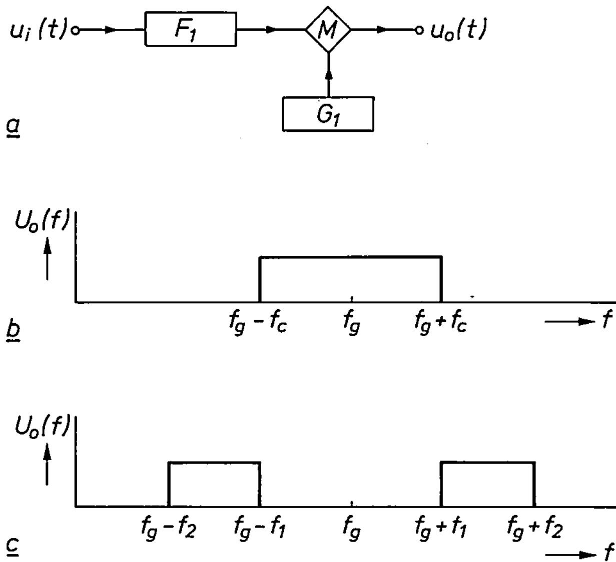

Fig. 3. *a*) Linear modulation stage consisting of filter F_1, a product modulator M and a carrier generator G_1, which gives a cosine carrier at a frequency f_g. The output signals of F_1 and G_1 are multiplied by each other in the modulator M. *b*) Frequency spectrum $U_o(f)$ of the output signal $u_o(t)$ obtained from the modulation stage when F_1 is a lowpass filter with cut-off frequency f_c. *c*) Frequency spectrum $U_o(f)$ of the output signal $u_o(t)$ obtained from the modulation stage when F_1 is a bandpass filter with a passband from f_1 to f_2.

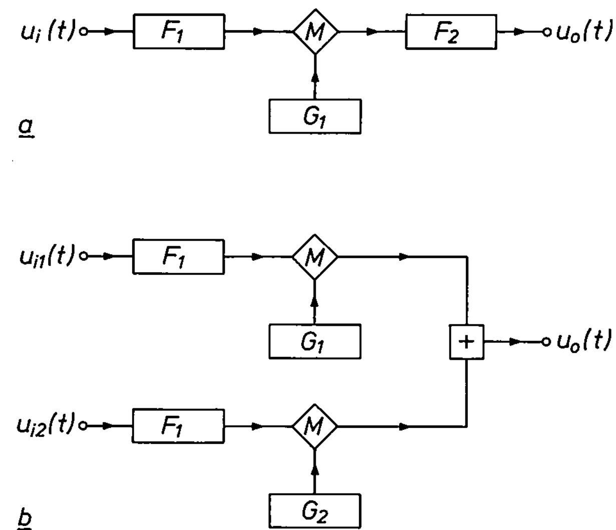

Fig. 4. *a*) Extension of the linear modulation stage to include a post-modulation filter F_2 for generating single-sideband- or vestigial-sideband-modulated signals. In the filter F_2 one of the sidebands produced in the modulation is now completely or partially suppressed. *b*) Duplicated version of the linear modulation stage for generating quadrature-modulated signals. Generator G_1 gives a cosine carrier signal and generator G_2 a sine carrier signal of the same frequency.

The digital linear modulation stage

In a digital version of the linear modulation stage there are only three elementary operations that can be performed on digital signals. The signal values can be:
- stored in a memory for a short or long period;
- added to give the sum;
- multiplied, either one by the other or one signal value can be multiplied by a constant ('coefficient').

Our digital modulation stage can therefore also be regarded as a special kind of small computer that calculates a digital output signal from the digital input signal in accordance with established rules. After digital-to-analog conversion, this output signal gives the same result that would have been obtained from the data signal if analog filters and modulators had been used. We should note here that the digital representation of the desired analog output signal from the data transmitter requires many more bits per second than the digital representation of the original data at the input. This can be seen from the fact that more digital words per second are necessary at the output of the modulation stage than at the input, and also from the fact that the required number of bits per word is greater; see fig. 1*b*. Our modulation stage has been designed to process 2400 input words per second, each of which can consist of one or two bits, while 13 800 words per second appear at the output, each consisting of eight bits. The ratio of 13 800/2400 = 23/4 between sampling frequencies at the output and the input was chosen deliberately, because the internal structure of the digital modulation stage can be kept relatively simple with these values, the modulator in particular [4].

Let us now turn our attention to a digital version of the filter F_1 in fig. 3. The filter requirements for data

[*] Important contributions to the design of this integrated circuit were made by H. A. van Essen, P. J. van Gerwen and W. A. M. Snijders.

[3] C. M. Hart and A. Slob, Integrated injection logic (I^2L), Philips tech. Rev. 33, 76-85, 1973.

[4] F. A. M. Snijders, N. A. M. Verhoeckx, H. A. van Essen and P. J. van Gerwen, Digital generation of linearly modulated data waveforms, IEEE Trans. COM-23, 1259-1270, 1975.

transmission do not include extremely high attenuation but they do include an accurately defined shape of the frequency characteristic. This requirement can readily be met by means of a digital transversal filter. The principle of such a filter is illustrated in *fig. 5.* The samples of the input signal are fed to a shift register. The output signal consists of the sum of the stored input samples, after each of them has been multiplied by a certain factor c_1, c_2 ... c_N (called the filter coefficients) [5]. The filter characteristic can be determined by the choice of the coefficient values, which can be stored as words of eight bits (for example) in a digital memory. In the configuration shown in fig. 5 all the N multiplications are carried out simultaneously and the products added. We use the more practical form, however, as illustrated on the left of *fig. 6.* Here the multiplications are carried out at an N-times accelerated rate one after the other, and the successive products are summed. The shift register now has only one output, where all the stored input samples appear in turn for multiplication by the appropriate coefficient c_i, supplied from the coefficient store. The feedback circuit presents the samples to the shift-register input in the same order for the calculation of the next filter-output sample. When a new input sample is available, it is supplied to the shift register by the switch *Sw*, and at the same time the oldest input sample present is discarded. As soon as a filter-output sample has been completely calculated and delivered (in our case to the modulator), the adder circuit with feedback (the accumulator) is reset to zero and a new calculation can begin. In the time that elapses between the occurrence of two successive input samples, the digital filter can if required calculate more than one output sample; this is known as 'interpolation'. In our case as many as 23 successive output samples can be calculated in the time in which four input samples are presented. This requires additional filter coefficients: our shift register consists of thirteen sections ($N = 13$), but in total the coefficient store contains $23N$ or 299 eight-bit coefficients for the calculations.

The input samples for our modulation stage consist of words of no more than two bits. Each shift-register section must therefore contain two bistable circuits, which can serve as the memory for two bits. The N multiplications of stored input samples with eight-bit coefficients require that the accumulator should be capable of processing longer words. We opted for an accumulator with a length of ten bits.

The product modulator M in fig. 3 can be produced in digital form by multiplying each filter output sample by a number from the digital carrier generator. This is illustrated in the right-hand part of fig. 6. The carrier generator consists of a digital memory containing a set

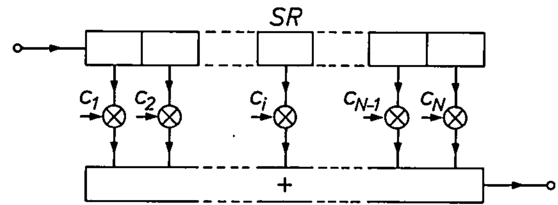

Fig. 5. Digital transversal filter. The input samples stored in the shift register *SR* are each multiplied by one filter coefficient c_1, c_2, ... c_i, ... c_N and the products are added together. The values of the coefficients determine the filter transfer function.

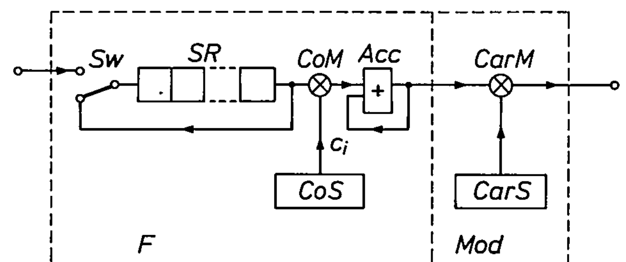

Fig. 6. Digital modulation stage consisting of a filter *F* and a modulator *Mod.* The digital transversal filter is arranged here in such a way that multiplication of the stored input samples by the filter coefficients (c_1, c_2, ... c_i, ... c_N) and addition of the resultant products are carried out sequentially at an increased rate. A feedback counter (the accumulator) *Acc* is used. The switch *Sw* feeds each new input sample to the shift register *SR*; the oldest input sample present is then discarded. In the modulator one multiplication of a carrier sample by the contents of the accumulator is performed for each output sample. *CoS* coefficient store. *CoM* coefficient multiplier. *CarS* carrier store. *CarM* carrier multiplier.

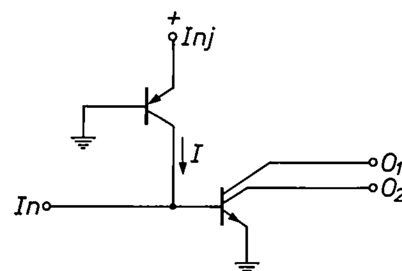

Fig. 7. Equivalent circuit for an I^{2}L gate. The base of a multi-collector transistor forms the input *In*, and the collectors form the outputs O_1 and O_2. The base current I of this transistor is supplied by a *P-N-P* transistor whose emitter *Inj* is at a fixed positive voltage. This emitter is generally called the injector.

of numbers that are periodically read out to represent a digital carrier. The quantity and the values of the different numbers to be stored in the carrier memory are determined by the ratio of the carrier frequency to the output sampling rate. It is very important to choose the right value for this ratio.

With the output sampling rate of 13.8 kHz that we have chosen for the modulation stage it is possible to

obtain modulated data signals whose carrier frequency is an arbitrary multiple of 300 Hz merely by multiplying by the values +1 and −1 in the modulator. This operation is so simple that it can easily be combined with the multiplications that are carried out in the digital filter. The modulator need therefore no longer be a separate part of the final circuit. In our practical design the modulation stage in fig. 6 is divided into four parts: the shift register, the combined coefficient multiplier, accumulator and modulator, the control circuit, and the coefficient store.

The generation of a single-sideband- or vestigial-sideband-modulated signal requires a second filter F_2 after the modulator to partly or completely suppress one of the two sidebands produced in the modulation; see fig. 4*a*. Now a digital-to-analog converter, as required after the digital modulation stage (fig. 1), always contains a simple analog filter. This filter can also perform the function of F_2 if we ensure that the two sidebands from the modulator are sufficiently separated, as indicated in fig. 3*c*. This can be done by making the filter F_1 in the digital modulation stage a bandpass filter instead of a lowpass one. This is simply a question of storing the appropriate filter coefficients c_i in the coefficient store. The replacement of a lowpass input filter by a bandpass input filter is made possible by the periodic spectral characteristics of digital signals. It would take us too far to go any deeper into this subject now [4] [6]. What is important here is the conclusion that the digital modulation stage in fig. 6 can also be used for generating single-sideband-modulated and vestigial-sideband-modulated data signals; examples of these have already been shown in fig. 2.

The design

On the basis of what has been said in the previous sections, we designed a digital linear modulation stage [4], which was finally made as an I²L circuit. The first step in the practical design was to specify the design parameters. A complete list of these would be outside the scope of this article, but *Table I* summarizes the design parameters mentioned so far.

The second step in the design was to build a functional model of the modulation stage, using commercially available electronic components or modules. This enabled us to verify whether the principles of the circuit and the choice of the various parameters were correct. At the same time, designing this functional model enabled us to directly determine the highest internal processing speed at any point in the circuit (220.8 kHz). It also gave us a good idea of the complexity and dimensions of the integrated version we intended to make. This completed the functional design of the modulation stage and we were then able to start on the design of the IC version. In the remainder of this article we shall discuss this in more detail, after first briefly explaining the IC technology (I²L).

Integrated injection logic (I²L)

Integrated injection logic is a suitable technology for making a circuit as complicated as the digital linear modulation stage described above. The main reasons for this are the high packing density to be obtained (100 to 200 gates/mm², depending on the regularity of the logic structure), the low power consumption per logic gate (e.g. 1 μW for a delay time per gate of 1 μs) and the relatively simple method of manufacture.

Fig. 7 shows the circuit diagram of an I²L gate, and *fig. 8* gives a cross-section and a plan view to illustrate

Table I. Some design parameters for the digital modulation stage.

Parameter	Value
Input sampling rate (f_i)	2.4 kHz
Word length of input samples	1 or 2 bits
Output sampling rate (f_o)	13.8 kHz
Carrier frequency	multiples of 300 Hz
Word length of filter coefficients	8 bits
Capacity of combined multiplier/accumulator	10 bits
Word length of output samples	8 bits
Length of shift register (N)	13 sections of 2 bits
Interpolation factor of digital filter ($f_o/f_i = K/M$)	13.8/2.4 = 23/4
Number of filter coefficients ($K \times N$)	299

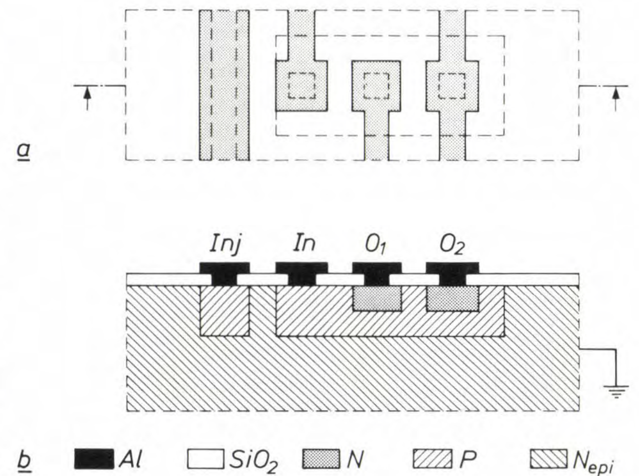

Fig. 8. Plan view (*a*) and cross-section (*b*) of an I²L gate. In addition to semiconductor material (N, P and N_{epi}), aluminium (*Al*) is used for conductors and silicon dioxide (SiO_2) is used for insulation. Because of their elongated shape (seen from above) the injectors join up adjacent gates to form an 'injector rail'. An aluminium conductor runs the whole length of the injector rail (*Inj*) to minimize the voltage loss along the rail. The number of outputs and the wiring pattern of input and outputs (*In*, O_1 and O_2) were chosen arbitrarily here. The locations of input and outputs are interchangeable.

[5] The theory underlying transversal filters is due to H. E. Kallmann, Proc. I.R.E. **28**, 302, 1940. The operation of such filters is also explained by P. J. van Gerwen in the article 'The use of digital circuits in data transmission', Philips tech. Rev. **30**, 71-81, 1969.

[6] L. R. Rabiner and B. Gold, Theory and application of digital signal processing, Prentice-Hall, Englewood Cliffs 1975.

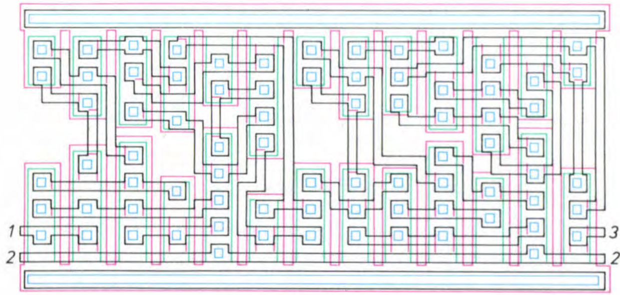

Fig. 9. Layout of the shift-register submodule. It contains 26 I²L gates that form four D-type bistable circuits and are positioned so as to produce a high packing density in a rectangular region. These submodules can thus be grouped together easily. In this drawing the circuit has an injector rail both at the top and at the bottom. Further I²L gates including these same injector rails can be added at the outside. *1* input. *2* through-lead for clock signal. *3* output.

the method of producing such a gate in semiconductor material. It consists of an *N-P-N* multicollector transistor whose base current is supplied by a *P-N-P* transistor operating as the current generator. Connecting this base to a preceding gate, conducting to earth or not, will determine whether the *N-P-N* transistor is conducting or not. The collectors of this transistor can then each be used separately for connecting the input of a following gate conductively or non-conductively to earth. Each gate has one input but may have several outputs. From input to output a gate acts as a logic inverter, and connecting the collectors of several gates together results in a logic AND function ('wired-AND'). Any logic circuit can be made from combinations of these two functions.

The layout

Making a layout for such a large and complex IC as this may be compared with making a jigsaw puzzle in which some of the pieces (e.g. the logic gates) are known in advance, while others (e.g. the connections between the gates) depend on the way in which pieces have been laid earlier. The designer has to observe certain rules. For example, the injectors of closely adjacent gates can best be made in the form of a long injector rail with the gates situated at right angles to the rail on either side. To make crossings a careful choice has to be made from various methods (e.g. multilayer interconnections or diffused crossunders). The layout must be rectangular and cover the smallest possible area. The connector pads must be distributed regularly around the edges.

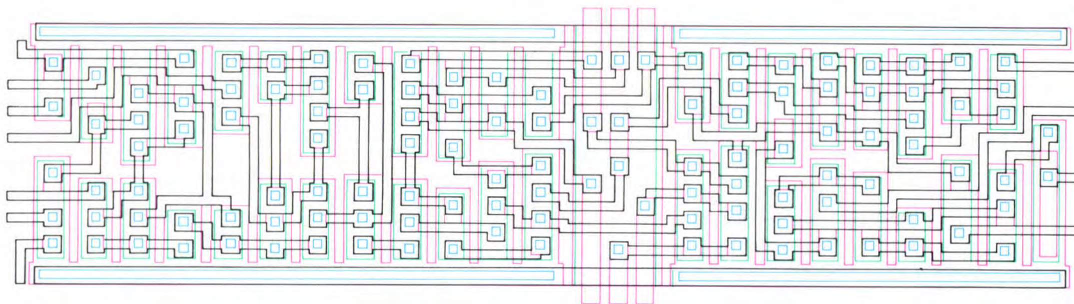

Fig. 10. Layout for one of the ten almost identical stages constituting the combined multiplier/accumulator. The left-hand part of the lay-out belongs to the multiplier and the right-hand part to the accumulator. The connections to the shift register, the coefficient store and the carrier store are situated on the left. The output is located on the right, together with a number of control inputs (including the connection for resetting the accumulator contents to zero). Three crossings for each injector rail can be seen near the centre for the connections to adjacent stages (the 'carries').

A common practice with a bipolar IC is first to make a 'breadboard' model of submodules consisting of integrated circuits each of which only contains a few gates. The breadboard model thus becomes a large circuit — for our digital modulation stage it contains as many as 170 breadboard ICs plus a few dozen discrete transistors — which has little resemblance to the IC of which it is the prototype. The breadboard model is used to check whether the design takes proper account of the typical characteristics of I²L gates (e.g. the delay time per gate for a given power consumption). The breadboard model is also used for testing the interfaces necessary for making an I²L circuit compatible with TTL circuits, which use different current and voltage values.

There are also a large number of rules for the permissible dimensions of components and connectors, the minimum spacing, and so on.

Meeting all of these many requirements at the same time for such a complicated circuit is a problem for which even a computer has no ready answer. The problem can be considerably simplified by partitioning the integrated circuit, i.e. dividing it into more or less independent functional sections. The number of connections between these sections is in general small. The

layout of each functional section is optimized separately with the aid of a computer, and finally the sections are combined to form a total layout. In partitioning the digital modulation stage we used the functional division discussed in the preceding sections of the article. As we saw earlier, the coefficient store (memory) is kept outside the I²L circuit, because it is then easier to change the coefficients; this makes the linear modulation stage more versatile in use. We shall now take a closer look at the layout of the three other functional sections, the shift register, the combined multiplier/accumulator and the control circuits. After this, we shall describe the additional provisions that were made, including interfaces, to arrive at the complete integrated circuit.

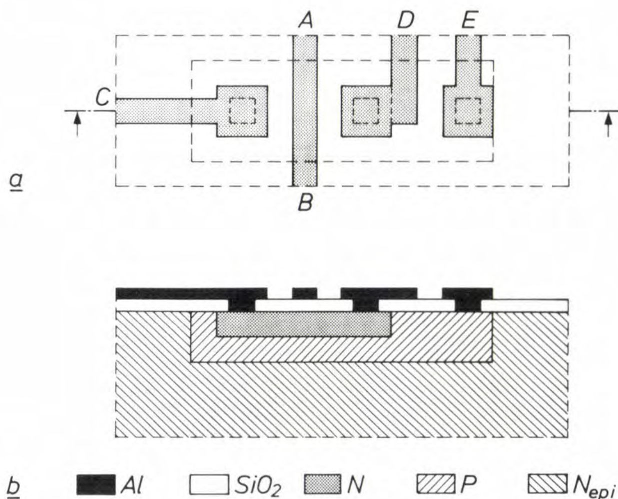

Fig. 11. Plan view (*a*) and cross-section (*b*) of a crossing of two conductors, *AB* and *CD*. *E* is a conductor that is earthed to ensure that the diode formed by the *N*- and *P*-type material is always reverse-biased. This is necessary to keep the *N*-type material forming part of the crossing isolated from its surroundings. To save space it is useful, where there are several crossings, to keep them together in one *P* region.

The shift register

As described above, the modulation stage contains 13 shift-register sections of two bits each, thus requiring 26 bistable circuits. These are of type D (D for delay), and each bistable circuit consists of seven I²L gates. It was not found necessary to make a separate layout for one such bistable circuit and then repeat it 26 times. One gate could be combined for every two bistable circuits (a maximum of four outputs per I²L gate was permitted) so as to connect four bistable circuits together to form a submodule of 26 gates; see *fig. 9*. The complete shift register thus consists of two rows of three submodules, to which two separate bistable circuits are added.

The combined multiplier/accumulator

The combined multiplier/accumulator performs the actual computation of the output samples from the linear modulation stage. In each calculation a two-bit number from the shift register is multiplied by an eight-bit filter coefficient and also by the sign of the digital carrier; it is then added to the contents of the accumulator. The multiplier/accumulator consists of ten nearly identical stages. The layout of one of these stages is shown in *fig. 10*. The left-hand part of the circuit contains the multiplier, the right-hand part the accumulator. A number of crossings can be seen in the centre of the diagram between the injector rails — the two large horizontal strips which also form the boundary of one stage — and the vertical connections between the neighbouring stages — the 'carries'. Various technologies are available for making the crossings; we decided to use diffused undercrossings. These are made by partially omitting the *P* region of the injector but continuing the aluminium conductor, which always runs above the injector rail to minimize the voltage loss along the rail. To make the crossings a large *P*-type region is first diffused into the IC under this aluminium conductor. The crossing connections take the form of strips of *N*-type semiconducting material inside this region; see *fig. 11*. The crossing conductors are insulated from each other by a thin (0.4 μm) layer of silicon oxide. The undercrossing connections (of *N*-type material) and the large *P*-type region in which they lie together form diodes, which have to be reverse-biased at all times. This is achieved by bringing the *P*-region, like the epitaxial *N*-region below it, to earth potential.

The control circuit

The least regular part of our IC is the control circuit. It consists mainly of an eight-bit up-and-down counter from which, by decoding the counter positions, the control signals for all parts of the modulation stage are derived. These include the addresses for the external coefficient store, the shift pulses for the shift register, the command signals for the multiplier/accumulator, and so on.

A closer examination of the logic diagram shows that there are four sections of about the same size, each consisting of 30 to 40 gates, which are reasonably independent of each other. It was therefore possible to write a computer program that would produce a layout design for each of these four sections. These designs were then modified slightly 'by hand' and finally combined. In the finished IC (*fig. 12*) it can still clearly be seen that the control circuit is a combination of four subsections.

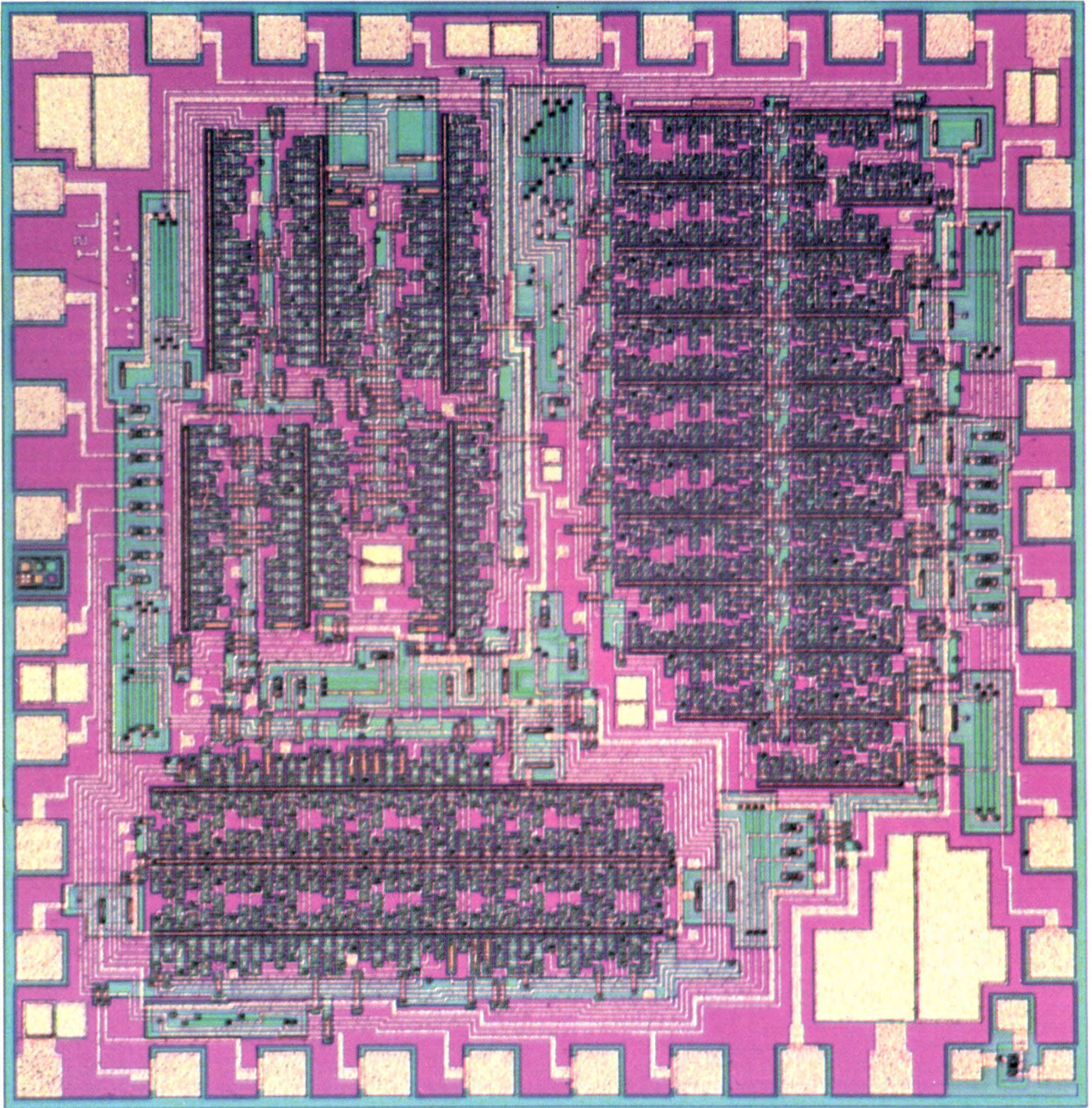

Fig. 12. Plan view of the integrated digital linear modulation stage in I²L. The upper part of the IC is taken up by the control circuit (*left*) and the combined multiplier/accumulator (*right*). The shift register is shown lower left. The injector rails, along which the I²L gates are grouped in long rows, are clearly visible. In the photograph these rows run vertically in the control section and horizontally in the shift register and the combined multiplier/accumulator. The dimensions for this IC are 3.6 × 3.7 mm.

Additional provisions

In an I²L circuit the difference between the voltage level representing a logic '1' and the voltage level representing a logic '0' is about 0.7 V, and the currents used are of the order of a few tens of μA. These are very different from the values found in the widely used TTL circuits (about 4 V and 1.5 mA). If an I²L circuit is to operate in conjunction with TTL circuits, it is therefore necessary to use interfaces, which should preferably be situated on the I²L circuit itself. Since our linear modulation stage requires about thirty of these interfaces, they must not take up too much space. The design of these circuits was therefore kept very simple. *Fig. 13* shows an input and an output circuit. The first consists simply of two resistors, the second contains an I²L gate with all its four collectors connected in parallel to increase the current gain, followed by a resistor and an *N-P-N* transistor. Because of its high current gain (about 60) and its 'open-collector' output, this *N-P-N* transistor can be connected in the usual way to a TTL

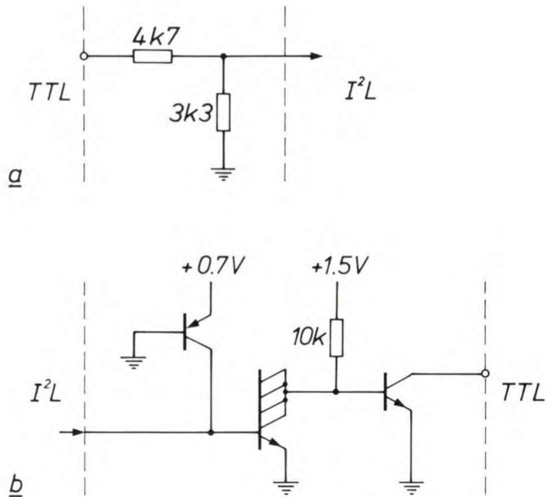

Fig. 13. Interfaces that can be used for operating conventional transistor-transistor logic (TTL) components in conjunction with an I²L gate (*a*) and vice versa (*b*). These interfaces can be made part of the I²L circuit. One consists of only two resistors, the other consists of an I²L gate, whose four collectors are interconnected, and a conventional *N-P-N* transistor operating as a current amplifier (gain about 60 times).

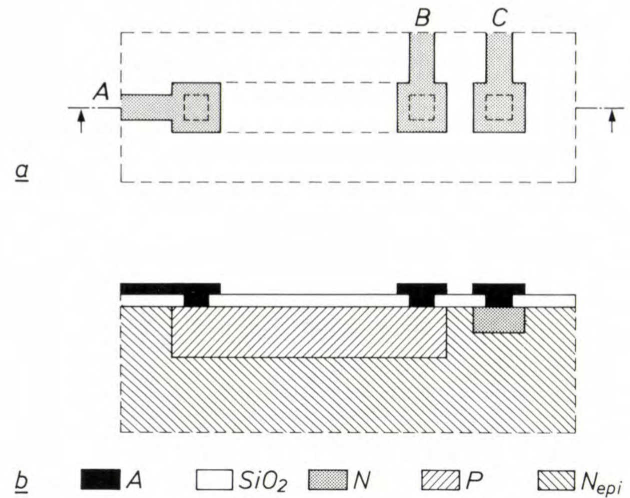

Fig. 14. Plan view (*a*) and cross-section (*b*) of a resistor suitable for combined fabrication with I²L gates on a single IC. The resistor (with connections *A* and *B*) is simply a piece of *P*-type material whose dimensions determine the resistance value. To keep the diode formed by this *P*-type material and the underlying N_{epi} material constantly reverse-biased, the N_{epi} region here should have the highest voltage that can ever appear across the resistance. This is ensured by connection *C*. To produce a well conducting contact between the Al and N_{epi} regions, an *N*-type diffusion is made under connection *C*.

circuit. *Fig. 14* shows how a resistor can be produced on an I²L circuit. In fact it is simply a piece of *P*-type semiconductor. Its dimensions determine the value of the resistance. Since the *P* region and the *N* region beneath it form a diode that must always be reverse-biased, the *N* region is connected to the maximum voltage that can ever occur at any point of the resistor — in our case the maximum supply voltage for TTL circuits, which is +5 V. The *N-P-N* transistor in the output circuit is shown schematically in *fig. 15*. The same type of transistor is also used as a current amplifier at nine other places in our integrated circuit, at the positions where the output signal of an I²L gate has to be applied to the inputs of more than four other I²L gates. A single transistor of the same type is also included for test purposes.

The method of applying the supply voltage to the I²L gates in an integrated circuit also imposes special requirements. This is because the relation between injector voltage and injector current is given by a diode characteristic that is highly nonlinear, so that a small variation in injector voltage can bring about a large variation in injector current. The injector currents of two directly interconnected logic gates should not however differ too greatly in value (by no more than a factor of 1.5) since otherwise the circuit may not function properly. This means that the potential difference between injector and earth for both gates should not differ by more than 5 to 10 mV. Differences between the supply voltages of the I²L gates arise mainly because of the voltage drop along the aluminium conductors connecting the positive supply voltage to the injector rails,

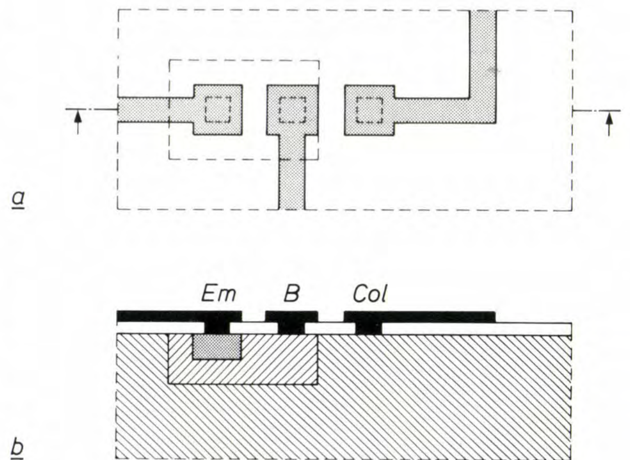

Fig. 15. Plan view (*a*) and cross-section (*b*) of a conventional transistor that can be used as a current amplifier in combination with I²L gates on one integrated circuit (simplified). *Em* emitter, *B* base, *Col* collector.

the voltage drop along the injector rails, and finally the voltage drop in the semiconductor material that acts as an earth lead. The second and third of these effects are removed by keeping the injector rails short (a maximum of thirty gates per rail) and by providing the IC with an external earth lead at more than one position. The voltage drop along the aluminium conductors could of course be reduced by increasing their dimensions and thus reducing their electrical resistance, but this would make the complete IC unnecessarily large. We therefore decided to adopt a different solution. The supply voltage for the IC is made approximately equal to twice the required injector voltage (1.5 V instead of 0.7 V) and

each injector rail is not connected to the supply lead directly but through a resistor, which has a voltage of 0.8 V across it. The combination of resistance and injector rail has a much less nonlinear relation between current and voltage than the injector rail itself. A larger voltage drop along the aluminium supply leads can then be tolerated (a few hundred mV) for the same maximum permissible spread in current.

application of a glassy protective layer over the complete IC, except for the connector pads, the test pads and the scribe lane. To illustrate the functions of the various masks, fig. 16 shows a cross-section through a part of our integrated circuit in which an I²L gate, a crossing, an earth connection, a resistor and a separate *N-P-N* transistor are situated. It can clearly be seen that the various types of component are completely sur-

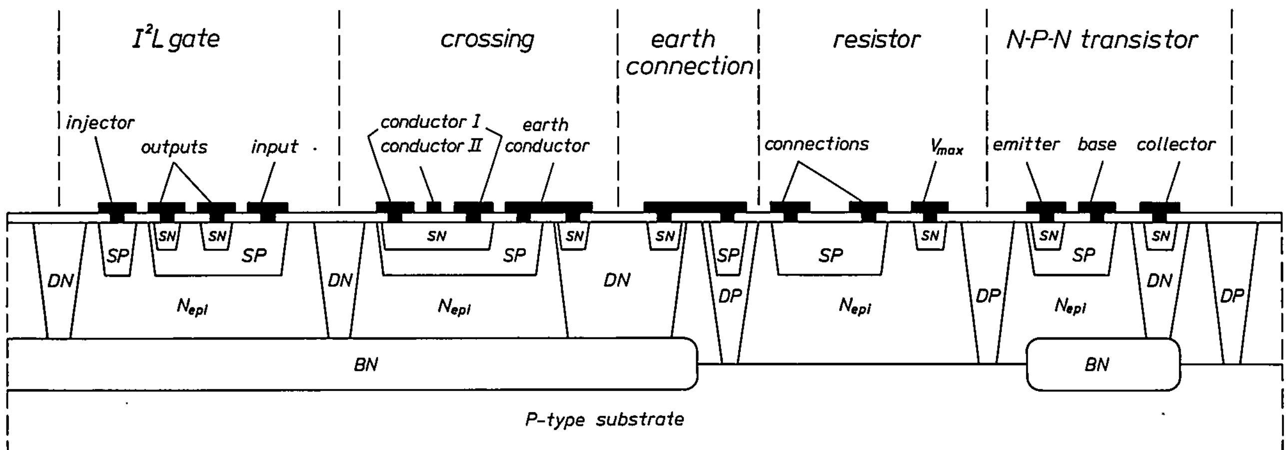

Fig. 16. Arbitrary cross-section through the I²L circuit in fig. 12, showing the principal components. The figure indicates the photomasks (*BN, DP, DN, SP, SN*) used for processing the various parts of the semiconducting material. No photomasks are necessary for producing the *P*-type substrate and the N_{epi} region. At places where a connection exists between *DN* (or *DP*) and an aluminium conductor, an *SN* (or *SP*) diffusion is always made for technological reasons. It can clearly be seen that the various types of component are completely surrounded by a 'trough' of *N*-type material (*DN* and *BN*) or by a *P*-type trough (formed by *DP* and *P*-type substrate). In this way they are kept electrically isolated from each other.

The photomasks

In making our modulation stage we start from a substrate of *P*-type silicon on which the complete circuit is produced step by step with the aid of eight photomasks [3] [7]; see *fig. 16*. With the first mask (the *BN* mask) an *N*-type diffusion is made at certain places in the *P*-type substrate, which will later act as a 'buried layer'. An *N*-type layer is then epitaxially grown over the whole surface of the crystal; no mask is of course required here. With the next two masks (the *DP* and *DN* masks) the deep *P* and *N* diffusions are made, which extend into the *P* substrate and the buried layer respectively. Two masks are then applied for relatively shallow diffusions, *SP* for a *P*-type diffusion and *SN* for *N*-type. The *CO* mask is then used to make contact holes in the insulating silicon-oxide layer that covers the entire circuit after the previous diffusion. An aluminium layer is next applied by vapour deposition, and a pattern is etched in it, with the aid of the *IN* (= interconnection) mask, to form the conducting connections between the various parts of the circuit. The eighth and final mask (the *CB* or protective mask) is used in the

Table II. The main electrical and technological features of the digital modulation stage.

Surface area	13.32 mm²
Number of masks	8
Power supply (nominal)	1.5 V, 10 mA and 5 V, < 10 μA
Highest internal clock rate	220.8 kHz
Number of I²L gates	786
Number of collectors per I²L gate — average	2.5
Number of collectors per I²L gate — maximum	4
Minimum width of aluminium conductors	8 μm
Number of separate *N-P-N* transistors	25
Number of *N-P-N* test transistors	1
Number of supply resistors	12
Number of bias resistors	49
Number of test pads	23
Number of crossings	237
Number of connector pads (four for earthing)	35
Number of encapsulation pins	32

[7] A. Schmitz, Solid circuits, Philips tech. Rev. 27, 192-199, 1966.
[8] C. Niessen, this issue, page 278.
[9] A. G. Bouwer, R. H. Bruel, H. F. van Heek, F. T. Klostermann and J. J. 't Mannetje, The Opthycograph, Philips tech. Rev. 34, 257-269, 1974.
[10] F. T. Klostermann, A step-and-repeat camera for making photomasks for integrated circuits, Philips tech. Rev. 30, 57-70, 1969.

rounded by a 'trough' of *N*-type silicon (formed by *DN* and *BN*) or a trough of *P*-type silicon (formed by *DP* and *P*-type substrate). Since these troughs are always earthed, the components are kept electrically isolated from each other and cannot therefore adversely affect each other's operation. Because of the need for this isolation the total number of masks used (eight) is greater than would have been expected from the simplified presentations in figs. 8, 11, 14 and 15.

The masks were made with the aid of a 'digitizer' [8], an Opthycograph [9] and a step-and-repeat camera [10]. With the aid of the digitizer a hand-drawn version of the layout was first converted into a description in the CIRCUITMASK computer language [8], and then recorded on magnetic tape. Owing to the use of the digitizer each measurement in the drawing and the associated recording of the result of the measurement only requires a movement of a measuring head and the pressing of a button. From the data recorded on the magnetic tape the Opthycograph produces photographic negatives ten times larger than the final circuit. The step-and-repeat camera produces ten-times reduced images of the Opthycograph negatives in large numbers of rows and columns for making the final working masks. In the fabrication of our IC we use masks on which the same digital modulation stage appears 191 times. After fabrication the modulation stages were tested one at a time on the wafers. The wafers were then broken into chips and mounted in their final housing.

Table II gives the main electrical and technological features of the modulation stage. It has been found from experiments with mounted modulation stages that the circuit also operates well at much higher clock rates than the nominal rate (220.8 kHz), up to 550 kHz. Thus, if required, input and output sampling rates two and a half times higher can be used.

Summary. In transmitting data signals via telephone lines use is made of 'modems', in which the signals are subjected to various operations such as filtering, modulation and demodulation before transmission and after reception. Depending on the transmission rate, different filter characteristics and different modulation methods may be used. A unit in fairly general use is the linear modulation stage, consisting of a filter and a product modulator. In digital form this modulation stage is particularly versatile, since it is only necessary to replace the contents of a digital memory to make the circuit comply with entirely different specifications. To produce a digital modulation stage in the form of an integrated circuit, it is not only necessary to make an accurate analysis of the logic design (word lengths, sampling rates), it is also necessary to make the best use of the special features of the semiconductor technology employed. This article describes the design and construction of a digital modulation stage for data-transmission applications in the form of an I^2L circuit, with particular attention to these two aspects.

An example of large-scale integration in a consumer product. A single integrated circuit performs all the functions associated with the digital clock in the Philips AS 570 clock radio: synchronization at 50 or 60 Hz, fast and slow resetting, storage of preset waking time, repetition of waking signal at intervals of about 10 minutes, switching off the radio after a preset period, control of the digital time indication by light-emitting diodes, brightness control for the digits, visual warning after a power failure. The integrated circuit was made in MOS technology with P-type channels.

Image sensor with resistive electrodes

H. Heyns, H. L. Peek and J. G. van Santen

Introduction

For some years now a considerable amount of research has been carried out on a solid-state alternative to the television camera tube: a silicon chip on which a moving image is projected and from which the video signal is 'directly tapped' [1]. As yet this 'solid-state image sensor' or 'flat sensor' is not a serious competitor of the camera tube, at least not where the image quality has to come up to the standards required in television broadcasting. It looks, however, as if solid-state sensors will fairly soon become an attractive alternative where images of poorer quality are acceptable. Possible applications include closed-circuit television systems for monitoring patients in hospitals, the extension of the audio baby alarm to 'baby vision', and the supervision of industrial processes in inaccessible spaces. Attention is currently directed mainly at flat sensors that could be used for home television cameras, with which scenes could be recorded on video tape and later played back on the home television set. The quality requirements here are quite high, but they do not have to rival the requirements for broadcasting.

The great impetus in the development of solid-state sensors came from the invention of the 'bucket-brigade shift register' at the end of the nineteen-sixties [2] and of other charge-transfer devices (CTDs) more recently. In a CTD a series of charge packets can be stored in potential wells under the surface of a silicon chip and can if required be shifted along at the rate set by an external clock, e.g. in the manner illustrated in *fig. 1*. This method permits many forms of signal processing (such as signal delay and filtering) to be performed electronically, the charge packets constituting samples of the signal. If the circuit elements are photosensitive, the device can be used for producing a video signal from an optical image converted into a pattern of charge packets.

The substrate material for sensors that work in this way ('CTD sensors') is usually *P*-type silicon. In each sensor element the incident light generates hole-electron pairs (*fig. 2*). The holes are conducted via the substrate to earth, while the electrons accumulate under an 'integration electrode'. Once in every picture period the signal charge is read out by shifting the charge packets along vertical CTDs to the bottom edge of the matrix,

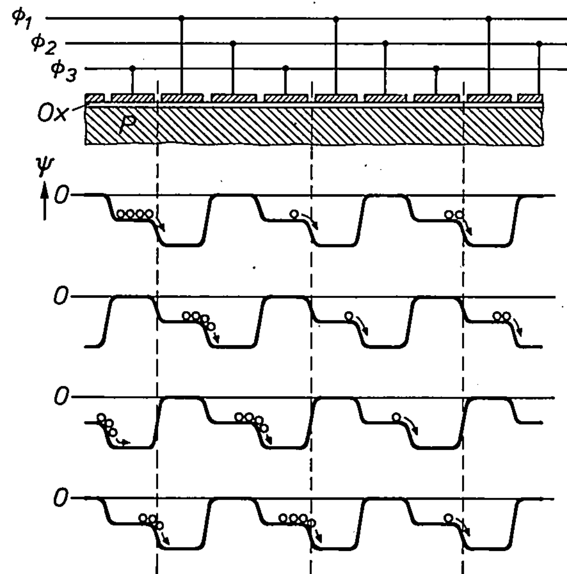

Fig. 1. Charge-transfer device (CTD) with three-phase clock signal. The clock signal (ϕ_1, ϕ_2, ϕ_3), applied to a closely packed network of electrodes on the surface of a chip of *P*-type silicon (*P*) generates a series of travelling potential wells for electrons. The electron potential ψ (of opposite sign to the conventional electrical potential) is shown here for four successive times, the first and fourth being one clock period apart. *Ox* oxide layer.

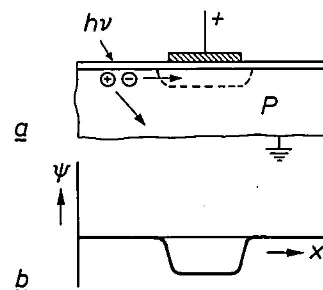

Fig. 2. *a*) A single element of a silicon sensor. The electrons from the hole-electron pairs generated by the incident light ($h\nu$) in the *P*-type material accumulate beneath the (positive) electrode; the holes are conducted to earth. *b*) Potential well $\psi(x)$ for the electrons beneath the electrode.

Ir H. Heyns was formerly with Philips Research Laboratories, Eindhoven, and is now with the IC laboratory of the Philips Video Division, Eindhoven. Ing. H. L. Peek and Drs J. G. van Santen are with Philips Research Laboratories, Eindhoven.

[1] See the articles on imaging devices in IEEE J. SC-11, No. 1, 1976 (pp. 109-146).
[2] F. L. J. Sangster and K. Teer, IEEE J. SC-4, 131, 1969.
F. L. J. Sangster, Philips tech. Rev. 31, 97, 1970.
W. S. Boyle and G. E. Smith, Bell Syst. tech. J. 49, 587, 1970.

where the packets are then processed into a video signal by means of a horizontal CTD.

There are also solid-state sensors that use an *X-Y* method for the read-out, e.g. the charge-injection device (CID) [3], illustrated in *fig. 3*. In this device the *X* electrodes are interconnected in rows and the *Y* electrodes in columns; a sensor element consists of one *X,Y* pair. If the voltage of row *i* and of column *j* is made zero, the sensor element *i,j* no longer forms a potential well, the signal charge is injected into the substrate and the associated current surge supplies the signal.

In this article we shall be concerned with CTD sensors. They can be divided into two types: 'frame-transfer' and 'interline-transfer' types. In frame-transfer sensors (*fig. 4*) the charge pattern that is accumulated in a frame period by the integration matrix M_i is transferred completely at the end of the period to a storage matrix M_s; to facilitate this transfer each column of M_i with the corresponding column of M_s forms a single CTD. The transfer time must be very short compared with the frame period to ensure that the charge packets are not significantly affected by incident light during the transfer. The storage matrix is shielded from light. In the next frame period a new charge pattern is formed in M_i, while the pattern in M_s is read out line by line via a horizontal output shift register. This takes up one frame period, so that the storage matrix is empty again at the end of the read-out and ready to receive a new charge pattern.

In the interline-transfer sensor (*fig. 5*) the integration and transfer functions are separated. The sensor elements are arranged in columns. At the end of each frame period the charge packets in each column are transferred by means of a pulse applied to the 'photo-electrode' into the cells of a CTD situated next to the column. These CTDs are shielded from light. While new charge packets are being formed in the sensor elements during the next frame period, the charge packets in the vertical CTDs are again read out via a horizontal CTD.

Two serious difficulties arise in both types of CTD sensor in their simplest form. In the first place the surface is covered with an array of (horizontal) electrodes, which have to be very close together to ensure good clock operation of the CTDs (see fig. 1). These electrodes must therefore be transparent for sufficient light to reach the silicon surface. In practice they consist of 'polysilicon' (polycrystalline silicon) which is more or less transparent except to blue light, which it barely passes. The *blue sensitivity* is therefore generally insufficient. This problem is overcome in frame-transfer devices by illuminating the silicon chip from *behind*. To have a reasonable resolution, however, the chip then has to be reduced by chemical etching to a thickness of

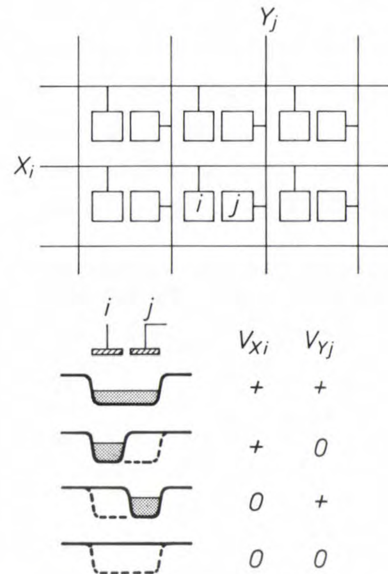

Fig. 3. Principle of an *X-Y* sensor (CID, charge-injection device). *Top:* the '*X* electrodes' of the sensor elements are interconnected in rows, the '*Y* electrodes' are interconnected in columns. *Bottom:* selection of the sensor element *i,j* takes place when V_{Xi} and V_{Yi} are both zero; the charge is then injected into the substrate.

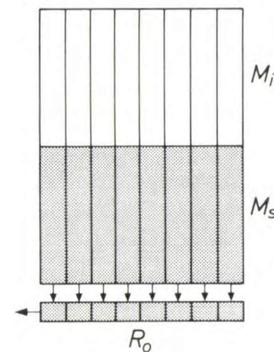

Fig. 4. CTD sensor with frame transfer. The charge pattern formed in the integration matrix M_i in one frame period is transferred to the storage matrix M_s via vertical CTDs in a time short compared with the frame period. During the next frame period it is read out line by line through the horizontal shift register R_o. The CTD cells of M_i are the sensor elements; M_s is shielded from light.

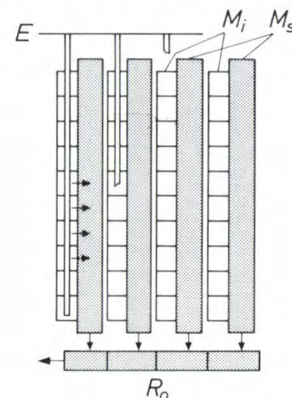

Fig. 5. CTD sensor with interline transfer. Compared with fig. 4, the columns of M_s are interposed between those of M_i. The charge in the elements of M_i (which are not CTD cells here) is transferred to M_s by means of a single pulse on the photoelectrodes *E*.

about 15 μm. This is not a practical proposition for the interline-transfer devices, because of the shielding required for the vertical CTDs.

In the second place the effect known as 'blooming', the spread of excess charge from an overexposed element, can become very troublesome. The electrons that overload a particular potential well are scattered over the vertical register, resulting in the appearance of vertical white lines or stripes in the picture. This is much more of a nuisance than the more or less 'natural' concentric blooming often encountered in other optical devices. To counteract this effect it must be possible to remove 'unobserved' any excess of electrons at every picture point. In the frame-transfer sensor one of the three clock electrodes is used for accumulating photo-electrons. The two others are made negative, so that holes accumulate at the silicon surface. The excess electrons in an overloaded potential well then disappear through recombination with these holes. In this way an overexposure of fifty times peak white can be handled [4]. Blooming in interline-transfer sensors is difficult to combat without sacrificing a large part of the silicon surface.

In this article we discuss a new image sensor in which neither the blue sensitivity nor blooming present a serious problem [5]. Vertical transfer does not take place in 'clocked' CTDs but in channels under resistive electrodes [6]. We shall first give a brief description of the new sensor, and then we shall take a closer look at the structure and operation of the vertical-transfer channel and at the method used to counteract blooming.

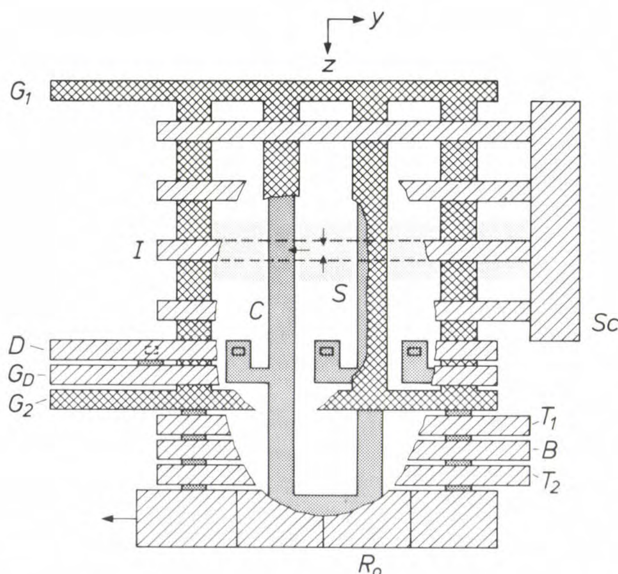

Fig. 6. Schematic diagram of the sensor with resistive electrodes for 4×4 sensor elements. In each line period the line selector *Sc* delivers a pulse to one of the integration electrodes (e.g. *I*), causing the charge under the sensor elements (*S*) to be transferred into the potential channels (*C*). The channels are depleted *N*-type regions in the *P*-type silicon. A voltage between the connections G_1, G_2 produces, via the resistive electrodes (cross-hatched), a potential gradient for the electrons; these 'slide' in a part of a line period to the buffer *B*; through T_1, *B* and T_2 they are transferred to the output register R_0 at the appropriate moment. During the time when no signal charge is travelling in *C* surplus electrons can be removed via the electrodes G_D and *D*.

The sensor with resistive electrodes

Fig. 6 shows the arrangement of the new sensor schematically for 4×4 sensor elements. The elements (*S*) of a row have a common integration electrode (*I*). Once in every frame period a pulse applied to this electrode transfers the accumulated charge into the vertical 'potential channels' *C* situated on the left of the sensor elements. In these channels the charge packets slide *during part of a line period* to the buffer zone *B*. From there they are transferred at a suitable moment to the cells of the shift register R_0. In one frame period all rows are successively read out once in this way. The 'driving force' in the potential channels *C* derives from a voltage between the connections G_1, G_2 of the resistive electrodes (cross-hatched).

The new sensor is still in an early experimental stage. *Fig. 7* shows one of the first ones built. The matrix of sensor elements has the standard super-8 format of 4.2×5.6 mm. The active surface, including the line selector and output register, measures 4.5×6.5 mm The dimensions of the chip itself are 5.5×7.5 mm. There are 300 lines and 200 columns; the pitch of the lines is thus 14 μm and that of the columns 28 μm. In the frame period of 20 ms the line period is 64 μs. *Fig. 8* shows a picture taken with this sensor.

The blue sensitivity is obtained because the electrode system leaves part of the silicon surface free. *Fig. 9* gives the spectral sensitivity of the system, measured on an experimental circuit of six columns whose output contacts are interconnected to increase the measuring signal. The columns are shorter than those of the actual sensor (96 elements, length 2.7 mm), but otherwise have the same structure (see fig. 12). It may therefore be assumed that fig. 9 is also representative of the actual sensor. As can be seen, the quantum yield for λ = 400 nm (violet) is still about 30%.

Considerable overexposure is permissible in this sensor because the vertical transfer of the signal charge takes place so quickly that enough time is left in one line period for the removal of excessive charge (via electrodes G_D and *D* in fig. 6). The manner in which this is done will be discussed later on.

[3] D. M. Brown, M. Ghezzo and M. Garfinkel, 1975 IEEE Int. Solid-State Circuits Conf. (ISSCC) Dig. tech. Papers, p. 34.
[4] W. F. Kosonocky, J. E. Carnes, M. G. Kovac, P. Levine, F. V. Shallcross and R. L. Rodgers III, RCA Rev. **35**, 3, 1974.
[5] J. G. van Santen, Jap. J. appl. Phys. **16**, Suppl. 16-1, p. 365, 1977.
[6] M. V. Whelan, L. A. Daverveld and J. G. de Groot, Philips Res. Repts. **30**, 436, 1975.

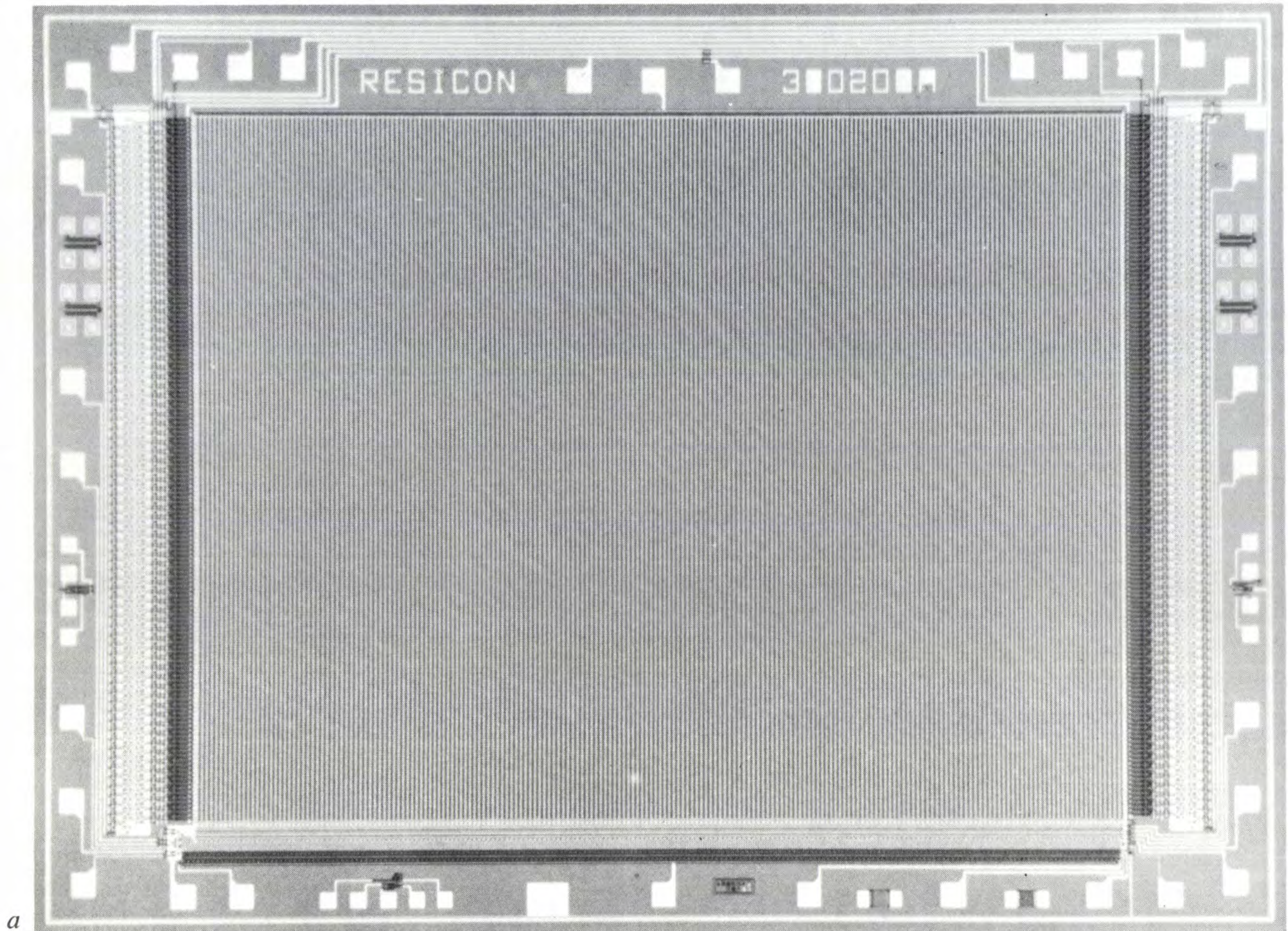

a

The vertical-transfer channel

Fig. 10 illustrates schematically the structure and operation of the vertical-transfer channel. The *P*-type silicon chip contains an *N*-type channel with a resistive electrode *G* above it, separated from the *N* channel by a thin oxide layer *Ox*. The *N* channel has an output contact *C*. A positive voltage V_C on *C* gives rise to a depletion layer at the *P-N* junction. Above a particular value of V_C the *N* channel is fully depleted. This value depends on the donor concentration N_d and on the thickness *d* of the *N* channel. The potential ψ for electrons in a cross-section *D* of the channel is then completely determined by the potential V_D of *G* in *D*. *Fig. 11* shows ψ as a function of the coordinate (*x*) perpendicular to the silicon chip, for the cross-sections at *A*, *B* and *D*. The minimum in these potential curves is due to the charge of the donors (the second derivative is proportional to N_d). The voltage across *G* gives rise to the tilted 'potential channel', as illustrated in fig. 10*c* and *d* together with fig. 11. The detailed structure of a column is shown in *fig. 12*. The charge transfer from a sensor element *S* to the *N* channel takes place via the crossunders in the channel.

The design of the sensor stands or falls with the time (T_{tr}) it takes to transfer electrons through the channel. For a single electron this time is given by the potential gradient $\Delta\psi$ across the channel, the length *L* of the channel and the mobility μ of electrons in silicon:

$$T_{tr} = L/v_d = L^2/\mu\Delta\psi. \qquad (1)$$

Here v_d is the drift velocity ($v_d = \mu\Delta\psi/L$). For $L = 4$ mm, $\mu = 1000$ cm²/Vs and $\Delta\psi = 10$ V we find $T_{tr} = 16$ μs. Under these conditions the transfer does in fact take up only a fraction of the line period, 64 μs. In the case of a packet of electrons it is also necessary to take into account the Coulomb repulsion between the electrons and the effect of thermal diffusion, both of which tend to 'smear out' the packet [7]. This means that the transfer time for a complete packet is longer. From a transfer model due to Y. Daimon *et al.*[8], it can be shown that 99% of a charge packet is transferred in less than 30 μs.

[7] K. Hoffmann, Solid-State Electronics **20**, 177, 1977.
[8] Y. Daimon, A. M. Mohsen and T. C. McGill, IEEE Trans. **ED-21**, 266, 1974.

Fig. 7. *a*) The sensor, magnification 22×. The line selectors can be seen to the left and right of the picture matrix, and the output register is below it. *b*) Detail from the lower left-hand section of the sensor. *c*) Detail of the picture matrix.

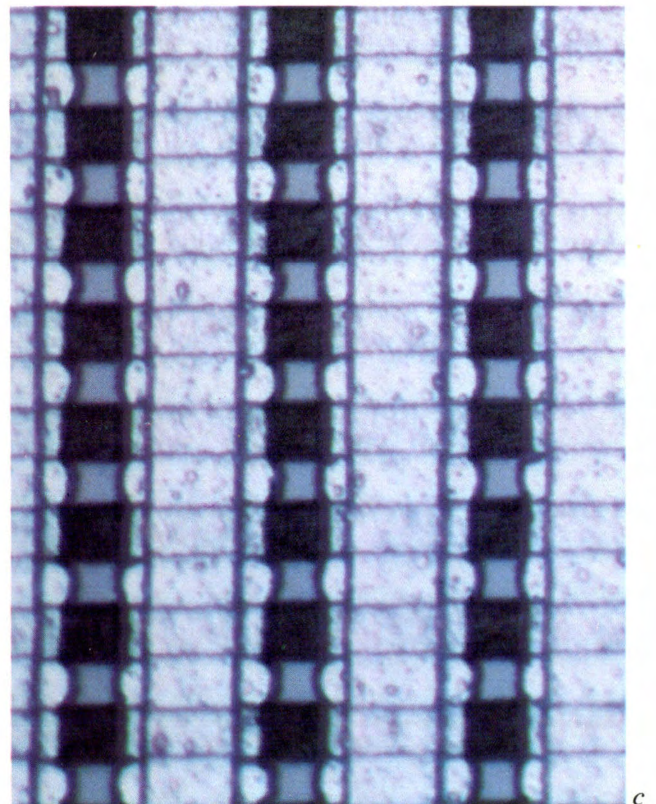

Fig. 13 gives T_{tr} as a function of the voltage V_{AB} across the resistive electrode, as measured on the experimental circuit mentioned above ($L = 2.7$ mm). In agreement with eq. (1), T_{tr} is approximately inversely proportional to V_{AB}. A calculation based on fig. 11, with data relating to the oxide layer and the doping profile, shows that $\Delta\psi$ is equal to 0.7 V_{AB}. The measured transfer times in fig. 13 are about 1.5 times as long as those given by eq. (1) with this value of $\Delta\psi$; this demonstrates the smearing-out effect of the charge packet.

Whether a given potential gradient $\Delta\psi$ (e.g. 10 V) can be achieved depends on the donor concentration N_d and the thickness d of the N layer. This can be explained as follows. The voltage at the interface N-Ox at A in fig. 10 must not be negative;

Fig. 8. Television picture recorded with the sensor in fig. 7.

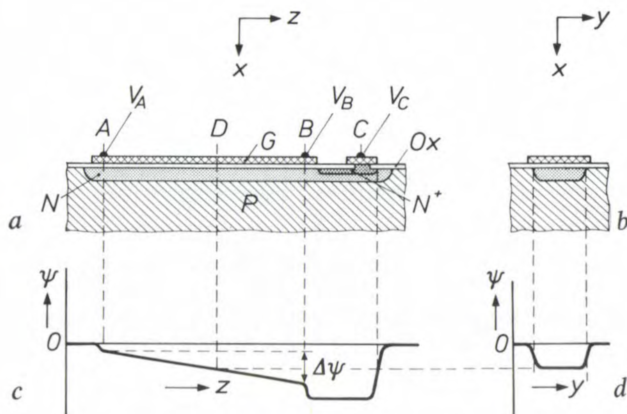

Fig. 10. Channel with resistive electrode, *a*) longitudinal section, *b*) lateral section. The *N* channel in the *P*-type material is depleted via the N^+ region and the output contact *C* (V_C = 10 to 20 V). *Ox* oxide layer, *G* resistive electrode. *c*) The electron potential ψ as a function of the length coordinate *z*; *d*) ψ in the section *D* as a function of the lateral coordinate *y*. The slope in (*c*) is due to the voltage $V_B - V_A$ applied across *G*.

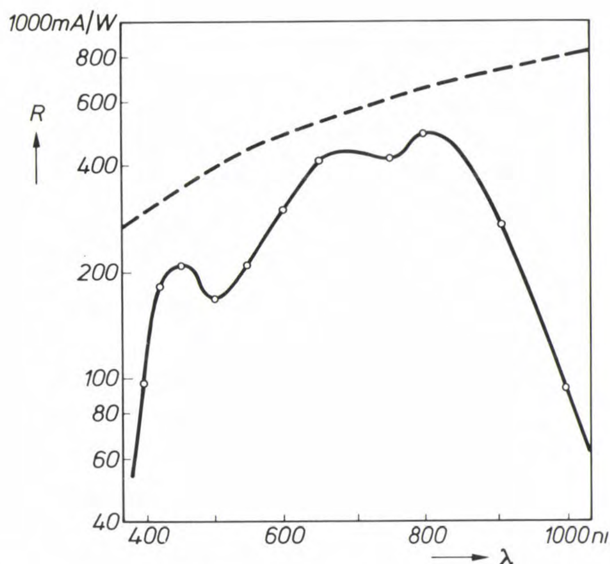

Fig. 9. The sensitivity *R* as a function of the wavelength λ of the incident light, for an experimental circuit of six columns whose output contacts are interconnected. The given values *R* relate to the part of the structure not screened with aluminium (see fig. 12). They thus give the current from the column structure divided by the power of the more or less monochromatic light that falls on the non-screened part. The dashed line gives the theoretical sensitivity at a quantum yield of 100%.

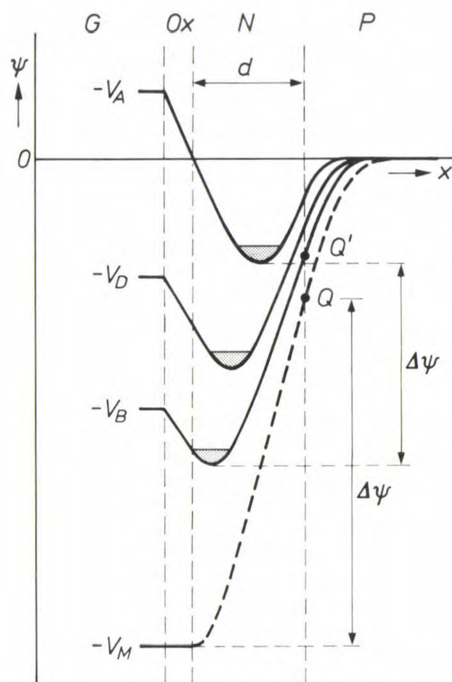

Fig. 11. The electron potential ψ as a function of the depth coordinate *x* for the cross-sections *A*, *D* and *B* in fig. 10. The parabolic shape in the N-type region is due to the space charge of the donors. The potential difference $\Delta\psi$ that can be obtained is limited by the fact that ψ in *A* at the interface *N-Ox* must not be positive and the curve $\psi(x)$ in *B* must have a distinct minimum; this is because the charge packets (*grey*) should preferably not travel along the surface.

this would cause inversion and give rise to holes in the channel. Also, V_B must remain smaller than V_M, the voltage at which the minimum in the potential curve just vanishes (see fig. 11). We now assume that $\Delta\psi'$, the potential difference across the *N* layer in the *x*-direction at the voltage V_M, is more or less representative of $\Delta\psi$. If N_d is now varied (and with it the steepness of the parabolic ψ-curves in this layer) then the thickness *d* must also be varied in order to obtain the same value of $\Delta\psi'$; the thickness *d* must be larger for smaller N_d and less for larger N_d. The curve at *Q* (really at *Q'*) must not, however, be so steep as to give rise to breakdown (avalanche ionization) at this location. This means that N_d is tied to a maximum. With $\Delta\psi'$ = 10 V this maximum is found to be 10^{16} cm^{-3}; the corresponding value of *d* is 0.7 μm. Fortunately, the maximum for N_d is so high that the *N* layer can be thin enough to guarantee the spatial separation in the lateral direction (*y*).

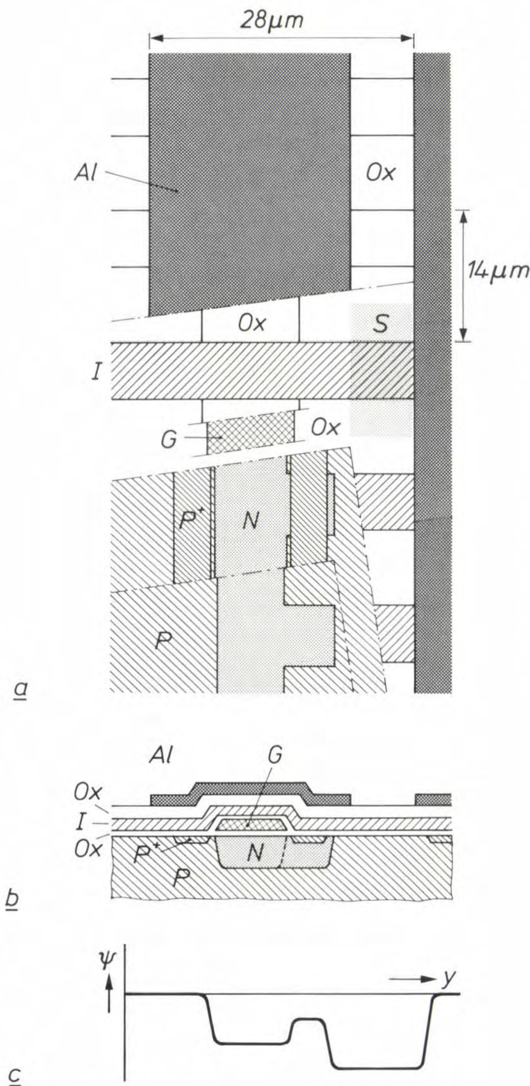

Fig. 12. Structure of a column. *a*) View from above with cut-away layers, *b*) lateral section. *P* substrate material, *N* channel, P^+ insulation strips of more strongly doped *P*-type material, *Ox* oxide layers. *G* resistive electrode (polysilicon), *I* integration electrodes (polysilicon), *Al* aluminium light-shield. *S* shows schematically the photosensitive part of a single sensor element. After the lower oxide layer has been cut away in (*a*), a layer of silicon is also removed, revealing crossunders in the *N* channel. These make selective charge transfer possible from a sensor element to the channel situated on the left. *c*) The potential ψ as a function of *y*, just under the surface, at the height of a crossunder. The P^+ strip, which is not itself entirely depleted and is thus at zero potential, keeps ψ in the underlying *N* region at a minimum of about 2 V below 0 (see the upper potential curve in fig. 11). Charge transfer takes place by means of a pulse applied to *I* which makes the potential in *S* equal to the threshold potential under the P^+ strip, i.e. a pulse that earths *I*.

Line selection; anti-blooming

The obvious choice for the line selector (*Sc* in fig. 6) is a digital shift register. It is not readily possible, however, to produce a conventional type of MOS register with a 'pitch' so small (14 μm) that it can link up with the line system directly. The system adopted is shown in *fig. 14*. Selection is carried out with two selectors, one on the left and one on the right of the matrix (fig. 14*a*). Also, each cell of the register serves *two* electrodes via a pair of MOS transistors (fig. 14*b*, *c*; further particulars are given in the caption). These two measures make the pitch required for the shift register four times that of the line system.

The switching programme for the integration electrodes and the other electrodes is shown schematically in *fig. 15* for the 4×4 sensor of fig. 6. At $t = 0$ μs of the first complete line period shown the charge packets under I_3 are transferred to the channel. In less than 30 μs they 'slide' to the buffer *B*; they are not impeded by G_D ('off') in this process, while T_1 ('on') transfers them to *B*. At $t = 54$ μs they are transferred by *B* and T_2 into the output register. In the subsequent periods the other electrodes take their turn in the same manner.

Blooming is minimized in this programme as follows. From $t = 30$ μs to $t = 34$ μs the potential wells beneath the integration electrodes have the 'normal' depth,

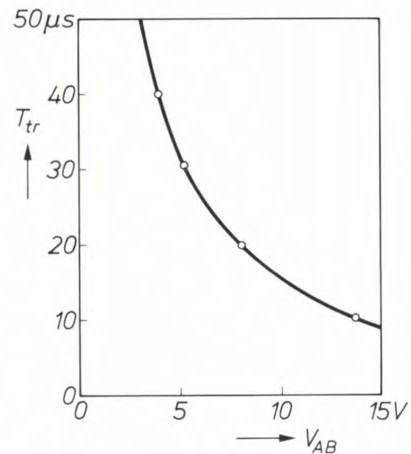

Fig. 13. The transfer time T_{tr} as a function of the voltage V_{AB} across the channel. In the experimental circuit mentioned earlier (six columns parallel, $L = 2.7$ mm) the frequency of the buffer pulses (*B* in fig. 6) was made twice as high as that of the selector pulses (*Sc* in fig. 6). With uniform illumination, the 'buckets' corresponding to the buffer pulses are then alternately full and empty. When the time interval between the selector pulses and the 'full' buffer pulses is gradually reduced, there will be an instant at which the packets from the upper electrode will begin to lose charge to the 'buckets' that were originally empty. At this instant the time interval mentioned is equal to the transfer time T_{tr}.

which determines the magnitude of the maximum packet ('peak-white' packet). From $t = 34$ μs to $t = 30$ μs in the next period, however, they are twice as deep, so that they can contain *two* peak-white packets. From the moment $t = 30$ μs they can again only contain one such packet; any surplus left spills

over into the channel. When this surplus arrives at G_D, at the most 30 μs later, it finds this gate open; it is then removed via the side channels and the electrode *D* in contact with them.

If it should prove possible to solve such problems, the potential uses of this sensor — and of other silicon-based sensors — will still be limited by the spatial and temporal fluctuations of the dark current (the current caused by thermal generation of hole-electron pairs). In a 'good' television picture the signal-to-noise ratio for 'white' is at least 100 (10^4 as a power ratio), whereas the 'fixed pattern noise', the signal difference between neighbouring points of a uniformly white picture area,

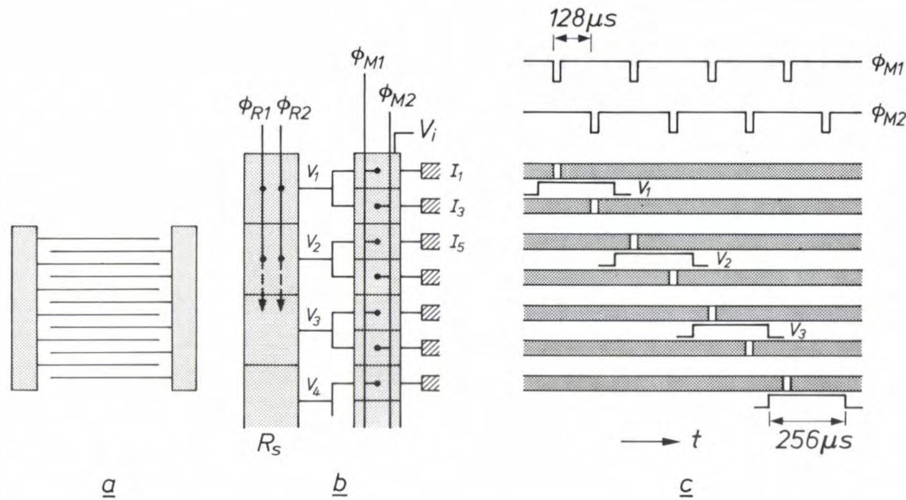

Fig. 14. Line selection. *a)* Division of the selection between a selector on the left and a selector on the right of the matrix. *b)* Switching diagram of the left-hand selector, *c)* timing of the pulses. The read-out cycle is started by a pulse on the input of R_s, a dynamic *N*-MOS shift register. Driven by two clock signals ϕ_{R1}, ϕ_{R2}, the pulse travels through the register; the output voltages V_1, V_2, ... of the cells are each successively positive during a complete clock period (256 μs). Each cell of R_s serves two MOS transistors. The upper MOS transistors of the MOST pairs are connected to a clock line ϕ_{M1}, the lower ones to a clock line ϕ_{M2}. The integration electrodes are in general at the positive integration potential V_i, but are earthed by the preceding MOST when the clock pulse (ϕ_{M1} or ϕ_{M2}) falls in a period when the preceding register cell is at a positive potential.

At the time $t = 34$ μs the wells beneath the integration electrodes thus contain at the most one peak-white package. Only if more than one peak-white packet should be added to the charge content of the well within the interval of 60 μs between $t = 34$ μs and $t = 30$ μs in the next period is it possible for unwanted electrons to arrive in the buffer. Since the signal packets are built up in one frame period (20 ms), the illumination can amount to about 300 times (20 ms/60 μs) the value for peak white before blooming occurs.

Further research

Further research is directed primarily at producing sensors in which the resistive and integration electrodes — together more than two metres of polysilicon 'wire' of 0.5×10 μm cross-section! — have no breaks or short-circuits; the horizontal and vertical stripes in fig. 8 are the consequence of such errors. Other aspects also require much attention. For example, the vapour-deposited resistive electrodes are not always found to have a suitable resistance, and there is sometimes charge cross-talk between neighbouring sensor elements.

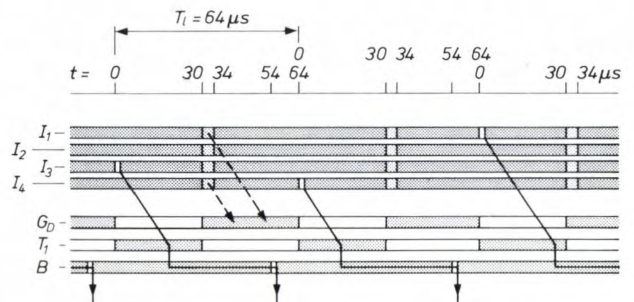

Fig. 15. Switching programme for the sensor in fig. 6. The different voltages on the electrodes are indicated by different shading. The potential wells under the integration electrodes have, in turn, normal depth (*light*) and double depth (*dark*). The solid lines indicate what happens to the signal charges, the dashed lines indicate what happens to the surplus charges. At $t = 34$ μs the wells of double depth contain at the most one peak-white packet. If overexposure causes so much to be added during the next interval of 60 μs that the total packet is greater than 'peak white', the surplus is transferred into the channel at $t = 30$ μs and removed via G_D ('on') to *D*.

is at the most 2%. In our sensor a 'peak-white' packet consists of some 3×10^5 electrons (with greater illumination the charge no longer increases). Taking a ten times smaller value for 'normal' white, the noise for a good picture should thus be no more than 300 electrons, and the variation from well to well should be no more than 600. The lowest dark current we have hitherto measured at room temperature is 2 nA/cm². This dark current corresponds to an average of 1000 electrons in a potential well in one frame period (20 ms), originating from the surrounding area of 14×28 μm. For a variety of reasons, in particular owing to material imperfections of various kinds, much greater fluctuations can occur in this number. What is more, the working temperatures may well be above room temperature, and with rising temperature the dark current increases very steeply. The concentration of such material imperfections in a sensor suitable for practical use would probably have to be less than one per cm². Considerable effort is now being expended in the search for technological processes that could make this possible.

Summary. Sensors based on charge-transfer devices (CTDs) are an important category of solid-state image sensors. They are small silicon chips in which once in every frame period an optical image, converted into a pattern of charge packets, is shifted via vertical CTDs to the bottom of the image matrix, where it is processed into a video signal by means of a horizontal CTD. Difficulties involved are the low blue sensitivity (dense electrode system) and 'blooming'. The article discusses an image sensor in which the vertical transfer takes place in 'potential channels' with a vertical gradient produced by resistive electrodes. The sensor matrix of 4.2×5.6 mm has 300 lines and 200 columns. Each line is transferred in a time much shorter than a line period; the rest of the time is available for the removal of charge due to overexposure. Since the electrode system is not very dense, the sensor is also sensitive in the blue.

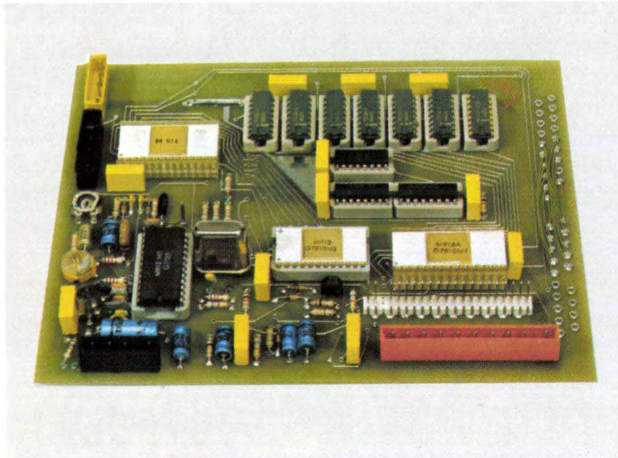

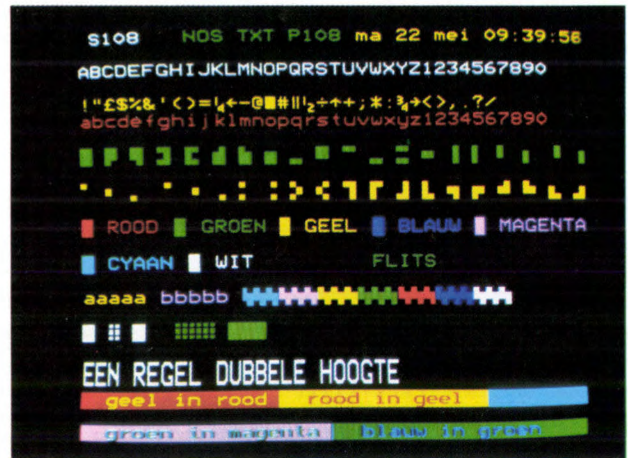

The television set now found in nearly every home can be used for more purposes than just showing television programmes. With LSI the size of the extra circuits required can be reduced to acceptable proportions. A single board with integrated circuits (top left) contains the decoder that adapts the television set to receive 'Teletext', a collection of about twenty pages containing current information that can be transmitted together with the programme. One of these pages contains the weather forecast (below). The pages consist of 24 lines of 40 characters, which are transmitted in digital code. The decoder contains a random-access memory (RAM) for 1000 words of 7 bits, in which the page is stored, and a read-only memory (ROM), which contains the different characters. These include both letters and digits as figure elements (top right). The pictures were taken from trial transmissions in the Netherlands.

A delta-modulation to PCM converter

L. D. J. Eggermont, M. H. H. Höfelt and R. H. W. Salters

Introduction

The present-day telephone network operates on the principle of baseband transmission on pairs of conductors. In the ordinary telephone exchange the appropriate conductor pairs are connected for the duration of a telephone call to form speech paths. In connections between exchanges that are far apart, other transmission systems are included. Their purpose is to replace the conductor pairs over most of their length for the transmission of signal components at frequencies in the speech band (300-3400 Hz). This replacement serves in the first place to reduce the attenuation. In the second place the aim is to give more economical use of the transmission paths by multiplex operation, that is to say, by the simultaneous transmission of multiple messages on a single telephone circuit. To limit the attenuation, amplifiers known as repeaters are incorporated in the multiplex circuit at fixed distances apart. At the ends of such a transmission system terminal equipment with multiplexers and demultiplexers provides the transition between the multiplex transmission within the system and the baseband transmission on separate conductor pairs outside it, so that the transmission system behaves to the outside world like a group of low-attenuation conductor pairs.

Multiplex transmission is usually based on the frequency-division multiplex (FDM) principle, although the time-division multiplex (TDM) principle is nowadays increasingly employed. In FDM transmission single-sideband modulation is used, in such a way that different frequency-shifted speech bands are stacked one above the other in the multiplex signal. In TDM transmission the signals are limited to the speech band by lowpass filters at the ends of the transmission system, and the transmission takes place by means of signal samples taken at fixed time intervals. During the sampling period the latest samples, originating from the individual input filters, are transmitted from one end of the circuit one by one to the associated output filters at the other end. At the transmitting end the signal samples are quantized in amplitude and digitally encoded so that, after decoding at the receiving end, they are supplied as quantized samples. Between this code modulation and demodulation there is thus a digital signal representation on the multiplex transmission path, unlike the analog signal representation in FDM transmission with single-sideband modulation. In both cases the signal representation on the multiplex path is standardized, ensuring compatibility between transmission and terminal equipment. The standard signal conversion for TDM transmission is called pulse-code modulation (PCM).

Standard FDM transmission has the advantage of making economical use of bandwidth for the multiplex transmission paths. Standard TDM transmission uses regenerative repeaters along the multiplex transmission path to restore the signal and free it from distortion and the effects of noise and cross-talk. This gives TDM transmission the advantage that it can be used for multiplex operation on pairs originally intended for baseband transmission and which would give too much cross-talk and noise with FDM. Another advantage of TDM is that the terminal equipment, with the multiplexers and demultiplexers, is less expensive than that for FDM. TDM transmission can therefore compete with unamplified baseband transmission on conductor pairs over distances even shorter than with FDM.

At the present time there is a distinct trend towards telephone exchanges operating on the digital TDM principle, which can transfer quantized signal samples between input filters and output filters so that the exchange behaves for speech in the same way as a TDM transmission system. In comparison with a conventional exchange, this gives in the first place a substantial reduction in the amount of wire and switching devices required. What is more, LSI circuits can be used for the digital electronics. The use of standard PCM in the digital telephone exchange allows the exchange to be directly connected to the multiplex-transmission paths of the TDM system, without the usual circuitous route using baseband transmission on conductor pairs. In this way much wire and equipment for conversion is saved, both at the transmitting end and in the exchange. Terminal equipment is then only necessary where connections have to be made to baseband transmission, as at the subscriber's end of such an exchange. A network of this kind is referred to as an IST (Integrated Switching and Transmission) network. Between two IST exchanges the digital TDM transmission system can be connected to each exchange without the need for any terminal equipment. The remaining converters between baseband transmission and PCM are then the major cost

Ir L. D. J. Eggermont, Ir M. H. H. Höfelt and Ir R. H. W. Salters are with Philips Research Laboratories, Eindhoven.

factor, and the challenge is to reduce the costs of such converters by designing them as integrated circuits.

Fig. 1 shows a possible structure for the local part of an IST network. Since not all the subscribers will be making telephone calls at the same time, traffic concentration can be effected at the input of the network by a 'concentrator'. Each of the outgoing lines from the concentrator is connected to a two-wire-four-wire converter (or 'hybrid') where the outgoing and the incoming signals are separated. The circuit in which the (analog) baseband signal is converted into the digital PCM signal forms the connection to the digital time-division multiplexer. The return path is arranged in a similar way. In the (de-)multiplexer the conversions take place between the spatially separated channels and the group of channels of the multiplex transmission paths. The transmission paths may consist, for instance, of a conductor pair for the outgoing paths and a conductor pair for the return paths. A (de-)multiplexer of this type can thus serve both for TDM transmission and for TDM switching equipment.

If the costs of the whole system (including signalling and the supply for the subscriber line) are low enough, the local IST structure in *fig. 2* is an attractive proposition. The converter is now located at the subscriber side of the (now digital) traffic concentrator. This structure makes the application of TDM and the use of ICs even more attractive, because digital signals are used in a larger part of the network.

In this article we shall describe an indirect conversion between baseband and PCM transmission. An intermediate form of digital signal representation is employed so that less critical circuits can be used: this cuts down on costs in the lowpass filters at the analog end and also in the converters between the analog and digital signals. The more exacting lowpass filter needed in PCM can be obtained with a digital filter, just as for the conversion between PCM and the digital intermediate format. The circuit for conversion between PCM and the intermediate form can be made in LSI. The way in which we have designed and built such a circuit will also be described. First of all, however, we shall review the functions involved in analog-to-digital (A/D) conversion. We shall then take a closer look at these functions to see if they can be designed in LSI, examining in particular the effect of the order in which they are performed. This will be followed by a more detailed discussion of the most suitable order of the functions for LSI. Finally it will be shown how an LSI circuit emerged from the conclusions drawn and the type of synchronous logic adopted, a silicon-gate N-MOS circuit.

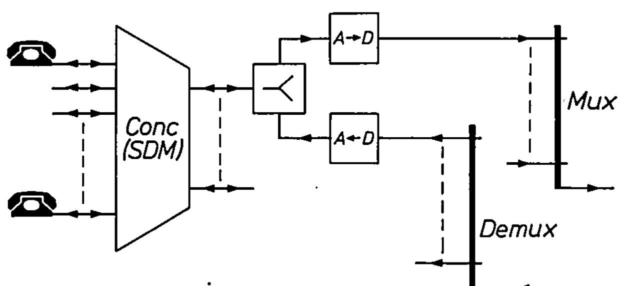

Fig. 1. Possible configuration of a local IST network for telephony (IST stands for Integrated Switching and Transmission). The signals from subscribers' calls are fed via a concentrator stage *Conc* to an A/D converter connected to a multiplexer *Mux*. The signals to the subscriber come via a D/A converter from the demultiplexer *Demux*. (*SDM* = space-division multiplexing.)

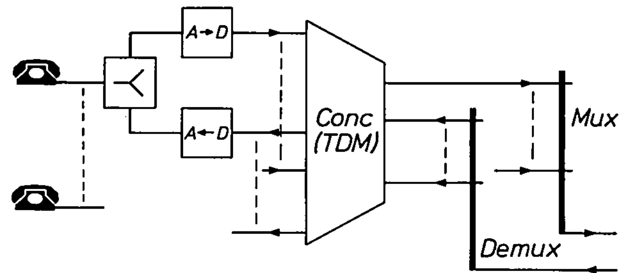

Fig. 2. In the local IST network represented here the signal is not connected to the multiplexer and demultiplexer via an SDM concentrator stage but via a TDM concentrator. This network configuration requires two connecting circuits with an A/D and a D/A converter for each subscriber. (SDM = space-division multiplexing; *TDM* = time-division multiplexing.)

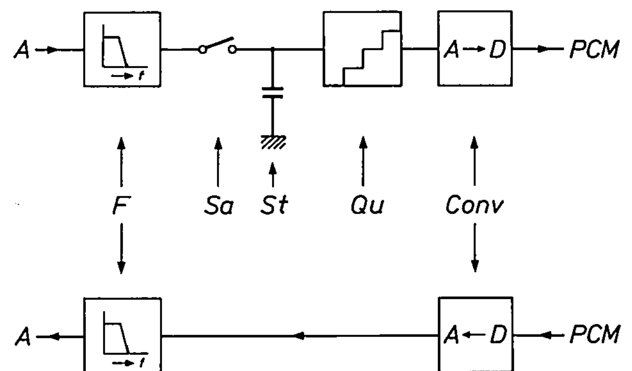

Fig. 3. Diagram of a common configuration for the connecting circuits (A/D) in fig. 1. In addition to an A/D converter (or a D/A converter) *Conv* the circuit also contains a lowpass filter *F* with a steep cut-off, and in the outward path a sampling circuit *Sa*, a buffer store *St* and a quantizer *Qu*.

The connecting circuit

The outward and return paths to and from standard PCM will be discussed with reference to *fig. 3*. The first operation which the analog signal has to undergo on the outward path is a bandwidth limitation. This step is necessary to satisfy the sampling theorem, which states that a signal $f(t)$ can be fully reconstructed from sampling values that are spaced a distance of $T = 1/f_b$

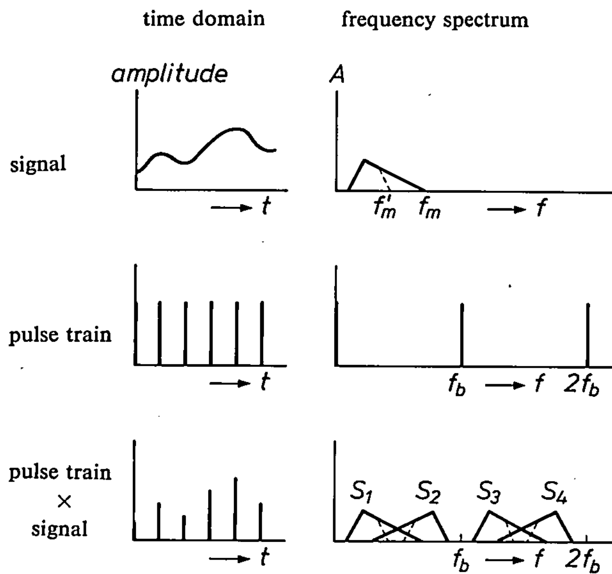

Fig. 4. The effect in both the time domain (*left*) and the frequency domain (*right*) of sampling a signal. In the time domain pulses are obtained that have the same amplitude as those of the original signal at the same time. The spectrum of the sampled signal (*lower right*) is repeated at intervals of f_b hertz. The spectrum thus formed also has fold-over symmetry about the frequencies $nf_b/2$ (n an integer). If, as applies to the spectrum of the unfiltered signal (*solid line*) the maximum frequency f_m is greater than half the sampling rate $f_b/2$, the tails of the original spectrum (S_1) and the spectrum folded about $f_b/2$ (S_2) will overlap. For signal components in the overlap region it is not possible to find the original value of the frequency, for example. The filtering in the outward path serves to prevent this undesired effect (fold-over distortion) by clipping the tail of the spectrum, so that $f_m < f_b/2$; see the dashed line. The filtering in the return path ensures that the spectra S_2, S_3, S_4, . . . due to the sampling are suppressed.

apart, provided that it contains no frequencies higher than $\frac{1}{2}f_b$. When a signal contains frequencies that are higher than half the sampling rate f_b, it is not possible to determine from the sampling values whether the original signal contains the frequency $\{(n + \frac{1}{2})f_b + f\}$ or $\{(n + \frac{1}{2})f_b - f\}$. This is illustrated in *fig. 4*.

To permit an unambiguous reconstruction of the signal, it is necessary to employ analog filtering when the standard sampling rate f_b (8 kHz) is used, so that frequencies in the speech band (300-3400 Hz) are passed, while high frequencies (above 4000 Hz) are strongly attenuated. The analog filters that can be used for this purpose are of at least fifth order and therefore expensive. A filter of this type in passive elements requires at least two inductors.

After the signal has been sampled the next steps are amplitude quantization and A/D conversion. To obtain standard PCM it is necessary to use non-uniform quantization, in which the quantized sample is converted into an eight-bit word. For small signal values the quantization unit is chosen so as to correspond to the quantization unit of a uniform quantizer for a twelve-bit coder. For larger signal values a lower resolution is accepted, so that with an eight-bit code word the same signal magnitude can be represented as with the twelve-bit code word of the uniform code. This does not alter the fact that the accuracy of the quantizer must meet a strict specification. In the past this has meant that common quantizers have been used in the outward path, or a common D/A converter in the return path, for 24 or 32 channels.

In the return paths the following operations are successively performed on the digital signal samples received. The digital/analog converter converts digital samples into a time-continuous signal with quantized amplitude at a rate of 8000 words per second. To obtain the best possible reconstruction of the original analog signal, this quantized signal is limited in bandwidth by an analog lowpass filter that has to meet the same strict specifications as the filter in the outward path.

These requirements for accuracy are in general difficult to satisfy in analog LSI. We therefore opted for a circuit in which analog functions are replaced as far as possible by digital ones. The accuracy that can be achieved in an analog circuit is related to the physical characteristics of the components. These depend on the production conditions, which are only partly controllable, and they are also dependent on the ambient conditions in which they operate (e.g. the temperature). In a digital circuit, on the other hand, the accuracy is structurally established by the choice of the number of bits per word used to represent a particular magnitude. Other advantages of digital circuits are that signals can be regenerated and that the information in these signals can readily be stored. As a result it is relatively easy to make digital circuits in LSI.

The essence of the approach we shall now describe consists in translating analog functions into digital functions for all the components in the connecting circuit. For the best possible design the translation should not be made separately for each function. By considering the connecting circuit as a whole, it becomes possible to change the internal sequence of functions if necessary.

Making the outward path suitable for digital circuits requires the use of a much higher sampling rate than the usual 8 kHz of standard PCM. As can be seen from fig. 4, when the sampling rate is high, the folded spectrum (S_2) will only overlap the original spectrum (S_1) slightly, if at all, so that an analog filter with a gently sloping characteristic will suffice. In addition this filter does not have to meet such a strict specification. The use of an extra-high sampling rate also means that the quantization noise enters only into part of the frequency band to be transmitted. Consequently, in this 'oversampling' it is permissible to quantize rather more coarsely. The resultant oversampled signal, for

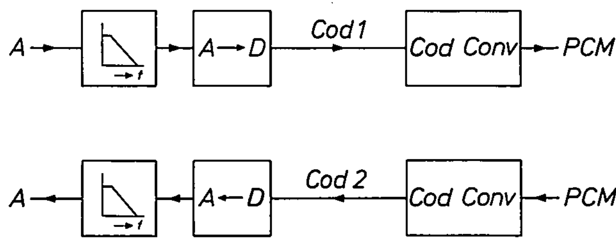

Fig. 5. Circuits for converting an analog signal (*A*) into a standard PCM signal (*PCM*) and vice versa for the outward and return paths in a local IST network of the type shown in fig. 2. A characteristic feature is the use of an intermediate code, which requires a digital code converter *Cod Conv* at the PCM end. In principle a separate intermediate code is possible for each of the two paths. The filter on the *A* side does not have to have a steep cut-off like the filter in fig. 3.

coincide with the sampling times of the 8-kHz standard PCM signal. This signal with high f_b is digitally converted into an intermediate code with coarser quantization than in standard PCM.

The resultant arrangement is shown in *fig. 5*. In principle there is no restriction on the choice of the intermediate codes for the outward and return paths. This allows the intermediate code for the outward path and the code for the return path to be optimized separately. As shown in *fig. 6*, however, attractive local IST structures are possible if the same intermediate code is used for the outward and return path. The configuration shown has the advantage that only digital code converters are required for connections with other ex-

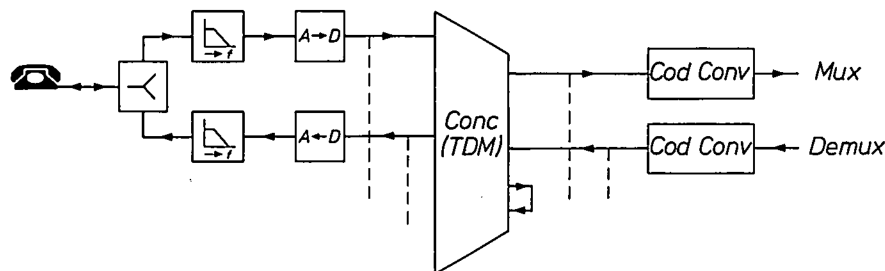

Fig. 6. Variant of the local IST network in fig. 2, in which the same intermediate code can be used in both the outward and the return paths (see fig. 5). The method discussed in this article is known as HIDM (High-Information Delta Modulation). The loop on the concentrator indicates that in this circuit connections between subscribers connected to the same concentrator are made without the need for code conversion.

which a digital intermediate code is used, has to be converted into 12-bit 8-kHz PCM. Obviously a digital lowpass filter is necessary to suppress signal components above 4 kHz. Finally the uniform 12-bit PCM has to be converted into the non-uniform standard 8-bit PCM.

It is also desirable to use a less steep analog filter in the return path. For reasons similar to those applicable to the outward path, this requires that the sampling rate f_b of the input signal to the analog filter should be much higher than follows from the sampling theorem, which says that $\frac{1}{2}f_b$ should be higher than the highest signal frequency f_m. When a high f_b is used the spectra obtained from the original spectrum are so far apart that a simple filter is sufficient to suppress them. Here again, the quantization noise enters into a broader frequency band than the band that contains the original signal spectrum. Consequently it is again permissible to quantize more coarsely, or to use fewer bits per word. A signal with a high f_b for the return path can be obtained by means of a digital interpolating filter, which calculates the additional intermediate samples for those sampling times of the intermediate code that do not changes. The local connections are established in the common intermediate code via the TDM concentrator. In our circuit the sampling rate f_b of the intermediate code is 64 kHz, so that a simple second-order filter is sufficient for both input and output. A special form of delta modulation called HIDM (High-Information Delta Modulation) was chosen for the intermediate code.

In PCM the instantaneous value of the signal is coded in digital form by the code words, but in delta modulation the *difference* between the present sampling value and the reconstruction of the previous sampling value is coded in a one-bit code [1]. The way in which the bit stream is calculated using HIDM is illustrated in *fig. 7*. An example of the structure of an HIDM encoder is given in *fig. 8*. A major advantage of HIDM compared with delta modulation with a continuously variable step size is that the step size can only assume values that are 2^n (n a positive integer) times larger than the minimum step size. Since only these simple powers of 2 occur in the step-size control, digital decoding of an HIDM signal is a relatively simple matter. Another advantage of HIDM compared with ordinary delta

modulation (with fixed step size) is the low bit rate necessary for encoding a signal in the speech band with a given signal-to-noise ratio over a wide range of signal values.

The functions in the digital code-converter

We shall now look at the functional structure of the 64-kHz HIDM/8-kHz PCM code converter. As shown in *fig. 9*, a digital code converter may be regarded as a cascade arrangement of a digital decoding circuit for the digital input code and a coding circuit to obtain the required digital output code [2]. As can be seen in fig. 8, the decoder consists of an 'expander', which regulates the step size, and an integrator. The operation of the integrator is digital, unlike that of the HIDM coder. In the coder the uniformly quantized PCM output signal from the digital integrator is filtered, because the signal components at frequencies above 4 kHz have to be suppressed to prevent fold-over distortion in the final 8-kHz PCM signal. At frequencies above its cut-off the lowpass filter reduces the quantization noise of the HIDM encoder, thus preventing the unwanted fold-over of noise to the final 4-kHz band. The uniform PCM output signal of the filter is then sampled at 8 kHz and finally the uniformly quantized signal is compressed to form the non-uniform quantized standard PCM signal.

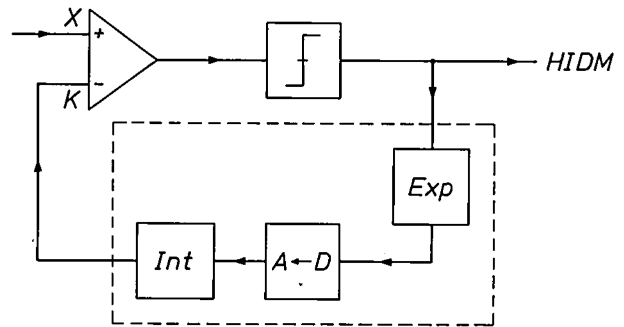

Fig. 8. A/D converter that forms the digital HIDM signal from the analog signal X. The part enclosed by the dashed lines is a decoder circuit that converts the HIDM signal into the comparison signal of fig. 7. This decoded signal K is compared with the filtered input signal X. If $X > K$, the associated HIDM bit, through the operation of the polarity detector, becomes $+1$, or otherwise -1. The expander *Exp*, which controls the step size, determines from the last and the two penultimate HIDM bits whether the step size is to be multiplied by 2^1, 2^0 or 2^{-1}. After D/A conversion the analog signal, which has now been given a sign, is integrated (*Int*). The decoded HIDM signal K appears at the output of the integrator.

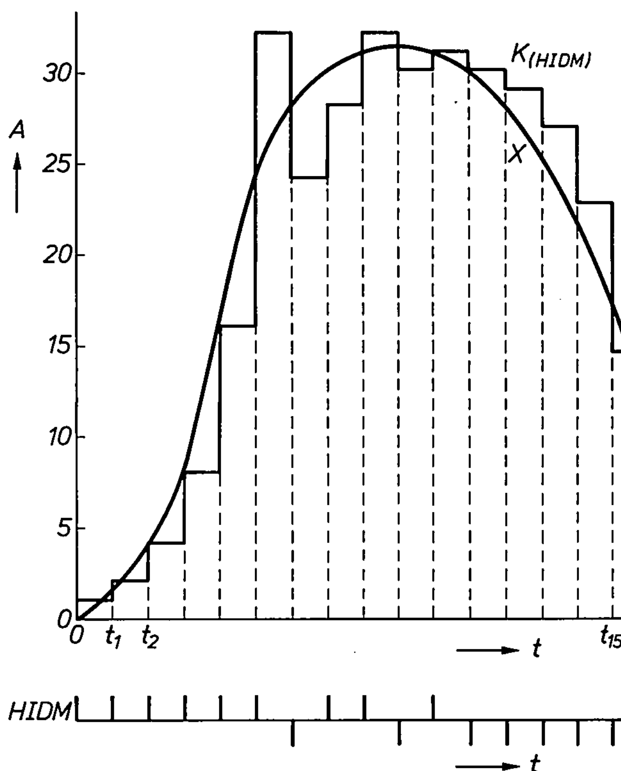

Fig. 7. Illustrating the relation between the HIDM bit stream and the sampled analog signal X. A amplitude. t time. (M. R. Winkler, IEEE Int. Conf. Rec. **11**, Part 8, 260, 1963.) The times t_1, t_2, etc. are the sampling times. The scale division along the vertical axis coincides with the equidistant quantization levels. Each step in the same direction is a factor of two greater than the preceding one, except in the case of the first two steps in the same direction after a change of direction. If successive steps are in opposite directions, the step size is successively halved. The step-size control is also limited by the existence of a minimum and a maximum step size. The HIDM bit pattern is plotted along the lower time axis.

In considering the lowpass filter in the PCM encoder it is first of all necessary to decide whether a recursive or non-recursive type of filter should be used. Now it can be shown from the theory of digital filters that unlike analog filters in the conventional connecting circuit, symmetrical non-recursive digital filters have the advantage that the signal delay in the filter is frequency-independent. Consequently the shape of analog signals is preserved, a point of particular importance for the transmission of data on a digital telephone network. A feature of non-recursive digital filters is that, if the sampling rate has to be reduced by a particular factor after the filter — as in the configuration in fig. 9, for example — the number of operations per unit time in the filter can be reduced by the same factor. With the aid of *fig. 10*, it can be seen that multiplication of the delayed signal samples by the appropriate filter coefficients a_k and addition of the products thus obtained need only take place at the times when the output signal is sampled. In a *recursive* filter, on the other hand, the output signal is added in each sampling period to the signal in the delay line (shift register), so that in general it is not possible to perform the addition and multiplication only at the times when the output signal has to be sampled.

[1] See for example part III of the review article by F. W. de Vrijer on modulation in Philips tech. Rev. 36, No. 11/12, 1976 (pp. 337-341).

Constructing a sequence of functions suitable for LSI

The sequence of the various operations to be carried out in the converter, as given in fig. 9, provides a general picture of the operations required to bring about the desired change in signal representation. This by no means implies, however, that the sequence is already decided. In making a design suitable for LSI it is necessary to consider which structure will occupy the smallest area. Important considerations here include the quantity of intermediate results and the number of bits required per word. The LSI technology chosen also sets limits to the speed at which operations can be carried out. With these considerations in mind, we shall now look at the operation of the converter. By way of description and analysis we shall first give an algebraic expression for the operation of the code converter.

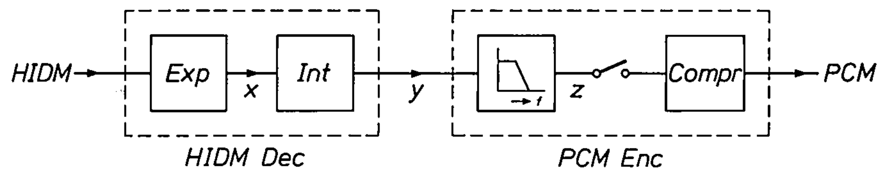

Fig. 9. Operating principle of the HIDM-PCM code converter. The two blocks in the dashed rectangle on the left (*HIDM Dec*) convert the HIDM code into a non-standard uniform PCM signal. The two blocks on the right (*PCM Enc*) make a standard PCM signal from this code. *Exp* expander. *Int* integrator. *Compr* digital compressor. The sampler is denoted by the switch symbol. This is preceded by a digital filter.

The value +1 or −1 is assigned to the delta-modulation bits of the converter input signal. The step size s_n at the time n is determined by the step size s_{n-1} and the factor m_n, which indicates the change in step size, through the relation

$$s_n = s_{n-1} \cdot m_n. \tag{1}$$

As already indicated in fig. 7, m_n assumes only the values 2, 1 and $\frac{1}{2}$. The value of m_n is found from the last three HIDM bits, as appears below:

b_{n-2}	b_{n-1}	b_n	m_n
1	1	1	2
−1	1	1	1
+1/−1	−1	1	$\frac{1}{2}$
−1	−1	−1	2
1	−1	−1	1
+1/−1	1	−1	$\frac{1}{2}$

(2)

It should be noted that s_n must not assume a value greater than s_{max} or smaller than s_{min}. The expanded input signal x of the integrator in fig. 9 has the form

$$x_n = b_n\, s_n, \tag{3}$$

while the output signal (the sum) is determined by

$$y_n = c y_{n-1} + x_n. \tag{4}$$

The signal y is processed by the non-recursive filter to form the output signal z:

$$z_n = \sum_{k=0}^{N-1} a_k y_{n-k}, \tag{5}$$

where a_k represents the filter coefficients of the filter of length N. The number of bits per word, the 'word length', is first increased by the expansion of the word length (see equation (3)) in the expander. However, the integration defined in equation (4) is particularly responsible for a considerable increase in word length. The output signals from the integrator, with their high word length, now have to be processed in the digital filter.

By substituting (4) in (5) we obtain an expression for z that allows us to see how this can be done. After substitution we find:

$$z_n = c\, z_{n-1} + u_n, \tag{6}$$

where

$$u_n = \sum_{k=0}^{N-1} a_k x_{n-k},$$

which means that the signal may also be filtered first and only then integrated. This interchange of functions has two advantages. The amount of memory capacity required decreases by about the same factor as that by which the word length decreases at the input of the filter. Consequently, depending on further detailed serial or parallel operation of electronic circuits, the required processing speed can be reduced by the same factor. An additional advantage of the interchange of integration and non-recursive filtering is that both operations can be performed with the same adder circuit, without it being necessary to store intermediate results separately. The constant c in (6) and (4) is chosen

[2] L. D. J. Eggermont, IEEE 1975 Int. Conf. on Communications (ICC75), San Francisco, Vol. III, p. 40.2.

in such a way that a simple electronic circuit can be used. The expression chosen was

$$c = 1 - 2^{-p}, \tag{7}$$

which only requires a shift and subtraction operation. The constant c was made less than 1 because the stability of the integrator is then guaranteed. The exponent p was made fairly large because this offers a good approximation to the integration ($c = 1$).

Apart from this interchange of integration and filtering, it is also possible to limit the size of the memory capacity required by including the step-size control for the expander in the filter. It is not then necessary to hold the step-size words x, all that need be stored are the HIDM bits and an initial step-size value, so that the memory can be about eight times smaller. The step size then has to be calculated for every shift-and-add operation, of course. But since the calculation of the step size from the bit stream, using equations (2) and (3), can run in parallel with the multiplications in the filter the incorporation of the step-size control in the filter has no effect on the processing speed, nor on the amount of electronics required.

The processing rate required for the filter can be substantially reduced because only one out of every eight samples need be calculated. We shall now look first at the interchange of integration and sampling necessary here. In the case of a reduction in the sampling rate at the input of the integrator by a factor R, equation (6) yields

$$z_{nR} = c^R z_{(n-1)R} + \sum_{i=0}^{R-1} c^i u_{nR-i}. \tag{8}$$

In terms of actual electronic circuits, this equation means that a non-recursive filter with filter coefficients c^i, separated by a sampler, precedes an integrator with the constant c^R. This interchange of integration and reduction in the sampling rate does not in itself give any advantage. But since the non-recursive filter, now even more necessary, can be combined with the existing non-recursive filter, an advantage is nevertheless obtained. The original non-recursive filter is expanded by $R - 1$ sections. The filter coefficients a'_k of this modified lowpass filter are obtained by substituting u (see equation (6)) in (8):

$$a'_k = \sum_{i=0}^{R-1} c^i a_{k-i}, \tag{9}$$

in which the unmodified filter coefficients a_m with m smaller than zero or greater than $N - 1$ are assumed to be equal to zero. From the above we see that the interchange of integrator and sampler leads to an increase in the filter length from N to $N + R - 1$; we shall call this length N'.

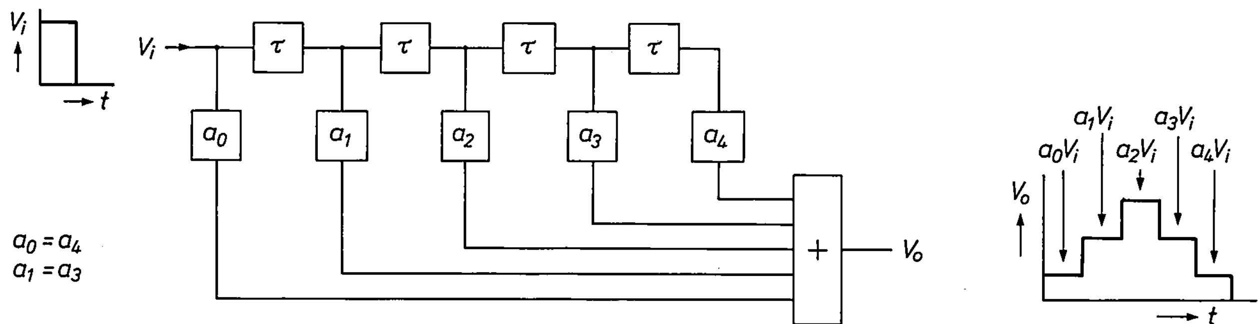

Fig. 10. A symmetrical non-recursive digital filter and the analog equivalent of its digital pulse response. The operation can be described as the addition of input-signal samples multiplied by fixed factors. The input signal V_i undergoes successive delays of τ (in this case four times). After each delay it is multiplied by a fixed factor a_i. The sum of the (four) products and a_0 times the non-delayed signal is the output signal V_o.

Now let us look at the interchange of the filter and reduction of sampling rate. This interchange, which gives a reduction in the required processing rate, as we saw earlier, also leads to a reduction in the number of samples that have to remain stored in the filter for calculating the next output sample. Without any reduction in sampling rate ($R = 1$) it is now necessary to store $N' - 1$ samples in the modified filter of length N'. For reduction factors greater than 1 but smaller than N', at least $N' - R$ samples must be stored in the filter for calculating the next output sample, whereas with values of R greater or equal to N' the next output signal is determined entirely by the samples arriving after the previous calculation. In this case, therefore, the filter does not need to retain any earlier sample value at all for the next calculation period [3]. The final result of

positioning the sampling reduction R before the filtering and integration stages is shown in *fig. 11.* The complete process of changing the sequence of the various operations is again summarized in *fig. 12.*

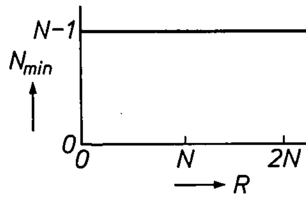

Fig. 11. The minimum number of samples N_{min} that must be stored in a filter is $N-1$ for each value of the sampling reduction R. N is the length of the unmodified filter.

between the parallel read-in of the R (= 8) HIDM bits, this register always shifts eight steps 'too far'. This leads to the desired situation in which, when the R new HIDM bits are input, the R oldest bits are transferred. At the same time, at the beginning of every calculation period in the filter, the step size stored for the previous one must be input to the expander. After R clock pulses the resultant step size is then stored for the next calculation period in the filter. This has to be done after R clock pulses (= shift pulses) because the bit at the location $N-R$, immediately after read-in of the R HIDM bits in the one calculation period has to arrive at location N at the beginning of the next one.

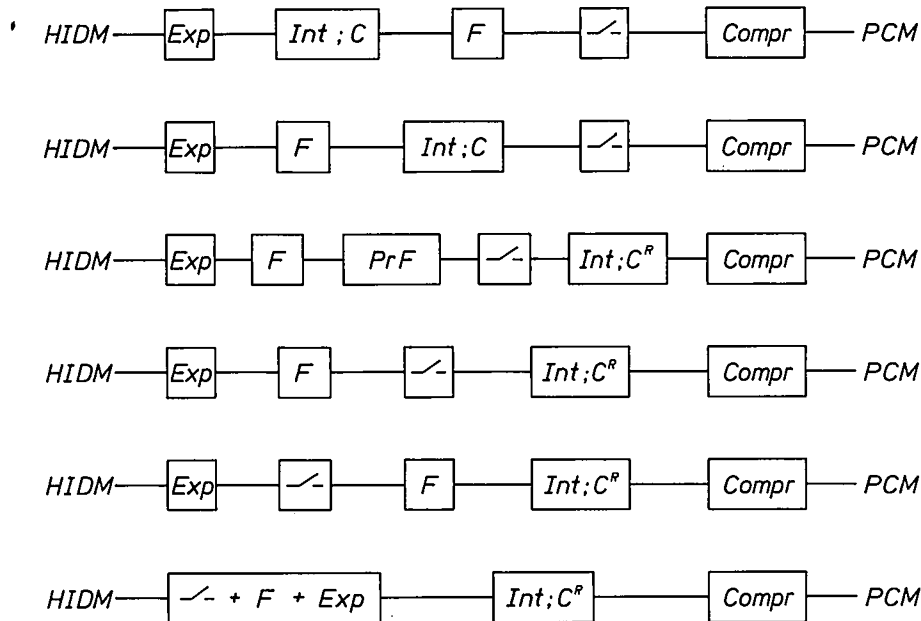

Fig. 12. Diagram showing the various steps in deriving a structure suitable for LSI from the diagram of fig. 9. The first step permits a smaller word length to be used in the filter. The second step, which limits the number of operations in the integrator, shows that the interchange of integrator and sampler leads to the introduction of an extra filter and to a change in the integration constant. In the third step these filters are combined, and the fourth step has the effect of reducing the number of operations in the filter. The last step is responsible for word-length expansion in the lowpass filter.

Block diagram of code converter

In circuits intended for telephony the dissipation should not be unduly high, and an integrated circuit should not therefore be required to operate at very high speeds if it can be avoided. For this reason we decided against serial operation for the digital signal processor, and chose parallel operation. The block diagram of the signal processor with the structure given in fig. 12 is shown in *fig. 13* [4]. This converter comprises a filter with 100 sections. The shift register belonging to the filter has 120 sections. Since there are 128 clock pulses

The multiplications of the filter coefficients by the step size of 2^n required for the filtering is achieved by shifting each filter coefficient by n places. The shifted filter coefficients — i.e. multiplied by a power of two — are then added in the accumulator, taking the signs into account. These nine-bit filter coefficients are stored in a 50-word ROM (read-only memory). The 50-word ROM is sufficient since only 50 different filter coefficients are required for the *symmetrical* non-recursive digital filter chosen. This implies that for the filter — but not for the integration — the constant c in (9) is made

equal to unity. From the discussion of eq. (9) we know that the interchange of integration and sampling has some effect (though only small) on the output signal.

The ROM is addressed by means of a shift register that contains exactly one '1'. Each position of this '1' in the address shift register, ASR, addresses one coefficient in the ROM in such a way that position i and position $101 - i$ ($i = 1, 2, \ldots 50$) in the ASR indicate the coefficient at position i in the ROM. This unusual addressing procedure is possible because the filter coefficients are always required in a *fixed* sequence. At the beginning of the calculation period the '1' in the ASR is shifted to position 1. By not resetting itself to zero, the accumulator operates as a 'leaky' integrator that shifts its own output a number of positions and then subtracts it from the original word. After completion of the multiplications for the filter, the accumulator — as will presently be discussed — requires a number of clock pulses to express the carry bits in the accumulator in its output signal. This is done by including 28 separate accumulator pulses which, together with the 100 associated additions of the filter, give an internal clock frequency of 1024 kHz (128 × 8 kHz). The 20-bit output signal from the accumulator is rounded off to 12 bits at the end of the complete cycle and then passed on to the digital compressor, which converts the 12-bit (uniform) PCM input signal into the non-uniform quantized standard 8-bit PCM code. Now that we have found a suitable block diagram for the code converter we shall look at the approach to the design of the electronic circuits.

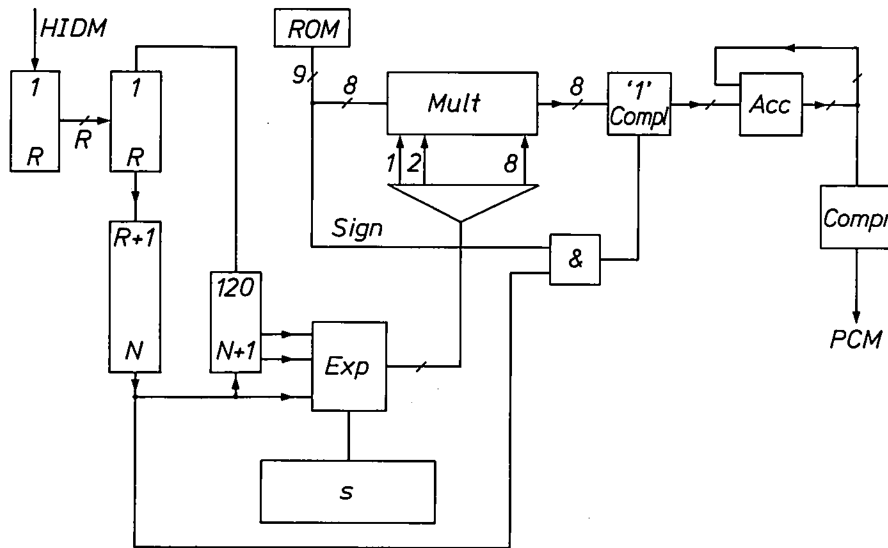

Fig. 13. Block diagram of the converter. An oblique stroke through a connection indicates that it consists of more than one line. *Mult* multiplier. *Comp* complement. *Acc* accumulator. *s* initial step size. The other symbols are the same as in fig. 9 and fig. 11.

From block diagram to detailed design

The essential feature to be borne in mind when designing LSI circuits is that there is little or no access to the various signals between the components of the IC. Nor it is possible to replace components of the IC. Because of these constraints it is necessary to use the aids described below. As the design progresses two particular problems are encountered. The design of a logic circuit amounts to the translation of a desired function into a set of binary logic relations (Boolean relations) that can be produced in the desired technology. The first difficulty consists in finding a functional structure (e.g. a block diagram) that will fulfil the desired function. When such a functional structure has been found, as described above, we come up against the second problem — how to reproduce its functions in the appropriate IC technology in logic circuits.

Since it would be no easy task to make a breadboard model for such a large circuit, and since a breadboard model would be of limited use for an MOS ciicuit, we checked the logic design of our circuit by means of a computer simulation.

This means of course that the logic-circuit description must be presented to the computer in a simple and well structured language. The simulation program must also be able to take account of the variations in the input signals during a given time interval. From this

[3] In fact, because of the relation between N' and R, this situation cannot occur in the system.

[4] G. P. Edwards, T. Preston, L. D. J. Eggermont and M. H. H. Höfelt, 1976 Int. Zürich Seminar on Digital Communications, p. B 3.1.

data relating to the structure and the input signals the simulation program determines the signal at the outputs and also a number of internal signals. The method is very versatile. Input signals can easily be changed. The logic design can also be modified quickly and easily if the result of the simulation shows that it is necessary.

For the simulation, the use of clocked or synchronous logic has considerable advantage over asynchronous logic, because the number of possible timing relations between the signals from a particular part of the circuit is very much smaller with synchronous logic. This means that simulation with this type of logic can be much faster and more reliable than with asynchronous logic. Largely for this reason we decided to use synchronous logic for the converter.

An important aspect to be considered in any design is the extent to which the IC resulting from a given design can be tested by finding the output signal associated with a given input signal. We do this by using the simulation program that works from a circuit description to which 'faults' have been added. With this description it is possible to see which gates are tested and which are not for any given input signal. This procedure is called test verification. If the result is not satisfactory, the designer may decide that either the use of additional (or different) test signals or the modification of the design would give successful testing. At an early stage in the design the problems of testing should be thoroughly examined, especially since there are some categories of circuit that are very difficult to test, in which a small modification can greatly facilitate the testing.

When using the test program or the simulation program it is necessary to know the output signal that should be obtained for a given input signal. Here we used a simulation program that does not work at 'gate level', like the one just described, but describes complete digital functional units (e.g. shift registers, accumulators and memories), without taking the internal structure of these units into account. The desired relation between the HIDM input signal and the PCM output signal of the digital code converter was determined with this block-simulation program with the aid of the block diagram shown in fig. 13.

If a breadboard model is used, characteristics such as quantization noise and the subjective perception can be determined in a simple way. But if it is not thought desirable to make a breadboard model, these characteristics will have to be determined from a simulation program. The gate-level simulator is not so suitable for this purpose, since it is not fast enough to simulate a few seconds of speech processing in the code converter. We have therefore also used the block-level simulator for these determinations.

Electronic design and technology

In the previous section we have described how we arrived at a block diagram for the digital code converter. Next we saw how the program simulating the operation of that block diagram and the gate-level simulation were used and compared with each other. We shall now discuss the four-phase dynamic MOS logic used in the converter.

Four-phase dynamic MOS logic

A circuit based on four-phase dynamic MOS logic is shown in *fig. 14.* The charge state of the capacitor C_1 determines the value ('true' or 'not true') of the Boolean function f. The value of f is arrived at as follows. In time interval *1* the capacitor C_1 is charged via T_1 as a result of the clock pulse ϕ_1. During the next time interval *2* the value of ϕ_1 is zero, but ϕ_2 keeps T_2 conducting. Thus, C_1 is discharged if there is a conducting path present in the logic circuit Log_1. This conducting connection occurs when the logic function $a(b + c) + de$ has the value 'true' [5]. In this case C_1 discharges, and the charge (and the potential) of C_1 represents the function $f = \overline{a(b + c) + de}$. The logic values formed in this manner remain in position until the next ϕ_1 pulse arrives, and can therefore be used as a reliable input signal for logic networks with type-3 gates, which are driven by the clock pulses ϕ_3 and ϕ_4 — in the same way as networks with type-1 gates are driven by the clock pulses ϕ_1 and ϕ_2. At the output a function g appears, which is represented by the state of charge of C_2. In their turn the output values of type-3 gates are stable during clock pulses ϕ_1 and ϕ_2, and are thus suitable for driving type-1 gates.

In addition to these two important types of gate there are also type-2 and type-4 gates. A slightly simplified configuration of a type-2 gate can be seen at the top of the circuit in fig. 14. The capacitor C_3 here contains the inverse of f. In time interval *1* capacitor C_3 is first charged via T_5 and then discharged via T_6 at the beginning of time interval *3*. Now type-3 gates only require their logic input signals during time interval *4*. As a result, type-2 gates deliver their output signal to the input of the type-3 gates at exactly the right time.

One advantage of separating the various operations into time intervals is that the dimensions and physical characteristics of the transistors do not have to be so critical for the circuits to function properly. Since any transistor can in principle be used in this configuration, the smallest transistor permitted by the technology will in general be used, provided the speed requirements allow it. Since it is also possible to achieve a fairly complicated function per gate, a high packing density can be obtained. It is often unnecessary to use flip-flops, since the charged capacitors perform their function.

Another virtue of four-phase logic is its low power, because there is no standing d.c. current. The circuit discussed here requires only 15 mW.

The circuit was made with an MOS process using the LOCOS field-oxide technology, which is based on a thick buried oxide layer. In this technology the tran-

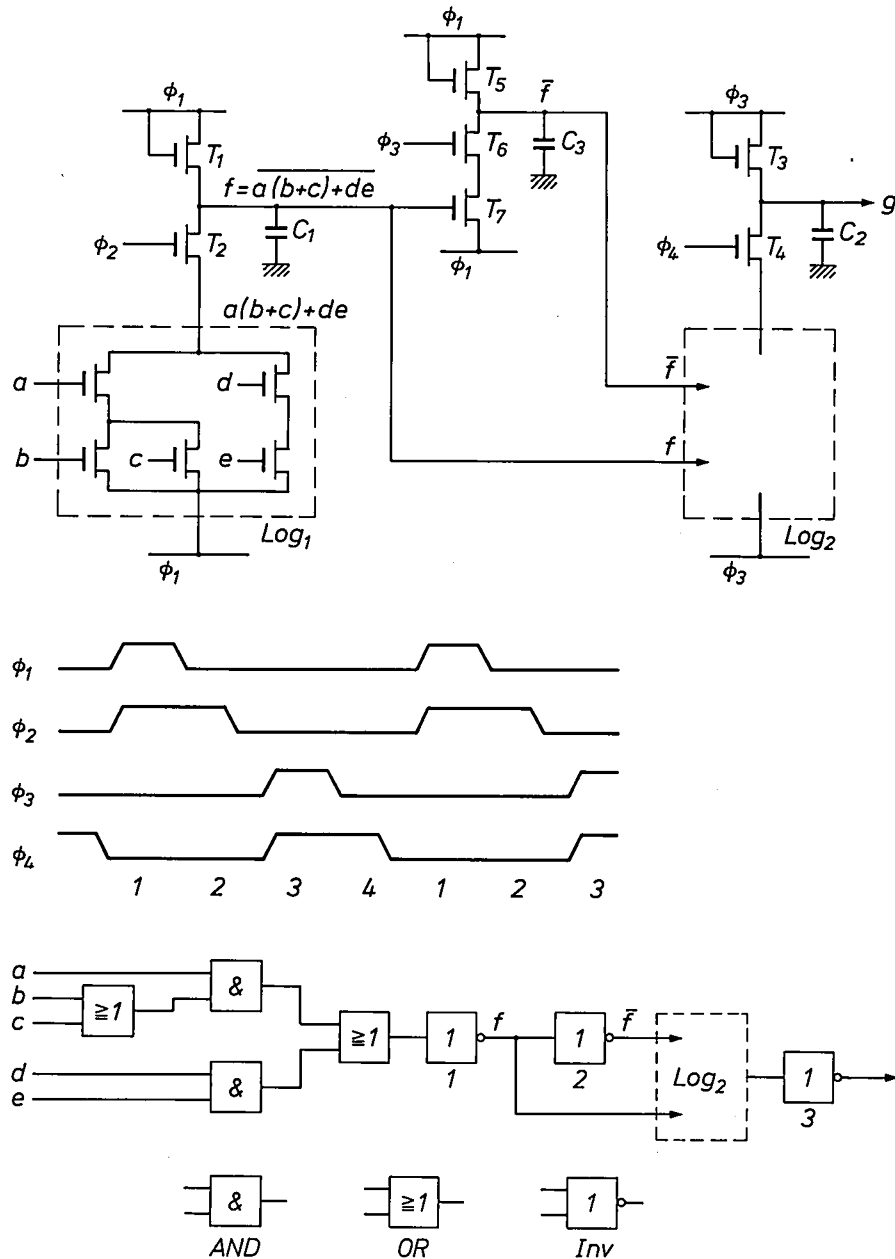

Fig. 14. Illustrating the operation of four-phase dynamic MOS logic. *From top to bottom:* a circuit, the four series of clock pulses ϕ and the logical representation of the circuit, *a*, *b*, *c*, *d* and *e* are arbitrary digital input signals. Log_1, Log_2 logic circuits. In the logical representation the gates of the various types are denoted by the appropriate digit. These gates are easily identified in the circuit.

It is necessary to check carefully, and separately from the simulation, whether the information stored in the IC as a charge on a capacitor might not be degraded on account of parasitic capacitances at crossings between the conductor connected to it and other connectors. If the parasitic capacitance to crossing lines is found to be too high compared with the buffer capacitance of the IC, the buffer capacitance must be increased.

sistors and the interconnections — which lie on the thick LOCOS oxide — have low parasitic capacitances. This allows fast circuits to be made that require

[5] $a(b + c) + de$ means: *a* and (*b* or *c*) or (*d* and *e*). This function has the value 'true' if (*a* and *b*) and/or (*a* and *c*) and/or (*d* and *e*) are true.

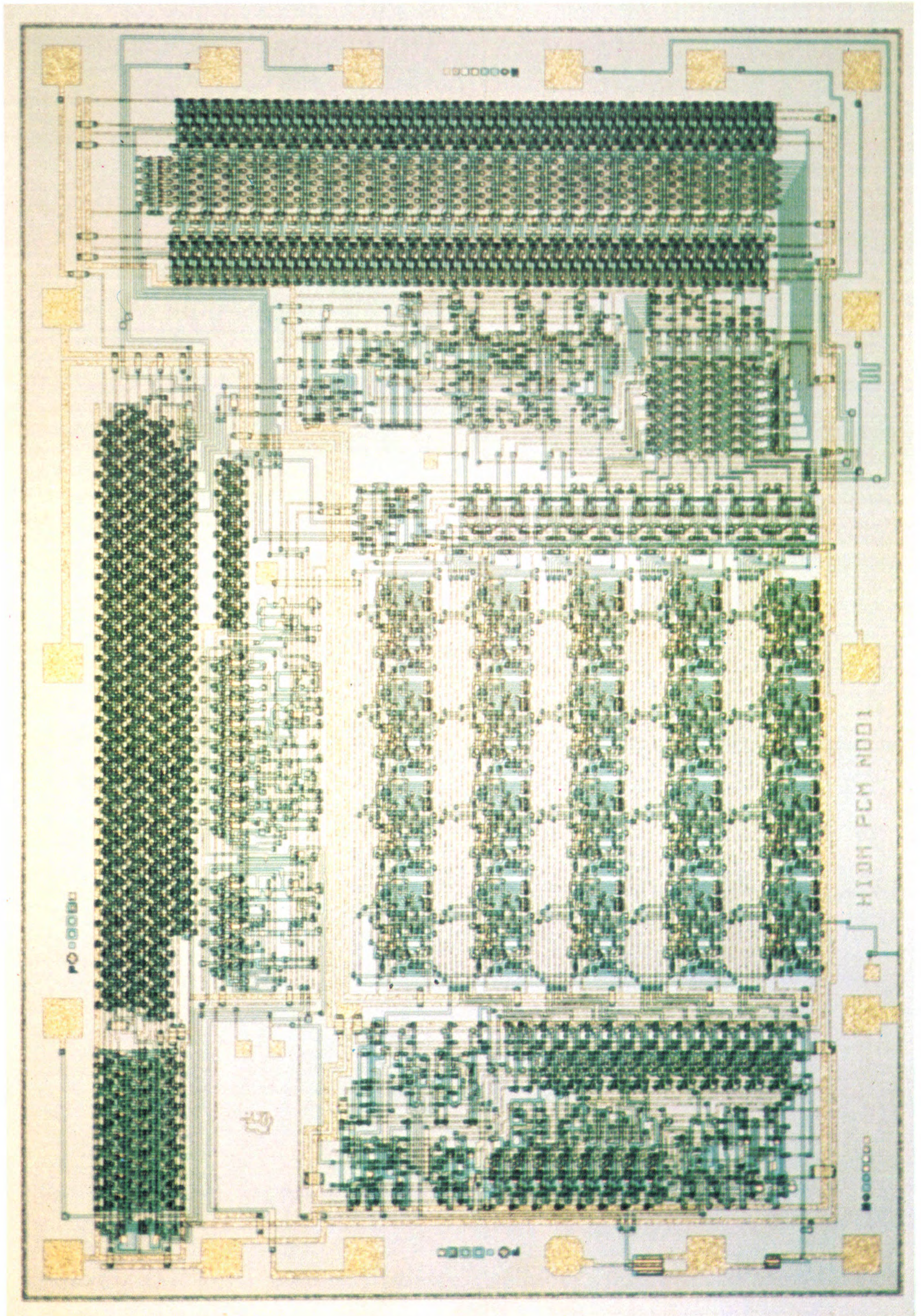

relatively little power. The desired clock freqμency (1.024 MHz) presents no problems.

In this technology, interconnections can be either diffused polysilicon or metal. Although a diffused interconnection and a polysilicon one cannot cross each other, it is very useful to have three kinds of interconnection available. Even with conservative layout rules for spacings and dimensions, a density of 200 NAND-gate-equivalents/mm² could be obtained with this technology.

Design of the layout

Our approach for the design of the layout could be described as semi-automated. The computer performs operations such as displacement, repetition and rotation of the patterns, but the structure of the layout is worked out by the designer and then supplied to the program.

One of the advantages of the semi-automated method is that a higher packing density can be obtained. This is because there are more degrees of freedom available. For the same reason, it is easier to optimize the processing speed for this circuit.

Since the circuit has high regularity, a fully automated method would not save much time compared with the semi-automated one. A disadvantage of the method we have chosen is that it is more difficult to check the correctness of the layout than with a fully automated procedure.

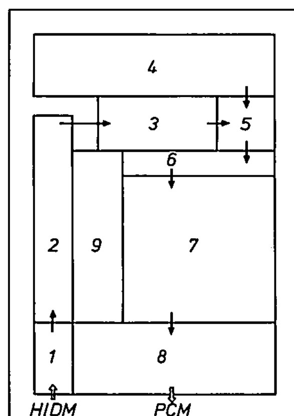

◁ **Fig. 15.** The IC of the HIDM-PCM converter, with an adjacent diagram showing the location of the various components on the IC. The arrows give the direction of the information flow. *1* eight-bit buffer register. *2* 120-bit shift register. *3* step-size control (expander). *4* ROM with filter coefficients. *5* multiplier. *6* converter to complement '1'. *7* 20-bit accumulator. *8* compressor. *9* control circuit. The dimensions of the chips are 3 by 5 mm.

The IC with the DM-PCM converter

We now come to the practical design of the block diagram of fig. 13 in four-phase dynamic logic. *Fig. 15* shows a photograph of the IC and a diagram indicating the location of the various functional units.

The accumulator and the shift register for the multiplier will now be discussed in more detail.

The accumulator

In the accumulator the filter coefficients multiplied by the numbers 2^0 to 2^7 are added to produce a sum with a maximum length of 20 bits. The adder is a 20-bit 'carry-save' accumulator, in which the carry is stored in each stage of the circuit. Each stage n of the adder functions as shown in the truth table given below.

	carry from preceding stage ↓ c_{n-1}	bit to be added ↓ a_n	old value of sum bit ↓ s_n	carry for next stage ↓ c_n	new value of sum bit ↓ s_n
Weight	2^n	2^n	2^n	2^{n+1}	2^n
Logic values	0	0	0	0	0
	1	0	0	0	1
	0	1	0	0	1
	0	0	1	0	1
	1	1	0	1	0
	0	1	1	1	0
	1	0	1	1	0
	1	1	1	1	1

An adder that obeys the rules given in the table stores the result of the addition of the sum bit, the bit to be added and the carry from the preceding stage at the location of the sum bit, and shifts any surplus as a carry of value '1' to the next stage. To obtain the sum at the end of the addition procedure the accumulator must be left to make a few more shifts so that it can pass on any carries of value '1' that may still be left. Finally, only sum bits remain, and these give the final result of the addition.

In the discussion of the design of the adder it is useful to describe the truth table in terms of logic functions:

$$s_n := (\bar{a}_n c_{n-1} + a_n \bar{c}_{n-1})\bar{s}_n + (\bar{a}_n \bar{c}_{n-1} + a_n c_{n-1}) s_n,$$

$$c_n := s_n c_{n-1} + a_n s_n + a_n c_{n-1},$$

where the new values of s_n and c_n appear on the left of the 'becomes equal to' sign (:=), and the old values of s_n and $\bar{c}_n$ on the right of it. *Fig. 16a* shows the logic diagram corresponding to these relations. It can be seen that no flip-flops are used here. The corresponding circuit diagram is shown in fig. 16*b*, while the layout and a photograph of the actual IC are shown in *fig. 17a* and *b*. In fig. 16*a* the bits a_n (of the signal to be added) and $\bar{c}_{n-1}$ (the inverse of the carry from the preceding stage) are shown entering the parts of the adder under discussion. Both the inverted and the non-

inverted signal are produced from these two signals in a type-1 and a type-2 inverter. At the same time, type-1 and type-2 inverters form s_n and $\bar{s}_n$ from the previous value of s_n. The six signals thus formed, a_n, $\bar{a}_n$, c_{n-1}, $\bar{c}_{n-1}$, s_n and $\bar{s}_n$, arrive next at the input of two type-3 gates. The new sum bit is formed in the left-hand type-3 gate, while the new carry is produced by the right-hand type-3 gate.

In the case where a_n and c_{n-1} are zero, the part of the circuit drawn in heavy lines forms a hold circuit for s_n. A circuit of this type is a very simple structure which could be said to be inherent in four-phase logic.

The IC contains the transistors at the locations where polysilicon crosses a diffusion path (black squares in fig. 17*a*). As can be seen in fig. 17*b*, the interconnections are either of aluminium (shown bright in the photo-

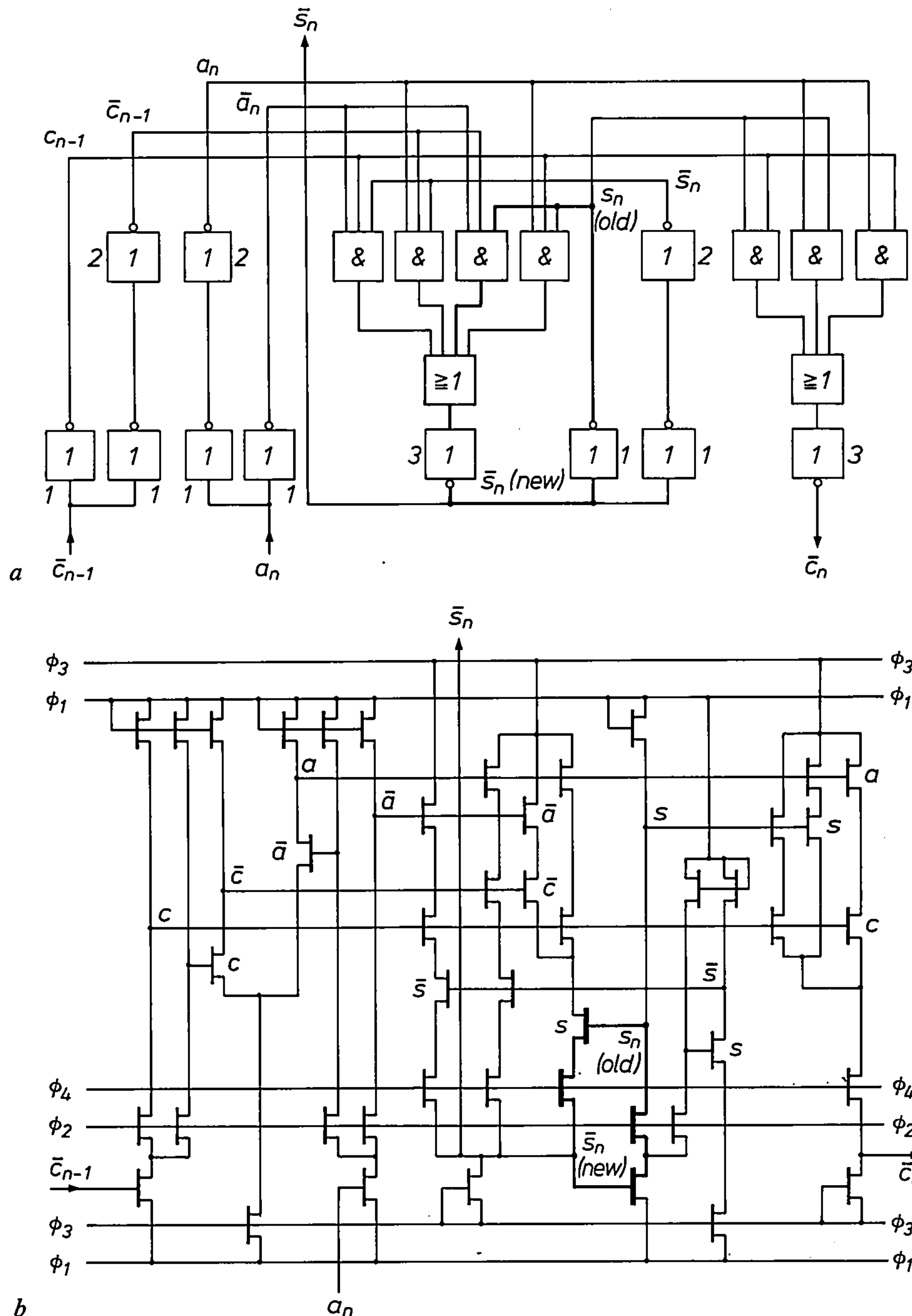

Fig. 16. The logic diagram (*a*) and the circuit (*b*) of a stage of the 'carry-save' accumulator (*Acc* in fig. 13). The types of gate used in four-phase logic are denoted by the appropriate digit. If a_n and the carry c_{n-1} are zero, the part of the circuit drawn in heavy lines forms a hold circuit for the sum bit s_n. In the two diagrams corresponding functions are located at the same place, where possible.

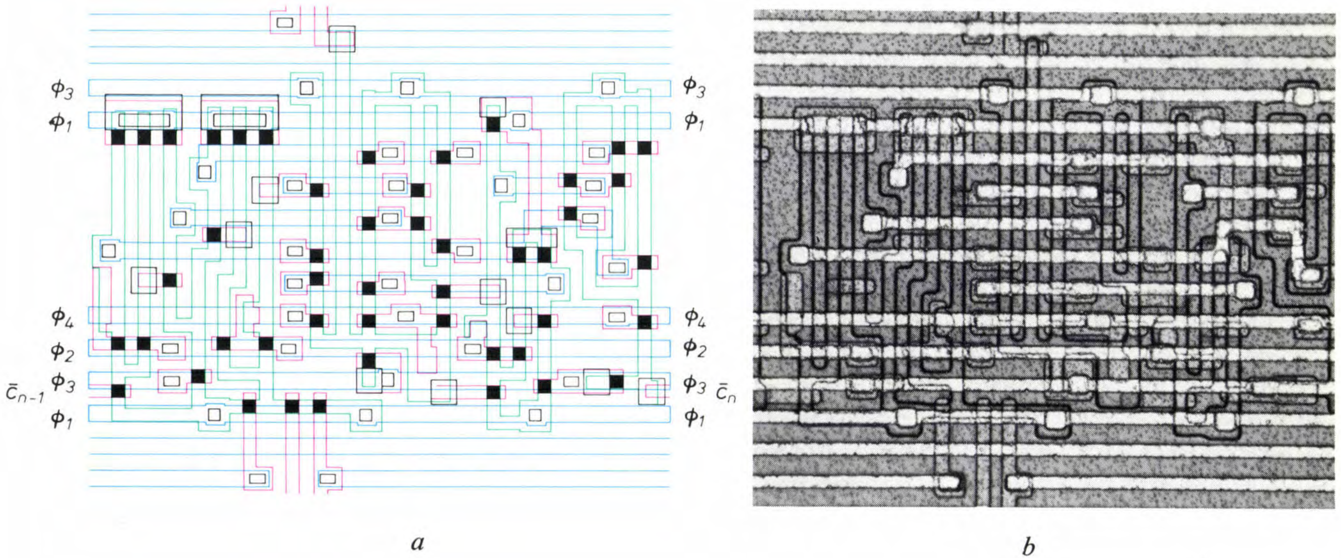

△
Fig. 17. *a*) The layout of the accumulator stage of fig. 16. The aluminium interconnections, mainly horizontal, are outlined in blue, and the polysilicon interconnections are shown in red. The diffusion channels lie inside the grooves in the thick oxide, marked green. Places where polysilicon covers the diffusion channel mark the location of an MOS (enhancement) transistor (*black squares*). No *N*-type dopant will penetrate into the channel at these locations. All parts of the channels not covered by polysilicon, on the other hand, receive *N*-type doping. The contact openings of the aluminium with the underlying material (polycrystalline silicon or silicon in the openings in the oxide) are outlined in black. At some positions where polysilicon crosses the diffusion channel an electrical contact between the two is required rather than a transistor. Here again, a special contact window is required; its openings are also outlined in black. *b*) Photograph of the accumulators on the chip. The light aluminium tracks are easily recognized, and so too are the polysilicon interconnections (mainly vertical). The diffused channels can be recognized from their dark edges.

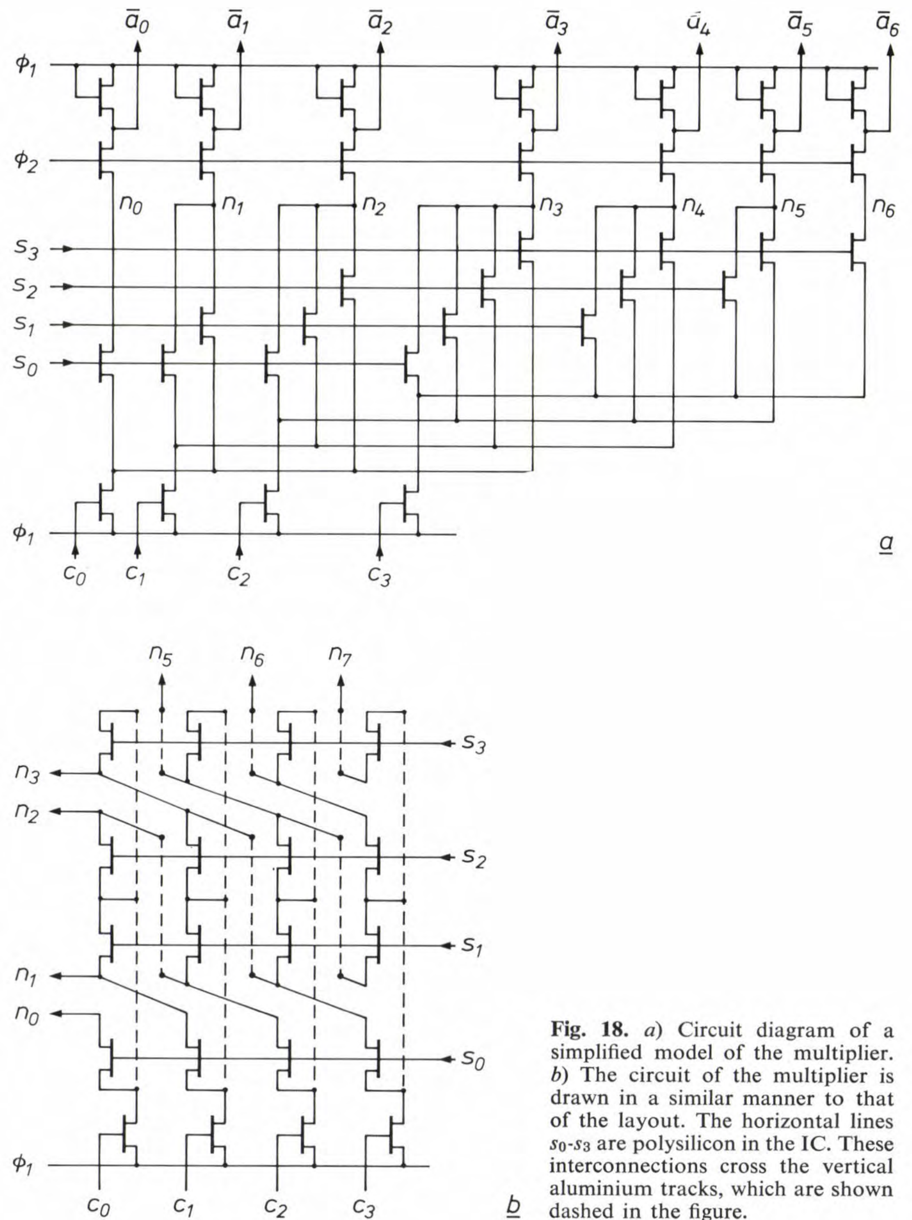

Fig. 18. *a*) Circuit diagram of a simplified model of the multiplier. *b*) The circuit of the multiplier is drawn in a similar manner to that of the layout. The horizontal lines s_0-s_3 are polysilicon in the IC. These interconnections cross the vertical aluminium tracks, which are shown dashed in the figure.

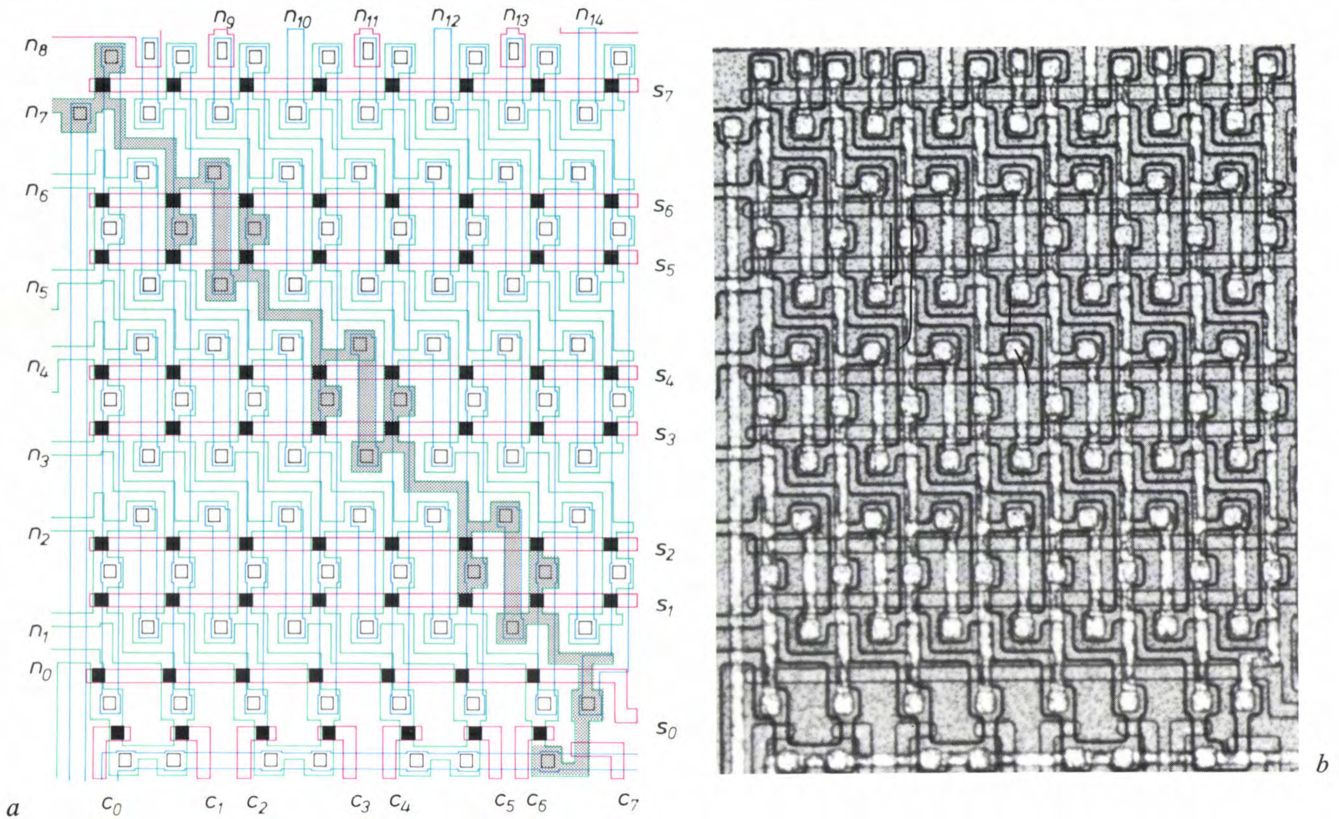

Fig. 19. *a*) Layout of the logic circuit for the multiplier. The colours have the same significance as in fig. 17*a*. The circuit for n_7 is shown in grey. *b*) Photograph of the multiplier section of the IC. The various structures can be recognized with reference to the layout in (*a*). The diffusion channels can be identified by their dark edges.

graph) or are diffused (mainly vertical in the photograph and recognizable by the dark edges). Polysilicon can also be used for interconnections. An example can be seen in the part of the IC shown here (above the $\bar{s}$ output). Twenty of these adder stages together form the accumulator. Each stage occupies about 0.08 mm², and including all the interconnections the accumulator occupies an area of 2.6 mm².

The shift register for the multiplier

Finally, we shall briefly discuss the multiplier shift register, with particular reference to the ability to obtain a high packing density through the use of three types of interconnection — aluminium, polysilicon and diffused. The multiplier has to multiply the filter coefficients by $2^0, 2^1, \ldots 2^6$ or 2^7, depending on the step size, before passing them on to the accumulator for summation. Multiplication by 2^n, apart from the sign, consists in shifting the eight-bit coefficients by n places. Each of the eight values of n has a corresponding separate control line, so that only one of the eight control lines, which are controlled by the expander, carries the high voltage at any given moment.

We shall illustrate the structure of the multiplier with the aid of a simplified example, in which 4-bit filter coefficients are shifted by zero to three places. The four bits of a filter coefficient are denoted by c_0, c_1, c_2 and c_3, while the control lines for shifting the filter coefficients by the appropriate number of places are denoted by s_0, s_1, s_2 and s_3. The seven outputs $a_0, a_1, a_2, \ldots a_6$ of the multiplier are given a logic value as indicated below:

$$
\begin{aligned}
a_0 &= s_0.c_0 \\
a_1 &= s_0.c_1 + s_1.c_0 \\
a_2 &= s_0.c_2 + s_1.c_1 + s_2.c_0 \\
a_3 &= s_0.c_3 + s_1.c_2 + s_2.c_1 + s_3.c_0 \\
a_4 &= s_1.c_3 + s_2.c_2 + s_3.c_1 \\
a_5 &= s_2.c_3 + s_3.c_2 \\
a_6 &= s_3.c_3.
\end{aligned}
$$

The variables c_0-c_3 each occur four times in the above logic expressions, which, in the usual configuration, requires four transistors per variable c_n. But since at any given moment only one of the control lines s carries the high voltage, it is possible, as shown in *fig. 18a*, to replace the four transistors normally used for c_n by a single transistor. If this were not the case, and if for example s_1 and s_2 could both be '1', then a conducting path could arise between c_0 and c_1, etc., with the result that the bits c_0, c_1, c_2 and c_3 would be made equal to

one another. This danger does not exist here, however. The compact structure permitted by the use of three types of interconnection is shown in fig. 18*b*, the layout of the multiplier is shown in fig. *19a*, and fig. 19*b* shows the final circuit, with an area of 0.25 mm².

Our objectives, arising from the requirements for an IST system, have thus been achieved: to structure the architecture of a digital code converter in such a way that the design would be suitable for LSI, and then to fabricate the circuit in the form of LSI hardware.

Summary. The development of LSI circuits makes it possible to use digital techniques in a telephone network, both for transmission and for switching. This can have considerable economic advantages, provided the analog/digital and digital/analog converters are inexpensive. This implies that the use of expensive analog filters has to be avoided. The article describes an A/D converter in which the analog signals are indirectly converted into the standard PCM code via an HIDM code ('High-Information Delta Modulation'). It is shown how the conversion of this intermediate code into the PCM code can be resolved into its elementary functions and subsequently combined so as to produce a design suitable for fabrication as an LSI circuit. A description is given of the design of the circuit in an LSI technology that combines a high packing density with low dissipation. The technology used is four-phase dynamic MOS logic.

 Philips tech. Rev. 37, 330-333, 1977, No. 11/12

The Silicon Repeater

The Silicon Repeater is a machine used in the manufacture of integrated circuits. The machine makes repeated and reduced projections of a single photomask directly on to accurately defined positions on a silicon wafer that has been coated with photosensitive lacquer (photoresist). In this way, as discussed in the introductory article in this issue [1], a number of steps of the process previously used are combined, that is to say the manufacture of a multiple mask with the step-and-repeat camera [2] and the subsequent production of a contact print of this multiple mask on the wafer. The method using the Silicon Repeater has two distinct advantages over the earlier one. To start with, repeated projections at a fifth of full scale are made of a single mask. The mask is consequently larger than the ultimate circuit. A single mask can be inspected much more quickly and easily than the multiple masks used earlier, and repairs are easier to carry out. Moreover, small im-

Fig. 1. The Silicon Repeater. The black column contains the illumination system. The cylindrical drum at the base of this column contains the turntable for the masks; the lighter-coloured unit underneath it accommodates the projection optics and the alignment system. All these are situated on one of the two carriages mounted on hydraulic bearings and driven by hydraulic motors. The other carriage, not shown in the photograph, carries the wafer table with the silicon wafer to be exposed. To change the wafers the table can be slid out of the equipment at the front. The monitor in the background shows the alignment marks on wafer and mask, which are used for the coarse alignment, set manually by the knobs on the control panel in the foreground. After this initial coarse alignment, the accurate alignment is carried out automatically by the computer in the background.

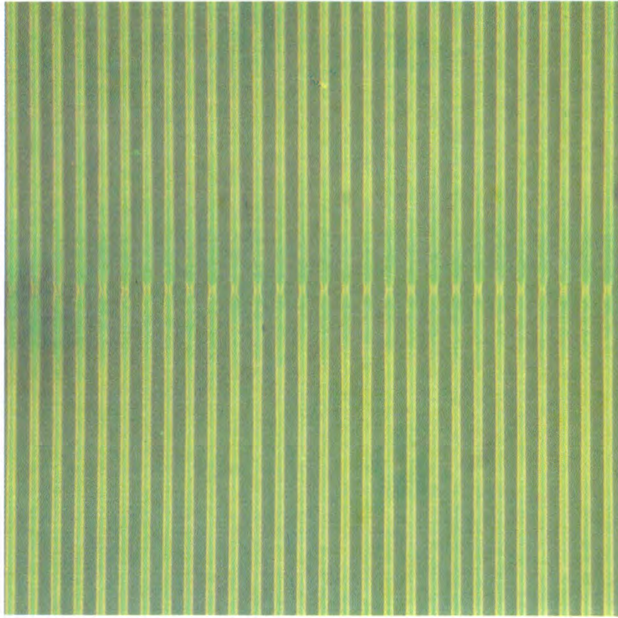

Fig. 2. Magnification of part of a grating pattern made with the Silicon Repeater from a number of consecutive projections of a mask. The boundary between two projections can just be discerned in the photograph at half height. The line width is 6 μm.

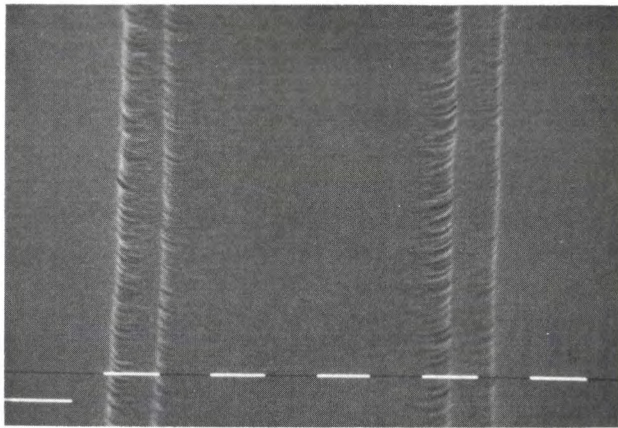

Fig. 3. Accuracy of the relative alignment of the results of two successive operations. A grating pattern is projected on to a silicon wafer coated with photoresist, developed and etched. The wafer is then given a new coating of photoresist, placed in the Silicon Repeater and the grating pattern is again projected on to it. The exposure is shorter for the second projection than for the first, giving narrower lines. The results of the second operation are accurately centred on those of the first. The black and white dashes at the bottom of the picture are each 1 μm long.

perfections in the mask and slight irregularities in the repair, owing to the five-times scale, have much less effect than in the masks for contact prints. The other great advantage is the absence of mechanical contact between the mask and the silicon wafer. This greatly reduces the risk of mechanical damage to the mask so that the mask has a longer useful life. As a result the work spent on inspecting the mask and making any repairs that may be necessary is more productive. There is also much less risk of damage being caused to the photoresist-coated silicon wafer.

To produce the maximum benefit from these advantages of the projection method, great care was taken at the design stage with the positioning accuracy of the successive projections and with the operating speed of the machine. For each of the successive operations carried out on the wafer a different mask is necessary. Each mask must always be accurately positioned with respect to the results of the previous operation on the wafer; the tolerances decrease with the size of the components of a circuit. For this positioning two permanent marks are made on each wafer, and the position of each projection of the successive masks is accurately determined with reference to these marks. The operating speed of the Silicon Repeater has to be high for it to compete with existing processes in which a single exposure is made of a multiple mask. The various measures necessitated by these requirements will now be dealt with in the discussion of the machine.

As with earlier machines for making photomasks [2] [3], the Silicon Repeater (*fig. 1*) has two carriages, mounted on hydrostatic bearings, which can be moved on beds at right angles to each other by linear hydraulic motors. On one carriage an adjustable holder is mounted that contains the photoresist-covered silicon wafer; the other carries the projection column. Two laser-interferometer systems [4] allow the position of the two carriages to be measured to the desired accuracy.

The projection column contains a super-high-pressure mercury-vapour lamp as the light source. An elliptical mirror behind the lamp and a special condenser system ensure sufficiently intense and homogeneous illumination of the mask to be projected. The mask lies on a turntable which can accommodate four masks. One position is used for the mask for the actual circuit, the other three positions are used for masks for projecting test patterns on to the wafer to check the various stages in the manufacture of an integrated circuit. The projection lens is designed as a telecentric lens system to ensure that a wafer with an uneven surface does not cause any variation in the enlargement on projection. The system consists of two sections, and the intermediate image between the two sections is at infinity. If the silicon wafer varies in thickness and the focusing has to be adjusted, this is done by displacing the lower

[1] See the introductory article by H. Bosma and W. G. Gelling in this issue, in particular fig. 2 (p. 267).
[2] F. T. Klostermann, Philips tech. Rev. 30, 57, 1969.
[3] A. G. Bouwer, R. H. Bruel, H. F. van Heek, F. T. Klostermann and J. J. 't Mannetje, Philips tech. Rev. 34, 257, 1974.
[4] H. de Lang and G. Bouwhuis, Philips tech. Rev. 30, 160, 1969.

section only; the magnification is not then affected.

The silicon wafer is clamped to the wafer table by gentle suction. The table can be adjusted so that the front of the wafer is perpendicular to the axis of the projection column. Any wedge-type deformity of the wafer then has no effect on the focus of the projection. The wafer table and the mask holder can rotate independently, so that the axes of both wafer and mask,

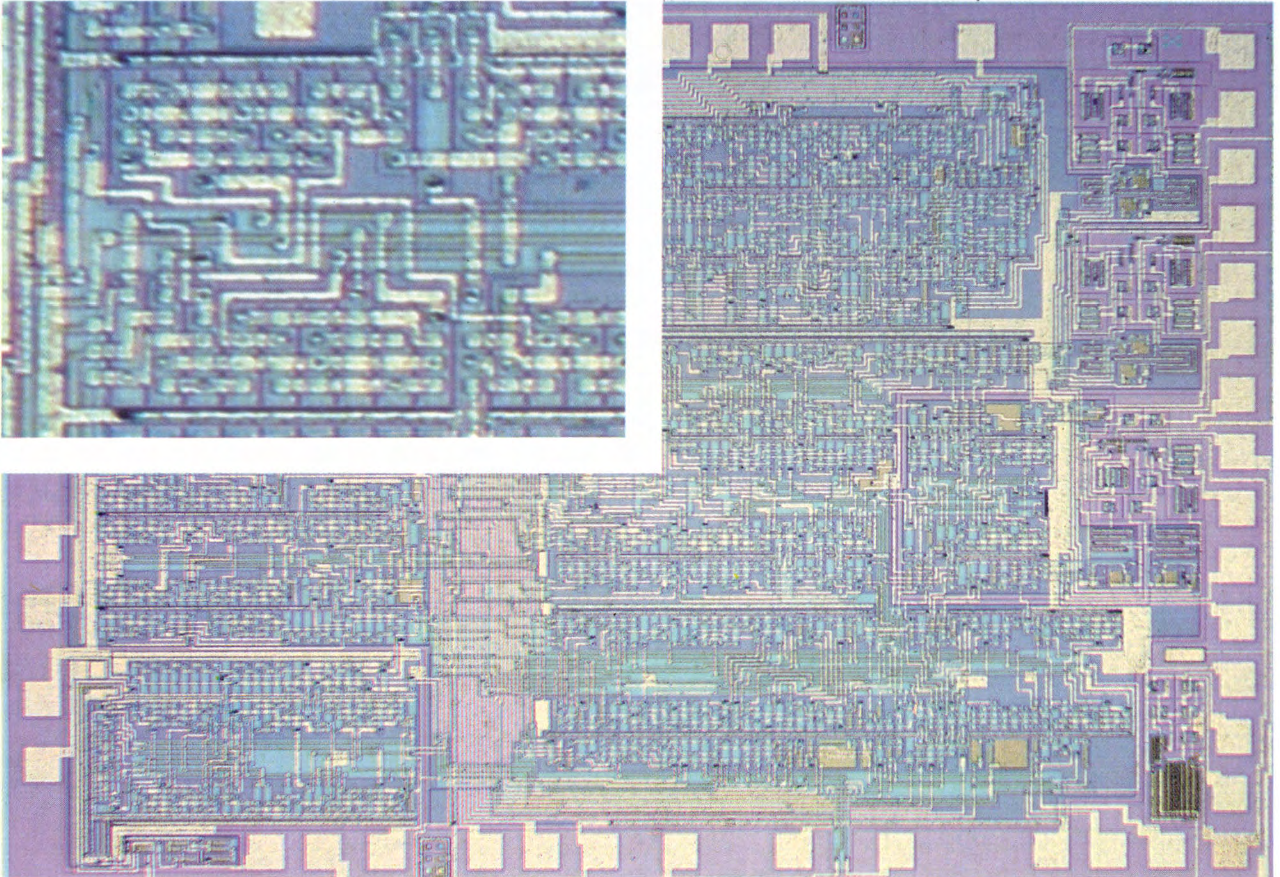

Fig. 4. A highly complex integrated circuit, which can only be made with a good yield by using the Silicon Repeater. The chip area is about 15 mm². Part of the circuit is shown at higher magnification in the top left-hand corner.

Table I. Numerical data relating to the Silicon Repeater.

Dimensions:	
mask image, maximum	50 × 50 mm
chip with IC, optimum focus	7 × 7 mm
chip of maximum dimensions and poor focus	10 × 10 mm
one silicon wafer	3 to 4 inches
smallest detail in a circuit	2 μm
Times:	
exposure per chip	0.5 s
displacement	0.5 s
exposure of a 3-inch wafer	2 min
Tolerances for flatness of wafer:	
wedge-type tolerance	10 μm/cm
focusing range	16 μm
Accuracies:	
realignment of a wafer	± 0.1 μm
positioning of each projection	± 0.1 μm

defined by the marks, can be set accurately parallel to the axes of the carriages with an automatic optical alignment system. The alignment marks on the wafer also fix the zero points on the axes of the wafer.

The electronic control system for the automatic adjustment of the wafer and masks and for positioning the successive projections was designed by our colleagues at the Philips Elcoma Division in Nijmegen.

Some figures giving an idea of the performance of the Silicon Repeater are presented in *Table I.* In achieving the accuracies quoted the quality of the optical alignment system is of great importance. To obtain some information about the quality of the system we made prints from a fine grid pattern. *Fig. 2* shows how accurately consecutive prints of this pattern can be joined

together so as to produce a grating that is larger than a single print of the mask. *Fig. 3* illustrates the accuracy with which the results of two successive operations can be adjusted in relation to one another. A grating is printed on the wafer coated with photoresist. The photoresist is developed, and the wafer is then etched. Following the application of another coating of photoresist, the same pattern is printed once again, now with a shorter exposure, wich gives narrower lines. The scanning electron photomicrograph shows a detail of the resulting grating line after a second etch. The narrow line of the second print lies exactly in the centre of the first line. Finally, *fig. 4* shows an integrated circuit made with the Silicon Repeater. This circuit is so complex that mask damage would have made the yield unacceptably low with existing methods.

A. G. Bouwer
G. Bouwhuis
H. F. van Heek
S. Wittekoek

A. G. Bouwer, G. Bouwhuis and Dr S. Wittekoek are with Philips Research Laboratories, Eindhoven; Drs H. F. van Heek, formerly with Philips Research Laboratories, is now with the Philips Elcoma Division, Eindhoven.

Philips tech. Rev. 37, 334-346, 1977, No. 11/12

Electron-beam pattern generator

J. P. Beasley and D. G. Squire

Introduction

The conventional process for making the masks which are used in the manufacture of integrated circuits is photolithography. A replica of the required pattern is first made and reduced photographically to the required size, using a very accurate optical system: often a very large demagnification is needed and the reduction may have to be made in two stages. The final replica is then used as a mask through which to expose a light-sensitive 'resist' which covers the material in which the pattern is to be made. After the resist is exposed and developed it forms a protective layer which shields the underlying material at the places where the pattern is to appear, while the rest can be etched away to leave the desired pattern. There are many possible variations, but all high-resolution processes share the need for a precise and usually high-definition mask.

Throughout the history of integrated-circuit manufacture there has always been a steady demand for smaller and smaller structures, and the resolution now required in the pattern and the mask approaches the fundamental limit set by the wavelength of light. If progress towards finer resolution is to continue, alternatives to optical techniques must be developed. The most promising of these is electron lithography, in which a beam of electrons is used to define the pattern in an electron-sensitive resist [1]. The pattern can be drawn directly on to the resist on the final substrate or used to make a mask which can be copied, for example using an electron-image projector such as that described in the article by J. P. Scott [2]. Electron lithography has two major advantages. First, the effective wavelength of an electron is typically very small; for an energy of 20 KeV, as used in the machine described here, the effective wavelength is about 0.05 nm — i.e. 10^4 times smaller than the wavelength of visible light. Such a machine is not limited by the wavelength and could in principle achieve a resolution many times higher than could be obtained optically, provided of course that the aberrations in the electron-optical system could be made sufficiently small. The second advantage is that since electrons are charged particles, the electron-optical system can be controlled and varied electrically while the pattern is being drawn. This feature can be used, for example, to adjust the alignment of the pattern on the substrate or to correct for any aberrations or distortions which may arise as the beam moves. This eases the requirements on the mechanical alignment and on the focusing and deflection systems.

The subject of this article is an electron-beam pattern generator which has been developed at Philips Research Laboratories, Redhill (PRL) [3]. This machine is normally used at a spot size of 0.25 μm, but this can be reduced to a value of 0.1 μm if required. The positional accuracy is close to $\pm \frac{1}{8}$ μm, and the machine can cover a mask measuring 42 × 42 mm with high-resolution patterns in from 1 to 3 hours, depending on the area taken up by the pattern.

The machine has been providing a pattern-generation service for PRL, for the Philips Research Laboratories in Eindhoven and for other establishments within the Philips company for the last two years. Patterns have been successfully made on several hundred substrates, some as masks for ordinary photolithography, some as masks for use in the electron-image projector and some drawn directly on to the required substrate (this process is called 'direct slice writing'). Most of the patterns have been used in the fabrication of experimental transistors and integrated circuits; other applications have been in magnetic-bubble circuits and surface-acoustic-wave devices. The high resolution of the machine gives an improved packing density in both applications, and in semiconductor devices the small dimensions attained also allow high operating frequencies.

In this article we shall first give a general outline of the machine and its operation and then more detailed descriptions of the most important features. In the final section the performance achieved will be described and some examples of work done on the machine will be shown.

J. P. Beasley, B.A., is with Philips Research Laboratories (PRL), Redhill, Surrey, England; D. G. Squire, B.Sc., formerly with PRL, is now with Philips Information Systems and Automation (ISA), at Croydon, Surrey.

[1] See for example E. D. Roberts, Philips tech. Rev. 35, 41, 1975. We use some of the special resists developed at PRL as well as the standard types based on polymethyl methacrylate.

[2] J. P. Scott, this issue, p. 347.

[3] A full technical description of the machine has been published in IEEE Trans. ED-22, 376, 1975.

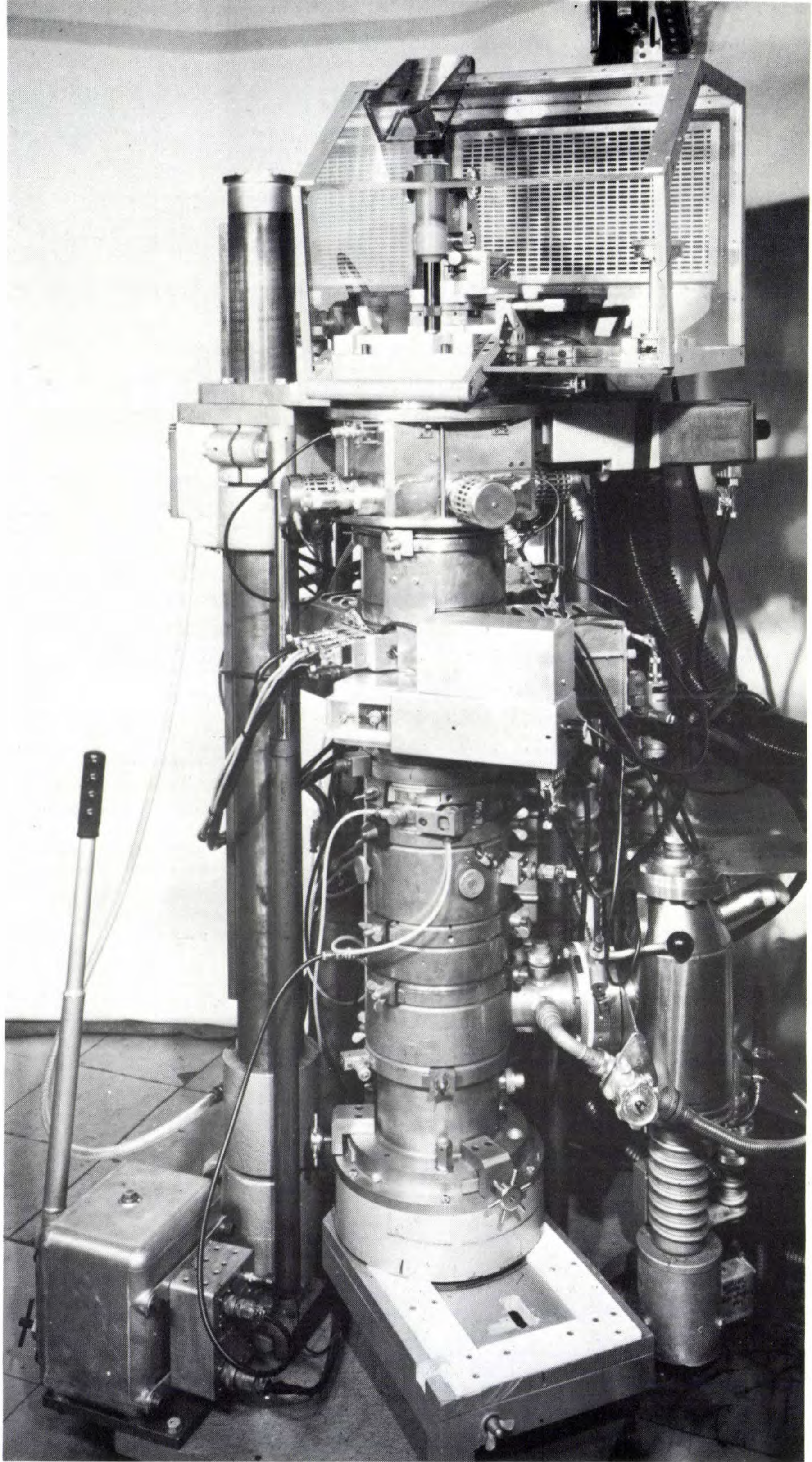

Fig. 1. The electron-optical column of the electron-beam pattern generator. The column is similar to that of a scanning electron microscope, and produces a beam of electrons focused to a spot of diameter 0.25 μm. This spot is scanned over the target under the control of a minicomputer so as to draw the required pattern directly on an electron-sensitive resist. Apart from the electron-optical column and the minicomputer the pattern generator consists of amplifiers and control circuits used for deflecting the beam, for adjusting the focus during scanning and for positioning the patterns.

General description of the pattern generator

The pattern generator is an adaptation of the scanning electron microscope (SEM) [4]. In the SEM a finely focused beam of electrons is scanned in a raster over the item of interest. Depending on the application the transmitted electrons, the reflected electrons, or the secondary-emission electrons are detected, and the signal produced is displayed visually by a synchronized raster on a screen. The pattern generator, which is shown in *fig. 1*, uses a similar electron-optical system, but a minicomputer is added, which drives the beam around in a complex path so as to draw a pattern directly on to a target covered in electron-sensitive resist. The resist is then developed and etched to produce a useful pattern directly or to make a mask which can be copied by other means. The pattern specification consists of a list of coordinates which are stored in the computer memory and so can be very easily altered or adjusted. Thus the process of pattern or mask making is both straightforward and flexible.

A mask for an integrated circuit contains a great deal of information — especially if the patterns are very finely detailed — although much of it is repetitive. For example a mask 42 × 42 mm contains 1.8×10^9 squares each 1 × 1 μm, so that even if the pattern occupies only 25% of the surface area, something like 4×10^8 squares may have to be drawn if a resolution of 1 μm is required throughout the mask. If the drawing is to take say 2 hours (a typical time for this machine), approximately 75 000 squares must be drawn each second. One of the main problems in electron-beam pattern generation is to obtain the required drawing speed without loss of resolution and accuracy. Particularly high demands are made of the deflection and focusing system, and in the PRL machine a two-stage deflection system together

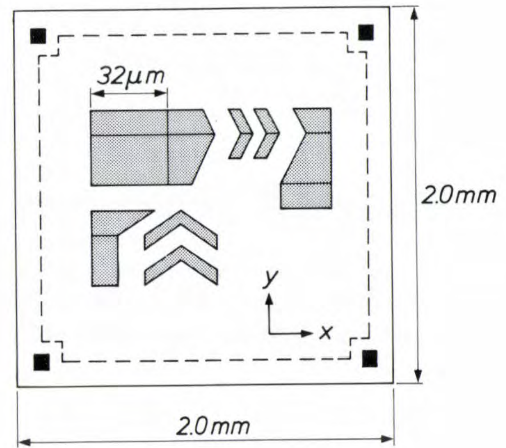

Fig. 2. The surface on which the pattern is to be drawn (maximum 42 × 42 mm) is divided up in squares each about 2 × 2 mm, which are filled one at a time. Within each square of patterns of any shape can be built up from trapezium-shaped elements. The trapezia are drawn by a fast-acting autonomous generator instructed by the computer. The main deflection system is used to place these elements accurately within the squares. The actual pattern area is 1.9 × 1.9 mm (see dashed lines) because part of the square is occupied by markers. The trapezia have a maximum size of 32 × 32 μm.

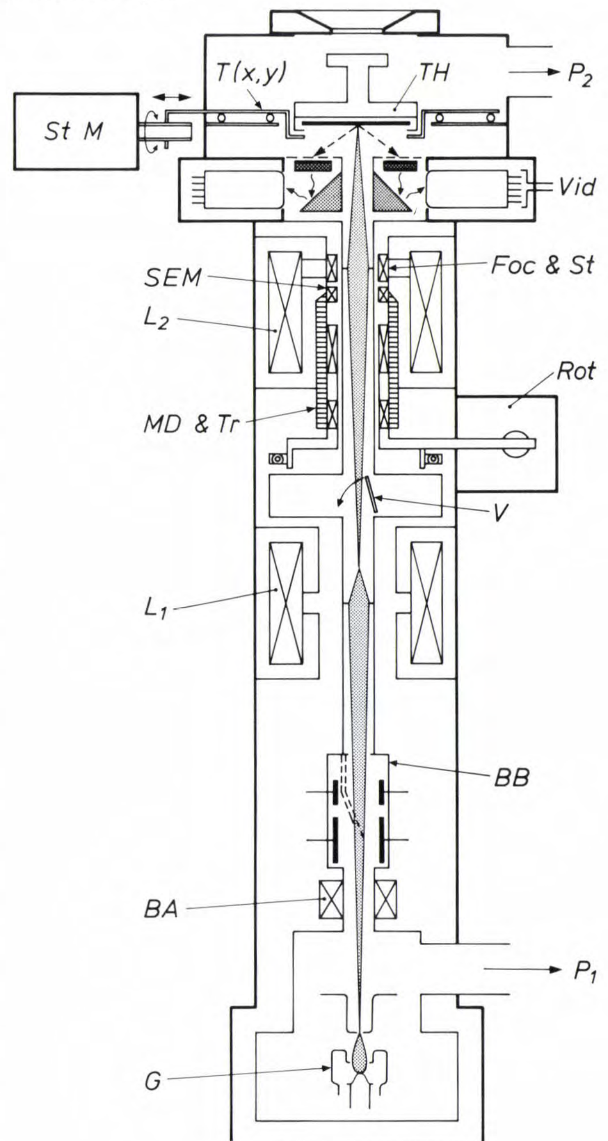

Fig. 3. Schematic sectional view of the electron-optical column. ▷ Starting from the bottom of the diagram, we have the electron gun *G*, a coil *BA* for beam alignment, a beam breaker *BB*, an electromagnetic lens L_1, a vacuum valve *V* and the objective lens L_2. The main deflection coils [*] and the coils of the trapezium generator (*MD* and *Tr*), separated from L_2 by a Mumetal cylinder (*hatched*), are located between L_1 and L_2. The entire column can be rotated about its axis by the mechanism *Rot* (a micrometer screw driven by a stepping motor). *Foc* and *St* are the coils for focusing and astigmatism correction (see also fig. 6). P_1 and P_2 connect with two diffusion pumps.

The slice to be processed is located in a target holder *TH* on the table *T(x,y)*, which can be displaced in two directions at right angles under the control of a computer. The electron beam (*light grey*) can scan a maximum of 2×2 mm and the mechanical stage allows an array of 22×22 such scanning areas to be drawn on a single target. Each area of 2×2 mm is marked out by an array of markers whose positions can be determined by making use of the back-scattered electrons. These electrons strike an annular phosphor-coated glass plate (*dark grey*), generating photons which are detected by four photomultipliers symmetrically arranged around the axis of the column. Photon collection by the photomultipliers is improved by the provision of aluminium mirrors. The video signal *Vid* thus produced is used for locating the markers and also for forming an image of the substrate as in an ordinary scanning electron microscope. This image is particularly useful for examining markers for defects.

with a mechanical stage are used to ease some of the problems.

The pattern which the machine has to draw — maximum dimensions 42×42 mm — is divided into subunits of about 2×2 mm, whose corners are determined by markers on the target surface. These markers are used for alignment purposes and also to help in focusing the beam, as we describe in more detail later. In the present machine a separate pattern, such as an integrated circuit, is drawn in each subunit, although patterns covering more than one subunit could be drawn. The target can be moved on a mechanical stage controlled by the computer so that a 22×22 array of separate patterns can be drawn on a single target. These may be different designs or repeats of a single type, as required.

The pattern which is to be drawn in the 2×2 mm scanning area is divided into small trapezium-shaped blocks, up to 32×32 μm in size. The main deflection system moves the beam to the correct point in the field and then hands over control to an autonomous trapezium-generator unit with its own deflection coils and control circuits, which rapidly fills in a block of the required shape and size. The pattern is thus built up from a large number of small blocks drawn side by side (*fig. 2*). The fact that these may be trapezoidal in form means that patterns with sloping sides can be drawn neatly without the rough edges which would occur if the basic elements were simply squares or rectangles. The trapezium generator can operate very quickly because it deflects the beam over only very short distances and so does not need great stability. On the other hand the main deflection circuit has to be able to deflect the beam very much further, and is correspondingly slow. By dividing control of the scanning process between the two units we obtain much greater speed than would be possible using the main deflection system alone.

A further element in the control system is concerned with retaining the focus of the beam so that high resolution can be obtained throughout the pattern. In general it is not possible to make an electron-optical system which is entirely free from aberrations and so an element of compromise in the design is inevitable. In our pattern generator the deflection system has been designed to minimize deflection distortion, but at the expense of appreciable aberrations, such as astigmatism and field curvature, which affect the size and shape of the spot. A precisely square scanning area is obtained which is accurate to within a small fraction of 1 μm throughout. The aberrations affecting the spot are predictable and are continuously corrected as the beam moves about by special circuits within the deflection amplifiers. A spot size smaller than ¼ μm is thus obtained. The fact that such correction is possible is one of the advantages of electron-beam systems compared with their optical counterparts.

The data input to the minicomputer (DEC PDP8) which controls the machine is in the form of lists of the coordinates, shapes and sizes of the trapezia which go to make up the patterns required. These are derived from the patterns themselves by a computer (ICL 1904S) using the CIRCUITMASK [5] language; a special processing program then generates the parameters of the trapezia and arranges them in the order in which they are to be drawn. The result is transferred to the PDP8 on magnetic tape and stored in the disc-memory unit to be called up when required. No further processing is needed. The patterns can be checked visually on a storage oscilloscope connected to the deflection system. Data relating to several circuits may be stored at one time and the computer operator feeds in separate information on how the different patterns are to be arranged together on the mask. This is particularly useful, as it allows the designer to include test patterns and circuit variations on a single mask.

Column and control system

In *fig. 3* a schematic sectional view of the machine is shown. Contrary to the usual practice the column has the electron gun at the bottom, which brings the work chamber to a convenient height for loading. The pumping system is fully automatic; there is a vacuum valve halfway along the column, which closes automatically when the work chamber is opened to load a substrate, so that the lower half of the column remains evacuated. The mechanical stage is propelled by rods which pass through vacuum seals to two ball screws. The screws are driven by stepping motors, each motor step moving the target area 25 μm for a total movement of 44 mm.

The electron gun is of our own design and is aligned mechanically with a little assistance from the beam aligner. The current to the target can be switched off when required by the 'beam blanker' halfway along the column. This works by deflecting the beam sideways so that it cannot reach the target. The deflection is electrostatic, with two sets of plates.

Fig. 4 shows a block diagram of the complete control system of the pattern generator. Some of its important parts and functions will be discussed in more detail in the following sections.

---

[*] The deflection coils directly beneath the electron detectors were designed by Ir R. Vonk and Ing. N. G. Vink of the Philips Video Division, Eindhoven.

[4] The Philips PSEM 500 scanning electron microscope is described by W. Kuypers and J. C. Tiemeijer in Philips tech. Rev. 35, 153, 1975.

[5] See for example C. Niessen, this issue, p. 278.

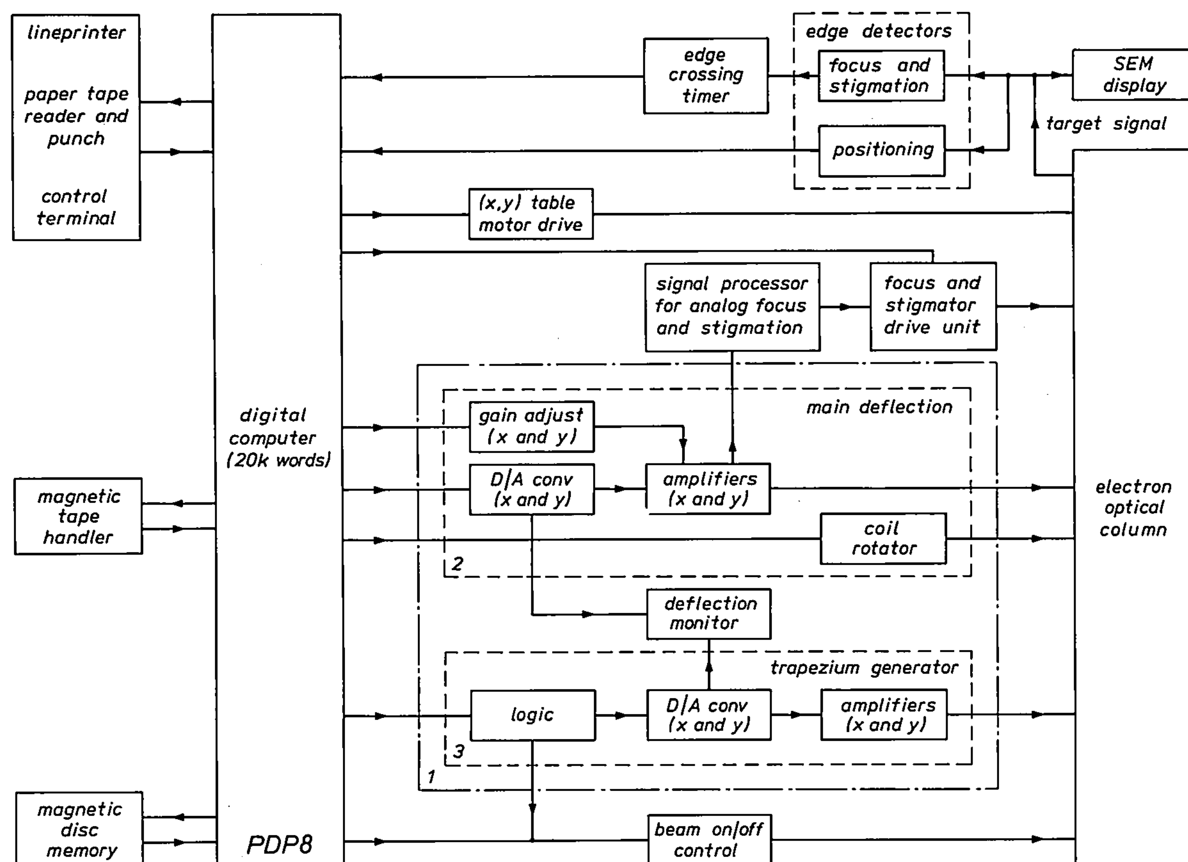

Fig. 4. Block diagram of the control unit. After the substrate has been placed on the table (see fig. 3) and the column has been evacuated, the pattern is drawn almost completely automatically. It is only necessary to feed the digital geometric data into the computer and to adjust the astigmatism-correcting coils (see fig. 3) when starting to draw each mask, so that a beam of circular cross-section is obtained. To the right of the computer, inside the large rectangle *1*, the main deflection system *2* and the trapezium generator *3* are shown, each with their digital-to-analog converters and amplifiers. The circuits at the top of the diagram are used in the investigation of the diameter and cross-section of the beam. This is done by determining the rise time of the signal — originating from electrons back-scattered by the markers — when the beam scans across two perpendicular edges of one of the markers.

The main deflection system

The main deflection system is used to move the electron beam across the 2 × 2 mm scanning area and place it accurately in the position required for each trapezium; control is then assumed by the autonomous trapezium generator. It is controlled directly by the computer via two 15-bit digital-to-analog converters which in turn drive the x and y amplifiers feeding the main deflection coils. The least-significant bit of the converters corresponds to 1/16 μm of deflection.

The size of the electron-beam scanning area is determined by the pattern resolution required and the reproducibility of the beam-scanning system. In this machine the beam diameter is normally about 0.25 μm and the deflection must be accurate to better than this if the resolution is to be fully used; 0.1 μm is usually required. Among the factors which affect the reproducibility of the beam position are drift in the power supplies and deflection amplifiers, eddy currents and build-up of contamination in the column. These limit the total number of separate points in the 2 × 2 mm scanning area which can be addressed to the required accuracy to 10^8. Higher accuracy would entail reducing the scanning area accordingly and the present 2 × 2 mm size was chosen as a suitable compromise.

Special care is taken to ensure that the scanning area is free from distortions, and in particular that its outline is precisely square. This is checked every few weeks using a calibrated substrate with a group of accurately spaced markers, and small electrical adjustments are made to ensure that the element is square to within $\frac{1}{8}$ μm.

The main deflection system does not need the very rapid response time of the trapezium generator but since the deflection distances are much greater some precautions still have to be taken to ensure an adequate

speed of operation. The deflection coils are therefore surrounded by annealed Mumetal rings 0.2 mm thick stacked axially and separated by spacers of the same thickness. The purpose of this is to prevent the magnetic flux from the coils from entering the objective lens where they would generate eddy currents during rapid changes in the deflection fields. These eddy currents would take a long time to decay and so would increase the time taken to stabilize the beam in a new position. As a further precaution the input data is arranged so that the beam does not take large jumps from one part of the scanning area to another. Pattern elements are drawn systematically from top to bottom and left to right, and even when there are no pattern elements to be drawn, the deflection system does not skip the region but moves through it with the beam current switched off. Thus rapid changes of magnetic fields are avoided and the effects of eddy currents and hysteresis in the coils are minimized. The system settles to within 0.03 μm within 100 μs.

The sensitivities of the x- and y-deflection systems are also in the control of the computer and can be varied by a few per cent to change the dimensions of the scanning area.

The trapezium generator

The trapezium generator has a special set of deflection coils which are similar to those of the main deflection system but have fewer turns and so are of lower inductance. The currents through them are determined by a logic unit driving very high speed digital-to-analog converters which feed a pair of fast amplifiers. The positions of the coils and the gain of the amplifiers are carefully adjusted in relation to the main system so that the trapezia are not drawn the wrong size, or tilted with respect to the x- and y-axes. It is also important that the deflection characteristics of the coils should match those of the main system. This is because when blocks are drawn side by side, the width of the blocks (which is determined by the trapezium generator) and their spacing (determined by the main deflection system) must be precisely the same if they are to fit together properly.

The logic unit is the heart of the trapezium generator. It receives from the computer numbers denoting the height, width and edge angles (see *fig. 5*) of the required trapezium and calculates, in digital form, the voltages needed to deflect the beam. These digital signals are applied to digital-to-analog converters which drive the beam to and fro in $\frac{1}{8}$-μm steps over the region in which the trapezium is required. This region can be up to 32 × 32 μm (256 steps), but the beam scans only within the required area, as shown in fig. 5. In this way trapezium shapes (including squares, rectangles and triangles as simple cases) can be filled in very rapidly; at the maximum stepping rate (corresponding to 10 MHz), each one takes at most 6.55 ms. The edges of the figures are reasonably smooth since the step size is somewhat less than the spot size.

Focusing the beam

The size of the spot which the electron-optical system can focus on the substrate determines the fineness of the detail which can be reproduced in the pattern. A number of measures have to be taken to ensure that the spot size is preserved throughout the pattern. The variations arise in three ways: first because the focus of the beam tends to vary during deflection; secondly because even with an undeflected beam the focus may drift slowly with time owing to variations in the EHT supply, build-up of contamination in the column and so forth; and thirdly because the target is unlikely to be exactly flat, nor will the movement of the mechanical stage be perfect, so that the height of the substrate will vary slightly as the stage moves.

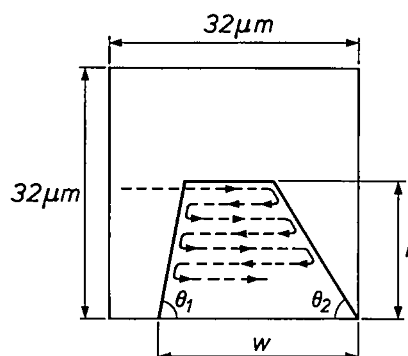

Fig. 5. The trapezium generator receives instructions from the computer indicating the height h, width w and edge angles θ_1, θ_2 of the trapezium. The spot scans in steps of $\frac{1}{8}$ μm in a raster up to 32 × 32 μm, always staying within the required region. At top speed it takes at most 6.55 ms to draw a trapezium.

The current density of the beam has an approximately Gaussian variation with distance from the centre-line. Near the focus the beam is circular in section, or elliptical if there is astigmatism. As the astigmatism does not vary greatly with time or with the position of the cross-section above or below the focus, it is sufficient to correct for it manually at the start of each mask. The variation in the position of the focus is greater: a correction for this is made automatically at the beginning of each 1.9 × 1.9 mm pattern. Both corrections are determined by scanning the beam across two perpendicular edges of one of the markers at a steady speed in an L-shaped pattern. The rise times of the signal as the edges are passed give a good estimate of the size and shape of the spot: two equal and short rise

times denote a narrow well focused beam; long and unequal rise times indicate that the beam is diffuse and elliptical. The information obtained from this measurement is used to adjust the current in a focus coil and in two astigmatism-correction coils (stigmators) which can be used to adjust the size and shape of the beam. The focus coil is a simple air-cored solenoid. The astigmatism is corrected by a pair of magnetic quadrupole lenses: one of these has its major axes parallel to the x- and y-directions of deflection, while the major axes of the other are rotated through 45°; see *fig. 6.* To find the value which gives the best focus a series of measurements are made as the focus-coil current is altered in small steps. When the stigmators have been adjusted, the currents in the stigmators and the focus coil are varied until the shortest possible rise times have been obtained. It is not sufficient to make the rise times equal; an elliptic spot inclined at 45° to the marker edges will also give equal rise times but they will be longer. Only *small* rise times provide a guarantee that the beam is free from astigmatism.

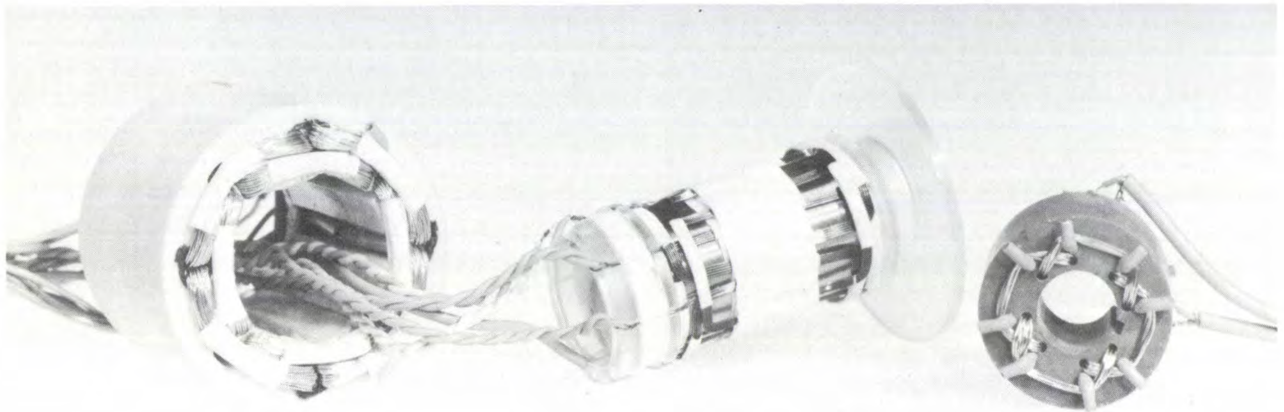

Fig. 6. The focus coil (*centre*), the coils for correcting astigmatism (the stigmators, *left*) and a coil for scanning the substrate (when the column is used as an SEM). Each stigmator consists of four vertically wound coils forming a magnetic quadrupole. One unit is aligned with the x- and y-axes, the other is at 45° to them. The focus coil is a simple solenoid, with compensating coils placed around it to improve the symmetry of the field. In reality it is mounted inside the stigmators.

As the deflected beam moves away from the marker new aberrations arise which depend on the position of the spot. The chief ones are curvature of the surface of best focus, which means that the beam reaches a focus which may be slightly above or below the target surface, and astigmatism. The aberrations do not change appreciably with time or with small variations in the height of the target. They can therefore be measured once and for all when the machine is made and the necessary corrections can be built into the design of the deflection amplifiers. The currents in the x- and y-deflection coils are monitored and a current proportional to $(x^2 + y^2)$ is applied to the focus coil to compensate for the known curvature of the focal surface. This is a well established technique used in some cathode-ray-tube displays. In addition, signals proportional to xy and $x^2 - y^2$ are used to derive the currents to the stigmator coils to correct for the known astigmatism. These corrections maintain the size of the spot substantially constant throughout the 2×2 mm scanning area.

A large number of the electrons in the beam pass through the layer of electron resist and into the substrate, where some are scattered and reflected back into the resist again a small distance from the point of entry. These 'back-scattered' electrons broaden the skirts of the intensity distribution in the spot. The effect of this is that the size of the pattern elements after development is altered by the presence of surrounding pattern material. This 'proximity effect' becomes important only for details of less than about 1 μm. In our machine we overcome the problem by increasing the dimensions of fine details in the pattern specification to compensate for the expected reduction during processing. This is readily done during processing of the pattern data before it is fed into the minicomputer.

The marker system

The manufacture of integrated circuits usually requires the use of several masks which are exposed successively on to the same silicon slice (*fig. 7*). Very often the final circuit contains patterns defined inside

each other by the successive masks and the relative positions of the masks are then at least as critical as the resolution of the fine details. The PRL electron-beam pattern generator can define pattern elements 1 μm wide to an accuracy of 1/16 μm and it must therefore be possible to align different masks to much the same accuracy. This could be achieved with a laser interferometer to control the mechanical stage, but an alternative, used here, is to rely on an accurate array of markers on the substrate; this can be located by the electron beam and used as a reference. The markers are deposited on the substrate before the processing in the machine begins.

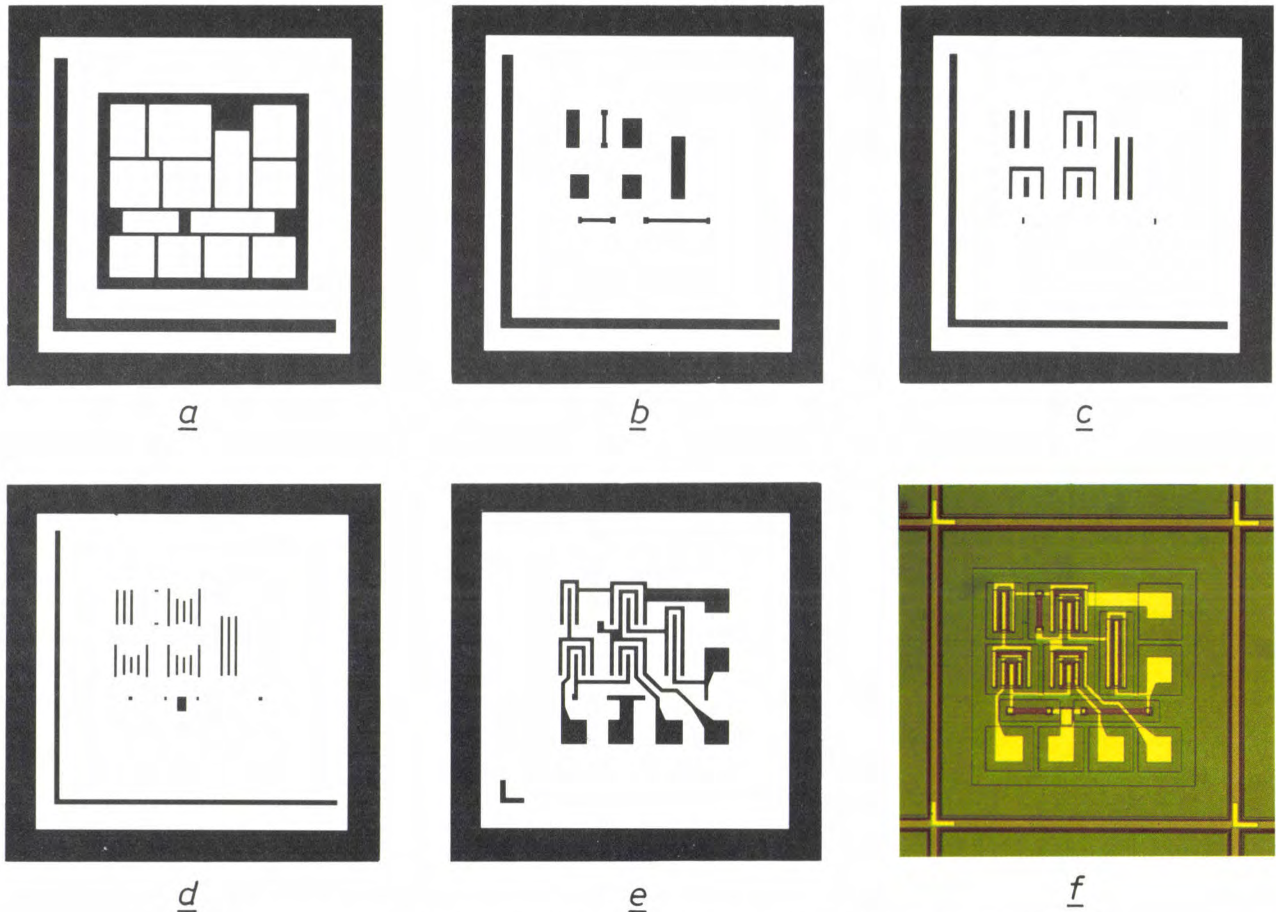

Fig. 7. A set of optical masks (*a-e*) used in making a simple integrated circuit (*f*). Magnification 40×. In conventional mask-making a simple pattern such as one of these (usually called a 'reticle') is repeated on a special 'step-and-repeat' camera to make a mask containing a large number of identical units in a two-dimensional array. The electron-beam pattern generator makes the complete mask directly from data stored in the controlling minicomputer; several different types of pattern can easily be included on the same mask if required. (This figure is taken from F. T. Klostermann [6].)

If, as is usually the case, each subunit is used for a separate circuit it is not necessary that all the markers should be equally spaced; it is necessary only that their positions should be identical for all the masks of a set. This is relatively easy to arrange if all the marker arrays for a particular set of masks are derived from the same master, using an electron-image projector or are defined using a very accurate optical repeater.

The markers are 20×20 μm squares and are arranged in a square with spacing of 1.9 mm so that each 2×2 mm area encompasses 4 markers at a time. The mechanical stage is used to position the substrate to ± 100 μm and the electron beam then searches a 128×128 μm square around the expected position to locate each marker precisely. The beam exposes the electron resist around the marker during the search and so regions of about 200×200 μm around the markers cannot be used for pattern making. The position of the markers is detected by the electrons back-scattered as the scanning beam passes over them and the marker material must, as well as being chemically compatible with the substrate, be such as to give a good back-scattering contrast with it. This means in practice that the

atomic number of the marker material must be very different from that of the substrate. Gold (atomic number $Z = 79$) and tantalum ($Z = 73$) are suitable for markers of chromium ($Z = 24$) on glass; tantalum is preferred for use on silicon ($Z = 14$) because it is compatible with the further processing of the device. It is usual to protect tantalum markers with a thin layer of silicon nitride, which does not unduly affect their back-scattering properties.

The markers are used to adjust the deflection system every time the mechanical stage is moved to present a new 2×2 mm scanning area to the beam. The procedure consists of 6 steps as follows; see *fig. 8*.

— The substrate is moved to bring four markers into one deflection area (*K*, *L*, *M* and *N* in fig. 8).

— Marker *K* is located by moving the beam rapidly over the surface in a raster covering a 128×128 μm square (the 'coarse search'). The centre of the marker is then defined accurately in terms of the beam-deflection coordinates by a 'fine-positioning' routine. The beam is stepped eight times across each edge of the marker in turn taking very small steps (1/16 μm), and the effective *x*- and *y*-coordinates of the centre are calculated from the signals received. Fine positioning takes about 80 ms and is repeatable within ± 1/16 μm for markers of 20×20 μm. The beam focus is checked and adjusted at this stage.

— A second marker *L* is found in the same way. The computer checks that the *x*-coordinates of *K* and *L* are identical; if they are not, owing to residual rotational errors in the mechanical stage or to the slight rotation of the deflection field in focusing, then the error is corrected by rotating the deflection coils about the column axis. This, too, is done under computer control.

— A third marker *M* is located and the sensitivities of the *x*- and *y*-deflection amplifiers are adjusted by the computer until the distances *KL* and *LM* as measured by the deflection system are both 1900 ± 1/16 μm. This completes the setting-up procedure for the area *KLMN*.

— The pattern is now drawn in this area. The setting-up procedure has ensured that distances and angles specified in the data will be accurately reproduced on the substrate. However, the coordinates of the details in the pattern as specified in the data are taken relative to the marker system. A simple translational adjustment has to be made to the coordinates during scanning to take account of the fact that owing to the inevitable inaccuracies in the mechanical stage the measured positions of the markers will always be slightly different from those expected.

— Finally, the substrate is moved until the next four markers, *MNOP*, appear in the scanning area and the process is continued.

For experimental purposes it is sufficient to draw a separate circuit in each subunit, but for production it may often be necessary to join patterns in several neighbouring subunits to form larger circuits. The deflection field has been tailored to have a precisely square outline to within a fraction of 1 μm, so the scanning system is capable of retaining its accuracy over a larger pattern provided that the array of markers can be made sufficiently regular. This is not a simple matter as a set of marker masks are needed, each of high accuracy. The best available step-and-repeat cameras [6] are capable of maintaining the marker spacings constant to about 0.1 μm, which is adequate for the present state of integrated-circuit development, and

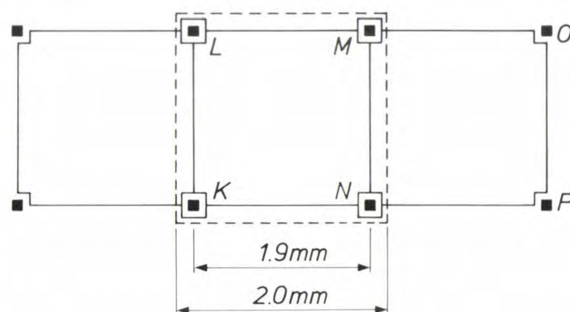

Fig. 8. Illustrating the use of markers for pattern registration. Markers *K*, *L* and *M* are located separately and the sensitivities of the *x* and *y* amplifiers are adjusted so that the distances *KL* and *LM* as measured by the deflection system are identical. The *x*-coordinates of *L* and *K* are checked and, if they are not identical, the deflection-coil assembly is rotated round the column to compensate.

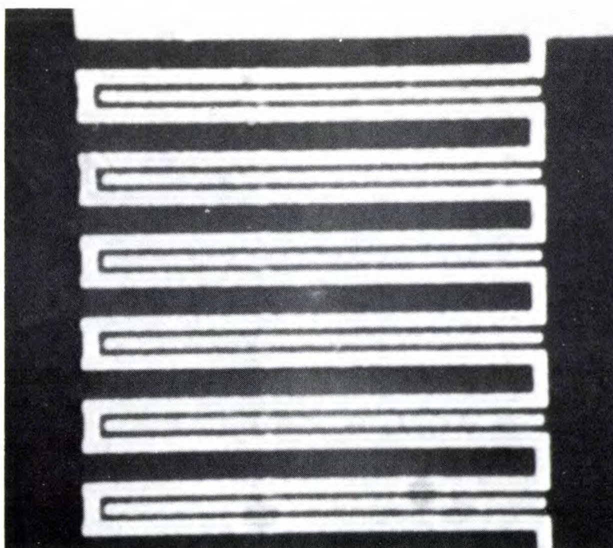

Fig. 9. Illustrating the accuracy with which a pattern can be placed in position. Two patterns were etched in chromium at different times; the substrate was removed from the machine between the two etchings. The mesh width of the pattern is 10 μm.

[6] See F. T. Klostermann, Philips tech. Rev. 30, 57, 1969.

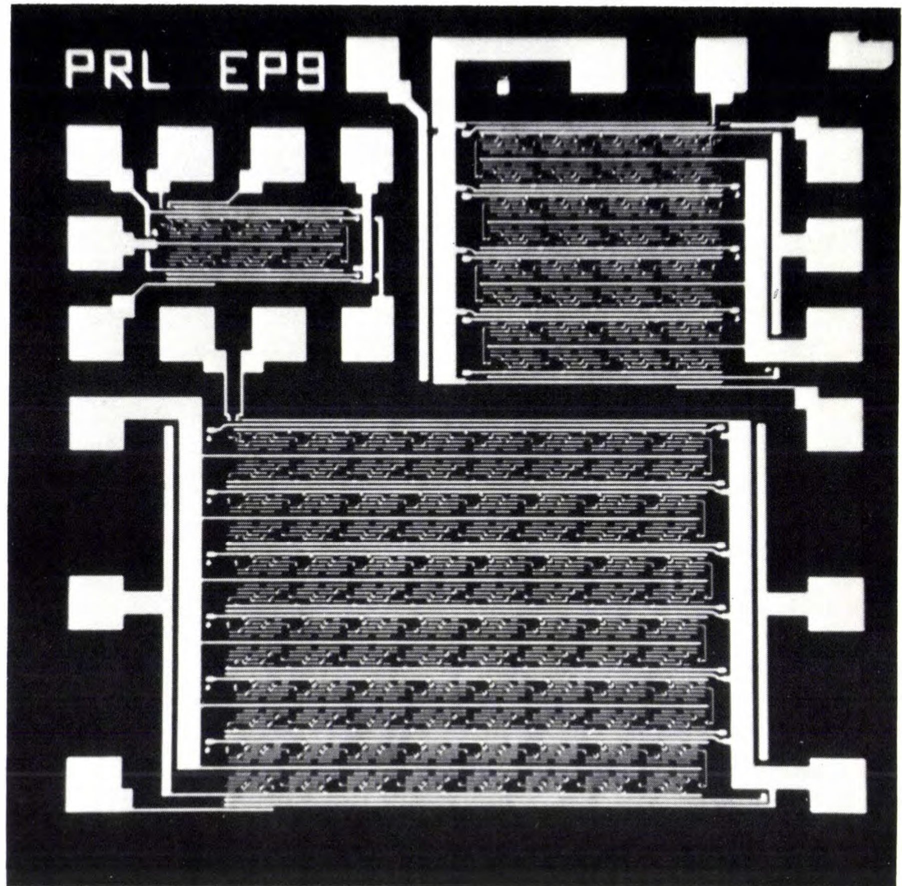

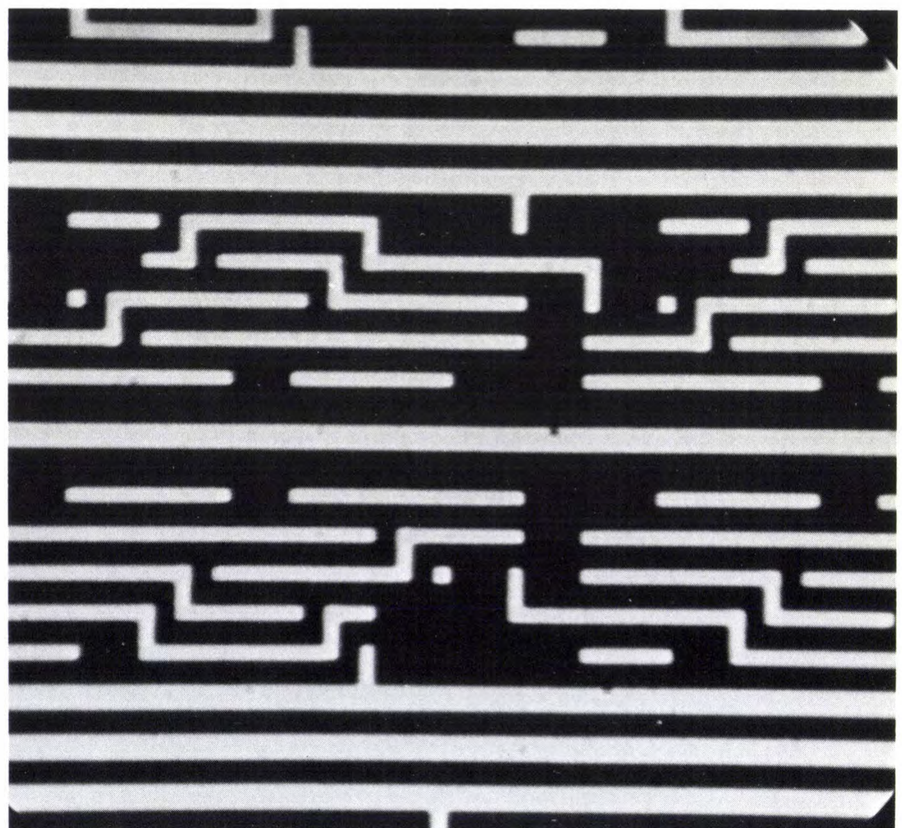

Fig. 10. Part of a mask for making metal interconnections for integrated circuits. The photograph shows how much detailed information can be present in a pattern.

one possible approach is to generate all the masks of the set separately on such a machine. An alternative is to make one master mask on a step-and-repeat camera and then copy it accurately to produce the other members of the set. It is found in practice that small but significant inaccuracies are introduced by conventional copying processes; the best method appears to be to use a high-accuracy electron-image projector such as that described in the article by J. P. Scott [2].

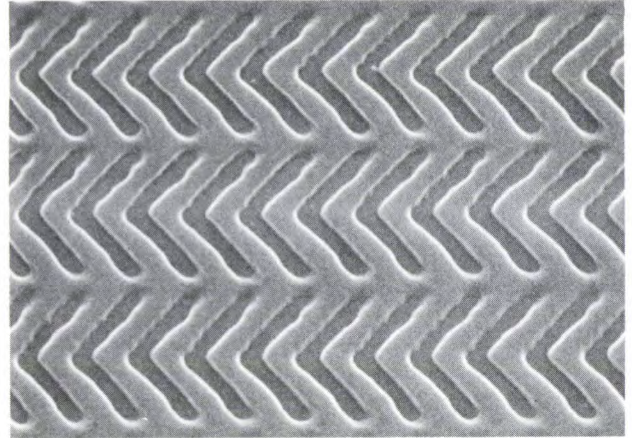

Fig. 11. Circuit for magnetic bubbles. Track width 0.5 μm.

Performance of the machine

The main criteria by which a mask-making machine should be judged are its speed, the positional accuracy of the patterns and the quality of the masks produced.

Speed

For patterns with low coverage, the dominant factor that determines the speed of operation is the time taken to move the mechanical stage; for complex patterns with high coverage the trapezium generator takes the most time.

The time taken to move the substrate so that all subunits have been covered and to adjust the focus of the beam and the gain and rotation of the deflection system is about 20 minutes for a 22 × 22 array of patterns making a 42 × 42 mm mask. Much of this is settling time to allow the mechanical table and the coil rotator to come to rest. A considerable reduction of this time is possible.

The trapezium generator takes 6.4 seconds to cover a 1-mm square, so to cover one third (a typical fraction for a high-coverage pattern) of a 42 × 42 mm mask takes about 60 minutes. To this must be added the settling time needed between trapezia to allow the digital-to-analog converters, the deflection amplifiers and the eddy currents induced in the metal parts to settle down. This takes about 100 μs, so for, say, 600 circuits each with 10^4 trapezia a further 10 minutes must be added for the settling time. Loading and unloading the substrate, pumping down and starting the program takes only 2 to 3 minutes. Adding up all these times, the total time for a 42 × 42 mm mask is in the range 1 to 3 hours, depending on the proportion of the area taken up by the pattern.

Positional accuracy

The machine was designed to make mask patterns with a positional accuracy of $\frac{1}{8}$ μm and this target has been reached. Reproducibility of pattern position can be measured by writing two images on the same substrate, which is removed from the holder and replaced between the two writings, with the same markers being used for registration on both occasions. *Fig. 9* shows

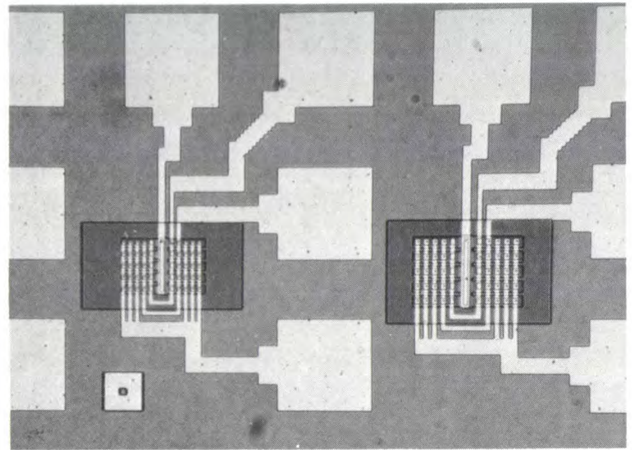

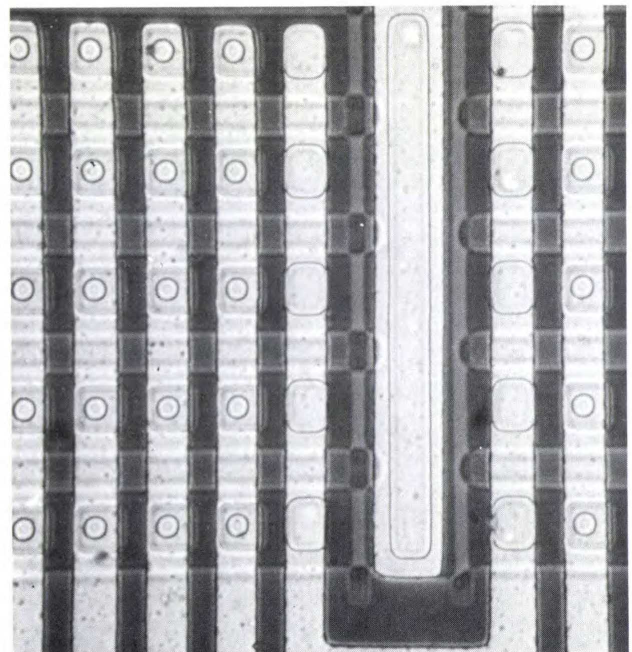

Fig. 12. Integrated circuit written directly on the slice by the electron beam. The smallest track width is 2 μm. The lower photograph shows a detail.

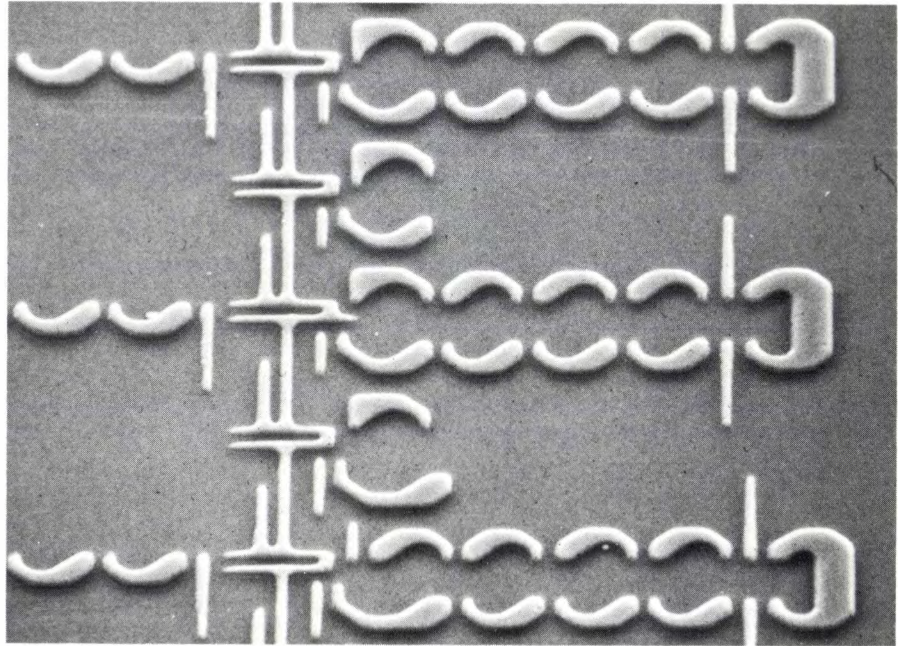

Fig. 13. Part of a magnetic-bubble circuit of permalloy, made by the electron-image projector [2], starting from a mask drawn by the electron-beam pattern generator. Since this machine assembles figures from trapezia whose shape and dimensions can be freely chosen, it can give very complicated shapes with smooth contours. The width of the narrowest tracks is 1 μm.

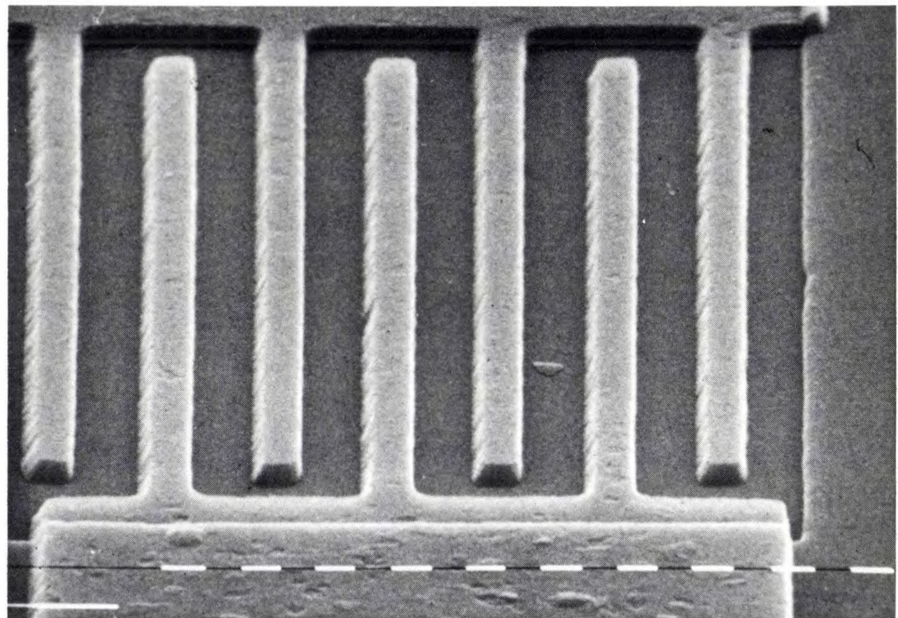

Fig. 14. Aluminium tracks on silicon made from a pattern written directly on the slice. The tracks are 1 μm wide. (The scale is in units of 1 μm.)

two such images etched in chromium. The alignment is very satisfactory. This level of precision is obtained except where there are very obvious defects in the markers.

Pattern quality

The quality of the patterns obtained with the electron-beam pattern generator can be seen from figs. 10 to 14; these are photographs made during the last two years. *Fig. 10* is a part of a mask for making the metal interconnections for experimental integrated circuits and shows how much information such a pattern can contain. *Fig. 11* is a pattern with 0.5-μm details, demonstrating the resolution that can be obtained. The very high resolution can also be seen from *figs. 12* and *13*: fig. 12 shows an integrated circuit written directly on the slice; fig. 13 shows a number of patterns for magnetic-bubble circuits, with a smallest line width of 1 μm. Finally, *fig. 14* shows 1-μm aluminium tracks on silicon; this pattern was again written directly on the slice.

New developments

A new research machine is now being commissioned which will handle 100-mm slices and will incorporate a number of improvements suggested by the experience of two years' operation. Among these will be a new mechanical table using a laser-based measurement system which improves the positioning accuracy and so overcomes the need for closely spaced markers. In some cases the presence of these markers is very undesirable, for example in VLSI circuits and in surface-acoustic-wave devices, both of which require an uninterrupted pattern over a large area.

Measures are also being taken to improve the settling time, and as a result the new machine will be several times faster; indeed an increase of at least ten times the speed of writing can be expected in the more distant future. This may make direct slice writing a reasonable commercial proposition.

Summary. An electron-beam machine for making complex and precise patterns such as those required for integrated circuits is described. A 0.25-μm diameter beam of electrons controlled by a computer draws patterns on a metallized substrate covered in electron-sensitive resist. After development and etching a pattern is produced (maximum dimensions 42×42 mm) which can be used directly or as a mask to be copied by other means. A two-stage deflection system is used. The first stage (relatively slow) deflects the beam to within a 2×2 mm square, the second stage (relatively fast) draws the appropriate part of the pattern inside the square. The pattern is made up from trapezia of maximum size 32×32 μm. The patterns can be positioned to an accuracy of $\pm \frac{1}{8}$ μm with the aid of a set of markers predeposited on the substrate. A complete mask containing details as small as 0.5 μm takes 1 to 3 hours to draw.

Electron-image projector

J. P. Scott

Background and principles

The article by J. P. Beasley and D. G. Squire [1] has described how an electron-beam machine can be used to make the very fine patterns which are increasingly in demand in modern integrated-circuit technology. The machine draws the pattern directly on to an electron-sensitive resist, coating the substrate on which the pattern is to be produced, and can achieve substantially greater resolution than can be obtained by optical methods. The technique is accurate and effective but the large patterns required in making integrated circuits on a slice (or wafer) take a long time to make. This makes the process unsuitable for the mass production of low-cost circuits. The solution to the problem is to use the electron-beam machine to make a master copy of the required pattern and then use other means to reproduce this cheaply and in large numbers. Clearly, optical methods cannot be used in the reproduction process since the reason for using electron-beam techniques in the mask making is to increase the resolution beyond the intrinsic limits of optical processes. An alternative approach with many advantages is to use electrons in the copying process. A machine which does so, called an electron-image projector, is the subject of this article.

The mask to be reproduced is first drawn by an electron-beam pattern generator on a layer of electron resist [2] covering a metallized quartz substrate. After processing, the required pattern is left on the substrate as metallization. The substrate is then coated with a thin layer of photoemitter which will release electrons when illuminated by ultraviolet radiation. If the illumination is from the back of the substrate electrons are only released where there is no metal.

In the electron-image projector, which is shown in *fig. 1*, the completed mask *M* is placed in an evacuated chamber some distance from the silicon slice *Si* on which the IC is to be produced. The slice is coated with an electron-sensitive resist. In the present machine the slice diameter is restricted to 50 mm but in an improved version, now being made, this is increased to 100 mm. Both mask and slice are situated in a magnetic field and a high voltage is connected between the mask and the silicon slice. The mask is now illuminated with ultraviolet light, which causes electrons to be emitted from the photoemitter behind the clear parts of the mask but not from the opaque regions. The electrons are accelerated by the electric field and focused by the combination of magnetic and electric fields [3] so as to produce an accurate image of the clear areas of the mask on the substrate. In this way the pattern can be transferred rapidly from the mask to the silicon slice at unit magnification.

J. P. Scott, M.A., Ph.D., was formerly with Philips Research Laboratories (PRL), Redhill, Surrey, England.

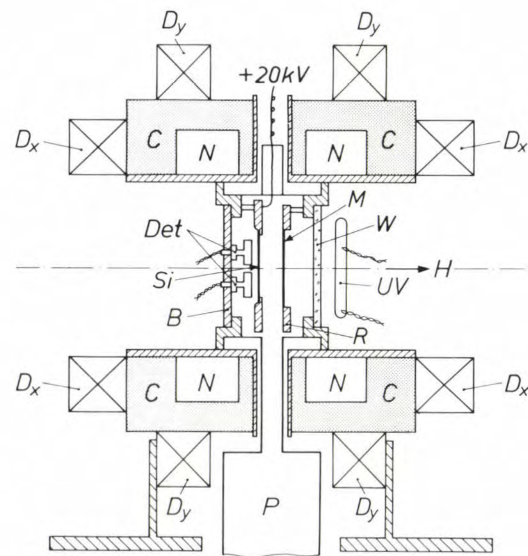

Fig. 1. Schematic cross-section of the electron-image projector. *M* is the mask, which is coated with a layer of caesium-iodide photoemitter and *Si* the silicon slice to be exposed, covered in an electron-sensitive resist. *M* and *Si* are situated in a vacuum chamber closed by the window *W* and the disc *B*. The chamber is pumped via a port *P*. Outside the vacuum, to the right of the window, is the ultraviolet lamp *UV*. The radiation from this lamp (184.9 nm) causes electrons to be emitted by the photoemitter behind the clear areas of the mask. The electrons are accelerated to *S* by an electric field (15 kV/cm) and focused by the highly uniform magnetic field *H* (about 1 kOe) provided by the split solenoid *C*, with correction notches *N*. The projected image is aligned in the *x*- and *y*-directions by means of currents through the deflection coils D_x, D_y; rotational alignment is provided by mechanical rotation of the mask holder *R*. Alignment signals are obtained by markers on the slice which emit X-ray signals which are detected by the solid-state detectors *Det*.

[1] J. P. Beasley and D. G. Squire, this issue, p. 334.
[2] See for example E. D. Roberts, Appl. Polymer Symp. **23**, 87, 1974.
[3] The basic idea of the electron-image projector was first proposed by T. W. O'Keeffe, J. Vine and R. M. Handy, Solid-State Electronics **12**, 841, 1969, and is sometimes called the Westinghouse system.

This method of reproducing patterns at very high resolution on silicon slices was first proposed in 1969 [3], but until recently has suffered from certain difficulties of operation which have prevented its widespread use. The present paper describes a number of improvements introduced at PRL which have made the method more generally applicable for the production of integrated circuits. The developments to be discussed are the use of caesium iodide as the photoemitter, a new design for the magnet and a method of automatic alignment using Bremsstrahlung X-rays, including improvements to the signal detection and processing. A final section describes some of the results obtained by one of these machines during two years of use in an experimental silicon-processing unit. *Fig. 2* shows a photograph of the electron-image projector.

The caesium-iodide photocathode

The photocathode material most commonly used in work on electron-image projectors has been palladium. The unsatisfactory behaviour of this material has been one of the major problems in the development of these machines and this has led us to search for an alternative. As a result of the search we have chosen caesium iodide (CsI), which fulfils all the major requirements for use in a mass-production machine. These are: ease of preparation, stability in air, reliable operation in relatively poor vacuum, and a stable photocurrent of at least 1 μA/cm^2.

Palladium is to some extent unsatisfactory in all of these respects except that of photocurrent density. It is very prone to contamination and in particular to the effects of minute traces of oxygen and water vapour. Thus its properties change when it is exposed to air, and it requires high-vacuum conditions (about 10^{-7} torr, i.e. 10 μPa) for effective operation. Even then the photocurrent is not reliable and may vary up to 50% during exposure because of the effects of contamination. The material is also difficult to prepare, and, because concentrated acids are required to remove it, special materials must be used for the mask so that it is not damaged during replacement of the photocathode.

A further requirement which involves the photocathode is that the energy of the electrons emitted when the photocathode is illuminated should be less than about 1 eV. This is because a large range of initial energies will produce the electron-optical equivalent of chromatic aberration in the image, impairing the resolution and depth of focus [4]. To achieve this one needs to select the right combination of lamp and photoemitter material. The essential requirement is that the quantum energy of the illumination must be only slightly higher than the work function of the photoemitter, because the emitted electrons will have a range of energies between zero and the difference between the work function and radiation energy. The lamp must be intense and monochromatic and the photoemitter must have a high and preferably unvarying emission less than 1 eV above its threshold.

To obtain high emission close to the threshold, the photoemitter should have a high density of states within 1 eV of the top of the highest filled band and a high escape probability. This suggests that insulating ionic crystals, which have valence bands generally narrower than the filled conduction bands of metals, should be suitable. In addition, these materials often have a large mean free path for the excited electrons, which results in a greatly increased escape probability for electrons excited deep inside the material.

In seeking a photocathode which is stable in the presence of air one can use the simple rule of thumb that the work function should be higher than 6 eV. This rule rests on the fact that the electron affinity of oxygen is 6 eV; if the work function is more than this it is likely to be energetically unfavourable for the oxygen to take an electron from the photocathode. This is a rather simplistic view of course, but it gives a useful pointer.

The above considerations give an indication of the wavelength limits of the source of illumination; a high-intensity source of photons of between 6 and 7 eV is required. A readily available source meeting this requirement is the low-pressure mercury-discharge lamp (wavelength 184.9 nm, photon energy 6.70 eV).

Among the materials most suitable as photoemitters for our purpose are ionic insulators such as alkali and other halides; the best is caesium iodide. Its work function is about 6 eV, so the photoelectrons emitted when illuminated by the Hg line at 184.9 nm have a maximum initial energy of about 0.5 eV. The average value is 0.3 eV.

The combination of caesium iodide and a low-pressure mercury lamp has two disadvantages. First, caesium iodide is an insulator so it is necessary to provide a conducting layer transparent to radiation at 184.9 nm between the CsI and the substrate. Secondly, the 184.9-nm radiation dissociates oxygen, leading to the formation of ozone, so the parts of the projector that are subject to the ultraviolet radiation have to be contained in an inert atmosphere such as nitrogen. Cleanliness is necessary in the vacuum part of the equipment, for any atomic oxygen formed there attacks residual organic matter; this results in breakdown of insulators and rapid deterioration of the photocathode.

These disadvantages are outweighed by the many advantages. The chief of these is that, as its high work function indicates, CsI is stable in dry air and requires

[4] J. P. Scott, Electron and ion beam science and technology, 6th int. Conf., San Francisco 1974, p. 123.

a vacuum of only 10^{-4} torr (10 mPa) for use as a photo-emitter (palladium cathodes require 10^{-7} torr, i.e. 10 μPa). It is therefore possible to open the apparatus to insert each silicon slice and to pump down the chamber quickly for each exposure. As a result the complete exposure cycle for each slice is less than three minutes, and the handling of the slices is a simple operation.

Another advantage is that the caesium-iodide layer is very easily prepared by sublimation at about 600 °C, and moreover can be simply rinsed off with water when a new layer is needed. The whole renewal operation takes only a few minutes.

In operation the CsI photocathodes give a lower current density than the Pd cathodes (20 μA/cm², compared with 100 μA/cm²) but the stability is far better; the current variation during exposure is less than 3 %, compared with 50 % for palladium. Up to fifty exposures can be made before renewing the layer.

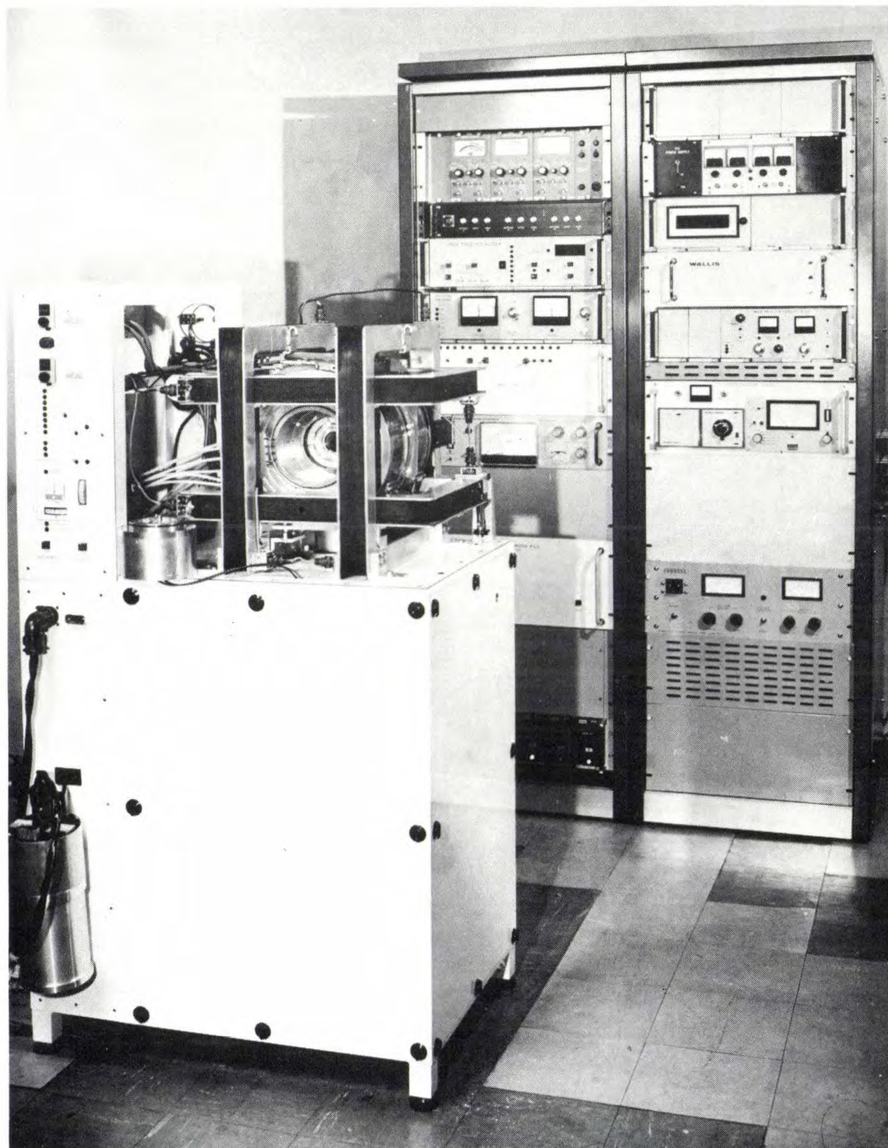

Fig. 2. Photograph of the prototype electron-image projector. The most prominent features visible are the deflection coils and the split solenoid. The vacuum pump is housed beneath the projector. Power supplies and all the electronics are situated in the two racks in the background.

The focusing solenoid

The electrons emitted from the photocathode are accelerated to the anode (the silicon slice with its electron-resist coating) by a voltage of about 20 kV, and focused by a magnetic field of about 80 kA/m (1 kOe) parallel to the direction of motion. The position of the focus depends on the magnitude of the

field, which has to be uniform to a few parts in 10^5 over the whole area of the silicon slice in order to keep the image distortion below 0.1 μm.

The design of the magnet which provides the focusing field has a major influence on the general configuration of the whole machine, as it determines the position of the pumping ports and the ease with which the silicon slices and the photocathodes can be introduced and extracted. A simple solenoid which would attain the required degree of uniformity would be unsuitable because of the restricted access to the central region of the field. We use a split solenoid giving good access from each end and consisting of two coils separated by a gap where the pumping port can be introduced; see *fig. 3*. In order to attain the required uniformity of field at the centre, the longitudinal section of the coil has rectangular 'notches' taken out of the windings – a principle well established for long solenoids but not hitherto developed for split coils [5]. A notch in the windings is equivalent to a small superimposed coil with current running in the opposite direction to that in the main coil, and the field from this can be adjusted to cancel out the more important non-uniformities in the field of the main coil.

Owing to the application of the principles mentioned above, our solenoid is substantially smaller and lighter than conventional designs and gives better access to the central field region. Its field is uniform to within 3 parts in 10^5 over a 50-mm disc about the centre of symmetry.

The magnetic field near the centre of a simple split solenoid can be described in terms of polynomials whose second and higher order terms represent the non-uniformity. With careful design the field from a second coil system with current in the opposite direction (equivalent to a notch) can cancel out the two lowest-order error components without much reducing the central field.

In any configuration of cylindrical symmetry with a plane of symmetry at the origin, as in the case of a simple solenoid (*fig. 4*), the axial and radial fields H_z and H_r at a point (r,θ) (spherical polar coordinates, origin at centre of symmetry, O) can be written as follows [5,6]:

$$H_z(r,\theta) = H_0 \left[1 + E_2 \left(\frac{r}{a}\right)^2 P_2(u) + E_4 \left(\frac{r}{a}\right)^4 P_4(u) + \ldots\right],$$

$$H_r(r,\theta) = H_0 \left[E_2 \left(\frac{r}{a}\right)^2 P_2'(u) + E_4 \left(\frac{r}{a}\right)^4 P_4'(u) + \ldots\right].$$

Here a is the inner radius of the windings, and H_0 is the field-strength at the centre of symmetry, given by:

$$H_0 = F\lambda ja,$$

where j is the current density, λ the filling factor, i.e. the ratio of the total cross-section of all the conductors in the coil to the cross-section of the coil itself. The quantity F is the 'field factor', which depends only on the geometry of the solenoid. The functions $P_2(u)$, $P_4(u)$,... are Legendre polynomials of the variable u, where $u = \cos\theta$; $P_2'(u)$, $P_4'(u)$,... are the derivatives with respect to u. The error coefficients E_2, E_4,... depend only on the geometry, like the field factor F. Because the expansions are made about the centre of symmetry, the coefficients E_1, E_3, ... are zero.

In choosing the superimposed coils j, λ and a were kept the same as for the main coil (so that the currents will cancel) and we chose the geometry such that the error coefficients $E_2{}^s$ and $E_4{}^s$ for the superimposed coil are much larger than for the main coil while the field factor F^s is smaller by the same factor. Thus the products $F^sE_2{}^s$ and $F^sE_4{}^s$ are made equal and opposite to FE_2 and FE_4 and the two lowest-order error coefficients will cancel out. The corrected field has magnitude:

$$H_0' = \lambda ja(F - F^s).$$

Thus by introducing a notch, which is equivalent to a superimposed coil, it is possible to design a solenoid with a slightly reduced magnetic field corrected to the fourth order. This is sometimes called a 'sixth-order' solenoid because deviations from the value H_0 are proportional to the sixth power of the distance from the centre. The magnitude of the sixth-order error is itself very small and the non-uniformity of the field can be kept to 10^{-5} over a usable volume.

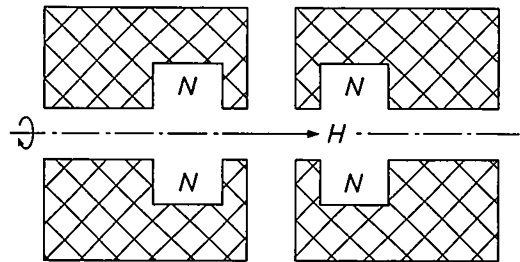

Fig. 3. Split solenoid with notches N. The notches are taken out of the windings to improve the uniformity of the field.

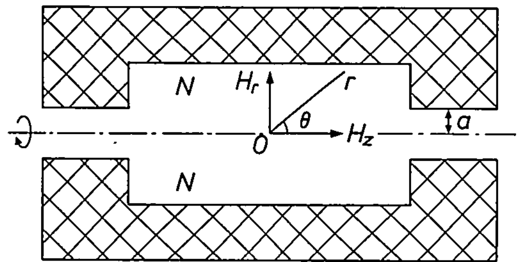

Fig. 4. Cross-section of a simple solenoid with one notch and system of coordinates relating to the calculation of its magnetic field H.

For a split solenoid as in fig. 3 the calculation is more complicated because of the additional parameters associated with the gap. There are now six variables defining the magnet (the length and diameter of the windings, the length and diameter of the notches, the gap between notches and the gap between the coils) and four constraints: the specified field; H_0; E_2 zero; E_4 zero; and minimum power. It is not normally necessary to set E_6 to zero.

In practice the requirement of minimum power leads to two useful rules of thumb for the design. First, the gap between the notches should be between $0.6a$ and $0.8a$. Secondly, the gap

between the coils should be kept to a minimum and, in any case, less than 0.6a. For larger gaps it is not possible to achieve compensation merely by taking a notch out of the windings; two separate split-pair magnets with currents flowing in the opposite sense are necessary, which wastes power. With the aid of these rules the equations may be solved to give a sixth-order field of a given strength, using minimum power. However, the process is intricate and lengthy even with the aid of a computer.

Automatic alignment

Integrated-circuit manufacture usually involves several steps using separate masks, which must be accurately aligned relative to one another. Usually the positional accuracy has to be comparable with the resolution of the finest detail in the pattern. In a machine intended for use in production it is clearly important to have an alignment system of the required precision which is both rapid and automatic. This has posed some difficult problems, mostly because of the restrictions on the ways of detecting a signal from a set of alignment markers. The detection of secondary electrons (which is the method used in the electron-beam pattern generator described in the article by Beasley and Squire [11]) is not possible, for electrons are trapped in the vicinity of the marker by the high electric and magnetic fields.

Instead we have adapted a method which uses the Bremsstrahlung X-rays generated by electrons striking markers of a heavy element on the slice [7]. In this method a marker grid (typically of tantalum oxide) is deposited on the silicon slice and an identical pattern is etched in the mask. When the projected image of the grid on the mask is exactly aligned with the tantalum-oxide grid on the slice, all the electrons from the mask grid fall on the tantalum oxide. If there is misalignment, however, some of the electrons fall on silicon, which is a less efficient generator of X-rays. Thus when the alignment is perfect, the X-ray output is a maximum. Detectors mounted behind the slice convert the X-rays which have passed through the slice into electrical signals. The point of maximum intensity is found automatically.

In our machine we use semiconductor X-ray detectors — this permits rapid alignment. The signals produced by the X-ray detectors are applied to a phase-sensitive circuit, which simplifies the electronics. These aspects will be described in more detail below. Two marker grids are used, one on either side of the pattern, so that both rotational and translational displacements can be readily detected. The translational corrections are made by the deflection coils but the rotations cannot be made in the same way without introducing unacceptable distortion of the image. Mechanical rotation of the mask holder is used instead.

Detecting the X-ray signal

Geiger-Müller tubes are the most widely used means for detecting X-ray signals, but they are not suitable for our purpose because they are limited to a count rate of about 10^4 per second. This implies long counting times to get sufficient counts to keep statistical fluctuations low, and hence a long time — typically about a minute — for the alignment. Semiconductor detectors, on the other hand, can be used at very high count rates and so signals with acceptable fluctuations can be obtained in one or two seconds. This makes semiconductor detectors preferable in spite of the fact that they have high background noise and are rather sensitive to interfering signals.

With these detectors the alignment can be carried out during the first 10% of the pattern exposure. In practice we use a 20-second period at a reduced dose rate to allow time for the rotation of the mask holder. The rest of the pattern is also being exposed during alignment, but this does not normally show in the developed image; there is also the great advantage that separate illumination is not required for the markers.

Processing the output from the detector

When the image of the marker pattern on the mask is swept over the matching pattern on the substrate the electrical signal produced by the detector is a triangular function of the image movement. This does not lend itself to automatic control because alignment occurs when the signal is a maximum, which is difficult to detect, particularly in the presence of noise. This is made worse by the very large d.c. leakage current from the solid-state detectors (normally about 1000 times larger than the signal to be detected).

We have therefore adopted a phase-sensitive detection method which rejects the d.c. component and produces a signal which passes through zero when the patterns are aligned. A small alternating current is passed through the deflection coils, which makes the image move regularly backwards and forwards over the marker and so causes a modulation of the detector signal. This a.c. signal is passed into a phase-sensitive detector, which compares its phase with that of the modulating current through the deflection coils. The output signal is proportional to the misalignment, being zero at the point of perfect alignment, and its sign indicates whether the error is to the right or to the left. The method requires relatively simple analog circuits and has the additional advantage that the x-axis and y-axis corrections can be made simultaneously by using

[5] J. P. Scott, J. Physics E 7, 574, 1974.
[6] D. B. Montgomery, Solenoid magnet design, Wiley-Interscience, New York 1969.
[7] B. Fay, 3e Colloque Int. A.V.I.SEM 71, Versailles 1971, p. 163.

different modulation frequencies for the two directions. The rotation-error signal is derived from the difference in the x signals from the two markers on either side of the mask.

Because the basic signal is triangular and not sinusoidal the modulated signal contains harmonics of the modulating frequency. The higher harmonics can be removed by filtering, but the lower ones must be left in because a filter which would remove them would also affect the phase of the component at the modulating frequency. For this reason the modulation frequencies used for the x- and y-axis corrections must be such that none of their low harmonics coincide either with each other or with harmonics of the mains frequency (50 Hz) which may be present through pick-up. The frequencies chosen in our machine are 93 Hz and 72 Hz.

The marker grids can be aligned to within 0.3% of their pitch by using phase-sensitive detection. Thus for a 0.1-μm alignment accuracy the marker grid must have a pitch of no more than 30 μm. However, the maximum misalignment that is expected on inserting the slice into its holder is of the order of 10 times this, so we use grid patterns containing both fine and coarse bars, the latter having a pitch of about 200 μm; see *fig. 5*. The coarse and fine patterns can be distinguished by the choice of the amplitude of the modulation current applied to the deflection coils: if the amplitude of the deflection is made equal to one pitch of the fine marker then the signal from the fine grid is reduced to zero and only the signal from the coarse grid is detected; if the modulation is restricted to less than half the pitch of the fine marker, the resulting signal is mainly due to the fine grid. A block diagram of the alignment system is shown in *fig. 6*.

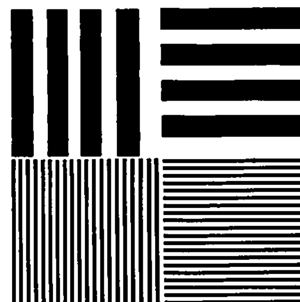

Fig. 5. Schematic diagram of part of one of the marker patterns for the automatic alignment. The full marker consists of 9 such patterns arranged in a square 6×6 mm. Two such patterns are etched in the mask and two are deposited as tantalum oxide on the silicon slice. Each pattern has coarse x and y grids (widths and spacings 200 μm) and fine x and y grids (widths and spacings 15 μm).

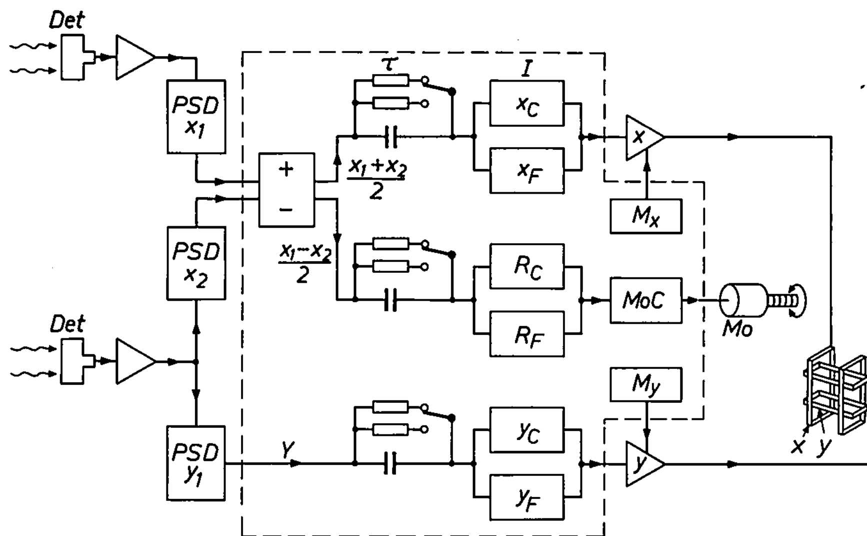

Fig. 6. Block diagram of the system for automatic alignment. The X-ray signals entering the detectors *Det* have been modulated by applying small alternating currents from the oscillators M_x and M_y to the x- and y-deflection coils (D_x, D_y, fig. 1) at frequencies which are different for the x- and the y-directions; the phase-sensitive detectors *PSD* can thereby separate out the x and y error signals. The mean value of the x signals from the two detectors gives the correction current for the x-direction; their difference gives the correction current for the rotation R. The y-correction current is derived from one detector only. The amplitude of the modulation applied to the deflection coils is first made such that the deflections of the image are exactly equal to the pitch of the fine grids (both x and y); in this way the signal due to the fine grid vanishes. After the coarse alignment, the amplitude is reduced to half the pitch of the fine grid or less: the signal is then substantially due to the fine grid. The networks marked τ represent the adjustable time constants, the networks marked x, R and y the gains of the circuits controlling the x displacement, the rotation and the y displacement respectively. The indices C and F refer to the coarse and fine controls.

Performance

Resolution and depth of focus

Extensive measurements have been made of the energy spectrum of the photoelectrons emitted from CsI when illuminated with the mercury line at 184.9 nm [8]. We have used these results as the basis for calculating the resolution and depth of focus which can be obtained by the electron-optical system. The results are illustrated in *fig. 7*, which shows the blurring of a line (the width between the points having 80% and 20% of the peak intensity) against position when working with a magnetic field of 1 kOe. The ultimate resolution is 0.01 μm, while 0.1 μm can be obtained over a depth of focus of about 100 μm. In fact the resolution achieved in the final pattern is somewhat less than that of the electron optics because of back-scattering of the electrons from the resist and substrate; see *fig. 8*. Experiments were performed to study the resolution achievable in a pattern under various conditions, and some results are shown in *fig. 9*. The best resolution obtained (0.25 μm) is essentially the same as that expected from electron scattering, indicating that the electrons to the substrate far away from the scattering point under the influence of the electric field. About 10% of the incident electrons are involved in this process and the extra background exposure given to the resist degrades the contrast. The effect can be serious if

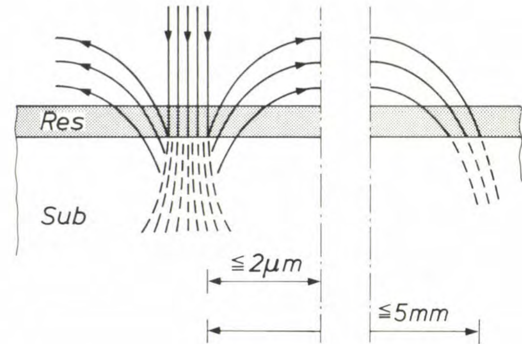

Fig. 8. Back-scattering of electrons in the resist *Res* and substrate *Sub* occurs in all electron-lithographic processes and limits the resolution obtainable. In the image projector the strong electric field also deflects the scattered electrons back to the substrate, up to 5 mm away from the scattering point. This affects the contrast and means that different exposures must be used for densely covered patterns, for which the back-scattered signal is highest.

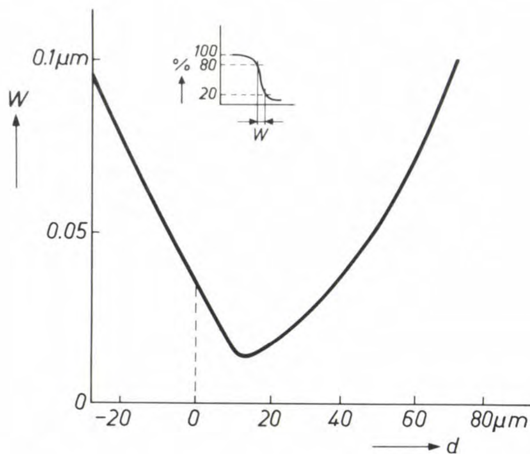

Fig. 7. The relation between the blurring W and depth of focus d in the electron image (calculated). The vertical axis shows the width W of an edge measured as the distance between points having 20% and 80% of the full exposure. In the range -25 μm $< d <$ 75 μm the resolution is better than 0.1 μm. The best resolution (approaching 0.01 μm) occurs slightly away from the nominal focus because of the finite energy of the electrons emitted from the photocathode. Scattering of electrons in the resist and substrate means that the high resolution of the electron image is not fully reproduced in the final pattern.

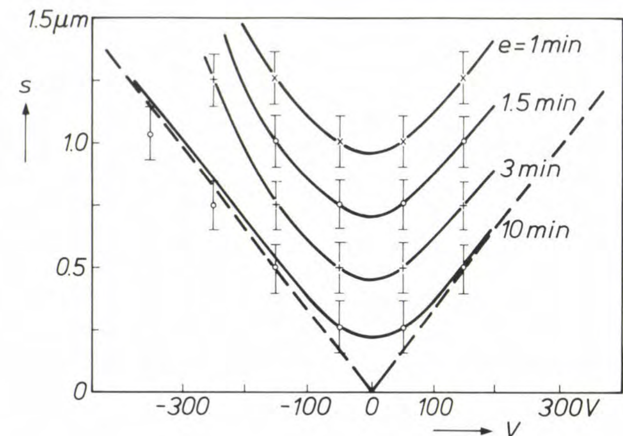

Fig. 9. Resolution s in the developed image as a function of the voltage between the pattern to be reproduced and the slice, for four values of the exposure e. The zero of the V-scale is chosen as the voltage that gives the best resolution. The dashed line represents the result of a calculation in which it is assumed that the resolution is determined entirely by the sharpness of the electron image and that the optimum exposure is made. The difference between the best experimental result and the calculated result is entirely due to electron scattering, which is the determining factor. In the most favourable conditions s is about 0.25 μm.

image resolution of the electron image is substantially better, in agreement with the calculation.

Back-scattering of electrons in the resist and substrate occurs in all electron-lithography processes. Fig. 8 also illustrates another problem which occurs only in image projectors: the return of back-scattered

more than half the mask is transparent, but this can be avoided by changing to a negative of the pattern and using a negative resist for the processing. Alternatively,

[8] H. R. Philipp and E. A. Taft, Phys. Chem. Solids 1, 159, 1956.
J. P. Scott, J. appl. Phys. 46, 661, 1975.

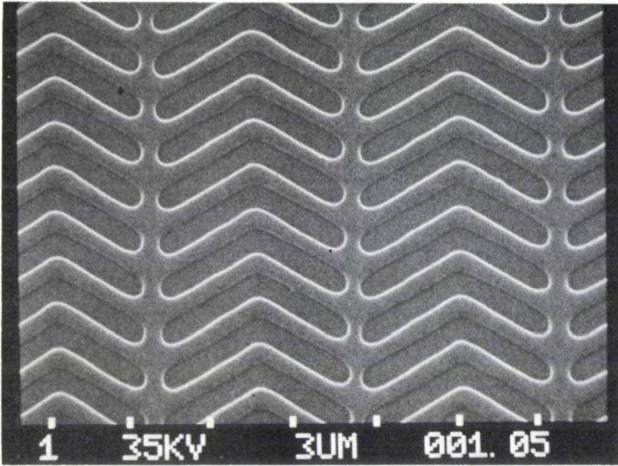

Fig. 10. Detail from an image in electron resist of a magnetic-bubble circuit made using the electron-image projector and illustrating the high resolution obtainable. The strips in the gaps are 1 μm wide.

Fig. 11. Experimental IC made using the electron-image projector. A number of 10-gate arrays can be seen in the photograph.

the problem can be overcome by using different exposures for lightly and densely covered patterns, though this is not always a convenient procedure for production purposes.

Image distortions

The success of any process for image transfer clearly depends on keeping the distortions to an acceptable level. For integrated-circuit manufacture distortions which are the same for all exposures are comparatively unimportant since they do not affect the relative positioning of the masks. In our machine the only significant reproducible distortions are those caused by the effect of the slice holder on the nearby electric field (the magnetic field is everywhere adequately uniform).

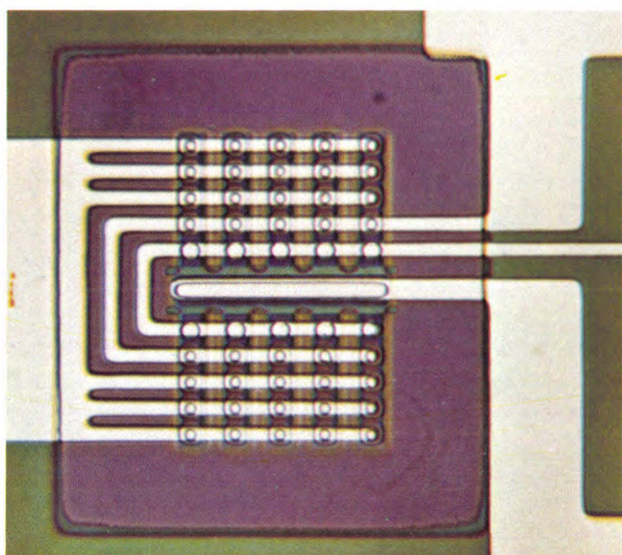

Fig. 12. One of the 10-gate arrays from fig. 11, but shown at greater magnification. The window dimensions are 2×2 μm and the aluminium conductors are 2.4 μm wide.

Irreproducible distortions, on the other hand, must be reduced to within the dimensional tolerance on adjacent components on the slice. The major irreproducible distortions arise from the charging up of the resist by absorbed electrons (which, however, can be kept within acceptable limits), and most important, the effects of bowing of the slice. The precision with which the pattern can be transferred is extremely sensitive to any departures from flatness of the slice because the slice forms the anode of the image projector; any change in its shape changes the electric field, giving corresponding shifts in the pattern. The lateral displacement in the pattern as a result of bowing is proportional to the mask-slice separation and is about 3% of the magnitude of the bowing for a mask-slice separation of 15 mm. The amount of bowing depends on the preparation of the slice but it can be as much as 30 μm in some cases; this implies lateral distortions of up to 1 μm. Distortions of this magnitude are quite unacceptable and it is therefore necessary to take active measures to reduce them.

In the electron-image projector the slice is exposed in vacuum: hence the normal method of holding down slices by a vacuum chuck cannot be used. A suitable alternative which we are now investigating is the electrostatic chuck [9]. This depends simply on the attraction of the silicon slice to a charged flat electrode separated from it by a thin insulator. In fact the same d.c. voltage used to expose the slice can also be used for the chuck; the silicon slice is thus held at +20 kV and the flat backing electrode is held at earth potential. In this way pressures of 0.2 to 0.4 bar are produced which are ample to hold the slice flat.

Experience with operating the machine

The electron-image projector described in this article has been operating in the experimental slice-processing unit at PRL for the last two years as part of a research programme aimed at developing processes for making integrated circuits with improved resolution and packing density [10]. All the masks used have been made on the electron-beam pattern generator [1].

The image projector has been used for approximately half its time for making masks of the marker arrays required by the pattern generator and half in developing a device-fabrication technology. Alignment accuracy has been found to be consistent within ± 0.1 μm in x and y; the rotational accuracy is also within ± 0.1 μm over the 1.9 mm separating the two marker areas. However, there can be distortions of up to 0.7 μm due to bowing of the slice; the electrostatic chuck should remove this. The resolution of patterns produced has been about 0.3 μm, a result dominated by the effects of electron back-scattering; the intrinsic resolution of the projector is considerably better. The machine has proved to be fast and convenient to operate. It uses short exposures and requires a total of 3 minutes for the full process including loading, pumping down, alignment and exposure and removal of the processed slice.

Figs. 10, 11 and *12* are photographs of patterns made with the machine. Fig. 10 is a pattern in electron resist for a very finely detailed magnetic-bubble

[9] The electrostatic chuck was first proposed by G. K. McGinty of PRL (British Patent 1443215), and independently by G. A. Wardly, Rev. sci. Instr. **44**, 1506, 1973.

[10] C. E. Fuller, D. J. Vinton and P. A. Gould, IEEE Trans. **ED**, in press.

circuit. Figs. 11 and 12 are experimental ICs made with the electron-image projector; they are examples of the manufacturing method developed at PRL and based on the electron-beam pattern generator and image projector.

The experience gained over the last two years is now being used in the design and construction of a new machine which will handle 100-mm slices and will incorporate an electrostatic chuck and several other improvements.

Summary. An electron-image projector is a machine for reproducing very fine patterns rapidly and at high resolution. Electrons are emitted from a photocathode material coating the mask and are accelerated and focused on the substrate by highly uniform electric and magnetic fields. This exposes an electron-sensitive resist coating the substrate and so reproduces the pattern at unity magnification. The PRL projector includes a number of new features which have made the method more generally applicable for the production of integrated circuits than hitherto. These include the use of caesium iodide as the photoemitter material, a new design for the magnet and a method of automatic alignment using Bremsstrahlung X-rays, including improvements to the signal detection and processing. The machine has been in use for two years and achieves an alignment accuracy of 0.1 μm and a resolution (limited by back-scattering of electrons in the substrate) of 0.3 μm. The complete cycle of loading, pumping down, alignment, exposure and removal of the processed slice takes about 3 minutes.